Transactions of the ASME®

FLUIDS ENGINEERING DIVISION
Technical Editor
DEMETRI P. TELIONIS (1999)
Executive Secretary
PAT WHITE (1999)
Assistant to the Editor
N. W. SCHAEFFLER
Calendar Editor
M. F. ACKERSON

Associate Technical Editors
S. BANERJEE (1999)
P. W. BEARMAN (2001)
P. BRADSHAW (2000)
M. N. DHAUBHADEL (1999)
J. K. EATON (1999)
G. ERLEBACHER (2000)
U. GHIA (2001)
M. HAJJ (2001)
J. KATZ (2001)
C. L. MERKLE (2000)
P. RAAD (2001)
B. SCHIAVELLO (1999)
M. SOMMERFELD (1999)
F. K. WASDEN (2000)
D. R. WILLIAMS (2000)
K. ZAMAN (2001)

BOARD ON COMMUNICATIONS
Chairman and Vice-President
R. K. SHAH

OFFICERS OF THE ASME
President, W. M. PHILLIPS
Exec. Director
D. L. BELDEN
Treasurer
J. A. MASON

PUBLISHING STAFF
Managing Director, Engineering
CHARLES W. BEARDSLEY
Director, Technical Publishing
PHILIP DI VIETRO
Managing Editor, Technical Publishing
CYNTHIA B. CLARK
Managing Editor, Transactions
CORNELIA MONAHAN
Production Assistant
MARISOL ANDINO

Transactions of the ASME, Journal of Fluids Engineering (ISSN 0098-2202) is published quarterly (Mar., June, Sept., Dec.) for $205.00 per year by The American Society of Mechanical Engineers, Three Park Avenue, New York, NY 10016. Periodicals postage paid at New York, NY and additional mailing offices.
POSTMASTER: Send address changes to Transactions of the ASME, Journal of Fluids Engineering, c/o THE AMERICAN SOCIETY OF MECHANICAL ENGINEERS, 22 Law Drive, Box 2300, Fairfield, NJ 07007-2300.
CHANGES OF ADDRESS must be received at Society headquarters seven weeks before they are to be effective. Please send old label and new address.
PRICES: To members, $40.00, annually: to nonmembers, $205.00. Add $40.00 for postage to countries outside the United States and Canada.
STATEMENT from By-Laws. The Society shall not be responsible for statements or opinions advanced in papers or . . . printed in its publications (B7.1, Par. 3).

INDEXED by Applied Mechanics Reviews and Engineering Information, Inc. Canadian Goods & Services Tax Registration #126148048.

Journal of Fluids Engineering

Published Quarterly by The American Society of Mechanical Engineers

VOLUME 121 • NUMBER 2 • JUNE 1999

(Contents continued on p. 253)

This journal is printed on acid-free paper, which exceeds the ANSI Z39.48-1992 specification for permanence of paper and library materials. ♾™
♻ 85% recycled content, including 10% post-consumer fibers.

(Contents continued)

(Contents continued on p. 258)

(Contents continued)

Announcements and Special Notices

Journal of Fluids Engineering

Editorial

Pump Research and Development Review

The 1997 Summer Meeting of the Fluids Engineering Division was the venue for the 3rd International Pumping Machinery Symposium. This symposium brings together engineers and researchers working mainly in the area of rotodynamic pumps every four years. Most workers in the field have experienced the challenges of new trends that are refocusing their efforts. These trends were addressed by invited speakers from the three major areas of the world that are involved heavily in the pump industry and the R&D that supports it, namely Japan, Europe, and the United States. Each addressed the topic, "Pump Research and Development—Past, Present, and Future." Each has a different perspective, which when taken together with the others forms an integrated whole that can benefit all who are associated with the pump industry. These three contributions were submitted to the *Journal of Fluids Engineering,* reviewed and now appear in the first few pages of this issue.

All three of these authors agree that the emphasis has changed from concentration simply on maximizing the performance and related design features to addressing how reliability, low maintenance and long life can be achieved at the same time. The commitment to technological improvements remains but in the context of these customer-oriented drivers.

Ohashi and Tsujimoto, in presenting the Japanese perspective, focus on three major socio-industrial stages that have occurred since 1955; namely expansion, conversion to a broader product emphasis, and globalization. These have steered pump R&D into the new direction mentioned. Impressive statistics are presented to illustrate this development. Hergt, by giving examples of three types of pumping machinery, illustrates how this change in direction is occurring in Europe. In addition to economies obtained for small pumps through better efficiency, he sees large pump technology leading to even larger machines. Gopalakrishnan sees the same shift in emphasis and insists that the basic given assumed by all customers is guaranteed and improved performance. He illustrates how this has been and can be done in the future through an in-depth review of the three technical areas of hydraulics, vibrations, and innovations in pump design.

These three contributions afford valuable insights for pump engineers, showing how future R&D efforts can be best attuned to recent developments vis-à-vis the environment, the changing economic landscape, and the new demands of present and future pump users and applications.

Paul Cooper
Ingersoll-Dresser Pump Company,
942 Memorial Parkway,
Phillipsburg, NJ 08865

A TRIBUTE TO HOWARD WILSON EMMONS
1912–1998

> One of the seven wonders of the world. A human slide rule.—Einstein's rival! Our eminent mathematician. He has made a name for himself in M.H.S. and will become famous some day. Look us up then, and tell us to what you attribute your success.

It is perhaps unfair to quote his Morristown, N.J. high school yearbook, but it clearly foreshadowed that Howard Emmons would accomplish a great deal in the following years. He graduated from Stevens Institute with a B.S. in Mechanical Engineering in 1933 and an M.S. in 1935, and then went on to Harvard, where he received a D.Sc. in 1938. Two years with Westinghouse, working on steam turbines and a year as associate professor at the University of Pennsylvania preceded his return to Harvard, which became the base for his professional life up to his death in November 1998, at age 86.

As it turned out, Howard Emmons significantly influenced several fields, most of them connected in one way or another with fluid mechanics and thermal phenomena, starting with his doctorate studies on drop condensation.

Numerical solution of fluid flows and heat conduction, including problems in shock waves and compressible boundary layers immediately followed, described in several publications beginning in 1941. He advised N.A.C.A. on the design of its first supersonic wind tunnel. It seems that at this time he developed the relaxation technique, apparently independently of Southwell. This extended into the numerical study of transition to turbulence in the mid-1940s.

This problem of transition to turbulence intrigued him, and in that context he is recognized as the first to describe the phenomenon known as the Emmons, or turbulent, spot. His detection of the "spot" was illustrative of the simplicity of some of his experiments. A thin layer of water flowed down a slightly inclined glass plate several feet in length and width, to be viewed or photographed either from above or below. At some Reynolds number, the clear laminar sheet would develop visibly rough patches that drifted and grew slowly downstream, a landmark observation leading to the recognition of the development and significance of large scale structures in turbulence.

But much of his research involved complex apparatus, major financial support, and a multi-person research team. For example, the studies of gas turbine compressor stall, supported by Pratt and Whitney, involved many Ph.D students, and led to the discovery of compressor stall, a major gas turbine problem, and evolution of hot wires concepts and applications.

It was interest in plasmas and fires that came to be his principal concern for forty years, and led to his being internationally recognized as "Mr. Fire Research," the initiator of scientific fire study, and the most significant contributor to that complex, and societally important subject. He argued before Congress for a Fire Research and Safety Act, which was adopted in 1968.

One in particular of the many experimental studies he and his colleagues devised will never be forgotten by any who witnessed the "fire whirl." A small cup of burning acetone with a flame a few inches high is at the bottom center of a wire cage seven feet in diameter rotating slowly a few times a minute. The flame with a roaring sound suddenly jumps to ten feet high, a spectacular demonstration of sudden transition in fuel/air mixing and radiant evaporation of fuel.

Paul Fitzgerald recalls the story of Howard's first association with Factory Mutual, Fitzgerald's insurance firm, back about 1960:

> Howard walked into a meeting of the Factory Mutual Joint Affair Committee, an executive board consisting of seven insurance company CEOs and the General Manager of Factory Mutual, and told them that they should invest in fundamental fire research—something none of their competitors were spending a dime on at that time. Not many people, let alone an engineering professor, were likely to have swayed that group. But Howard persuaded them to think "out of the box" and convinced them of its value. And fortunately, they accepted his recommendation. Howard went on to become the Scientific Advisor to our basic research program.

Complex investigations followed, such as studies of fire propagation under various circumstances of ignition and propagation of fires in buildings. These led to revisions of flammability rating techniques for combustible materials, development of new sprinkler concepts, and ultimately the development of the "Harvard Computer Fire Code," which predicts the growth of fire in buildings and remains a useful tool today.

Professor Emmons's involvement in engineering and scientific organizations was extensive. He was a member of both the National Academy of Sciences and the National Academy of Engineering. He served on many committees and panels within the Government, and was extensively involved in the American Physical Society, the Combustion Institute, and The American Society of Mechanical Engineers. Within ASME he was:

Chairman, Applied Mechanics Division, 1943
Chairman, Fluids Engr., 1960
Chairman, Policy Board, Basic Engr., 1967–70
Chairman, Com. on Tech. Affairs, 1967–70
Vice President, Exec. Com. of Council, 1967–70
Recipient of the Timoshenko Medal, 1971
Made Honorary Member, 1978, ASME's highest honor

Professor Emmons's legacy to society goes beyond his teaching and research, and the 51 Ph.D.s of whom many went on to distinguished careers in engineering and science. He was a member of advisory committees established by the Mayor of Boston and the Governor of Massachusetts. He was a selectman for his home town, Sudbury, and a very constructive Chairman of the Lincoln-Sudbury School Committee for twenty years.

Paul Croce, Vice President and Manager of Research for Liberty Mutual, with which Professor Emmons coordinated much of his fire research, notes most aptly:

> He looked at the world as a place where he could solve problems and make it a better place, whether through science, education, government service or everyday life, never stopping, always looking onward to the next challenge, the next problem he could solve and always reaching beyond what others thought to be the limit.

Richard I. Land
Lloyd M. Trefethen

Photograph by Clay Allen

Howard Wilson Emmons

Journal of Fluids Engineering

Industry Perspectives

Steady and Unsteady Computations of Turbulent Flows Induced by a 4/45 Degree Pitched-Blade Impeller[1]

Marcus W. A. Hoefken.[2] The authors are the first to present an extensive study on the influence of the calculation method, namely steady versus unsteady computations, on the accuracy of the computational results for a Pitched-Blade Turbine (PBT) in turbulent operation. They validated their results with experimental data published by Schaefer et al. (1998), which are known to be the most complete and accurate data base for the validation of CFD-simulations on PBTs to date. All computational results were in excellent agreement with the experimental data. Even the turbulent predictions, which normally represent a major problem, showed no significant deviations. For this reason, the work presented in this paper is of great value to industry, because up to now properly verified and thoroughly validated computational fluid dynamic codes and processes were very rare. Now, one can use this validated code for optimizations of the impeller/reactor configuration by changing the location of the impeller, the number of baffles etc. and still achieve results of excellent accuracy.

In many of the earlier papers (see text) the influence of the impeller was represented by boundary conditions around the impeller derived from experimental data, neglecting the most important region of the reactor, which is the region in and around the impeller. Such computations cannot be used for any kind of optimizations of the impeller, since the geometry of the impeller is not represented properly. In the computations of the present paper, a clicking grid method was used to accurately simulate the momentum caused by the impeller rotation. Due to the clicking grid method and the reliability of the results, the authors offer for the first time a code which could be used for the optimizations of impeller geometries. This is of great importance to industry since it could help to optimize not only impellers but also reactor designs and chemical processes.

The authors have shown that steady computations satisfy accuracy requirements, thus reducing the computational time and the parallelization of the code allows for the use of clusters of standard PCs as well as supercomputers for such computations. It can be envisaged that such methods will find their way into industry within the next few years and will become a very useful tool for the layout and design of chemical reactors.

[1] By K. Wechsler, M. Breuer, and F. Durst, published in this issue pp. 318–329.

[2] Managing Director, INVENT Umwelt-Und Verfahrenstechnik GmbH&Co. KG, Am Weichselgarten 36, D-91058, Germany.

Predictable Model for Characteristics of One-Dimensional Solid-Gas-Liquid Three-Phase Mixtures Flow Along a Vertical Pipeline with an Abrupt Enlargement in Diameter[1]

Kouji Takatani.[2] The authors analyzed the flow characteristics of solid-gas-liquid three-phase mixtures flowing upward in a vertical pipe with a sudden expansion in diameter. In order to do so, they modified the numerical procedure of their own theoretical model (Hatta et al., 1998) capable of predicting multi-phase flow field in steady-state. They built up the system of governing equations based on a quasi-one-dimensional multi-fluid model, taking into account the transitions of gas flow pattern, interaction between different phases and external forces. Therefore, their model is theoretically rigorous compared with another model based on the simple momentum conservation law (Yoshinaga et al., 1996). The predictions obtained by the present model agree reasonably well with experimental data. Accordingly, the present model is suitable to predict the performance of an air-lift pump system for conveying solid particles.

The authors represented numerically, as well as experimentally, that an abrupt expansion of pipe diameter contributes an improvement of pump-efficiency. The reduction of volumetric fraction for gas-phase is effective to control the gas flow pattern due to the abrupt expansion of pipe. This finding is very practical for designing a high-performance air-lift pump system in particular, a very large-scale air-lift system.

The authors also provide fundamental information concerning the motion of solid particles in a vertical pipe from a photographic viewpoint. The moving processes of solid particles in gas-slug as well as liquid were shown under several flow conditions by means of high-speed video camera. Their experimental data are very useful to physically understand the flow field of three-phase mixtures.

References

Hatta, N., Fujimoto, H., Isobe, M., and Kang, J. S., 1998, "Theoretical Analysis of Flow Characteristics of Multiphase Mixtures in a Vertical Pipe," *International Journal of Multiphase Flow,* Vol. 24, pp. 539–561.

Yoshinaga, T., and Sato, Y., 1996, "Performance of an Air-Lift Pump for Conveying Coarse Particles," *International Journal of Multiphase Flow,* Vol. 22, pp. 223–238.

[1] By N. Hatta, M. Omodaka, F. Nakajima, T. Takatsu, H. Fujimoto, and H. Takuda, published in this issue pp. 330–342.

[2] Deputy Chief, Department of Fundamental Technology, Corporate Research and Development Laboratories, Sumitomo Metal Industries, Ltd., 16-1 Sunayama, Hasaki-machi, Kashima-gun, Ibaraki-ken 314-0255, Japan.

Pump Research and Development: Past, Present, and Future—An American Perspective

S. Gopalakrishnan
Flowserve Corporation,
Vernon, CA 90058
e-mail: sgopalakrishnan@flowserve.com

Pump research and development efforts are primarily driven by the needs of the customer. Today, these needs are centered around cost and reliability issues with the understanding that certain threshold levels of performance are achieved. As centrifugal pumps have reached high levels of maturity in most industrial applications, we can anticipate, that in the future, customer expectations will change subtly but significantly. They will demand continuously reducing costs with the understanding that reliability and technology needs will be satisfied. This would lead to a strong emphasis on consistent predictability of performance in the field and to less of a focus on innovations in design. R&D efforts in the past were intended to stretch the envelope to produce better hydraulic performance, to improve mean-time-between-failures, and to operate at higher speeds. In contrast, R&D efforts in the future would be aimed towards cost reduction, accurate hydraulic guarantees, and flawless performance in the field. In this paper, the R&D efforts of the past, present, and future are discussed in terms of three core competencies, which are essential for today's pump manufacturer. These are hydraulics (with an emphasis on improving predictability of performance and improving impeller life), vibrations (with a view to providing cost effective problem solving/avoidance capability), and pump designs which capitalize on improved understanding of the underlying technologies.

Introduction

Significant advances are being steadily made in the understanding of key technical phenomena relating to centrifugal pumps. These advances are in those disciplines which constitute the core competencies that are required to be in the business of offering pumps to the users in power, petroleum, water supply or similar industries. In this paper, these advances are viewed from the perspective of a pump manufacturer supplying to a world-wide customer base. Although the business is rapidly becoming global, the author's experience is primarily with American customers and hence the paper probably represents an American perspective. Today, the primary requirements of the end-user, at least in the industries mentioned earlier, relate to cost and reliability. This is not to imply that the technical performance is of low priority, but only that a certain level of technical performance has to be met before a pump can be treated as an acceptable offering. Once this minimum hurdle is met, issues of cost and reliability become the judging factors in the final choice. Thus, in this paper, only those R&D efforts which are deemed to contribute to the key customer issues of cost and reliability are discussed. In the author's opinion, these issues can be broadly divided into three categories—hydraulics (including cavitation), vibrations, and pump design. These three categories are discussed in terms of past R&D efforts, the state-of-the-technology today, and the author's opinion of what is likely in the near future.

Hydraulics

No other field of pump technology has shown more dramatic advances than pump hydraulics. State-of-the-art calculation techniques of ten years ago appear archaic today. While obsolescence at this pace is not at all uncommon in certain fields, e.g. electronic communications, progress in pump technology has been slow in general. However, in hydraulics, calculation capabilities have increased dramatically primarily because of inexpensive access to high speed computers with tremendous number-crunching capability. Today, it is possible to predict the complete head-flow curve of a pump given the full geometric information of the impeller and the stationary diffusing passage.

Figure 1 shows the results of an early attempt at this prediction (Gopalakrishnan, 1981). In this method, the basic flow field in the impeller is calculated using a meridional plane method developed at NASA (Katsanis, 1964). A quasi-orthogonal net is made to cover the meridional plane, and the flow equation is solved along the quasi-orthogonal. Since no viscous terms were included, the resulting solution exhibits no losses. In order to predict the actual head developed for any given flow, assumptions have to be made not only for the losses but also for the slip that occurs in the flow of a fluid that has viscosity. The slip factor and losses were calculated using empirical coefficients. These coefficients were deduced through elaborate back calculations from known test data for a class of vertical pumps.

In contrast to this work, what can be done today is truly a significant leap. Very accurate predictions of flow field within an impeller are now possible for a wide range of geometries and specific speeds. Gopalakrishnan, et al, (1995) contains a description of the prediction capability for a high specific speed mixed flow impeller. The numerical flow field calculation of the mixed flow impeller was performed by using a commercially available Computational Fluid Dynamics (CFD) code known as TASCflow. TASCflow solves the Reynolds Stress Averaged Navier-Stokes equations, and is applicable to incompressible and compressible (subsonic, transonic, and supersonic) flows. The effects of turbulence are modeled by the standard k-ε turbulence model, and log-law wall functions are used to simulate the

Contributed by the Fluids Engineering Division for publication in the JOURNAL OF FLUIDS ENGINEERING. Manuscript received by the Fluids Engineering Division September 8, 1998; revised manuscript received December 21, 1998. Guest Editor: P. Cooper.

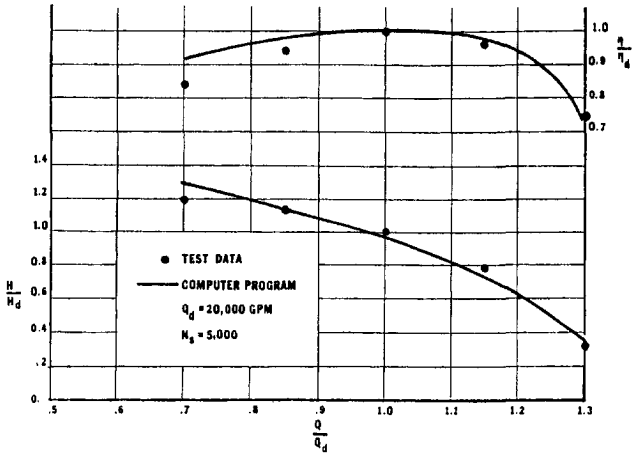

Fig. 1 Comparison between measured and calculated performance of a mixed flow pump (from Gopalakrishnan, 1981)

boundary layers. The code is a general-purpose CFD program, however, it is especially well adapted for calculation of rotating machinery flows for its inclusion of the Coriolis acceleration terms and added schemes to better cope with convergence problems that could arise from large grid aspect ratios (at the leading edge of the blade and high-curvature surfaces). It utilizes non-orthogonal, boundary fitted, structural grid, and has several features such as multi-blocking and grid-embedding to further enhance modeling complex features. The code employs an element-based finite volume method, and is a pressure based (as opposed to density based, time marching) code. The computational domain used for generating the results contained 116,000 nodes.

Figure 2 shows the comparison between prediction and measurement at the trailing edge. Since the measuring instrument used was a fixed traversing probe, what the probe measured was a circumferential average of the velocity field. The CFD calculations at each radial location was mass averaged for comparison purposes. It can be seen that the agreement is very good indeed for a wide range of flow from 53 to 120 percent of best efficiency point (BEP) flow. This comparison shows that it is no longer necessary to use a slip factor correlation or even to specifically invoke a Kutta condition to define vane circulation. Figure 3 shows the meridional velocity and relative flow angle comparison showing once again a very satisfactory correlation.

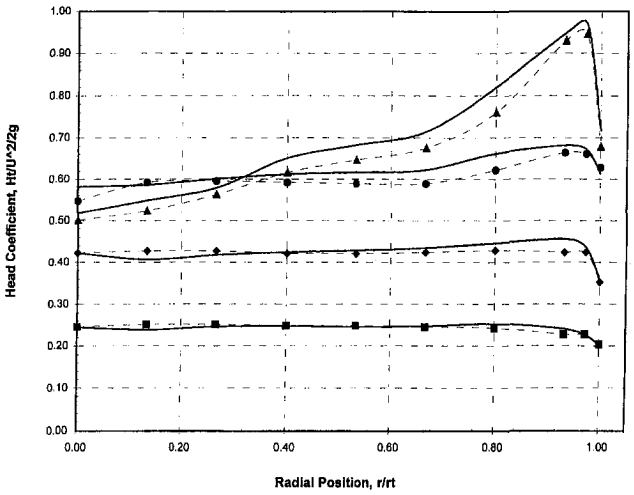

Fig. 2 Comparison between measured and calculated impeller discharge head coefficient—CFD calculations; ▲ 53 percent Q_{BEP}; ● 74 percent; ♦ 100 percent; ■ 120 percent (from Gopalakrishnan et al., 1995)

It must be pointed out that the quality of predictions shown in Figs. 2 and 3 can be achieved without having to use a full 3D viscous code. Graf (1993) shows that quasi-3D non-viscous calculations can provide enough accuracy to be useful at the design stage.

The key advantage of CFD is that it holds the promise for predicting the *H-Q* curve and efficiency without using empirically derived coefficients. While there is nothing wrong with using empirical coefficients from a pump designer's point of view, it must be remembered that progress to improved designs is not possible if the technology is based on past practice. Goto (1997) contains a comparison between calculation and measurement for the *H-Q* and efficiency of a mixed flow impeller stage. The authors used a Baldwin-Lomax turbulence model in the stage version of Dawes CFD Code. To make comparisons possible for the measured pump head and flow downstream of the diffuser, certain losses had to be calculated separately. These included leakage, disk friction, and mechanical losses. As shown in Fig. 4, the trend for power is very well predicted. The performance at design point is somewhat over predicted. Results at high flows show high deviations between calculations and measurements.

The results of Gopalakrishnan et al. (1995) and Goto (1997) are for individual pumps and there is a concern whether the CFD analysis would provide good results for a range of pump specific speeds. Gülich and Favre (1997) contains a thorough analysis of the validity of CFD technique. Thirty impellers ranging in specific speed from 12 to 160 metric (620 to 8000 in U.S. units) were analyzed and tested for head and efficiency. The analysis was conducted using a commercially available CFD code using a standard k-ε model. The authors found that the theoretical head could be predicted with a standard deviation of ± 2.5 percent. The evaluation of losses need further improvement and should include the effect of impeller outlet flow distribution on volute or diffuser performance.

The ability to analyze the flow field inside pump stages using CFD has led to advanced pump designs. In Valenti (1996), examples are cited where vendors have improved pump efficiency (by as much as 5 to 10 points), improved impeller life (from six months to four years or more), reduced noise, and developed monotonic *H-Q* curves even at high specific speed. CFD capability has also speeded up the design process as it reduces the number of time-consuming model tests that are sometimes required.

While CFD holds promise of becoming a useful tool for pump design, it must be noted that a major unknown in fluid dynamics today is a realistic model for turbulence. This may take years of fundamental work. It appears that for the foreseeable future, pump designers will use some of the existing turbulence models and calibrate their CFD results against test data thereby introducing some empiricism into their analysis. This will remain necessary as in the pump business, the penalty for failure to meet performance guarantees is severe indeed.

Another future need is more user friendly mesh generation software that can use the designer's CAD files directly. Much progress is being made in this direction, and it is reasonable to forecast that the cycle time for a CFD analysis on a new design can be reduced from the present seven days to about a day or two.

Another area in hydraulics where significant progress has been made is in cavitation. The key practical requirement in this area is to determine the NPSH required under any given flow and speed conditions to prevent cavitation damage and vibration consequences. Early attempts have been almost entirely empirical. Recognizing that the damage rate is proportional to some exponent of the bubble length, correlations were developed with this as a key parameter. The EPRI sponsored work in boiler feed pumps led to important publications in this field (Gülich, 1989). While it was recognized that damage rate was affected by a number of factors including details of vane

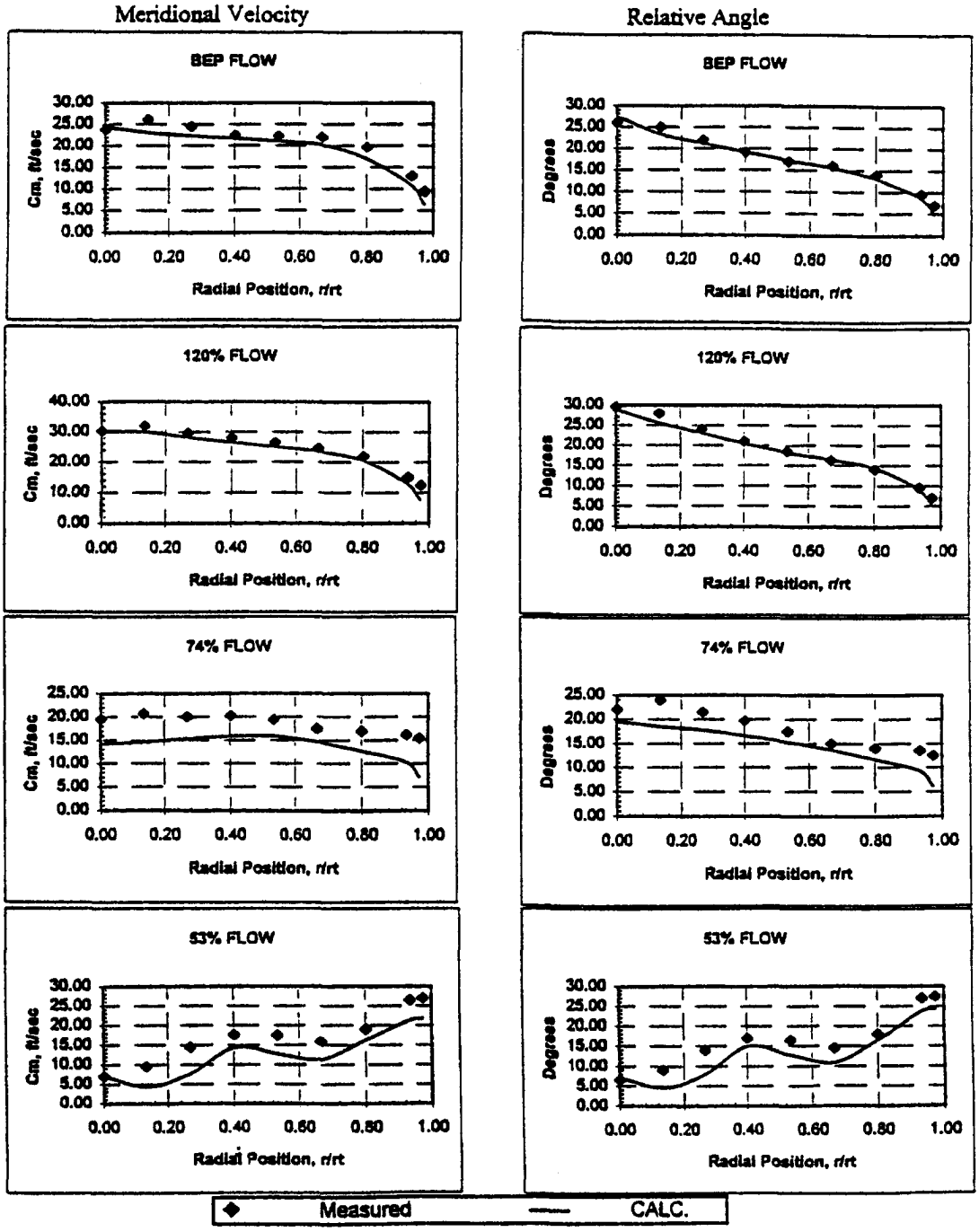

Fig. 3 Comparison between measured and calculated impeller discharge velocity parameters (from Gopalakrishnan et al., 1995)

geometry, it was found that a usable correlation could be deduced with cavitation bubble length as the primary independent variable. This correlation is of the form

$$\frac{dE}{dt} \propto L^{2.83} \tag{1}$$

Here dE/dt is erosion rate and L is cavity bubble length. Although, it may be risky to project a useful impeller life on an absolute basis from this correlation, it is very reasonable to project a change in impeller life when the geometry is changed to yield a different bubble length, all other factors remaining the same. An example of this approach may be found in Ferman et al. (1997). Here the first stage of a large two stage boiler feed pump was suffering cavitation damage in an unacceptably short time of about 10,000 hours. It was required to increase the life to about 80,000 hours. This meant that with the 2.83 exponent, the bubble length had to be reduced by a factor of 2.0. Ferman et al. (1997) describes the methodology and verification used to generate the new impeller.

Continuing improvements in understanding of cavitation phenomena have led to practical benefits. On the one hand, pump vendors are able to better specify the NPSH characteristics of their pumps both in terms of the NPSH required and in terms of the acceptable operating range. On the other hand, pump vendors are better able to design the impellers to provide acceptable cavitation characteristics. Both of these enhancements are described below.

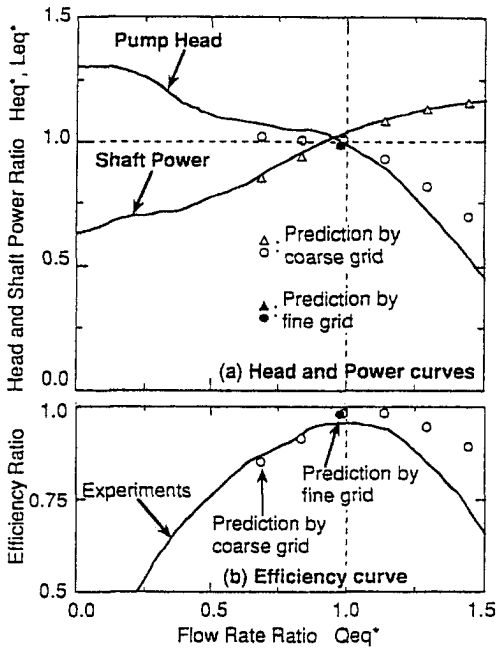

Fig. 4 Comparison between measured and calculated pump performance (from Goto, 1997)

To calculate the required NPSH to avoid damage, a method using the findings of Gopalakrishnan (1993) start with a ratio $R_{d\cdot f}$ defined as:

$$R_{d\cdot f} = \frac{\tau_{d\cdot f} - \tau_{3\%}}{\tau_i - \tau_{3\%}} \tag{2}$$

where τ is NPSH nondimensionalized through dividing by $U_e^2/2g$ with U_e being eye velocity of the impeller and g the acceleration due to gravity. The subscripts $d\cdot f$ refers to damage-free condition, i the inception and 3 percent, the condition at which pump head has decreased by 3 percent due to cavitation. It is shown in Gopalakrishnan (1993) that after representing bubble length as a function of R_A where

$$R_A = \frac{\tau_A - \tau_{3\%}}{\tau_i - \tau_{3\%}} \tag{3}$$

with subscript A representing available conditions,

$$R_{d\cdot f} \propto U_e^b \tag{4}$$

with exponent b being approximately 2.0. In order to use this expression for predicting damage-free NPSH, it is necessary to establish $\tau_{3\%}$ and τ_i for a given impeller. The latter can be calculated from a potential flow analysis with the assumption of thermodynamic equilibrium i.e. bubbles form as soon as local pressure reaches vapor pressure corresponding to the upstream temperature. This analysis can be made with very simple computer programs. In Gopalakrishnan (1985), a two-dimensional method based on solving a set of singularity equations provided good agreement with test data for inception as shown in Fig. 5. The value for $\tau_{3\%}$ is best obtained from NPSH tests on the pump. Thus it is possible to estimate NPSH required to avoid damage for given eye geometry and operating conditions.

Table 1

Feature	Benefit
a) Elliptical noses on blades	Local pressure-drop spike minimized
b) Blade camber angle matched to analyzed flow	Cavity reduced or eliminated at BEP
c) Biased-Wedge blade thickness development	Widens range of cavity-free flow rate
d) Biased-Wedge blade designed to avoid increase of NPSHR due to loss of effective area between blades	Maintains NPSHR of conventional impeller designs
e) Concave blade leading edge, blended forward into hub	Removes hub-fillet cavitation and damage

The second aspect of the improved understanding of cavitation is the development of cavitation avoidance features. Sloteman et al. (1991) contains a detailed analysis of this phenomenon and Table 1 reproduced from this reference summarizes the geometrical features that reduce cavitation activity.

A representative blade design containing these features is shown in Fig. 6. It can be seen that blading that would result in improved cavitation characteristics call for a more demanding and precise design approach than has been utilized in the past.

Determination of cavitation bubble length today requires a flow visualization testing capability. Such testing is generally very expensive and therefore, the need for a good calculation technique is strong. A very promising attempt in this direction is shown in Hirschi et al. (1997). In this method, the single phase flow is first computed by assuming a free surface boundary which confines the cavitation activity. The free surface is then iteratively altered to maintain a constant relative pressure. Figure 7 shows a typical result for the shroud streamline of a centrifugal pump impeller. The flattening of the C_p curve on the suction surface from the leading edge shows the extent of the cavitation bubble. Figure 8 shows the comparison between

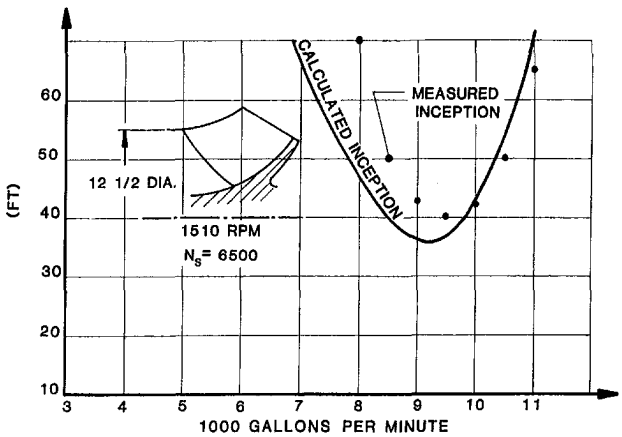

Fig. 5 Cavitation inception prediction (from Gopalakrishnan, 1985)

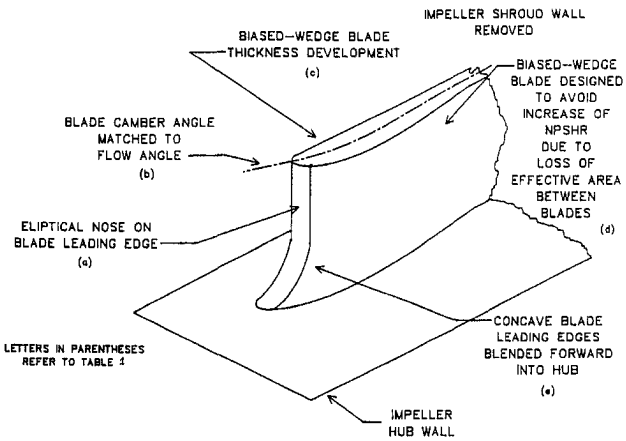

Fig. 6 Cavitation avoidance features (from Sloteman et al., 1991)

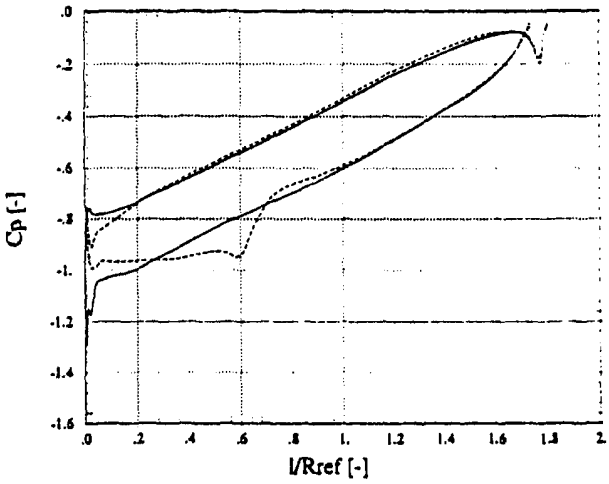

Fig. 7 Effect of cavitation on surface pressure distribution; —— without cavitation; --- with cavitation (from Hirschi et al., 1997)

calculated and measured bubble length at design point for several suction pressures. The overall agreement is excellent.

It is not believed that in the near future it would be possible to calculate damage rate from first principles. Bubble length calculation capability will certainly improve and combined with approaches as in Gülich (1989), Gopalakrishnan (1993), and Sloteman et al. (1991) confident predictions will be made of impeller life and advanced designs with reduced susceptibility to cavitation will emerge.

Vibrations

One of the key symptoms which accompany a potentially drastic reduction in pump life is excessive vibrations. In general, the measured vibrations on a pump arise as a consequence of operation close to a resonance or of the presence of high exciting forces. In this section, we will deal with these two issues from the perspective of recent advances that have the potential to improve pump reliability.

Resonance. Resonance related problems can occur if the operating speed and some of its harmonics (particularly the vane passing) coincide with the natural frequency of a stationary part (e.g., bearing housing) or coincide with that of the rotating system. The former occurs much more frequently in practical

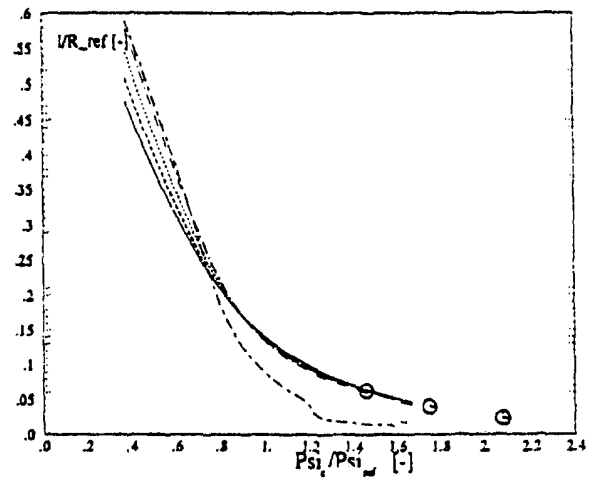

Fig. 8 Calculation of cavitation bubble length —— hub; --- shroud; ⊙ measurements (from Hirschi et al., 1997)

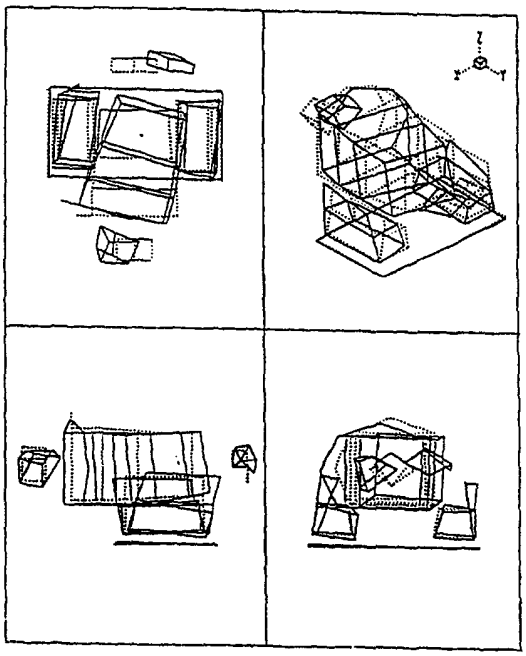

Fig. 9 Measured structural mode shape of a high energy feed pump (from Gopalakrishnan, 1996)

installations, and fortunately very good techniques are now available to resolve such problems. A key tool in this arsenal is experimental modal analysis to directly measure the natural frequency of the stationary component at the pump installation. In this analysis, the pump structure is excited at one or more locations (generally in three mutually perpendicular directions), and the response is measured at many locations. The excitation and measurement locations are input into modal analysis software which constructs a wire frame model. Then the normalized response at one location due to one excitation is plotted as a function of frequency, generating the so-called frequency response function (FRF). In a typical case, 200 to 300 FRFs may be generated. These are curve fitted and solutions are developed for eigen values, mode shapes and damping ratios. The results can thus be exhibited as an animation of the structure at each eigen value. Figure 9 taken from Gopalakrishnan (1996) shows the displaced shape of the wire frame at one instant of time during the animation. The animation clearly shows the structure that is resonant and the analyst can come up with modifications to the structure to move the resonance to a safe frequency.

Structural resonance calculations can also be effectively made with commercially available finite element analysis programs. However, certain assumptions regarding bolt and foundation stiffnesses have to be made. Thus direct calculations do not always give accurate results for a given installation. At this time, it is safer to "calibrate" the analysis for the baseline installation and compute the change in frequency due to a proposed structural modification.

Another type of resonance that can occur in pumps and pumping systems is when the natural frequency for the formation of a standing acoustic wave in a pipe coincides with an exciting force frequency. This typically occurs at vane passing frequencies and can generate pressure pulsations strong enough to break small bore piping and cause high structural vibrations leading to premature bearing and seal failure. It is possible to calculate standing wave natural frequencies by using finite element modeling. Figure 10 shows the results of such a calculation for a large two stage reactor feed pump, when the internal cross-over piping from the first to the second stage acoustically resonated with the vane passing force.

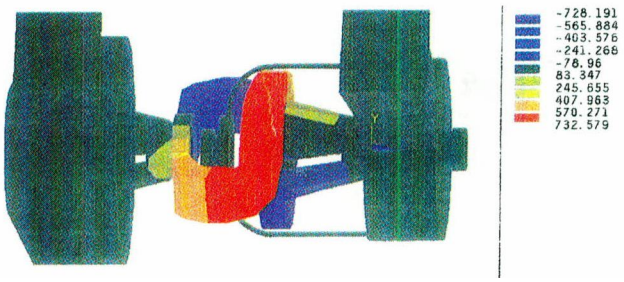

Fig. 10 Pressure plot at acoustic resonance in the long cross-over of a two-stage reactor feed pump

Although, as mentioned before, rotor critical speeds are problems only infrequently, much research has been done in this area. In the early 80s, it was understood that pump rotor dynamics is fundamentally affected by the presence of liquid in the close clearance running fits of the rotating element in the stationary casing. The general rotor dynamic equation for a two degree of freedom system is:

$$\begin{bmatrix} F_x \\ F_y \end{bmatrix} = \begin{bmatrix} k_{xx} & k_{xy} \\ k_{yx} & k_{yy} \end{bmatrix} \begin{bmatrix} x \\ y \end{bmatrix} + \begin{bmatrix} C_{xx} & C_{xy} \\ C_{yx} & C_{yy} \end{bmatrix} \begin{bmatrix} \dot{x} \\ \dot{y} \end{bmatrix} + \begin{bmatrix} M_{xx} & M_{xy} \\ M_{yx} & M_{yy} \end{bmatrix} \begin{bmatrix} \ddot{x} \\ \ddot{y} \end{bmatrix} \quad (5)$$

where

F is the applied force,
k is the dynamic stiffness
C is the dynamic damping
M is the hydrodynamic mass
x, y are the two displacements
$\dot{x}$, $\dot{y}$ are the two velocities and
$\ddot{x}$, $\ddot{y}$ are the two accelerations

In the calculations of Gopalakrishnan (1982), only the direct stiffness term was used. It was found that the k_{xx} term arising out of the Lomakin effect in wear rings, center-stage pieces, balance sleeves, etc. is very strong and increases as a square of the operating speed. It could be shown that for most practical multistage pump executions, critical speed is totally suppressed.

Later research began to show that it is optimistic to suppose that pumps do not exhibit a critical speed. Experimental and

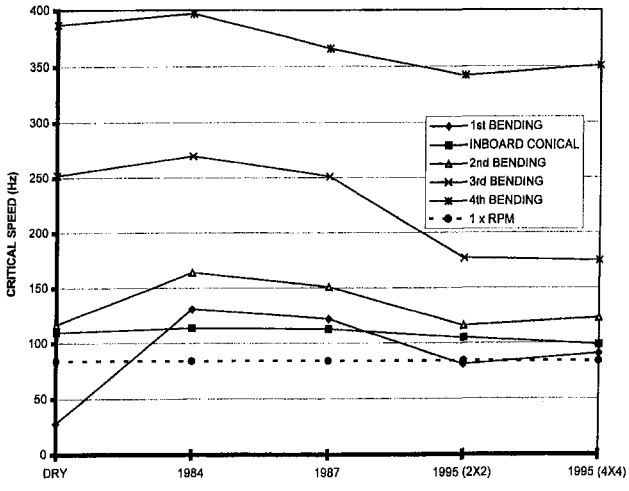

Fig. 11 Critical speed calculation results based on improved modeling assumptions

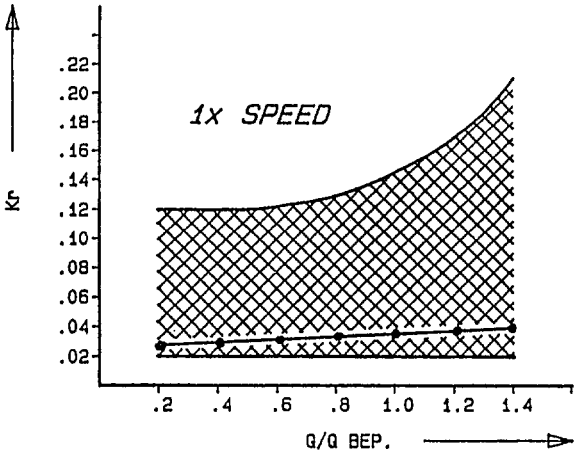

Fig. 12 Maximum and minimum radial force at synchronous frequency for a number of similar pumps (from Verhoeven, 1988)

analytical work were pursued (notably Childs and Moyer (1985)) and estimates for all the terms in the 2 × 2 dynamic matrices became available. At the same time, it was also recognized that motion dependent interaction forces occur in the gaps between the impeller tip and the inlet of the stationary diffusing passage be it volute or diffuser (Jery, et al. (1985)). Also similar forces were shown to arise in the space between the impeller shroud and the stationary casing side walls (Guinzburg, 1992), this force being fairly strong for low specific speed impellers. Very recently it has been demonstrated (Feng et al., 1992) that it is not adequate to consider the dynamic interaction in running fits to be a 2 × 2 matrix. Angular motion of the shaft through the clearance rings (particularly the long rings like the balance sleeve and center stage piece) is important, and thus the dynamics has to be represented by a 4 × 4 matrix, which includes the direct and cross-coupled moment coefficients.

The effect of such an evolution can best be seen by reviewing the eigen modes calculated for the same pump using the modeling assumptions of the past decade. Figure 11 shows the results for a seven stage boiler feed pump (impeller diameter ≅ 13.0 in.) with a nominal operating speed of 5082 rpm (84.4 Hz). In the 1970s when calculations were made without fluid effects, the first bending mode occurred at 28 Hz well below operating speed and the log decrement was 0 indicating that operation of the pump near this speed would be catastrophic. In 1984, calculations included wear ring and balance sleeve coefficients, without however any fluid inertia effects. Now the first bending mode is moved well beyond operating speed. (As pointed out before, if the direct stiffness only is included, the critical speed becomes infinite, i.e., is suppressed.) By 1987, volute/impeller interaction effects were included, and this reduced the first critical speed somewhat. The first calculation of 1995 uses a 2 × 2 matrix and the coefficients are computed with state-of-the-art numerical solutions for the fluid dynamic equation including the k-e turbulence modeling. Now the critical speed drops just below operating speed. Fortunately, the calculations show a logarithmic decrement value in excess of five indicating a stable motion. The second calculation of 1995 uses a full $4X4$ matrix. Now the critical speed is above the operating speed still with a healthy decrement in excess of 4.0.

Table 2

Mechanical Unbalance (G 2.5)	14.5 lb at $1 \cdot N$ frequency
Hydraulic Unbalance (k_H = .015)	74 lb at $1 \cdot N$ frequency
Vane Passing (k_H = 0.025)	1233 lb at $Z \cdot N$ frequency
Rotating Stall, etc. (k_H = .01)	49 lb at low frequency

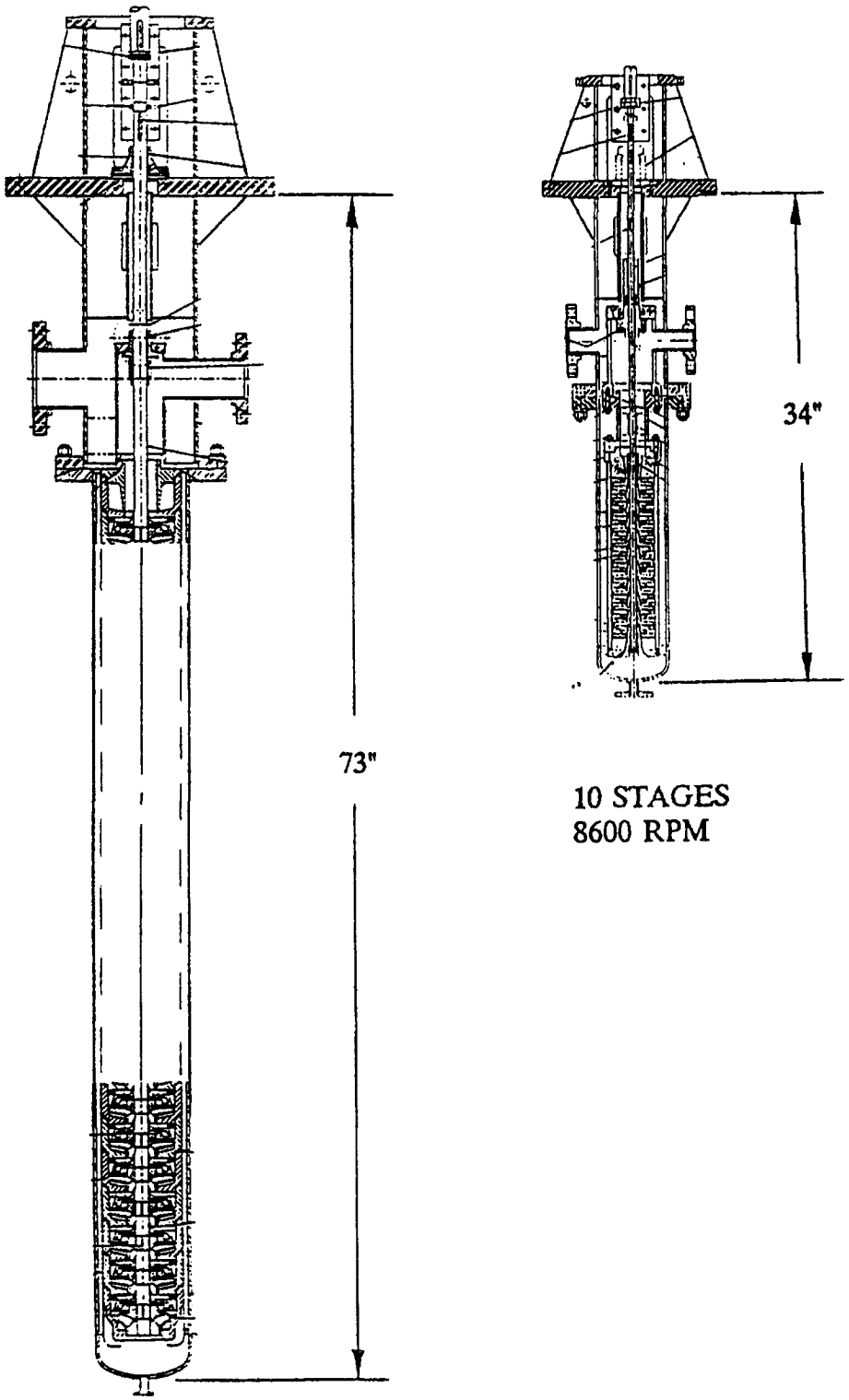

Fig. 13 Liquid oxygen pump size comparison resulting from increased speed

The second eigen mode shown is the inboard conical mode arising due to the coupling mass overhanging from the bearing. As this mode is unaffected by fluid effects, it remains at substantially the same frequency for all calculations.

Modes 3, 4, and 5 are all higher order bending modes and they are affected by fluid modeling. From this analysis, it can be seen that the technology for computing critical speeds has become very complex and it will continue to remain so in the foreseeable future.

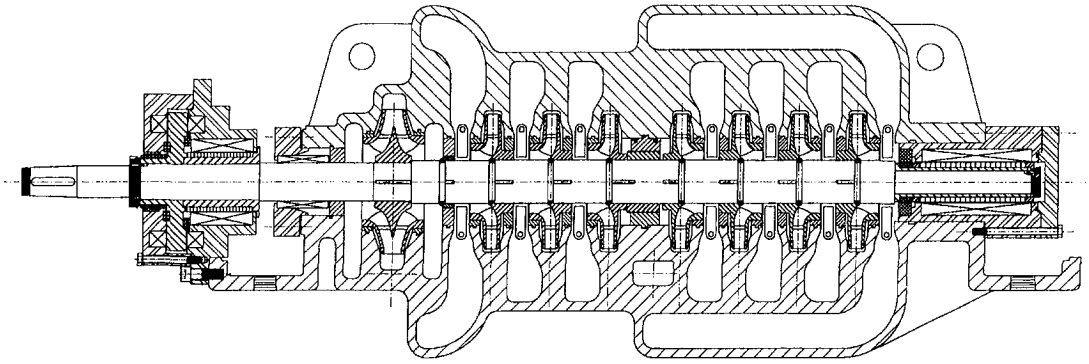

Fig. 14 Multistage feed pump with magnetic bearings (from Hanson, 1996)

Another development is this area is the calculation of response to excitation forces as it is now being understood that adequate separation margin between critical and operating frequencies may not assure a smooth running pump (Pace et al., 1986). Therefore, much effort is being exerted for estimating the excitation forces, as will be discussed subsequently.

A major problem today in this field is that, although accurate calculation techniques are available to solve the rotor dynamic equations, the coefficients themselves cannot be reliably predicted. Large quantity of experimental and analytical data are available, but for practical applications, confidence is still lacking. This situation is particularly true for the hydrodynamic mass terms and for the volute/diffuser-impeller interaction coefficients.

In the absence of reliable predictive capability, once again the rotor dynamic model has to be calibrated against test data. Such calibration can be done fairly easily for variable speed pumps or when critical speeds are captured on coast-down. (Speed dependent coefficients have to be included to deduce the critical speed under normal operating conditions). When such data cannot be obtained, direct modal analysis on the rotating shaft becomes necessary. In this technique described in Marscher (1986), the running shaft is impacted with a calibrated hammer a very large number of times. By cumulative time averaging the responses, the shaft natural frequencies show up on the response spectrum. While this method is direct and reliable, it requires impacting a running shaft with a heavy hammer (approx. 12 lb) many times (in excess of 200 impacts). Although such an artificial excitation will not cause pump damage, it can damage the operator of the hammer! This method is therefore used only in cases where direct measurement is critical.

Forces. As the critical speed issues in pumps were being understood, it became increasingly clear that the rotor dynamic performance was controlled by the magnitude of the exciting forces acting on the rotor. These forces occur naturally as the impeller rotates and adds energy to the fluid and are independent of the lateral motion of the shaft. This is in distinction to the forces generated in the clearances which are strongly motion-dependent. The excitation forces occur at several frequencies predominant among these being the once per rev and vane passing. The effects of the $1\times$ excitation are identical to those of a mechanical unbalance and hence the hydraulic source cannot be distinguished.

The $1\times$ force arises primarily as a result of asymmetry of the vane passages, which in turn is due to casting irregularities. Since direct measurement of the forces is difficult, a method has been developed to calculate it indirectly from a set of measured vibrations using an inverse transfer function method (Verhoeven, 1988). Vibration characteristics were measured for a number of multi-stage pumps and the excitation forces were back calculated. As these pumps had all been balanced to the same fine grade of balance, the calculated forces were due to

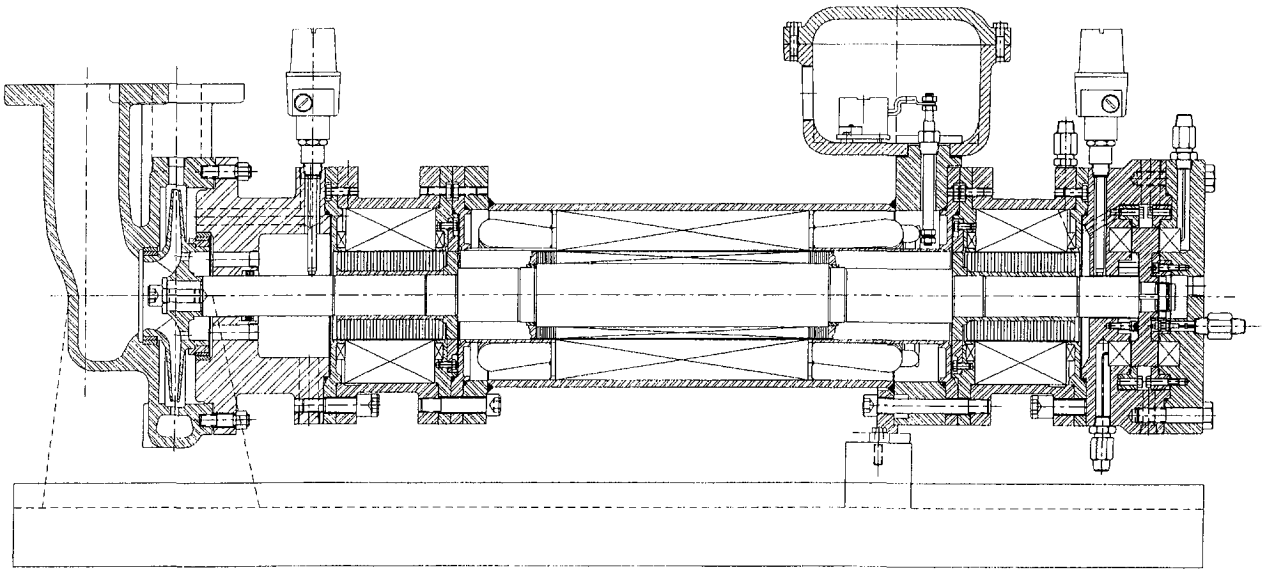

Fig. 15 Canned motor magnetic bearing process pump for the Petroleum Industry (from Hanson et al., 1992)

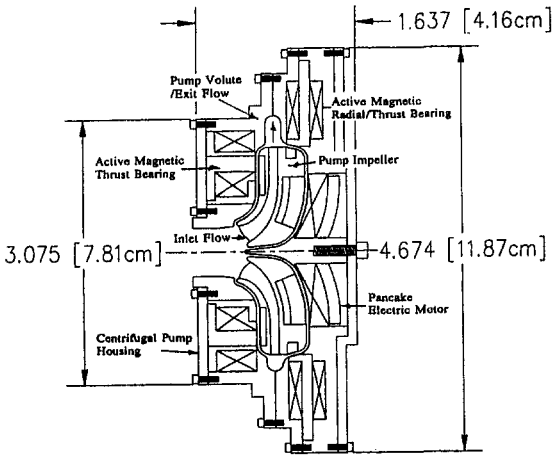

Fig. 16 Schematic of blood pump (from Olsen et al., 1996)

hydraulic unbalance. The results shown in Fig. 12 are very surprising in that the magnitude varied by a factor of six or more although all of the impellers were made with the state-of-the-art sand casting methods.

It is instructive to compare the magnitude of the hydraulic unbalance force against mechanical unbalance. A simple calculation for a typical high speed boiler feed pump is shown in Table 2. Here k_H is the hydraulic unbalance force nondimensionalized through division by pump head, outlet diameter and width.

Such results, which are not untypical (see Florjancic and Frei, 1993), lead one to believe that very fine mechanical balance is futile when impellers are not made with great control over passageway uniformity.

As mentioned before, hydraulic forces are manifested at other frequencies. Verhoeven (1988) contains results for forces at vane passing frequency, which is typically generated by the impeller wake interaction with the diffuser/volute leading edge, and at sub-synchronous frequencies, which arise due to rotating stall and other impeller recirculation phenomena. The results clearly show, as for the 1× forces, a wide variation from one pump to the next.

From the foregoing it is clear that hydraulic excitation forces are nearly impossible to predict accurately. But as the magnitudes of the forces are significant, the pump designer has to adopt conservative strategies to minimize the effect of these forces. These include proper pump design in terms of impeller/diffuser or volute clearances, shaft deflections, etc. Further, advanced technologies for impeller manufacture need to be looked into.

In the near future, it is unlikely that prediction capability for hydraulic forces will significantly improve as the calculations require proper and accurate simulation of vane-to-vane asymmetries and the complex flow situation in the gaps surrounding the impeller. On the other hand, significant improvements in impeller quality can be expected through advances in manufacturing technology. Direct machining of closed impellers from forgings are now possible. The vane passages in such impellers can be quite accurate and should have the potential to generate very low hydraulic unbalance forces. At this time, however, such impellers are significantly more expensive and it is hard to forecast wide spread use of this technique. Rapid prototyping techniques are also finding applications in pumps but mainly in the R&D arena as the materials are now primarily restricted to polymers, etc. Whether impellers in steel can be directly fabricated using advanced rapid prototyping methods remains to be seen.

Pump Design

Advances in the knowledge of rotor dynamics and cavitation behavior have led over the years to a steady increase in operating speed. Speed increases lead to a decrease in size and hence cost of the machine. When the design properly accounts for the speed effects, such machines can be built to provide the same degree of reliability as other slower speed pumps. Figure 13 shows the comparative designs when speed is increased

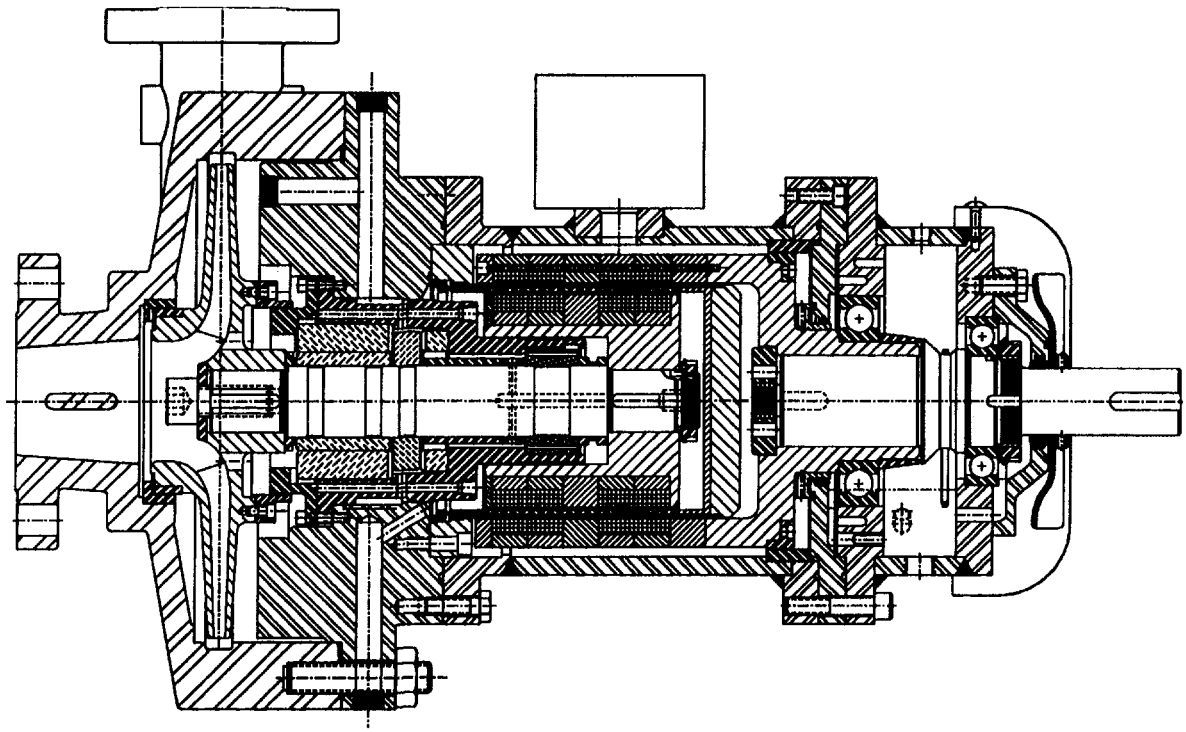

Fig. 17 Magnetic drive process pump conforming to API 610 specifications

significantly. The pump shown on the right replaced the one shown on the left six years ago and has since provided excellent service.

A factor that prevents wider application of high speeds is the cost associated with the variable frequency drive or gear box. Further, new reliability issues arise due to the addition of another component in the system. A further fundamental problem is that customers generally suspect that higher speeds will lead to lower mean time between replacements. Customers are also normally reluctant to depart from proven designs with an extensive user history list. All these factors imply that operating speeds other than direct drive will be restricted to special situations or when turbine drives are provided.

An exciting innovation in the past few years has been the application of magnetic bearings to large pumps. Because these bearings eliminate tribological contact, they offer the potential of unlimited life. They also eliminate the conventional lube oil system, and associated oil contamination problems. Their ability to provide on-line information on shaft position and forces is also an advantage. One application for a large utility boiler feed pump is described in Hanson (1996). In this execution, operating efficiency is also improved because balance line leakage loss is eliminated (Fig. 14). Another application for a large double suction refinery process pump uses a homopolar magnetic field arrangement (Ashley, 1996).

Magnetic bearings in conjunction with canned motors can offer zero leakage capability for overhung pumps. These are especially useful in refineries where strict emission controls are increasingly being enforced. The advantage of using magnetic bearings is that they are relatively immune to abrasive particles in the liquid or occasional dry running. These conditions normally destroy conventional product lubricated bearings. A description of a magnetic bearing equipped process pump can be found in Hanson and Imlach (1992). Figure 15 shows the schematic of this pump.

While these applications have demonstrated that magnetic bearings can be applied for large utility and refinery pumps, the commercialization potential is largely unproven. At present, magnetic bearings are much more expensive than the bearings which they replace. Although the magnetic bearing cost can come down if they are purchased in quantity, the volume is not likely to increase unless the costs come down. Additionally, there is considerable user reluctance to adopt a completely new technology that would require extensive training of field personnel to maintain equipment. So, the future for magnetic bearings in pump applications for the general utility and refinery industry does not look very bright.

However, there are special niche applications where magnetic bearings become the essential enabling technology. One example is an innovative blood pump (Fig. 16, Olsen et al., 1996) that is totally suspended in magnetic bearings and rotated by a disk shaped brushless DC motor. Such projects are in the innovative stage and whether these become commercially successful remains to be seen.

Zero leakage capability for API refinery process pumps can be achieved using magnetic drives. These drives are well known in the chemical process industry typically employing low horsepower units. For API applications, the liner that contains the process liquid has to be thick to hold the pressure. This causes such large eddy current losses that the application is often not feasible. A novel innovation for the liner (Smith and Oliver, 1991), consisting of an outer metal shell with longitudinal slots and an inner shell made up of a number of hoops separated by non-conducting material, has been proposed for an API pump as shown in Fig. 17. Except for a few applications in Europe, such pumps have not obtained wide acceptance. The main reason is that mechanical seals have greatly improved in reliability and with tandem or gas mechanical seals, nearly zero atmospheric emission has been achieved.

Conclusions

The pump research and development efforts in the United States today are strongly driven by the perceived needs of the customer viz. cost and reliability. Because of this drive the R& D strategy in the US has changed significantly from the past. This is reflected in the focus on certain technology fields in which great progress has been accomplished. These include:

(i.) Hydraulics: Prediction technology based on computerized fluid dynamics is poised to replace the previous "black book" empirical approaches. The drive is to produce pump designs which meet performance specifications with minimal trial and error and thus reduce pump cost. In cavitation, the approach is to provide advanced impeller designs which can guarantee long impeller life.

(ii.) Vibrations: Diagnostic technology is now well advanced to quickly identify sources of problems and provide cost effective solutions. Rotor dynamic technology is now being understood well enough to offer high speed designs which have the potential of reduced cost without sacrificing reliability.

(iii.) Pump Design: Other than high speed applications, innovations have been made in magnetic drives and magnetic bearings for pumps. While these have demonstrated technical suitability for the intended services, their commercial acceptability has not yet been proven. It appears that their near-term future will be in niche applications, where they become the enabling technology.

References

Ashley, S., 1996, "Magnetic Bearing Retrofit for Pumps," in Technology Focus Section, *Mechanical Engineering,* Dec.

Childs, D. W., and Moyer, D. S., 1985, "Sample Rotor Dynamic Calculations Using Cal-Tech Rotor Dynamic Coefficients," Addendum to paper by B. Jery et al., *2nd International Pump Symposium,* Texas A&M University.

Feng, T. et al, 1992, "Identification of Fluid Structure Interactions in Centrifugal Pumps," *5th International Conference on Vibrations in Rotating Machinery,* University of Bath.

Ferman, R. et al, 1997, "Boiler Feed Pump Rerate for Increased Head and Reduced Cavitation," *3rd ASME Pumping Machinery Symposium,* Vancouver, Canada.

Florjancic, S. and Frei, A., 1993, "Dynamic Loading on Pumps—Causes for Vibrations," *10th International Pump Symposium,* Texas A&M University.

Gopalakrishnan, S., 1981, "Computer Based Hydraulic Design of Pumps," 7th Technical Conference of the British Pump Manufacturer's Association, York, England.

Gopalakrishnan, S., Cugal, M., and Ferman, R., 1995, "Experimental and Theoretical Flow Field Analysis of Mixed Flow Pumps," 2nd International Conference on Pumps and Fans, Tsinghua University, Beijing, China.

Gopalakrishnan, S., 1993, "Impact of Hydraulic Design on Pump Reliability," Rotating Machinery Conference and Exposition, Somerset, NJ.

Gopalakrishnan, S., 1985, "Modern Cavitation Criteria for Centrifugal Pumps," *2nd International Pump Symposium,* Texas A&M University.

Gopalakrishnan, S., 1996, "Diagnosis of Service Water Pump Problems," *EPRI SWSRI Seminar, Daytona Beach, FL.*

Gopalakrishnan, S., et al, 1982, "Critical Speed in Centrifugal Pumps," ASME Paper No. 82-GT-277.

Goto, A., 1997, "Prediction of Diffuser Pump Performance Using 3-D Viscous Stage Calculation," *3rd ASME Pumping Machinery Symposium,* Vancouver, Canada.

Graf, E., 1993, "Analysis of Centrifugal Impeller BEP and Recirculating Flows," ASME *Pumping Machinery Symposium,* Washington, DC.

Guinzburg, A., 1992, "Rotor dynamic Forces Generated by Discharge to Suction Leakage Flows in Centrifugal Pumps," Ph.D. thesis, California Institute of Technology.

Gülich, J. E., and Favre J. N., 1997, "An Assessment of Pump Impeller Performance Predictions by 3-D Navier Stokes Calculations," *3rd ASME Pumping Machinery Symposium,* Vancouver, Canada.

Gülich, J., 1989, "Guidelines for Prevention of Cavitation in Centrifugal Feed Pumps," *EPRI GS 6398.*

Hanson, L., 1996, "A Commercial Threshold for Magnetic Bearings," World Pumps, May.

Hanson, L., and Imlach, J., 1992, "Development of a Magnetic Bearing API Process Pump with a Canned Motor," *9th International Pump Symposium,* Texas A&M University.

Hirschi, R., et al, 1997, "Centrifugal Pump Performance Drop due to Leading Edge Cavitation," *3rd ASME Pumping Machinery Symposium,* Vancouver, Canada.

Jery, B., et al, 1985, "Forces on Centrifugal Pump Impellers," *2nd International Pump Symposium,* Texas A&M University.

Katsanis, T., 1964, "Use of Arbitrary Quasi Orthogonals for Calculating Flow Distribution in the Meridional Plane of a Turbomachine," NASA TN D-2546.

Marscher, W. D., 1986, "Determination of Pump Critical Speeds during Operation through Use of Modal Analysis," ASME *Symposium on Fluid Machinery Trouble Shooting,* Anaheim, CA.

Olsen, D. B., et al, 1996, "Status Report on the Utah Continuous Flow Ventricular Assist Device," 4th Cong. International Society Rotary Blood Pumps, Tokyo.

Pace, S. E., et al, 1986, "Rotordynamic Developments for High Speed Multistage Pumps," *3rd International Pump Symposium,* Texas A&M University.

Sloteman, D. P., Cooper, P., and Graf, E., 1991, "Design of High Energy Pump Impellers to Avoid Cavitation Instability and Damage," *EPRI Power Plant Pumps Symposium,* Tampa, FL.

Smith, J. and Oliver, J., 1991, "Techniques for Eddy Current Reduction in Magnetic Drives Using Metallic Containment Barriers," *8th International Pump Symposium,* Texas A&M University.

Valenti, M., 1996, "CFD Software Improves Pump Design," *Mechanical Engineering,* Nov.

Verhoeven, J. J., 1988, "Unsteady Hydraulic Forces in Centrifugal Pumps," *Proceedings of the Institution of Mechanical Engineers C348/88.*

Pump Research and Development: Past, Present, and Future

Peter H. Hergt
Dipl.-Eng.,
Senior Research Engineer,
Central Hydraulic Department,
KSB A.G.,
Johann-Klein-Straße 9,
D-67227 Frankenthal, Germany

As in all areas relevant to the development and production of pumps the tasks the hydraulic engineer has to deal with have undergone a remarkable change in recent decades: from a more or less unrestricted design of components to design roles dictated by manufacturing techniques. These general trends are accompanied by developments related to changes of the market requirements. This is demonstrated for three particular pump types. The consequences of the demand to save energy—with all the different aspects—are described for the example of heating circulation pumps. The still growing environmental awareness is a challenge for an enlargement of the presently valid operation limits of sealless pumps and for the development of intelligent monitoring systems. It is demonstrated that the developments in the field of boiler feed pumps are closely related to the growing unit sizes. Availability and reliability, and as far as very large pumps are concerned the efficiency, have always been and still are the dominant criteria.

General Research and Development Trends

Over the last 25 years, all areas of relevance to the development and production of centrifugal pumps have undergone fundamental changes which is of course only realized by those who have worked in the same field over a long period of time. These changes will be illustrated in the following by the example of research and development in the field of fluid dynamics. They become obvious:

- ◇ in the objectives and hence the research focuses
- ◇ in the approaches to problem solving and in the last couple of years
- ◇ in an intensified cooperation with external organizations, especially universities
- ◇ in the concentration on projects evaluated according to the cost-benefit principle only

When talking about changing research focuses here, it is not only the change inherent in all technical progress and development of new products. It must be realized that irrespective of the product and its field of application, production technology has influenced fluid dynamics research to such an extent that it is now heading into a completely different direction.

In the early 1960s, the main concern was to create fundamentals which allowed the engineer to achieve optimum efficiency, stable characteristic curves, and a good suction behavior. The complexity of the geometric forms developed in the process was hardly ever discussed since the machines were mostly manufactured from cast components and aspects of component castability were neglected. From the beginning of centrifugal pump engineering to the 1970s, the focus was on what the theory of turbomachinery describes as the "primary task of turbomachinery design," namely:

Given are the operating data, and needed are:

- the geometry of the rotor (impeller)
- the geometry of the stator (casing)
- the optimum speed or the possible speed ranges

which will yield maximum efficiency and operating reliability within the required operating range.

Although the goals—such as maximum efficiency—are still the same, the problem definition has changed in so far as the researchers question is no longer: how can we find the best of all possible designs (not considering any manufacturing aspects) but: how can we design the hydraulic contours to meet the requirements of modern, low-cost manufacturing methods (forging, milling, bending, moulding), that is, in general, how can we simplify them without causing an impermissible deterioration of the desired characteristics.

This highlights the significance of the "second task of turbomachinery design," namely:

Given are:

- the possible geometric forms of rotor and stator (for example as defined by the optimal manufacturing process)
- the possible speeds
- the operating behavior and operating range
- the fluid and its characteristics

Needed are:

- the head and
- the flow rate

which can be achieved with an optimum efficiency while satisfying the requirements regarding

- the operating range and operating behavior

The fluid engineer had therefore to acquire a thorough knowledge of the possibilities provided by the production methods and he was faced with the fact that the parameters required for the design of these geometries were out of the range of his experience. At this time, mainly empirical approaches were used for the design of pumps, i.e., Euler's simple turbine theory improved and adapted to experimental results by so-called "coefficients of experience."

With the development of computers and the improvement of CFD-codes, tools became available which could help to replace experimental experience by a purely theoretical analysis—at least to some extent. Nevertheless, since all theory must stand the test of practice, practical experience gathered very systematically and thoroughly will continue to be of great value as a calibration standard. It will still be some time before theoretical

Contributed by the Fluids Engineering Division for publication in the JOURNAL OF FLUIDS ENGINEERING. Manuscript received by the Fluids Engineering Division September 8, 1998; revised manuscript received December 21, 1998. Guest Editor: P. Cooper.

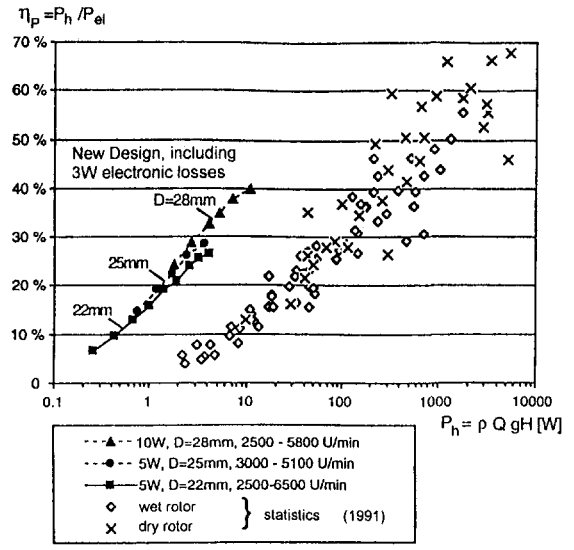

Fig. 1 Total efficiencies of small centrifugal pumps versus hydraulic power P_h

methods are reliable enough to make most experiments obsolete, but the trend is already discernible and for cost reasons also desired.

As far as the research topics are concerned, from the very beginning of the period under review they have been determined by the product requirements. However, there was always adequate scope for fundamental research work not directly related to the products, which, as experience shows, pays in the long run. In addition, there was sufficient room for checking and verifying concepts for the next pump generation and the generation after that. Nowadays we often do not find this, since today projects are evaluated according to the cost-benefit principle only. In other words, our fast-moving times also produce short-term research approaches.

In the wake of increasing energy awareness, research focuses once more on improving efficiency. While in the past improvements were counted in percentage points, targets are now set to tenths of a percent. Indispensable prerequisites for achieving these targets are the use of all the modern theoretical and experimental tools available.

Since industrial research departments usually concentrate on the essentials, they often cannot cope with the variety of methods applied and questions to be treated. This is why fundamental research work is increasingly carried out in cooperation with external organizations. It goes without saying that companies must nonetheless retain the relevant technical competence to translate the research findings into practice.

In addition to these basic changes, specific progress, of course, has been made in all fields of pump engineering. The following illustrates this progress by three typical examples.

Heating Circulation Pumps

At present, approximately 15 million circulation pumps are being manufactured in Europe annually, about $\frac{1}{3}$ of which (i.e., 5 million) are fitted in new installations. Assuming a rather low power consumption of 60 W per pump, this leads to an additional power of 300 MW per year. Whoever has such a small pump fitted in the heating system of his house will most likely not be aware of this fact. Whether the pump input power is 60 or 70 W will probably make no difference to him, since this accounts for less than 1 cent per day on average. Everybody is interested only in the pump price, which is therefore, as ever, a very important factor of success for the manufacturer.

The incentive for developing energy-saving circulation pumps does not originate from customer demands but from overall economic considerations. These insights resulted in a recently published study conducted by the Swiss Federal Energy Agency in the framework of its "Electricity" research programme (Nipkow et al., 1994). The study revealed that the efficiency of the circulator pumps currently available on the market could still be significantly increased and called for a sort of required minimum efficiency. Thus, "saving energy" will be one of the major development goals in the future as it was in the past. However, the term "energy saving" has several aspects.

Internal Pump Efficiency. The study mentioned above shows that some, but by far not all, of the pumps under investigation achieved fairly good efficiency in comparison with the efficiency attainable according to Anderson (1975). The question is, however, if this is really the standard to be applied today. Of course this calls for the trivial task of adjusting the unfavorable hydraulics to the level of the better ones. But the use of supersynchronous speeds offers, in addition, a broad range of possibilities. If it is possible to cover all design points with $nq = 45 \div 55$, ($Ns = 2300$ to 2800 or $SL_s = 0.84$ to 1.03), it will mean a great step forward.

Motor Efficiency. Another issue the above study treated at length is motor efficiency. For various reasons, conventional asynchronous motors with low power output, exhibit low efficiency, which in combination with pump efficiency might result in wire-to-water efficiencies of only a few percent. By contrast, electronically controlled motors with permanent magnet rotors have an efficiency η of up to 80 percent. If combined with improved hydraulics (see above), this could easily lead to an overall efficiency which corresponds to less than the half of the required energy. This is illustrated in Fig. 1 (Nipkow et al., 1994).

Matching the Pump to the Operating Points. Typical operating points of a complex heating system are shown in Fig. 2. It is plain to see that they look like the points of the resistance curve of a system with a high static component. At $Q < Q_{max}$ and with constant need, the power loss caused

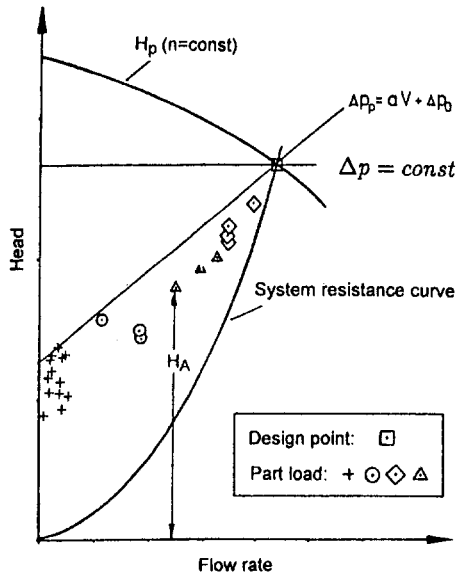

Fig. 2 Typical operation points in a heating network

by throttle control is $Q\ (H_P - H_A)/\eta$. A first step toward energy saving was speed control in accordance with Δp = const, i.e., the pump is controlled via sensors so as to deliver identical discharge pressures irrespective of the flow rate. Today, advanced integrated power electronics offer new control options: provided a defined electrical signal value can be attributed to each operating point, it is possible not only to keep Δp = const but also to match the H/Q data to the requirement and thus to avoid the losses completely.

Optimization of the Piping Network. Again and again larger pumps than originally planned must be retrofitted into heating systems, because the supply to some of the consumer installations proves to be insufficient. This in turn entails throttling of consumer installations then supplied with excessive water.

A project funded by the German government dealt with the development of a practical and not too complex method for analyzing existing plants (Bach et al., 1989). Application of this new method in installed plants corroborated the assumption that in many cases heating system layouts are not optimal, which causes an enormous waste of energy.

In one case in which optimization of the existing plant by simple installation of appropriate throttling devices at the correct points within the system brought the total pump input power down from 4 KW to 0.4 KW. In another case, the same procedure resulted in a reduction from 170 KW to 37 KW. Similar amounts of energy cannot be saved by any other measures, which means that in the future great significance must be attached to correct system layout.

Costs. In addition to energy consumption, manufacturing costs, and thus the pump price, have been and will always be an important criterion. The European circulator pump market is dominated by two manufacturers (Grundfos and Wilo), and success largely depends on the product prices. The consequences derived from this fact, namely

- optimized design
- lightweight construction
- high performance → small pump, high speed
- low-price materials
- optimized manufacturing processes
- optimized production methods
- etc.

are well-known and do not only apply to circulation pumps.

Sealless Pumps

In the late 1970s, I. Karassik predicted that sealless pumps would gain importance in the years to come, and he was right.

Increasing environmental awareness in the last couple of years and pertinent anti-pollution regulations contributed toward a drastic limitation of permissible pollutant emission. Such regulations can only be adhered to with difficulty, if at all, when using pumps with mechanical seals. As a consequence, hermetically sealed pumps are used for critical applications such as:

- transport of media detrimental to health
- transport of media involving a risk of fire or explosion
- recirculation under vacuum or high pressure conditions
- handling media at extremely low or high temperatures
- handling media in pharmaceutical or bioengineering applications

There are two types of hermetically sealed pumps: canned motor pumps and mag-drive pumps. Only the former will be discussed in this paper.

The Swiss Benjamin Gräminger invented the canned motor as early as 1914, but it was not before the 1930s, when for the first time austenitic steels were used for the can, that this type started to become a true alternative to conventional designs. The next important step forward was the development of a pump for the nuclear submarine *Nautilus* by the Philadelphia-based Chempump Corporation in 1948. European manufacturers started their own developments in the 1950s and 1960s. Real progress was only made, however, when motors with higher rating could be built and the admissible operation temperature and pressure ranges could be increased.

Today, the limits are approximately the following:

$$\left.\begin{aligned} P &\le 250\ \text{kW} \\ -120°\text{C} \le t &\le 450°\text{C} \\ P_{\text{syst}} &\le 1200\ \text{bar} \end{aligned}\right|$$

While the pump efficiency is as a rule similar to that of other pump types, the efficiency of canned motors is significantly, i.e., 10 to 15 percentage points, lower than standard motor efficiency. So far, this fact has been of minor importance, since safety is the vital aspect in canned motor pump applications. The possible future use of cans made from plastics holds a considerable energy savings potential.

A comparison of canned motor and standard motor pump prices reveals that canned motor pumps, particularly in cast iron design, are more expensive. According to the statistics of a large German chemical company, however, canned motor pumps require around one third less repair work than pumps fitted with mechanical seals. They are obviously more reliable and their life cycle costs are lower, which in many cases more than compensates for the higher price.

As a result of more and more stringent anti-pollution regulations, engineers must concentrate their efforts on leak-free pumps. In the future, this pump type will have to meet ever more exacting demands in terms of increased performance and a broader application range. The development of new materials, especially for plain bearings, will open up new chances and opportunities regarding improved wear resistance and dry-running features, as well as reliability in general. For the transport of fluids having no or just minimum lubricating characteristics, canned motor pumps fitted with active magnetic bearings are an excellent choice and have already been used in one or the other application. The relatively high price is however still a prohibitive factor as to universal use of such magnetic bearings.

As the efficiency of chemical plants is being more and more improved, monitoring of hermetically sealed pumps will gain importance. On-site monitoring of the flow rate, pressure and power input is already quite common today. In the case of canned motor pumps, the liquid level within the motor and the temperature are monitored in addition. Critical applications might require additional vibration and/or shaft position measurements. It will be only a matter of time until these different monitoring systems will be replaced by one single intelligent diagnostic system permitting early recognition of pump failures.

Boiler Feed Pumps

As illustrated in Fig. 3, the further development of boiler feed pumps was—and still is—determined by the fact that the boiler capacity and the output of individual units have become larger over the years.

In the mid-1950s, the increasing unit output also brought a change in the feed water treatment, thereby improving the conditions for steam generators and turbines but at the same time increasing the corrosion risk for boiler feed pumps. With impellers and diffusers being already made of high-alloy cast chrome steel, it became necessary now to manufacture other components from high-alloy materials as well, which had a

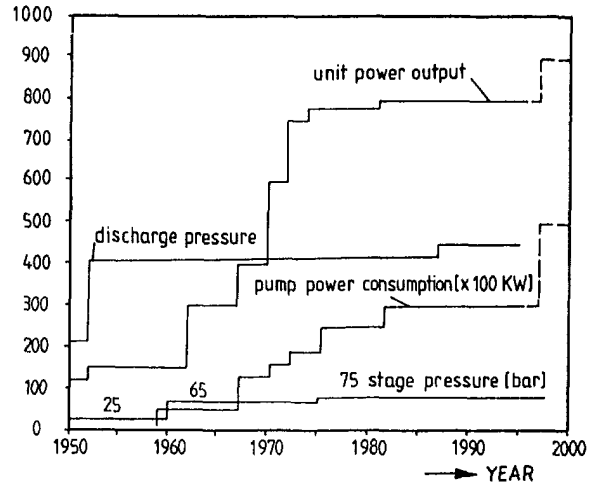

Fig. 3 Development of conventional power stations

detrimental effect on the anti-seizure behavior, however. The result of a large-scale research project was a corrosion-resistant special alloy with improved anti-seizure properties as well as the insight that it was impossible to achieve the favorable properties of the previously used low-alloy materials again. A change in design compensated for this disadvantage. With a large number of stages, the casing was matched to the rotor's deflection curve and the sealing gap was provided with a groove profile.

In the early 1960s, unit outputs increased up to 150 MW, and for the first time, stage pressures up to 65 bar were reached. Meanwhile, drive technology enabled speed levels up to a max. of 6000 rpm, which allowed the use of high specific speed hydraulics. This way, even with a small number of stages and increased internal clearances, high efficiencies could be reached.

Larger pump sizes and higher speeds made for a considerable energy concentration. The stage pressure rose by up to 2.5 times, causing increased hydraulic forces and hence axial thrust balancing and vibration stability problems. These issues triggered thorough investigations regarding the build-up and balancing of radial and axial forces.

Thus the development of boiler feed pumps in ring-section design had reached a high level of perfection in the 1960s and made possible the design of pumps for further increases in output. In the late 1960s, unit outputs reached 300 MW. In principle, these application requirements could be met by the ring-section pump concept. However, in view of possible further increases in output the barrel casing design was also discussed with European consultants. At that time, this type was the standard design in the U.S. As a result, both pump types were used from then on, with barrel casing pumps being preferred when high-output machines were concerned. In the case of low-output pumps the ring-section design still predominated for price reasons.

At the beginning of the 1970s, the first 600 MW plants were built. Since long-term practical experience with the use of pumps in 300 MW plants could not be drawn upon in Germany, barrel casing pumps, were the exclusive choice for power plants of this size. Although commissioning was usually effected without problems, after about one year of operation the first-stage impellers showed unexpectedly heavy cavitation erosion. The reason was the high velocity level resulting from the pump size. Until then, the commonly used method for determining the required suction head had failed. In order to avoid damage, a new generation of impellers was developed for the first stage. A number of papers describing the different steps of the development have been published (e.g., Hergt, 1991).

The 1980s and 1990s saw just a minor increase in outputs (from 600 to 700 to 800 MW) with pump power consumptions rising up to 30 MW. Meanwhile, the pumps had become very large so that the analysis of the temperature-induced deformations became important. Before start-up and after shutdown, temperature layers occur in the pump resulting in temperature-induced deformations. As a result, the casing becomes distorted so that the rotor is at risk of rubbing against the casing. The use of honeycomb joint rings enabled the rotor to run without contact again with no loss of efficiency, as well as with reduced vibrations. In small and medium-sized pumps, honeycomb sealing rings even make for an increase in efficiency. But top efficiency could also be achieved in large pumps by additional hydraulic and design improvements.

Among the different boiler plant developers, a certain degree of standardization can be observed as far as the small and medium sized boilers are concerned. The feed pumps for these applications are available, but that does not mean there is no need for further development. Future research and development will focus on the following points:

- Increasing the overall efficiency of boiler feed pumps
- Further improvement of the suction impellers in order to avoid the need for booster pumps, or to allow the feed water tank to be installed at a lower level and, consequently, reduce the cost of piping and elevated steel structures
- Design of pumps without auxiliary systems which reduces the cost of monitoring, which includes, mechanical seals without cooling water circuits and water-lubricated bearings, among others
- Lowering production costs and at the same time improving product quality
- Prolonging maintenance intervals so they coincide with planned boiler inspections
- Shortening delivery times

The pumps designed for the large coal-fired power stations of the future will have to meet a different set of requirements. From the literature and several meetings with a number of end users, it can be concluded that, at least in Germany, power stations with a unit output of 900 MW will be built in the near future. And 1200 MW are by no means impossible. From today's perspective, this prospect calls for the development of new turbines and generators or twin turbines. Stainless steel still remains the material used for boilers, although heat-resistant austenitic steels will definitely be tested in the future.

The new stainless steels used for turbines are suitable for inlet temperatures of 600°C and inlet pressures of up to 300 bar, which means that the total heads of boiler feed pumps will increase once more and that the flow rates will increase considerably.

From our current experience with boiler feed pumps installed in 700 MW units, only 100 percent full load pumps are used, with one, or at the most two, considerably smaller starting pumps. The driving turbines will have a speed of between 5000 and 6000 rpm. Speeds higher than 6000 rpm are not expected because of economical reasons as discussed by Hergt et al. (1990). In terms of the pumps, this means that (Schill, 1995):

- The efficiency of the double-entry boosters will have to reach 88 percent
- The hydraulic systems of the main pumps have to be optimized in terms of efficiency

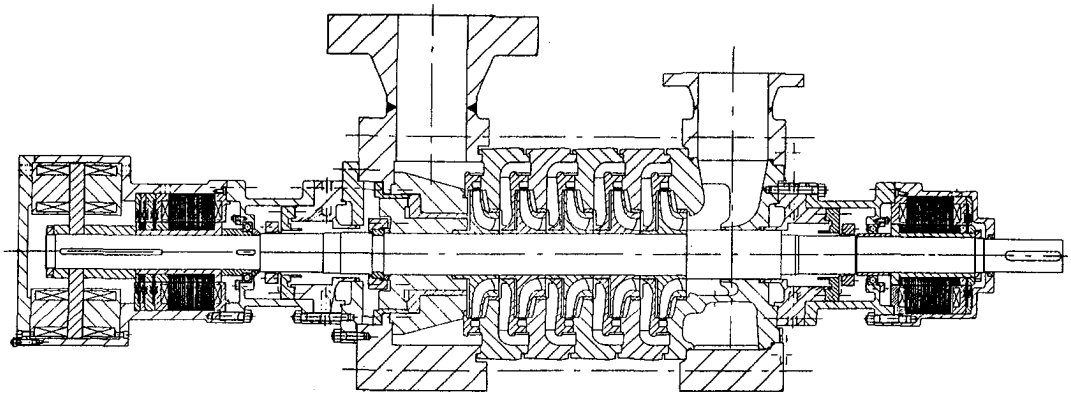

Fig. 4 Boiler feed pump with magnetic bearings

- The end volute downstream of the last stage is a must
- Cellular profile casing wear rings will be a standard feature
- Research will concentrate on improving the cavitation behavior, the interaction between impeller and diffuser, and on the pressure distribution in the impeller side gaps. The targets are stable characteristics without even the smallest instabilities as well as the accurate prediction of the axial thrust
- In view of the high power density of up to 8000 kW per stage and the required geometrical accuracy combined with physically smooth surfaces, impellers and diffusers will be made more and more often of forged materials. The channels will be pre-turned, milled, and drilled on numerically controlled machining centers and the final tuning will be done by EDM.
- Today's impeller materials—stainless steels—will possibly be replaced, e.g., by titanium
- Gas seals may eventually take the place of today's shaft seals
- The oil-lubricated radial and axial bearings will probably be replaced by active magnetic bearings at some point. A prerequisite for this is that the widely criticized balance disk experiences a renaissance. By a change of bearings alone, it is possible to improve the efficiency by 0.8 percent. What a pump like this looks like, is shown in Fig. 4 (depicted with a double piston).

Future Prospects in General

Questions such as: what basic features do end users expect of their pumps in future? are of course of interest in addition to the general and special trends described above. This is why the German Association of Pump Manufacturers commissioned a Delphi study consisting of 21 questions. One of the most interesting questions concerned the importance of the pump characteristics listed below:

Energy consumption	Suction behavior
Reliability, availability	Zero leakage
Control range, controllability	Sound emission
Price	Pulsations
Recyclability	Supersynchronous speeds

The answers of 40 end users, consultants, institutes, etc. covered by the survey resulted in the ranking illustrated in Fig. 5. The fact that the price ranks fourth must not be misinterpreted to mean that it is of minor importance. The following conclusion can be drawn however: it seems that the customer is willing to pay a higher price for a highly reliable pump with good efficiency. This is already common knowledge as far as high-performing pumps are concerned. But the fact that also relatively small machines are increasingly evaluated in terms of their so-called life cycle costs, i.e., purchase costs, operating costs, maintenance costs, downtime costs, etc. is an indication as to which product features the manufacturer must optimize. A difficult situation arises only if the end user, whose main concern is life cycle costs, and the consultant, who is exclusively judged by the investments required, are not identical.

The high ranking of the zero leakage feature corroborates the well-known trend toward hermetically sealed pumps in process engineering applications.

A number of comments emphasized the ever-increasing importance of sound emission characteristics.

One problem not directly covered by the study but touched upon by comments on other questions and discussed at length in workshops at the 1996 Pump Conference in Karlsruhe was the frequent lack of communication between manufacturer and user. There was widespread agreement that in many cases the optimum solution to pumping duties cannot be found because on the one hand, the manufacturer receives incomplete specifications and on the other hand, the user is not sufficiently familiar with the physical characteristics and limits of pumps.

So in the future, the manufacturer must think in terms of "providing solutions" rather than "selling products." If this is true and if the pump features described above are to be optimized, computer simulation will gain importance in the future. Reliable computation methods are indispensable for finding out how a pump interacts with a system. The same applies to the question of reliability. Critical phenomena like abrasion, cavitation, transient stress on components or flow processes in seal chambers cannot be economically controlled

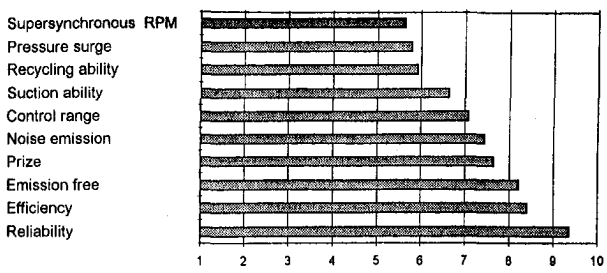

Fig. 5 Importance of pump characteristics

by merely conducting experiments, although what has been said earlier holds true here also: in the long run, practical experience will continue to be the "calibration standard" for theoretical findings.

Acknowledgments

The author wishes to thank Mr. Schmalfuß from WILO Company, Mr. Krämer from Hermetic Pumps, and Mr. Schill from KSB AG for their support in getting the relevant data and their readiness to answer all questions concerning history and technical trends in the future.

References

Nipkow, J., et al., 1994, Klein-Umwälzpumpe mit hohem Wirkungsgrad, Forschungsprogramm Elektrizität, ENET-Nr. 5107700-2, Bundesamt für Energiewirtschaft/Bern.

Anderson, H.H., 1995, "The Economic Aspect of Pump Efficiency," Pumps for Progress, 4th Techn. Conf. of the BPMA, Durham, 9–10, Apr.

Bach, H. et al., 1989, "Rechnergestützte Analyse und hydraulischer Abgleich von Rohrnetzen angewandt auf die Betriebsoptimierung der Pumpe," BMFT-Proj.-Nr. 0338163B.

Hergt, P., 1991, "Design Approach for Feed Pump Suction impellers" *Power Plant Pumps Symposium,* Tampa.

Hergt, P. et al., 1990, "Status of Boiler Feed Pump Development," *IAHR-Symposium,* Belgrade.

Schill, J., 1995, "The State of the Art and the Future Development of Boiler Feed Pumps," *2nd Intern. Conf. on Pumps and Fans,* Tsinghua Univ., Beijing.

Pump Research and Development: Past, Present, and Future—Japanese Perspective

Hideo Ohashi
President,
Kogakuin University,
Tokyo 163-8677, Japan

Yoshinobu Tsujimoto
Professor,
Engineering Science, Osaka University,
Toyonaka, Osaka 560-8531, Japan
e-mail: tsujimoto@me.osaka-u.ac.jp

The evolution of pump research and production in Japan after 1955 is surveyed. The post-war period has been divided into three stages of development with unique social and industrial characteristics: expansion, conversion, and globalization. The growth of pump production in sales amount and quantity is shown for various types of pumps. The post-war direct and indirect research on pumps is classified into eight groups of topics and their past trends are analyzed. These changes are correlated with the characteristics of the corresponding background stage. These analyses with the past suggest new trends of research for pumps of tomorrow.

Introduction

Pumps are an industrial product which meets the most basic needs of humanity. They supply city water for daily life; they feed water to boilers for power generation; and they circulate fluids in every kind of liquid-handling system including human bodies. Because of this, the production and development of pumps have been strongly influenced by society and industry. The present paper attempts to show how the characteristics of pump research and development can be explained in terms of the needs of society and industry in each respective age.

In order to crystallize the characteristics of society and industry, the present paper divides the post-war development of Japan into three stages with unique social and industrial characteristics, that is, the Stage of Expansion (1955–1973), The Stage of Conversion (1973–1991), and the Stage of Globalization (1991–present).

The growth of pump production in sales amount and quantity is analyzed for various types of pumps based on the annual industrial statistics (The Japan Association of Industrial Machinery 1995–1996). The post-war research on pumps, both with direct and indirect concern, is classified into eight groups of topics and their past trends are analyzed. These changes are correlated with the characteristics of the background stage.

The last stage started in 1991, at the beginning of the last decade of the 20th century. A paradigm shift of pump research and development may be required in the years to come. The shift of value can be described in simple wording as "from pre-delivery to post-delivery."

Change of Background—Three Stages of Social and Industrial Development

The social, political, economic, and industrial development of post-war Japan can be classified into three stages with unique characteristics (Ohashi, 1996). Following are the descriptions of each stage.

The First Stage: Period of Expansion, 1955–1973 (18 years). Ten years (1945–55) were needed to overcome the post-war chaos caused by the surrender and occupation. In 1955, the Liberal Democratic Party gained political control and continued to hold the government until recently. This political stability allowed a consistent policy necessary for farsighted development of the society and industry. The government started "Double the Income Initiative" to accelerate economic development and the domestic market grew accordingly.

Heavy industries, such as steel, petrochemical, synthetic fiber, ship building, automobiles, and heavy electric machinery; and infrastructure industries, such as power generation and construction, took the leadership in expansion. Exports increased rapidly and the international trade balance turned from deficit to surplus in spite of huge imports of oil and raw material.

As industries started to expand rapidly, the shortage of engineers became an urgent issue. The plea of industry leaders for more engineers evoked a national consensus and the government launched plans to quadruple the number of graduate engineers. This expansion in quantity had its peak around 1965 and the target was reached by the end of this expansion stage.

The influence of industrial waste on the pollution of the local environment gathered little attention until the end of sixties. This ignorance caused many severe and tragic consequences such as the Minamata-syndrome (pollution by organic mercury) in the decades to follow.

The Second Stage: Period of Conversion, 1973–1991 (18 years). The first oil crisis in 1973 terminated the expansion story of the first stage. Industries found that they thrived mainly by consuming huge amounts of oil and raw material. They were forced to reform themselves to be less dependent on the supply of energy and material. Conversion from "Heavy-Thick-Long-Large" to "Light-Thin-Short-Small" became a typical slogan of Japanese industries.

The information age started about this period with accelerated proliferation of computer and communication technologies. Products featuring the application of micro-electronics and precision-manufacturing, such as VCRs, DRAMs, and LCDs, became the front running exports, replacing previous heavy products such as steel and ships. Industries achieved this conversion far quicker than anticipated and regained competitiveness in the world market.

In the latter half of this stage, the GNP grew rapidly again, and Japan became the no. 2 economic power with a huge trade surplus. A booming economy and surplus money triggered an overheated investment rush on stocks and lands, leading to a spree called a bubbly economy. The bubbles started to burst in 1991, and the second stage terminated. History may explain that the essential and hidden cause of this collapse was the ending of the cold war.

The Third Stage: Period of Globalization, 1991–?. The end of the cold war relieved mankind of the nightmare of nuclear massacre and lowered the barriers between nations. It

Contributed by the Fluids Engineering Division for publication in the JOURNAL OF FLUIDS ENGINEERING. Manuscript received by the Fluids Engineering Division March 2, 1998; revised manuscript received September 21, 1998. Associate Technical Editor: D. P. Telionis.

triggered the start of a borderless age. This new situation initiated, on the other hand, a war of a different nature, namely, competition of industries on a global scale. Leaders of every nation are now clearly aware that science and technology are the key factors for maintaining competitiveness and sound development of industries, thus ensuring employment and a growing standard of living. Every industrialized nation started to enhance "Strategic Research" with the determined object of maintaining leadership in industrial development.

In the age of globalization just started, Japanese industries are facing many difficulties: high costs of products owing to the over-evaluation of currency, shift of production plants abroad, over-capacities of domestic industries caused by production moving abroad ('hollowing'), change of the Japanese style management, decrease in the size of the young generation and so on.

The most competitive of Japanese industries have been mass production technologies of standardized products such as automobiles and electronic devices. These technologies can be transferred abroad together with transplanted production facilities. Industries urgently need new products which replace obsolete products and fill the large hollows of domestic factories. The fate of many Japanese industries depends on whether they are capable of replacing their mainstream products from traditional to globally competitive ones.

The industrial development of newcomer nations such as China and southeast Asian countries, is accelerating the consumption of energy and material at an enormous rate. The consequence will be the shortage of natural resources on a global scale and an ever worsening influence on the environment.

At the very start of the present stage in 1992, the Earth Summit in Rio de Janeiro (UN Conference on Environment and Development) declared that the environment is a global issue. Discharge of carbon dioxide or CFC gas at a location induces the greenhouse effect or depletion of ozone over the entire globe. The largest value and target of industrial development in the present stage lie in the key words "Sustainable Development."

Growth of Pump Production

The Japan Association of Industrial Machinery publishes annual statistics on the domestic production of industrial machinery of various kinds (The Japan Association of Industrial Machinery 1995–1996). The following data are taken and processed from these sources.

Figure 1 indicates how the annual sales of pumps in yen have increased since 1955, the start of the first stage. The sales amount is further divided into three categories according to the nature of clients, that is, export, the public sector, and the private sector. The clients of the public sector are the government and local authorities, and the pumps in this category are mainly for public infrastructure such as irrigation, drainage, water supply, sewage, dredging, water desalination, and so on. Pumps for the private sector include those for power plants, chemical and petrochemical plants, industrial facilities like steel works, ships, mining, buildings and miscellaneous purposes. Small in size, but huge in number, pumps installed in automobile engines, electric appliances, house heating and cooling devices, etc., are excluded from the present statistics.

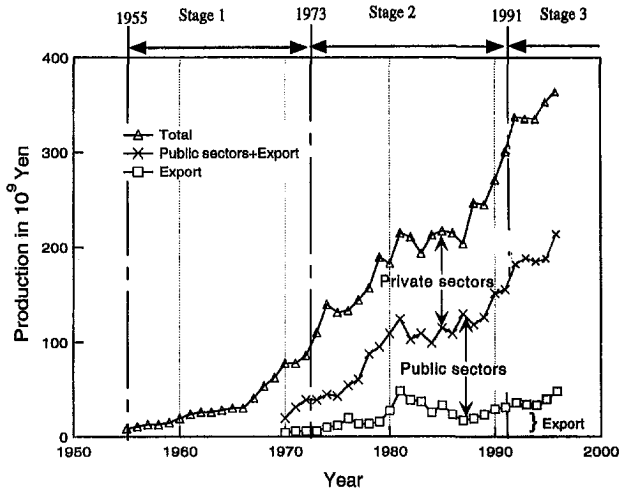

Fig. 1 Annual production of pumps in sales amount

As seen from the figure, the sales amount on a linear scale has been increasing remarkably (divide by 120 for a rough conversion to U.S. dollars). However, if we see this figure on a logarithmic scale, that is, in terms of growth rate, the situation seems quite different. The sales amount increased 15.3 times during the first Stage with an annual growth rate of 16.4 percent. This was indeed a period of expansion. The growth rate of the Gross National Product (GNP) during the same period was 12.5 percent, namely 4 percent less than that of pump production. This fact indicates that pumps used to be the forerunner of industrial expansion, since they are an indispensable element of investment in plants and facilities.

This situation changed in the second stage. The sales amount increased three times during stage 2 with an annual growth rate of 5.8 percent during the same 18 years. This change was triggered, of course, by the oil crises which urged the industrial conversion as described above. The annual growth rate dropped to 2.9 percent between 1975 and 1988, and the rate was far lower than that of GNP (7.5 percent), of the same period. Pumps proved to be the forerunner of industrial trends also in this case, but in a negative sense.

In the last few years of the second stage (1988–1991), the growth rate of pump production recovered to 7.3 percent and exceeded again the GNP growth, 5.7 percent, considerably. This fact indicates that Japanese industries had overcome the aftermath of the oil crises and recovered confidence for investing in the future. If we scrutinize the production of pumps during the second Stage by client categories, it is found that the growth rate of pumps for the private sector was 1 percent lower than the average, while the rate for the public sector 1 percent higher. This difference was due to the political decision of the government to increase the budget for social infrastructure as the means of stimulation for the stagnating national economy. Exports increased six times in sales amount during this period. However, the conversion rate of currency fluctuated so drastically, from 360 yen/$ to 80 and again to 120 at present, that it is difficult to find any meaningful trends.

The outlook for the third stage is still opaque. The growth of pump production parallel to the GNP may be fundamental as the rule of thumb for such basic products as pumps.

Figure 2 indicates the annual production of pumps in number of units on a logarithmic scale. Besides the total number of pumps produced, the number of centrifugal pumps (single and multi-stage), of axial and mixed flow pumps, of rotary and reciprocating pumps (including regenerative pumps), of submerged-motor pumps, and of non-corrosive pumps (stainless pumps) are shown respectively. Centrifugal pumps kept the majority as easily imagined. A rapid increase of submerged-motor pumps since the late sixties and that of noncorrosive pumps since the middle of the eighties are two remarkable cases which reflected the interests of pump users. Demand for easy maintenance and stain-free water may be the underlying incentive of this rapid expansion.

Figure 3 illustrates the evolution of the largest unit output of electric power stations in Japan, both for fossil-fuel and nuclear power plants. Responding to ever increasing demand for electric power, unit output of oil-burning power plants had increased tenfold from 60 to 600 MW during the first Stage. It reached

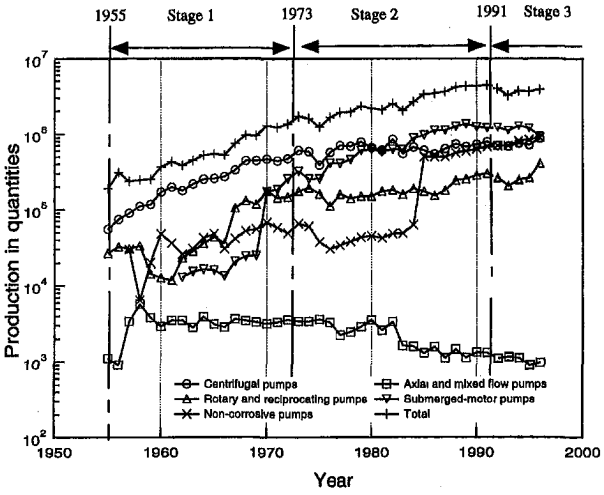

Fig. 2 Annual production of pumps in quantity

1000 MW in 1975 and has saturated since then. The situation of nuclear power plants is quite similar. The largest unit output of PWR and BWR plants reached the 1100 MW class at the end of the first stage and stayed almost constant till 1996 when an ABWR of 1300 MW class started operation.

The demand for bigger unit capacity has gone hand-in-hand with the demand for higher thermal efficiency. Figure 3 shows also the evolution of the highest delivery pressure and shaft power of boiler feed pumps (BFP). The pressure and temperature condition of oil-burning power stations jumped from sub-critical to super-critical in 1968. The development of BFPs succeeded in following the plant demands and played an essential role for the improvement of thermal efficiency.

The story of BFPs is just an example of many other success stories. Tankers became bigger and bigger. The capacity of blast furnaces expanded year after year. We could find the introduction of numerous record-breaking pumps every year in the Annual Review Issue of *JSME Journal* during the first stage. This glorious age of pumps was terminated by the assault of the oil crises. The development of pumps thenceforth became difficult to recognize from the superficial figures of specifications. Improved efficiency, higher reliability, easy maintenance, rationalized design, and manufacturing processes leading to cost reduction; all these advances are invisible but quite essential to the demands of present society.

Evolution of Research

For the survey of past research on pumps carried out in Japan, papers published in the *Transaction of JSME,* Series B were

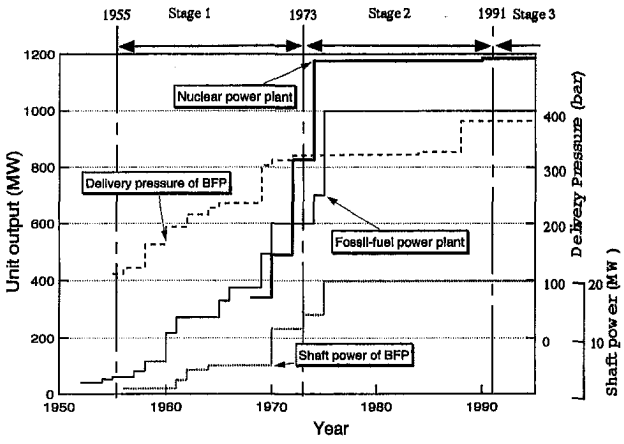

Fig. 3 Evolution of the record capacities

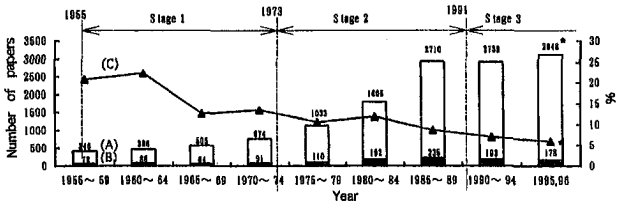

Fig. 4 Number of papers published in the *Transactions of JSME,* Series B

surveyed. Series B includes papers on fluids engineering (fluid mechanics and turbomachinery) and thermal engineering (thermodynamics, heat transfer and thermal power plant) of roughly equivalent number.

Figure 4 shows the evolution of research publications. To reduce an excessive fluctuation, the number of papers published in the five years duration is summed and shown by histogram. The height of white bars (A) indicates the total number of papers published in Series B, while the shaded height (B) that of pump-related papers. Research on gas-handling machinery such as fans and blowers are considered as pump-related, as long as the effect of compressibility does not play a primary role on the result. The ratio of pump-related papers to the total, B/A, is indicated by line C. The number of pump-related papers has been increasing, however, the increase is relatively low compared to the increase of total papers. The ratio has decreased from 22 percent to 6 percent over the last 40 years. In the fifties and early sixties, nearly half of fluids engineering research was pump-related, a vast field of application. The pump share has decreased by two-thirds since then, and this fact shows that fluids engineering has cultivated new fields of application in emerging technologies.

It is interesting to observe that the increase of pump-related papers was rather low (1.2 percent annually) in the first stage when pump production was soaring. On the contrary, the pump research was remarkably activated by the annual growth rate of 5.2 percent in the second stage when the pump production was rather stagnant. This implies that a booming economy may spoil the driving force for innovative products. Difficulty is the mother of progress. In order to follow the shift of interest in pump research, pump-related papers were classified into the following eight groups of topics:

(1) Flow phenomena in pump elements such as impellers and diffusers, sub-divided into steady and unsteady phenomena.
(2) Analysis and prediction of overall performance of pumps, sub-divided into steady and unsteady aspects.
(3) Fluid force on pump elements like vanes and impellers, sub-divided into steady and unsteady phenomena.
(4) Cavitation study; inception, collapse, performance, noise and acoustics, damage, etc., sub-divided into fluid phenomena and material damage.
(5) Multi-phase flow in pumps; phenomena and performance of pumps handling solid particles in liquid and gas bubbles in liquid.
(6) Application of Computational Fluid Dynamics (CFD) to pumps, and active control of performance.
(7) Unsteady phenomena in piping system.
(8) Non-turbo pumps; rotary and reciprocating pumps, jet pumps, water-hammer pumps, air-lift pumps, etc.

The number of papers in each group is summed up for five years duration and the percentage of each group to the total pump-related papers in the same period is plotted in Fig. 5. It can be seen from this figure that the study of steady flow phenomena in pump elements and unsteady phenomena in piping

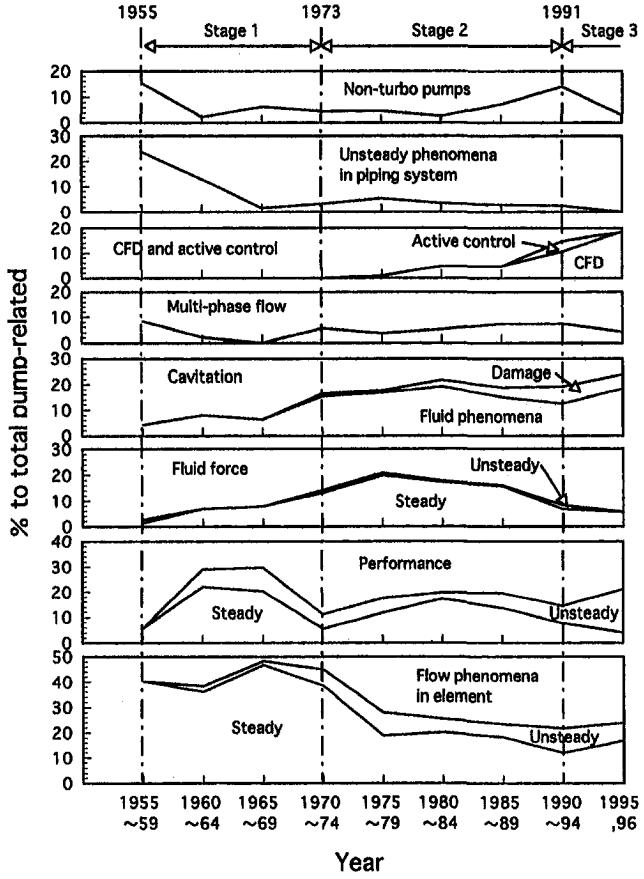

Fig. 5 Composition of the topics of pump-related papers

systems showed a drastic decrease from the first to the second stage. The opposite tendency is obvious in the study of unsteady flow phenomena in pump elements, fluid force, cavitation, gas/liquid multi-phase flow, CFD, and active control of performance.

The research trends may be characterized by a closer approach to real internal flow mechanisms and diversification of research topics. In stage 1, most of the studies were on axial or centrifugal machines characterized by 2D linear or circular cascade analysis. This evolved into the studies of mixed flow impellers, diffusers and volutes in stage 2, with the shifts through quasi 3D to pure 3D analysis. Studies in stage 3 include detailed internal flow measurements and CFD to correlate the development of secondary flows including tip leakage flows with over-all performance, studies on specific pumps such as inducers, screw pumps, regenerative pumps, pumps for high viscosity fluids and so on. Recent increase of non-turbo pumps includes jet pumps, air-lift pumps, oscillating-pipe pumps and pumps utilizing Weis Fogh mechanisms. Developments of drainage pumps operable at any suction water level in stage 3 symbolize the diversification of demand from classical performance to reliability in operation.

Turning to unsteady flow research, classical studies of cascade flutter, surge, rotor-stator interactions and unsteady performance in stage 1 are followed by studies that include the effects of stall, boundary layer response, cavitation and 3D effects. Studies of transient performance and those of rotordynamics were started in stage 2 and extended to cover various cases.

The evolution of cavitation studies is somewhat different from others. In stage 1, observation of cavitation and cavitation performance in real pumps were of major interest. More fundamental studies of cavitating flows on foils and cascades, bubble dynamics and damage were made in stage 2, leading to the efforts to quantitatively predict damage in real pumps in stage 3. Cavitation surge, is more closely correlated with internal flow effects and the mechanisms of rotating cavitation were studied in stage 3.

The study of fluid force and cavitation is closely connected with the assurance of noise and vibration-free operation, which became increasingly important to meet the regulations for the surrounding environment. The largest feature of the second stage is the proliferation of computer and information technologies. The application of CFD to the research and design of pumps will accelerate further into the third stage. Application of the inverse method will become a common tool of design also in this stage.

Papers on active control of performance appeared a decade ago and have been increasing. If active control of turbulent flow becomes a realistic technology, it will evoke new research that apply it to the internal flow of pumps.

Pumps in the Third Stage

Pumps have two different faces. One is the face of a record-challenging machine with the utmost in advanced technologies. Pumps are the heart of every liquid-handling system. The more challenging the system, the more difficult the development of the required pumps becomes. A good example is the turbopumps of liquid-propellant rocket engines. High performance rocket engines require the most advanced pumps in terms of compactness and lightweight. This face is worth demonstrating in the showcase of pumps.

The other is a quite common face as a component of a piping system. The function of pumps in a piping system is to increase the pressure and is just opposite to that of valves, which reduce pressure by adjusting flow resistance. Pumps are merely one of numerous piping components, as it is the case for valves, bends, branches, etc. The majority of pumps bear this common face. The value of these common pumps consists in high reliability, easy maintenance and operation, and low cost.

Engineers and researchers who have a stake in pumps, wish naturally to be involved in the R&D of record-breaking pumps with the former face. Such cases have been, however, quite scarce in recent years and we can mention only a few examples such as the hydrogen and oxygen turbopumps for the LE-7 rocket engine (Kamijo, 1993), a down-hole pump for geothermal power generation (submerged-motor pump in 200°C water) (Katsuta, 1996), a compact, high-powered pump for water jet propulsion (Kawakami, 1993), a 600 bar high pressure centrifugal pump for sea bedrock crushing (Manabe, 1981), etc. Such opportunities may be also scarce, sorry to say, in the present stage as was the case in the second stage.

A pump has a life cycle. Research, design, manufacturing, test, and installation constitute the predelivery cycle, while operation and maintenance do the postdelivery cycle. The costs incurred during the predelivery cycle make up the initial cost, while those during the postdelivery cycle the operational cost. Poor reliability pays a big penalty as a consequence in term of increased operational cost.

Let us consider the case of a Primary Loop Recirculating Pump of a BWR plant. The pump is expected to operate for 40 years (plant life) with the highest reliability, since any trouble with the pump, even an excessive leakage from the shaft seal, leads to a shutdown of the whole plant. In order to maintain a high level of reliability for plant life, the costs during the postdelivery cycle become essentially higher than the initial cost (for pump reliability, refer to Makay and Szamody, 1978).

For the majority of pumps in service, long life, reliability and life-cycle costs will become the largest concern in the decades to come. This sort of target is not easy to handle, since a variety of engineering disciplines are involved and must be coordinated and integrated effectively. There are still a variety of key technologies that are waiting further advance and breakthrough. To

mention a few, countermeasures for cavitation erosion, quantitative prediction of unsteady fluid loading, air/water two-phase flow pumps with large void fraction, structural vibration analysis under liquid/structure interaction, maintenance-free bearings and shaft-seals, pumps with a wide operational range, fluid dynamical design for easy manufacturing, etc. are the examples of such technologies. Fluids engineering plays a fraction of the total role in the development of pumps; however, it has the possibility of making a fundamental breakthrough for higher reliability and lower costs.

Conclusion

The social and industrial background of post-war Japan has been classified into three stages of development with unique characteristics. The production of pumps in sales and quantity was analyzed by statistical data and the evolution was correlated with the features of the corresponding background stages. Similar analysis was made also for papers on pump-related research published in the *Transaction of JSME,* Series B (fluids and thermal engineering).

As the value of pumps, such qualifications as high reliability, easy maintenance/operation and low costs will be sought as top priority in the decades to come. The shift of value can be described in a simple wording as "from predelivery to postdelivery." Fluids engineering has the possibility of making an essential break-through for these targets.

Acknowledgments

The authors express their gratitude to the pump manufactures of Japan for offering information on state-of-the-art pump technology. They thank also Dr. S. Satake of Kogakuin University and Dr. K. Sato of Osaka University, for their assistance in preparing this paper.

References

Gopalakrishnan, S., 1999, "Pump Research and Development—Past, Present, and Future, an American Perspective," ASME JOURNAL OF FLUIDS ENGINEERING, Vo. 121, June, pp. 237–247.

Hergt, P. H., 1999, "Pump Research and Development, Past, Present and Future," ASME JOURNAL OF FLUIDS ENGINEERING, Vol. 121, June, pp. 248–253.

Kamijo, K. et al., 1993, "Hydraulic and Mechanical Performance of LE-7 LOX Pump Inducer," AIAA *Journal of Propulsion and Power,* Vol. 9, No. 6, pp. 819–826.

Katsuta, S., 1996, "Japanese Submergible Pump," Geothermal Down-Hole Production Pump Workshop, Geothermal Resources Council, March 1996, Ontario, CA.

Kawakami, T., et al., 1993, "Water-Jet Propulsion Unit for High Speed Hydrofoil Catamaran," *Proceedings of the Second International Conference on Fast Sea Transportation,* Dec., Yokohama, Japan, 1499–1510.

Manabe, N., et al., 1981, "Development of Super High Pressure Centrifugal Pump for Water Jet Bedrock-Crushing," *Technical Review,* Mitsubishi Heavy Industries, Ltd., Oct., pp. 211–221.

Makay, E., and Szamody, O., 1978, "Survey of Feed Pump Outages," EPRI Report FP-754, Apr.

Ohashi, H., 1996, "Evolution of Engineering Education—Past, Present and Future," *Journal of Japan Association of Engineering Education,* Vol. 44, No. 4, pp. 6–11.

The Japan Association of Industrial Machinery, 1955–1996, Statistics of Industrial Activities, Annual Report (in Japanese).

Yoshiki Yoshida
Associate Professor.
e-mail: yoshida@me.es.osaka-u.ac.jp

Yoshinobu Tsujimoto
Professor.

Graduate School of Engineering Science,
Osaka University,
1-3, Machikaneyama, Toyonaka,
Osaka 560-8531, Japan

Nobuhiro Ishii
Engineer, Hitachi Construction
Machinery Co., Ltd.,
650, Kandatsu, Tsuchiura,
Ibaraki 300-0012, Japan

Hideo Ohashi
President, Kougakuin University,
1-24-2, Nishishijuku Shinjuku,
Tokyo 163-8677, Japan

Fumitaka Kano
Professor, Nara National
College of Technology,
22, Yata, Yamatokoriyama,
Nara 639-1058, Japan

The Rotordynamic Forces on an Open-Type Centrifugal Compressor Impeller in Whirling Motion

In recent years, increasing interest has been given to the rotordynamic forces on impellers, from the view point of the shaft vibration analysis. Previous experimental and analytical results have shown that the fluid-induced forces on closed-type (with shroud) centrifugal impellers in whirling motion contribute substantially to the potential destabilization of subsynchronous shaft vibrations. However, to date nothing is known of the rotordynamic forces on open-type (without shroud) centrifugal impellers. This paper examines the rotordynamic fluid forces on an open-type centrifugal compressor impeller in whirling motion. For an open-type impeller, the variation of the tip clearance due to the whirling motion is the main contribute to the rotordynamic forces. Experiments were performed to investigate the rotordynamic forces by direct measurement using a force balance device, and indirectly from the unsteady pressure on the casing wall over a range of whirl speed ratio (Ω/ω) for several flow rates. In this paper, the following results were obtained: (1) Destabilizing forces occur at small positive whirl speed ratio ($0 < \Omega/\omega < 0.3$) throughout the flow range of normal operation; (2) At smaller flow rate with inlet backflow, the magnitude of the fluid force changes dramatically at a whirl speed ratio close to $\Omega/\omega = 0.8$, resulting in destabilizing rotordynamic forces. From the measurement of unsteady inlet pressure, it was shown that the drastic changes in the fluid force are related to the coupling of the whirling motion with a rotating flow instability, similar to "rotating stall"; (3) The forces estimated from the unsteady pressure distribution on the casing wall and those estimated from the pressure difference across the impeller blades were compared with the results from the direct fluid force measurements. The direct fluid forces correlate better with the forces due to the pressure distribution on the casing wall.

Introduction

Over the last ten years many experimental and analytical data have been obtained on the fluid-induced rotordynamic forces on pump impellers, mainly at Caltech and the University of Tokyo. It is now widely recognized that for closed-type (with shroud) centrifugal impellers, the fluid forces become destabilizing for the forward whirl generally at whirl speed ratio (Ω/ω) less than 0.5 (Jery et al., 1985; Bolleter et al., 1987; Ohashi et al., 1988). The destabilizing forces are caused by the unsteady interaction between the impeller and volute casing (Adkins et al., 1988; Tsujimoto et al., 1988a) or vaned diffuser (Tsujimoto et al., 1988b), or by unsteady leakage flow that surrounds the impeller shroud (Childs, 1989; Guinzburg et al., 1994). All these works have been summarized in the recent textbooks of Childs (1993) and Brennen (1994), which are extremely helpful and useful for shaft vibration analysts.

For axial turbomachines, the destabilizing mechanism associated with the tip clearance flow was first postulated by Thomas (1958) and Alford (1965). Their model explaining the destabilizing tangential force has been widely accepted. They pointed out that: in a turbine operating with an eccentric rotor, blades with smaller tip clearance would produce greater circumferential driving force than blades at the diametrically opposite position with larger tip clearance. This difference in blade loading results in a tangential force promoting the forward whirl. Recently, for axial compressors operating with rotor eccentricity, it was reported that the destabilizing whirl direction depends on the flow rate (Colding-Jorgensen, 1992; Ehrich, 1993). In addition, an MIT group investigated the rotordynamic forces on the axial flow turbine for the SSME (Space Shuttle Main Engine), both experimentally (Martinez-Sanchez et al., 1995) and analytically (Song et al., 1997). They reported that the fluid force on the rotor is basically generated as a result of the nonuniform blade loading, as explained by Thomas and Alford, with some fraction of the force caused by the nonuniform pressure distribution around the rotor.

Open-type impellers have been widely used for high-speed and high-pressure centrifugal compressors. Nevertheless, as far as the authors are aware, no rotordynamic data for these machines are available. This paper presents the results from an investigation of the rotordynamic fluid forces on an open-type centrifugal compressor impeller. Fluid forces were measured directly with a force balance device. Discussions on the unsteady pressure measurements on the casing wall, and blade to blade pressure distributions are also presented.

Experimental Facility

Description of Test Facility. Figure 1 shows the mechanism to generate the whirling motion. The inner sleeve supports the main shaft through two eccentric inner bearings set to produce a pure whirling motion. The main shaft is driven by an AC motor with the rotational speed (ω) through the universal joint, and the outer sleeve is driven by a DC motor controlled to run at a prescribed whirling speed (Ω). The main shaft speed was maintained at 400 ± 1 rpm, and the whirl speed ratio (Ω/ω) was varied in the range from −1.4 to +1.4. Uncertainty in the whirl speed

Contributed by the Fluids Engineering Division for publication in the JOURNAL OF FLUIDS ENGINEERING. Manuscript received by the Fluids Engineering Division August 17, 1998; revised manuscript received March 15, 1999. Associate Technical Editor: B. Schiavello.

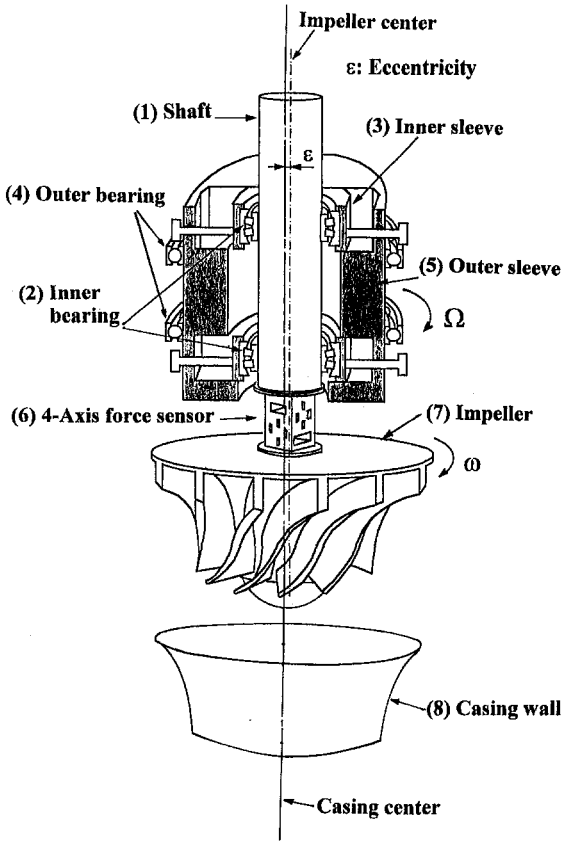

Fig. 1 Mechanism to produce the impeller whirling motion

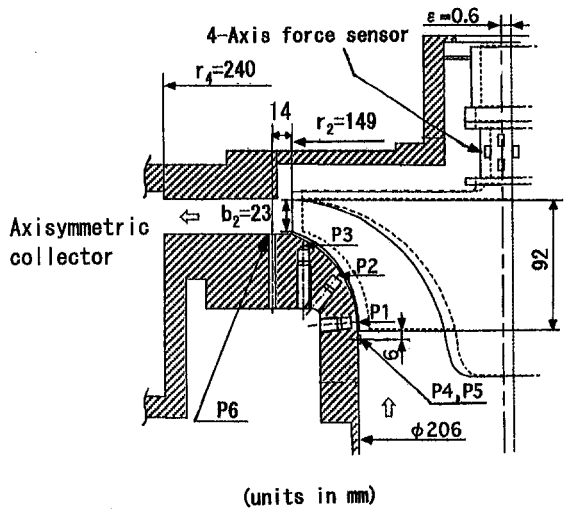

Fig. 2 Cross section of the test rig (impeller, casing and instrumended shaft)

ratio, Ω/ω, is ± 0.002. A detailed description of the facility can be found in Ohashi et al. (1991).

Figure 2 shows the details around the impeller. The test impeller is a model of an industrial centrifugal compressor with 12 blades (Z_i), inlet blade angle 32 deg and outlet 45 deg at the tip (i.e., back swept blade), outer radius (r_2) 149 mm, exit width (b_2) 23 mm; its nondimensional type number is 1.3. The impeller was running inside a vaneless diffuser with radius ratio $r_4/r_2 = 1.61$ and a symmetrical collector to minimize the interaction with stationary parts. Although the test impeller was designed for gas, water was used as the working fluid to facilitate the measurement of the fluid forces. The Reynolds number ($\mathrm{Re} = u_2 r_2/\nu$, $u_2 = r_2\omega$) is $3.0 \sim 4.0 \times 10^6$ for actual condition (air, $u_2 = 300 \sim 400$ m/s), and 0.92×10^6 for this laboratory test condition (water, $u_2 = 6.2$ m/s). The effect of compressibility of actual working fluid (gas) is neglected in the test condition (water). Under the condition without eccentricity, the blade tip normal clearance is constant (1 mm)

Nomenclature

b_2 = impeller axial width at outlet = 23 mm (see Fig. 2)
C = dimensionless direct damping coefficient, normalized by $\rho\pi r_2^2 b_2 \omega$
c = dimensionless cross-coupled damping coefficient, normalized by $\rho\pi r_2^2 b_2 \omega$
ΔG_p = coefficient of unsteady pressure Δp, normalized by $\rho(r_2\omega)^2$
$\Delta C_{p'}$ = coefficient of unsteady pressure $\Delta p'$, normalized by $\rho(r_2\omega)^2$
$\Delta C_{p''}$ = coefficient of unsteady pressure $\Delta p''$, normalized by $\rho(r_2\omega)^2$
F_1, F_2 = lateral fluid force in rotating frame (see Fig. 3)
F_n, F_t = fluid force, normal (n) and tangential (t) to whirl orbit (see Fig. 3)
f_n, f_t = dimensionless fluid force, normal (n) and tangential (t) to whirl orbit, normalized by $\rho\pi r_2^2 b_2 \varepsilon \omega^2$
f'_n, f'_t = dimensionless fluid force due to pressure difference across blades: $\Delta p'$, normal (n) and tangential (t) to whirl orbit, normalized by $\rho\pi r_2^2 b_2 \varepsilon \omega^2$
f''_n, f''_t = dimensionless fluid force due to pressure distribution on casing wall: $\Delta p''$, normal (n) and tangential (t) to whirl orbit, normalized by $\rho\pi r_2^2 b_2 \varepsilon \omega^2$
f = frequency (Hz)
j = imaginary unit
K = dimensionless direct stiffness coefficient, normalized by $\rho\pi r_2^2 b_2 \omega^2$
k = dimensionless cross-coupled stiffness coefficient, normalized by $\rho\pi r_2^2 b_2 \omega^2$
M = dimensionless direct added mass coefficient, normalized by $\rho\pi r_2^2 b_2$
m = dimensionless cross-coupled mass coefficient, normalized by $\rho\pi r_2^2 b_2$
p = pressure
Δp = unsteady pressure
$\Delta p'$ = peak-to-peak of unsteady pressure on casing wall at blade passing frequency
$\Delta p''$ = amplitude of unsteady pressure on casing wall with whirling frequency
Re = Reynolds number = $u_2 r_2/\nu$ (where $u_2 = r_2\omega$, ν: kinematic viscosity)
r_2 = impeller outlet radius = 149 mm (see Fig. 2)
t = time
Z_i = number of impeller blades = 12
β = circumferential angular difference between pressure taps P4 and P5 = 60 deg
γ = phase difference (deg)
ε = radius of circular whirl orbit = 0.6 mm
θ = circumferential angle
ρ = fluid density
ϕ = flow coefficient = flow rate/$(2\pi r_2^2 b_2 \omega)$
ψ = pressure coefficient = $(p - p_{t1})/\rho(r_2\omega)^2$, p_{t1}: total pressure at inlet
Ω = whirling angular velocity
Ω' = angular velocity of pressure pattern
ω = angular velocity of impeller
Ω/ω = whirl speed ratio

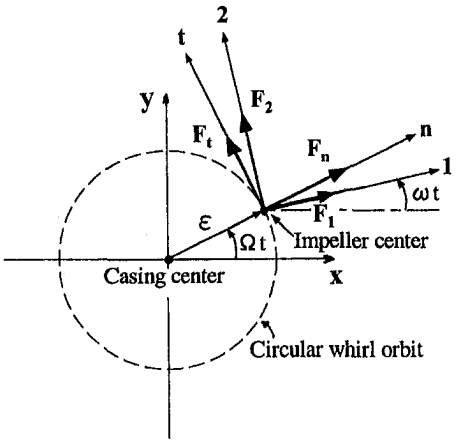

Fig. 3 Scheme showing the rotordynamic forces. F_n and F_t are the normal and tangential component to the whirl orbit. (ε: eccentricity, ω: shaft rotational speed, Ω: whirling speed, (1, 2): rotating frame of the force balance, (n, t): normal and tangential to the whirl orbit)

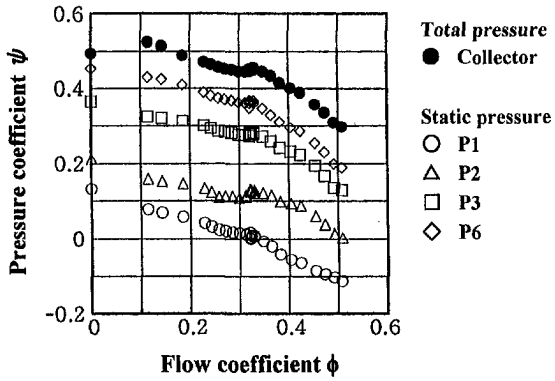

Fig. 4 Pressure performance of the test impeller and steady pressure on the casing wall without eccentricity, pressure coefficient ψ versus flow coefficient ϕ (uncertainty in $\psi \pm 0.005$, in $\phi \pm 0.01$)

from the inlet to outlet. In the present tests, an eccentricity $\varepsilon = 0.6$ mm was used for the whirl orbit radius. In this condition, the tip clearance varies in the angular direction in the range of 0.4 mm~1.6 mm at the inlet and 0.8 mm~1.2 mm at the outlet in phase respectively, due to the whirling motion.

Instrumentation and Data Acquisition System. The impeller is supported by the main shaft through a rotating force balance with a 4-axis force sensor, as shown in Fig. 1. The force balance is composed of two couples of parallel plates and 4 strain gauges per plate to measure the 4-axis forces (2 forces and 2 force moments). The strain signals were taken out through a slipring. The output signals from the strain gauges are converted to the forces (two) and moments (two) components using a transfer matrix determined from a dynamic calibration test. The outputs start to be recorded at the instant when both the direction of the eccentricity (Ωt) and the impeller rotational angle (ωt) come to a prescribed orientation. Figure 3 shows the situation at time t after the start of data recording, with both of the above directions set to be in x-direction. Output signals were ensemble-averaged over 32 whirl orbits based on the triggering signal that indicates the instant $\Omega t = \omega t = 0$ in Fig.3. The forces measured by the rotating force balance give the lateral components of the fluid force, F_1 and F_2 in a frame rotating with the impeller. The force components normal (F_n) and tangential (F_t) to the whirl orbit, which are useful for the rotor vibration analysis, were obtained from F_1 and F_2 using the angle $(\omega - \Omega) \times t$ between the frame (1, 2) and (n, t), as shown in Fig. 3. Both the fluid forces and force moments on the test impeller were measured in the present study. However in this paper, we focus only on the fluid forces, which play a primary important role for the whirl stability. Measured fluid forces are normalized as f_n, $f_t = F_n$, $F_t/(\rho\pi r_2^2 b_2 \varepsilon\omega^2)$, where ρ is fluid density. Uncertainty in the dimensionless fluid forces f_n and f_t is ± 1.5. We should note here that the tangential fluid force, f_t, is destabilizing for the whirling motion when $f_t \times (\Omega/\omega) > 0$. (i.e., f_t and Ω/ω are both positive or both negative.) In the case of the normal fluid force, f_n, a positive (outward) force could be considered as a destabilizing force in the sense that it tends to increase the radius of the whirl orbit.

P1~P6 in Fig. 2 show the location of pressure taps to measure the steady and unsteady pressure. P1~P3 and P6 were used to measure the steady pressure with a manometer. P6 is located downstream of the impeller at radius $r = 163$ mm (i.e., $r/r_2 = 1.09$.) In addition to this, P1~P3 and P4, P5 were used to measure the unsteady pressure with pressure transducers. P1~P3 on the casing wall are facing the impeller tip. P4 and P5 are located just upstream (6 mm) of the impeller inlet at different circumferential positions (separation angle, $\beta = 60$ deg.) to facilitate examination of the circumferential propagation of a rotating flow instability (described later). The diameter of the pressure taps, P1~P3, is 1 mm and silicone oil was filled in the cavity in front of the pressure transducers. The pressure transducers at P4 and P5 were installed flush with the casing wall. The resonance frequency of the measurement system is 2.2 kHz, while the blade passing frequency is 80 Hz ($Z_i \times \omega/2\pi$).

Results and Discussions

Compressor Pressure Performance. Figure 4 shows the static pressure coefficient (ψ) and steady pressure on the casing wall at various axial locations plotted against the flow coefficient (ϕ), under the conditions without eccentricity. The design flow coefficient is $\phi_d = 0.424$. From the flow visualization through the transparent casing made of acrylic resin with air bubble injection, backflow onset at the inlet was observed at $\phi = 0.32$, where the pressure rise reaches a local peak. The performance curve has a positive slope in a range of $\phi = 0.30$~0.32. The flow rates less than $\phi = 0.32$ will be called hereafter the low flow rates. For the measurements of fluid forces, the flow rate was varied from $\phi = 0.185$ to $\phi = 0.508$.

Fluid Forces Measured With Force Balance. Figure 5 shows the dimensionless normal, f_n, and tangential, f_t, fluid forces measured directly by the force balance versus the whirl speed ratio, Ω/ω, for various flow rates. From these results, it can be seen that the tangential fluid forces, f_t, on the unshrouded centrifugal impeller are destabilizing at small positive whirl speed ratio in the range $0 < \Omega/\omega < 0.3$ throughout all the flow range, even without the interaction between the impeller and volute casing or vaned diffuser. At the design flow rate of $\phi_d = 0.424$, the normal component is roughly quadratic and the tangential component is linear with whirl speed ratio. This was also found to be true for the case of a shrouded pump impeller in volute casing (Jery et al., 1985). From the quadratic behavior, it is suggested that the added mass effect contributes substantially to the normal component at the design flow rate. The direct added mass (M), cross-coupled added mass (m), direct damping (C), cross-coupled damping (c), direct stiffness (K), and the cross-coupled stiffness (k) can be obtained from rotordynamic force data if force can be expressed as a quadratic function of Ω/ω (Childs (1993) and Brennen (1994)). Table 1 presents the dimensionless rotordynamic coefficients obtained from the fluid forces in Fig. 5 (e) at the design flow rate. The dimensionless direct added mass coefficient, M, is 3.04, and "whirl ratio", k/C, is 0.34. These characteristics are the same as a shrouded pump impeller in volute casing (Jery et al., 1985). The dimensionless direct stiffness coefficient, K, is 1.82 (positive), while it is negative for a shrouded pump impeller. However, it should be noted here that the fluid forces change dramatically at

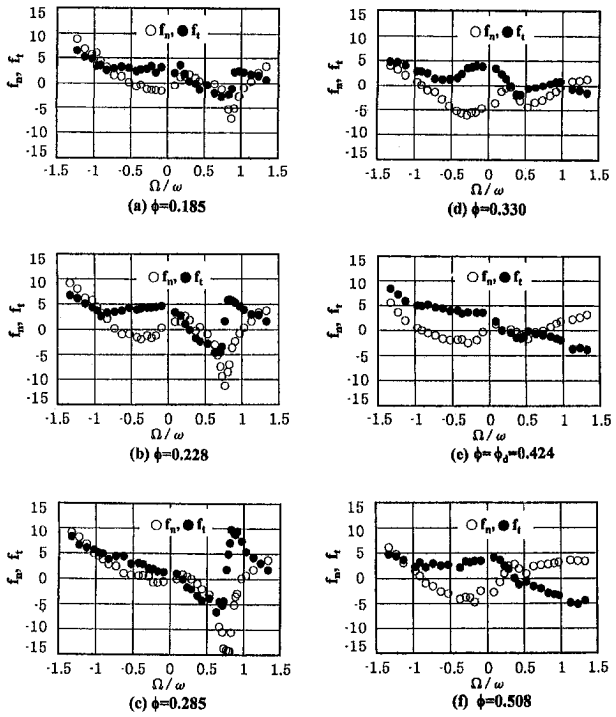

Fig. 5 Dimensionless fluid forces for ϕ = 0.185, 0.228, 0.285, 0.330, 0.434 ($=\phi_d$), and 0.508 ± 0.01, normal f_n and tangential f_t components versus while speed ratio Ω/ω (uncertainty in f_n, f_t ± 1.5, in Ω/ω ± 0.002)

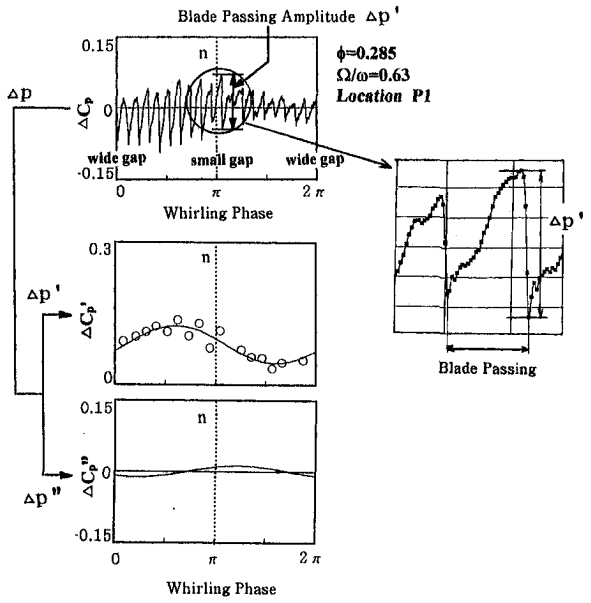

Fig. 6 Evaluation of the peak to peak of the blade passing ($\Delta p'$) and the unsteady pressure with whirling frequency ($\Delta p''$) from the unsteady pressure on the casing wall (Δp), for location of P1, ϕ = 0.285, and Ω/ω = 0.63 (uncertainty in ΔC_p ± 0.005, in ϕ ± 0.01, in Ω/ω ± 0.002)

the low flow rates in the presence of backflow. In particular, at whirl speed ratio close to Ω/ω = 0.8, the tangential component changes significantly from being negative to a high positive value.

Ohashi et al. (1990) reported experimentally that the destabilizing tangential fluid force on a shrouded pump impeller with vaned diffuser increased suddenly at low flow rate for the whirl speed ratio of Ω/ω = 0.05. They attributed this to the rotating stall in the vaned diffuser. Moreover, Tsujimoto et al. (1987) calculated the fluid forces on a whirling impeller in a vaneless diffuser using 2-dimensional vortical flow analysis. They also reported that, at low flow rate, the tangential fluid force becomes destabilizing at the whirl speed ratio (Ω/ω) close to the propagating speed ratio Ω'/ω = 0.157 of the diffuser rotating stall, and Ω'/ω = 0.988 of the impeller rotating stall. Recently, Bently et al. (1998) reported from the experimental results of perturbation test of a centrifugal compressor, that the fluid-induced direct stiffness drops dramatically during rotating stall. The significant change of the fluid forces for Ω/ω = 0.8 in the present study will be discussed later from the detailed examination of the unsteady pressure on the casing wall.

Table 1 Dimensionless rotordynamic coefficients for ϕ_d = 0.424

M, m : normalized by $\rho\,\pi r_2^2 b_2$

C, c : normalized by $\rho\,\pi r_2^2 b_2 \omega$

K, k : normalized by $\rho\,\pi r_2^2 b_2 \omega^2$

M	3.04
m	-0.053
C	4.30
c	-0.081
K	1.82
k	1.48

Force Estimated From Unsteady Pressure Distribution. The fluid forces on the impeller are estimated from the unsteady pressure measurements on the casing wall to possibly obtain a better understanding of their origin. Two simple ways of estimation are employed. The first is to integrate the blade forces that are evaluated from the pressure difference across the blade measured on the casing wall. This corresponds to the nonuniform blade loading model proposed by Thomas (1958) and Alford (1965). The second is simply to integrate the pressure distribution on the casing wall to estimate the reaction forces. In this case the forces due to the pressure distribution and the momentum transfer at the inlet and outlet, and the rate of change of fluid momentum in the impeller are neglected.

Unsteady pressure on the casing wall (Δp at locations P1, P2, and P3) consists of the blade passing frequency and the whirling frequency components. Figure 6 shows a typical example of unsteady pressure, Δp, measured on the casing wall at the location of P1, for ϕ = 0.285, and Ω/ω = 0.63. In this figure, the horizontal axis represents the phase of the whirling during a period, in which the clearance gap is widest at 0, 2π, and smallest at π, at the location of pressure measurement (P1). During one period of the whirling, the number of blades passing by the pressure transducer is $Z_i \times |\omega/\Omega|$. For the condition shown in Fig. 6, nineteen waves ($Z_i \times |\omega/\Omega|$ = 19.05) due to the blade passing are clearly observed. The amplitudes of the component with blade passing frequency, denoted as $\Delta p'$ used for the estimation of the blade loading, were obtained from the reading of peak-to-peak values for each blade passing, as shown in the top of Fig.6. A detail of the pressure wave form of the blade passing is shown in the figure. On the other hand, the pressure fluctuation with whirling frequency, denoted as $\Delta p''$ used for the casing pressure force evaluation, was obtained from the Fourier transform analysis of Δp, as shown in the bottom of Fig. 6.

For the blade load evaluation, it is assumed that $\Delta p'$ shows the pressure difference across the blade at the tip, and the pressure differences from the tip to hub are proportional to the square of its radius. The forces (f_n', f_t') are estimated by integrating the assumed pressure differences on the three segments of the blade using $\Delta p'$

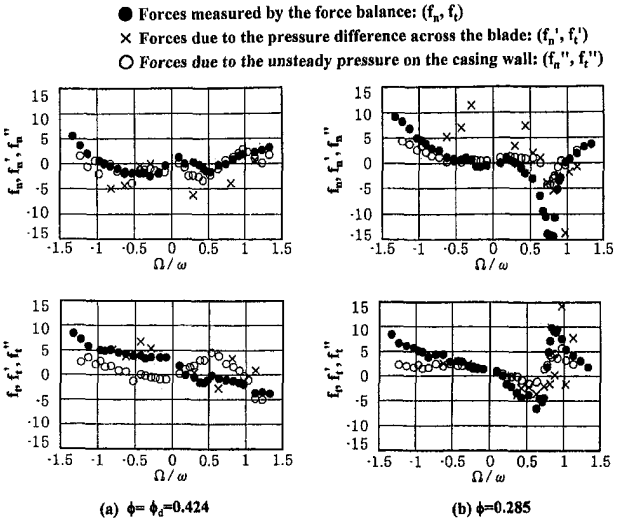

Fig. 7 Comparisons of the dimensionless direct fluid forces (f_n, f_t) with the estimated fluid forces (f_n', f_t') due to the pressure difference across the blade, and (f_n'', f_t'') due to the unsteady pressure on the casing wall (uncertainty in f_n, f_t ± 1.5, in Ω/ω ± 0.002)

at P1, P2, and P3 in consideration of the back swept blade. For the casing pressure force evaluation, the fluid forces (f_n'', f_t'') are obtained by integrating the pressure distributions $\Delta p''$ from the blade leading edge to trailing edge on the casing wall. The pressure distributions are interpolated and extrapolated from $\Delta p''$ at P1, P2, and P3.

Figure 7 shows the comparison of the direct fluid forces (f_n, f_t) measured with the force balance and the estimated forces (f_n', f_t'), and (f_n'', f_t''), for the design ($\phi_d = 0.424$) and low flow rate ($\phi = 0.285$) conditions. The fluid forces (f_n'', f_t'') agree fairly well with (f_n, f_t), while (f_n', f_t') are not in good agreement. Thomas (1958) and Alford (1965) explained the destabilizing mechanism in axial flow turbines from the blade loading nonuniformity due to the change in tip clearance. The present results may suggest that some fraction of the fluid force on the impeller is caused by the nonuniform pressure distribution on the casing wall, so that a different flow model is needed to explain the rotordynamic forces on unshrouded centrifugal impellers.

Coupling of Whirling Motion With Rotating Flow Instability at Low Flow Rate. Figures 8 and 9 show the unsteady pressure at the inlet at the design ($\phi_d = 0.424$) and lower flow rate ($\phi = 0.285$) conditions, without eccentricity. Figures 8 (*a*) and 9 (*a*) show the wave forms measured at the locations of P4 and P5; P4 and P5 are at the same axial location, but P5 is 60 deg ahead of P4 in the direction of the impeller rotation. Figures 8 (*b*) and 9 (*b*) show the time averaged cross spectra between P4 and P5, and Figs. 8 (*c*) and 9 (*c*) the phase (γ) of the pressure at P5 relative to that at P4. At the design flow rate, the blade passing ($f = 80$ Hz ($Z_i \times \omega/2\pi$)) is clearly shown in the wave form. However, it is not very clear at the lower flow rate. At the low flow rate, there are some peaks in the cross spectrum (Fig. 9(*b*)), although the cross of amplitudes ($\Delta p_4 \times \Delta p_5$) of these peaks are much smaller (approximately 1~3%) than that of the blade passing frequency. The discrete components (i), (ii), and (iii), in Figs. 9 (*b*) and (*c*), have the frequency of $f = 5.3$, 10.8, and 17.0 Hz, and the phase $\gamma = -60$, -150, and -200 deg, respectively. These values of phase difference are close to integer multiples of circumferential angular distance ($\beta = 60$ deg) of two sensors; i.e., $\gamma \cong -n\beta$, $n = 1$, 2, and 3. This suggests that pressure patterns with the number of cells $n = 1$, 2, and 3 are rotating at the inlet much like conventional rotating stall. However, unlike conventional rotating stall, these frequency components (i), (ii) and (iii) are found only at the inlet. The propagating speed ratio of these components is $\Omega'/\omega = f/n(\omega/2\pi) \approx 0.79$ which is very close to the value of $\Omega/\omega = 0.8$ where the abrupt change in f_n and f_t is found at the low flow rate under whirling motion. The group of frequency components (iv) distributed over a wide range of frequency $f = 20$~60 Hz has the characteristic that the phase (γ) decreases linearly with the increasing frequency f. Here, when we assume a circumferentially propagating pressure pattern Δp with frequency f and propagating speed Ω', that is $\Delta p \propto \exp\{2\pi f j \times (t - \theta/\Omega')\}$, the phase γ measured between P4 and P5 is expressed as $\gamma = -2\pi f\beta/\Omega'$ (where $\theta = \beta = 60$ deg). With constant Ω', this relation between γ and f is linear. This situation agrees with the component (iv) found in the range of $f = 20$~60 Hz as shown in Fig. 9 (*c*). From the slope of $\Delta\gamma/\Delta f$ in Fig. 9 (*c*), the propagating speed ratio was estimated to be $\Omega'/\omega = 0.43$ in the present study. From the above discussion, frequency components (i)~(iii) correspond to discrete frequencies where $2\pi f/\Omega' = n = 1$, 2, and 3 (where $\Omega'/\omega = 0.79$), while for the frequency component range (iv) the value of $2\pi f/\Omega'$ varies continuously from 7 to 21 as f varies from 20~60 Hz ($\Omega'/\omega = 0.43$). All of the components (i)~(iv) appeared at lower flow rate $\phi < 0.32$ where the inlet backflow was observed from the flow visualization. However, further study is needed to clarify the relation between the backflow and these pressure fluctuations.

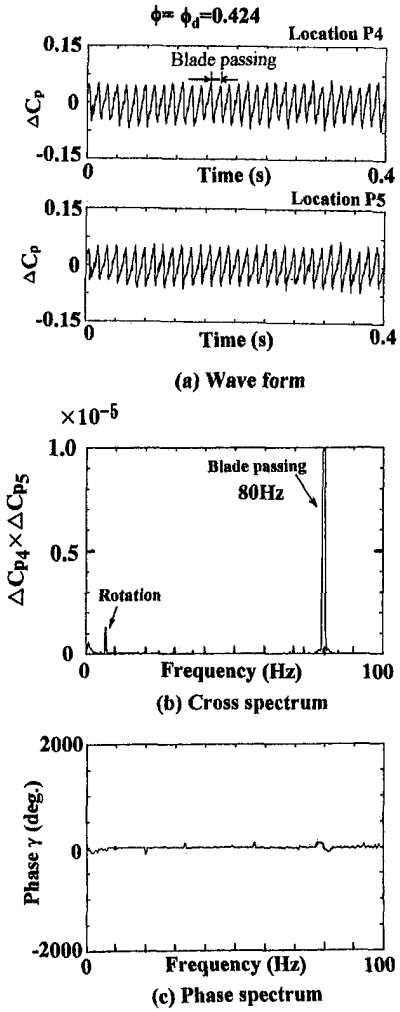

Fig. 8 Typical wave form of unsteady pressure, cross, and phase spectrum at the impeller upstream locations P4 and P5, $\phi = \phi_d = 0.424$ ± 0.01, without eccentricity (uncertainty in ΔC_p ± 0.005, in frequency f ± 0.4 Hz, in phase γ ± 5 deg)

Kameier et al. (1997) also observed similar rotating pressure pattern with a constant slope $\Delta\gamma/\Delta f$ at low flow rate in an axial compressor. In this case, the propagating speed ratio increased

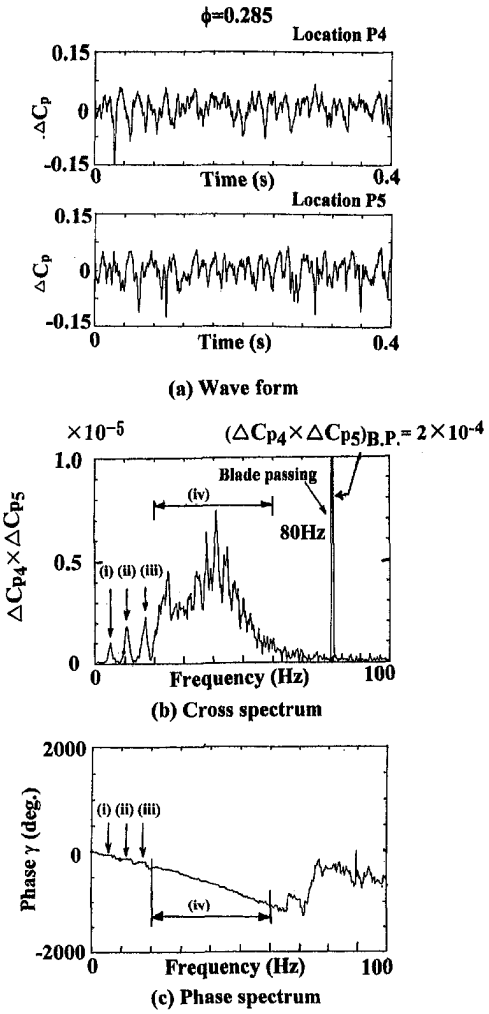

Fig. 9 Typical wave form of unsteady pressure, cross, and phase spectrum at the impeller upstream locations P4 and P5, ϕ = 0.285 ± 0.01, without eccentricity (uncertainty in ΔC_p ± 0.005, in frequency f ± 0.4 Hz, in phase γ ± 5 deg)

from 0.3 to 0.55 as the flow rate decreased. From their experimental results for the cases with two tip clearances (wide and small) and a test with Velcro tape inserted in the tip clearance, they concluded that these patterns of pressure fluctuation are associated with the leakage flow through the tip clearance under reversed flow condition.

Figure 10 shows the comparison of the pressure fluctuations measured at the location P1 with a whirl eccentricity, ε = 0.6 mm. The wave forms of pressure fluctuation were ensemble-averaged 32 times based on the triggering signal that indicates the instant when the direction of the eccentricity and the impeller rotation angle are at a prescribed orientation relative to the pressure transducer. The dotted line, denoted as "n" in the figures, indicates the instant when the smallest tip clearance passes by the pressure transducer. The amplitude of the blade passing component, or the blade loading, varies with the whirling. At the design flow rate (Fig. 10 (*a*)), the variation of the blade loading is not strongly affected by the whirl speed ratio within Ω/ω = 0.63~1.13. However at low flow rate (Fig. 10 (*b*)), the blade loading changes significantly with the whirling motion, and the location of the maximum blade loading (corresponding to the highest peak-to-peak fluctuation) relative to the location of the minimum tip clearance (n) shifts with the change in Ω/ω. The difference of the blade loading is largest at Ω/ω = 0.81. This and the large change of the fluid forces near Ω/ω = 0.8 at low flow rates may be caused by the coupling of the whirling motion with the rotating pressure

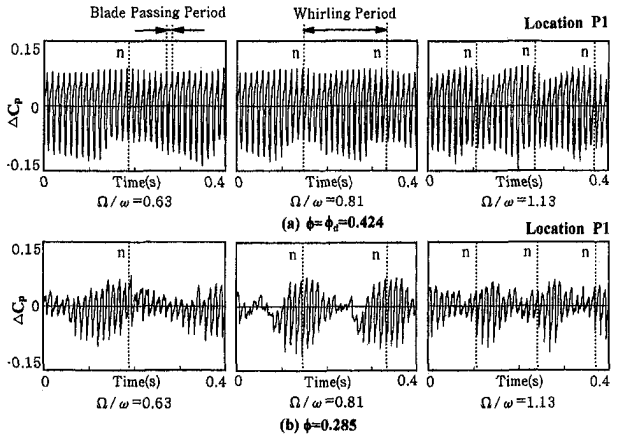

Fig. 10 Comparison of the pressure fluctuations on the casing wall between $\phi = \phi_d$ = 0.424 and ϕ = 0.285 with whirling motion ε = 0.6 mm, at location P1 for Ω/ω = 0.63, 0.81, 1.13 (uncertainty in ΔC_p ± 0.005, in Ω/ω ± 0.002, in ϕ ± 0.01)

pattern, i.e., component (i), found at the impeller inlet (Figs. 9(*b*) and 9(*c*)).

Conclusions

From the experimental results and discussions, the following conclusions can be drawn:

1. For an open-type centrifugal compressor impeller, the tangential fluid forces become destabilizing at small positive whirl speed ratio ($0 < \Omega/\omega < 0.3$) throughout all the flow range even without the interaction with a volute or vaned diffuser.
2. The forces estimated from the unsteady pressure on the casing wall agree well with the forces measured directly by the force balance. However, the forces estimated from the pressure difference across the impeller blades are not in good agreement with the direct force measurements.
3. The fluid forces change dramatically near the whirl speed ratio Ω/ω = 0.8 at the low flow rates. As a result, the tangential fluid force has a large positive value and enhances whirling close to this whirl speed ratio.
4. When the rotor has no eccentricity, it was found that pressure patterns with 1, 2 and 3 cells rotate at the impeller inlet with the speed ratio of Ω'/ω = 0.79 at low flow rates. In addition to this, it was found that the pressure patterns without definite number of cells propagate with the speed ratio of Ω'/ω = 0.43.
5. From the pressure measurements just downstream of the blade leading edge in presence of whirling motion, it is suggested that the destabilizing fluid force around Ω/ω = 0.80 is caused by the strong interaction of the whirling motion with the rotating flow pattern with Ω'/ω = 0.79.

Acknowledgments

The authors wish to express their gratitude for the effort of Mr. Shin Ishizaki in establishing the experimental procedure as a graduate project at Osaka University. They are also deeply grateful to Dr. Bruno Schiavello of Ingersoll-Dresser Pump Company for his extremely helpful and useful comments. The present study was partly supported by the Ministry of Education, Science, Sports and Culture through the Grant-in Aid for Developmental Scientific Research (No.06555055).

References

Adkins, D. R., and Brennen, C. E., 1988, "Analyses of Hydraulic Radial Forces on Centrifugal Pump Impeller," ASME JOURNAL OF FLUIDS ENGINEERING, Vol. 110, pp. 20–28.

Alford, J. S., 1965, "Protecting Turbomachinary from Self-Excited Rotor Whirl," ASME *Journal of Engineering for Power*, Vol. 87, pp. 334–344.

Bently, D. E., and Goldman, P., 1998, "Destabilizing Effect of Aerodynamic Forces in Centrifugal Compressors," *Proceedings of the 7th International Symposium on Transport Phenomena and Dynamics of Rotating Machinery*, Honolulu, Hawaii, Vol. A, pp. 306–315.

Bolleter, U., Wyss, A., Whelte, I., and Sturchler, R., 1987, "Measurement of Hydraulic Interaction Matrices of Boiler Feed Pump Impeller," ASME *Journal of Vibration, Acoustics, Stress and Reliability in Design*, Vol. 109, pp. 144–151.

Brennen, C. E., 1994, *Hydrodynamics of Pumps*, Concept ETI, and Oxford University Press.

Childs, D. W., 1989, "Fluid Structure Interaction Forces at Pump-Impeller-Shroud Surfaces for Rotordynamic Calculation," ASME *Journal of Vibration, Acoustics, Stress and Reliability in Design*, Vol. 109, pp. 144–151.

Childs, D. W., 1993, *Turbomachinery Rotordynamics*, Wiley, New York.

Colding-Jorgensen, J., 1992, "Prediction of Rotor Dynamic Destabilizing Forces in Axial Flow Compressor," ASME JOURNAL OF FLUIDS ENGINEERING, Vol. 114, pp. 621–625.

Ehrich, F., 1993, "Rotor Whirl Forces Induced by the Tip Clearance Effect in Axial Flow Compressor," ASME *Journal of Vibration and Acoustics*, Vol. 115, pp. 509–515.

Guinzburg, A., Brennen, C. E., Acosta, A. J., and Caughy, T. K., 1994, "Experimental Results for the Rotordynamic Characteristics of Leakage Flow in Centrifugal Pump," ASME JOURNAL OF FLUIDS ENGINEERING, Vol. 116, pp. 110–115.

Jery, B., Acosta, A. J., Brennen, C. E., and Caughy, T. K., 1985, "Forces on Centrifugal Pump Impellers," *Proceedings of the 2nd International Pump Symposium*, Houston, Texas, pp. 21–32.

Kameier, F., and Neise, W., 1997, "Experimental Study of Tip Clearance Losses and Noise in Axial Turbomachines and Their Reduction," ASME *Journal of Turbomachinery*, Vol. 119, pp. 460–471.

Martinez-Sanchez, M., Jaroux, B., Song, S. J., and Yoo, S., 1995, "Measurement of Turbine Blade-Tip Rotordynamic Excitation Forces", ASME *Journal of Turbomachinery*, Vol. 117, pp. 384–392.

Ohashi, H., Sakurai, A., and Nishihama, J., 1988, "Influence of Impeller and Diffuser Geometries on the Lateral Fluid Forces of Whirling Centrifugal Impeller," NASA CP. 3026, pp. 285–306.

Ohashi, H., Imai, H., Sakurai, A., and Nishihama, J., 1990, "Lateral fluid Forces of Whirling Centrifugal Impellers with Various Geometries," *The 3rd Japan-China Joint Conference of Fluid Machinery*, Vol. II, pp. 147–153.

Ohashi, H., Imai, H., and Tsuchihashi, T., 1991, "Fluid Force and Moment on Centrifugal Impeller in Precession Motion," ASME *Fluid Machinery Forum*, FED-Vol. 119, pp. 57–60.

Song, S. J., and Martinez-Sanchez, M., 1997, "Rotordynamic Forces Due to Turbine Tip Leakage: Part I - Blade Scale Effects, Part II - Radius Scale Effects and Experimental Verification," ASME *Journal of Turbomachinery*, Vol. 119, pp. 605–703, and pp. 704–713.

Thomas, H. J., 1958, "Instabile Eigenschwingungen von Turbinenlaeufern Angefacht durch die Spaltstroemung in Stopfubuchsen und Bechauchflug (Unstable Nature Vibrations of Turbine Rotors Induced by the Clearance Flows in Glands and Blading)," *Bulletin de L.A.I.M.*, Vol. 71, No.11/12, pp. 1039–1063.

Tsujimoto, Y., Acosta, A. J., 1987, "Theoretical Study of Impeller and/or Vaneless Diffuser Attributed Rotating Stall and Their Effects on Whirling Instability of Centrifugal Impeller," Work Group on the Behavior of Hydraulic Machinery under Steady Oscillatory Conditions, Lille, France.

Tsujimoto, Y., Acosta, A. J., and Brennen C. E., 1988a, "Theoretical Study of Fluid Forces on Centrifugal Pump Impeller Rotating and Whirling in a Volute," ASME *Journal of Vibration, Acoustics, Stress and Reliability in Design*, Vol. 110, pp. 263–269.

Tsujimoto, Y., Acosta, A. J., and Yoshida, Y., 1988b, "A Theoretical Study of Fluid Forces on Centrifugal Pump Impeller Rotating and Whirling in a Vaned Diffuser," NASA CP. 3026, pp. 307–322.

Performance Analysis of Automotive Torque Converter Elements

E. Ejiri
Senior Researcher.

M. Kubo
Research Engineer.

Nissan Research Center,
Nissan Motor Co., Ltd.,
1, Natsushima-cho,
Yokosuka-shi 237-8523, Japan
e-mail: e-ejiri@mail.nissan.co.jp

The hydrodynamic performance of a three-element automotive torque converter is analyzed by measuring flow between the elements with five-hole Pitot tubes. The performance of each element, including head, head loss, and efficiency, is defined and evaluated. The results show that the pump is the major source of loss in the speed ratio range where vehicles are most frequently operated in everyday driving. The loss coefficients for the three elements are also evaluated using a one-dimensional flow model. The friction loss coefficient of the turbine shows small variation over the entire tested speed ratio range, whereas the coefficients of the pump and stator vary considerably according to the operating speed ratio. The cause of loss in the pump and stator is investigated by flow visualization and three-dimensional numerical flow analysis. A low kinetic energy region in the pump and leading edge separation in the stator are clearly visualized or computed.

Introduction

A torque converter is a kind of turbomachine that is widely used in today's automatic transmissions for automobiles. It consists of three major elements—a pump, a turbine, and a stator. Its functions include damping of engine torque fluctuation, damping of noise and vibration in the driveline, and automatic amplification of torque according to the difference in rotational speed between the input and output shafts without requiring any external control. Internal flow investigations and development of performance prediction methods for the torque converter have been carried out over the years, as its hydrodynamic performance has a significant influence on vehicle fuel economy and driving performance.

Some experimental work has been done to elucidate internal flow characteristics. Numazawa et al. (1983) reported their results of flow visualization in the pump and turbine blade passage obtained with a liquid resin method. Unsteady flow just behind the pump impeller was measured by Browarzik (1994). Brun et al. (1996) used a laser Doppler velocimeter to investigate the internal flow in the three elements. Dong et al. (1998) measured complex unsteady flow fields at the pump and turbine exits using five-hole Pitot tubes with high-response pressure transducers.

Flows through the three elements were computed by using CFD codes employing a finite difference method (Fujitani et al., 1988) and a finite volume method (Cigarini et al., 1995), thanks to the improvement of computer hardware and computational schemes. Some of the computational results showed good qualitative agreement with the measured flow patterns. This approach, however, cannot be considered practical yet for making overall performance predictions, in view of the considerable manpower and time required for mesh generation and program execution, among other drawbacks. Therefore, a simple and practical performance prediction method is still needed, one which employs empirical constants but yields results in a relatively short time with sufficient accuracy for practical application.

Practical performance prediction has mainly been performed on the basis of a one-dimensional angular momentum theory (Ishihara, 1955), which assumes a stream line representing internal flow in a torque converter. Efforts have been made to improve the prediction accuracy of this approach in order to apply it to various blade and channel specifications and performance requirements. Some researchers have introduced the exit flow angle and total pressure loss characteristics of the stator as computed by numerical simulation using a discrete vortex method (Minato et al., 1987) or viscous flow analysis (Kubo et al., 1994). One paper describes an attempt to adjust the stator exit flow angle as a way of obtaining good agreement between the calculated and measured torque converter performance (Abe et al., 1996). However, none of these studies sufficiently examined the pump and turbine hydrodynamic characteristics, and systematic approaches were not used to evaluate the performance characteristics of each element of the torque converter. Therefore, these methods have the drawback of poor performance prediction accuracy when design parameters such as the blade angles change considerably.

This paper describes an experimental procedure for clarifying the hydrodynamic characteristics of the three elements, defining the unit performance of each element and evaluating it on the basis of data measured with five-hole Pitot tubes between any two elements. It also examines the friction loss coefficients of each element in a one-dimensional flow model, and investigates the cause of loss generated in the pump and and stator where the friction loss coefficients change substantially. This is done in reference to the flow visualization results in the blade passage walls and the CFD results for the three-dimensional flow in the pump.

Experimental Apparatus and Procedure

Test Rig. A torque converter with a 236 mm nominal diameter and a circular torus cross-section was used, as shown in Fig. 1. The inlet and exit blade angles on the design path, a line that bisects the flow passage cross-sectional area, and the blade number for the three elements are shown in Table 1. The blade angle is defined as an angle from the meridional plane. The minus sign in the table indicates the rotational direction of the impellers, which means that the tested pump impeller had forward lean blades. The characteristic curves of the test torque converter without the Pitot tubes are shown in Fig. 2.

The input and output shafts of the torque converter were connected to DC dynamometers, with tachometers and torquemeters installed in between. These dynamometers were controlled so that the input torque was constant in a given speed ratio. As the stator was fixed, measurements were performed in a speed ratio range

Contributed by the Fluids Engineering Division for publication in the JOURNAL OF FLUIDS ENGINEERING. Manuscript received by the Fluids Engineering Division December 1, 1997; revised manuscript received March 12, 1999. Associate Technical Editor: B. Schiavello.

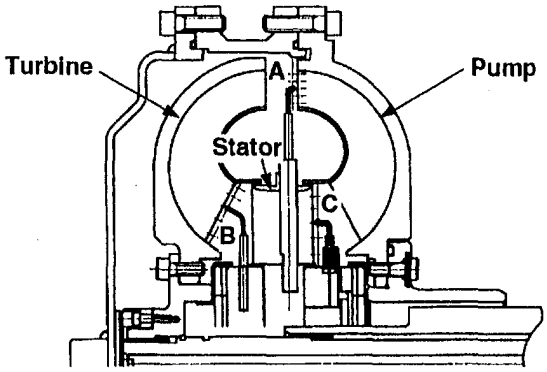

Fig. 1 Torque converter and Pitot tubes

between 0 to 0.8, where the output torque was larger than the input torque. The pump and turbine speeds for three typical speed ratios are shown in Table 2 for reference. An ordinary automatic transmission fluid was provided as the working fluid from an external pressure source and controlled so that the inlet pressure was 0.17 MPa, the outlet pressure 0.14 MPa and the exit temperature 80 ± 1°C for the torque converter.

Five-Hole Pitot Tube. Three different types of spherical five-hole Pitot tubes (with a 2 mm probe diameter and a 0.2 mm pressure hole diameter) were made in order to measure flow between any two elements. They were calibrated for yaw and pitch angle in steady-state uniform flow in an oil tunnel. The calibration was conducted at the velocity near the Reynolds number under actual machine operation.

The measurement points (location of probe front) of the three measurement sections A, B, and C (pump exit, turbine exit and stator exit, respectively) are also shown in Fig. 1. The probe was traversed over 5 points to measure sections A and B, and over 25 points (5 points radial × 5 points peripheral) to measure section C. The probe was installed tightly in the test rig and flow velocity and pressure were calculated using the calibration curves for yaw and pitch angle. When calculating one-dimensional performance, the average for the section was found by weighting the data according to the mass flow at the measurement points.

Flow Visualization. The visualization method employed here resembles the oil film method and is outlined below. First, a material made primarily of heat deformable epoxy resin was liquified at high temperature and coated thinly on the blade passage walls. Second, the flow pattern was created on the surface of the material by operating the torque converter under the specified conditions. It took at least several minutes to create the flow pattern on the blade passage walls. Therefore, a short period of time (10–20 seconds) each for start up and shut down did not affect the steady flow pattern. Third, after hardening the material surface at room temperature, liquid silicon rubber was poured over it to form a thin film. The rubber film with the transcribed flow pattern was then detached from the material some hours later after the rubber had solidified. Finally, the rubber surface was covered with dye powder in order to make the engraved flow pattern more visible.

Table 1 Specification of three elements

Element	Inlet angle	Exit angle	Blade number
Pump	38°	-36°	31
Turbine	-60°	57°	29
Stator	0°	-58°	16

Computational Method

Viscous calculations were performed by using STAR-CD (Computational Dynamics, 1995), a general flow analysis code which employs a finite volume method of discretization. Three-dimensional incompressible time-averaged Navier-Stokes equations were solved with the code. A standard k-ε model (Launder et al., 1974) was used for turbulence closure modeling. In discretizing the convection terms of the equations, the QUICK scheme (Leonard, 1979), a third-order upwind differencing scheme, was used to obtain a stable solution while suppressing numerical diffusion. The SIMPLE algorithm (Patankar et al., 1972) was employed to solve the algebraic finite-volume equations resulting from the discretization operation.

To represent the complex geometry of the torque converter hydraulic elements accurately and distribute the computational meshes in an appropriate fashion, an in-house mesh generation program was used. Mesh-point clustering was performed near the boundary and cell deformity was checked with the program. The computational grid used in the present study is given in Fig. 3 where one blade passage is shown in each element to illustrate the

Nomenclature

e = speed ratio ($= \omega_2/\omega_1$)
H = head (nondimensional)
I = rothalpy ($= P/\rho + 1/2W^2 - 1/2U^2$)
h = head loss (nondimensional)
N = rotational speed
P = static pressure
P_T = total pressure
r = radius
s = distance along the design path (a line that bisects the cross-sectional area in the meridional plane), starting from upstream boundary and ending at downstream boundary of the computation domain of an element
T = torque
t = torque ratio ($= T_2/T_1$)
U = peripheral velocity
V = absolute velocity
W = relative velocity
α = relative flow angle from meridional plane
β = blade angle from meridional plane
ΔI = rothalpy change from upstream boundary of the computation domain of an element
ϕ = shock loss coefficient
η = efficiency
ρ = density
τ_1 = input torque capacity coefficient ($= T_1/N_1^2$)
ω = angular velocity
ζ = friction loss coefficient

Subscripts

0 = reference position (design path position at pump exit)
1 = pump
2 = turbine
3 = stator
A = measured section A (pump exit)
B = measured section B (turbine exit)
C = measured section C (stator exit)
f = friction
p = circulatory component (a direction perpendicular to measurement line or computation mesh line from shell to core in meridional plane)
s = shock
θ = tangential component
(i, j) = i = 1: pump; = 2: turbine; = 3: stator; j = 1: inlet; = 2: exit

Superscript

* = nondimensional

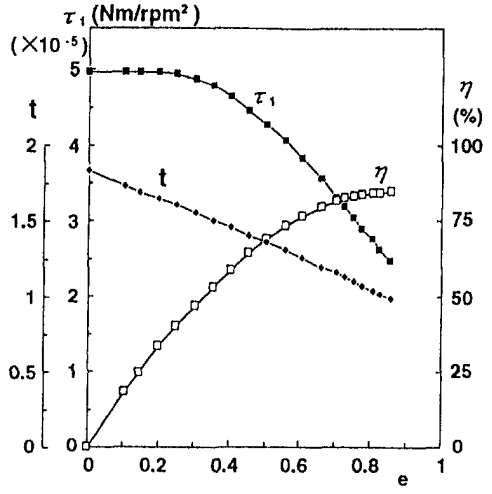

Fig. 2 Characteristic curves of torque converter

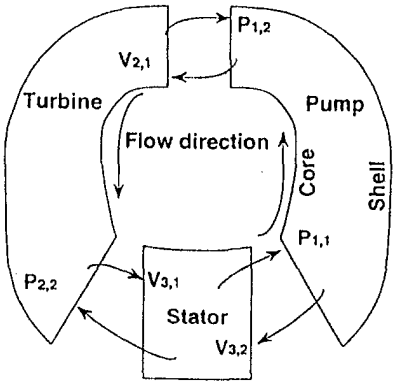

Fig. 4 Interface boundary conditions

grid distribution in the computational field for a total of about 68,000 grid cells.

The wall function for the velocity vector was used to reduce the grid points near the wall. A cyclic boundary condition was imposed on both peripheral boundaries outside a blade passage. The computation is performed on one element after another along the flow direction in a manner where either velocity or pressure is given as the inlet and exit boundary condition of each element. Computed pressures and velocities in each iteration are averaged circumferentially, transferred to the adjacent element and used as the boundary condition of the next iteration (Fig. 4).

The solution is assumed to have converged when all the normalized residuals of the mass and the momentum conservation equations are less than 10^{-2} and the rate of change in mass flow rate in two consecutive circulatory iterations is less than 10^{-3}. Typically, about 12 hours of CPU time were required to obtain a converged solution on an SGI INDIGO2-IMPACT (R4400, 250 MHz) for about 168,000 grid cells in total.

Several types of grid systems were used to evaluate the grid number dependence of the computational results. Figure 5 shows the grid number dependence of the solution in terms of the element efficiencies. The comparison suggests that a grid-independent solution was obtained with more than about 170,000 grid cells in total.

Table 2 Rotational speed of pump and turbine

Speed ratio	Pump	Turbine
0	1414rpm	0rpm
0.6	1596rpm	957rpm
0.8	1860rpm	1486rpm

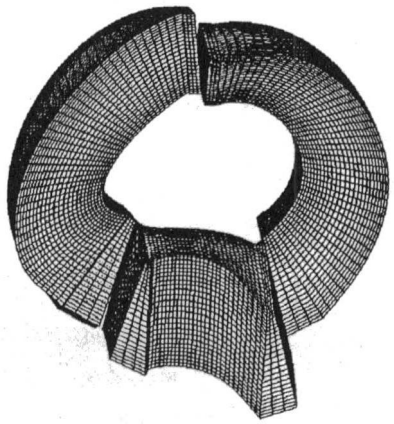

Fig. 3 Computational grid

Uncertainty in Experiment

The flow blockage effect, caused by the presence of any type of probes, on the torque transmission capacity τ_1 was less than 4%, which means circulatory flow rate decreased by at most 4% due to the blockage of the probe. A correction in the measured velocity and flow angle could be employed, however, such correction was not made here in order to avoid complexity. It was judged that the original flow field was almost entirely maintained even if a probe was present. Pressures from the five-hole Pitot tubes were transmitted to semiconductor transducers through the shortest tubes possible and the system showed a flat frequency response characteristic to 2 kHz in the design calculations. Although the flow was unsteady, the pressure data obtained were treated under the assumption of quasi-steady flow (Matsunaga et al., 1980).

The level of unsteady fluctuations measured by the probe varied with torque converter operating condition and measuring point. Generally speaking, the relative magnitude of velocity and pressure unsteadiness (RMS value of fluctuating quantities divided by time mean value) was 5–10% and 2–5% for the pump exit, and 4–7% and 2–3% for the turbine exit. The blade passing frequency of the pump (higher than that of the turbine) was at most 960 Hz in the measurement. Therefore, the fluctuation up to at least the second harmonic was captured, which was thought to be enough to evaluate the major part of the fluctuation. A set of 1,024 data were sampled at each measuring point and mass-averaged using instantaneous circulatory flow velocity at the point.

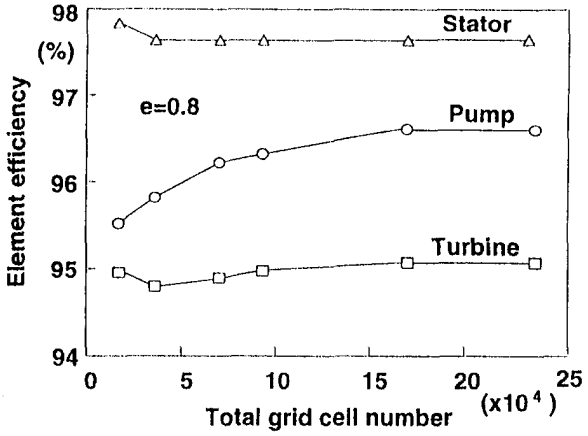

Fig. 5 Grid number dependence of solution

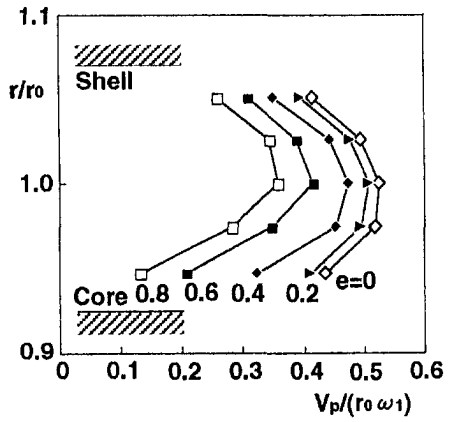

Fig. 6 Circulatory velocity distribution at pump exit

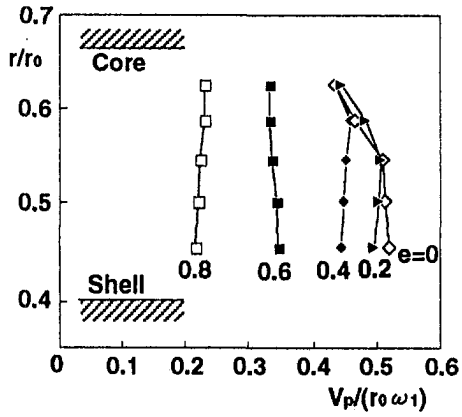

Fig. 7 Circulatory velocity distribution at turbine exit

Calibration curves for the five-hole probes were approximated by high-order polynomials so that the deviation of the approximated results from the measured data would fall within a 1% band with 95% confidence. Uncertainty of the pressure measurement obtained with the pressure transducers used in the experiment was estimated at 0.2%. Uncertainty of the steady flow velocity calculated from the pressure measured with the five-hole probes was estimated at 3%, based on the uncertainty of the pressure measurements and the uncertainty of the flow angles measured during the calibration process using the standard procedures (Kline, 1985).

The static pressure inside the torque converter was neither measured nor subtracted from the pressure measured by the five-hole probe. The probe was not calibrated for the range of static pressure variation. However, the effect of static pressure on the probe characteristics is regarded as negligibly small because the working fluid inside the torque converter was pressurized enough to avoid cavitation near the probe.

Note that a small error in the angle measurement can result in large error in resolved velocity components at the pump exit (Dong et al., 1998). This is because the absolute velocity is much larger than the relative velocity since the blade peripheral velocity is very high. The measurement error of the relative flow angle at the pump exit was estimated at about six times as large as that at the turbine exit, judging from the velocity triangles. Uncertainty of the relative flow angle at the pump and turbine exit was estimated as ± 12 and ± 2 deg, respectively.

Results and Discussion

Circulatory Velocity Distribution. Figures 6 to 8 show the nondimensionalized tangentially mass-averaged circulatory velocity distribution for $e = 0$–0.8 at the pump exit, the turbine exit, and the stator exit, respectively. Here, the circulatory velocity V_p is defined as a component whose direction is perpendicular to the measurement line from the shell (outer channel wall) to the core (inner channel wall) in the meridional plane.

The velocity distribution from the shell to the core at the pump exit for $e = 0$ resembles a profile of two-dimensional turbulent channel flow. It shows even more peaky and asymmetric profiles with growth in the velocity deficit near the core as the speed ratio e increases, i.e., at a lower flow rate (Fig. 6). In contrast, the distribution has flatter profiles at the turbine exit for all speed ratios tested (Fig. 7). Note that a small deficit in velocity is observed at the core in the lower speed ratio range.

Figures 8(a)–(b) show the velocity distribution in the contour profiles at the stator exit for $e = 0$ and 0.8, respectively. It is seen from Fig. 8(a) that flow deviated toward the shell on the suction surface. The cause of this deviation is thought to be that inflow to the stator has a large positive incidence angle while keeping a large downward pitch angle. The velocity peak moved slightly toward the core surface at $e = 0.8$ (Fig. 8(b)), and the biggest difference between the two figures is that it has a flatter distribution at $e = 0.8$.

Exit Flow Angle. Figure 9 shows the exit flow angle α mass-averaged from the shell to the core of the three elements, together with the exit blade angle β. The deviation angle ($|\alpha - \beta|$) was around 8 deg for the pump and the turbine regardless of the speed ratio, whereas it was about 10 deg in the higher speed ratio range and tended to increase in the lower speed ratio range for the stator. These results can be explained as follows. The pump and turbine blade passages are long and their deviation angle at the exit is not likely to be influenced by the flow rate and the inlet flow angle so much, whereas the stator blade passage is apt to be influenced by the inlet flow condition as its axial cascade solidity is around 1.0 and the inlet flow angle itself varies significantly (see Fig. 17).

Head. The theoretical head of the pump, H_1, actual head of the turbine, H_2, and head loss of the three elements, h_1, h_2, and h_3 (all nondimensional), are defined as follows and were obtained by mass-flow averaging of the velocity and pressure data measured with the Pitot tubes for each section.

$$H_1 = \frac{2\omega_1(r_A V_{\theta A} - r_C V_{\theta C})}{(r_0\omega_1)^2} \tag{1}$$

$$H_2 = \frac{2\omega_2(r_A V_{\theta A} - r_B V_{\theta B})}{(r_0\omega_1)^2} \tag{2}$$

$$h_1 = H_1 - \frac{2(P_{TA} - P_{TC})}{\rho(r_0\omega_1)^2} \tag{3}$$

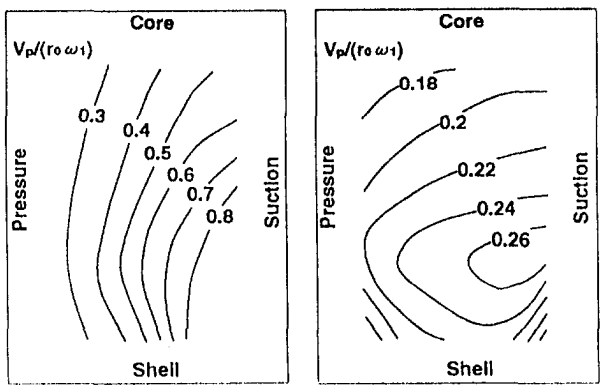

Fig. 8 Circulatory velocity distribution at stator exit

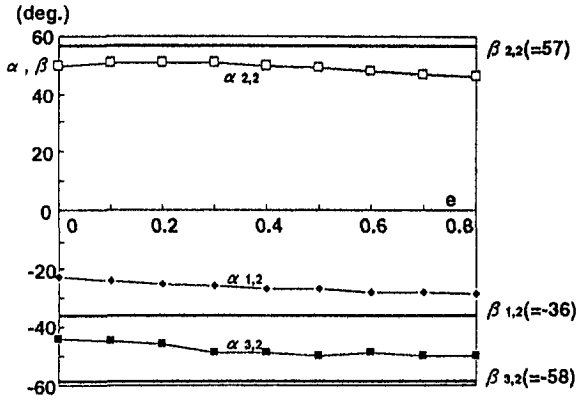

Fig. 9 Exit relative flow angle α (β: blade angle)

$$h_2 = \frac{2(P_{TA} - P_{TB})}{\rho(r_0\omega_1)^2} - H_2 \tag{4}$$

$$h_3 = \frac{2(P_{TB} - P_{TC})}{\rho(r_0\omega_1)^2} \tag{5}$$

Figure 10 shows the composition of each head over the speed ratio range tested. The combined head loss of the three elements equals the difference between the theoretical head of the pump and the real head of the turbine. It should be noted that the head loss of the pump was the greatest of the three in the higher speed ratio range ($e > 0.6$) while the loss of the stator increased abruptly in the lower speed ratio range ($e < 0.2$).

Efficiency. The individual hydraulic efficiencies of the pump, turbine and stator, η_1, η_2, and η_3, are defined by the following expressions:

$$\eta_1 = \frac{(P_{TA} - P_{TC})}{\rho\omega_1(r_A V_{\theta A} - r_C V_{\theta C})} \tag{6}$$

$$\eta_2 = \frac{\rho\omega_2(r_A V_{\theta A} - r_B V_{\theta B})}{(P_{TA} - P_{TB})} \tag{7}$$

$$\eta_3 = 1 - \frac{(P_{TB} - P_{TC})}{(P_{TA} - P_{TC})} \tag{8}$$

The following relation then holds true between the hydraulic global efficiency η and η_1, η_2, and η_3, as the hydraulic global efficiency is defined as the ratio of output power to input power.

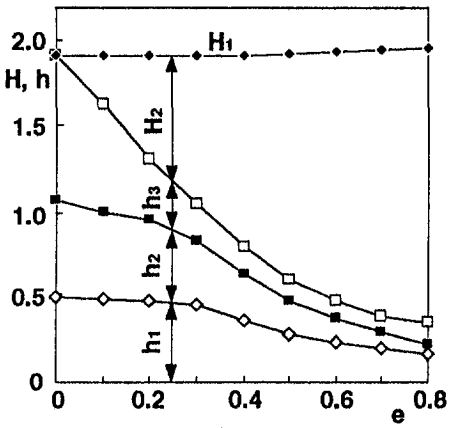

Fig. 10 Head and head loss

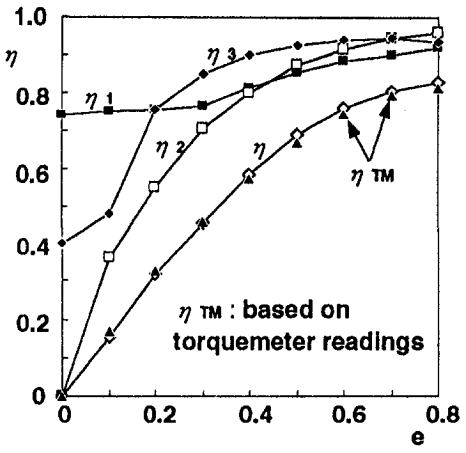

Fig. 11 Efficiency

$$\eta = \eta_1\eta_2\eta_3 = \frac{\omega_2(r_A V_{\theta A} - r_B V_{\theta B})}{\omega_1(r_A V_{\theta A} - r_C V_{\theta C})} \tag{9}$$

Overall efficiency η_{TM} was calculated from the following expression based on the torquemeter and tachometer readings. Here, T_1 and T_2 were obtained by compensation of mechanical losses in the bearings and the oil seals (measured beforehand), disk friction loss between the turbine shell and the casing, and windage loss (using empirical formula).

$$\eta_{TM} = \frac{T_2\omega_2}{T_1\omega_1} \tag{10}$$

Figure 11 shows the hydraulic efficiency of each element and hydraulic global efficiency derived from Eq. (9). Pump efficiency was the lowest of the three elements in the speed ratio range ($e > 0.6$) where vehicles are operated most frequently in everyday driving. The overall efficiency η_{TM} defined by Eq. (10) showed lower values by 2–3 points in this speed ratio range. It is mainly because the number of measuring points was finite and they did not cover the flow fields near the shell and the core where considerable losses occurred. It is partly because the leakage flow not only between the elements (within the core) but also between an element and the external flow field was disregarded in the measurement.

Friction Loss Coefficient. The loss model in the one-dimensional flow model employed in the literature (Ishihara, 1955) consists of the friction loss, h_{fi}, and the shock loss, h_{si}, which are given by the following expressions:

$$h_{fi} = \zeta_i(W_{i,1}^2 + W_{i,2}^2)/2/(r_0\omega_1)^2 \tag{11}$$

$$h_{si} = \phi_i\{(r_{i,1}\omega_i - V_{pi,1}\tan\beta_{i,1}) - (r_{i-1,2}\omega_{i-1} - V_{pi-1,2}\tan\alpha_{i-1,2}) \cdot (r_{i-1,2}/r_{i,1})\}^2/(r_0\omega_1)^2 \tag{12}$$

Here, a suffix "i" indicates one of the three elements (pump or turbine or stator). If $i = 1$ (pump), then "$i - 1$" means stator. If $i = 2$ (turbine), then "$i - 1$" means pump. For example, V_{pi-1} means V_p at the pump exit if $i = 2$. Figures 12–14 show the calculated values of $(h_{fi} + h_{si})$ for the three elements along with the experimental values of h_i. These values were calculated on the basis of the averaged circulatory velocity in measured section B for all elements, taking ζ_i as a parameter. The values of ϕ_i used in the calculations were $\phi_1 = \phi_2 = 1.0$ and $\phi_3 = 0.5$.

The experimental value of ζ_1 stayed around 1.0 in the range of $e = 0$–0.5, whereas it appeared to increase to 1.5–2.0 in the higher speed ratio range. The value of ζ_2 remained as low as 0.5 over the entire tested speed ratio range because the turbine was of the acceleration cascade type and a serious separation was not

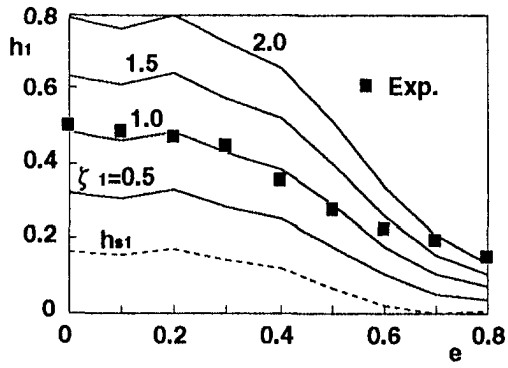

Fig. 12 Head loss for pump

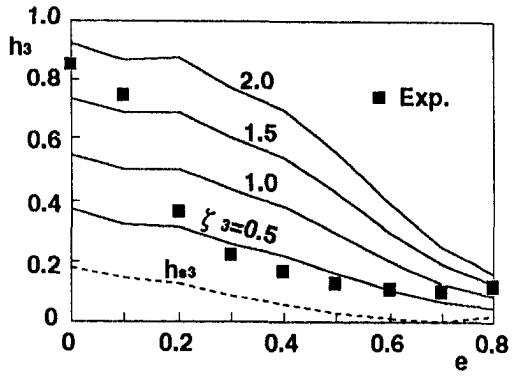

Fig. 14 Head loss for stator

likely to occur there. The value of ζ_3 increased to as great as 1.5–2.0 in the lower and higher speed ratio ranges.

Flow Visualization. The loss generation mechanism for the pump and stator, which both showed considerable variation of the apparent friction loss coefficients, was investigated by flow visualization near the blade passage walls.

Figures 15(*a*)–(*b*) show photographs of the visualized flow pattern on the core and suction surfaces of the pump impeller at speed ratios of 0.6 and 0.8, respectively. A low kinetic energy region is apparent in both cases over the corner where the suction and core surfaces intersect. The separation begins just behind the inlet and the separated width increases gradually along the streamwise direction for $e = 0.6$ (the separation area is smaller for $e < 0.6$), whereas the separation area is much larger for $e = 0.8$ than for $e = 0.6$. (Separation lines are shown in the sketches.) Reverse flow is also observed in the fore part of the region in both cases. The increase in the apparent friction loss coefficient for the pump from $e = 0.6$ to 0.8 is thought to be directly related to the growth in the low kinetic energy region noted above, as a significant low kinetic energy region was not found anywhere else in the pump. Similar growth in the low kinetic energy region in the higher speed ratio range was also observed in the LDV measurements reported by Brun et al. (1996).

The separation condition observed in the visualized flow near the stator blade surface in the three speed ratios is summarized in Table 3. In this table, the definition of trailing edge separation includes not only the separation near the trailing edge but also the separation on the latter half of the blade surface. It is seen that leading edge separation occurred in the lower and higher speed ratio ranges, where the friction loss coefficient for the stator increased. Photographs of the visualized flow on the pressure surface (leading edge separation) and on the suction surface (trailing edge separation) of the stator at $e = 0.8$ are shown in Fig. 16(*a*)–(*b*) as examples.

Figure 17 shows the one-dimensional velocity vectors on the design path at the stator inlet, which are based on measurements made with the five-hole Pitot tubes. The inlet flow angle varied significantly from $\alpha = 49$ deg ($e = 0$) to $\alpha = -39$ deg ($e = 0.8$). Therefore, it is only natural that large-scale separation would occur on the suction surface at $e = 0$ and on the pressure surface at $e = 0.8$ because of the excessive incidence angle of the stator, even though a relatively thick blade profile was employed. This observation well explains the visualization results in Table 3. A large-scale separation results in an apparent increase in the friction loss coefficient for the stator in Fig. 14 as the shock loss only simulates a small-scale separation near the leading edge (it often reattaches and forms a separation bubble) (Senoo, 1984).

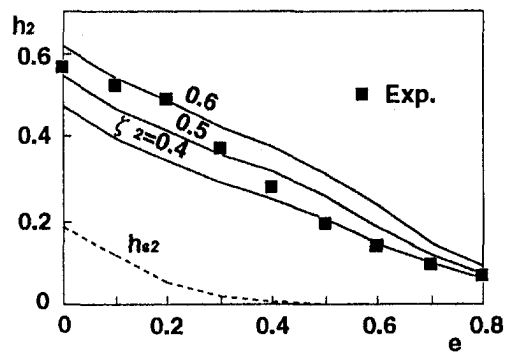

Fig. 13 Head loss for turbine

CFD Analysis. In order to better understand the loss generation mechanism in the pump, three-dimensional viscous calculations were performed through the three elements. A total of 166,800 grid cells ($26 \times 30 \times 80$: pitch × span × longitude for the pump and turbine, $28 \times 30 \times 50$ for the stator) were used in the calculations.

Main Stream. Figures 18(*a*)–(*b*) show the computed nondimensional circulatory velocity distribution from the shell to the core in five cross sections (0/4–4/4) in the pump at $e = 0.6$ and $e = 0.8$, respectively. Here, the circulatory velocity V_p is defined as a component whose direction is perpendicular to the computing mesh line from the shell to the core in the meridional plane. The circulatory velocity near the core tends to decrease in the range from the inlet (0/4) to the middle (2/4) of the passage and the distribution becomes more nonuniform as the speed ratio increases, whereas the distribution is relatively uniform near the exit (4/4) at both speed ratios. The corresponding experimental data in Fig. 6 do not show such a fully developed flow profile at $e = 0.6$ and 0.8. It is probably because the computation was conducted with the k-ε turbulence model, which is based on high Reynolds number flow, whereas the actual flow in the torque converter was low Reynolds number turbulent flow.

Figure 19 shows the computed relative inlet flow angle distribution at three speed ratios together with the blade inlet angle. The incidence angle is negative over almost the entire span at $e = 0.05$ and $e = 0.6$ as the flow rate is distant from that of the design point. The incidence angle shows a small negative value from the midspan to the shell at $e = 0.8$ as the speed ratio is near that of the design point, whereas it displays a large positive value near the core. This large positive incidence angle is caused mainly by the circulatory velocity deficit near the core noted above, and partly by the large peripheral velocity of the pump impeller near the core.

Figure 20 shows the computed nondimensional circulatory velocity distribution from the shell to the core in four cross sections (1/4–4/4) in the stator at $e = 0.8$. The distribution is relatively uniform just behind the stator inlet (1/4), whereas the velocity deficit near the core increases in the downstream direction (toward the pump), which means the circulatory velocity deficit in the pump ranges to the middle of the stator passage upstream in the

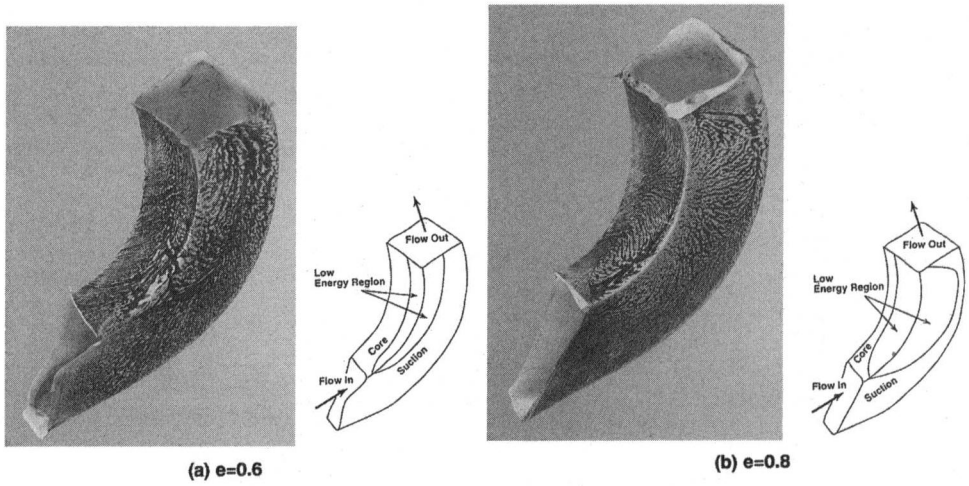

Fig. 15 Visualized flow patterns in pump

pump. The inlet loss and the velocity reduction loss increase toward the core at $e = 0.8$ because the stator works as a deceleration type cascade and the incidence angle has a larger negative value. The earlier leading edge separation near the core on the pressure surface is verified in Fig. 16(*a*).

Figures 21(*a*)–(*b*) show the computed circulatory velocity distribution in the middle and the exit cross sections of the pump, respectively. Reverse flow is observed near the core on the suction surface in the middle of the passage while no reverse flow is seen at the exit. This is because the flow is decelerating in the fore half, but is accelerating in the latter half as the test impeller was of the forward lean type. The area of flow reversal is smaller in the middle of the passage at $e = 0.6$ compared with that at $e = 0.8$, but the tendency is the same at both speed ratios.

Flow Near the Wall. Figures 22(*a*)–(*b*) show the computed secondary flow vectors on the core and suction surfaces of the pump at $e = 0.6$ and $e = 0.8$, respectively. The magnitude of the arrows was nondimensionalized by the mean circulatory velocity at the pump exit. Compared with the corresponding visualized results in Fig. 15, the computation results show satisfactory prediction of the major features of the flow pattern. Qualitative but essential characteristics of the flow pattern were simulated by the computations, including: (1) the location of a low kinetic energy

Table 3 Separation condition

Speed ratio	Pressure surface	Suction surface
0	No separation	L.E. separation
0.6	No separation	T.E. separation
0.8	L.E. separation	T.E. separation

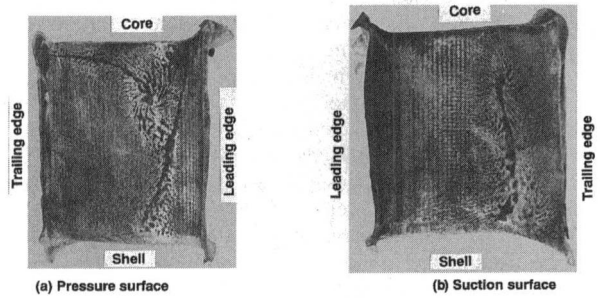

Fig. 16 Visualized flow patterns in stator at $e = 0.8$

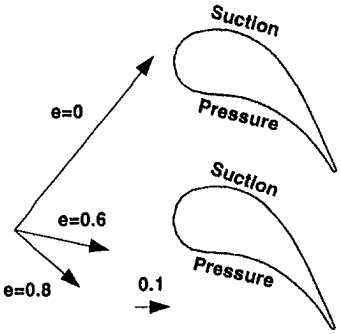

Fig. 17 Velocity vectors at stator inlet

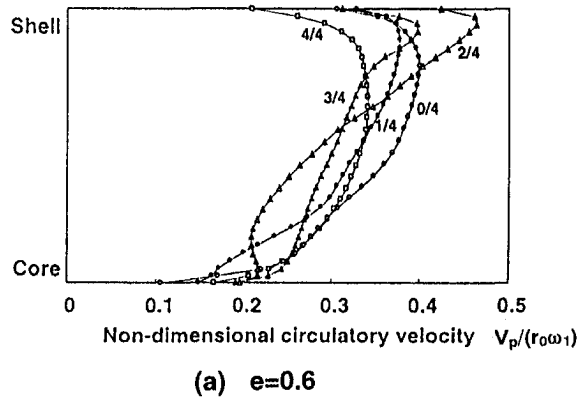

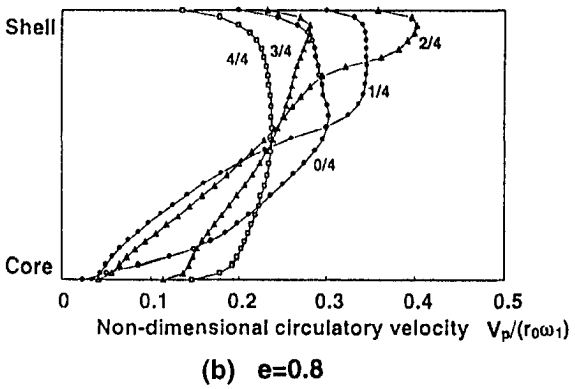

Fig. 18 Circulatory velocity distribution in pump

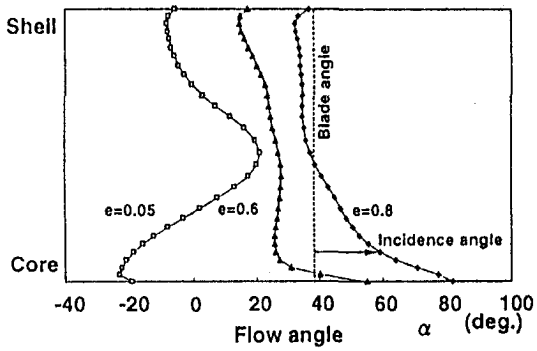

Fig. 19 Relative flow angle at pump inlet

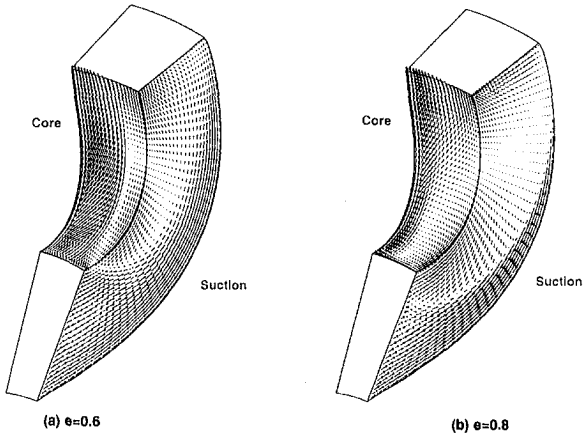

Fig. 22 Computed secondary flow vectors in pump

region covering the core and suction surfaces, (2) the growth of the region from $e = 0.6$ to 0.8, and (3) the presence of reverse flow in a fore part of the region.

A secondary flow, the velocity of which has a component going from the pressure to the suction surface on the core surface and from the core to the shell surface on the suction surface, is seen in the fore part of the region. Another secondary flow, the velocity of which has a component going from the shell to the core surface on the suction surface, is seen in the latter part of the region, on the contrary.

Loss Distribution. Figure 23 shows the nondimensional rothalpy change distribution from the inlet to the exit, $(\Delta I)^*$, where the rothalpy change from the inlet, ΔI, was normalized by the theoretical head of the pump, H_1. s^* is the distance nondimensionalized by the full length of s. The leading edge corresponds to about $s^* = 0.05$, and the trailing edge corresponds to about $s^* = 0.95$. A concentrated loss occurs just behind the inlet due to a so-called shock loss. The following region where the slopes of the curves are less steep than in the inlet region corresponds to the area where reverse flow occurs. The slopes of the curves become more moderate after the reverse flow region and reach the exit with a smaller loss. The large change in rothalpy observed just behind the exit is due to the mixing loss resulting from the mixing of the boundary layers on the pressure and suction surfaces. The figure indicates that the nondimensional rothalpy change at $e = 0.6$ was lower than that at $e = 0.8$ at the exit, which means the pump efficiency was lower for $e = 0.6$ than for $e = 0.8$. This tendency coincides with the experimental result of η_1 in Fig. 11.

Figures 24(*a*)–(*b*) show the computed nondimensional rothapy change distribution in the two major cross-sections, middle and exit for $e = 0.6$. The lowest rothalpy change occurred near the corner where the suction surface and core surface intersected. The lowest rothalpy change was more on the suction surface in the middle of the passage, whereas it was more on the core surface at the exit.

Flow in the boundary layer of the radial impeller is generally dominated by the pressure field of the main stream corresponding to the centrifugal force due to the stream line curvature on the meridional plane (MC force), similarly to flow within elbow, the Coriolis force due to impeller rotation (CO force), and the centrifugal force due to the stream line curvature on the blade-to-blade surface (BC force), as shown in Fig. 25(*a*) (Tsujita et al., 1996).

The main stream axially enters the pump impeller and flows nearly radially through most of the passage as in an ordinary radial impeller. The combined effect of the CO force and BC force in the main stream is the blade loading (i.e., the pressure difference between the blade pressure and suction surfaces). Fluid with lower velocity than that of the main stream flows from the pressure

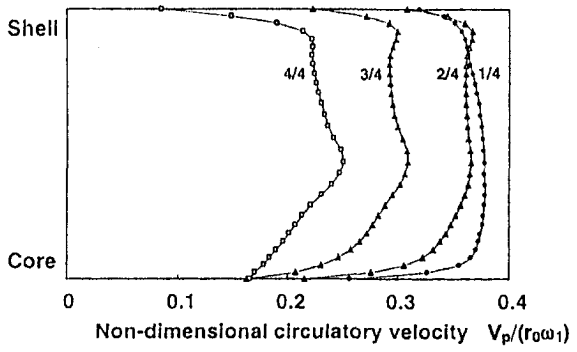

Fig. 20 Circulatory velocity distribution in stator at $e = 0.8$

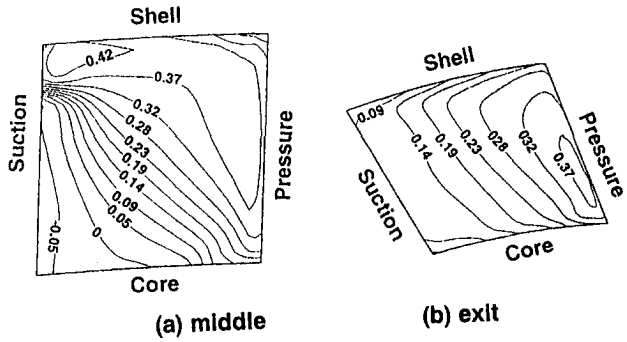

Fig. 21 Nondimensional circulatory velocity distribution in cross sections of pump at $e = 0.8$

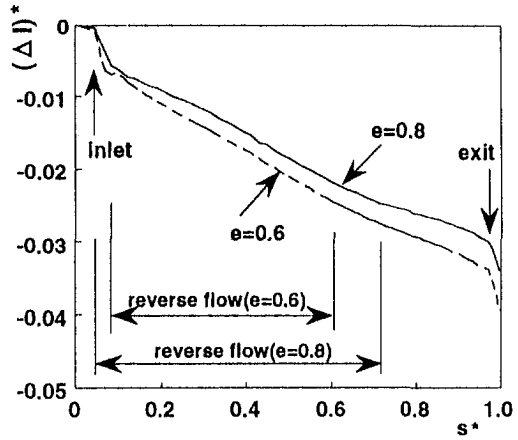

Fig. 23 Nondimensional rothalpy change distribution from inlet to exit in pump

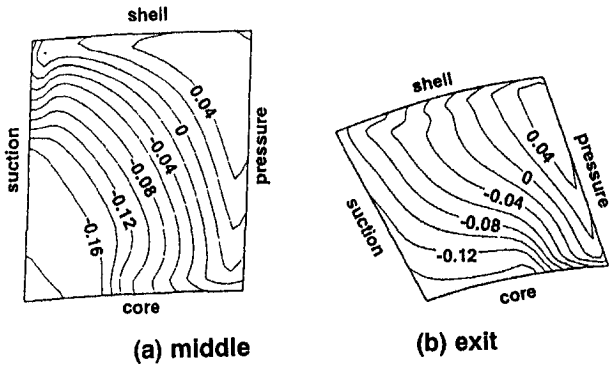

Fig. 24 Nondimensional rothalpy change distribution in cross sections of pump at $e = 0.6$

surface to the suction surface, as the total of the two forces in the slow fluid is smaller than that of the main stream and does not overcome the pressure difference between the pressure and the suction surfaces (Fig. 25(*a*) (ii)). The MC force drives the fluid on the blade surfaces towards the core (Fig. 25(*a*) (i)). There is more accumulation of low kinetic energy fluid on the suction surface in the middle of the passage in Fig. 24(*a*) because the total of the CO force and BC force is larger than the MC force.

The main stream turns from the radial to the axial direction towards the exit, where the blade loading approaches zero. As a result, the secondary flow shown in Fig. 25(*b*) (ii) is very weak. Low kinetic energy fluid accumulated more on the core surface at the exit in Fig. 24(*b*) because the radial pressure gradient increased, as the MC force due to the stream line curvature in the meridional plane was added by the CO force, $2W_\theta\omega$, and the centrifugal force, W_θ^2/r (RC force), both stemming from the forward lean exit angle of the impeller (Fig. 25(*b*) (i)).

Figures 26(*a*)–(*b*) show the computed secondary flow vectors in the two major cross-sections, middle and exit for $e = 0.6$ in the pump. The figures are viewed from the upstream of the pump impeller, and the length of vectors are normalized by the peripheral

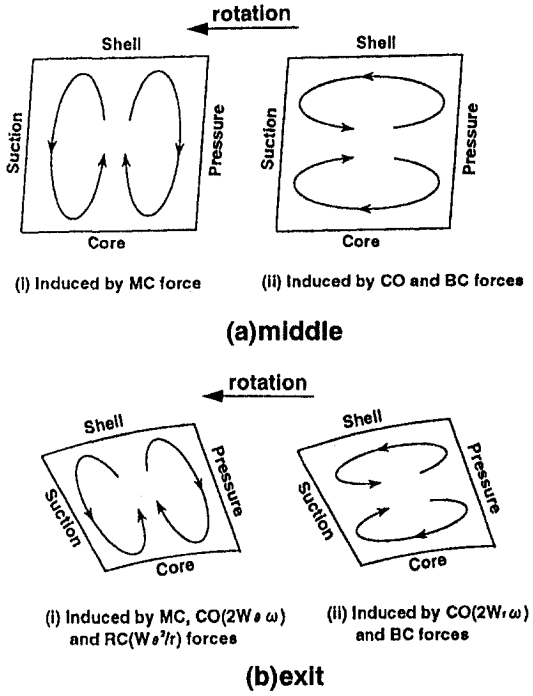

Fig. 25 Schematic of typical secondary flow patterns in cross sections of pump

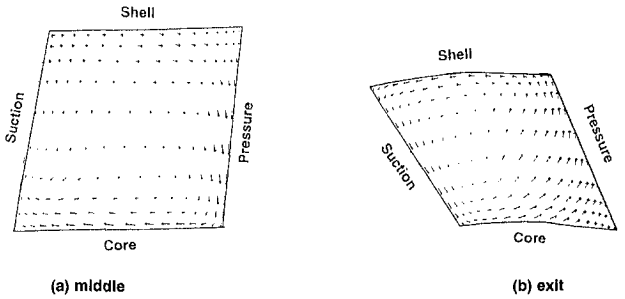

Fig. 26 Computed secondary flow vectors in cross sections of pump at $e = 0.6$

velocity of the pump exit, $r_0\omega_1$. A clear secondary flow, whose vorticity is clockwise, is found in the middle of the passage on the one hand (Fig. 26(*a*)). A stronger secondary flow, whose vorticity is counter-clockwise, is found in the exit of the passage on the other hand (Fig. 26(*b*)). The behavior of the low kinetic energy fluid in the vicinity of the corner, where the suction surface and core surface intersected (Figs. 24(*a*)–(*b*)), can be well explained by these secondary flows.

Concluding Remarks

- The individual performance of the three torque converter elements, which has rarely been discussed so far, was defined and evaluated on the basis of flow data measured with five-hole Pitot tubes. The head loss was the highest and efficiency the lowest for the pump in the speed ratio range where vehicles are most frequently operated in everyday driving.
- Calculations performed with a one-dimensional flow model revealed that the apparent friction loss coefficient of the turbine was nearly constant over the entire tested speed ratio range, whereas the coefficients of the pump and stator varied considerably according to the operating speed ratio.
- Flow visualization by a liquid-resin film method revealed that an increase in the apparent friction loss coefficient of the pump in the higher speed ratio range was directly related to an increase in the area of a low kinetic energy region spreading over the corner where the suction and core surfaces intersected. The increase in the apparent friction loss coefficient of the stator in the lower and higher speed ratio ranges was caused by leading edge separation on the suction and pressure surfaces, respectively.
- Flow in the pump in the higher speed ratio range was analyzed numerically by using a general CFD code. The results predicted that a circulatory velocity deficit occurred near the core at the pump inlet, which ranged to the middle of the stator passage. Reverse flow was also computed near the core on the suction surface in the middle of the passage while no reverse flow was seen at the exit. The computation results of the flow pattern near the core and suction surfaces showed good qualitative agreement with flow visualization indications. The results predicted the loss distribution from the inlet to the exit and indicated that the pump efficiency was lower for $e = 0.6$ than for $e = 0.8$, which coincided with the measured results. The results also showed that the low kinetic energy region was more on the suction surface in the middle of the passage, whereas it was more on the core surface at the exit.
- The procedure presented here is useful not only in improving performance prediction accuracy for the torque converter but also in determining a direction for design improvement. In the next stage of the study, it will be necessary to make more detailed measurements and more accurate computations of flow in the three elements.

Acknowledgments

The authors are grateful to Dr. Yasutoshi Senoo, Professor Emeritus of Kyushu University, who has continuously offered

instructive advice to them during this study. The authors would like to thank Nissan Motor Co., Ltd. for permission to publish this paper, as well as Yoshihiko Ishii for his help in conducting the experiments and Ikuo Aoki for his assistance in performing the computations.

References

Abe, H., Miyoi, N., Yamashita, T., and Shirakigawa, K., 1996, "Practical Simulation Method for the Performance of a Hydraulic Torque Converter," FISITA '96 Technical Paper, P1641 (CD-ROM).

Browarzik, V., 1994, "Experimental Investigation of Rotor/Rotor Interaction in a Hydrodynamic Torque Converter Using Hot-Film Anemometry," ASME Paper 94-GT-246.

Brun, K., and Flack, R. D., 1996, "The Flow Field Inside an Automotive Torque Converter: Laser Velocimeter Measurements," SAE Paper No. 960721.

Cigarini, M., and Jonnavithula, S., 1995, "Fluid Flow in an Automotive Torque Converter: Comparison of Numerical Results with Measurements," SAE Paper No. 950673.

Computational Dynamics Ltd., 1995, STAR-CD Version 2.3 Manual.

Dong, Y., Lakshminarayana, B., and Maddock, D., 1998, "Steady and Unsteady Flow Field at Pump and Turbine Exits of a Torque Converter," ASME JOURNAL OF FLUIDS ENGINEERING, Vol. 120, pp. 538–548.

Fujitani, K., Himeno, R., and Takagi, M., 1988, "Computational Study on Flow through a Torque Converter," SAE Paper No. 881746.

Ishihara, T., 1955, "A Study of Hydraulic Torque Converter," *Report of the Institute of Industrial Science,* University of Tokyo, Vol. 5, No. 7, pp. 150–202.

Kline, S. J., 1985, "The Purpose of Uncertainty Analysis," ASME JOURNAL OF FLUIDS ENGINEERING, Vol. 107, pp. 153–160.

Kubo, M., Ejiri, E., Kumada, H., and Ishii, Y., 1994, "Improvement of Prediction Accuracy for Torque Converter Performance: One-Dimensional Flow Theory Reflecting the Stator Blade Geometry," *JSAE Review,* Vol. 15, pp. 309–314.

Launder, B. E., and Spalding, D. B., 1974, "The Numerical Computation of Turbulent Flows," *Computer Methods in Applied Mechanics and Engineering,* Vol. 3, pp. 269–289.

Leonard, B. P., 1979, "A Stable and Accurate Convective Modeling Procedure Based on Quadratic Upstream Interpolation," *Computer Methods in Applied Mechanics and Engineering,* Vol. 19, pp. 59–98.

Matsunaga, S., Ishibashi, H., and Nishi, M., 1980, "Measurement of Instantaneous Pressure and Velocity in Nonsteady Three-Dimensional Water Flow by Means of a Combined Five-Hole Probe," ASME JOURNAL OF FLUIDS ENGINEERING, Vol. 102, pp. 196–206.

Minato, K., Sakamoto, K., Fujitani, K., and Takagi, M., 1987, "Performance Prediction of Torque Converters," *Journal of the Flow Visualization Society of Japan* (in Japanese), Vol. 7, No. 26, pp. 81–84.

Numazawa, A., Ushijima, F., Fukumura, K., and Ishihara, T., 1983, "An Experimental Analysis of Fluid Flow in a Torque Converter," SAE Paper No. 830571.

Patankar, S. V., and Spalding, D. B., 1972, "A Calculation Procedure for Heat, Mass and Momentum Transfer in Three-dimensional Parabolic Flows," *International Journal of Heat and Mass Transfer,* Vol. 15, pp. 1787–1806.

Senoo, Y., 1984, *Turbomachinery* (in Japanese), Vol. 12, No. 4, pp. 214–220.

Tsujita, H., Mizuki, S., and Ejiri, E., 1996, "Analysis of Flow within Pump Impeller of Torque Converter," ASME Paper 96-GT-404.

Experimental Study on the Aeroacoustic Behavior of a Forward-Curved Blades Centrifugal Fan

Sandra Velarde-Suárez
Associate Professor.

Carlos Santolaria-Morros
Professor.

Rafael Ballesteros-Tajadura
Associate Professor.

Universidad de Oviedo,
Área de Mecánica de Fluidos,
Campus de Viesques,
33271 Gijón Asturias,
Spain
e-mail: RBALLEST@sci.cpd.uniovi.es

In this paper, an aeroacoustic study on a forward-curved blades centrifugal fan has been carried out. As a first step, the fan performance curves, i.e., total pressure, power, efficiency and sound power level versus flow rate were obtained, showing its unstable behavior over a wide operating range. Second, the fan sound power level spectra for several working conditions were determined. For this purpose a normalized installation for testing in laboratory was designed and constructed. Afterwards, the velocity and pressure fields, both at the inlet and outlet planes of the impeller were measured using hot wire probes and pressure transducers, for different operating conditions. Finally, the aeroacoustic behavior of the fan was determined measuring the vorticity field at the impeller outlet, which is known to be related to tonal noise generation. This relation is worked out using the theory of vortex sound, developed by several authors during the second half of this century. The paper shows that the generation of tonal noise is produced at the blade passing frequency and it increases with the flow rate. Although the main contribution to fan noise generation is due to mechanical sources, the bands in which aerodynamic noise is generated by these fans correspond to frequencies especially unpleasant to the human ear. Therefore, the research presented in this paper may be of considerable interest, establishing a starting point for the design of quieter and more efficient fans.

Introduction

Forward-curved blades centrifugal fans usually exhibit instability phenomena, which reduce their operating range. A basic feature of their impellers is the inefficient flow guiding, as a result of the short radial length of the blades and their strong curvature. Usually, this effect is counterbalanced by a greater number of blades. Such an arrangement can cause the flow to stall, even at design conditions. A perturbation at the inlet or at the outlet planes can be amplified, giving rise to flow instabilities both in the fan and in the system. Cau et al. (1987) show in their work that the poor design of the flow channel in these fans causes a severely distorted primary flow, with early flow separation on the suction side at both design and low flow rates. They ascribed the inefficiencies of these machines to the sharp axial to radial bend, to the large inlet gap between inlet cone and impeller shroud and to the poor matching between impeller outlet and volute.

Most of the studies on aerodynamic noise generated by moving blades are based on the acoustic analogy (Lighthill, 1952). Another interesting theory, used in this work, is Powell's theory of vortex sound (1964), that expresses noise generation as a function of velocity and vorticity fields. Thompson and Hourigan (1992) made a prediction of the blade passing tone of a centrifugal fan by solving the Powell's wave equation using a finite element method. The acoustic forcing term was derived from experimental velocity data obtained by Shepherd and Lafontaine (1992) using a Particle Image Velocimetry (PIV) method.

In the solution of the wave equation presented by Ffowcs Williams and Hawkings (1969), some terms are identified with the different aeroacoustic generation mechanisms which appear when solid surfaces are moving: quadrupolar noise, related to turbulence shear stresses; dipolar noise, produced by steady and unsteady forces exerted by the moving surfaces on the flow; and monopolar or thickness noise, due to the volume displacement of the moving surfaces. Among the above mentioned mechanisms, the main contribution to the noise generated by fans is due to the forces acting on the blades, vanes and casing, produced by their interaction with the turbulent flow. Forces on the blades can be periodic or random, and so the resulting sound field will have either discrete or broad band components (Neise, 1992). Discrete components due to this mechanism are produced at the blade passing frequency and their harmonics as usually encountered in industrial fans.

In this paper, an experimental study of the aeroacoustic behavior of a forward-curved blades centrifugal fan is carried out. First, the fan performance curves and the fan sound power level were measured. Second, the vorticity field was calculated from velocity and pressure measurements and it was used to explain some noise generation features of the fan, using Powell's theory to relate noise generation to aerodynamic phenomena.

Performance and Noise Testing

The tests were made on a simple aspirating centrifugal fan. The shrouded rotor has an inlet diameter of 300 mm, an outlet diameter of 400 mm and a width of 150 mm. It has 38 forward-curved blades and is driven by an AC 9.2 kW motor. The impeller rotates at 1460 rpm with a fluctuation level lower than 0.5 percent for the whole range of the analyzed flow rates. The volute has a width of 248 mm.

Figure 1 shows a sketch of the fan with the main dimensions expressed in mm. The minimum distance between the fan impeller and the volute is 50 mm at the tongue. The inlet blade angle is 0 deg with respect to the radial direction and therefore there is non-zero incidence and flow separation occurs for all the flow conditions. The outlet blade angle is 74° relative to the radial direction. The fan inlet is open to the ambient air.

Contributed by the Fluids Engineering Division for publication in the JOURNAL OF FLUIDS ENGINEERING. Manuscript received by the Fluids Engineering Division August 10, 1998; revised manuscript received March 25, 1999. Associate Technical Editor: B. Schiavello.

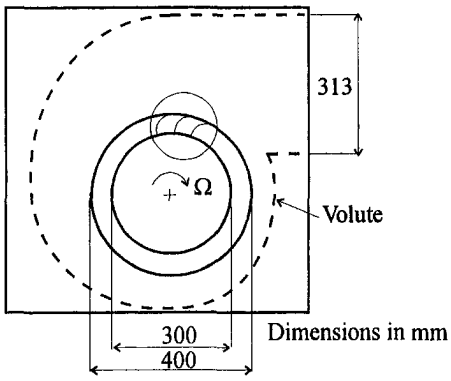

Fig. 1 Test fan

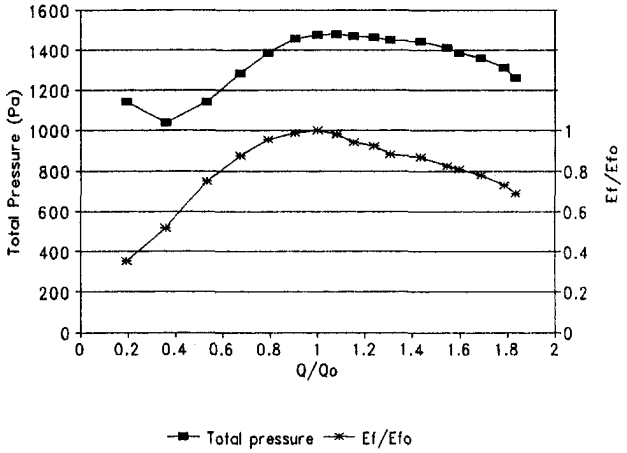

Fig. 3 Total differential pressure and efficiency versus flow rate

A test facility was designed and built following British Standard BS 848: Part 1 (1980) and BS 848: Part 2 (1985). In this way, the same facility could be used to measure the fan performance curves and the fan acoustic behavior. Figure 2 shows a sketch of this test facility with its main elements. After leaving the fan, air passes through a straightener in order to remove the swirl generated by the fan; the measurement instruments were placed at sections A (static pressure) and B (flow rate and sound pressure level). At the end of the facility, an anechoic termination removes undesired noise reflections and the regulation cone permits to modify the fan operating point.

The performance curves and the SWL spectra were obtained following the procedures indicated on the already mentioned British Standards. The flow rate was measured with a Pitot-static tube, placed at section B, using the traversing method described in the Standard. Static pressure was measured using a differential manometer with one side connected to four wall tappings evenly distributed at Section A and the other side open to the atmospheric pressure in the laboratory. Velocity head was deduced from the flow rate and the duct cross section.

The following uncertainties were established for the measured and calculated magnitudes:

—Differential total pressure: ±1.4% (±21 Pa).

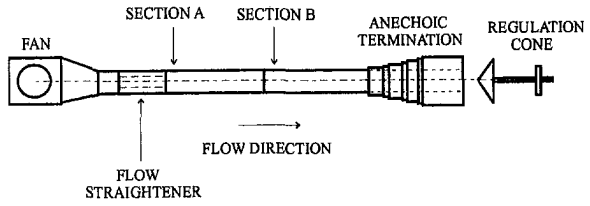

Fig. 2 Test facility

—Flow rate: ±2% (±0.06 m^3/s).
—Shaft power: ±2% (±0.19 kW).
—Sound power level: ranges between ±1.6 dB and ±4 dB depending upon the frequency band considered:

Frequency (Hz)	Uncertainty (dB)
50	3.5
63	3.0
80	2.5
100	2.5
125	2.0
160 to 2500	1.6
3150 to 4000	2.0
5000	2.5
6300 to 8000	2.5
10000	4.0

Figure 3 shows differential total pressure and efficiency against the flow rate and Fig. 4 shows shaft power and sound power level (SWL) versus flow rate. Qo refers to the flow rate at the best efficiency point and Efo refers to the corresponding efficiency. The values obtained for these variables were $Qo = 1.7$ m^3/s and Efo = 0.63. On the differential total pressure curve a wide zone with positive slope, in which some aerodynamic unstable phenomena may appear, can be observed. Furthermore, the design point, corresponding to the highest efficiency falls within that zone, revealing an unsuitable fan design. The references consulted by the authors mention the following aerodynamic instability phenomena which are responsible for the increase in noise generation and level of mechanical vibrations and the decrease in aerodynamic performance: flow separation in the blade channels, reverse flow and prerotation at fan suction. The shaft power curve increases with the flow rate, thus causing a drive overload when working at high flow rates during long periods of time.

The sound pressure level was measured with a Brüel & Kjaer

Nomenclature

c_0 = sound velocity
Ef = efficiency
Efo = maximum efficiency
p = pressure
p' = pressure fluctuation
Q = flow rate
Qo = design flow rate
r = radial coordinate
SWL = sound power level
t = time
$\vec{u}$ = velocity field without the acoustic fluctuations
V = absolute velocity
V_r = radial component of the absolute velocity
V_{rm} = mean radial component of the absolute velocity
V_{tg} = tangential component of the absolute velocity
U = blade speed at rotor exit
θ = tangential coordinate
ρ = density
ρ_0 = density of the mean flow
$\vec{\omega}$ = vorticity field without the acoustic fluctuations
ω_z = axial component of vorticity
Ω = impeller rotation velocity

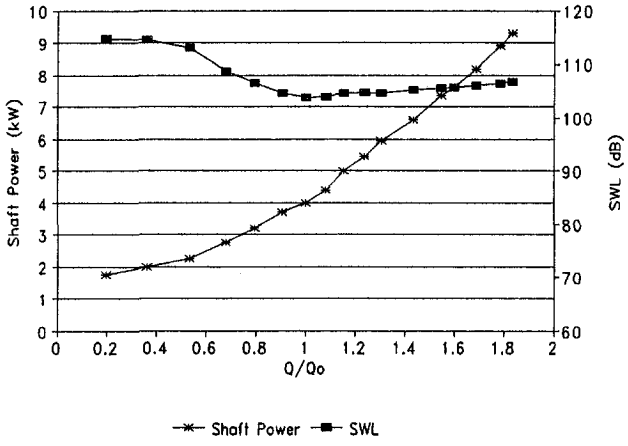

Fig. 4 Shaft power and SWL versus flow rate

modular sound level meter with a level 1 precision. A $\frac{1}{2}$ in. microphone protected with a nose cone was used. The sound level meter incorporates analogical filters and a frequency analysis module. The fan sound power level was obtained using the sound pressure levels measured and the procedure described in the already mentioned British Standard.

In the SWL curve shown in Fig. 4, higher levels were measured at the lower flow rates. The lowest value of this level corresponds with the highest value of efficiency, and after that point, its value increases slightly with the flow rate.

Figure 5 shows the SWL spectrum measured at 40 percent of the design flow rate. Noise at low frequencies is dominant and the band with the highest value includes the impeller rotational frequency (25 Hz band). Its fifth harmonic (160 Hz band) is also clearly shown, while the blade passing frequency, included in the 1000 Hz band, contains much less power when compared to the lower frequencies.

On Fig. 6 the SWL spectrum measured for the design point is plotted. Even though low frequency noise is remarkably reduced in comparison with the previous case, the most predominant frequency is again the impeller rotational frequency; (its second and fifth harmonics can also be clearly observed). The level of the fifth harmonic is invariable with the flow rate, indicating a mechanical origin of the noise generated in this band. The levels of the blade passing frequency and its second harmonic are still small if compared to the lower frequency levels. Moreover, the measured pressure distribution around the impeller exit did not reveal a significant axisymmetry that could explain the behavior at low frequencies. This behavior is not apparent in other fan geometries for which the blade passing frequency is dominant. As was stated by Neise (1992), this is not the typical behavior of an industrial fan: in backward-curved bladed fans with a better aerodynamic design, a bigger contribution of the tonal noise at the blade passing frequency should be expected.

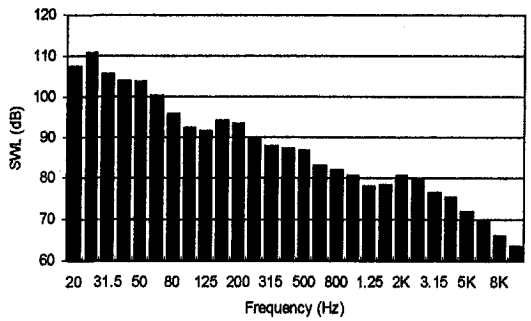

Fig. 5 SWL spectrum, 0.4 × *Qo*

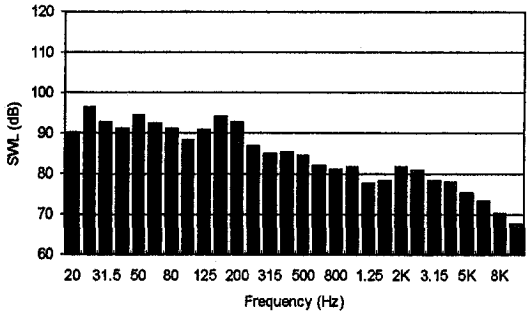

Fig. 6 SWL spectrum, *Qo*

Figure 7 shows the evolution of the SWL for the impeller and the blade passing frequency with the flow rate. The noise generated at the impeller rotational frequency exhibits its lowest values between 1 and 1.4 times the design flow rate, and increases dramatically at lower flow rates. Regarding the blade passing frequency, the generated noise is much lower than its value at the impeller rotational frequency for all the flow rates investigated showing a lowest value at 0.7 times the design flow rate. Below that value the level increases slightly and above that value the level increases remarkably. The noise generated at the blade passing frequency (so-called *tonal noise*) is mainly due to the interaction between the blades wakes and the volute tongue. It is well known (Neise, 1992) that for industrial fans, when the flow rate increases, the wakes become bigger and this noise also increases.

Aerodynamic Testing

For three operating conditions (the design flow rate Qo, $0.4 \times Qo$ and $0.7 \times Qo$, all included in the positive slope zone of the total pressure curve), the flow field at the impeller exit plane was measured. For that purpose, pressure and velocity signals were measured on two radial locations, taking measurements on 12 circumferential points evenly distributed on each location (Fig. 8). The inner location (named **I**) has a radius of 210 mm and the outer location (named **E**) has a radius of 240 mm. These measurements were taken at mid span; in addition, the spanwise variation of the flow field was obtained by taking velocity measurements in different axial positions for several circumferential points. Although the tangential component was found to be almost constant over the rotor width, the radial component decreased clearly at both impeller width ends.

Pressure signals were taken with a Brüel & Kjaer 4135 $\frac{1}{4}''$ microphone, for which the frequency response and pressure range

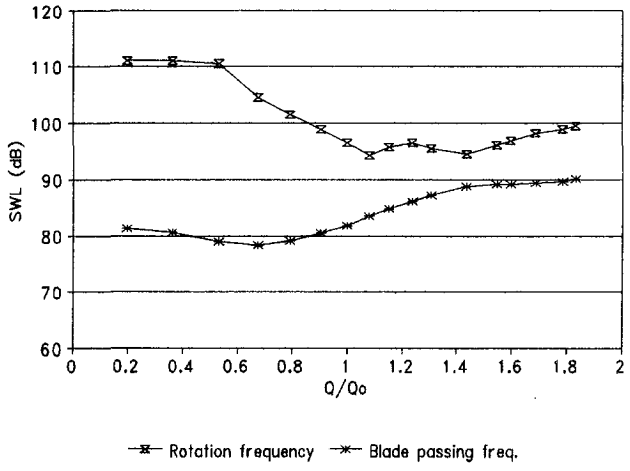

Fig. 7 SWL versus flow rate

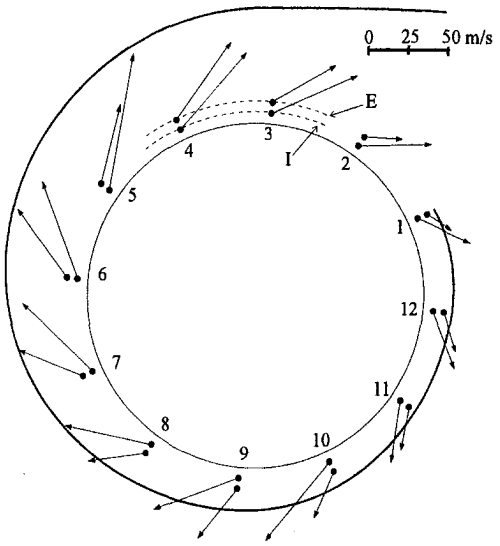

Fig. 8 Measurements points and absolute velocity vectors at impeller outlet, 0.7 × *Qo*

were 20 kHz and $2 \cdot 10^{-5}$ – 6400 Pa, respectively. The microphone was calibrated using the Brüel & Kjaer 4230 sound level calibrator and was placed at 90 deg to the flow direction, only protected with its standard grid. The uncertainty of the pressure measurements was estimated to be ±1 dB ($\pm 2.3 \times 10^{-5}$ Pa).

To measure the radial and the tangential components of the absolute velocity at the impeller exit, a two-wire probe was used. Hot wire anemometry is able to get the two-dimensional character of the flow with a high temporal resolution (Comte-Bellot, 1976). A direct calibration procedure of the probe was selected. It is possible to derive two calibration coefficients to represent flow angle and velocity magnitude changes. The variation of these coefficients is established through an angular calibration and the resulting curves were used instead of the response equations of the wires. Full details of the calibration procedure and the methodology used can be found in Blanco-Marigorta et al. (1998) and Velarde-Suárez (1997). For the two-wire probe, the angular and velocity uncertainties were estimated to be 2 deg and 2 percent, respectively. The probe support has a diameter of 4 mm. The wires are in a plane perpendicular to the axis of the support and they form an angle of 120 deg. The length of the wires is 2 mm and their diameter 5 μm; therefore, their aspect ratio is 400. The minimum distance between the wires is 1 mm. These dimensions can be compared to the impeller blade span: 33 mm, and the distance between the impeller and the volute tongue: 50 mm.

Velocity data were acquired with the anemometer IFA-100 of TSI Inc. and registered with the digital recorder STOREPLEX DELTA of RACAL Recorders Ltd. Apart from the wires signals, a one pulse per revolution trigger signal was also acquired. This signal helps to delimit the impeller revolutions in the wires signals. Then, data were introduced in a personal computer using an analog-to-digital card DAS16/330i of ComputerBoards Inc. Data were stored in files and transformed according to the calibration charts of the probe to obtain the flow velocity and the flow angle. The data acquisition frequency was chosen equal to 11.4 kHz per channel (380 points per revolution) to obtain a good resolution and the filtering frequency was set at 5 kHz per channel, to avoid aliasing.

Pressure and velocity measurements were also taken at the inlet of the fan by placing an aspiration duct. Contrary to what could be expected from the literature survey, they did not reveal the existence of inlet reverse flow or prerotation in the flow rate range under analysis.

Figure 8 shows the mass-averaged absolute velocity field for 0.7 × *Qo*, at two radial locations at the outlet of the impeller,

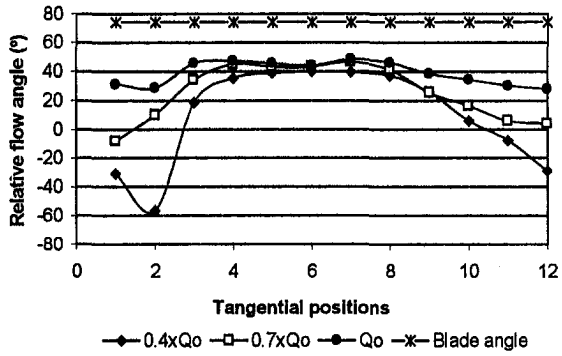

Fig. 9 Mean relative flow angle at impeller outlet

which were placed 10 mm and 40 mm from the impeller exit plane in the radial direction. Data were averaged for 20 impeller rotations. The measurement positions were at the middle plane of the impeller width. The mean absolute flow velocity at the impeller outlet was split up in the impeller tip velocity, U = 32 m/s, and the mean relative flow velocity, thus obtaining the mean relative flow angle, which is compared in Fig. 9 to the blade outlet angle, both measured with respect to the radial direction, for all the circumferential positions.

Figure 10 shows the absolute velocity field pitch-averaged, at point 6 of the inner circumferential location. 20 rotor revolutions were averaged to obtain these results. The radial component, V_r, was normalized using the mean value V_{rm} of that component at that radial location for all the 12 measurement locations. The tangential component, V_{tg}, was normalized using the impeller tip velocity. The numbers 1, 2 . . . refer to evenly distributed points between two impeller blades. The jet-wake structure is not so clear as in backward-curved blades centrifugal fans, although the presence of the blade wakes can be observed in both velocity components for all the measured flow rates. Behind the wake, both components have a minimum. The tangential component increases with the flow rate, as expected as these flow rates belong to the unstable zone, in which total pressure increases with flow rate. Figure 11 shows the same distributions as Fig. 10 but at point 10 of the inner radial location. The jet-wake structure is not so clear as in the previous case. Whereas at point 6 the normalized radial component remains higher than 1, at point 10 is always lower than 1, revealing a flow asymmetry around the impeller outlet.

Figure 12 shows the frequency spectrum of the tangential absolute component corresponding to 0.7 × *Qo* at point 5 of the inner radial location. In this figure, the peaks due to the blade passing frequency and its second harmonic can be clearly observed. However, the jet-wake structure and the peak due to the

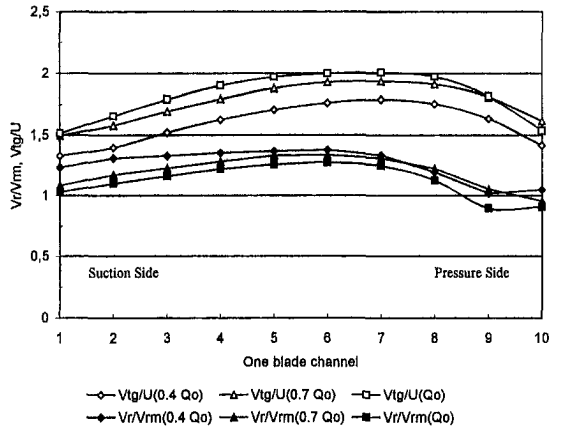

Fig. 10 Absolute velocity components in a blade channel, Point 6 /

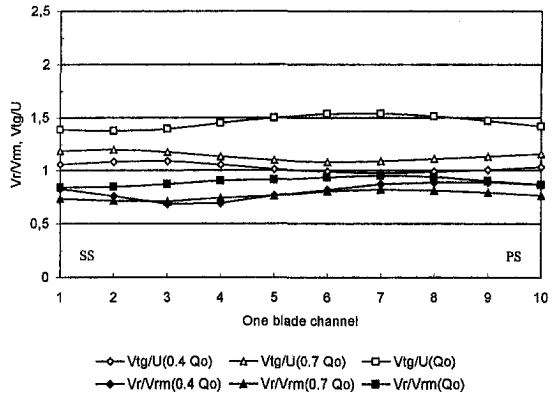

Fig. 11 Absolute velocity components in a blade channel, Point 10 /

blade passing frequency are not so clear at all the circumferential positions, showing a lack of flow uniformity around the impeller outlet. Broad band components appear in the circumferential positions closer to the volute tongue, whereas the peak due to the blade passing frequency disappears.

Aeroacoustic Coupling

Once the flow was determined, some of the aerodynamic features observed were to be related to the fan noise generation, by means of Powell's equation (1964):

$$\frac{1}{c_o^2}\frac{\partial^2 p'}{\partial t^2} - \Delta p' = \rho_o \nabla(\vec{\omega} \times \vec{u}) \tag{1}$$

where p' represents the acoustic pressure fluctuations. Lighthill's analogy considers the flow field as a superposition of a small amplitude fluctuating sound field and a nonperturbed aerodynamic field that generates the fluctuating field. Powell's equation is an alternative to Lighthill's analogy that relates the change with space and time of the pressure fluctuations to the unperturbed aerodynamic field.

With the measurements taken only in two radial locations, the source term on the right hand was not fully determined because no derivative could be made in the radial direction. Therefore, the aeroacoustic coupling was studied using only the axial component of the vorticity, ω_z. This vorticity component was obtained using Crocco's formulation of the Euler's equation:

$$\frac{\partial \vec{u}}{\partial t} + \nabla\left(\frac{p}{\rho} + \frac{V^2}{2}\right) = -\vec{\omega} \times \vec{u} \tag{2}$$

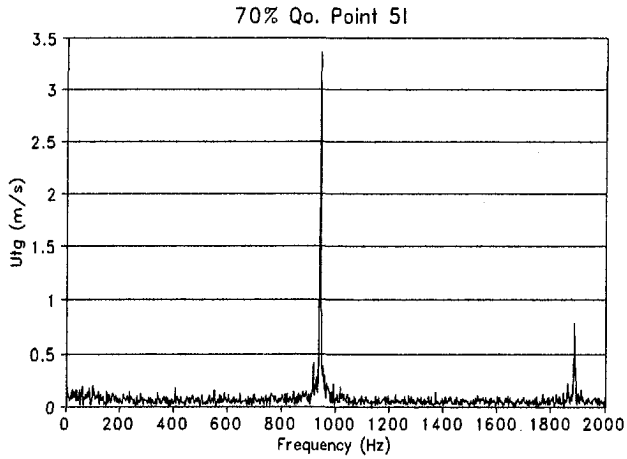

Fig. 12 Spectrum of the tangential component of velocity, 0.7 × *Qo*, Point 5 /

Considering the circumferential component of that equation, ω_z can be calculated as follows:

$$\frac{\partial V_{tg}}{\partial t} + \frac{1}{r}\frac{\partial}{\partial \theta}\left(\frac{p}{\rho} + \frac{V^2}{2}\right) = V_r \omega_z \tag{3}$$

Chu et al. (1995) make a similar approach to obtain the pressure field in a centrifugal pump, using Particle Displacement Velocimetry (PDV) to obtain velocity and vorticity fields.

The time derivative of the tangential component is estimated by the following quotient:

$$\frac{\partial V_{tg}}{\partial t} \approx \frac{V_{tg}(n+1) - V_{tg}(n)}{\Delta t} \tag{4}$$

where $V_{tg}(n)$ and $V_{tg}(n+1)$ are two values acquired at consecutive instants at a fixed circumferential position, and Δt is the inverse of the acquisition frequency.

The spatial derivative in the circumferential direction of the total pressure is represented by the following quotient:

$$\frac{\partial}{\partial \theta}\left(\frac{p}{\rho} + \frac{V^2}{2}\right) \approx \frac{1}{\rho}\frac{p(n+1) - p(n)}{\Delta \theta} + \frac{1}{2}\frac{V^2(n+1) - V^2(n)}{\Delta \theta} \tag{5}$$

where $p(n)$, $p(n+1)$, $V(n)$ and $V(n+1)$ are values acquired at consecutive instants. In this case, the angular step $\Delta\theta$ is calculated taking into account that the signal at point $(n+1)$ is equivalent to the signal at point (n), but displaced Δt in time, i.e., $\Delta\theta = \Delta t \times \Omega$.

A computer code based on Eq. (5) was written in C language in order to calculate the vorticity field starting from the experimental data of pressure and velocity fields. The vorticity was calculated for all the measurement points and for the three flow rates studied. The maximum uncertainty for the vorticity was estimated to be four percent. A trigger signal activated with the impeller rotation was used in order to ensure a right synchronization between pressure and velocity signals. Once the time evolution of the vorticity was computed, a Fast Fourier Transform (FFT) algorithm was applied in order to obtain the corresponding spectra.

Figure 13 shows the evolution of the vorticity, normalized with the impeller rotation velocity and mass-averaged over the circumferential extent of a blade channel at point 6 of the outer plane. The jet-wake structure can be observed again, mainly for increasing flow rates. Zones of high levels of vorticity (in absolute value) correspond approximately with the wake zone, whereas low absolute values of the vorticity correspond with the central core of the flow between the blades. In Fig. 14, the vorticity spectrum for the same position is plotted for $0.4 \times Qo$, and Fig. 15 shows the spectrum for the same point and Qo. In the former, the broad band components prevail, although the peak due to the blade passing frequency can be appreciated. This peak is clearer in the latter spectrum in which even the second harmonic can be appreciated (around 2000 Hz). As with the velocity field, the vorticity field exhibits substantial changes among the different positions. Only

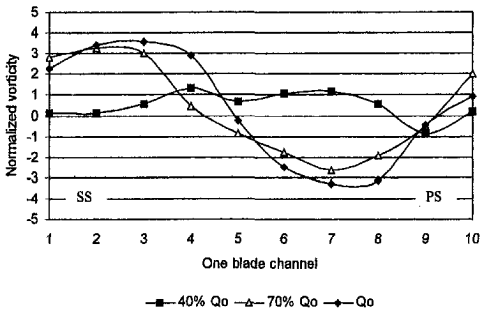

Fig. 13 Axial component of the vorticity in a blade channel

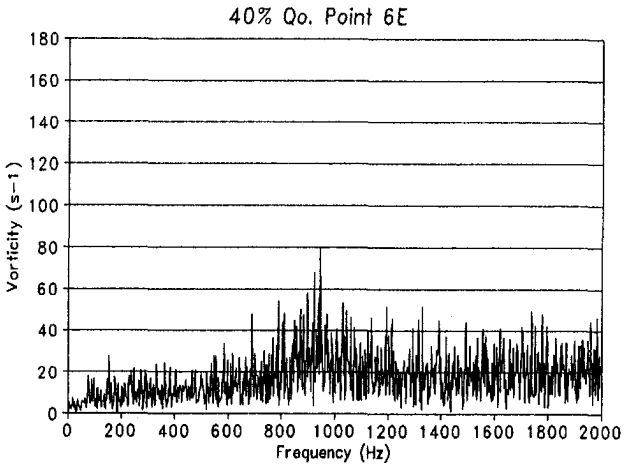

Fig. 14 Vorticity spectrum, 0.4 × *Qo*, Point 6 *E*

broad band spectra were obtained in the circumferential positions closer to the volute tongue, thus not revealing any peak due neither to the blade passing frequency nor to its second harmonic.

The vorticity spectra did not show relevant peaks at low frequencies, which could imply that the noise generated at those frequencies has not aerodynamic origins.

Conclusions

An experimental characterization of the flow field in a forward-curved blades centrifugal fan with unstable performance curves was carried out. The flow field measurements allow the study of the aerodynamic noise generated by the fan, which can be related to the vorticity and velocity fields at two impeller exit radial locations.

The fan sound power level spectrum was measured, from which it can be concluded that the main contribution to the noise was the impeller rotational frequency. On the other hand, the tonal noise due to the blade passing frequency was much lower compared to the normal behavior of an industrial fan with a better aerodynamic design. Blade passing frequency is dominant in the velocity spectra, and its effects decrease with flow rate, although in the vicinity of the volute tongue the spectra contains broad band components at lower frequencies.

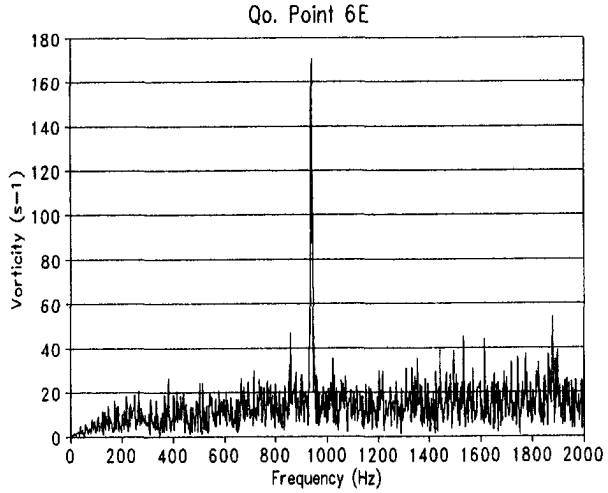

Fig. 15 Vorticity spectrum, *Qo*, Point 6 *E*

Regarding the flow field at the two impeller exit radial locations considered, there is great asymmetry, with considerable changes in both magnitude and direction among the different circumferential positions. In particular, big differences appear between the circumferential locations closer to the volute tongue and the other ones.

Finally, the aerodynamic features were related to the fan noise generation. The vorticity field shows that the main contribution to the fan noise is the blade passing frequency, although with great differences with respect to the flow rate and position around the impeller. As the velocity field, the vorticity spectra contain broad band components in the vicinity of the volute tongue. These results agree with the reduced importance of the tonal noise at the blade passing frequency in the sound power level spectra.

Analyzing the vorticity distributions and spectra, it can be concluded that the tonal aerodynamic noise is produced at the blade passing frequency, and to a lesser extent, at its second harmonic, increasing with the flow rate. Some other features of the noise spectra (the supremacy of noise at the impeller rotational frequency and at other low frequencies) were not related to aerodynamic phenomena, so they may be caused by mechanical sources. However, the tonal noise has to be reduced and has to be investigated because it occurs over a range of frequencies especially unpleasant to the human ear. Therefore, the research opened with this work may be of considerable interest, establishing a starting point for the design of quieter and more efficient fans. Although the results obtained in this work could be extrapolated to some other forward-curved bladed fans, the influence of key design parameters such as blade angles, blade number, blade aerodynamic loading, distance to the volute tongue and some others identified in the course of the research, has still to be studied.

Acknowledgments

This work was supported by the Research Project "Estudio de los mecanismos aerodinámicos de generación acústica en ventiladores axiales," Ref. PB-TDI97-01, FICYT, Asturias, Spain.

References

Blanco-Marigorta, E., Ballesteros-Tajadura, R., and Santolaria, C., 1998, "Angular Range and Uncertainty Analysis of Non-Orthogonal Crossed Hot Wire Probes," ASME JOURNAL OF FLUIDS ENGINEERING, Vol. 120, pp. 90–94.

British Standard BS-848, 1980, "Fans for General Purposes. Part 1. Methods of Testing Performance."

British Standard BS-848, 1985, "Fans for General Purposes. Part 2. Methods of Noise Testing."

Cau, G., Mandas, N., Manfrida, Nurzia, F., 1987, "Measurements of Primary and Secondary Flows in an Industrial Forward-Curved Centrifugal Fan," ASME JOURNAL OF FLUIDS ENGINEERING, Vol. 109, pp. 353–358.

Chu, S., Dong, R., and Katz, J., 1995, "Relationship Between Unsteady Flow, Pressure Fluctuations, and Noise in a Centrifugal Pump-Part A: Use of PDV Data to Compute the Pressure Field," ASME JOURNAL OF FLUIDS ENGINEERING, Vol. 117, pp. 24–29.

Chu, S., Dong, R., and Katz, J., 1995, "Relationship Between Unsteady Flow, Pressure Fluctuations, and Noise in a Centrifugal Pump-Part B: Effects of Blade-Tongue Interactions," ASME JOURNAL OF FLUIDS ENGINEERING, Vol. 117, pp. 30–35.

Comte-Bellot, G., 1975, "Hot-Wire Anemometry," *Annual Review of Fluid Mechanics,* Vol. 8, pp. 209–231.

Ffowcs Williams, J. E., and Hawkings, D. L., 1969, "Sound Generation by Turbulence and Surfaces in Arbitrary Motion," *Proceedings of the Royal Society,* Series A, Vol. 264, pp. 321–342.

Lighthill, M. J., 1952, "On Sound Generated Aerodynamically. I. General Theory," *Proceedings of the Royal Society,* Series A, Vol. 211, pp. 564–587.

Neise, W., 1992, "Review of Fan Noise Generations Mechanisms and Control Methods," *Proceedings of the SFA Symposium on Fan Noise,* Senlis, France.

Powell, A., 1964, "Theory of Vortex Sound," *Journal of the Acoustical Society of America,* Vol. 16.

Shepherd, I. C., and Lafontaine, R. F., 1992, "Measurement of Vorticity Noise Sources in a Centrifugal Fan," *Proceedings of the SFA Symposium on Fan Noise,* Senlis, France.

Thompson, M. C., and Hourigan, K., 1992, "Prediction of the Noise Generation in a Centrifugal Fan by Solution of the Acoustic Wave Equation," *Proceedings of the SFA Symposium on Fan Noise,* Senlis, France.

Velarde-Suárez, S., 1997, "Comportamiento Aeroacústico de Ventiladores Inestables" (*in Spanish*), Ph.D. thesis, Univ. of Oviedo, Spain.

A. C. Mueller
Graduate Student.

S. A. Kinnas
Associate Professor.

ECJ 8.502, Ocean Engineering Group,
Department of Civil Engineering,
The University of Texas at Austin,
Austin, TX 78712
e-mail: kinnas@mail.utexas.edu

Propeller Sheet Cavitation Predictions Using a Panel Method

A boundary element method is used to predict the time-dependent cavitation on a propeller subject to nonaxisymmetric inflow. The convergence of the method is studied. The predicted cavities agree well with those observed in CAPREX, an experiment performed at MIT's variable pressure water tunnel. The method is modified so that prediction of cavities detaching at mid-chord regions is possible. An algorithm for predicting the cavity detachment location on the blade is described and applied on a blade geometry which exhibits mid-chord cavitation.

Introduction

In recent years, the design of high speed marine vehicles has become increasingly competitive. The design of efficient propulsion systems is a very important aspect of the overall design process. However, as these vehicles attain higher speeds, cavitation can become an inhibitor to the propulsion systems. The need for accurate modeling of cavitation is clear since accurate prediction of the cavities may result in better propulsor designs.

Recent advancements in the propulsor design industry have placed heavier demands on the available modeling tools. For example, a well-designed propulsion system will permit cavitation if higher efficiencies and speeds can be obtained. In extreme cases, racing propellers may have only a few uses because of the extremely high amount of permitted cavitation. This class of propellers in particular, is often designed to exhibit mid-chord cavitation (Vorus and Mitchell, 1994) in order to reduce the cavity thickness and subsequently the cavity drag. Mid-chord or bubble cavitation may also appear on modern, conventional propeller blade designs. Tip-vortex (developed or incipient) and face cavitation are also very common in modern propeller designs.

With the advent of faster computers, the development of codes with "more involved" modeling has become possible. A vortex and source lattice method based on a linearized cavity model was available as early as 1979 (Lee, 1979). The corresponding computer code is called PUF-3. This method was modified to include the leading edge corrections which accounted for the non-linear effect of the blade thickness on the cavity size (Kerwin and Kinnas, 1986; Kinnas, 1991). The option for prescribed cavity detachment downstream of the blade leading edge was also implemented in PUF-3 Kinnas and Fine, 1989). A list of more recent versions of PUF-3 may be found in (Kinnas et al., 1997).

A cavitating propeller computer program using a boundary element method (BEM or panel method) was developed in 1992 (Kinnas and Fine, 1992; Fine, 1992). The method implemented a nonlinear cavity model and also allowed for prescribed cavity detachment. While the vortex and source lattice method's predictions seem to be close to those of the boundary element method for some cases, the latter method always offers a more accurate modeling of the flow at the leading edge and of the blade thickness/loading coupling. The boundary element method (PROPCAV)[1] also provides a better foundation for future improvements, such as the modeling of the developed tip-vortex, face, and mid-chord cavitation.

In the present work, the effect of the grid parameters on PROPCAV's predicted results is studied for a recent propeller design. The predicted cavity shapes are compared to those observed at an experiment performed at MIT's variable pressure water tunnel. In an effort to model mid-chord detachment, a method is proposed and implemented in PROPCAV. Since no universally accepted definition for mid-chord detachment exists, we will loosely define it here as detachment of the cavity "well behind" the leading edge of the propeller blades. The present method uses the predicted pressure distributions from the wetted (non-cavitating) run in order to formulate an initial cavity detachment line.[2] This detachment line is used in PROPCAV (with cavitation allowed) and adjusted accordingly until the resulting cavity thickness is positive everywhere on the cavity and the pressures on the wetted blade are larger than vapor pressure. The method is used to predict the mid-chord detachment line for a given blade geometry.

Formulation

A propeller subject to a general inflow wake,[3] $\vec{q}_{\text{wake}}$, is shown in Fig. 1. The following equations are more extensively described in (Kinnas and Fine, 1992). They are summarized here for completeness.

The goal of the mathematical formulation is to determine the velocity, $\vec{q}$, at any point on and near the propeller blade. With the velocity known, it is then possible to determine pressures, blade forces, thrust and torque coefficients, and the formation of water vapor due to low pressures (cavitation). In the coordinate system (x_P, y_P, z_P), which rotates with the propeller, the velocity vector, $\vec{q}$, can be expressed as a sum of the local inflow velocity, $\vec{q}_{\text{in}}$, and the perturbation potential velocity (the velocity induced by the propeller), $\vec{q}_{\text{pert}}$, as follows:

$$\vec{q} = \vec{q}_{\text{in}} + \vec{q}_{\text{pert}} \tag{1}$$

In the case of inviscid flow, the perturbation velocity can be expressed in terms of the perturbation potential, ϕ, as follows:

$$\vec{q}_{\text{pert}} = \nabla\phi \tag{2}$$

The inflow velocity, $\vec{q}_{\text{in}}$, with respect to the propeller fixed system can be expressed as the sum of the inflow wake velocity, $\vec{q}_{\text{wake}}$, and the propeller's angular velocity, $\vec{\omega}$, at a given location, $\vec{r}$:

[1] The boundary element method will also be referred to as "PROPCAV," the name of the corresponding computer code.

Contributed by the Fluids Engineering Division for publication in the JOURNAL OF FLUIDS ENGINEERING. Manuscript received by the Fluids Engineering Division October 14, 1997; revised manuscript received February 24, 1999. Associate Technical Editor: J. Katz

[2] The detachment line is the locus of points on the blade where cavitation begins (also referred to as detachment locations).

[3] The inflow wake is the "effective" wake to the propeller, i.e., it includes the interactions between the vorticity in the nominal wake and the propeller.

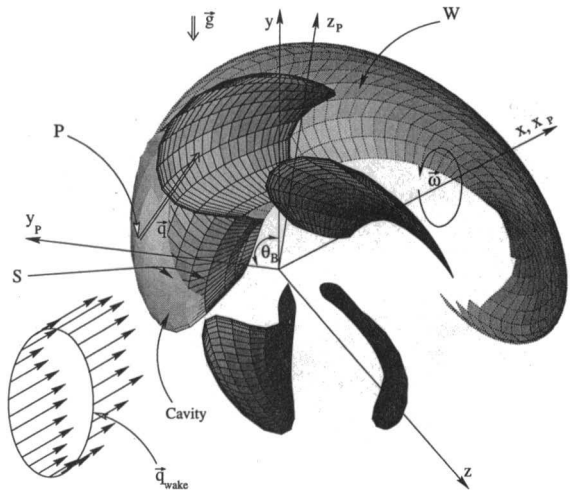

Fig. 1 Propeller subject to general inflow wake. The propeller fixed (x_P, y_P, z_P) and the inertial (x, y, z) coordinate systems are shown.

$$\vec{q}_{\text{in}} = \vec{q}_{\text{wake}} + \vec{\omega} \times \vec{r} \tag{3}$$

The perturbation potential, ϕ, satisfies Laplace's equation in the fluid domain:

$$\nabla^2 \phi = 0 \tag{4}$$

Green's third identity is applied to solve the potential problem on the blade and cavity surface, S, and on the trailing wake sheet, W:

$$2\pi\phi = \oint_S \left[\phi \frac{\partial}{\partial n}\left(\frac{1}{r}\right) - \frac{\partial \phi}{\partial n}\frac{1}{r} \right] dS + \oint_W \Delta\phi \frac{\partial}{\partial n}\left(\frac{1}{r}\right) dW \tag{5}$$

Several boundary conditions are needed to determine ϕ:

- The kinematic boundary condition is applied on the wetted part of the blade:

$$\frac{\partial \phi}{\partial n} = -\vec{q}_{\text{in}} \cdot \vec{n} \tag{6}$$

The dynamic boundary condition is applied on the cavity surface:

$$P = P_{\text{vapor}} \tag{7}$$

The Morino Kutta condition is applied at all spanwise locations of the blade trailing edge (Morino and Kuo, 1974):

$$\Delta\phi_{T.E.} = \phi^+_{T.E.} - \phi^-_{T.E.} = \Gamma \tag{8}$$

The closure condition is applied at all spanwise locations of the cavity trailing edge.

$$\delta = 0 \tag{9}$$

$\phi^+_{T.E.}$ and $\phi^-_{T.E.}$ are the potentials at the blade trailing edge of the suction side and pressure side, respectively, and Γ is the circulation around the blade at the same spanwise location. δ is the cavity height at the trailing edge of the cavity. Equation (5) and these boundary conditions, Eqs. (6), (7), (8), and (9), determine the perturbation potential on the cavity and blade.

Once ϕ has been evaluated, the pressures are determined via Bernoulli's equation:

$$\frac{\partial \phi}{\partial t} + \frac{P}{\rho} + \frac{1}{2}|\vec{q}|^2 + gy = \frac{P_\infty}{\rho} + \frac{1}{2}|\vec{q}_{\text{in}}|^2 \tag{10}$$

where P is the pressure at a point on the blade or cavity, gy is the hydrostatic term, and P_∞ is the pressure at the level of the propeller shaft. Equation (10) is based on the Bernoulli equation with respect to a rotating system of coordinates (Batchelor, 1967). Note that the right-hand side of Eq. (10) only contains the pressure at the level of the shaft due to the assumption that the inflow pressure obeys the hydrostatic law. If a point on the blade and the blade angle, θ_B, are specified, then the terms gy, and $\vec{q}_{\text{in}}$ are known. $\partial\phi/\partial t$ is evaluated numerically via a backward finite differencing scheme (Fine, 1992). Thus, with all terms accounted for, it is possible to solve for P. Hence, it is possible to examine pressures at any point on the blade. A derivation of Eq. (10) may be found in Mueller (1998).

As shown in Kinnas and Fine (1992), the dynamic boundary condition, Eq. (7), is equivalent to having known values of ϕ on the cavity. The Green's identity, Eq. (5), is then solved with respect to ϕ on the wetted blade and $\partial\phi/\partial n$ on the cavity.

The pressure coefficient, C_p, is defined as:

$$C_p \equiv \frac{P - P_\infty}{\frac{\rho}{2}n^2D^2} \tag{11}$$

where D is the diameter of the propeller and n is the rotational frequency (rev/s) of the propeller. The cavitation number, σ_n is defined similarly:

$$\sigma_n \equiv \frac{P_\infty - P_{\text{vapor}}}{\frac{\rho}{2}n^2D^2} \tag{12}$$

such that cavitation will occur whenever:

$$-C_p \geq \sigma_n \tag{13}$$

The advance ratio is defined as:

$$J_s = \frac{V_s}{nD} \tag{14}$$

where V_s is the ship speed.

The cavity heights can be determined by applying the kinematic boundary condition on the cavity surface. It should be noted at this point that in order to determine the cavity shape an iterative process is required as described in Kinnas and Fine (1993). However, in that work of Kinnas and Fine (1993) it was found that the cavity shape from the first iteration (when the panels are located on the blade under the cavity) is very close to the cavity shape determined from the iterative process.

$$\nabla\phi \cdot \vec{n}_c = -\vec{q}_{\text{in}} \cdot \vec{n}_c \tag{15}$$

where $\vec{n}_c$ is the normal vector on the cavity surface. By executing the dot product in Eq. (15) and by expressing $\vec{n}_c$ in terms of the derivatives of h (Kinnas and Fine, 1993), the following partial differential equation can be obtained:

$$\frac{\partial h}{\partial s}\left[\frac{\partial \phi}{\partial s} + q_s - \cos\beta\left(\frac{\partial \phi}{\partial v} + q_v\right)\right] + \frac{\partial h}{\partial v}\left[\frac{\partial \phi}{\partial v} + q_v - \cos\beta\left(\frac{\partial \phi}{\partial s} + q_s\right)\right] = \sin^2\beta\left(\frac{\partial \phi}{\partial n} + q_n\right) \tag{16}$$

where h is the cavity height. The unit vectors, $\vec{s}$, $\vec{v}$ and $\vec{n}$ depend on the geometry of the panel. The vector $\vec{n}$ is normal to the blade, while the vectors $\vec{s}$, and $\vec{v}$ are tangent to the blade. The angle between the vectors $\vec{s}$ and $\vec{v}$ is β. The panel coordinate system is shown in Fig. 2. The values q_s, q_v, and q_n are the components of $\vec{q}_{\text{in}}$ expressed in the local coordinate system.

Equation (16) is integrated to provide the cavity heights. Finite difference approximations for the derivatives, $(\partial h/\partial s)$ and $(\partial h/\partial v)$, are used to determine the heights at all panels. In general, the heights at the trailing edge of the cavity at each radial section

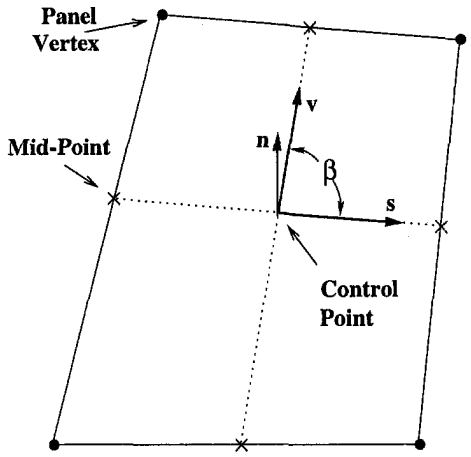

Fig. 2 The local panel coordinate system showing $\hat{s}$, $\hat{v}$, $\hat{n}$ and β. The vectors $\hat{s}$ and $\hat{v}$ are formed by the lines connecting the mid-points of the lines connecting the panel vertices. The vector $\hat{n}$ is normal to $\hat{s}$ and $\hat{v}$.

will be nonzero unless the cavity lengths have been guessed correctly. The value of the height at the trailing edge of the cavity at a particular radial section is designated as δ. When the cavity lengths (at each radial section) are adjusted and the problem is solved again, the values of δ will change. Thus, the problem must be solved in an iterative manner. The secant method is used to provide subsequent guesses for cavity length. A correct guess of the cavity length will yield a value of δ which is small. After several iterations, the cavity will close on the blade or wake to within a certain tolerance, δ_{tol}. Figure 3 shows a cavity that has closed to within this tolerance. The algorithm which solves for the potential and determines the cavity planform is described in more detail in (Fine, 1992).

After a solution is obtained at a particular blade angle (or timestep), the propeller will then "click" one timestep to the next blade angle where the problem is solved in the same manner, but possibly with different inflow conditions.

Solution Convergence

Comprehensive studies of the convergence of the predicted cavity planforms from PROPCAV were performed by Fine (1992) and Fine and Kinnas (1993). The convergence of the predicted cavity planforms and cavity volume from PROPCAV is investigated for a recent propeller design (DTMB N4990), the geometry of which is given in Appendix A. The code was run under unsteady conditions. A non-uniform inflow wake was used. Figure 4 shows the nondimensionalized velocity in the x-direction. The velocities are nondimensionalized by the ship speed and the y and z axes are nondimensionalized by the propeller radius.

In the method, the effect of the other blades on the key blade is accounted for iteratively over several propeller revolutions until convergence is achieved. The effect of the number of revolutions on the results is shown in Fig. 5. The graph should be read from left to right; the program's earlier revolutions are to the left of the graph. Fifty panels were used in the chordwise direction of the blade (includes upper and lower surfaces) with ten panels in the spanwise direction. This is denoted as 50 × 10. As the figure shows, a converged solution was reached after the first two revolutions. This is indicated by the "leveling off" of the maximum

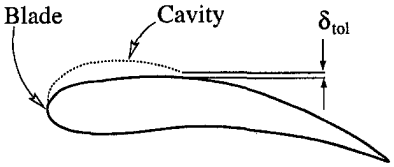

Fig. 3 Cavity closure condition

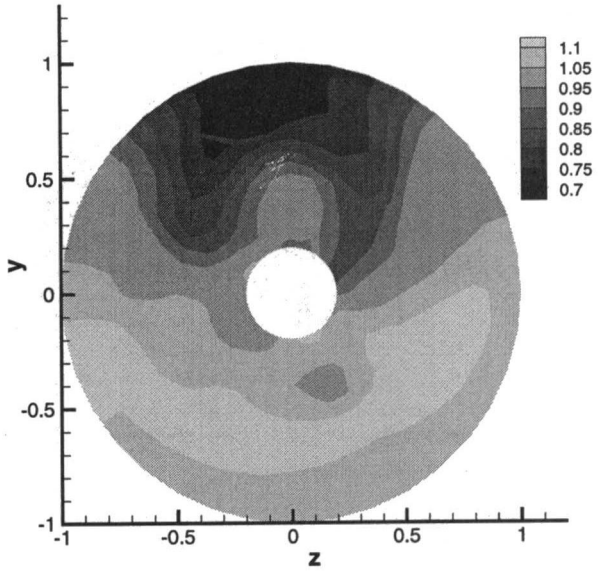

Fig. 4 Inflow velocities in the X-direction. The velocities are nondimensionalized by the ship speed, V_s.

cavity volume for the last three revolutions. Slightly better convergence is seen for the final two revolutions (as indicated by the extremely similar shapes near the bases of the last two peaks). This indicates that 2.5 revolutions are required for convergence. If slightly better convergence is desired (especially during the cavity collapse stage), then 3.5 revolutions may be required. For the runs mentioned in this paper, at least 2.5 revolutions were completed.

The effect of the panel discretization on the predicted cavity volume and planform is shown in Figs. 6 and 7. Figure 6 shows that there is a slight difference in the predicted cavity volume for the 50 × 10 panel configuration. However, the convergence of the predicted volumes has been achieved for panel configurations with 60 × 12 or more panels. Also, the predicted cavity planforms, shown in Fig. 7, are quite similar in shape, even when comparing the 50 × 10 run to the 80 × 16 run. The cavities plotted in Fig. 7 occur at a blade angle of 30 deg, where the cavity volume reaches its maximum value, as indicated by Fig. 6. Table 1 shows the computational requirements for the above runs. All runs were done on a DEC Alpha 600-5/266.

The run times of PROPCAV have recently been reduced by

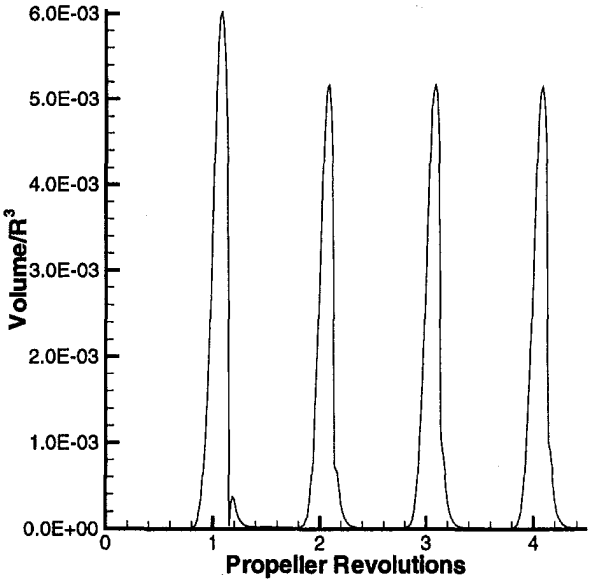

Fig. 5 Cavity volume history through 4.5 revolutions. for the N4990 propeller. 50 × 10 panels. J_s = 1.0. σ_n = 3.0.

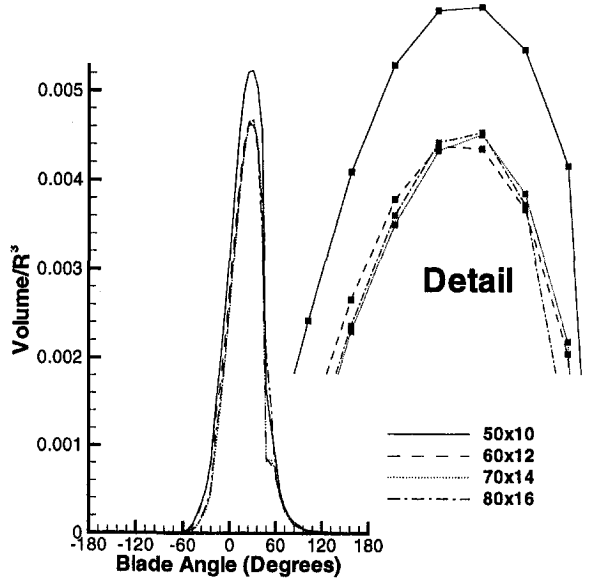

Fig. 6 Cavity volume plot for final revolution for 50 × 10, 60 × 12, 70 × 14, and 80 × 16 panel configurations. Blade angle of 0 degrees is the top of propeller revolution. N4990 propeller. J_s = 1.0. σ_n = 3.0.

modifying the cavity length computation algorithm. A complete description of the modifications to the code is given by Mueller (1998).

Experimental Validation

PROPCAV was used to predict the cavitation for the David Taylor Model Basin N4148 propeller. This propeller was recently tested at MIT's water tunnel in a screen generated non-axisymmetric inflow (Mishima et al., 1995). The geometry of N4148 is given in Appendix A. The predicted cavity shapes from PROPCAV are shown in Figs. 8 and 9 together with the photographs from Mishima et al. (1995) for two different conditions. PROPCAV used the corresponding inflow wake in order to take into account the effects of the tunnel walls (Choi and Kinnas, 1999). The advance ratio based on tunnel speed was 0.91. The advance ratio in PROPCAV has been adjusted for thrust identity with the experiment (Young and Kinnas, 1999). A more comprehensive investigation of the modeling of the tunnel walls is given in (Choi and Kinnas, 1999).

The computer generated results agree fairly well with the experimental observations as shown in Figs. 8 and 9. Some disagreement exists near the blade tip. PROPCAV has over-predicted the sheet cavitation near the tip. As seen in the lower part of Figure 8, the tip-vortex cavity and the sheet cavity "connect" to each other near the tip at the blade angle of −30 deg, but not at the other blade angles. In Fig. 9, the vortex and sheet cavity almost connect at −30 deg. The tip-vortex cavities and sheet cavities seen in the photos appear to interact with each other in a seemingly unpredictable manner. This behavior is completely missed by the present method. The present cavity model is inaccurate at the tip region and therefore the predictions in this region are unreliable. Comparisons with the same photographs were also made with the results of HPUF-3AL (a more recent version of PUF-3) (Choi and Kinnas, 1999), and the predicted cavity shapes also agreed well with the observed, except at the tip.

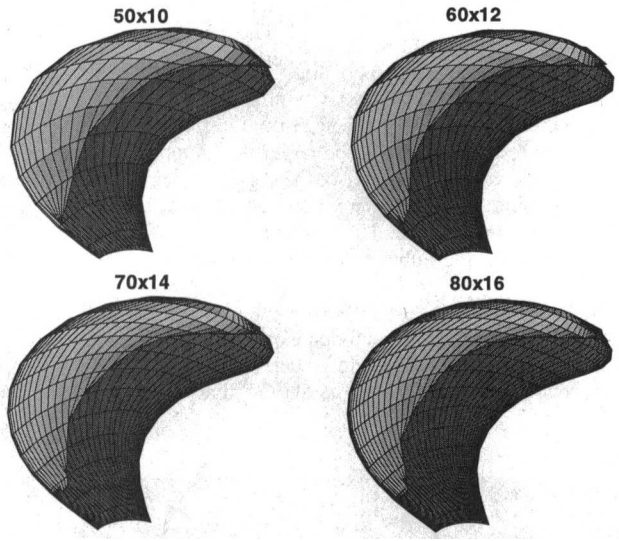

Fig. 7 Cavity shapes for blade angle of 30 degrees for 50 × 10, 60 × 12, 70 × 14, and 80 × 16 panel configurations. N4990 propeller. J_s = 1.0. σ_n = 3.0.

Table 1 CPU times and RAM requirements for different panel configurations

Paneling	CPU Time	RAM required
50 × 10	29 min	65 Meg
60 × 12	1.0 hr	92 Meg
70 × 14	1.6 hr	128 Meg
80 × 16	2.6 hr	175 Meg

Mid-Chord Detachment

A critical assumption for most cavitating propeller models is that the cavity always begins at the leading edge of the propeller blade. For most applications, this is a fair assumption. Propellers are often designed so that cavitation begins at the leading edge, thereby avoiding the potentially harmful effects of mid-chord or bubble cavitation. In some cases though (such as high speed, high efficiency propellers), the propeller can benefit from a non-leading edge detachment. Mid-chord cavities generally tend to be much thinner than leading edge cavities, thereby creating less cavity drag. If these characteristics are desired, then the designer will look for the "flat" pressure distributions that are typical of mid-chord cavitation (Vorus and Mitchell, 1994). These "flat distributions" can also be found in modern, conventional propeller designs and may lead to either mid-chord or bubble cavitation (Jessup et al., 1994). In all of these cases, the assumption of leading edge detachment is grossly invalid.

PROPCAV has (since its creation) had the ability to allow the user to specify a constant chordwise cavity detachment location. The user may specify (in terms of a panel number) the position on the strips that cavity detachment occurs. Figure 10 shows an example of leading-edge detachment and detachment at 2.4 percent x/C.

For the case on the left of Fig. 10, detachment was forced at the leading-edge of the propeller blade. For the case on the right of the same figure, detachment was specified on the third panel. That is, the cavity detached at 2.4 percent of the chordlength at each strip. The figure clearly shows the effect of the detachment location on the predicted cavity extent. A shorter cavity can be seen in the case of detachment downstream of the leading edge. This cavity also has smaller thickness and volume than the cavity that detached at the leading edge. A similar trend was reported by Kinnas and Fine (1989). Note that neither of these runs predicts the correct detachment location; they simply demonstrate how the cavity shape may be affected by moving the detachment locations.

PROPCAV is first refined so that the detachment location is determined via an iterative algorithm. A mid-chord cavitating propeller, MC-1, was studied using a nonconstant detachment line. The geometry of MC-1 is given in Appendix A. An appropriate advance ratio (J_s = 1.04) was chosen so that flat pressure distributions occurred on the suction side. For this investigation, PROPCAV was run in a steady mode (uniform inflow wake with the gravitational and time varying potential terms set to zero).

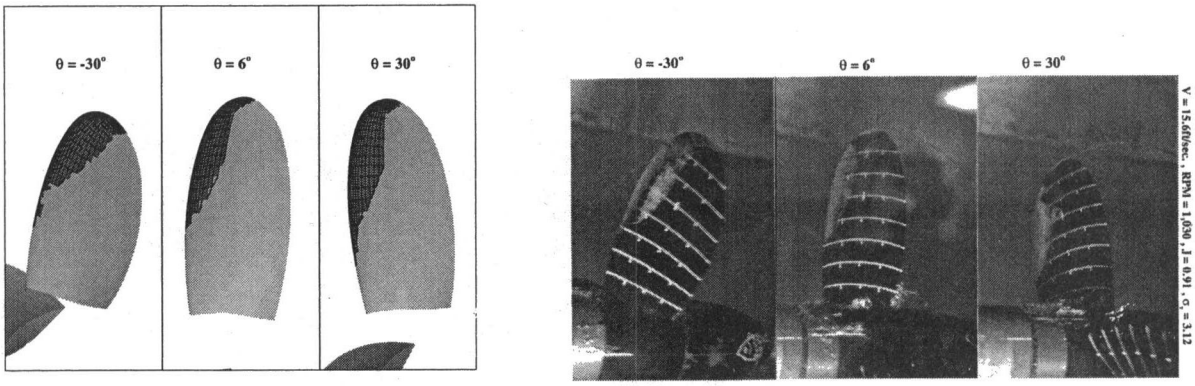

Fig. 8 Comparison of PROPCAV's prediction to the experimental observations. σ_n = 2.58, Panel Configuration: 60 × 15.

Figure 11 shows the pressure distribution for the wetted (non-cavitating) run of the propeller, MC-1.

Note that the contour legend shows the higher values of $-C_p$ as the lighter shades. The lighter the contour plot, the more likely cavitation is to occur. Recall from Eq. (13) that cavitation will occur whenever $-C_p$ exceeds σ_n. Thus, if our cavitation number is anywhere between about 0.8 and 1.45, mid-chord cavitation is likely. Accordingly, if the cavitation number is specified as σ_n = 1.22, it is possible to determine (as an initial guess) where the cavity is likely to detach based on the wetted pressure distribution. PROPCAV numerically determines this detachment line by performing a simple search at each strip. Figure 11 shows this initial detachment line superimposed on the figure. Note that it is simply the panel node nearest the leading edge with a value of $-C_p$ which is greater than or equal to 1.22.

The prediction of the detachment line based on the wetted pressure distribution is not sufficient. It is true that for the cavitation number of 1.22, cavitation will develop whenever $-C_p$ is greater than 1.22. However, the development of a cavity on the blade alters the flow around the blade. The cavity itself must be considered when computing the flow around the blade. The detachment line must be solved in an iterative fashion, just as PROPCAV solves for the cavity shape using a different iterative algorithm.

Following two fully wetted revolutions of the propeller, PROPCAV began the cavitating computations based on the initial detachment line. After the cavity computations are completed at a given blade angle, the detachment line is modified based on the results at that blade angle. The cavitating pressure distributions for the initial and final location of the detachment line are shown in Figs. 12 and 13. The detachment location at a particular strip is adjusted according to the following criteria:

- If the cavity at the strip has negative thickness, then the detachment location is moved toward the trailing edge of the blade.
- If the pressure at the strip is below vapor pressure at a point upstream of the cavity, then the detachment location is moved toward the leading edge of the blade.

These criteria when applied in two dimensions are equivalent to the Villat-Brillouin cavity detachment condition (Villat, 1914; Brillouin, 1911).

After several revolutions of the propeller, the detachment line begins to "stabilize"; major adjustments to the detachment line do not occur. In this case, the stabilization of the detachment line occurred after five cavitating revolutions of the propeller blade. With the method, it is possible to have a slight "back and forth" movement of the detachment locations at certain strips. This occurs when the detachment location is continually adjusted first according to the height criterion, and then according to the pressure criterion (or vice versa). The authors consider these adjustments to have only a slight impact on the final solution. They are presently considered acceptable. A "split panel" refinement of the detachment location would alleviate this behavior. A similar split panel refinement was described by Kinnas and Fine (1993).

The cavity shape for the final detachment line is shown in Fig. 14. Because of the nature of mid-chord cavitation, the cavity is plotted using a different method than that used to show the other cavities in previous sections of the paper. A black line on a strip indicates a thin cavity. If the cavity at a strip is thick enough, one can see the thickness with offsets normal to the blade surface. The predicted pressures appear to be larger than vapor pressure everywhere on the wetted blade. Also, the converged cavity thicknesses after the third revolution are non-negative (although they are remarkably thin). Figure 15 compares the cavity heights at the third strip from the hub for the first and final revolutions of the propeller.

The predictions of mid-chord cavitation by PROPCAV are based on a sheet cavitation model. Consequently, these predictions of mid-chord cavitation should be considered susceptible to errors because of bubble or cloud cavitation that can occur in these

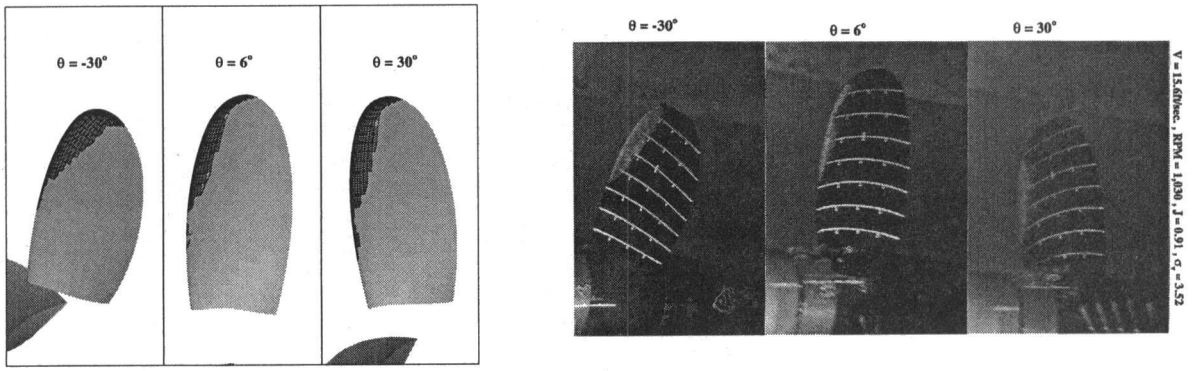

Fig. 9 Comparison of PROPCAV's prediction to the experimental observations. σ_n = 2.91, Panel Configuration: 60 × 15.

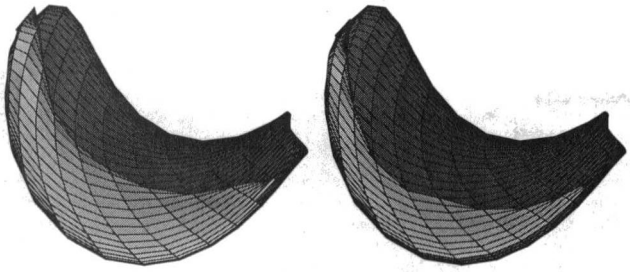

Fig. 10 Cavity shape predicted with detachments at leading-edge (left) and x/C = 2.4 percent (right). The propeller is N4990 with 60 × 12 panels. σ_n = 3.0. J_s = 1.0.

regions. PROPCAV cannot predict when bubble cavitation will occur; the modeling of bubble and cloud cavitation is a very complex problem not addressed in this paper. However, coupling these results with observations of a cavitating propeller experiment may provide insight into these phenomena. This is further discussed in the Future Work section.

Conclusions

The cavity volumes predicted by the boundary element method were found to converge quickly with the number of revolutions for the DTMB N4990 propeller. The panel configuration had a slight impact on the volumes, but minimal impact on the cavity planform.

The results of the boundary element method were successfully correlated with the cavitation experiment performed at MIT. Near the tip region, however, the BEM was found to overpredict appreciably the amount of cavitation. Recent extensions, refinements, and comparisons with experiments, can be found in Kinnas et al. (1998) and in Young and Kinnas (1999).

An iterative method was implemented into the BEM in order to predict mid-chord sheet cavitation. The criteria for choosing the detachment location are the existence of positive cavity thicknesses and pressures everywhere on the wetted surface which are greater than vapor pressure. Note that this method considers inviscid flow. Viscous phenomena can have an effect on the cavity

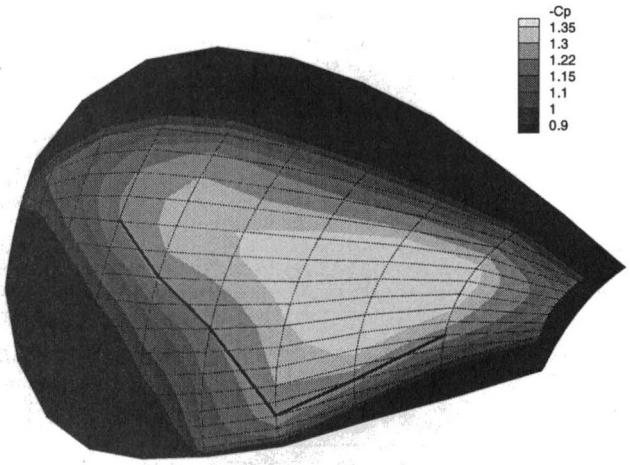

Fig. 11 Pressure distribution, wetted (non-cavitating) run. Propeller MC-1. J_s = 1.04. Also shown is the initial detachment line for σ_n = 1.22.

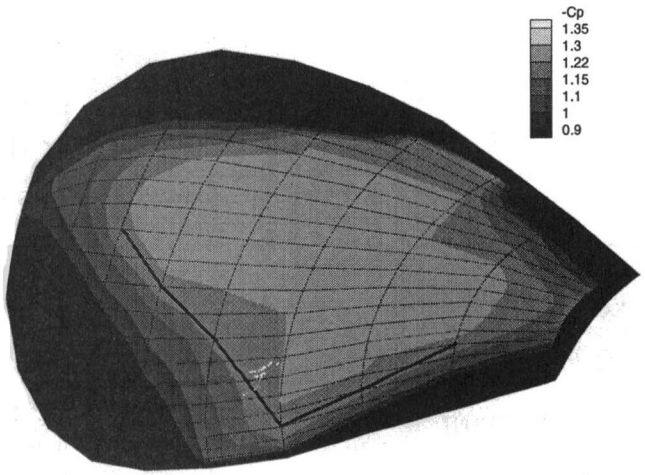

Fig. 12 Cavitating pressure distribution for initial detachment line. σ_n = 1.22

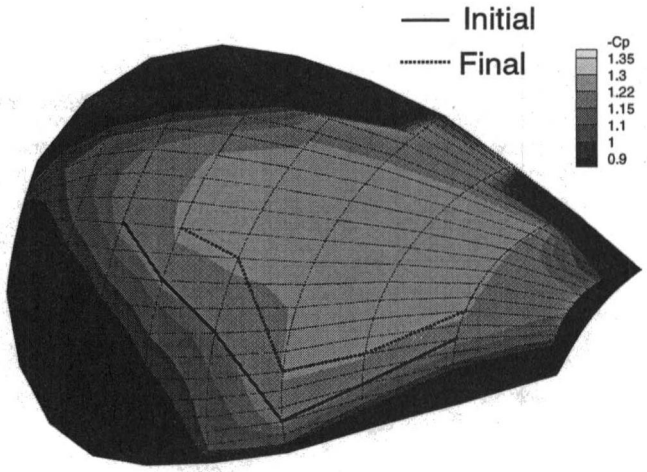

Fig. 13 Cavitating pressure distribution for final detachment line. σ_n = 1.22

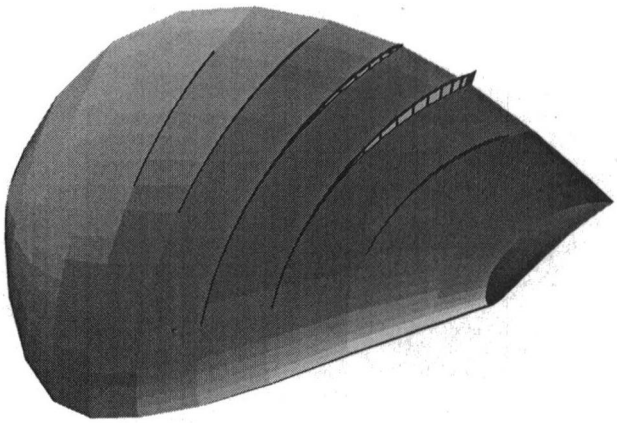

Fig. 14 Predicted cavity shape for final detachment line

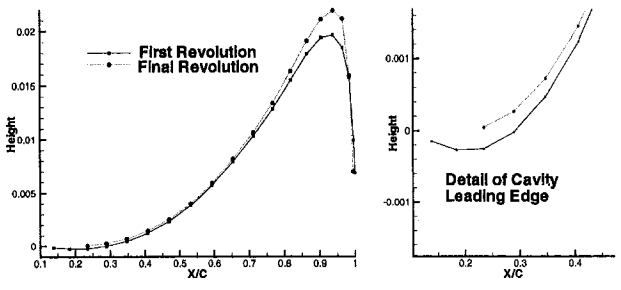

Fig. 15 Cavity heights on the third strip from the hub for the first and final cavitating revolutions

detachment as was shown by Franc and Michel (1985). In order to locate the detachment location based on the criterion of Franc and Michel (1985), the boundary layer on the propeller blades must be solved. This could be done in PROPCAV in a stripwise sense, but the additional computation and memory requirements would greatly increase the program's run times. A two-dimensional boundary layer solver coupled with a panel method has been applied on cavitating hydrofoils by Brewer and Kinnas (1997).

Future Work

- Continue testing and improving the mid-chord cavitation model. Test the model for an unsteady flow case and a supercavitating propeller.
- Improve modeling of developed tip-vortex cavitation. Work is underway in this area.
- Validate modeling of mid-chord cavitation. Compare the cavitation predictions with experimental observations of mid-chord or bubble cavitation. Correlate predictions with other observed phenomena such as bubble and cloud cavitation. Combined analysis and experiments could lead to an answer of the fundamental question: How thin must a cavity be in order to transform from mid-chord sheet to bubble cavitation?

Acknowledgment

Support for this research was provided by Phase II of the "Consortium on Cavitation Performance of High Speed Propulsors" with the following members: David Taylor Model Basin, Daewoo Shipbuilding and Heavy Machinery, El Pardo Model Basin, Hamburg Ship Model Basin, Hyundai Maritime Research Institute, KaMeWa AB, Michigan Wheel, Rolla SP Propellers SA, Sulzer-Hydro GMBH, Ulstein Propellers, Volvo-Penta of the Americas, and Wärtsilä Propulsion.

References

Brewer, W. H. and Kinnas, S. A., 1997, "Experiment and Viscous Flow Analysis on a Partially Cavitating Hydrofoil," *Journal of Ship Research,* Vol. 41(3), pp. 161–171, Sept.

Brillouin, M., 1911, "Les surfaces de glissement de Helmholtz et la resistance des fluides," *Annales de Chimie and de Physique,* Vol. 23, pp. 145–230.

Choi, J.-K. and Kinnas, S. A., 1999, "Numerical Model of a Cavitating Propeller Inside of a Tunnel," ASME JOURNAL OF FLUIDS ENGINEERING, Vol. 121, published in this issue pp. 297–304.

Fine, N. E., 1992, "Nonlinear Analysis of Cavitating Propellers in Nonuniform Flow," PhD thesis, Department of Ocean Engineering, MIT, Oct.

Fine, N. E. and Kinnas, S. A., 1993, "The Nonlinear Numerical Prediction of Unsteady Sheet Cavitation for Propellers of Extreme Geometry," *Sixth International Conference On Numerical Ship Hydrodynamics,* pp. 531–544, University of Iowa, Iowa, Aug.

Franc, J. P. and Michel, J. M., 1985, "Attached Cavitation and the Boundary Layer: Experimental Investigation and Numerical Treatment," *Journal of Fluid Mechanics,* Vol. 154, pp. 63–90.

Jessup, S., Berberich, W., and Remmers, K., 1994, "Cavitation Performance Evaluation of Naval Surface Ship Propellers with Standard and Advanced Blade Sections," in *Twentieth Symposium on Naval Hydrodynamics,* pp. 101–116, University of California, Santa Barbara, Aug.

Kerwin, J. E., Kinnas, S. A., Wilson, M. B., and McHugh, J., 1986, "Experimental and Analytical Techniques for the Study of Unsteady Propeller Sheet Cavitation," *Proceedings of the Sixteenth Symposium on Naval Hydrodynamics,* pp. 387–414, Berkeley, CA, July.

Kinnas, S. A., 1991, "Leading-Edge Corrections to the Linear Theory of Partially Cavitating Hydrofoils," *Journal of Ship Research,* Vol. 35(1), pp. 15–27, Mar.

Kinnas, S. A. and Fine, N. E., 1989, "Theoretical prediction of the midchord and face unsteady propeller sheet cavitation," in *Fifth International Conference on Numerical Ship Hydrodynamics,* pp. 685–700, Hiroshima, Japan, Sept.

Kinnas, S. A. and Fine, N. E., 1992, "A Nonlinear Boundary Element Method for the Analysis of Unsteady Propeller Sheet Cavitation," *Nineteenth Symposium on Naval Hydrodynamics,* pp. 717–737, Seoul, Korea, Aug.

Kinnas, S. A. and Fine, N. E., 1993, "A Numerical Nonlinear Analysis of the Flow Around Two- and Three-Dimensional Partially Cavitating Hydrofoils," *Journal of Fluid Mechanics,* Vol. 254, pp. 151–181, Sept.

Kinnas, S. A., Griffin, P. E., and Mueller, A. C., 1997, "Computational Tools for the Analysis and Design of High Speed Propulsors," *The International CFD Conference,* Ulsteinvik, Norway, May 29–31.

Kinnas, S. A., Lee, H., and Mueller, A. C., 1998, "Prediction of Propeller Blade Sheet and Developed Tip Vortex Cavitation," *22nd Symposium on Naval Hydrodynamics,* pp. 182–198, Washington, D.C., Aug. 9–14.

Lee, C.-S., 1979, "Prediction of Steady and Unsteady Performance of Marine Propellers with or without Cavitation by Numerical Lifting Surface Theory," PhD thesis, M.I.T., Department of Ocean Engineering, May.

Mishima, S., Kinnas, S. A., and Egnor, D., 1995, "The CAvitating PRopeller EXperiment (CAPREX), Phases I & II," Technical Report, Department of Ocean Engineering, MIT, Aug.

Morino, L. and Kuo, C.-C., 1974, "Subsonic Potential Aerodynamic for Complex Configurations: A General Theory," *AIAA Journal,* Vol. 12(no 2), pp. 191–197, Feb.

Mueller, A. C., 1998, "Development of Face and Mid-Chord Cavitation Models for the Prediction of Unsteady Cavitation on a Propeller," Master's thesis, UT Austin, Dept. of Civil Engineering, May.

Villat, H., 1914, "Sur la validité des solutions de certain problem d'hydrodynamique," *Journal de Mathematiques,* Vol 6(No. 10), pp. 231–290.

Vorus, W. and Mitchell, K. W., 1994, "Engineering of Power Boat Propellers," *Propellers/Shafting '94 Symposium,* pp. 1–16 (paper No. 12), Virginia Beach, VA, September 20–21. Society of Naval Architects & Marine Engineers.

Young, Y. L. and Kinnas, S. A., 1999, "Numerical and Experimental Validation of a Cavitating Propeller BEM Code," *Cavitation and Multiphase Flow Forum,* San Francisco, CA, July. Fluids Engineering Division, ASME, to be presented.

APPENDIX A

Propeller Geometries

Table 2 The geometry of MC-1. 3 blades. NACA66 thickness distribution. α = 0.8 meanline camber distribution

r/R	*P/D*	*C/D*	*f/C*	*t/D*
0.200	1.000	0.174	0.0351	0.02865
0.250	1.000	0.202	0.0369	0.03600
0.300	1.150	0.229	0.0368	0.04410
0.400	1.351	0.275	0.0348	0.04410
0.500	1.351	0.312	0.0307	0.03600
0.600	1.359	0.337	0.0245	0.02865
0.700	1.350	0.347	0.0191	0.02190
0.800	1.150	0.334	0.0148	0.01575
0.900	0.800	0.280	0.0123	0.01010
0.950	0.600	0.210	0.0128	0.00720
1.000	0.300	0.000	0.0120	0.00440

NOTE: The geometry of this propeller has been exaggerated to some extent so that mid-chord cavitation will be likely in certain regions (middle of the blade). Structurally, this propeller is unsound, but from a modeling perspective, it is a useful tool for these initial studies of mid-chord cavitation.

Table 3 The geometry of DTMB N4990. 5 blades. NACA66 thickness distribution. α = 0.8 meanline camber distribution

r/R	*P/D*	Rake	Skew	*C/D*	*f/C*	*t/D*
0.30	1.183	−0.0004	0.00	0.1776	0.00202	0.04442
0.35	1.360	−0.0123	−4.53	0.2099	0.00533	0.03820
0.40	1.516	−0.0237	−7.53	0.2412	0.01059	0.03377
0.45	1.642	−0.0338	−9.21	0.2714	0.01657	0.03121
0.50	1.731	−0.0414	−9.75	0.3020	0.02297	0.03041
0.60	1.795	−0.0458	−7.96	0.3620	0.02980	0.02929
0.70	1.719	−0.0395	−3.12	0.4200	0.02834	0.02780
0.80	1.547	−0.0278	4.12	0.4690	0.02036	0.02533
0.90	1.341	−0.0141	13.41	0.4650	0.00932	0.02102
0.95	1.245	−0.0072	18.82	0.3900	0.00333	0.01642
1.00	1.163	0.0000	24.74	0.0010	−.00270	0.00000

Table 4 The geometry of DTMB N4148. 3 blades. NACA66 thickness distribution. α = 0.8 meanline camber distribution

r/R	*P/D*	*C/D*	*f/C*	*t/D*
0.2000	0.9921	0.1600	0.0174	0.0329
0.3000	0.9967	0.1818	0.0195	0.0282
0.4000	0.9987	0.2024	0.0192	0.0239
0.5000	0.9975	0.2196	0.0175	0.0198
0.6000	0.9944	0.2305	0.0158	0.0160
0.7000	0.9907	0.2311	0.0143	0.0125
0.8000	0.9850	0.2173	0.0133	0.0091
0.9000	0.9788	0.1806	0.0125	0.0060
0.9500	0.9740	0.1387	0.0115	0.0045
1.0000	0.9680	0.0010	0.0000	0.0000

T. M. Pham
Research Assistant.

F. Larrarte[1]
Research Assistant.

D. H. Fruman
Professor.

Ecole Nationale Supérieure
de Techniques Avancées
Groupe Phénomènes
d'Interface
Chemin de la Hunière,
91761 Palaiseau Cedex,
France

Investigation of Unsteady Sheet Cavitation and Cloud Cavitation Mechanisms

Sheet cavitation on a foil section and, in particular, its unsteady characteristics leading to cloud cavitation, were experimentally investigated using high-speed visualizations and fluctuating pressure measurements. Two sources of sheet cavitation instability were evidenced, the re-entrant jet and small interfacial waves. The dynamics of the re-entrant jet was studied using surface electrical probes. Its mean velocity at different distances from the leading edge was determined and its role in promoting the unsteadiness of the sheet cavitation and generating large cloud shedding was demonstrated. The effect of gravity on the dynamics of the re-entrant jet and the development of interfacial perturbations were examined and interpreted. Finally, control of cloud cavitation using various means, such as positioning a tiny obstacle (barrier) on the foil surface or performing air injection through a slit situated in the vicinity of the leading edge, was investigated. It was shown that these were very effective methods for decreasing the amplitude of the instabilities and even eliminating them.

1 Introduction

Designers of hydromechanical systems try to avoid all sources of instability because the induced vibrations may lead to serious structural damages. Sheet cavitation can develop on the rotor or stator blades of pumps and may exhibit, under specific conditions, an unstable behavior characterized by the periodic shedding of vapor structures. This situation, usually referred to as "cloud cavitation," generates nondesirable vibrations. Thus, it is of practical interest (i) to define the operating conditions leading to such a behaviour and to know the associated shedding frequencies, (ii) to determine the generation mechanisms of instability in order to control cloud cavitation or, at least, to have a comprehensive understanding of the physical processes leading to it.

Knapp et al. (1970), in his comprehensive study on cavities attached to a two-dimensional body, pointed out the existence of a re-entrant flow in the cavity closure region and listed the cyclic cloud shedding process as being formed by three main phases, namely, formation and growth, filling, and breakoff. Furness and Hutton (1975) numerically modelled the unsteady cavity and predicted that a liquid jet should form during the growth phase. Later, numerous investigations confirmed the existence of the re-entrant jet by visualizing the cavity closure using dye injection (Le et al., 1993) or high speed cinematography (De Lange et al., 1994). In spite of the fact that the re-entrant jet seems to be the major cause responsible for sheet cavitation instability, other possible mechanisms have been proposed. We can mention the role played by condensation shock waves as Jacobsen (1964) pointed out in his investigation of cavitating inducers, or the growth of surface waves propagating downstream on the cavity interface until transition to turbulence occurs, as Brennen (1969) observed for natural and ventilated cavities. Avellan et al. (1988) considers that cloud cavitation results from the growth of these interfacial instabilities. In contrast, Kawanami et al. (1997) recently observed that cloud cavitation was never generated when the re-entrant jet was obstructed by an obstacle fitted on the foil surface and concluded that the re-entrant jet was responsible for cloud cavitation. Therefore, whether the cavity dynamics is determined by the re-entrant jet or the growth of surface instabilities, or a combination of both, remains an open question. In order to be able to answer these interrogations it is necessary to gain information concerning the re-entrant jet dynamics and the interface instabilities, by using non intrusive techniques.

This paper reports the main results of an experimental investigation of the unsteady sheet cavitation. It is organized as follows: Section 2 is devoted to characterizing the unsteady behavior of an attached cavity by means of visualizations and fluctuating pressure measurements. Section 3 contains the results of an investigation of the mechanisms of cloud cavitation and in particular of the re-entrant jet dynamics using electrical probes. Finally, in Section 4 is discussed the possibility of controlling cloud cavitation using various means such as positioning an obstacle on the foil surface or performing air injection through a slit situated in the vicinity of the leading edge.

2 Investigation of the Unsteady Behavior of Sheet Cavitation

2.1 Experimental. Experiments were conducted in the ENSTA Cavitation Tunnel with a test section 150 mm height, 80 mm width, 640 mm length. A two-dimensional foil of 150 mm chord and 80 mm span made in solid brass, sketched in Fig. 1, was used. Its cross-section had a flat upper surface and a convex lower surface of 195 mm radius. The foil was mounted mid-height in the test section and sheet cavitation was produced on its upper surface. The unsteady behavior of sheet cavitation was investigated by means of high-speed imaging in order to examine the cavity morphology, and by fluctuating pressure measurements in order to define the operating conditions leading to periodic cloud shedding and to measure the associated shedding frequencies. The experimental conditions were known with a 1% precision on the foil angle of attack, a 1% and a 2% precision on the flow velocity and the upstream pressure respectively, which leads to a 4% uncertainty on the cavitation number.

Visualizations of the cavities were performed using either a Hycam cine camera operated at a maximum rate of 10,000 images per second or a Kodak Spin Physics video camera (SP2000) operated at 6000 images per second (Larrarte et al., 1995). Side views were obtained by means of the SP2000 camera, which enabled to collect information concerning the cross-section of the

[1] Current address: Laboratoire Central des Ponts et Chaussées—Centre de Nantes. BP 19-44340 Bouguenais, France.

Contributed by the Fluids Engineering Division for publication in the JOURNAL OF FLUIDS ENGINEERING. Manuscript received by the Fluids Engineering Division January 21, 1998; revised manuscript received December 21, 1998. Associate Technical Editor. J. Katz.

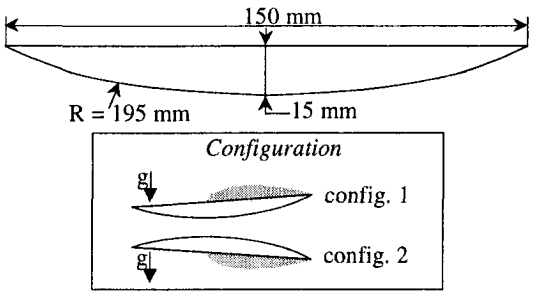

Fig. 1 Sketch of the foil—flow configurations

cavities, thereby their volume. Top views of the cavities were obtained with the film camera in order to examine the characteristic features of the interface. All the tests were conducted with cavities exhibiting periodic vapour cloud shedding. The selected film sequences and video images were numerized and the Optimas® software computed aided procedures were implemented to facilitate the data analysis. For the side views, the cavity outline was determined by a grey level threshold procedure. Its cross-section area was automatically computed by Optimas®. As an example, Fig. 2 illustrates one frame visualized on the TV monitor (Fig. 2(*a*)), and one enlarged image of the cavity outline (Fig. 2(*b*)). Although there was a clear visual indication that the cavity was broken down into two smaller cavities, the threshold method did not permit to individualize them. This was made by manually introducing a cut as shown in Fig. 2(*c*) and Fig. 2(*d*). For the top views, assuming that the cavity was two-dimensional, the mean grey level at different distances from the leading edge was calculated by averaging the grey level of sixteen pixels equally distributed along the span direction. This allowed to obtain a grey level signature along the foil chord which could be interpreted in terms of waves or perturbations of the interface. For a detailed description of the data analysis procedure, we refer the reader to Larrarte et al. (1995).

The far field unsteady pressures generated by the cavitation were measured by means of a PCB model M106B50 piezo-electric pressure transducer (resonant frequency 40 kHz, sensibility 0.07 mV/Pa). The latter was mounted flush on one of the vertical walls of the test section, 30 mm upstream the foil. The pressure data were processed by a HP 35665A spectrum analyzer whose frequency full span and default resolution were, respectively, 102.4 kHz and 400 lines. Apart from very low frequencies, the signals were not filtered. The Fourier transforms of the signals were digitally performed from 1024 sampled data. They were averaged over 50 samples. Note that these measurements were intended to characterize the pressure fluctuations associated with the global behavior of the cavity and not the pressure pulses resulting in noise emission.

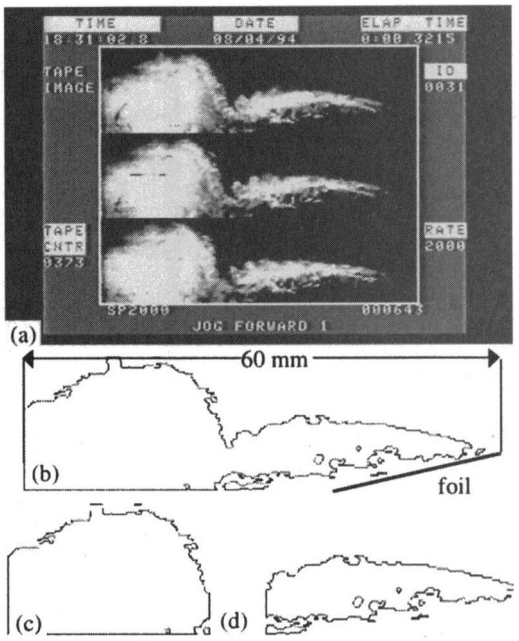

Fig. 2 (*a*) Example of a frame on the TV monitor, (*b*) global outline of the cavity, (*c*) outline of the convected cavity and (*d*) Outline of the developing cavity

2.2 Results and Interpretation. Side views of the cavity, Fig. 3, were obtained with the high-speed video camera for a foil incidence, α, of 4°, a free-stream velocity, U_∞, of 8 m/s, a cavitation number, σ, of 1.2. For these flow conditions the cavity had a mean cavity length, l, of 60 mm and the Reynolds number based on the foil chord, Re, was 1.2×10^6. Under the assumption of a two-dimensional flow, the volume of the cavity could be obtained by multiplying its cross-sectional area, given by the analysis of the video images, by the width of the test section. In Fig. 4, the continuous line shows the volume obtained using the total area of the cavity cross-section (see Fig. 2(*b*)) as a function of time. The measurement uncertainty on the cavity volume was estimated at about 5%. The individual symbols denote the volume of the cavity which developed from the leading edge (see Fig. 2(*d*)), from its initiation up until its disappearance when the cloud shedding was completed. The periodic character of the cavity behavior, emerging from Fig. 4, can be described as follows:

(i) The leading edge cavity growth is initiated at 0.013 (cavity 2), 0.05 (cavity 3), 0.08 second (cavity 4);
(ii) The growth is nearly linear and reaches a maximum at 0.03 (cavity 2), 0.062 (cavity 3), 0.092 second (cavity 4).

Nomenclature

c = foil chord (m)
d = distance between two neighbouring probes (m)
f = cloud shedding frequency or occurrence frequency of the re-entrant jet on the electrical probes (Hz)
g = gravity acceleration (m/s^2)
l = maximum length of the cavity (m)
p = pressure (pa)
P_∞ = upstream pressure (Pa)
Q = air flow rate (m^3/s)
q = dimensionless air flow rate $q = Q/U_\infty cs$ (—)
Re = Reynolds number Re $= U_\infty c/\nu$ (—)
$R_{n-1,n}$ = cross-correlation function between the outputs from the probes #$(n-1)$ and #n (V^2)
s = foil span (m)
St = Strouhal number St $= fl/U_\infty$ (—)
t = time (s)
U = fluid velocity (m/s)
U_∞ = free-stream velocity (m/s)
$\bar{v}$ = local mean velocity of the re-entrant jet (m/s)
x = distance from the leading edge (m)
y_n = output signal from probe #n (V)
α = angle of attack (degree)
$\Delta t_{n-1,n}$ = time delay between the outputs from probes #$(n-1)$ and #n (s)
γ = surface tension (N/m)
λ = wavelength (m)
ν = kinematic viscosity (m^2/s)
ρ = liquid density (kg/m^3)
σ = cavitation number $\sigma = 2((P_\infty - P_v)/\rho U_\infty^2)$ (—)

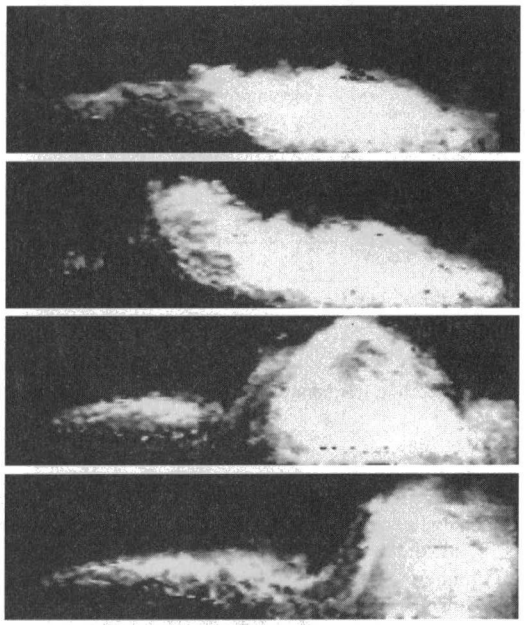

Fig. 3 Timewise evolution of the cavity (1.67 ms between two images—flow from left to right)—α = 4°, U_∞ = 8 m/s, σ = 1.2

Meanwhile, the cloud of the preceding cavity is totally evacuated;

(iii) After the leading edge cavity reached its maximum volume, a saddle type shape is seen to occur before the cavity is separated from the foil and the volume decreases. A new cycle begins.

From the time period of the cycle, we can estimate the shedding frequency f at 29 Hz, which leads to a Strouhal number based on the length of the cavity, St, of 0.22.

Top views of the cavity interface, for which examples are given in Fig. 5(*a*), were obtained using the cine camera for $\sigma = 0.7$, $U_\infty = 6.6$ m/s, $\alpha = 4°$, which corresponds to Re = 9.9×10^5 and l = 50 mm. Figure 5(*b*) presents the evolution of the average grey level with the distance from the leading edge at increasing times, from bottom to top. Two main phases can be singled out in this figure:

Phase A: A precursor front wave (indicated by an arrow) rushes from the rear of the cavity toward the leading edge. This is an evidence of the perturbation created on the interface by the re-entrant jet propagation. The initiation of Phase A corresponds to the maximum cavity volume in Fig. 4.

Phase B: After the re-entrant jet reached the leading edge and collided with the cavity interface, a partial break-off ensues and a cloud gets organized and is convected downstream. A new leading edge cavity begins to grow as indicated by the downstream limit of the perturbed region. This growth phase is called Phase B and corresponds to the positive rate of growth of the cavity volume in Fig. 4. During this phase, small scale waves trains, having a mean

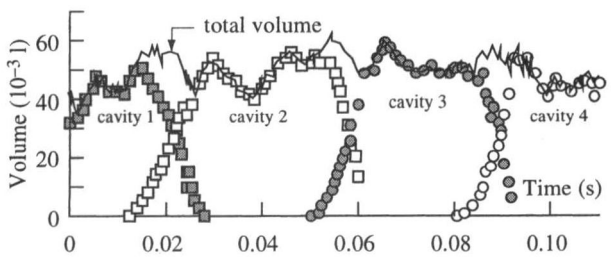

Fig. 4 Timewise evolution of the cavity volume α = 4°, U_∞ = 8 m/s, σ = 1.2

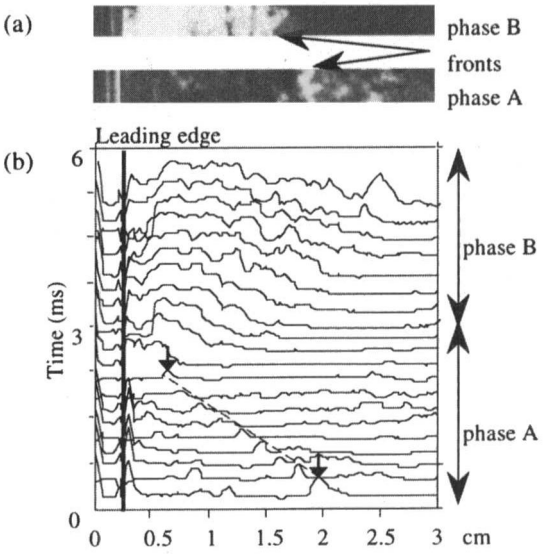

Fig. 5 Grey level profiles at different times α = 4°, U_∞ = 6.6 m/s, σ = 0.7

wavelength of 3 mm, propagate toward the trailing edge. This phase is illustrated in Fig. 3, where it can be clearly seen how the sheet cavity progresses from the leading edge while the previous detached cloud is carried downstream (Frames 3 and 4). A third phase which can be of very short duration, not shown in Fig. 5(*b*), corresponds to a well developed cavity without major surface perturbations. The cycle repeats consistently once the unstable situation is reached.

The visualizations have clearly demonstrated that the phases of cloud shedding are as those very early schematized by Knapp et al. (1970) and further confirmed by other authors. Moreover, the interface perturbation linked to the probable propagation of a re-entrant jet suggests that the unsteady behavior, and the subsequent cloud cavitation, can be attributed, at least in part, to the impact of the re-entrant jet with the cavity interface. However, small interfacial wave trains, whose precise role remains as yet to be defined, have been also observed.

On account of the fastidious, time consuming and off-line analysis procedures to be used to analyze the visualizations, only data for a limited number of operating conditions were obtained. Since Kubota et al. (1989) and Reisman et al. (1996) have shown that the unsteadiness of a sheet cavity is strongly correlated with the unsteady pressure signature, it was decided to carry out fluctuating pressure measurements. These can be analyzed in terms of shedding frequencies on-line, in order to determine a much larger range of operating conditions leading to cloud cavitation. According to Reisman et al. (1996), the far-field pressure is mainly related to the coherent collapse of the cavitation cloud. Kubota et al. (1989) consider that the low frequency component of the pressure fluctuation is caused by the large scale cyclic development and convection of the cavitation cloud whereas the high frequency component is related to its local structure. Therefore, it was decided to restrict our study to relatively narrow spans of frequency, namely 0–800 Hz, 0–400 Hz, 0–200 Hz. This permitted to achieve a greater frequency resolution (i.e., 0.5 Hz for the frequency span of 0–200 Hz).

All the tests were performed for a fixed free-stream velocity, 8 m/s (i.e., Re = 1.2×10^6) and α was varied between 0° and 5° by steps of 0.25°. σ ranged from 0.94 to 1.4.

Figure 6 presents, for σ = 1.1, the spectra of the fluctuating pressure signal for eleven incidence angles. They show that, depending the incidence angle is lower or larger than 2°, two main regimes, respectively illustrated in Fig. 6(*a*) and Fig. 6(*b*), can occur.

(i) For $\alpha < 2°$, the spectra reveal relatively high dominant frequencies distributed in broad ranges of few hundreds

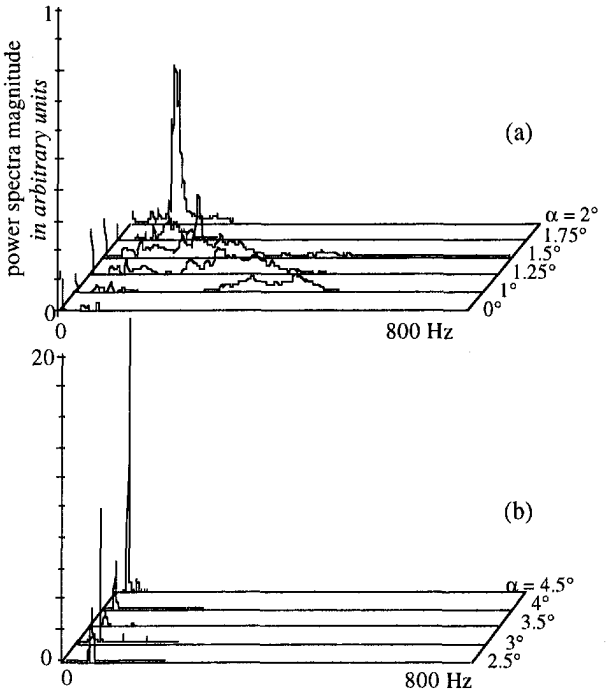

Fig. 6 Power spectra of the fluctuating pressure signal at different angles of attack σ = 1.1, U_∞ = 8 m/s

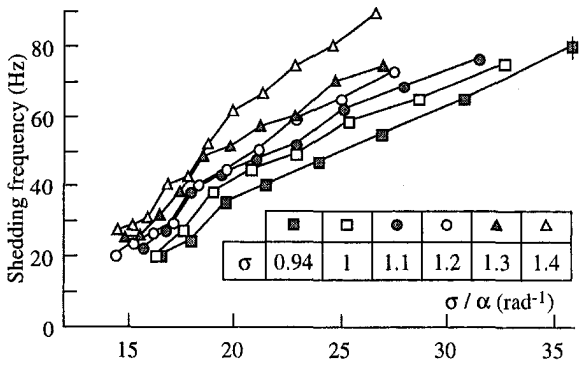

Fig. 7 Cloud shedding frequency as a function of the parameter σ/α – U_∞ = 8 m/s

Hertz width. Visually, cavitation sheet appears to be stable or undergoing localized fluctuations in its closure region. The frequency components above 100 Hz may be due to interfacial instabilities (Kjeldsen, 1997) or to the shedding of small vapor clouds (De Lange et al., 1994).

(ii) For $\alpha > 2°$, the spectra show sharp dominant spectral peaks (notice the change of the scale on the vertical axis). The dominant frequencies are smaller than 70–80 Hz and are distributed in much narrower ranges than in Case (i). The cavities exhibit large scale cloud shedding and the dominant spectral frequencies can be identified with the cloud shedding frequencies. Therefore, this operating domain will be referred to as the periodic cloud shedding regime.

The existence of the periodic cloud shedding regime was observed for all the tested σ.

Next, attention was focused on this regime and in particular on the cloud shedding frequencies. Acosta (1955) introduced in his linearized theory of partial cavitation of flat plate hydrofoils the parameter $\sigma/2\alpha$ which he related to the ratio of the cavity length over the foil chord. Le et al. (1993), when experimentally investigating partial cavitation with a similar hydrofoil as ours, successfully correlated the maximum cavity length l with σ/α. Those authors, among others, found that the Strouhal number St based on l and the free stream velocity U_∞ was nearly constant around 0.3. If so, at a fixed U_∞, one can expect the shedding frequency f to be a single function of σ/α. We tentatively plotted in Fig. 7 the frequency f, determined by spectral analysis, as a function of σ/α, with α in radians. For σ/α smaller than 17 or greater than 20, the spectra showed a unique dominant peak at a very well defined frequency. For σ/α comprised between 17 and 20, it was more difficult to define a unique shedding frequency as the spectral energy was distributed in a slightly larger range of frequency of 20–25 Hz width, and secondary peaks of smaller magnitude were present in addition to the dominant spectral peak. In these cases, we disregarded the secondary peaks and considered the shedding frequency as being given by the frequency of the dominant peak. It can be seen in Fig. 7 that f increases with σ/α, and that, contrary of what was expected, a dependency on σ which exceeds the maximum uncertainty, estimated at 3 Hz, exists. This shows the nonlinear character of the shedding phenomenom. Figure 8(*a*) presents for all the tested incidences and cavitation numbers the Strouhal number, St, based on the maximum cavity length l visually determined under stroboscopic lightning and on the free stream velocity U_∞. All points fall in the range of 0.2–0.4 with an average St value of .28 and a .044 standard deviation. The observed data scattering may be partly explained by the important measurement uncertainty on l, estimated at 5 mm. The scattering is smaller when St is scaled by the velocity at the interface $U_\infty\sqrt{1+\sigma}$ rather than U_∞ (see Fig. 8(*b*)). In this case, the mean St value is equal to .19 with a .026 standard deviation. This indicates that the velocity at the interface, which takes into account a σ effect, is a more relevant characteristic velocity scale for normalizing the shedding frequency.

3 Investigation of the Re-Entrant Jet Dynamics

This section aims to investigate the re-entrant jet dynamics by means of a nonintrusive measuring method and to link it to the unsteadiness of sheet cavitation. For this purpose, the flat surface of the foil was equipped with electrical probes in order to detect, for the periodic cloud shedding regime defined in the previous section, the passage of a water front corresponding to the penetration of the re-entrant jet. The effect of gravity on the propagation of the water front and on the interfacial waves was also examined

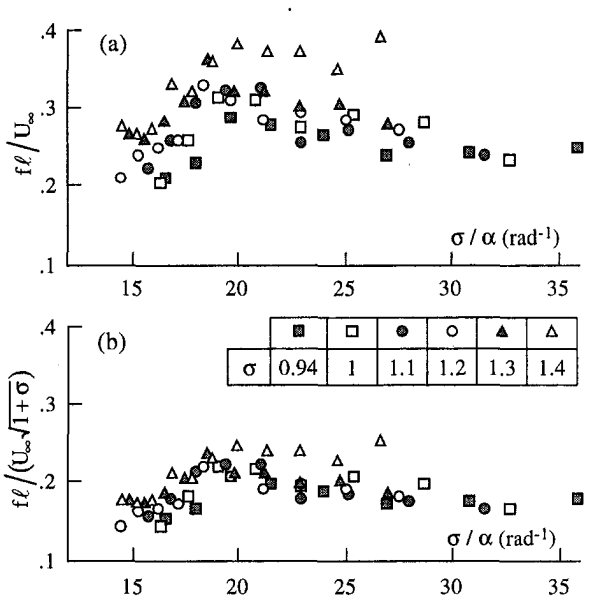

Fig. 8 Strouhal number based on different velocity scales, as a function of the parameter σ/α – U_∞ = 8 m/s

by performing tests with the flat surface facing the upper or lower horizontal wall of the test section.

3.1 Experimental Methods and Instrumentation. Electrical impedance techniques are commonly used in the field of multiphase flows for measuring spatially averaged flow properties, such as void fraction (Ceccio and George, 1996). Derived from this instrumentation, Ceccio and Brennen (1991) developed a novel equipment to study travelling bubble cavitation and, more recently, implemented it to the investigation of the dynamics of stable attached cavities on bodies of revolution (Ceccio and Brennen, 1992). The same type of technique was employed in this study for detecting the water front corresponding to the re-entrant jet. For this purpose, specific instrumentation and signal processing system were developed and validated by preliminary experiments. After validating the instruments, tests were conducted in the ENSTA Water Tunnel on the foil equipped with surface electrical probes in cloud cavitation conditions for $U_\infty = 8$ m/s.

A series of six electrodes having a diameter of 2 mm and made of stainless steel were arrayed mid-span on the upper flat surface of the hydrofoil in the flow direction. The electrodes were equally spaced 10 mm apart, starting at $x = 30$ mm (probe #1) and ending at $x = 80$ mm (probe #6) from the leading edge. They were flush mounted on patches of 4 mm diameter made with Araldite in order to electrically isolate them from the foil which played the role of the general ground and, we recall, was fabricated in solid brass. The impedance of each of the sensors (i.e., the impedance of the local conducting medium between the electrode and the ground) played the role of a branch of a Wheastone bridge supplied with a constant electrical potential. When the impedance was changed, because of the presence on the sensor of water, vapour or a mixture of both, an appropriate electronic set-up gave a variable voltage which was function of the impedance. The output signal was measured and monitored by the HP 35665A spectrum analyzer. In order to link cloud cavitation with the re-entrant jet information, the results were compared with fluctuating pressure measurements performed using the piezo-electric transducer described in Section 2.1.

The re-entrant jet dynamics was detected through processing of the unsteady component of the electrodes signal: the output of the electrodes was Fourier analyzed and the spectra were averaged on 50 samples. A cross-correlation function between the output signals from two neighbouring probes, defined by,

$$R_{n-1,n}(\tau) = \lim_{T\to\infty} \frac{1}{T} \int_0^T y_{n-1}(t) y_n(t+\tau) dt \quad \text{for } n = 2 \ldots 6$$

where $y_n(t)$ designates the output signal from probe #n, was performed using the Correlation Analysis Mode of the analyzer. The cross-correlation function was averaged over 100 samples of a duration of 3.9 ms. The data collection was triggered by a positive voltage ramp from probe #n with a pretrigger time of 500 μs (i.e., arrival of the water front on #n).

3.2 The Re-Entrant Jet Dynamics. A typical output signal from an electrode situated under the cavity is shown in Fig. 9, for cloud cavitation conditions. The maximum level of the velocity signal corresponds to the liquid phase fully wetting the surface of the electrode. When the re-entrant jet recedes, a more or less thick layer of water remains on the surface and drains away. Depending on the duration of the process, and the more or less completed draining, the output voltage, while decreasing, reaches variable levels. What seems to be certain is that the sensor is not often in contact with pure vapour and "sees" most of the time a combination of water and vapour. In spite of the apparently noisy output signal, a trend, which determines a duration of the events, is quite well defined.

Direction of Propagation, Velocity of the Re-Entrant Jet. For all the electrodes ($n = 2 \ldots 6$), the mean cross-correlation function for probes #$(n-1)$ and #n exhibited a well defined maximum, at a time delay $\Delta t_{n-1,n}$ corresponding to the time required for the front to advance from probe #n to probe #$(n-1)$. The direction of propagation of the front was given by the sign of the time delay, and the local mean velocity of the re-entrant jet between the probes #$(n-1)$ and #n, $\bar{v}_{n-1,n}$, was given by $\bar{v}_{n-1,n} = d/\Delta t_{n-1,n}$, where d is the distance between two electrodes (10 mm). $\Delta t_{n-1,n}$ was of positive sign, which conclusively demonstrated that a liquid front actually rushed from the trailing edge towards the leading edge. Figure 10 presents for $\sigma = 0.94$ and $\alpha = 3.5°$ and at different nondimensional abscissas x/l, the local mean velocity of the re-entrant jet divided by the free-stream velocity. The velocity at the point midway between probes #n and #$(n-1)$ is approximated as $\bar{v}_{n-1,n}$. It can be seen that the velocity of the re-entrant jet is of the same order of magnitude as the main flow velocity and increases with the distance from the leading edge. The standard deviation has a maximum at the electrodes close to the cavity closure region on account of the inherent unsteady character of this region. For comparison, Fig. 10 also includes the inviscid value of the re-entrant jet velocity, $U_\infty\sqrt{1+\sigma}$, and one experimental result of Kawanami et al. (1997), obtained using a hot wires velocimeter for a cavity of length $l/c \approx 50\%$ pulsing at about 20 Hz. Both values are consistent with our results.

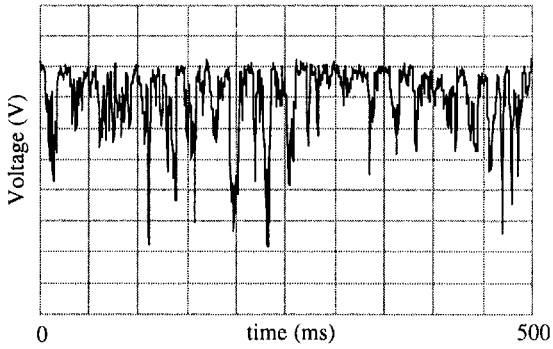

Fig. 9 Typical output signal from an electrode situated under the cavity for cloud cavitation conditions

Frequency of Occurrence of the Re-Entrant Jet on the Probes. The averaged spectra of the output signal from the probes situated under the cavity show dominant peaks at an equal frequency which can be reasonably identified with that of the re-entrant jet passage on the electrodes. As in Section 2.2, for σ/α comprised between 17 and 20, secondery peaks of smaller magnitude were present in addition to the dominant spectral peak.

For all the operating conditions tested, the results obtained from local impedance and unsteady pressure measurements matched

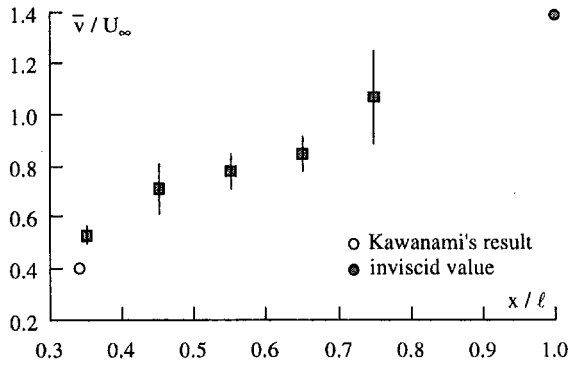

Fig. 10 Local mean velocity of the re-entrant jet divided by the free stream velocity as a function of the distance from the leading edge normalized by the cavity length – $\sigma = 0.94$, $\alpha = 3.5°$, $U_\infty = 8$ m/s

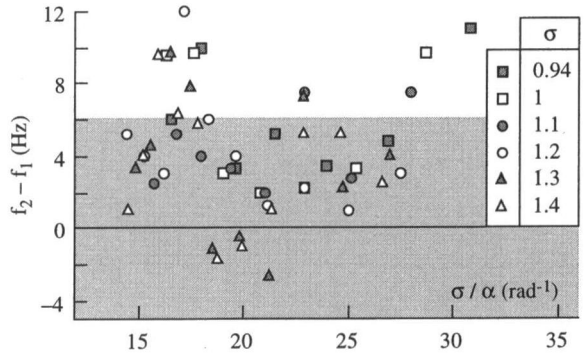

Fig. 11 Difference between the cloud shedding frequencies in config.2 and in config.1 as a function of σ/α.

very well: for $\sigma/\alpha < 17$ or $\sigma/\alpha > 20$, it was found that the frequency of occurrence of the re-entrant jet on the electrodes was equal to the cloud shedding frequency determined by unsteady pressure measurements, to within the measurement uncertainty. For $17 < \sigma/\alpha < 20$, the pressure and the electrode signal spectra revealed dominant frequencies in exactly the same range. This result clearly indicates the major promoting role of the re-entrant jet in cloud cavitation. However, we can not ignore that the small interfacial perturbations, which were observed by high-speed imaging (see Section 2.2.), may have an effect on the large scale shedding of cavitation clouds.

3.3 Gravity Effect. Local impedance and unsteady pressure measurements were performed with the flat surface of the foil facing the test section floor (configuration 2), for incidences so as sheet cavitation was produced on the flat side (see Fig. 1). By comparison with the results obtained with the initial set-up (configuration 1) presented in Section 2.1, these tests allow to investigate the effect of gravity on the re-entrant jet and on the stability of the interfacial waves. The consequences on the cavity behaviour were then examined. The test conditions corresponded to periodic cloud shedding.

Avellan et al. (1988) and Kjeldsen (1997) consider that the interfacial perturbations of an attached cavity result from the development of Kelvin-Helmoltz instabilities. In this theory, the plane interface separating two unbounded inviscid fluids of different densities, which have different mean horizontal velocities, is unstable if,

$$\frac{\rho_1\rho_2}{\rho_1+\rho_2}(U_1-U_2)^2-\frac{g}{2\pi}\lambda(\rho_1-\rho_2)-\gamma\frac{2\pi}{\lambda}>0$$

where γ is the surface tension, λ is the wavelength of the waves travelling at the interface and the indices 1 and 2 respectively denote the lower and upper fluid layers. Considering this inequality, one notes that gravity will have a stabilizing effect if the heavier layer is under the lighter one (i.e., $\rho_1 - \rho_2 > 0$). As in configuration 2 the gravity acceleration is directed from the cavity towards the liquid, it can be inferred that the cavity interface will be stabilized. Consequently, if the interfacial perturbations do have a significant effect on cloud shedding, it can be speculated that it will be mitigated in configuration 2 compared with configuration 1.

This type of investigation was first conducted by Larrarte et al. (1995) who showed by high-speed video, for $\sigma = 1.2$ and $\alpha = 4°$, that the frequency of the cloud shedding was increased as compared to configuration 1, from 29 Hz to 41 Hz. Our measurements of the response of the surface electrical sensors, conducted for numerous operating points, support this finding. Figure 11 shows the difference between the frequencies of passage of the water front on the electrodes, equal to the cloud shedding frequencies, in configuration 2, f_2, and in configuration 1, f_1, plotted versus σ/α. The difference is always positive, besides for few data points which are within the two standard error interval indicated by the shaded area. We can thus conclude that, indeed, the cloud shedding frequency is increased in configuration 2 and that, as opposed to what was initially expected, the instability is enhanced. The reason for this behaviour, as initially suggested by Larrarte et al. (1995), can be traced to the action of gravity on the re-entrant jet. In configuration 2, the re-entrant jet deviates from the foil surface due to the gravity effect, and strikes the cavity interface slightly downstream the leading edge. This leads to the shedding of smaller vapour clouds at higher frequencies than in configuration 1.

In view of these results, it seems quite reasonable to consider that the role played by the re-entrant jet is preponderant over that of the interfacial instabilities in the generation of periodic cloud shedding. Therefore, it may be speculated that controlling the re-entrant jet flow may allow to control cloud cavitation.

4 Control of Cloud Cavitation

4.1 Control of Cloud Cavitation by Means of an Obstacle. The results of Kawanami et al. (1997) indicate that cloud cavitation can be prevented by using an obstacle in order to hold back the re-entrant jet. Based on their results, we conducted a series of experiments by placing a bar having a width of 4 mm, protruding from the foil surface by 2 mm and as large as the foil span, in-between probes #1 and #2, at $x = 35$ mm ($x/c = 0.233$) from the leading edge. Simultaneous fluctuating pressure and local impedance measurements were conducted in cloud cavitation conditions, at $\sigma = 0.94$, $U_\infty = 8$ m/s and for three incidences of 3°, 3.25°, and 3.5°, which respectively correspond to mean cavity lengths of 80, 90, and 100 mm.

For example, Fig. 12 shows the cross-correlation analysis of the signals from electrodes #2 and #3, from #1 and #2, for $\alpha = 3.5°$. For the #2–3 pair, we observe a maximum indicating a satisfactory correlation and the existence of a characteristic advance velocity of the water front. For the #1–2 pair, the correlation is deficient and no indication of an advancing velocity can be noted. Therefore, the re-entrant jet was effectively held back or deviated by the obstacle. As a consequence, the magnitude of the fluctuating pressure induced by cloud cavitation was significantly reduced. Indeed, the magnitude of the dominant peak in the power spectra of the fluctuating pressure, which characterized the cloud cavitation "intensity" as far as the periodic regime was concerned, was divided by two compared with the situation without obstacle. Depending on the incidence angle, the fluctuating pressure could be reduced by a factor four. In view of these results, we can conclude that the re-entrant jet loses part of its momentum or is deviated due to the obstacle. This causes the modification of the cloud shedding mechanism and the reduction of the amplitude of the pressure fluctuations associated with it.

4.2 Effect of Air Injection. The air injection technique has been used for many years by Navies as a countermeasure to avoid propeller cavitation induced erosion, noise and vibration. Its effectiveness was demonstrated by Rusmussen (1956), Huse (1976), Okamoto et al. (1977) and was interpreted as a "cushioning effect"

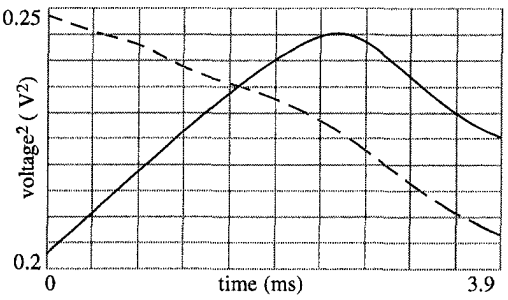

Fig. 12 Cross-correlation functions between the outputs from probes #2 and #3 (solid line), #1 and #2 (dashed line) – $\sigma = 0.94$, $\alpha = 3.5°$, $U_\infty = 8$ m/s

of the air contained in the cavities. The principle of our experiment is slightly different. We intend stabilizing the fluctuating cavity by inhibiting the instability source, that is the re-entrant jet, rather than damping the cloud cavitation collapse. Indeed, the visualizations of Larrarte et al. (1995) by high-speed video indicated that ventilated cavities do not undergo large scale break-off and filling. Instead, the air is continuously evacuated at the rear of the cavities and no evidence of a re-entrant jet can be observed. Based on this observation, the idea is to inject air into the fluctuating cavitation sheet in order to create a wake which would impede the re-entrant jet. This principle of operation is also supported by ship measurements performed by English (1998).

Tests were performed with and without air injection through a slit, 1 mm wide, situated 2 mm from the leading edge. The air was supplied at room temperature and pressure. On account of the large difference between the air supply pressure (the room pressure) and the injection one (the cavity pressure), a pressure reducer was necessary in order to create a sufficient head loss to achieve flow rates of the order of 10–20 l/min. An air flow control valve was installed on the air supply line. The flow rate measured at the room pressure, using a BROOKS Sho-Rate 13355 rotameter, has to be converted to a value, Q, for the conditions prevailing in the cavity. Brennen (1969) showed that the cavity pressure increases nearly linearly with the volume rate of supplied air. However, direct pressure measurements in the fluctuating cavity involve numerous difficulties (Brennen, 1969) and can only give access to an average pressure between the tunnel and the cavity pressures. Therefore, we decided to estimate Q at the cavity pressure supposed to remain equal to the vapour pressure at the water temperature.

The foil was operated in cavitating conditions, at $\sigma = 1.0$, $U_\infty = 8$ m/s, for $\alpha = 2.5°$ and $\alpha = 3.5°$, with a cavity fluctuating at 47 Hz and 20 Hz, respectively. For increasing air flow rates, we measured the far field low frequency fluctuating pressure and determined the magnitude of the dominant spectral peak exhibited by the averaged power spectra of the pressure signal. It is plotted, normalized by the peak value obtained without air injection, as a function of the air injection rate in Fig. 13. For flow rates larger than about 5 l/min, the peak magnitude is reduced by a factor about 100, which is a vivid indication of the cloud cavitation mitigation. Visually, this corresponds to a complete modification of the cavity appearance, which becomes stable and longer.

Arndt et al. (1993) and, later, Reisman et al. (1997) quantified the noise reduction which could be possibly achieved by air injection, for a cloud cavitation on a stationary foil and on an oscillating foil, respectively. They introduced a dimensionless air flow rate $q = Q/(U_\infty cs)$. It was found that a flow rate q_{lim} of less than 0.001 was sufficient to achieve a substantial noise reduction, in both steady and oscillating foil experiments.

In the present study, for our experimental conditions $-U_\infty = 8$ m/s, $c = 150$ mm, $s = 80$ mm, $5 < Q_{lim} < 6$ l/min $- 8.7\ 10^{-4} < q_{lim} < 1\ 10^{-3}$, which compares favorably with Arndt et al. (1993) and Reisman et al. (1997) results. Thus, air injection seems to be particularly efficient in suppressing the cloud cavitation.

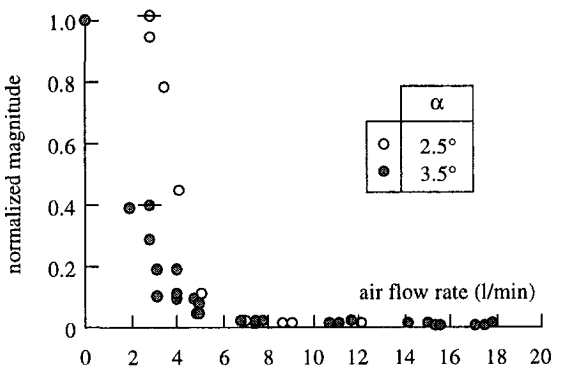

Fig. 13 Normalized magnitude of the dominant spectral peak as a function of the air flow rate – $\sigma = 1.0$, $\alpha = 2.5°$ and $3.5°$, $U_\infty = 8$ m/s

5 Summary and Conclusions

The unsteady behavior of an attached cavity was experimentally investigated. Attention was focused on the physical mechanisms leading to cloud cavitation. The main results of the present work can be summarized as follows:

- Visualizations by high-speed video and cine enabled to describe the morphology of the cavity. The cloud shedding cycle was described from examining the time evolution of the cavity volume. Two types of interfacial perturbations were observed: a precursor front wave rushing from the cavity rear toward the leading edge, evidencing the re-entrant jet propagation, and, small scale waves travelling on the interface.
- The pressure fluctuations associated with cloud cavitation were examined. This permitted to determine by spectral analysis the cloud shedding frequencies as a function of σ/α and to define the initiation of the periodic regime.
- The re-entrant jet dynamics was studied using surface electrical probes. In particular, its direction of propagation and mean velocity were established. For all the operating conditions, the frequencies of occurrence of the re-entrant jet on the electrodes were found to be equal to the cloud shedding frequencies determined by unsteady pressure measurements. This demonstrated that the cloud shedding was actually driven by the re-entrant jet.
- For the same flow conditions, the gravity effect increases the cloud shedding frequency despite the fact that the cavity interface is expected to be more stable. This might be explained by the earlier collision of the re-entrant jet with the interface. The present result suggests that the role played by the re-entrant jet is preponderant over the interfacial instabilities in the generation of periodic cloud shedding.
- Cloud cavitation was successfully controlled, first, by means of an obstacle fitted on the foil which held back the re-entrant jet, second, by air injection. Air injection appeared to be particularly efficient in suppressing the periodic cloud shedding.

Acknowledgments

Financial support for this research was provided by the Centre National d'Etudes Spatiales (CNES), France. T.M. Pham benefited from a post-doctoral scholarship from CNES. The authors wish to express their gratitude to Dr. G. Albano, from CNES, for his continuous support. They are also grateful to Mr. H. V. Nguyen and Mr. H. Fricou for their support in conducting experiments.

References

Acosta, A. J., 1955, "A Note on Partial Cavitation of Flat Plate Hydrofoils," *California Institute of Technology, Report N° E-19.9.*

Arndt, R. E. A., Ellis, C. R., and Paul, S., 1993, "Preliminary Investigation of the Use of Air Injection to Mitigate Cavitation Erosion," *Proceedings of the ASME Symposium on Bubble Noise and Cavitation Erosion in Fluid Systems,* Vol. FED-176, pp. 105–116.

Avellan, F., Dupont, P., and Ryhming, I., 1988, "Generation Mechanism and Dynamics of Cavitation Vortices Downstream a Fixed Leading Edge Cavity," *Proceedings of the 17th Symposium on Naval Hydrodynamics,* pp. 317–329.

Brennen, C. E., 1969, "Air and Heat Balance in Cavity Flows," *Journal of Fluid Mechanics,* Vol. 37, pp. 115–127.

Ceccio, S. L., and Brennen, C. E., 1991, "Observations of the Dynamics and Acoustics of Travelling Bubble Cavitation," *Journal of Fluid Mechanics,* Vol. 233, pp. 633–660.

Ceccio, S. L., and Brennen, C. E., 1992, "Dynamics of Attached Cavities on Bodies of Revolution," ASME JOURNAL OF FLUIDS ENGINEERING, Vol. 114, pp. 93–99.

Ceccio, S. L., and George, D. L., 1996, "A Review of Electrical Impedance Techniques for the Measurement of Multiphase Flows," ASME JOURNAL OF FLUIDS ENGINEERING, Vol. 118, pp. 391–399.

De Lange, D. F., De Bruin, G. J., and Van Wijngaarden, L., April 1994, "On the Mechanism of Cloud Cavitation—Experiment and Modelling," *Proceedings of the 2nd International Symposium on Cavitation,* Tokyo, Japan.

English, J. W., 1998, "Air Injection as a Mean of Reducing Propeller Cavitation Induced Ship Vibration," *Proceedings of the 3rd International Symposium on Cavitation,* Apr., Grenoble, France.

Furness, R. A., and Hutton, S. P., 1975, "Experimental and Theoretical Study of Two-Dimensional Fixed-Type Cavities," ASME JOURNAL OF FLUIDS ENGINEERING, Vol. 97, pp. 515–522.

Huse, E., 1976, "Air Injection to Avoid Cavitation Erosion in Propeller Ducts," *Norwegian Maritime Research,* No. 1, pp. 21–40.

Jacobsen, J. K., 1964, "On the Mechanism of Head Breakdown in Cavitating Inducers," ASME *Journal of Basic Engineering,* Vol. 111, pp. 291–305.

Kawanami, Y., Kato, H., Yamaguchi, H., Tanimura, M., and Tagaya, Y., 1997, "Mechanism and Control of Cloud Cavitation," ASME JOURNAL OF FLUIDS ENGINEERING, Vol. 119, pp. 788–794.

Kjeldsen, M., 1997, "Theoretical and Experimental Investigations of the Instability of an Attached Cavity," *Proceedings of the ASME Fuids Engineering Division Summer Meeting.*

Knapp, R. T., Daily J. W., and Hamitt, F. G., 1970, *Cavitation,* McGraw-Hill.

Kubota, A., Kato, H., Yamaguchi, H., and Maeda, M., 1989, "Unsteady Structure Measurement of Cloud Cavitation on a Foil Section Using Conditional Sampling Techniques," ASME JOURNAL OF FLUIDS ENGINEERING, Vol. 111, pp. 204–210.

Larrarte, F., Pauchet, A., Bousquet, Ph., and Fruman, D. H., 1995, "On the Morphology of Natural and Ventilated Cavities," *Proceedings of the ASME Fuids Engineering Division Summer Meetingg,* Vol. FED-210, pp. 31–38.

Le, Q., Franc, J. P., and Michel, J. M., 1993, "Partial Cavities: Global Behavior and Mean Pressure Distribution," ASME JOURNAL OF FLUIDS ENGINEERING, Vol. 115, pp. 243–248.

Okamoto, H., Okada, K., Saito, Y., Takahei, T., 1977, "Cavitation Study of Duct Propellers on large Ships," *Transactions of the Annual Meeting of the Society of Naval Architects and Marine Engineers,* No. 7, pp. 168–191.

Reisman, G. E., and Grennen, C. E., 1996, "Pressure Pulses Generated by Cloud Cavitation," *Proceedings of the ASME Fuids Engineering Division Summer Meeting,* Vol. FED-236, pp. 319–328.

Reisman, G. E., Duttweiler, M. E., and Brennen, C. E., 1997, "Effect of Air Injection on the Cloud Cavitation on a Hydrofoil," *Proceedings of the ASME Fluids Engineering Division Summer Meeting.*

Rusmussen, R. E. H., 1956, "Some Experiments on Cavitation Erosion in Water Mixed With Air," *Cavitation in Hydrodynamics,* NPL, Paper No. 20, pp. 1–25.

Numerical Model of Cavitating Propeller Inside of a Tunnel

Jin-Keun Choi
Graduate Student.

Spyros A. Kinnas
Professor.

Ocean Engineering Group,
Department of Civil Engineering,
University of Texas at Austin,
Austin, TX 78712
e-mail: kinnas@mail.utexas.edu

The unsteady cavitating flow of a propeller subject to a nonaxisymmetric inflow inside of a tunnel is addressed. A numerical method is developed which solves for the fully unsteady propeller problem and the tunnel problem separately, with the unsteady effects of one on the other being accounted for in an iterative manner. The propeller influence on the tunnel walls is considered via potential while the tunnel walls influence on the propeller is considered via velocity. The iterative process is found to converge very fast, usually within three iterations, even for a heavily loaded propeller. The effect of the tunnel extent and the number of panels on the predicted mean propeller forces is investigated. In the case of uniform inflow the equivalent open water velocity is calculated and then compared to that predicted from Glauert's formula. The two velocities are found to be very close to each other in the case of light propeller loading, and to deviate from each other as the propeller loading increases. In the case of nonuniform flow the predicted unsteady propeller forces are found not to be affected appreciably by the tunnel effects in the case of noncavitating flow. In the case of cavitating flows the tunnel effects have been found to be appreciable, especially in terms of the predicted cavity extent and volume. The predicted cavity patterns are shown to be very close to those observed in CAPREX, a CAvitating PRopeller EXperiment performed at MIT's cavitation tunnel.

Introduction

When a propeller experiment is performed in a cavitation tunnel, the experimental results have to be corrected for the tunnel wall effects. One of the most widely used formulas for the tunnel wall correction is Glauert's formula, which is based on simple axisymmetric momentum theory (Glauert, 1947). The correction in Glauert's formula consists of replacing the mean inflow velocity (flow rate divided by the tunnel sectional area) with an equivalent open (unbounded) flow velocity for the same thrust. However, in Glauert's formula the propeller is treated with an actuator disk and thus the effects of the propeller characteristics (pitch, chord, number of blades, rake, etc.) are not accounted for. Most importantly, the effects of the nonuniformity of the inflow (usually simulated in a tunnel with a wake screen) are not included at all. The tunnel walls effects in this case can be crucial in determining the unsteady forces or unsteady cavity shapes on the blades.

The objective of the research described in this paper is to solve the *fully* unsteady flow of a cavitating propeller inside of a tunnel. In this way, experimental results can be compared *directly* to the computational results without the need for any corrections. In other words, the complete tunnel wall effects on the propeller performance, including cavitation, are computed numerically.

A lifting-surface vortex-lattice method has been developed for the unsteady flows around cavitating propellers in an unbounded fluid (Lee, 1979; Breslin et al., 1982; Kerwin and Kinnas, 1986). This method has been extended recently to include the wake alignment in inclined flows (Pyo and Kinnas, 1997).

The effects of a duct or hub on the propeller flow have been considered in the case of steady flow (Kerwin and Kinnas, 1987; Hughes et al., 1992), and in the case of unsteady noncavitating flows (Hughes and Kinnas, 1993; Kinnas et al., 1993). In these works, the flow around a duct though is still treated as an external flow with its interaction with the propeller being accounted for iteratively. One might say that the effect of a tunnel could be simulated as that of a duct with "infinite" chord. This approach however, would require adjustment of the inflow to the "duct" until the flow distribution inside the duct upstream of the propeller is equal to that measured in the tunnel. The propeller inside of a tunnel flow could also be treated with methods for the hydrodynamic analysis of pumps (Brennen, 1994). These methods though treat the blade sections as cascades of 2-D sections and model the unsteady cavity shapes in a quasi-steady manner.

In the present paper, a numerical method is developed which solves the fully unsteady cavitating propeller problem and the tunnel problem separately, with the unsteady effect of one on the other being accounted for in an iterative manner. The flow inside the tunnel is solved via a panel method applied to the tunnel walls and two sectional stations (lids), one upstream and the other downstream of the propeller, as shown in Fig. 1. The propeller influence on the tunnel walls is considered via potential while the tunnel walls influence on the propeller is considered via velocity.

Cavitating Propeller in Open Flow

The prediction of propeller sheet cavitation in open nonaxisymmetric inflow can be accomplished by using a Vortex/Source-Lattice method developed at MIT and UT called HPUF-3AL. A brief description of the method is given next.

The analysis method models the three-dimensional unsteady cavitating flow around a propeller by representing the blade and trailing wake as a discrete set (lattice) of vortices and sources which are located on the blade mean camber surface and trailing wake surface.

The strengths of the blade thickness sources are given in terms of derivatives of the thickness in the chord-wise direction and are independent of time. The unknown bound vortices on the blade and the unknown cavity sources are determined by applying the kinematic boundary condition and the dynamic boundary condition at certain control points located on the blade mean camber surface. A more detailed description of the control point location is given in (Kinnas and Fine, 1989).

The kinematic boundary condition requires that the sum of the influences for all of the vortices, sources, and the inflow normal to a particular control point on the blade is equal to zero. Another way to say this is that the kinematic boundary condition requires the flow to be tangent to the blade surface. The dynamic boundary

Contributed by the Fluids Engineering Division for publication in the JOURNAL OF FLUIDS ENGINEERING. Manuscript received by the Fluids Engineering Division May 27, 1997; revised manuscript received May 22, 1999. Associate Technical Editor: J. Katz.

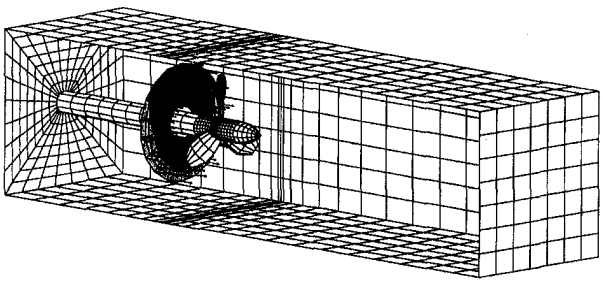

Fig. 1 Modeling of the problem with paneled tunnel and propeller

condition requires that the pressure must be equal to vapor pressure at control points covered by the cavity. The fully unsteady linearized dynamic boundary condition (Lee, 1979; Breslin et al., 1982) is applied with the incorporation of the non-linear leading edge correction, as will be described later in this section. The area of application of the dynamic boundary condition changes with time, as the cavity extent changes with time. The unknown cavity extent is determined by searching for the cavity length along each span-wise location. The desired cavity length is the one which renders the cavity pressure equal to vapor pressure. A closed cavity condition (zero cavity thickness at the cavity end) is applied at all times. Cavity thickness is determined by integrating the cavity source distribution over the cavity surface along each strip. Cavity volume is calculated by numerically integrating the cavity thickness over the mean camber surface area.

The problem is solved in the time domain, with each time step representing an angular rotation of the propeller. The time domain solution allows for the effects of all strips and blades to be accounted for in an iterative fashion. After the first complete propeller revolution, the method achieves the fully wetted steady solution. Three more propeller revolutions produce the fully wetted unsteady solution. Finally, the converged cavitating unsteady solution is attained after three (or more) additional propeller revolutions.

Many major modifications have been made to HPUF-3AL since the original version (called PUF-3) developed by Lee (Lee, 1979) and Breslin et al. (1982). These modifications include the follows:

- Nonlinear leading edge correction (Kerwin et al., 1986) in order to predict the correct effect of blade thickness on cavity size (Kinnas, 1991).

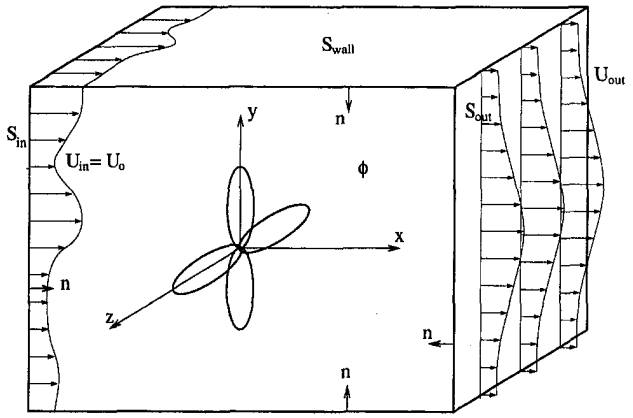

Fig. 2 Propeller and tunnel coordinate system

- An improved numerical scheme and the option for cavity detachment at a known location (Kinnas and Fine, 1989).
- Hub effects using the method of imaging (Kinnas and Coney, 1992).
- General blade thickness sections, allowing for supercavitating sections with finite trailing edge thickness (Kudo and Kinnas, 1995).
- Wake alignment for uniform and inclined flows (Pyo and Kinnas, 1996; Kinnas and Pyo, 1997).

Propeller/Tunnel Interaction

Formulation. In general, there are two possible formulations for internal potential flow problems; the total potential formulation and the perturbation potential formulation. In most propeller applications though the ship wake is non-axisymmetric and the inflow cannot be described via a velocity potential, thus leaving the perturbation potential method as the only viable alternative. It should be noted that only the potential part of the propeller-tunnel interaction will be considered with this method.

The coordinate system shown in Fig. 2 is used because of its consistency with the propeller coordinate system used in HPUF-3AL explained earlier. The normal vector points into the flow domain. The outer boundary of the flow domain, S_T, is composed of the tunnel walls and two imaginary planes; one upstream, S_{in},

Nomenclature

A = cross-sectional area of the tunnel
D = propeller diameter
F_n = Froude number; $F_n = (n^2D/g)$
g = gravitational acceleration
H = tunnel height
J = advance ratio, $J = (V_x/nD)$
K_T = thrust coefficient, $K_T = (T/\rho n^2D^4)$
K_Q = torque coefficient, $K_Q = (Q/\rho n^2D^5)$
n = number of propeller rotation per second
$\vec{n}$ = normal vector, positive when pointing into the fluid
p = pressure on the tunnel wall
Q = cavity volume
r = distance between field point and source point
R = propeller radius
S_{in} = inflow boundary part of the tunnel boundary surface
S_{out} = outflow boundary part of the tunnel boundary surface
S_P = propeller boundary and trailing wake surface
S_T = tunnel boundary surface, $S_T = S_{wall} + S_{in} + S_{out}$
S_{wall} = solid wall boundary part of the tunnel boundary surface
$\vec{U}_{in}$ = velocity vector field at S_{in}
$\vec{U}_o$ = velocity vector field inside the tunnel in the absence of propeller
$\vec{U}_{out}$ = velocity vector field at S_{out}
$\vec{V}$ = velocity vector
V_{open} = inflow velocity to the propeller in unbounded open flow for the same thrust as in tunnel flow
V_{tun} = inflow velocity to the propeller inside tunnel
V_x = axial velocity
(x, y, z) = coordinate systems fixed on tunnel, nondimensionalized by R (x downstream direction, y upward, z port side)
Z = number of blades
λ = the ratio of tunnel velocity to the equivalent open water velocity; $\lambda = V_{tun}/V_{open}$
ϕ = perturbation potential
ϕ_{prop} = perturbation potential induced by propeller
ρ = density of water
σ_n = cavitation number based on RPS n; $\sigma_n = (p_{shaft} - p_v/0.5\rho n^2D^2)$
θ = blade angle
τ = nondimensionalized thrust; $\tau = (T/\rho AV^2) = (4K_T/\pi J^2)$

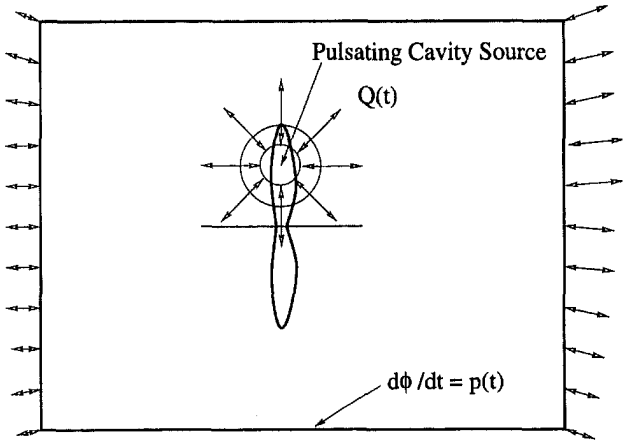

Fig. 3 Pulsating cavity source effect applied on both "lids" of the tunnel

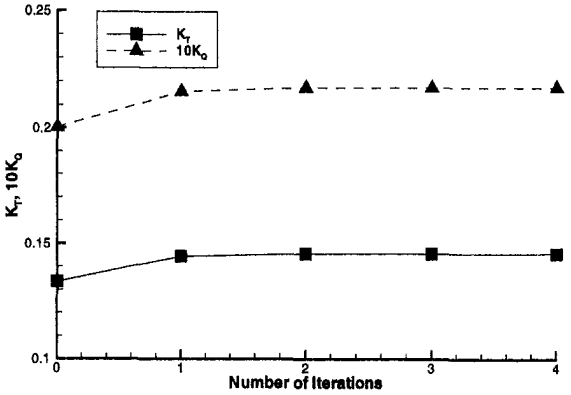

Fig. 5 Convergence of K_T and K_Q, N4148 propeller, $H = 3.333R$, $J = 0.8$, noncavitating flow

and the other downstream, S_{out}, of the propeller plane, as shown in Fig. 2.

$$S_T = S_{wall} + S_{in} + S_{out} \tag{1}$$

The velocity field can be expressed in terms of the perturbation potential ϕ.

$$\vec{V} = \vec{U}_o + \nabla\phi \tag{2}$$

$\vec{U}_o$ is the nonuniform flow field inside the tunnel in the absence of the propeller, appropriately adjusted in order to take into account the interaction of the incoming vorticity with the propeller (effective wake) (Huang and Groves, 1980).

By applying Green's theorem to the flow domain bounded by S_T and the propeller surface S_P (which also includes the propeller trailing wake surface), the following integral equation for the perturbation potential on S_P and S_T is derived.

$$2\pi\phi = \int\int_{S_T+S_P} \left\{ \phi \frac{\partial}{\partial n}\left(\frac{1}{r}\right) - \frac{\partial\phi}{\partial n}\frac{1}{r} \right\} dS \tag{3}$$

On the other hand, in the case of an unbounded propeller flow the perturbation potential everywhere in the flow field (except on the propeller surface) is given as follows.

$$4\pi\phi_{prop} = \int\int_{S_P} \left\{ \phi \frac{\partial}{\partial n}\left(\frac{1}{r}\right) - \frac{\partial\phi}{\partial n}\frac{1}{r} \right\} dS \tag{4}$$

Combining Eq. (4) with Eq. (3) the perturbation potential on S_T can be expressed as follows (Kinnas and Coney, 1992).

$$2\pi\phi = \int\int_{S_T} \left\{ \phi \frac{\partial}{\partial n}\left(\frac{1}{r}\right) - \frac{\partial\phi}{\partial n}\frac{1}{r} \right\} dS + 4\pi\phi_{prop} \tag{5}$$

Boundary Conditions. The unperturbed velocity field $\vec{U}_o$, which is in general nonuniform and nonaxisymmetric, satisfies the tunnel wall boundary condition;

$$\vec{n} \cdot \vec{U}_o = 0 \quad \text{on } S_{wall} \tag{6}$$

Then, the boundary condition on the solid tunnel wall S_{wall} becomes

$$\vec{n} \cdot \vec{V} = \vec{n} \cdot \vec{U}_o + \vec{n} \cdot \nabla\phi = \frac{\partial\phi}{\partial n} = 0 \tag{7}$$

At the inflow boundary S_{in}, which is assumed to be far enough from the propeller, the flow field will remain unperturbed.

$$\vec{n} \cdot \vec{V} = \vec{n} \cdot \vec{U}_o + \vec{n} \cdot \nabla\phi = \vec{n} \cdot \vec{U}_o \tag{8}$$

As a result, the boundary condition on S_{in} can be written as follows.

$$\frac{\partial\phi}{\partial n} = 0 \quad \text{on } S_{in} \tag{9}$$

At the outflow boundary, S_{out}, which like S_{in} is also assumed to be far enough from the propeller, the flow could differ from the unperturbed, depending on how far the action of the propeller trailing vorticity would persist. In the ideal case, where the propeller trailing wake extends to infinity, an outflow profile similar to that shown in Fig. 2 will exist. In this case $\partial\phi/\partial n$ in S_{out} should be different than zero, even though its surface integral should be equal to zero for the mass to be conserved. It is shown by Choi and Kinnas (1998) that for the case of a propeller subject to a uniform

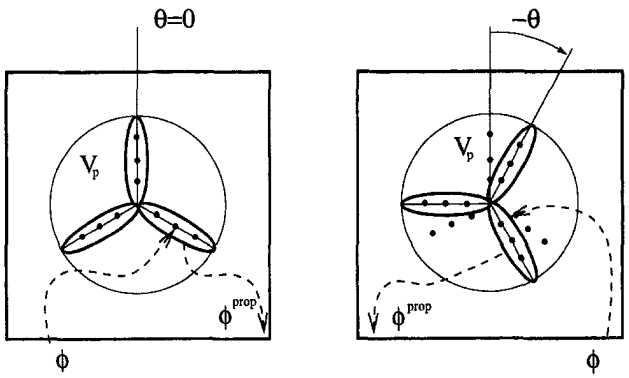

Fig. 4 Solution method in the time domain (looking from downstream)

Table 1 The geometry of DTMB propeller N4148. Thickness section: Modified NACA66, Zero skew, Camber section: NACA $a = 0.8$, Zero rake

radius/R	Pitch/D	Chord/D	Max. Camber/Chord	Max. Thickness/D
0.2000	0.9921	0.1600	0.0174	0.0329
0.3000	0.9967	0.1818	0.0195	0.0282
0.4000	0.9987	0.2024	0.0192	0.0239
0.5000	0.9975	0.2196	0.0175	0.0198
0.6000	0.9944	0.2305	0.0158	0.0160
0.7000	0.9907	0.2311	0.0143	0.0125
0.8000	0.9850	0.2173	0.0133	0.0091
0.9000	0.9788	0.1806	0.0125	0.0060
0.9500	0.9740	0.1387	0.0115	0.0045
1.0000	0.9680	0.0010	0.0000	0.0000

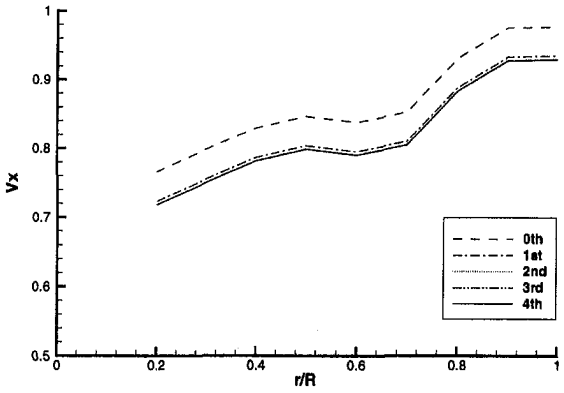

Fig. 6 Convergence of circumferential mean axial velocity V_x in tunnel with number of iterations, N4148 propeller, $H = 3.333R$, $J = 0.8$, noncavitating flow

tunnel flow the value of $\partial\phi/\partial n$ affects very little the flow in the vicinity of the propeller. For simplicity, the following boundary condition is applied on S_{out}.

$$\frac{\partial \phi}{\partial n} = 0 \quad \text{on } S_{out} \tag{10}$$

The effect of the tunnel length on the solution will be discussed later in this paper.

Applying the boundary conditions, Eq. (7), Eq. (9), and Eq. (10) to the integral equation Eq. (5) results in the distribution of only dipoles on S_T.

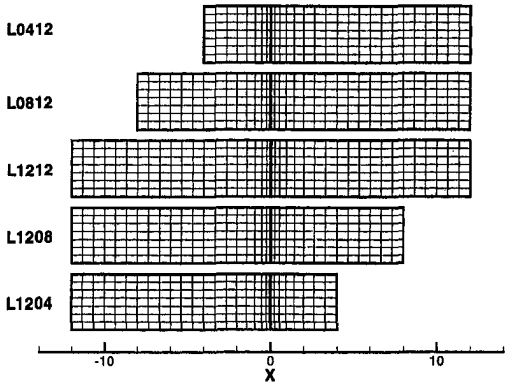

Fig. 7 Five combinations of tunnel extents upstream and downstream of the propeller; scaled with respect to propeller radius R

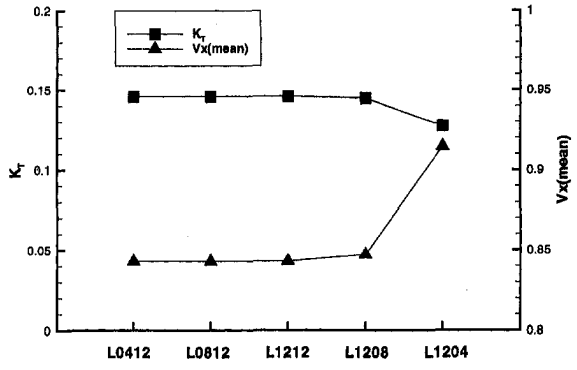

Fig. 8 Effect of tunnel extent on K_T and V_x, N4148 propeller, $H = 3.333R$, $J = 0.8$, without cavitation

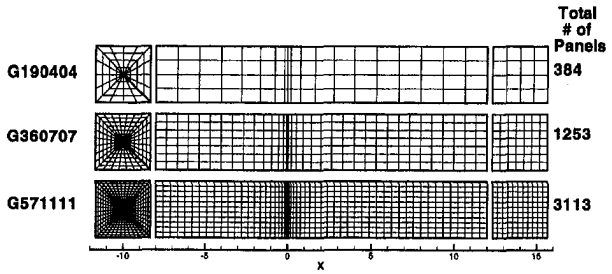

Fig. 9 Three different tunnel discretizations; scaled with respect to propeller radius R

$$2\pi\phi = \iint_{S_T} \phi \frac{\partial}{\partial n}\left(\frac{1}{r}\right) dS + 4\pi\phi_{prop} \tag{11}$$

Constant strength dipole distributions are used over each panel and the corresponding influence coefficients are computed by subdividing each panel into a sufficient number of sub-panels which are then approximated with discrete dipoles. Equation (11) is applied at the centroids (control points) of each tunnel panel. Details on the evaluation of influence coefficients are given in (Choi and Kinnas, 1998). The value of ϕ_{prop} is evaluated as the superposition of the effects of the propeller vortex- and source-lattice on the tunnel control points (Greeley and Kerwin, 1990).

The inflow velocity to the propeller is the sum of the inflow velocity $\vec{U}_o$ and that due to the tunnel. The velocity induced by the tunnel can be determined by taking the gradient of the perturbation potential induced by the tunnel. The perturbation potential in the flow field is given from the equation;

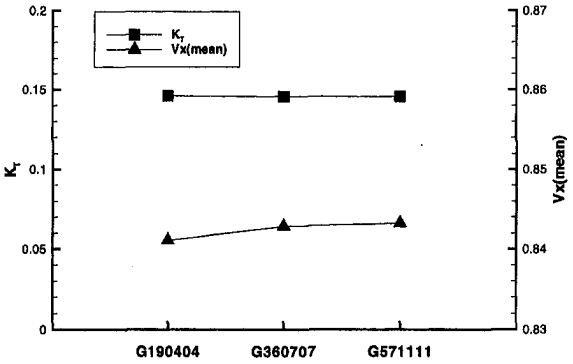

Fig. 10 Effect of number of panels on K_T and V_x, N4148 propeller, $H = 3.333R$, $J = 0.8$, without cavitation

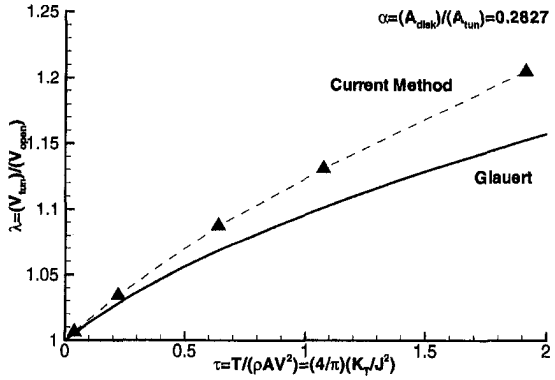

Fig. 11 Comparison with Glauert's momentum theory

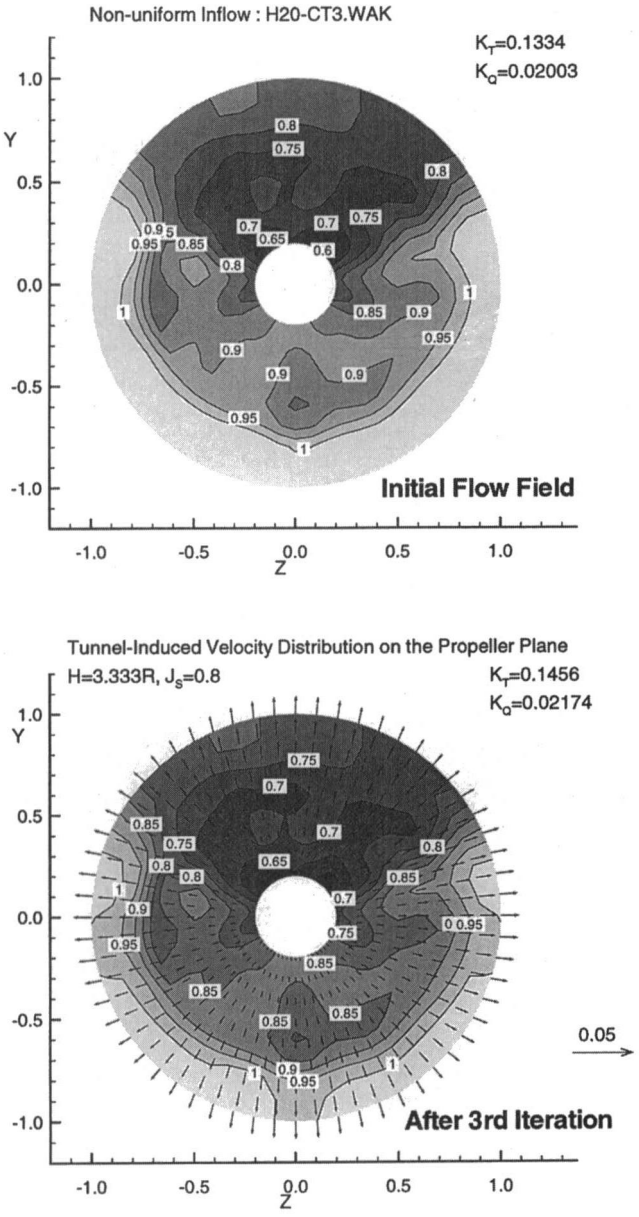

Fig. 12 Change of propeller inflow velocity field (evaluated at the propeller plane); noncavitating flow, $J = 0.80$

$$4\pi\phi = \int\int_{S_T} \phi \frac{\partial}{\partial n}\left(\frac{1}{r}\right) dS + 4\pi\phi_{\text{prop}} \tag{12}$$

The first term at the RHS of Eq. (12) corresponds to the perturbation potential induced by the tunnel, while the second term is the perturbation potential induced by the propeller. The inflow velocity to the propeller can thus be expressed as;

$$\vec{V} = \vec{U}_o + \frac{1}{4\pi}\int\int_{S_T} \phi\nabla\left\{\frac{\partial}{\partial n}\left(\frac{1}{r}\right)\right\} dS \tag{13}$$

Cavity Source Effect. The previous formulation, Eq. (11), with the boundary conditions, Eq. (7), Eq. (9), and Eq. (10), is valid only when the cavity volume is not changing with time. That is, the formulation is applicable for non-cavitating unsteady propeller flows and cavitating propeller flows with constant cavity volume. If the cavity volume changes, the boundary conditions should be modified to satisfy the continuity of the flow inside the tunnel.

One way of handling the cavity volume change inside the tunnel is depicted in Fig. 3. The cavity volume, $Q(t)$ is known from the solution of the propeller solver. The boundary condition on S_{in} and S_{out} should be modified to allow this volume change. A uniform velocity profile is applied on both sides of the tunnel.

$$\frac{\partial\phi}{\partial n} = -\frac{dQ}{dt}\frac{1}{2A} \text{ on } S_{\text{in}} \text{ and } S_{\text{out}} \tag{14}$$

where, A is the cross-sectional area of the tunnel. Half of the cavity volume change, $(dQ/dt)/2$ is assumed to make an out flux through S_{in}, and the other half through S_{out} in Eq. (14).

Alternatively, the total cavity volume change dQ/dt can be assumed to make an out flux only through S_{out}. In this case, the boundary conditions are as follows.

$$\frac{\partial\phi}{\partial n} = -\frac{dQ}{dt}\frac{1}{A} \text{ on } S_{\text{out}} \tag{15}$$

$$\frac{\partial\phi}{\partial n} = 0 \quad \text{on } S_{\text{in}} \tag{16}$$

The numerical solution of the integral equation, Eq. (5) is found to remain practically the same whether the boundary conditions, Eq. (7) and Eq. (14) are used or the boundary conditions, Eq. (7), Eq. (15), and Eq. (16) are used. This is primarily due to the relatively small values of the velocities to set-off the change in the cavity volume. The later set of boundary conditions has been chosen in the calculations because of its simplicity.

Equations (11) and (13) must now be modified to include the non-zero terms of $\partial\phi/\partial n$ at the tunnel lids. For example the following general equation replaces Eq. (13).

$$\vec{V} = \vec{U}_o + \frac{1}{4\pi}\int\int_{S_T}\left\{\phi\nabla\frac{\partial}{\partial n}\left(\frac{1}{r}\right) - \frac{\partial\phi}{\partial n}\nabla\left(\frac{1}{r}\right)\right\} dS \tag{17}$$

It should be noted that if a calculation involving pressures on the tunnel walls had to be performed the acoustic impedance of the rigid tunnel, as well as the flexibility of the tunnel walls (the tunnel Plexiglas windows in particular) would need to be considered, as described by Kinnas et al. (1998).

Solution Method in Time Domain. The integral equation Eq. (5) must be solved in the time domain. The numerical solution is carried over a finite number of time steps, which is taken equal to that used in the unsteady propeller problem (60 per revolution). The time-marching solution scheme is depicted in Fig. 4.

The following iterative procedure is employed:

Step 1: Calculate $\phi_{\text{prop}}(x, y, z, \theta)$, the propeller influence at (x, y, z) on S_T when the key blade is at the θ position. This potential $\phi_{\text{prop}}(x, y, z, \theta)$ is given by Eq. (4) and is calculated by PUF3FPP, a post-processing code of HPUF-3AL which calculates the unbounded potential field induced by a cavitating propeller (Greeley and Kerwin, 1990). The calculation is performed for $60/Z$ time-steps (key blade angles).

Step 2: Solve the tunnel problem to obtain $\phi(x, y, z, \theta)$, the perturbation potential at (x, y, z) on S_T when the key blade is at the θ position. The potential $\phi(x, y, z, \theta)$ is obtained by solving Eq. (5). This calculation is performed for $60/Z$ time-steps.

Step 3: Calculate the inflow to the propeller, $\vec{V}$ $(x = 0, r, \theta + i2\pi/Z)$, as given by Eq. (17). $\vec{U}_o$ corresponds to the unperturbed inflow velocity at $(r, \theta + i2\pi/Z)$, $i = 1, \ldots, Z$, on the propeller plane when the key blade is at θ position, where Z is the number of blades. This velocity is evaluated along the mid-chord line of the blade (in the lifting line sense).

Steps 1–3 are repeated until convergence of the solution. Notice that the flow field in the tunnel is periodic with frequency Zn where n is the propeller RPS. Thus, the tunnel problem has to be

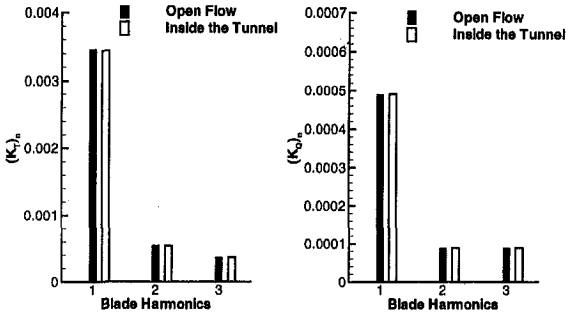

Fig. 13 Tunnel effects on the unsteady forces of a propeller; noncavitating flow, $J = 0.8$

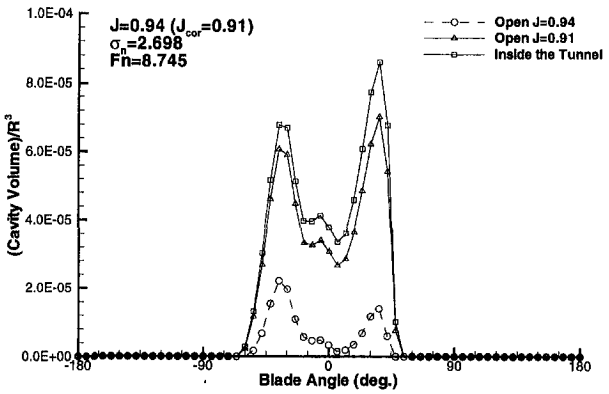

Fig. 15 Tunnel effect on cavity volume; $J = 0.94$, $\sigma_n = 2.7$

solved only for $60/Z$ time-steps per iteration. The coefficient matrix that corresponds to the tunnel problem does not change with time, and is LU decomposed only once, while the solution at each time step is carried out via backward substitution. An advantage of the present iterative method is that there was no need to modify the existing propeller analysis code, HPUF-3AL.

Convergence of the Method

The convergence history with iteration number for the mean thrust coefficient, K_T, and the mean torque coefficient, K_Q, is shown in Fig. 5. The propeller geometry, the tunnel section dimensions, and the wake inflow for the CAPREX II experiment performed at the MIT cavitation tunnel are used (Mishima et al., 1995). The 3-bladed 12 inch diameter propeller model N4148 (designed by DTMB) is used, with characteristics given in Table 1. The tunnel has a 20 inch square cross section. The paneling for the tunnel is L1212 shown in Fig. 7. The paneled tunnel length is $24R$; $12R$ upstream of the propeller and $12R$ downstream of the propeller, with R being the propeller radius.

Figure 6 shows the convergence history with iteration number for the circumferential mean axial velocity in the propeller plane. It is concluded from Figs. 5 and 6 that the iterative method converges very fast. After applying the iterative process to several cases, it has been found that generally three iterations are enough, even for heavily loaded propellers.

In the formulation, it is assumed that the upstream and downstream boundaries are far enough from the propeller. Thus the effect of the extent of the paneled tunnel on the solution is of great importance. The predicted K_T and V_x are shown in Fig. 8 for the various tunnel extents shown in Fig. 7.

The middle part, x from -4 to 4, for each of the cases shown in Fig. 7 is modeled with the same paneling, so that only the tunnel extent effect is observed. It may be concluded from Fig. 8 that; (a) the upstream tunnel length is not important, and (b) the downstream extent of the tunnel should be longer than $8R$. For this propeller condition, the length of the ultimate wake is slightly greater than $8R$ in HPUF-3AL. This suggests there could be a relation between the length of the ultimate wake and the required downstream tunnel extent. More detailed investigation on the downstream tunnel length confirms that the downstream tunnel length should be longer than the ultimate wake to get results which are not affected by the modeled tunnel length (Choi and Kinnas, 1998).

The effect of number of panels on the solution for fixed tunnel size is given in Fig. 10 for the grids shown in Fig. 9. A relatively mild dependence on the number of panels is found. The grid G360707 has been found as the most suitable for a large variety of tried cases. The corresponding CPU time for this grid and for three propeller-tunnel iterations is about 20 minutes on a DEC Alpha 600 5/266.

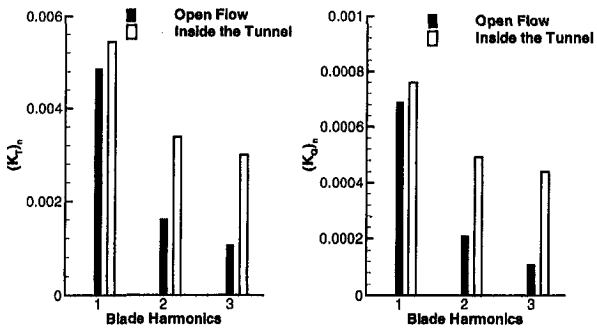

Fig. 14 Tunnel effects on the unsteady forces of a propeller; cavitating flow, $J = 0.94$, $\sigma_n = 1.9$

Numerical Results

All results in this section are obtained for propeller N4148 and the conditions in CAPREX II already mentioned (Mishima et al., 1995). The method is first applied in the case of uniform flow and the results are compared to those of Glauert. Glauert modeled the propeller with an actuator disk and assumed that the axial velocity is uniform upstream of the tunnel, in propeller slip stream, and outside of the slip stream. Then, by applying continuity, Bernoulli's equation, and axial momentum conservation he obtained a simple relation between the equivalent open flow speed and thrust for various tunnel cross sectional areas (Glauert, 1947). He defined λ as the ratio of the actual mean velocity through the tunnel, V_{tun} to that of an open flow, V_{open}, which would result the same propeller thrust. He also gave the value of λ as a function of the thrust coefficient and the ratio of the propeller disk to the tunnel cross-sectional area. This ratio can also be predicted by the present numerical method by running the propeller in open flow and inside of a tunnel.

Figure 11 shows the λ versus τ curves given from Glauert's theory and from applying the present method. Non-cavitating conditions were used and the viscous flow effects were not included in the propeller analysis method, in order to replicate the assumptions in Glauert's theory. Notice that the two curves are very close to each other in the case of light propeller loading (small τ), and that they start deviating from each other as the loading increases. The differences are attributed to the different propeller models (actuator disk vs. lifting surface) used in the two methods, as well as to the assumptions in Glauert's theory that were mentioned previously. A more thorough comparison of the present method to Glauert's theory is given by Choi and Kinnas (1998). The effect of having a square tunnel instead of a circular one on the solution has been investigated for the conditions of CAPREX II and found to be negligible. However, this effect should become more significant for heavily loaded propellers and larger propeller disk to tunnel sectional area ratios. It should be noted that the range

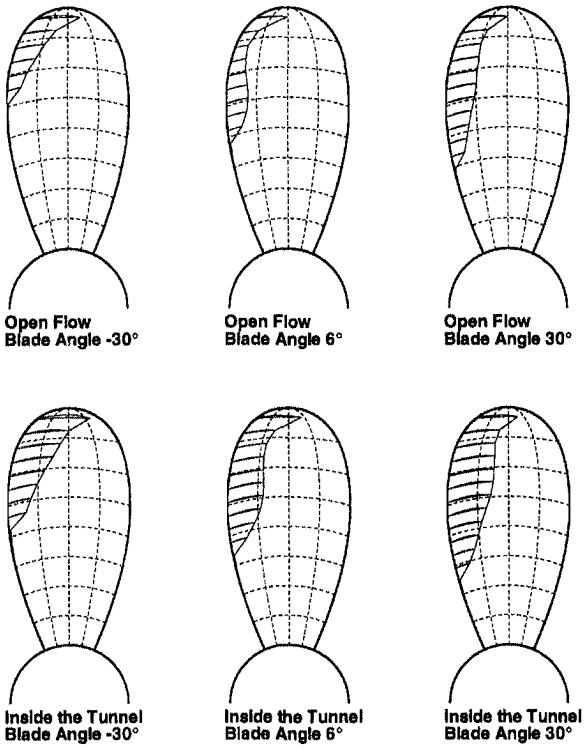

(a) Predicted cavity shapes; WITHOUT the tunnel effect (top) and WITH the tunnel effect (bottom)

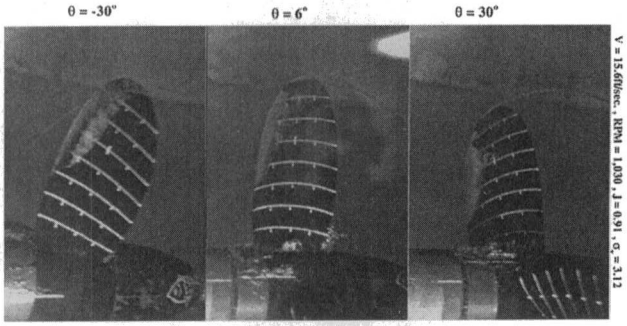

(b) Photograph taken from CAPREX

Fig. 16 Comparison of cavity shapes, $J = 0.9087$, $\sigma_n = 2.576$, $F_n = 9.159$

of τ in CAPREX II is $0.01 \leq \tau \leq 0.3$, where the two curves are in very good agreement.

Figure 12 shows the non-uniform inflow at the propeller plane inside the tunnel at the zeroth iteration (open flow) and at the third iteration after convergence of the solution has been achieved. The values of the corresponding thrust and the torque coefficients are also given in Fig. 12. The advance ratio is equal to $J_s = 0.8$ and the flow is noncavitating. The initial inflow at the propeller plane is the effective wake, as predicted from the nominal wake (measured in CAPREX) by using WKPROC (Wilson and Van Houten, 1983), an extension of the method described in (Huang and Groves, 1980). Only the axial component of the measured inflow has been considered, knowing that the other two components of the inflow velocity are negligible. In open flow the mean thrust and torque of the propeller are $K_T = 0.1334$ and $K_Q = 0.02003$, respectively. The converged thrust and torque inside the tunnel are $K_T = 0.1456$ and $K_Q = 0.02174$, respectively. This thrust corresponds to $\tau = 0.3652$, while the converged mean axial velocity corresponds to $\lambda = 1.0565$. The modified inflow, which includes the tunnel propeller interaction, is shown at the bottom part of Fig. 12. Notice that for this propeller geometry and flow conditions the effect of the tunnel on the inflow is an almost "uniform" reduction in the values of the axial velocity. Also, in the same figure the existence of a small radial outward flow is shown. This outflow off-sets the contraction of the propeller flow so that the resulting flow is aligned with the tunnel walls.

The harmonics of the unsteady propeller forces in open and tunnel flow are shown in Fig. 13. The effect of the tunnel on the unsteady forces is negligible in this noncavitating flow case. This is consistent with the velocity profiles shown in Fig. 12. The harmonics of the forces are also shown in the case of cavitating flow in Fig. 14. Notice now that the differences are larger.

The effect of the tunnel on the predicted cavity volume is shown in Fig. 15. The cavity volume shown in the figure is that of a single blade. The advance ratio $J = 0.94$ based on the tunnel inflow velocity or $J_{cor} = 0.91$ based on the equivalent (for mean thrust identity) unbounded inflow velocity. The reason the cavity volume has two "peaks" is that the propeller inflow wake has two slow velocity regions, as seen in Fig. 12. The drastic increase in cavity volume due to the effect of the tunnel is clearly shown. In Fig. 15, cavity volume for $J = 0.91$ calculated under open flow condition

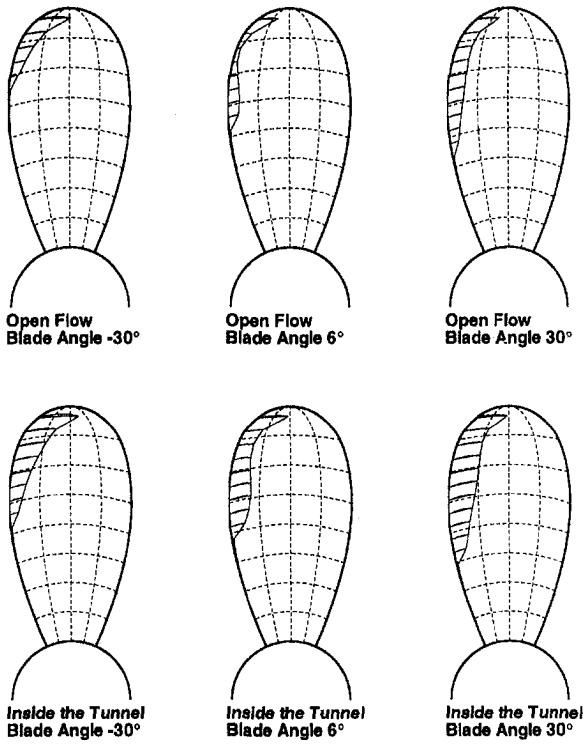

(a) Predicted cavity shapes; WITHOUT the tunnel effect (top) and WITH the tunnel effect (bottom)

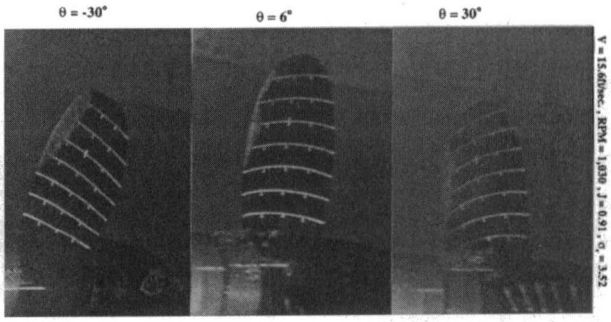

(b) Photograph taken from CAPREX

Fig. 17 Comparison of cavity shapes, $J = 0.9087$, $\sigma_n = 2.907$, $F_n = 9.159$

is also shown. The difference between the curves "Inside the Tunnel" and "Open $J = 0.91$" is relatively small. However, this difference shows that the tunnel interaction computed by the current method is more than a simple adjustment of the mean axial velocity.

The predicted cavity shapes for one of the cases in CAPREX are shown in Fig. 16(*a*). The advance ratio J based on tunnel velocity is 0.9087. The cavitation number based on RPS n is $\sigma_n = (p_{shaft} - p_v/0.5\rho n^2 D^2) = 2.576$, and the Froude number is $F_n = (n^2 D/g) = 9.159$. The corresponding photographs of the blade at three different angles are shown in Fig. 16(*b*). Dashed lines corresponding to painted curves and marks on the blade shown in the photographs are drawn on top of the computed cavity shape plots in order to facilitate the comparison. A similar comparison for a different cavitation number ($\sigma_n = 2.907$) is shown in Fig. 17. The drastic effect of the tunnel on the cavity shape is clearly shown in Figs. 16 and 17. The increase of the cavity size in the tunnel is due to the reduction of the inflow velocity at the propeller plane. Note the good agreement of the predicted cavity shapes to those shown in the photographs, except in a region very close to the blade tip where the present cavity model is expected to break down.

Conclusions

In this paper, the problem of a cavitating propeller inside of a tunnel is formulated via the perturbation potential method. An iterative method that accounts for the fully unsteady tunnel—propeller interaction problem is developed. One advantage of this iterative method is that there is no need to modify the existing cavitating propeller analysis code, HPUF-3AL (or its future upgrades). The iterative process is found to converge very fast, usually within three iterations even for a heavily loaded propeller. The effect of the tunnel extent and the number of panels on the predicted propeller forces and cavity shapes has been found to be insignificant. The equivalent open water velocity is calculated and then compared to that predicted from Glauert's formula. The two velocities are found to agree well in the case of light propeller loading, but deviate from each other as the propeller loading increases. The effect of the tunnel on unsteady forces has been found to be negligible in the case of non-cavitating flows, but appreciable in the case of cavitating flows. The effect of the tunnel on the predicted cavity extent and volume has been found to be drastic. Application of the numerical method has shown that a uniform adjustment to the inflow is not sufficient in the case of cavitating flows. Predicted cavity shapes have been found to be in very good agreement to those observed in CAPREX II, a cavitating propeller experiment.

Acknowledgment

Support for this research was provided by the "Consortium on Cavitation Performance of High Speed Propulsors" with the following members; DTMB, OMC, Mercury, Volvo-Penta, IHI, Daewoo, El Pardo MB, HSVA, KaMeWa, Rolla, Sulzer-Escher Wyss, Hyundai, Wärtsilä, Ulstein, and Michigan Wheel.

References

Brennen, C. E., 1994, *Hydrodynamics of Pumps,* Concepts ETI, Inc., and Oxford University Press.

Breslin, J. P., Van Houten, R. J., Kerwin, J. E., and Johnsson, C.-A., 1982, "Theoretical and Experimental Propeller-Induced Hull Pressures Arising from Intermittent Blade Cavitation, Loading, and Thickness," *Trans. SNAME,* Vol. 90.

Choi, J.-K., and Kinnas, S. A., 1998, "Numerical Water Tunnel in Two and Three Dimensions," *Journal of Ship Research,* Vol. 42(2), pp. 86–98, June.

Glauert, H., 1947, *The Elements of Aerofoil and Airscrew Theory, 2nd Edition,* Cambridge University Press, New York.

Greeley, D. S., and Kerwin, J. E., 1990, "A Numerical Method for the Calculation of the Field Point Potential Due to a Cavitating Propeller MIT-PUF3FPP Documentation and Listings," Technical Report 90-6, MIT, Department of Ocean Engineering, Feb.

Huang, T. T., and Groves, N. C., 1980, "Effective Wake: Theory and Experiment," *13th Symposium on Naval Hydrodynamics,* Tokyo, Oct.

Hughes, M. J., and Kinnas, S. A., 1993, "Unsteady Flows Around Multi-Component Integrated Propulsors," *Forum on Unsteady Flows* (FED-Vol. 157), pp. 21–31. Fluids Engineering Division, ASME.

Hughes, M. J., Kinnas, S. A., and Kerwin, J. E., 1992, "Experimental Validation of a Ducted Propeller Analysis Method," ASME JOURNAL OF FLUIDS ENGINEERING, Vol. 114(2), pp. 214–219.

Kerwin, J. E., Kinnas, S. A., Lee, J.-T., and Shih, W.-Z., 1987, "A Surface Panel Method for the Hydrodynamic Analysis of Ducted Propellers," *Trans. SNAME,* Vol. 95.

Kerwin, J. E., Kinnas, S. A., Wilson, M. B., and McHugh, J., 1986, "Experimental and Analytical Techniques for the Study of Unsteady Propeller Sheet Cavitation," *Proceedings of the Sixteenth Symposium on Naval Hydrodynamics,* pp. 387–414, Berkeley, CA, July.

Kinnas, S. A., 1991, "Leading-Edge Corrections to the Linear Theory of Partially Cavitating Hydrofoils," *Journal of Ship Research,* Vol. 35(1), pp. 15–27, Mar.

Kinnas, S. A., and Coney, W. B., 1992, "The Generalized Image Model—An Application to the Design of Ducted Propellers," *Journal of Ship Research,* Vol. 36(3), pp. 197–209, Sept.

Kinnas, S. A., and Fine, N. E., 1989, "Theoretical Prediction of the Midchord and Face Unsteady Propeller Sheet Cavitation," *Fifth International Conference on Numerical Ship Hydrodynamics,* pp. 685–700, Hiroshima, Japan, Sept.

Kinnas, S. A., Hsin, C.-Y., and Keenan, D. P., 1991, "A Potential Based Panel Method for the Unsteady Flow Around Open and Ducted Propellers," *Eighteenth Symposium on Naval Hydrodynamics (1990),* pp. 667–685, Washington D.C., National Academy Press.

Kinnas, S. A., Kimball, R. W., and Choi, J.-K., 1998, "Cavitating Propeller Experiment (CAPREX III): Measurement and Prediction of Tunnel Pressures," *Journal of Ship Research,* Vol. 42(3), pp. 233–248, Sept.

Kinnas, S. A., and Pyo, S., 1997, "Propeller Wake Alignment Models in Uniform and Inclined Inflow," *Propellers/Shafting '97 Symposium,* pp. 1–15 (Paper No. 28), Virginia Beach, VA, Sept., Soc. Naval Arch. & Marine Engnrs.

Kudo, T., and Kinnas, S. A., 1995, "Application of Vortex/Source Lattice Method on Supercavitating Propellers," *24th American Towing Tank Conference,* College Station, TX, Nov. 2–3.

Lee, C.-S., 1979, "Prediction of Steady and Unsteady Performance of Marine Propellers with or without Cavitation by Numerical Lifting Surface Theory," PhD thesis, M.I.T., Department of Ocean Engineering, May.

Mishima, S., Kinnas, S. A., and Egnor, D., 1995, "The CAvitating PRopeller EXperiment (CAPREX), Phases I & II," Technical report, Department of Ocean Engineering, MIT, Aug.

Pyo, S., and Kinnas, S. A., 1996, "User's Manual for HPUF-3AL (Cavitating Propeller Analysis with Wake Alignment)," Technical report, Ocean Engineering Group, UT Austin, Apr.

Wilson, H. B., and Van Houten, R. J., 1983, "A Program for Interpolation, Smoothing, Fourier Analysis, and Effective Wake Estimation of Propeller Inflow Fields: MIT-WKPROC User's Manual," Technical Report 83-7, MIT, Department of Ocean Engineering, June.

The Cavermod Device: Hydrodynamic Aspects and Erosion Tests

E. G. Filali[1]
Assistant.

J. M. Michel
Research Director.

Laboratoire des Écoulements Géophysiques et Industriels, CNRS
and University of Grenoble.
(Laboratory common to U.J.F., I.N.P.G., C.N.R.S.),
B.P. 53, 38041 Grenoble Cedex 9, France
e-mail: jean-marie.michel@hmg.inpg.fr

The Cavermod (CAVitation ERosion MODel) is an erosion test device first described by Dominguez-Cortazar et al. (1992, 1997). Recently, it was modified in two steps: first by increasing its maximum rotation rate (from 4500 to 8000 rpm) and second by shortening its vapor core (from 156 to 66 mm). This paper plans to present the main results which are obtained in both configurations (long and short vortex) and for "slow" or "rapid" regime of rotation. They mainly concern 1. the hydrodynamic aspects of the vapor core collapse, as deduced from observation of rapid films (evolution of the vortex length, collapse velocity), 2. the erosion patterns produced on metallic targets such as pure aluminium and copper. A second companion paper will present the results of force measurements in both configuration and an attempt to estimate the local erosive pressures.

1 Introduction

The Cavermod is an apparatus which uses the axial collapse of the vapor core of a liquid vortex in order to produce high forces concentrated on small areas over a finite time so that significant erosive effects on hard materials are obtained. It was first described in Dominguez-Cortazar et al. (1992) and more recently in Dominguez-Cortazar et al. (1997). The latter paper gives details on the genesis of the idea of vapor vortex axial collapse and its achievement in the Cavermod device. Let us recall only that the vapor vortex is formed near the axis of a rotating chamber, initially filled with deaerated water, by the small displacement **a** of a piston which results in the increase of the chamber volume (see Fig. 1(*a*) in which the parallel lines denote the vapor core). Then the rapid motion of the piston, due to the shock of a mass moving under a pressure difference $\mathbf{\Delta P}$, compels the vortex to collapse axially, at a high velocity **V**. At the end of the collapse, the closure region hits either a force transducer or a metallic target, which allows the measurement of the force exerted on the wall or the observation of the erosion patterns.

Recently, that device was modified in two steps (Filali, 1997). First, its maximum rotation rate was increased from 4500 to 8000 rpm, which results in a smaller minimum initial radius for a stable cylindrical vapor core (Rosenthal, 1962), and then in a possibly higher collapse velocity. Second, the shape of the piston was modified (see Fig. 1(*b*) in which the shaded area denotes the modified piston), so that the initial vortex length became 66 mm instead of 156 mm, which is the chamber length. The shortening of the vortex aimed to limit the development of the free surface unstabilities, which are believed to be at the origin of the dispersed pattern of erosion pits, in the case of the long vortex (Dominguez-Cortazar et al., 1997, Filali, 1997).

In this paper, we present the results of works which were undertaken with both configurations (long and short vortices) and for different values, middle and high, of the rotation rate. They relate first to hydrodynamic aspects: vortex length evolution, collapse velocities, size of the residual vapor core and second to erosion effects: erosion patterns, pits number, eroded volumes, correlation with material properties and comparison of Cavermod with other classic erosion tests devices. In the second, companion paper (Filali et al., 1999), results of force measurements are given, which were obtained from three different methods, and estimates of the erosive pressures are attempted.

2 Main Parameters

Besides the piston radius **R** (R = 21 mm) and the initial length $\mathbf{L}'$ of the vapor core ($\mathbf{L}' = \mathbf{L}$ for the long vortex), the main control parameters of the Cavermod are the rotation rate $\mathbf{\Omega}$, the displacement of the piston **a** and the driving pressure $\mathbf{\Delta P}$ by which the mass which produces the shock against the piston is moved. The resulting parameters are the initial vapor core radius $\mathbf{r_0}$, which depends on **a** and $\mathbf{\Omega}$ through centrifugal forces, and the collapse velocity **V** which depends on $\mathbf{\Delta P}$ and $\mathbf{r_0}$. The effect of centrifugal forces on the deformation of the lucite chamber wall can be estimated from classical relations coming from Elasticity theory. Table 1 gives the corrective coefficient which must be applied to the geometrical value of $\mathbf{r_0}$ (given by $\mathbf{r_0} = R\sqrt{a/L'}$ from the conservation of liquid volume) in order to estimate the effect of the centrifugal forces.

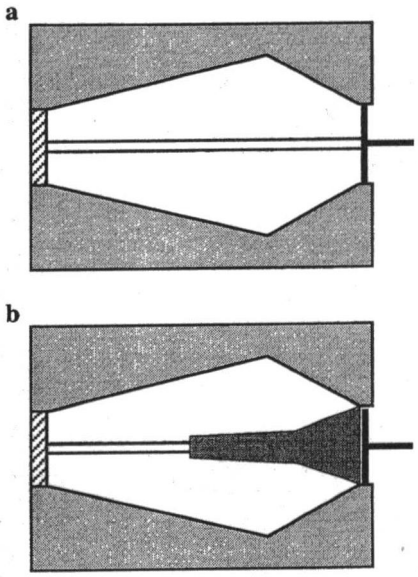

Fig. 1 The two kinds of working, (*a*) Long vortex; (*b*) short vortex

[1] Now at Alger University, Algeria.

Contributed by the Fluids Engineering Division for publication in the JOURNAL OF FLUIDS ENGINEERING. Manuscript received by the Fluids Engineering Division March 12, 1998; revised manuscript received February 8, 1999. Associate Technical Editor: J. Katz.

Table 1

r_0 (mm)	Ω (rpm)		
	4000	6000	8000
0.5	1.41	1.80	2.25
1.0	1.12	1.25	1.42
1.5	1.05	1.12	1.20
2.0	1.03	1.07	1.48

The effect of centrifugal forces is important for high rotation rates and small radii. At high Ω-values, it may happen that the vapor core appears as a consequence of centrifugal forces only. In such a case, it would be possible to reduce the initial radius until its limiting stable value is attained by giving a negative value to the parameter **a**. However, such a possibility was not used in the present study. In the following, the size of the vortex is indicated by either **a** or the geometrical value of $\mathbf{r_0}$.

3 Hydrodynamic Aspects

In the case of the long vortex, sixteen rapid films (at a frame rate close to 40,000 im/s) were taken to observe the evolution of the vapor vortex core. At each "shot" of the Cavermod, several collapses and rebounds are observed over a total duration of about 50 ms. In general, the first collapse takes less than one millisecond as shown on Fig. 2, which gives the evolution of the vortex length during its first collapse for three values of the initial radius. The evolution versus time is approximately linear, however, significant variations in the slope can be observed. It must be noted that such evolutions are fairly repeatable. Figure 3 shows an example of three first collapses and rebounds. Of course, the first collapse is the fastest one, and from the measurement of forces, it appears that erosion takes place at the end of the first collapse. Figure 4 shows the dependency of the mean velocity of the first collapse on the driving pressure **ΔP**, for low and high rotation rates and two values of the initial radius. In the case Ω = 7,000 rpm, the real value of the radius is of the order one millimeter, as given by Table 1, which explains that the difference between the results of both experimental cases is not too important. In the range of the experimental values, the dependency can be considered roughly linear. Attention has to be drawn to the high values of the collapse velocities which can exceed 1000 m/s. In fact, instantaneous velocities can reach 1200 m/s. The dependency **V(ΔP)**, for **ΔP** smaller than one bar, is not known. From an elementary mechanical model, which does not take friction forces into account, and assumes an inelastic shock between the moving mass and the piston, the piston velocity should vary as $(\Delta P)^{1/2}$. Then **V** could vary also according to the same approximate law for the small values of **ΔP**.

In the case of the short vortex, the collapse is not so easily observed and only small values of **ΔP** were tested. Figure 5 shows an example of first collapse for **ΔP** = 1 bar and a = 0.1 mm, which corresponds to $\mathbf{r_0}$ = 0.82 mm. In this case, the collapse is preceded by a noticeable time of acceleration: this is probably due to the larger value of the piston mass. It results in a significant difference between the mean (V_m) and the maximum (V_{max}) values of the collapse velocity. As expected, the perturbations of the free surface are less developed in the case of the short vortex and the two-phase torus which appears at the end of the first collapse

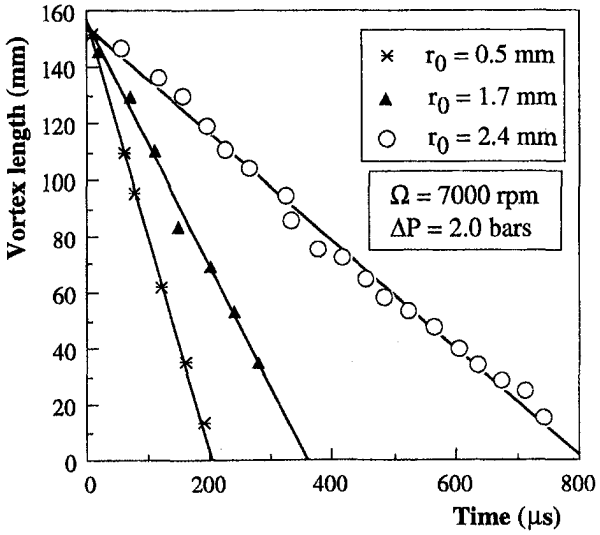

Fig. 2 **Evolution of the vortex length (first collapse) (Uncertainties: ±1 percent on time, ±3 mm on length)**

(Filali, 1997, Dominguez-Cortazar et al., 1997) is reduced with respect to the case of the long vortex.

In Dominguez-Cortazar et al. (1997) the role of Coriolis forces, by which the total axial moment of momentum of the liquid body is kept constant, was discussed. They prevent the total closure of the vapor vortex core and favor the existence of a thin vapor residue, visible on Fig. 8, downstream the pressure wave. In order to model this phenomenon (Filali, 1997), calculations were undertaken on the base of the rotating flow model developed in the Batchelor's textbook, except that here a pressure condition is imposed on the vortex core, upstream and downstream the transient overpressure which reduces the core size. In Fig. 6 the variations of the residual vortex radius $\mathbf{r_3}$ versus the rotation rate are displayed for different conditions of working of the Cavermod. In Fig. 7 the tangential velocity V_b profile near the vapor residue is shown: it is linear except near the residue itself where a $\mathbf{r}^{-1}$ law is obtained. The $\mathbf{r_3}$-values are rather small, of the order ten micrometers. This is mainly due to the small value of the similarity parameter $\Omega \mathbf{r_0}/\mathbf{U}$ (the inverse of the Rossby number) in the present experiment: for example, for Ω = 7000 rpm = 733 rd/s, the larger value of this parameter for the three cases under consideration in Fig. 6 is lower than 0.001. Despite this small value, Coriolis forces prevent the formation of a reentrant jet which otherwise would appear in the region of vortex core closure. We can mention another example of the efficiency of Coriolis forces: instead of the cylindrical vapor core, with Cavermod it is possible to form a chain of small bubbles, with diameter equal to about one millimeter, on the rotation axis: under the transient overpressure those bubbles don't disappear but remain visible and can be observed on rapid films (Filali, 1997). This finding should be considered as a guide for any modeling of the bubble behavior in a rotating liquid medium.

Finally, Fig. 8 shows a photograph of the two-phase torus for the case of the long vortex: it was taken under a short flash lighting, at a time close to the end of the first collapse. On the original some rough structures are visible inside the torus, which can be put in

Nomenclature

a = piston displacement (mm)
ΔP = driving pressure (bar)
L = chamber length (mm)
L′ = vortex core length (mm)
R = piston radius (mm)
V = axial collapse velocity (m/s))
Ω = rotation rate (rpm)
$\mathbf{r_0}$ = initial vortex radius (mm)
$\mathbf{r_3}$ = residual vortex radius (mm)
$\mathbf{V_b}$ = tangential velocity (m/s)

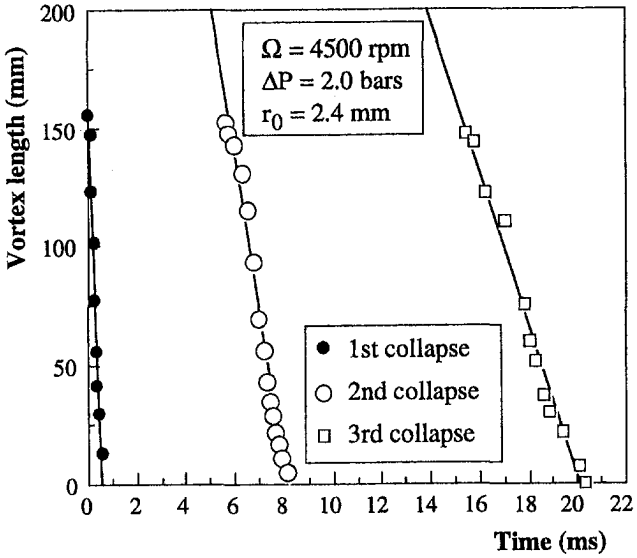

Fig. 3 History of the vortex collapse (Uncertainties as in Fig. 2)

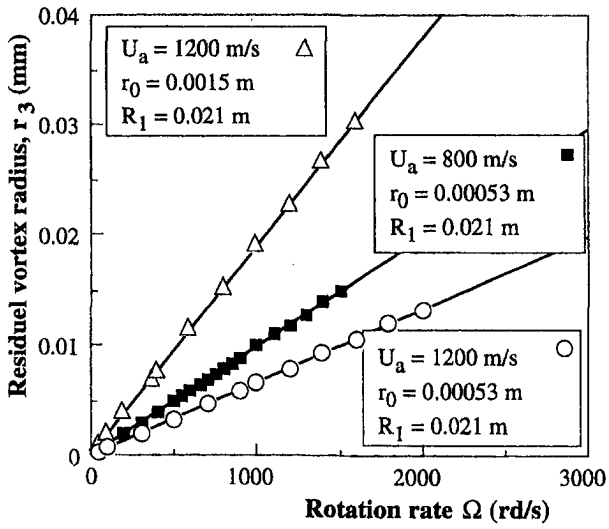

Fig. 6 Residual vortex radius vs the rotation rate (calculation results)

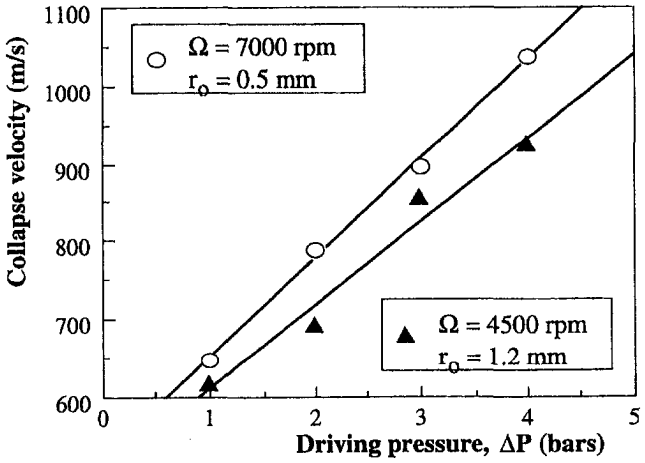

Fig. 4 Collapse velocities vs the driving pressure (Uncertainties: ±2 percent on ΔP, ±5 percent on the velocity)

relation with the dispersed patterns of erosion pits on metallic targets (see hereafter).

4 Erosion Tests

Figure 9 shows two photographs of the erosion patterns obtained from one Cavermod shot on pure aluminium samples in the cases of long and short vortices for the same driving pressure $\Delta P = 2$ bars. It is visible that the short vortex gives a concentrated erosion figure, contrarily to the long vortex. In order to quantify this aspect, we consider the real values of the radius r_0 by taking the effect of centrifugal forces into account. We obtain 1.2 mm and 1.3 mm approximately for the long and short vortex, respectively, while the maximum values of the corresponding erosion pattern sizes are 3 mm and 1.4 mm. Thus the size of the erosion pattern given by the short vortex on a soft material such as pure aluminium is rather smaller than the diameter of the initial vapour core, while it is larger in the case of long vortex. This reinforces the link between the hydrodynamic aspects—perturbations of the free surface, final two-phase torus—and the erosion damage on solid materials.

The eroded areas are also described using a microscope with a Mirau interferometric objective (Belahadji et al., 1991). In general, such an apparatus allows only the observation of a limited window,

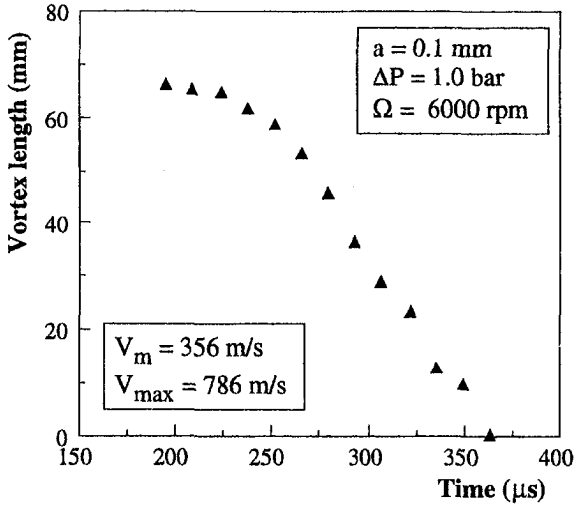

Fig. 5 Evolution of the short vortex length (Uncertainties: as in Fig. 2)

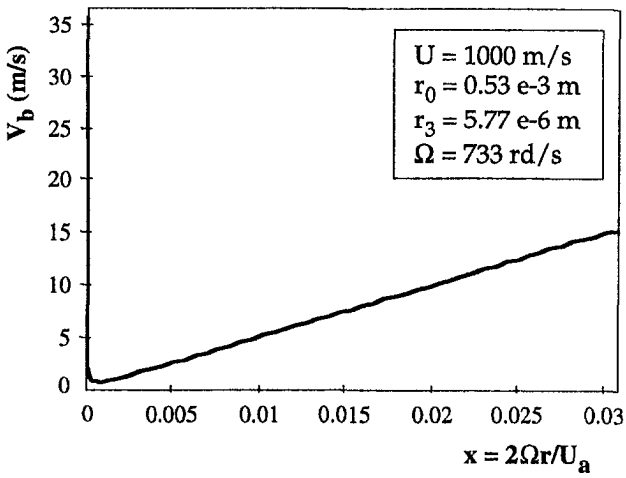

Fig. 7 Profile of the circumferential velocity near the vapor residue (calculation results)

Fig. 8 The two-phase flow torus at the end of the collapse. Case of the long vortex (diameter of the two-phase torus on the left: about 5 mm).

the size of which is smaller than the present erosion patterns. Figure 10 shows the whole patterns corresponding to Fig. 9, as reconstructed from photographs of elementary windows. In such a representation, two neighboring black fringes correspond to differences in altitude of $\lambda/2$, where λ is the mercury light wavelength, i.e., $\lambda/2 = 0.273$ μm. The dispersed pattern given by the long vortex is apparent in that view also. Concerning the short vortex, the photograph shows a global depression, the diameter of which is about 1.4 mm and the depth cannot be easily estimated, as the number of fringes is high. In addition, a complicated pattern of secondary craters is seen inside the global depression. A three-dimensional image of the same erosion figure, obtained from a laser profilometer, is given in Fig. 11: it allows us to have a more realistic idea of the erosion pattern and to emit some assumptions on the probable mechanisms leading to its formation. The isolated craters seem to be due to the collapses of individual bubbles existing in the two-phase medium at the end of the first collapse, which possibly influence their vicinity by emitting shock waves, as described by Tomita and Shima (1986) and Alloncle et al. (1992). This should be true also for the dispersed patterns given by the long vortex. Regarding the global depression of Fig. 9(*b*), it is difficult to assign it a precise origin: may be the global effect of the vortex closure region which hits the solid wall, or may be the result of the individual bubble collapses. As the region of craters is far enough from the frontier of the global depression in Fig. 10(*b*), the first hypothesis might be preferred. Anyway, subsequent experi-

Fig. 9(*a*) Case of long vortex: diameter 3 mm

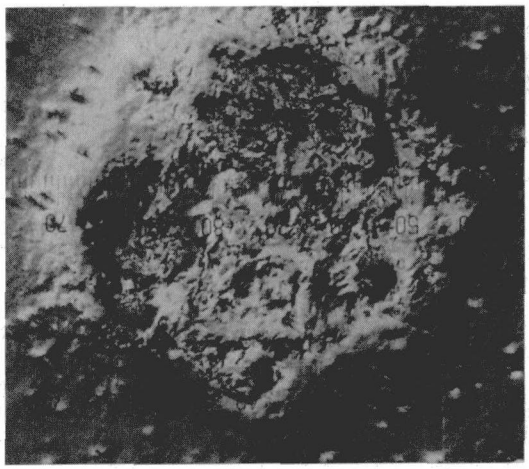

Fig. 9(*b*) Case of short vortex: diameter 1.4 mm

Fig. 9 Erosion patterns on aluminium samples

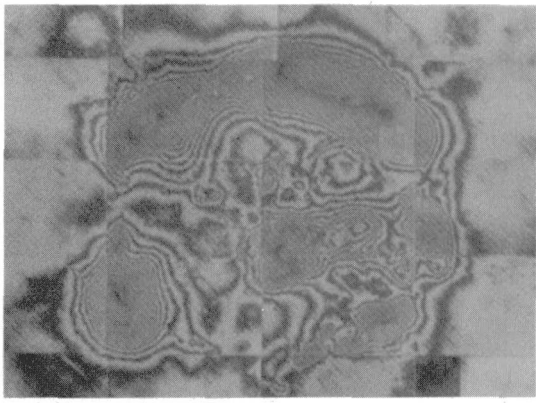

Fig. 10(*a*) Long vortex

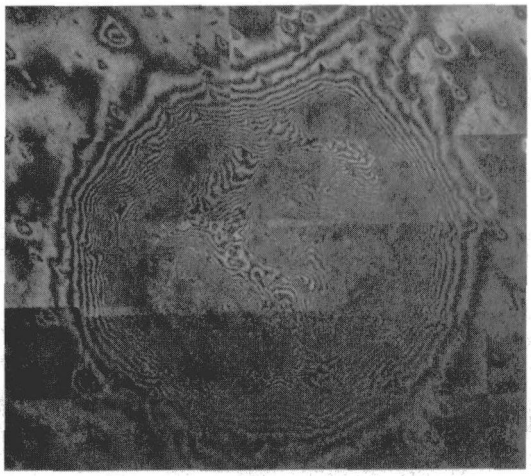

Fig. 10(*b*) Short vortex

Fig. 10 Reconstruction of the eroded areas by interferometric method

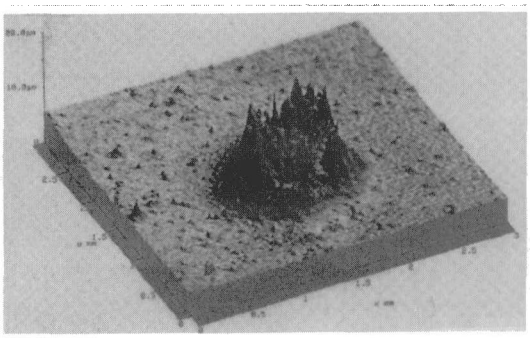

Fig. 11 Profile of the eroded area by laser profilometer

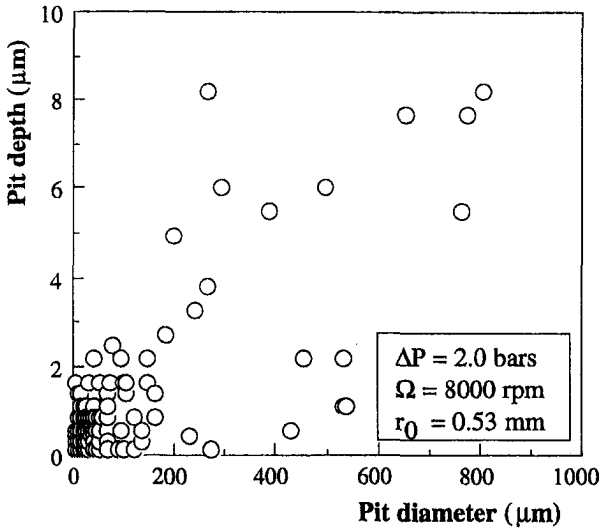

Fig. 12 Correlation between the pit depth and the pit diameter (Uncertainties: ±5 percent on the diameter, ±.130 μm on depth)

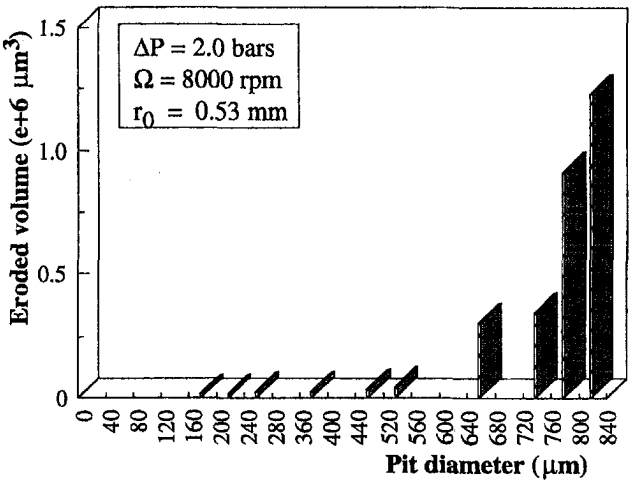

Fig. 14 Histogram of eroded volume (aluminium)

ments with hard materials and short vortex have shown that the global depression does not appear necessarily and that erosion figures can be limited to isolated craters in a restricted area.

By means of the interferometric microscope, it is possible to measure the pits number and the pits size—depth and diameter—if the erosion pits are isolated, which is the case for the erosion patterns given by the long vortex. Figures 12 to 14 give results on the erosion pattern produced by one shot of the Cavermod, under a driving pressure of two bars, on a pure aluminium sample. Here statistics are possible as the number of pits, i.e., 329, is high. Correlation between pits depth and diameter is given in Fig. 12: in general, the ratio is between .2 and 3 percent. The histogram of pits number given in Fig. 13 displays the overwhelming number of small pits, with diameter lower than 20 μm, but from the viewpoint of damage, the histogram of eroded volumes (volumes are estimated from the cone approximation) of Fig. 14 shows that only larger pits, although rare, are significant. In Fig. 15, the total eroded volumes of aluminium and copper, corresponding to one shot of the Cavermod, are shown as functions of the total impact force exerted on the sample (see the companion paper for the force measurement): it appears that the dependency is roughly linear.

Figure 16 shows correlations between material properties of the erosion samples—Brinnel hardness and breaking resistance—with the eroded volumes and the number of pits produced on four materials: pure aluminium (329 pits), copper (300), brass (150) and stainless steel 316 L (74) under the same working conditions of Cavermod: **a** = 0.1 mm, Ω = 8,000 rpm, **ΔP** = 2 bars). While the increase of pits number when the material properties decrease is regular enough (Fig. 16(*b*)), a large difference on volumes is seen between aluminium and copper in Fig. 16(*a*): this is mainly due to the difference in the number of big pits produced on both materials. As those experiments were not repeated, it is difficult to know if such a behavior is essential or is in relation with some variations of the Cavermod in the production of large erosive structures at the end of the first collapse.

Finally, Fig. 17(*a*) and 17(*b*) compare correlations (pits depth)/(pits diameter) for aluminium and copper, as given either by Cavermod or by usual erosive test devices such as the vibratory A.S.T.M. G32 device or the venturi device developed at the Fukui University (Japan). It appears that the ratios depth/diameter are roughly the same, with a possible larger value in the case of aluminium. However, the major information is relative to the size of the largest pits produced by the Cavermod, which can be twice the size found in usual test devices. Such a comparison is corroborated by the comparison concerning *the forces* produced in those different devices: for example (Filali, 1997), for Ω = 4,500 rpm,

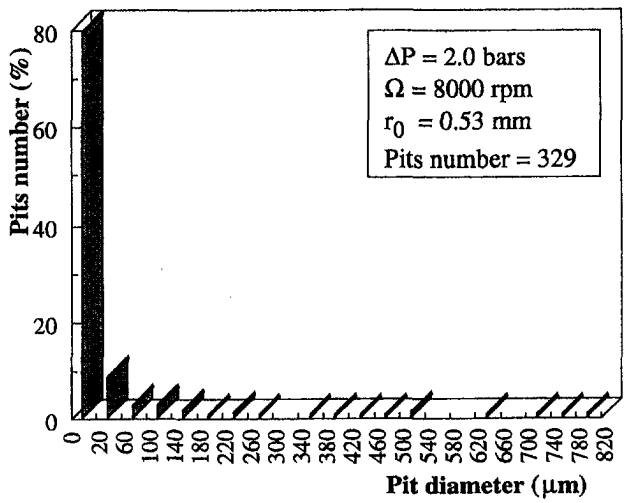

Fig. 13 Histogram of pits number (aluminium)

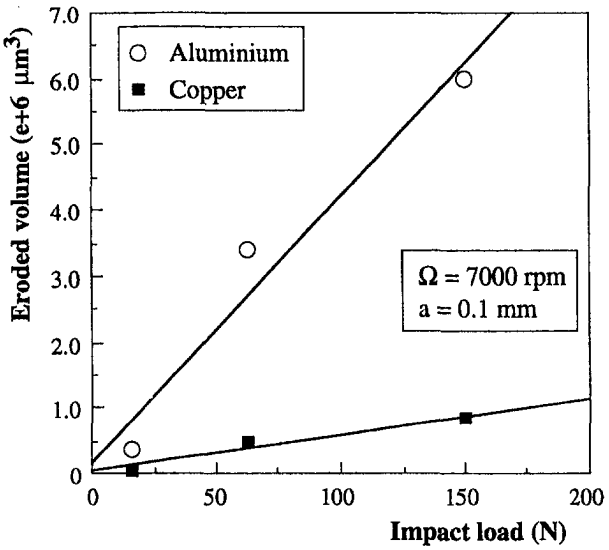

Fig. 15 Eroded volumes vs the impact load (Uncertainties: ±5 percent on the load, ±15 percent on the volume)

r_0 = 1.2 mm, ΔP = 4 bars, the force is larger than 150 N, i.e., five times larger than the force obtained in the venturi device with a water velocity equal to 30 m/s.

5 Conclusion

The Cavermod device was recently modified by the increase of its rotation rate and the shortening of its vapor core. In the present paper, the main results concerning hydrodynamics aspects and erosion figures, as obtained with long and short vortices, are compared. They relate first to the vortex length evolution, the collapse velocities (which can reach and even exceed 1000 m/s in the case of the long vortex) and the size of the two-phase region which takes place at the end of the first collapse. In particular, it appears that the reduction of the vortex length results in a least development of the free surface perturbations of the vortex core, and then in a smaller two-phase region. As to erosion results, contrarily to the long vortex which gives dispersed patterns of erosion pits, the small vortex allows us to get concentrated erosion patterns, at least on soft materials such as pure aluminium. In this case, the size of the erosion pattern, about 1.4 mm, is smaller than the diameter of the vapour core, and a unique depression can be seen, with secondary craters inside it, deeper than the main depression. Other results are relative to the number and size of pits produced by the long vortex. As a result, the comparison with other erosion devices displays the capacity of Cavermod to produce larger damage figures.

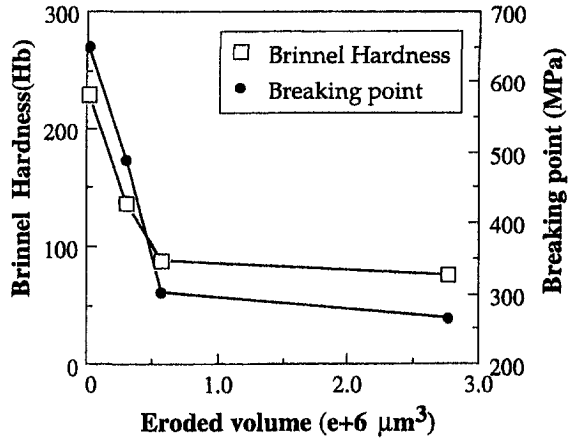

Fig. 16(*a*)

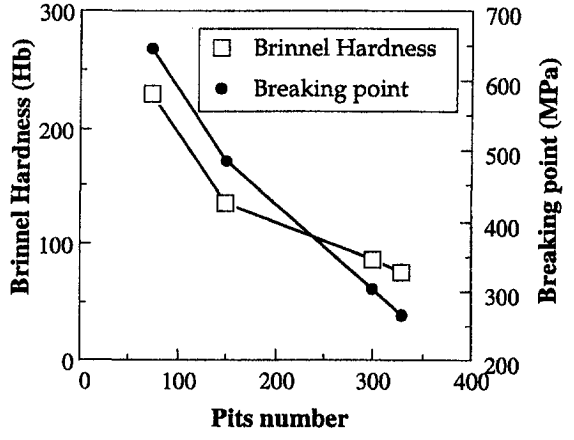

Fig. 16(*b*)

Fig. 16 Correlation of eroded volume (*a*) and pits number (*b*) with material properties (Uncertainties ±5 percent on ordinates, ±15 percent on volume)

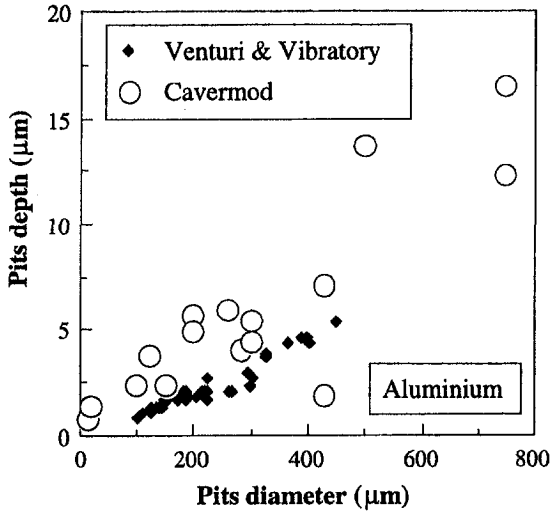

Fig. 17(*a*)

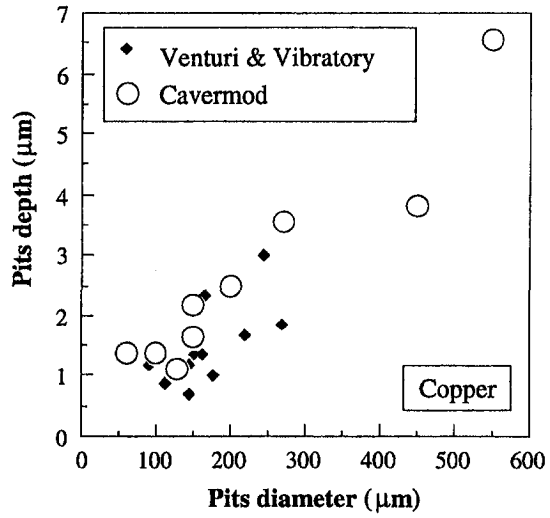

Fig. 17(*b*)

Fig. 17 Correlations pits diameter/pits depth in cavermod (case of long vortex), and other erosion devices

In the companion paper, results concerning force measurements are presented. From the results given here concerning the size of the indentations obtained with the short vortex, it appears that new developments of Cavermod can be envisaged: as that size exceeds the smaller diameter of available pressure transducers (about one millimeter), the direct measurement of the mean value of the erosive pressure, not only of the global forces, becomes possible.

Uncertainties

The geometrical parameters R, L, L', **a**, and the rotation rate Ω are known within uncertainties lower than 0.5 percent, which can be considered as negligible. The driving pressure ΔP is known at about 2 percent. For the vortex evolution given by rapid films (Figs. 2, 3, and 5) the time is known thanks to an oscillator which controls a lamp at a rate of 1000 Hz. Thus the precision on time is better than 1 percent. The major uncertainties is in the estimate of the vortex core length, as the vortex closure region may be poorly determined, particularly at the end of the collapse: the error on the length is ±3 mm. It gives a relative uncertainty on the mean collapse velocities of 5 percent calculated with the total length (Fig. 4), and a larger value (at

least 10 percent) for the instantaneous velocities. For the size of erosion pits, the depth is known within $\lambda/4$ (about .130 μm), which makes a better precision for deeper pits. If the pit is not exactly circular, the pit diameter is estimated as the mean value of the greatest and the smallest value of the diameters. The ends of the diameter are taken at the exterior of the external fringe and the uncertainty on the diameters is of the order the width of fringe, which makes a poor relative precision for small pits (about 20 percent).

Acknowledgments

The Research was partly supported by D.G.A. (Direction Générale de l'Armement), under Contract D.R.E.T. 93-145. We are indebted to Mr. A. Archer, from Electricité de France, for the analysis of erosion pits by laser profilometer (Fig. 11). Information on performances of classical erosion tests devices (Fig. 17) was given by Professor Hattori, from the Fukui University (Japan).

References

Batchelor, G. K., 1967, *An Introduction to Fluid Dynamics,* University Press, Cambridge, pp. 543–550.

Belahadji, B., Franc, J. P., and Michel, J. M., 1991, "A Statistical Analysis of Cavitation Erosion Pits," ASME JOURNAL OF FLUIDS ENGINEERING, Vol. 113, pp. 700–706.

Dominguez-Cortazar, M. A., Franc, J. P., and Michel, J. M., 1992, "Cavitating Vortex: Collapse Visualizations and induced damage," *Proceedings of the International IMechE Conference on Cavitation,* Cambridge (U.K.), pp. 43–48.

Dominguez-Cortazar, M. A., Franc, J. P., and Michel, J. M., 1997, "The Erosive Axial Collapse of a Cavitating Vortex: an Experimental Study," ASME JOURNAL OF FLUIDS ENGINEERING, Vol. 119, pp. 686–691.

Filali, E. G., 1997, "Etude Physique de l'Implosion Axiale de Tourbillons Cavitants formés dans une Chambre Tournante," PhD Thesis, Université Joseph Fourier, Grenoble, France.

Filali, E. G., Michel, J. M., Hattori, S., and Fujikawa, S., 1999, "The Cavermod Device: Force Measurements," ASME JOURNAL OF FLUIDS ENGINEERING, Vol. 121, published in this issue pp. 312–317.

Rosenthal, D. K., 1962, "The Shape and Stability of a Bubble at the Axis of a Rotating Liquid," *Journal of Fluid Mechanics,* Vol. 12, pp. 358–386.

E. G. Filali[1]
Assistant.

J. M. Michel
Research Director,

CNRS & University of Grenoble. Laboratoire des Écoulements Géophysiques et Industriels (Laboratory common to U.J.F., I.N.P.G., C.N.R.S.)
Grenoble, France

S. Hattori
Professor,
Department of Mechanical Engineering,
Fukui University,
Fukui, Japan

S. Fujikawa
Professor,
Department of Mechanical Systems Engineering,
Toyama Prefectural University,
Toyama, Japan

The Cavermod Device: Force Measurements

The Cavermod device, as described in the companion paper (Filali et al., 1999), allows us to produce the axial collapse of a cavitating vortex at high velocities. From a global point of view, we can consider that it produces a high momentum in the axial direction. Large forces, concentrated on a small area and able to produce erosion pits on hard materials, result from the sudden momentum stopping against a solid wall. In this paper, the results of the forces measurements are given. Four different measurements devices are used to analyze the Cavermod performance in both cases of long and short vortex: dislocations in MgO (Magnesium Oxide) single crystal, two special piezoelectric ceramic transducers and a PVDF film transducer. Special attention is given to the PVDF film response which is found twice the response of other devices. In addition, an attempt is made to interpret the temporal force signal given by a ceramic transducer in terms of local erosive pressure.

1 Introduction

It is well known that the analysis of erosion damage caused by cavitation is a complicated task as it addresses diverse fields of applied sciences, such as fluid and solid mechanics, metallurgy or material science etc. Outside of the fact it is difficult (if not impossible) for the researchers to gain a deep ability in such different fields of knowledge, it appears that a technical difficulty brings an additional challenge to progress in the knowledge of cavitation erosion: at the present time, it is not possible to know the exact value of the pressure arising from the erosive fluid events at the fluid/solid interface. This is mainly due to the size of the available pressure transducers which usually exceeds the very small size of the pressure peaks by one or several orders of magnitude, the ratio between those sizes remaining anyway unknown. That difficulty is a hard and frustrating point since pressure justly is the physical parameter common to the fluid and solid domains and it controls the response of the solid material. In such a situation, the best that can be done is to limit prospects to the measurements of forces under repeatable conditions and seize any favorable circumstance to proceed to the estimate of the erosive pressure.

The Cavermod device, such as described in the paper by Dominguez-Cortazar et al. (1997) and the first companion paper (Filali et al., 1999), is well suited to force measurements. From a global point of view, the axial collapse of the cavitating vortex can be considered as a high impulse in the axial direction. Large forces, concentrated on a small area and able to produce erosion pits on hard materials, result from the sudden stopping of the liquid momentum against the solid wall. Thus, the conditions of forces occurrence are fairly well controlled and repeatable, and the impact location is known in advance: those expected features make forces measurements desirable, and from the beginning some attempts were made to characterize the impact force by a commercially available transducer (Dominguez-Cortazar et al., 1997). However, such transducers don't resist a long time to the agression of collapses, and other ways have to be taken to get valuable information on forces.

The first way was to use PVDF (Polyvinylidene fluorure) films in order to make by hand force transducers directly in contact with the erosive events and to calibrate them dynamically (Nguyen et al., 1994; Soyama et al., 1999). The other methods were brought to the LEGI Labotatory by Professors Hattori and Fujikawa, on the occasion of stages as invited professors: firstly the measurement of dislocation etch-pit patterns produced on Magnesium Oxide single crystal (Hattori et al., 1988; Okada et al., 1994) and second two kinds of pressure transducers, both of them being built on the same principle (Jones and Edwards, 1960) but different in their practical achievement. Subsequently, they will be called ceramic transducers 1 and 2, respectively. The results of the four methods are given in the present paper, for the long and short vortices configurations (see the companion paper): a general result is the approximately linear dependence of the forces on the driving pressure ΔP of Cavermod. Another peculiar result deserves a special attention: it is found that the PVDF film, although calibrated by the same method (dropping ball) as ceramic transducers 1 and 2, gives a response approximately twice when it is submitted to the Cavermod shot.

In the conclusion of the companion paper, it was suggested that, as the size of the erosion pits produced by the short vortex on a pure aluminium sample is larger than one millimeter, hopefully we can anticipate that at least the mean pressure over the area of such a pit will be measured in the near future. Here, taking advantage of the ceramic transducers features, we proceed to another attempt toward the erosive pressures. It leads us to values in the range of 0.45 to 3 GPa, which seem to be relevant to the erosion phenomena.

2 The Measurement and Calibration Methods

2.1 Dislocation Patterns in MgO Single Crystal. This measurement technique, first used in the field of lubrication (Dufrane and Glaeser, 1976; Hattori et al., 1988), was then adapted to

[1] Now at Alger University, Algeria.

Contributed by the Fluids Engineering Division for publication in the JOURNAL OF FLUIDS ENGINEERING. Manuscript received by the Fluids Engineering Division March 12, 1998; revised manuscript received February 8, 1999. Associate Technical Editor: J. Katz.

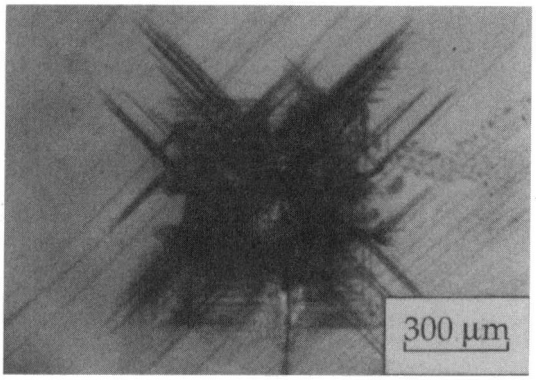

Fig. 1 Rockwell indent in hardness test

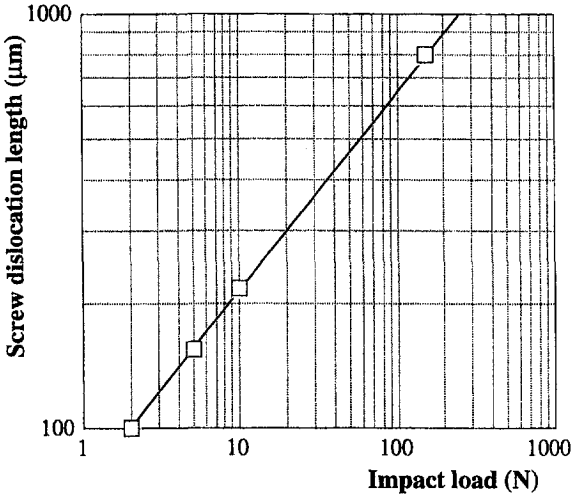

Fig. 2 Calibration of the MgO crystal

cavitation erosion by Brooks et al. (1992) and Okada et al. (1994). Under an external, large enough stress, dislocations appear at the surface {100} of the MgO crystal. Normal stresses produce screw dislocations in the four planes similar to {110} and {101} which are at 45 degrees with respect to the surface plane and intersect it along directions {001} and {010}. At the opposite, tangential stresses produce edge dislocations in the two planes such as {011} which are perpendicular to the surface and intersect it along directions at 45 degrees with the directions {011} and $\{01\bar{1}\}$. The details of the methods are given by Okada et al. (1994). Figure 1 shows the indent due to a static Rockwell hardness test aimed to the calibration of the MgO crystals. Figure 2 gives the result of the calibration, from which it results that the length of screw dislocations (the uncertainty of which is +5 percent) approximately varies as $F^{1/2}$, where F is the total force. In Fig. 1, it appears that both systems of dislocations are present, and indeed the Rockwell test produces normal and tangential stresses on the surface of the crystals. On the contrary, under the shock of Cavermod (Fig. 3, with the following condition of run: Ω = 7,000 rpm, **a** = 0.1 mm, $\Delta\mathbf{P}$ = 3.0 bar), almost all dislocations are of the screw type, and then the stresses applied to the liquid solid interface are mainly normal to it.

2.2 PVDF Film Transducer. The use of PVDF films for the measurement of cavitation impacts is described with some details in Soyama et al. (1998). By comparison to the work of those authors, the present tests were made by using films with thickness 40 μm (instead of 110 μm), the natural frequency of which is of the order 25 MHz (instead of 10 MHz), and the transducer was stuck on the metallic target between two polyamide tapes, one to ensure electrical insulation, the other to protect it against the erosive agression of the vortex collapse. Then the transducer thickness is of the order 0.2 mm. Several transducers were built, whose sensing area diameters spread from one to eight millimeters. Their dynamical calibration uses the dropping ball method, for which the time of contact, lower than 25 μs, is measured by means of a digital oscilloscope. Figure 4 shows the result of the calibration for a PVDF transducer with diameter 5 mm. The least square line does not come exactly through the origin (which does not seem too grave, as the measured forces on Cavermod are rather large) and its slope entails a high sensitivity $s = dV/dF = 0.073$ V/N. Differences between the dropping ball calibration and the working of PVDF films transducers under Cavermod shocks have to be noted: first, the maximum force measured on the Cavermod device (see Fig. 10) is larger by one order of magnitude approximately. Second, although the total shock duration, as given by piezo-ceramics transducers, is approximately the same (see Fig. 13), the individual peaks are shorter (about 5 μs). On the whole, it will appear that the results of the PVDF film measurements, if correctly interpreted, fairly agree with the results of other methods, which gives some confidence in that method.

2.3 Piezo-Ceramics Transducers. Figure 5 shows the main elements of the ceramic transducer 1. The impact force is measured by a ceramic disk, with thickness 0.25 mm and natural frequency 8 MHz, sandwiched between two metallic rods (copper or other metal). One of them has its free end mounted flush the wall and receives the impact force due to cavitation events. The force wave is transmitted to the ceramic disk and then to the second metallic rod. The length of the second rod is adjusted so that the reflected wave can be distinguished from the incident wave in the signal output given by the ceramic disk. Several diameters of rods are used to analyze the force exerted by the Cavermod.

In ordinary erosion devices, such transducers allow the measurements of forces together with the loss of mass. When using them on the Cavermod device, we can measure the force given by one shot only and observe the corresponding erosion pits. For most of the present tests, the interest was in the dependency of the forces on the control parameters, mainly the driving pressure $\Delta\mathbf{P}$. However, an attempt to estimate the local pressure by considering the erosion pits area was also made, as described hereafter (Section 4).

The ceramic transducer 2 (thickness of the ceramisc disk 0.09 mm, natural frequency around 29 MHz) is basically similar to the first one except that some details are aimed to improve its response: the first rod is mechanically isolated from the surrounding by a soft material and it is made of titanium in order to improve the transmission of the force wave to the ceramic disk. Also, the conical shape of the second rod end tends to weaken the reflected wave.

Both kinds of transducers were calibrated by the dropping ball method, the duration of the impact being in the range 10 to 20 μs. It was found that the calibration coefficient was close enough to the value given by the manufacturer, which gives some confidence

Nomenclature

a = piston displacement (mm)
$\Delta\mathbf{P}$ = driving pressure (bar)
L = chamber length (mm)
L' = vortex core length (mm)
F = impact force (N)
R = piston radius (mm)
V = axial collapse velocity (m/s)
Ω = rotation rate (rpm)
r_0 = initial vortex radius (mm)
Φ = transducer diameter (mm)

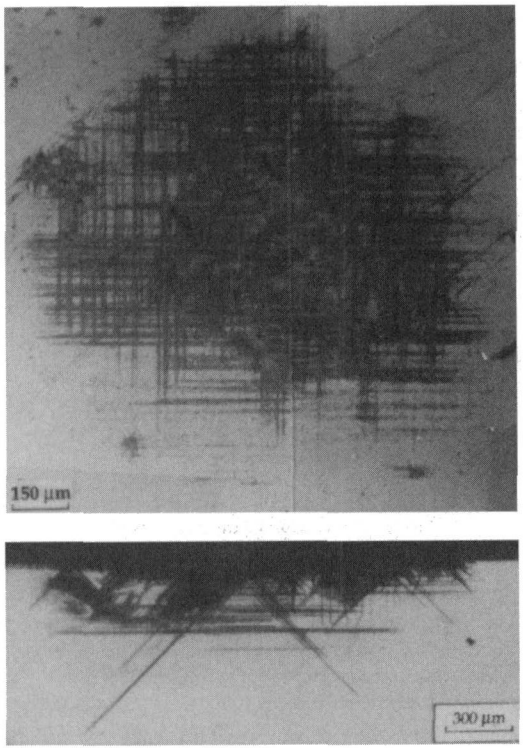

Fig. 3 Dislocation patterns on MgO crystal surface and cross section (Ω = 7,000 rpm, a = 0,1 mm, ΔP = 3 bars)

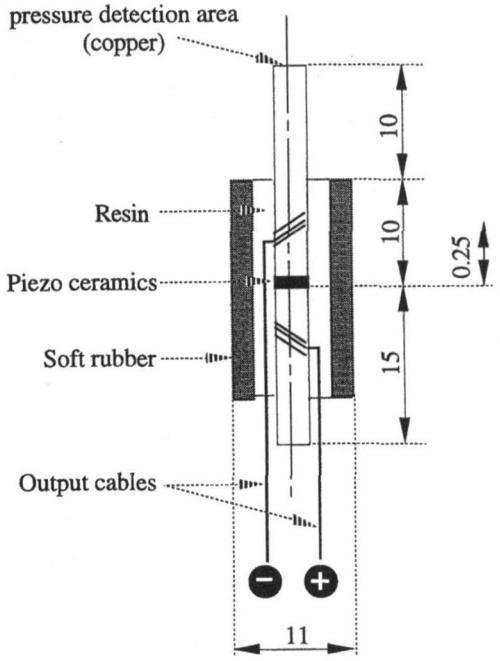

Fig. 5 Ceramic pressure transducer

in the behavior of those transducers. For the following results (Figs. 7 to 12), the force F is obtained as the average of the maximum amplitude of the signal for ten shots of the Cavermod at least. The uncertainty on F is estimated to 10 percent. Due to limitation in the speed of the rotating contact, the measurements of forces by PVDF and piezo-ceramic transducers were made at a rotation rate Ω = 4,500 rpm only. The uncertainty on $\Delta\mathbf{P}$ is 2 percent.

3 Results of Forces Measurements on the Cavermod Device

3.1 Case of the Long Vortex. Figure 6 shows the results of the *MgO* measurements of forces for different values of the driving pressure $\Delta\mathbf{P}$. The tendency is an approximately linear dependence, with a value F = 20 N for $\Delta\mathbf{P}$ = 1 bar and a maximum value F = 150 N for $\Delta\mathbf{P}$ = 4 bars.

With the ceramic transducer 1 (diameter Φ = 5 mm), see Fig. 7, we obtain the linear dependency of F versus $\Delta\mathbf{P}$ (together with uncertainty bars on F), and the maximum value F = 160 N for $\Delta\mathbf{P}$ = 4 bars. The same linear tendency is found (see Fig. 8) for other rod diameters 1 and 3 mm. Meanwhile, the comparison of the force increments between the cases 1 and 3 mm, and between the cases 3 and 5, gives an idea of the mean pressure distribution: the forces increments are lower than the sensing areas increases, which involves a higher mean pressure near the centre. In Fig. 9, the influence of the initial piston displacement **a** is shown: for a constant value of $\Delta\mathbf{P}$, the force is larger if **a** is smaller, due to the resulting increase in the collapse velocity.

With the PVDF film transducer also we obtain a roughly linear dependency of F on $\Delta\mathbf{P}$, and it was checked that the responses with transducer diameters 5 and 8 mm are practically the same. Surprisingly, however (see Fig. 10), we obtain a maximum value (for $\Delta\mathbf{P}$ = 4 bars) close to 300 N, i.e., approximately twice the value

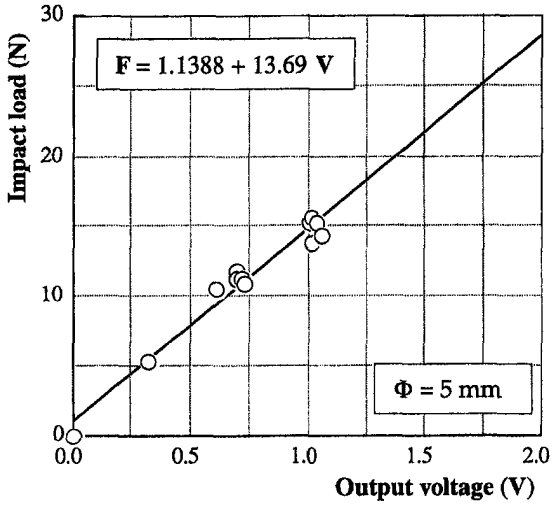

Fig. 4 *Calibration curve of a PVDF transducer*

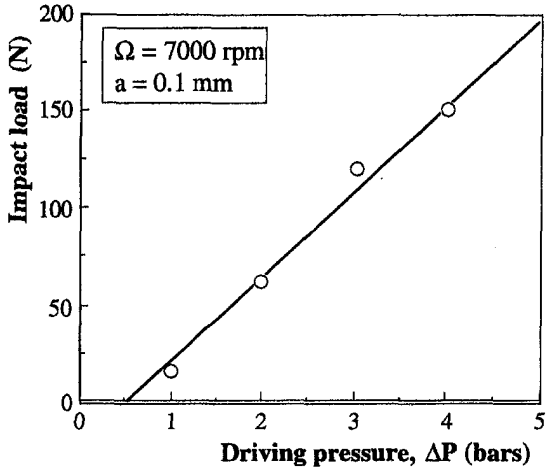

Fig. 6 Force measurements by MgO crystal (Uncertainties: ±2 percent on ΔP, ±8 percent on the load)

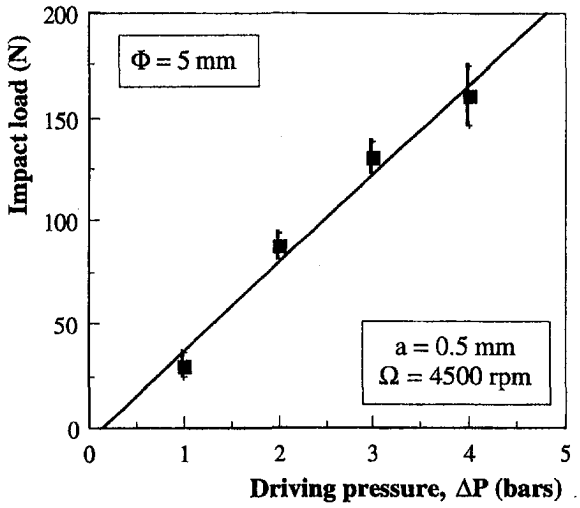

Fig. 7 Transducer 1 force versus the driving pressure (Uncertainties: ±2 percent on ΔP, ±5 percent on the load)

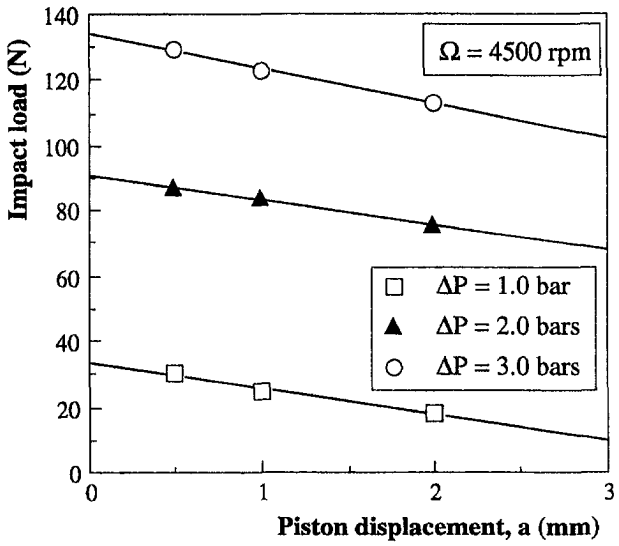

Fig. 9 Variations of the impact load force with the piston displacement (Uncertainties: ±0.1 mm on a, ±5 percent on the load)

given by the ceramic transducer 1, although the diameters of the sensing areas are the same. This singular behavior appears somewhat troublesome, all the more the calibration methods are the same for both kind of transducers. In our opinion, the explanation is to be searched on the side of the wave transmission. On the one hand, for ceramic transducers, the transmission of the force wave at the interface rod/ceramic disk is the same in both cases of calibration and work on Cavermod. On the other, for the PVDF film, the steel ball imposes a condition of solid frontier (and thus of deformation itself) to the sensing film during calibration tests, while during work in Cavermod a pressure condition is imposed and the pressure wave is reflected against the solid wall which supports the film, then doubling its value. Details of calculation—which indeed are classic—can be found in Filali (1997). The results of the force measurements by three methods are presented in Fig. 11, the values corresponding to PVDF films being first modified by the coefficient 0.5.

3.2 Case of the Short Vortex. Both ceramic transducers 1 and 2 (with a rod diameter equal to 2 mm) were used in the case of the short vortex. The results are shown in Fig. 12. Here also the variations of the force versus the driving pressure are markedly linear. Attention is to pay to the slope of the line which roughly is twice the slope obtained in the case of Fig. 11. Thus for $\Delta P = 4$ bars, the force is larger than 300 N in the case of the short vortex instead of 160 N for the long vortex. That happens although the collapse velocities are rather smaller in the case of the short vortex: as already mentioned, the hydrodynamic impact is concentrated on a smaller area in that case, and it appears that the Cavermod device is more efficient when working with the short vortex. As a matter of fact, the mean pressure resulting from the maximum force value just found is not far from 100 MPa: this result is to be compared to the erosion pattern presented in Figs. 9(*b*) and 10(*b*) of the companion paper, in which a global depression, with diameter 1.4 mm, is produced on a soft material such as pure aluminium, the elastic limit of which is approximately 70 MPa, under a driving pressure of 2 bars. In that case, it appears that the mean pressure in the central part of the impact area is sufficient to make that some plastic limit criterion is exceeded over all this area.

4 Toward Pressure Estimates

The following observations are made considering the long vortex configuration. In that case, the value of the mean pressure

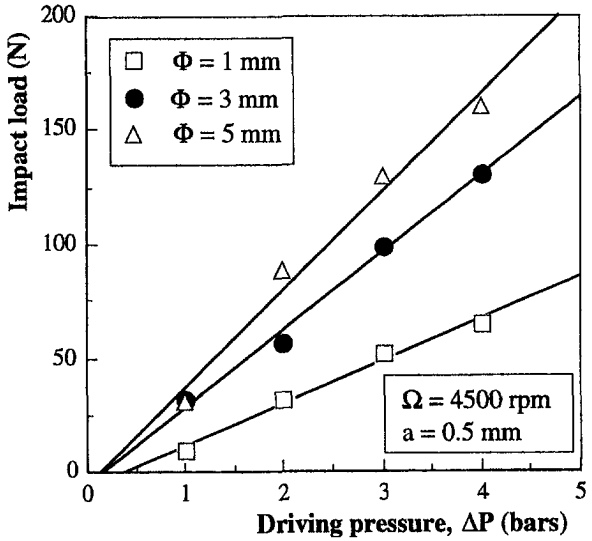

Fig. 8 Responses of transducer 1 with different diameters (Uncertainties: as in Fig. 7)

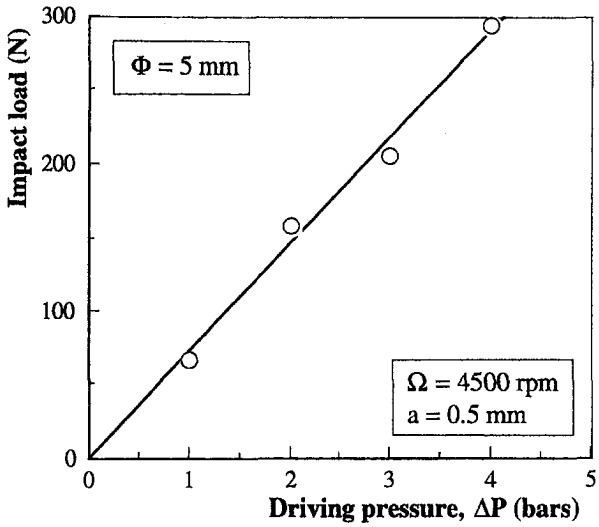

Fig. 10 PVDF transducer—Force versus the driving pressure (Uncertainties: as in Fig. 7)

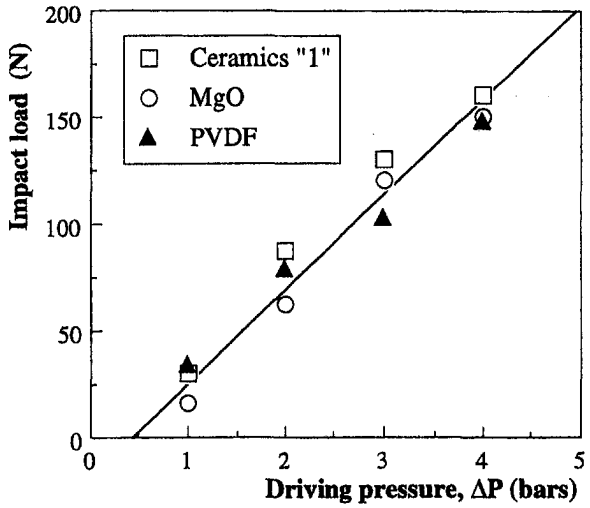

Fig. 11 Long vortex: comparison of the responses of the three transducers (Uncertainties: as in Fig. 7)

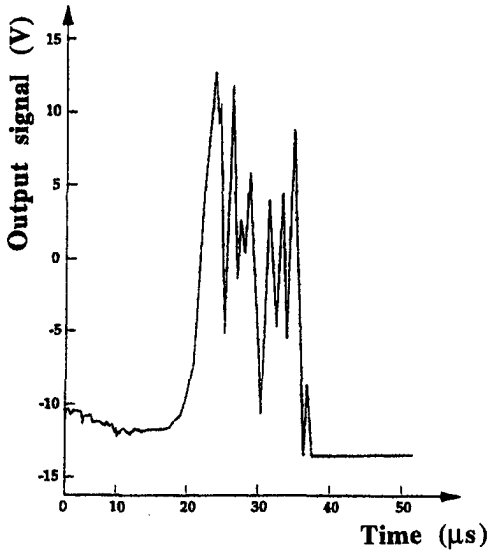

Fig. 13 Example of output signal given by ceramic transducer 1—Φ = 5 mm—Long vortex (Uncertainties on the output signal: ±10 percent)

corresponding to a force of 160 N and a rod diameter of 5 mm is approximately 8.15 MPa, which is lower by far than the yield stress of metallic targets. However, the force signal delivered by transducer 1 (see Fig. 13) exhibits a number of peaks with amplitudes V_i at time t_i. Figure 14 shows that the number of peaks tends to increase with the driving pressure (in that figure, each point corresponds to a shot of the Cavermod). The histograms of peaks amplitudes (Fig. 15) are spread more largely in the case of the larger values of the driving pressure. The time intervals $t_{i+1} - t_i$ are largely distributed between 0.3 and 3 μs, as shown on Fig. 16, so that the peaks cannot due to some wave system established in the transducer or its neighbouring, which would give a spectrum with a unique peak. More, we can note that the extreme values 0.3 to 3 μm correspond to distances 0.46 to 4.6 mm for a velocity equal to the sound speed 1450 m/s in water. Those distances are of the same order than the distances between bubbles inside the torus which is observed at the end of the vapour vortex collapse (see Fig. 8 in the companion paper). Thus it could be inferred that some influences between bubbles, due for example to wave shocks emitted at the instant of their individual collapses (Tomita et al., 1986; Giovanneschi-Testud et al., 1990) occur during the global process of collapse of the vapour core. Anyway, whatever the scenario may be, it is possible at least to assume that the peaks in Fig. 13 are due to the collapse and rebound of individual bubbles, as described in the companion paper.

On the basis of that assumption, it is natural to associate the largest signal peak to the largest pit observed on the rod end section (this is made with a copper rod) and, more generally, to associate peaks and pits previously put in a decreasing order of size (in general, the number of pits on copper is larger than the peaks number, so that the pits in excess, the smallest ones, are disregarded). The results of such correlations are given in Fig. 17, for several Cavermod shots, under a driving pressure $\Delta P = 1$ bar (the Cavermod shots are identified by different marks). The resulting local pressures are in the range 0.45 to 3 GPa, which can be considered realistic in comparison with the values of the yield stresses of solid materials.

5 Conclusion

Four methods, especially tailored for the measurement of forces due to cavitation events impacts, have been used on the Cavermod apparatus. The first one, based on the development of dislocations in a MgO macrocrystal under external forces, is deeply different from the three others, which use the piezoelectric effect on either

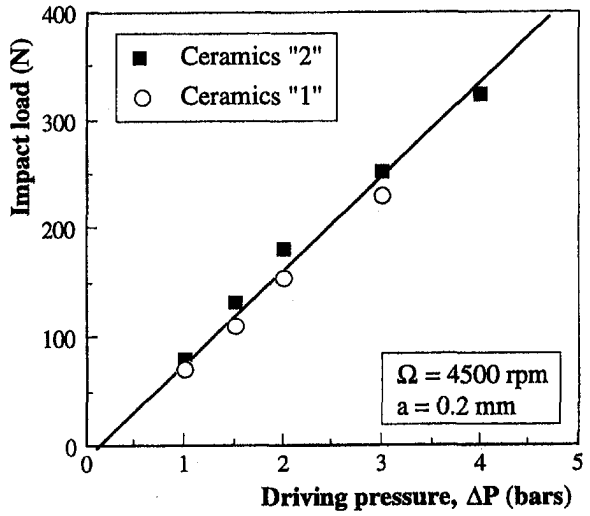

Fig. 12 Force measurements in case of short vortex (Uncertainties: as in Fig. 7)

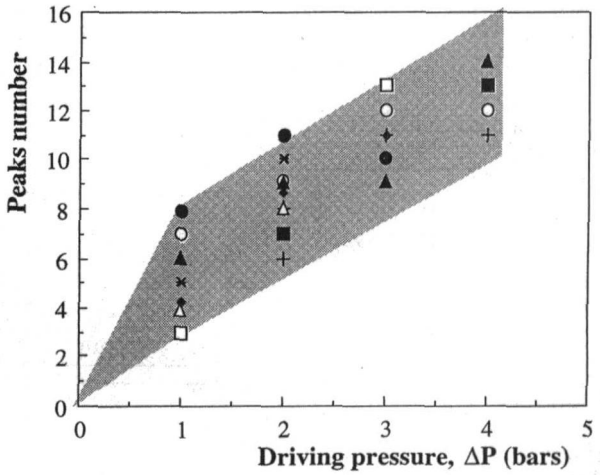

Fig. 14 Peaks number versus the driving pressure

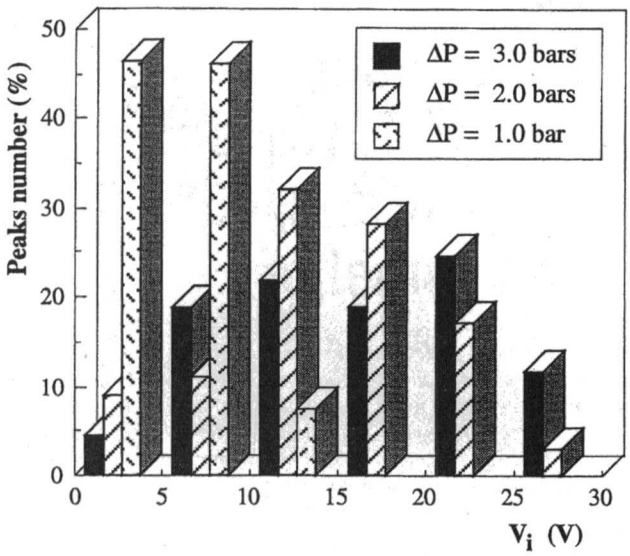

Fig. 15 Histograms of peaks amplitudes

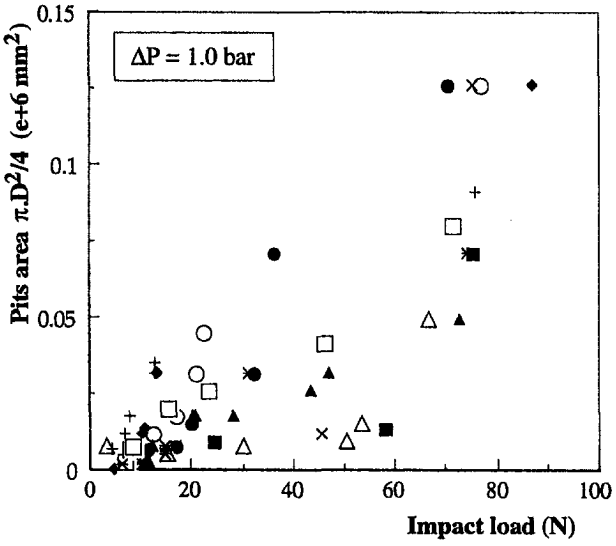

Fig. 17 Pressure estimates—long vortex (Uncertainties: ±10 percent on pits area, ±5 percent on the load)

PVDF films or ceramic disks. The results of the four methods agree fairly well, under the condition that the results of the PVDF film method are correctly interpreted. They allow us to analyze the main features of the Cavermod device. An important result is the linear dependency of the impact force on the driving pressure **ΔP**. The maximum force, obtained in the case of the short vortex, is of the order 300 N for a driving pressure equal to 4 bars. It compares well with classical erosion test devices, for which the measured force is 30 N at most. Endly, when we use ceramic disk transducers, we can associate the elementary peaks of the electric signal and the size of the erosion pits produced on the end section of the metallic rod: such a correlation gives estimates of the local pressures in the range 0.45 to 3 GPa, which seems to be the right order of magnitude of erosive pressures.

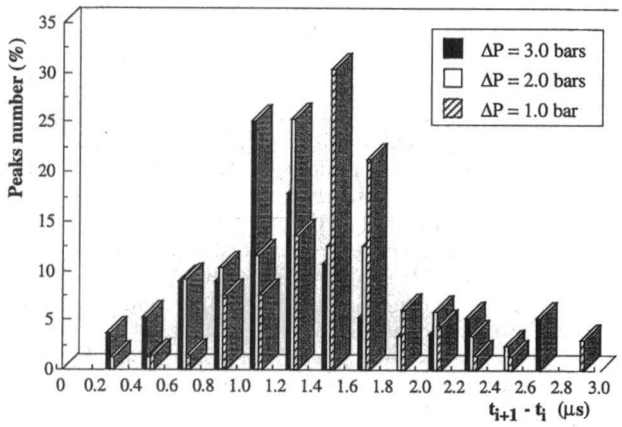

Fig. 16 Histograms of the time intervals between consecutive peaks

Acknowledgments

The financial support of both Japanese Ministry of Education (Joint Research, Prof. Kato, 07044124) and French Ministry of Education is gratefully acknowledged.

References

Brooks, C. A., Green, P., James, R. D., Wallis, R. L., and Kerry, P. R., 1992, "Observations on Localized Plasticity and Work-Hardening in Magnesium Oxide Crystals During the Initial Stages of Cavitation Damage," *Proceedings of the IME International Conference on Cavitation,* Cambridge, pp. 139–145.

Dominguez-Cortazar, M. A., Franc, J. P., and Michel, J. M., 1997, "The Erosive Axial Collapse of a Cavitating Vortex: an Experimental Study," ASME JOURNAL OF FLUIDS ENGINEERING, Vol. 119, pp. 686–691.

Dufrane, K. F., and Glaeser, W. A., 1976, "Rolling-Contact Deformation of MgO Single Crystals," *Wear,* Vol. 37, pp. 21–32.

Filali, E. G., 1997, "Étude physique de l'implosion axiale de tourbillons cavitants formés dans une chambre tournante," P.H.D. thesis, Université Joseph Fourier, Grenoble, France.

Filali, E. G., and Michel, J. M., 1999, "The Cavermod Device: Hydrodynamic Aspects and Erosion Tests," ASME JOURNAL OF FLUIDS ENGINEERING, Vol. 121, published in this issue pp. 305–311.

Giovanneschi-Testud, P., Alloncle, A. P., and Dufresne D., 1990, "Collective Effects of Cavitation: Experimental Study of Bubble-Bubble and Bubble-Shock Wave Interactions," *Journal of Applied Physics,* Vol. 67, 8, pp. 15sq.

Hattori, S., Miyoshi, K., Buckley, D. H., and Okada, T., 1988, "Plastic Deformation of Magnesium Oxide {001} Surface Produced by Cavitation," *Lubrication Engineering,* 44, p. 53.

Jones, I. R., and Edwards, D. H., 1960, "An Experimental Study of the Forces Generated by the Collapse of Transient Cavities in Water," *Journal of Fluid Mechanics,* Vol. 7, pp. 596–611.

Nguyen, T. H., 1994, "Développement et validation d'une méthode analytique de prévision de l'érosion de cavitation," P.H.D. thesis, INPG, Grenoble, France.

Okada, T., Hattori, S., and Shimizu, M., 1994, "A Fundamental Study of Cavitation Erosion using a Magnesium Oxide Single Crystal: Dislocations and Surface Roughness," *Proceedings of the 2nd International Symposium on Cavitation,* Tokyo, pp. 185–190.

Soyama, et al., 1999, paper accepted for publication in the ASME JOURNAL OF FLUIDS ENGINEERING.

Tomita, Y., and Shima, A., 1986, "Mechanism of Impulsive Pressure Generation and Damage Pit Formation by Bubble Collapse," *Journal of Fluid Mechanics,* Vol. 169, pp. 535–564.

Steady and Unsteady Computations of Turbulent Flows Induced by a 4/45° Pitched-Blade Impeller

K. Wechsler
Researcher.

M. Breuer
Researcher.

F. Durst
Professor.
e-mail: durst@lstm@uni-erlangen.de

Institute of Fluid Mechanics,
University of Erlangen-Nürnberg,
Cauerstr. 4, D-91058 Erlangen, Germany

The present paper summarizes steady and unsteady computations of turbulent flow induced by a pitched-blade turbine (four blades, 45° inclined) in a baffled stirred tank. Mean flow and turbulence characteristics were determined by solving the Reynolds averaged Navier-Stokes equations together with a standard k-ϵ turbulence model. The round vessel had a diameter of T = 152 mm. The turbine of diameter T/3 was located at a clearance of T/3. The Reynolds number (Re) of the experimental investigation was 7280, and computations were performed at Re = 7280 and Re = 29,000. Techniques of high-performance computing were applied to permit grid sensitivity studies in order to isolate errors resulting from deficiencies of the turbulence model and those resulting from insufficient grid resolution. Both steady and unsteady computations were performed and compared with respect to quality and computational effort. Unsteady computations considered the time-dependent geometry which is caused by the rotation of the impeller within the baffled stirred tank reactor. Steady-state computations also considered neglect the relative motion of impeller and baffles. By solving the governing equations of motion in a rotating frame of reference for the region attached to the impeller, the steady-state approach is able to capture trailing vortices. It is shown that this steady-state computational approach yields numerical results which are in excellent agreement with fully unsteady computations at a fraction of the time and expense for the stirred vessel configuration under consideration.

1 Introduction and Brief Literature Survey

The importance of impeller stirred reactors for production processes in the chemical industry is undisputed. According to Tatterson et al. (1991), half of the $750 billion per year output of the US chemical process industry is circulated through stirred tank reactors (STRs). Additionally, Tatterson et al. (1991) estimate that $1–20 billion per year is lost due to inadequate design of mixing processes, and they urgently recommend further research studies to increase the understanding of mixing processes in order to permit reliable process optimization. For this reason, numerous experimental investigations have been carried out in order to study both single- and multi-phase flow fields inside the vessel, applying techniques such as laser sheet illumination (LSI) for qualitative visualization of flow patterns or laser Doppler anemometry (LDA) for measuring individual velocity components. However, these studies are restricted to smaller scale processes, since the analysis of real full-size equipment is often impossible. The scale-up rules which are applied to transfer the knowledge obtained on the laboratory scale are often not straightforward. This uncertainty in the scale-up criteria leads to non-optimal design of full-size equipment causing the large losses mentioned above.

Computational fluid dynamics (CFD) provides an alternative opportunity for the analysis of industrial fluid flow processes. Within this framework, digital computers are used to determine the flow field inside STRs by solving the underlying transport equations of flow variables such as mass, momentum or temperature. In contrast to most experimental investigations, the size of the setup within the CFD simulation is not restricted to the laboratory scale, thus providing the possibility of performing the respective analysis on the scale of the full-size equipment. However, using CFD as a pure design tool requires accurate knowledge of the performance and validity of the solution method employed. Errors in CFD predictions can be mainly caused by insufficient grid resolution or deficiencies of the applied models. Thus, detailed studies on the possibility of CFD to reflect and reproduce physical effects and flow characteristics are necessary. These studies have to be combined with experiments and usually require very high computational effort as they include sensitivity studies also on extremely fine grids in order to isolate discretization and model errors. As soon as the performance of the applied models and the required grid resolution are known, CFD can be used as a design tool in engineering practice. Additionally, efficient computational methods are required in order to achieve short computation times and high throughput to allow parametric studies.

The application of CFD to STRs dates back to the late 1970s. Obviously, a particular challenge in simulating the flow in baffled stirred tank reactors (BSTRs) is presented by the variation of the shape of the flow domain with time. This inherently time-dependent underlying flow domain requires special attention and divides the approaches applied to CFD of BSTRs. Since both fully time-dependent and three-dimensional flow simulations are very demanding with respect to computer resources such as memory and computing power, early investigations were restricted to steady and two-dimensional flow simulation. The possibility of steady-state treatment was achieved by considering the azimuthally averaged impact of the impeller in terms of appropriate momentum source and sink terms in a 2-D cylindrical coordinate system (Harvey and Greaves 1982, Pericleous and Patel 1987). The tangentially averaged impact of the impeller on the swept volume was also obtained by specifying measured profiles of mean and fluctuating velocity components at parts of the boundary of this volume (Ranade and Joshi, 1990, Bakker and Van Den Akker, 1994 and others). However, the usefulness of this approach is

Contributed by the Fluids Engineering Division for publication in the JOURNAL OF FLUIDS ENGINEERING. Manuscript received by the Fluids Engineering Division July 13, 1998; revised manuscript received January 25, 1999. Associate Technical Editor: P. Bradshaw.

restricted since no such detailed experimental data are available for industrial mixing applications.

The steady-state concept was also applied to three-dimensional flow simulations by Middleton et al. (1986), perhaps for the first time in the open literature. It should be mentioned that an alternative way to describe the tangentially averaged impact of the blade passage can be realized by prescribing swirling radial jet models, as it was done by Ju et al. (1990) and Kresta and Wood (1991). However, azimuthally averaging in any of the ways mentioned above hinders the simulation of transient structures such as the eddies shed by the impeller blades because they are smeared out in the averaging processes. Since these trailing vortices have been demonstrated to play an important role in different processes and for different types of impellers, there is a strong need for simulating these structures. Fully time-dependent computations of the flow in the time-varying flow domain of a BSTR (Luo et al., 1993, Perng and Murthy, 1993) are capable of simulating these structures, as they consider the complete geometry including impeller shape, baffle shape and relative movement. But, applying time-dependent moving and/or deforming grids (sliding or clicking) requires excessive computational resources, especially computing time, since the start-up flow behaviour has to be overcome, which is really not substantial for the operation of the BSTR. Combining both full description of geometry and a steady-state analysis for computational savings can only be achieved by neglect of the relative movement of impeller and baffles. Such an approach is very promising as a design tool since it is not constrained by experimental input but allows computational savings due to the steady-state approach. However, within the stationary geometry, the flow has to be induced with some computational method: Ranade and Dommeti (1996) induced the flow by applying source and sink terms for the flow variables on the impeller surface. The flow can also be induced by solving the transport equations in a rotating frame of reference in a region attached to the impeller. Other regions of the tank including the baffles are simulated in a frame of reference at rest. A fictitious cylindrical boundary with a radius intermediate between that of the impeller blade tips and the baffle edges defines the interface between these regions. While azimuthally averaging the flow solution over this surface is called the inner-outer method, Harvey et al. (1995) called it an approximate steady-state method without averaging during the computation.

Pitched-blade turbines (PBTs) are commonly used in industrial mixing applications, partly because they are more efficient than the Rushton turbine, e.g., for processes requiring solid suspension. The trailing vortices have also been identified as very important for ligament and sheet production in liquid-liquid systems, as shown by Ali et al. (1981). However, computational investigations on the performance of pitched-blade turbines are very limited, in spite of their importance: Ranade et al. (1989) performed three-dimensional steady-state simulations and applied the standard k-ϵ turbulence model with boundary conditions developed from experimental data. In 1991, Ranade et al. extended this study to mixing of an inert tracer. Although the work of Sahu and Joshi (1995) is limited to two-dimensional steady-state simulations with the standard k-ϵ turbulence model, it should be mentioned because they are perhaps the only workers to report on the impact of computational issues such as convergence rates depending on the pressure-correction approach or initial values for the iterative methods. Since such studies are very time consuming, Sahu and Joshi (1995) limited their investigations to two-dimensional flow simulations. An approximate steady-state method applied to the laminar three-dimensional simulation of PBT flow has been presented by Harvey et al. (1995). They performed detailed grid sensitivity studies in order to demonstrate the impact of grid resolution on the predictions. Additionally, their work is remarkable since they consider the finite thickness of the PBT's blades. Harvey and Rogers (1996) compared these results with those of unsteady computations and Harvey et al. (1997) applied this approach to multiple impeller flows. However, all these studies were performed in a laminar operation mode.

PBT in turbulent operation was simulated by Xu and McGrath (1996) by a momentum source model. They pointed out that no experimental input is necessary and therefore the approach is suitable for industrial applications. However, the time-dependent characteristics are smeared out since the flow inside the impeller is averaged tangentially, thus hindering the simulation of flow around the blades and especially the trailing vortices. Bakker et al. (1996) compared three different turbulence models for the turbulent operation of a PBT. They reported very little difference between the prediction of the turbulence models. They were disappointed about the errors in the prediction of the power number. As they did not carry out both grid sensitivity studies and investigations of the trailing vortices and therefore the energy dissipated inside the vortices, the benefit from these data is unclear. Simulations of flow characteristics within the impeller swept volume of a PBT were presented for the first time by Ranade and Dommeti (1996). Within their steady-state snapshot approach, the impeller blades were fixed at one particular position and appropriate source and sink terms for cells adjacent to impeller were prescribed. They reformulated the time derivatives in terms of spatial gradients and were able to describe transient structures of the flow inside the impeller swept volume at significantly lower computational costs than fully time-dependent simulations. Sliding mesh simulations were reported by Bakker et al. (1997). They confirmed the high computational costs of sliding mesh predictions due to revolution numbers of up to 35 necessary to yield fully developed periodic solutions. They admitted that finer grids will be necessary to resolve effects of possible turbulent tip vortices.

The present paper compares two different modeling approaches for three-dimensional flows induced by PBTs operating in the turbulent mode. Section 2 describes the governing equations, the boundary conditions and the method of solution for the discretized equations. In Section 3, the different modeling approaches both based on a complete representation of the impeller and its impact on the flow are explained. A detailed description of the computational setup is given in Section 4. Finally, the computed results are discussed and compared with available experimental data. This includes a discussion on the computational performance of the code in addition to a critical evaluation of the two different modeling approaches concerning the quality of the results and the computational efforts required.

2 Computational Basics

2.1 Governing Equations. For the unsteady, incompressible and isothermal fluid flow under consideration, the Reynolds averaged Navier-Stokes equations combined with the well known standard k-ϵ turbulence model (Jones and Launder, 1972 and Launder and Spalding, 1974), including the constants reported by Launder and Sharma (1974), are solved. The mathematical model is based on the conservation equations for mass, momentum, turbulent kinetic energy k and dissipation rate of turbulent kinetic energy ϵ. For rotor-stator configurations such as the stirred vessel under consideration, a transformation of the governing equations to a rotating frame of reference is necessary for the present approach. This transformation leaves the conservation equations of mass, turbulent kinetic energy and dissipation rate unchanged, while additional source terms representing Coriolis and centrifugal forces must be added to the conservation equations of momentum.

The conservation equations for all transport variables in a Cartesian coordinate system can be written by

$$\frac{\partial(\rho\Phi)}{\partial t} + \frac{\partial}{\partial x_i}\left(\rho u_i \Phi - \Gamma_\Phi \frac{\partial \Phi}{\partial x_i}\right) = S_\Phi, \tag{1}$$

where Φ denotes the transport variable, x_i the i-th Cartesian coordinate, u_i the i-th Cartesian velocity component in the rotating reference frame, ρ the density of the fluid, Γ_Φ the diffusivity of Φ,

Table 1 Transport variable Φ, diffusivity Γ_Φ and source term S_Φ for all transport equations applied in the model. Additional relations and constants not mentioned in the text: $\mu_t = c_\mu \rho(k^2/\epsilon)$, $c_\mu = 0.09$, $\sigma_k = 1.0$, $\sigma_\epsilon = 1.3$, $c_{\epsilon 1} = 1.44$, $c_{\epsilon 2} = 1.92$.

Conservation variable	Φ	Γ_Φ	S_Φ
Mass	1	0	0
Momentum (j-th component)	u_j	$\mu + \mu_t$	$-\frac{\partial p}{\partial x_j} + \frac{\partial}{\partial x_j}\left((\mu+\mu_t)\frac{\partial u_j}{\partial x_i}\right)$ $+2\varepsilon_{mnj}u_m\omega_n - \varepsilon_{mnj}\omega_m(\varepsilon_{pqn}\omega_p x_q)$
Turbulent kinetic energy	k	$\mu + \frac{\mu_t}{\sigma_k}$	$\mu_t\left(\frac{\partial u_i}{\partial x_k} + \frac{\partial u_k}{\partial x_i}\right)\frac{\partial u_i}{\partial x_k} - \rho\epsilon$
Dissipation rate of k	ϵ	$\mu + \frac{\mu_t}{\sigma_\epsilon}$	$\frac{\epsilon}{k}c_{\epsilon 1}\mu_t\left(\frac{\partial u_i}{\partial x_k} + \frac{\partial u_k}{\partial x_i}\right)\frac{\partial u_i}{\partial x_k} - c_{\epsilon 2}\rho\frac{\epsilon^2}{k}$

and S_Φ the source term of Φ. Table 1 gives the values of Φ, Γ_Φ and S_Φ for all transport equations applied in the model. For simplicity, all equations are given here in Cartesian coordinates. However, the computations were performed on curvilinear boundary-fitted grids. The corresponding conservation equations can be derived by a coordinate transformation. Equation (1) is applicable to both a stationary and a rotating frame of reference. The velocity vector in a stationary reference frame **U** and the velocity vector in a rotating reference frame **u** are related by

$$\mathbf{U} = \mathbf{u} + \boldsymbol{\omega} \times \mathbf{x}$$

resp.

$$U_i = u_i + \varepsilon_{ijk}\omega_j x_k \tag{2}$$

where $\boldsymbol{\omega} = (\omega_1, \omega_2, \omega_3)$ represents the angular velocity vector and $\mathbf{x} = (x_1, x_2, x_3)$ the position relative to the rotation axis. ε_{ijk} is equal unity if (ijk) is a cyclic permutation of (123), ε_{ijk} is equal minus unity if (ijk) is an anti-cyclic permutation of (123), and zero otherwise.

2.2 Discretization, Boundary Conditions and Method of Solution. The numerical solution method is based on a fully conservative finite volume discretization on non-orthogonal boundary-fitted grids with a non-staggered arrangement of the variables. In order to ensure the correct coupling of pressure and velocity fields, the well known momentum interpolation technique of Rhie and Chow (1983) is applied. Second-order discretization is used for all terms (central differences, linear interpolation) together with flux blending and a deferred correction approach for the convective fluxes.

Based on the continuity equation, a pressure-correction equation is derived according to the SIMPLE algorithm of Patankar and Spalding (1972). The linearized equations for the velocity components, the pressure-correction and other scalar variables are assembled and solved sequentially, where the ILU approach of Stone (1968) is employed as a linear system solver. Outer iterations are performed to take into account the non-linearities, the coupling of the variables, and the effects of grid non-orthogonality, which are treated explicitly in all equations. In the case of unsteady computations, the discretization of the time derivatives is done by a three-time-level, second-order fully implicit scheme reported by Arnal et al. (1992).

Block-structured grids, where the blocks are globally unstructured but the grids are locally structured, are used as they can be viewed as a compromise between the high geometric flexibility of fully unstructured grids and the high numerical efficiency achieved on globally structured grids. The coupling of the blocks along the block interfaces, i.e., the transfer of information among neighboring blocks, is realized by adding auxiliary control volumes along the block interfaces containing the corresponding boundary values of the neighboring block. To ensure the coupling of the subdomains, the boundary data in the auxiliary control volumes of neighboring blocks is updated after each inner iteration of the iterative linear system solver.

Only solid walls, partially moving, delimit the flow domain in the configuration under consideration. Thus, solid walls are modeled by wall functions according to Launder and Sharma (1974) for all quantities used within the standard k-ϵ turbulence model.

2.3 High-Performance Computing. For parallelization, a grid partitioning technique directly related to the block-structuring is employed. The principle idea is to transform the block-structure which results from the requirements to model the geometry (geometric block-structure) by some suitable mapping process to a new block-structure (parallel block-structure), and the resulting blocks are assigned to the available processors. The blocks of the parallel block-structure, in addition to the geometric ones, also have to meet the requirements for efficient implementation on a parallel computer. Although there are several requirements, the most important one is to obtain similar numbers of control volumes per processor in order to ensure good load balancing on the parallel machine. A measure for this is the load balancing efficiency E^{lb}, which is the ratio of the total number of control volumes to the number of processors times the largest number of control volumes of one processor. If the control volumes are equally distributed to the processors, the load balancing efficiency is 100%. Details of the parallelization technique were given by Durst et al. (1996) and Durst and Schäfer (1996). The vectorized version of the applied linear system solver was presented by Leister and Perić (1993).

3 Modeling Approaches for the Impeller Motion

During operation, a baffled stirred tank reactor obviously changes its shape because of the relative motion of the impeller and baffles. This time-dependent solution domain inherently requires a fully time-dependent computation of the flow in the tank. However, starting from a fluid initially at rest, it is very time consuming to overcome the start-up flow patterns, because 10–30 complete revolutions of the impeller have to be simulated. In the following two different modeling approaches for the impeller motion and their advantages and disadvantages will be addressed.

3.1 Fully Time-Dependent Computations. The most realistic approach is based on a fully time-dependent computation which was performed by the method of clicking grids in the present study. This approach takes the relative motion of the rotor (impeller) and the stator (baffle) into account, see Fig. 1(*a*). For that reason the computational domain is subdivided into two main regions (block R and block S). Based on the block-structured grid a cylindrical region is defined which contains the whole impeller and which is solved in a rotating reference frame. The rest of the tank, including the baffles, however, is solved in a fixed reference frame, see Fig. 1(*b*). In order to handle the interface between rotating and stationary parts of the grid within the block-structured code, the update of the velocities in the auxiliary control volumes has to take into account the transformation into the other reference system (equation (2)). This issue is demonstrated in Fig. 1(*b*). An equidistant distribution of the grid points in circumferential direction ensures that, at every discrete time level, the grid lines of the two regions of the grid are connected to each other, see Fig. 1(*c*). This makes additional interpolations at the interface unnecessary which is an advantage of the clicking grids method in comparison to the sliding mesh approach. However, the time step of the clicking grids method is directly coupled with the circumferential resolution at the interface. In the present computations the minimal time step at each grid level was chosen which corresponds to a clicking procedure with only one CV at each time step. In contrast to this basic idea of the clicking grids method, the rotating part of the grid stays internally at the same position within the current implementation, which is shown in Fig. 1(*d*). This has the advantage that no rotation of coordinates and velocities of the old time step solution has to be performed. However, during the iterations within each time step, a modification of the update of auxiliary control volumes is necessary which compensates for the rotation of the blocks attached to the rotor. Rotation of coordinates and

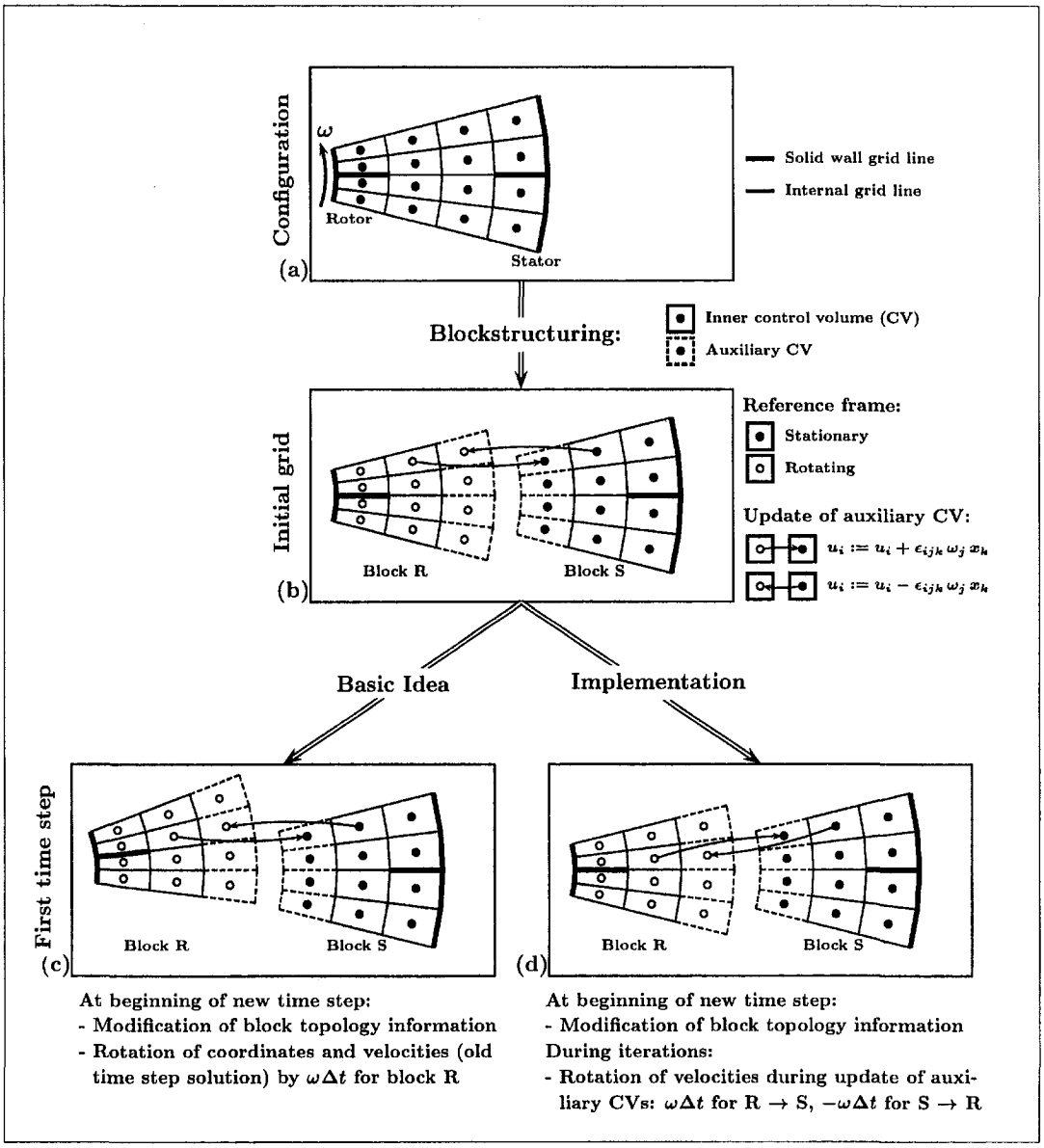

Fig. 1 Illustration of the method of clicking grids: Rotor-stator configuration (*a*), block-structure of rotating and stationary parts of the grid (*b*), basic idea of the time-dependent topology (*c*), and current implementation (*d*)

velocities within the rotating blocks is only done for visualization purposes.

In the present study, the unsteady computations were started with predictions of the steady-state modeling approach described in the next section because this technique already provides excellent initial values for the unsteady simulations.

3.2 Steady-State Computations. The main drawback of the fully time-dependent computation is the CPU-time consumption. An alternative for the solution of the baffled tank problem is given by the steady-state modeling approach, which is also the subject of the present investigation. It is based on the assumption that the relative motion between the impeller and the baffles can be neglected. This reduces the inherently time-dependent geometry to a stationary configuration which consists of a single position of the impeller relative to the side baffles.

Harvey et al. (1995) called this technique an approximate steady-state method and applied it for computing the laminar flow field in a baffled, pitched-blade impeller-stirred tank reactor. Ranade and Dommeti (1996) called the method a computational snapshot approach in their work on turbulent operation of a standard pitched-blade turbine. However, the way in which the flow is induced in the two studies differs. Whereas Ranade and Dommeti (1996) added source and sink terms at the blades and transformed the time derivatives in terms of spatial gradients, Harvey et al. (1995) solved the transport equations in a rotating frame of reference in a region attached to the impeller.

The present steady-state modeling approach is very similar to that proposed by Harvey et al. (1995). Like it is done for the clicking grids method, a cylindrical region is defined based on the block-structured grid which contains the whole impeller and which is solved in a rotating frame of reference (block R). The rest of the tank, including the baffles, however, is solved in a fixed reference frame (block S). Again, equation (2) is taken into account in order to handle the interface between blocks solved in the rotating reference frame and the stationary reference frame.

In conclusion, the main difference between the two modeling approaches is the fact, that the topology of the neighboring CVs at the interface between the blocks R and S is fixed in the steady-state modeling approach, whereas in the unsteady computations the corresponding CVs for the data update at the interface are chang-

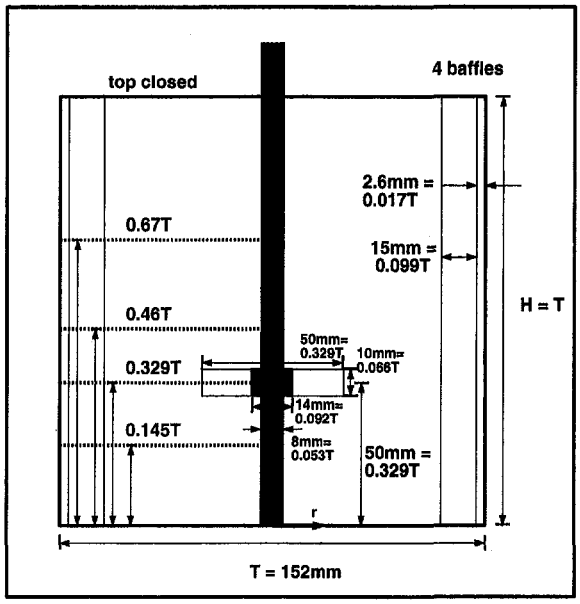

Fig. 2 Stirred vessel configuration: cross-sectional view. Dotted lines indicate locations of radial profiles for comparison of experimental with computational large-scale flow field results.

ing form time step to time step in order to take the relative motion of the impeller and the baffles into account.

The objective of the present study is to investigate the influence of the different approaches on the solution of the pitched-blade impeller flow.

4 Computational Setup

Computations were performed for the stirred vessel configuration experimentally investigated by Schäfer et al. (1998) in order to allow accurate comparison of the results. The experiments were carried out in a cylindrical vessel of diameter $T = 152$ mm and the liquid height was $H = T$. Sketches of the vessel configuration are shown in Fig. 2 (cross-sectional view) and Fig. 3 (plane view). The tank angle θ denotes the circumferential location for the visualization of the large-scale flow field, whereas the blade angle ϕ defines the position of the plane relative to the leading blade used for visualization of the impeller flow field. Four equally spaced vertical baffles of width $B = T/10$ were fitted along the periphery of the vessel with a gap of $0.017T$ between the vessel wall and the rear of each baffle. The top of the vessel was closed by a lid in order to prevent air bubbles from entraining into the liquid at the free surface. The impeller had four blades and a diameter $D = 0.329T$ with a blade height of $0.2D$ and a blade pitch of 45°. The clearance between the bottom of the mixing vessel and the middle of the impeller blades was $C = T/3$. The working fluid was silicon oil of density $\varrho = 1039$ kg/m^3 and dynamic viscosity $\mu = 0.0159$ Pa s. The impeller rotated at $N = 44.56$ rps, resulting in a Reynolds number of $\mathrm{Re} = \varrho N D^2/\mu = 7280$ and a tip velocity $U_{tip} = \pi N D = 7$ m/s.

All dimensions reported above were used to set up the computational grids. In contrast to the experiments, however, no finite thickness of the impeller blades and the baffles was considered. Furthermore, only one quarter of the solution domain was discretized because of the periodicity of both the impeller and the vessel geometry. This fourfold periodicity of the flow field was also assumed by Schäfer et al. (1998) for the evaluation of the corresponding experiments. Of course, the reduction of the vessel geometry to one quarter significantly reduces the requirements on computational power and computer resources such as main memory.

Three grid levels were generated in order to permit investigations on the grid sensitivity of the predicted computational solution and will be referred to below as fine, medium and coarse grid. The medium grid is a subset of the fine grid which is generated by removing every second grid point in each direction, leading to a grid size of one eighth of the fine grid. The same procedure is applied to generate the coarse grid from the medium grid. The underlying geometry is described by eight blocks within the frame of block-structured grids described above. The part of the tank which is computed in a rotating frame of reference is of cylindrical shape: it is confined to a radial distance of $r = 0.329T$ and is located between the axial positions $z = 0.067T$ and $0.39T$. Although this region covers only 21% of the vessel volume, 51% of the grid points were located in this region in order to resolve the trailing vortices which emerge from the operation of the pitched-blade impeller. In the case of the fine grid, each surface of the blade is covered by 32×32 control volumes. One quarter is discretized by 80 control volumes in the azimuthal direction, and the total number of control volumes for the fine grid is 1,003,520. Accordingly, the numbers for the medium and coarse grid are 125,440 and 15,680, respectively.

It is well known that the wall function formulation is valid only in the limited range of $30 < y_2^+ < 300$, where y_2^+ is the dimensionless, sublayer-scaled wall distance of the first interior grid point. For $y_2^+ < 30$, the surface shear stress predicted by the wall function becomes too high with a completely unsatisfactory situation for $y_2^+ < 11$. Furthermore, the relations for k and ϵ near solid boundaries are not valid if the wall distance of the first interior grid point is too small. This criterion was severely violated for the computation with $\mathrm{Re} = 7280$ for the fine grid. Thus, the grid sensitivity studies, which compare the numerical results with experimental results, were performed at a higher Reynolds number of $\mathrm{Re} = 29{,}000$ in order not to violate the range of validity of the wall functions at solid surfaces. It was demonstrated by Schäfer et al. (1998) that the flow field already scales with U_{tip} for $\mathrm{Re} > 5500$, which enables a comparison of experimental data at $\mathrm{Re} = 7280$ and numerical results at $\mathrm{Re} = 29{,}000$, as long as the results are normalized with U_{tip} in case of the velocity data and U_{tip}^2 for the turbulent kinetic energy.

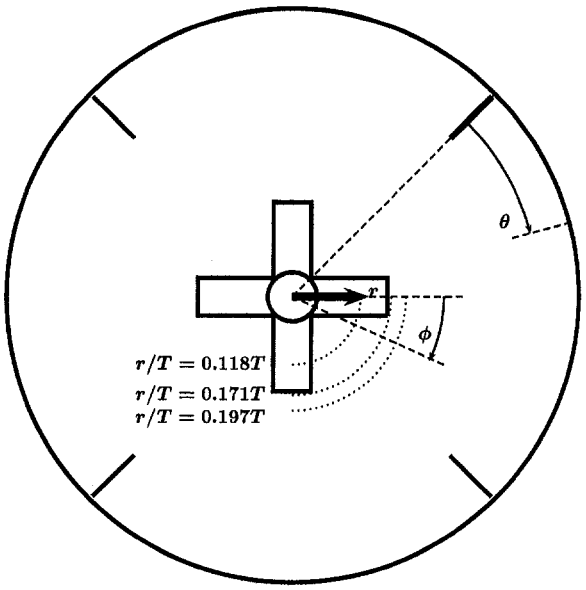

Fig. 3 Stirred vessel configuration: plan view. Dotted lines indicate locations of circumferential profiles for comparison of experimental with computational impeller flow field results. θ indicates large-scale tangential coordinate and ϕ describes blade angle for impeller flow field data.

Table 2 **Computational performance in MFlops for different computers, different grid sizes N_{CV} and varying number of processors N_P. The numbers in parentheses indicate load balancing efficiency E^{lb} for parallel computations.**

		Fujitsu VPP 700			Sun Ultra 1
N_{CV}	N_P=	1	4 (89%)	8(90%)	N_P= 1
15,680		361			28
125,440		530			24
1,003,520		605	1,945	3,605	

5 Results and Discussion

5.1 Computational Performance. All computations were carried out on a Fujitsu VPP 700 parallel vector processor system which is equipped with 2 GByte of main memory per node and which can theoretically operate on each node at a peak performance of 2.2 GFlops. The Fujitsu VPP 700 is a distributed memory system, where a crossbar permits access to data which are located in the main memory of other processors. However, this peak performance usually cannot be reached by a complex application program of several thousands of lines because ideal conditions have to be present in order to run the computer code at peak performance of the vector processor. This includes extremely long vector lengths and a simultaneous use of the add and multiply units of the vector processor usually possible only for simple benchmark applications such as the vector triad. Table 2 gives the computational performance in MFlops which was achieved with the present code FASTEST-3D for the various grids mentioned in the preceding section and various numbers of processors. The numbers in parentheses indicate the load balancing efficiency E^{lb} for the parallel computations which describes the deviation from ideal speedup due to the idle time of the processors caused by uneven load, i.e. different number of CVs per processor. For complex applications such as the stirred vessel configuration, great efforts are required to achieve an appropriate load balancing. Therefore, the given values for E^{lb} are usual for practically relevant flow simulations. The computational performance for a Sun Ultra 1 workstation operating at 170 MHz was also added in order to give the possibility of comparing the applied computing power with that of common desktop workstations. Table 2 demonstrates that parallel vector computers afford more than 100 times the computing power of common workstations even for a small number of processors and thus permit the three-dimensional computations of flow in stirred vessels. In order to get an impression of the computational resources necessary for such simulations it should be mentioned that the steady computation on the finest grid (about one million CVs) took about 2.5 hours on four processors of a VPP 700 and requires a core memory of 828 MBytes. As will be shown below the unsteady simulations even demand CPU-time resources which are at least one order of magnitude larger. More details

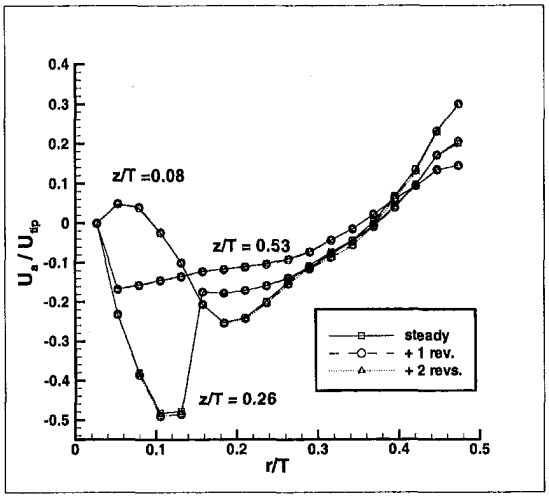

(a)

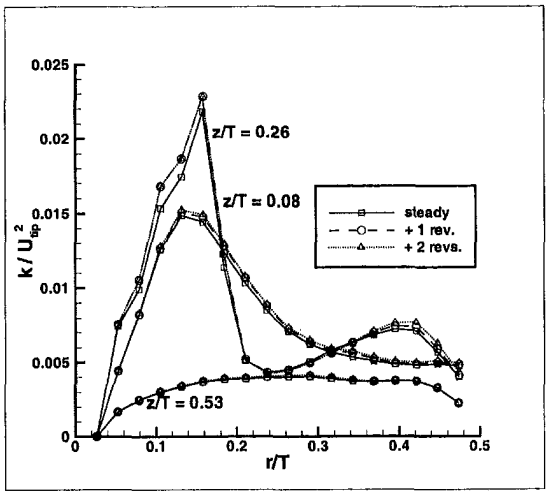

(b)

Fig. 4 Radial profiles of normalized axial velocity component (*a*) and normalized turbulent kinetic energy (*b*) for different axial positions.
— □ — steady-state computation, Re = 7280
– – ○ – – unsteady computation, Re = 7280, one revolution started from steady-state solution
···△··· unsteady computation, Re = 7280, two revolutions started from steady-state solution.

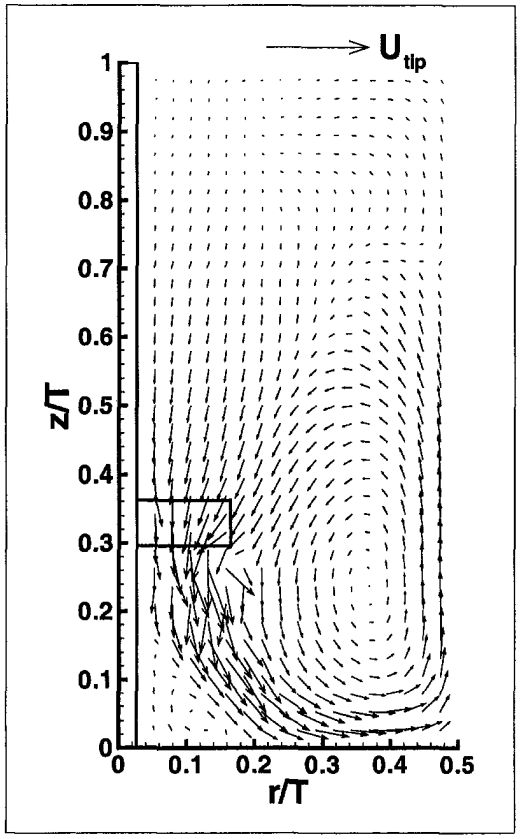

Fig. 5 Secondary flow field in mid-baffle plane (θ = 45°), Re = 7280

about the performance of the code can be found in Durst and Schäfer (1996) and Durst et al. (1996).

5.2 Steady-State Versus Unsteady Computations. In order to compare the predictions of the applied steady-state modeling technique with fully time-dependent simulations, steady-state and unsteady computations of turbulent pitched-blade impeller flow were performed for the second grid level with 125,440 CVs at Re = 7280. The unsteady computation was not started from a fluid at rest but with initial values taken from the solution of the steady-state computation. This was done in order to overcome the start-up flow patterns which are computationally very expensive, as described earlier. A total of 2010 iterations was necessary to drop the sums of the absolute residual sources below 10^{-6} for the steady-state computation. Starting from this steady-state solution, it took approximately another 15000 iterations to overcome two complete revolutions in a fully time-dependent computation. Figure 4 compares radial profiles of normalized axial velocity component (a) and normalized turbulent kinetic energy (b) for different axial positions. Square symbols connected by solid lines give the results of the steady-state computation. Circles connected by dashed lines indicate the solution of one revolution of the unsteady computation started from the steady-state solution. Triangles connected by dotted lines show the solution after two revolutions of unsteady computation which was also started from the steady-state solution. The agreement of the different solutions is excellent. Almost no visible difference is present for the normalized axial velocity. Small deviations can be seen for the normalized turbulent kinetic energy. However, the solutions of the two unsteady computations are again very close to each other, indicating that in the unsteady computation the periodic motion is fully developed after just one additional revolution of the impeller. The results demonstrate that the applied steady-state approach is very well suited for saving excessive computational effort for fully time-dependent computations of turbulent pitched-blade impeller flow, at least in the present configuration.

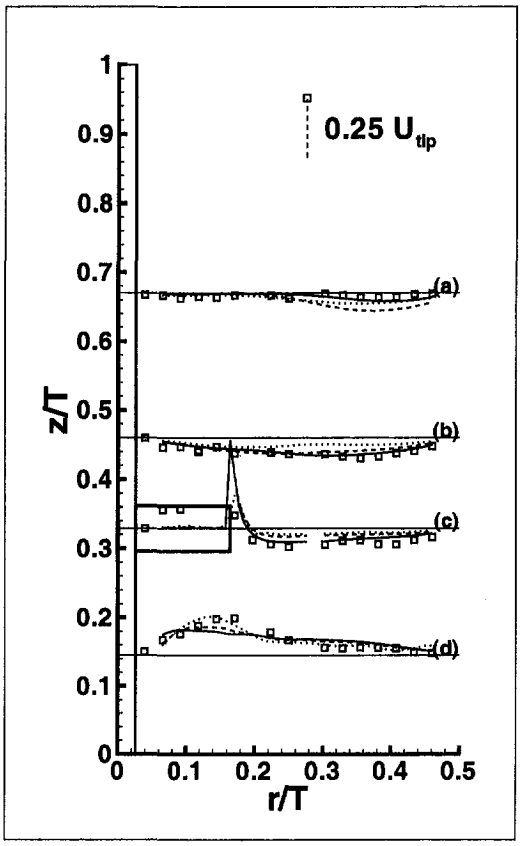

Fig. 7 Radial profiles of normalized radial velocity U_r/U_{tip} in mid-baffle plane (θ = 45°) at four different axial positions (sketched in Fig. 2): (*a*) z/T = 0.67; (*b*) z/T = 0.46; (*c*) z/T = 0.33; (*d*) z/T = 0.145. Symbols and lines as in Fig. 6.

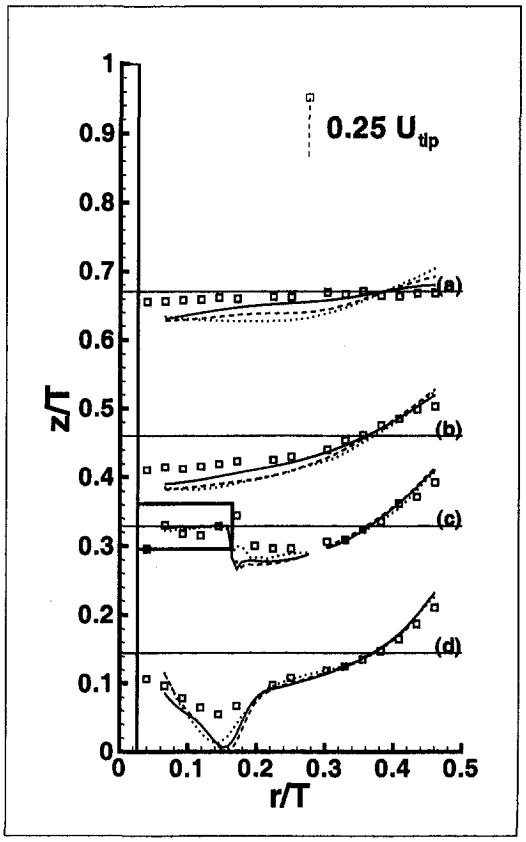

Fig. 6 Radial profiles of normalized axial velocity U_a/U_{tip} in the mid-baffle plane (θ = 45°) at four different axial positions (sketched in Fig. 2): (*a*) z/T = 0.67; (*b*) z/T = 0.46; (*c*) z/T = 0.33; (*d*) z/T = 0.145.
□□□□□□ experimental data of Schäfer et al. (1998), Re = 7280
——— steady-state simulation, Re = 29,000, fine grid
– – – – – – steady-state simulation, Re = 29,000, medium grid
····· steady-state simulation, Re = 29,000, coarse grid

5.3 Large-Scale Flow Field. The secondary flow field in the θ = 45° plane (see Fig. 3) obtained by steady-state computation on the grid consisting of 125,440 CVs is shown in Fig. 5 for Re = 7280. The discharge flow is nearly axial below the impeller, although evidence for the trailing vortices can already be seen from this large-scale velocity vector plot. Below the impeller, the discharge flow becomes more and more radial, reaches the bottom at around r/T = 0.25 and forms a main recirculation region which reaches up to about z/T = 0.65. In addition to this main recirculation vortex, a small vortex below the discharge flow which is rotating in the opposite direction with small velocities can be observed in Fig. 5. All the mentioned flow features are in encouraging agreement with the experiments reported by Schäfer et al. (1998). In order to evaluate the predictions in more detail, normalized mean flow velocity components and normalized turbulent kinetic energy were directly compared with the experimental data of Schäfer et al. (1998) via radial profiles at different axial positions in the mid-baffle plane (θ = 45°). The axial positions of the radial profiles are sketched in Fig. 2. The experimental results are plotted in combination with the results of the steady-state computations on all grid levels, thus allowing grid sensitivity analysis of the predicted results. As already mentioned, the Reynolds number had to be increased in case of the computations in order to enable grid sensitivity studies. This difference and the discrepancy of the geometry (zero thickness of the blades in the computations) have

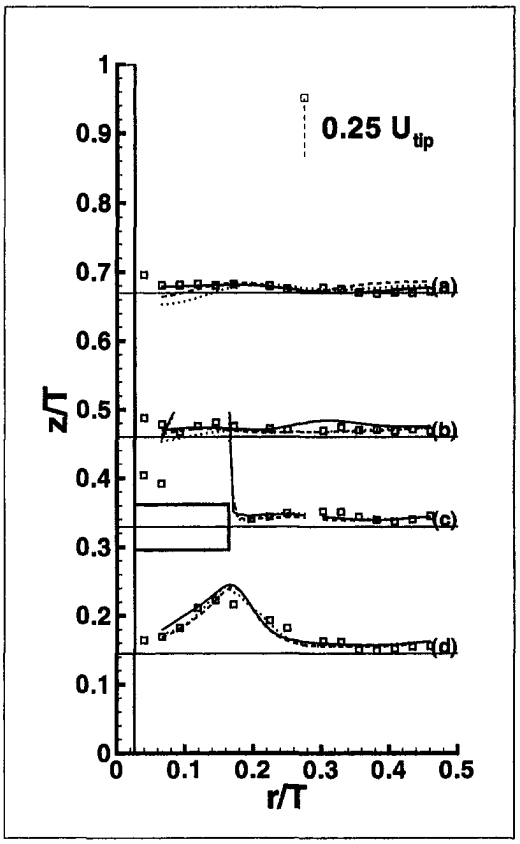

Fig. 8 Radial profiles of normalized tangential velocity U_t/U_{tip} in mid-baffle plane (θ = 45°) at four different axial positions (sketched in Fig. 2): (*a*) z/T = 0.67; (*b*) z/T = 0.46; (*c*) z/T = 0.33; (*d*) z/T = 0.145. Symbols and lines as in Fig. 6.

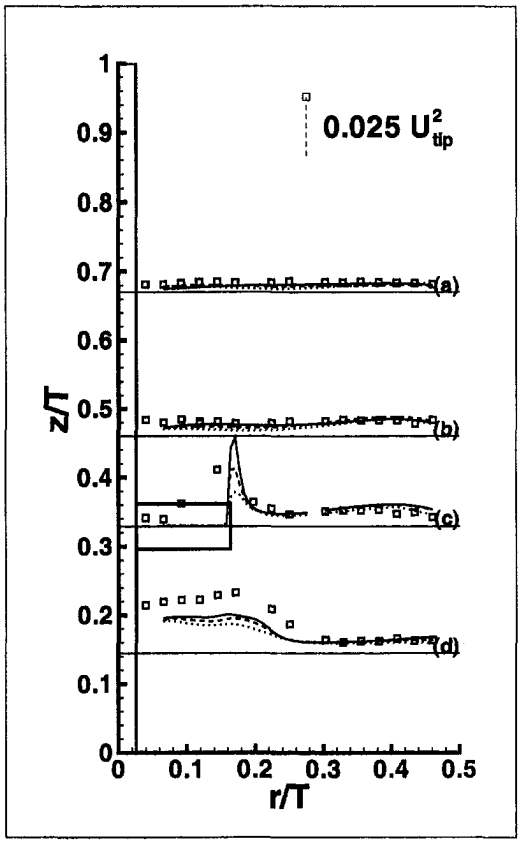

Fig. 9 Radial profiles of normalized turbulent kinetic energy k/U_{tip}^2 in mid-baffle plane (θ = 45°) at four different axial positions (sketched in Fig. 2): (*a*) z/T = 0.67; (*b*) z/T = 0.46; (*c*) z/T = 0.33; (*d*) z/T = 0.145. Symbols and lines as in Fig. 6.

to be kept in mind during the comparisons. Figures 6–9 show results for normalized axial, radial and tangential velocity components and normalized turbulent kinetic energy at four different axial positions and Re = 29,000, respectively.

Figure 6(*a*) (z/T = 0.67) shows that the axial velocity is very low in the upper third of the tank, making accurate predictions very difficult. Only the fine grid solution (solid line) is close to the experimental results (symbols), but there are too high negative axial velocities for all grid levels in the inner part of the tank. The presence of the main recirculation vortex is obvious from Fig. 6(*b*). Figure 6(*d*) shows that the axial velocity of the discharge flow at z/T = 0.145 is overpredicted by the computations. To conclude, the magnitude of the negative axial velocity is overpredicted in the whole tank for $r/T < 0.24$, which indicates too high pumping activity of the impeller. Rutherford et al. (1996) showed that thin bladed Rushton turbines have a significant higher flow number than thick bladed turbines. The difference in the blade thickness between experiment and simulation can at least partially explain the differences in the normalized axial velocity component between experiments and simulation in the present study.

Similar quality and behavior of the computational results are evident for the normalized radial velocity in Fig. 7(*a–d*). Very low radial velocities in the upper third of the tank again render accurate predictions difficult, but agreement between experiments and fine-grid results is satisfactory. Similar agreement can be seen for z/T = 0.46, where the coarse grid solution is wrong, indicating insufficient grid resolution; the fine grid solution, however, is excellent compared with the experimental data. Agreement for z/T = 0.33 is good also for the normalized radial velocity. However, radial velocities for z/T = 0.145 again show some deviations from experiment, indicating a deficiency of the turbulence model in predicting correct values of the magnitude of the discharge flow velocity. Evidently, further refinement of the grid will not change the magnitude of the predicted radial velocity in this region. The values of U_t/U_{tip} are in close agreement with the experiment within the whole tank, as can be seen from Fig. 8.

Predictions of the turbulent kinetic energy are rarely reported in

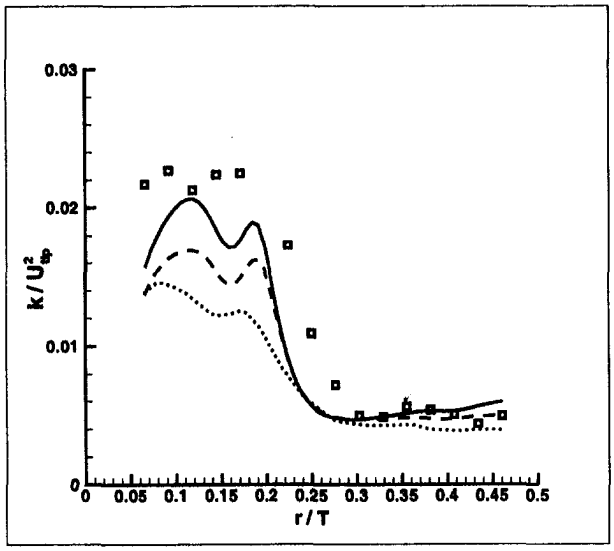

Fig. 10 Radial profiles of normalized turbulent kinetic energy k/U_{tip}^2 for tank angle θ = 5° at axial position z/T = 0.145 (sketched in Fig. 2). Symbols and lines as in Fig. 6.

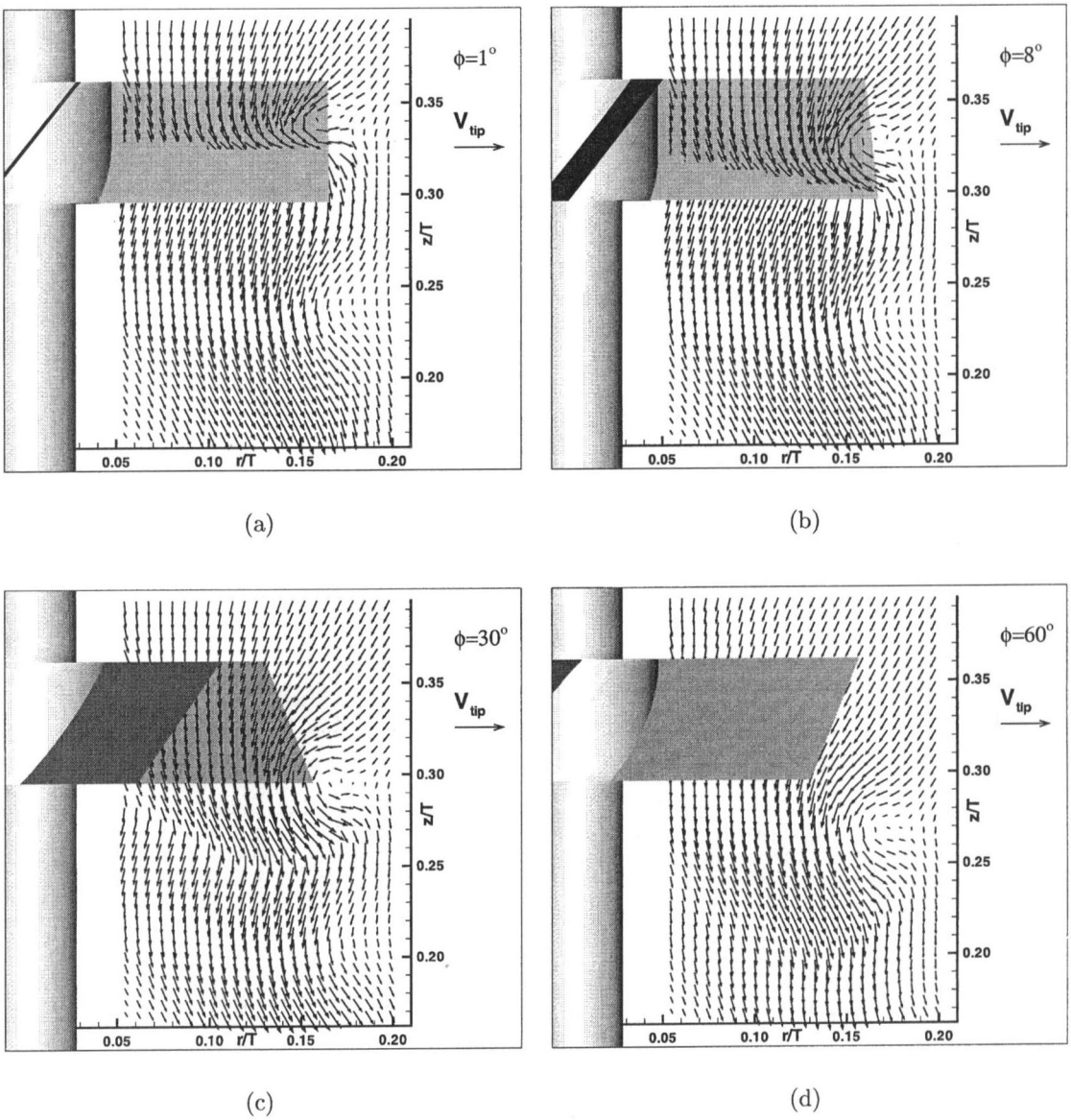

Fig. 11 Secondary impeller flow field for different blade angles ϕ: (*a*) $\phi = 1°$; (*b*) $\theta = 8°$; (*c*) $\phi = 30°$; (*d*) $\theta = 60°$; Re = 7280

the literature, perhaps mainly owing to the problems encountered with its prediction. The present study shows, however, that it is possible to obtain reasonable agreement even for the turbulent kinetic energy, which can be seen from Fig. 9(*a–d*). Predicted values of k/U_{tip}^2 are encouraging for the upper part of the tank and the region next to the impeller. But, there is an underprediction of k/U_{tip}^2 in Fig. 9(*d*), and the grid sensitivity study shows that the predictions will not reach the experimental values even on finer grids. However, Fig. 9(*d*) shows the most severe underprediction of k/U_{tip}^2 at $z/T = 0.145$ ($\theta = 45°$). At other tank angles, the agreement with experimental values is much better, which can be seen from Fig. 10, showing k/U_{tip}^2 at $z/T = 0.145$ and a tank angle of $\theta = 5°$. This figure also demonstrates clearly that the use of coarse grids can lead to severe underprediction of the turbulent kinetic energy overemphasizing the deficiency of the turbulence model. To conclude, although there is quantitative disagreement in some parts of the tank (see, for example, Fig. 9(*d*)), the prediction at the fine grid level shows encouraging results in the light of the problems reported in the literature in determining the correct turbulent kinetic energy level.

5.4 Impeller Flow Field. Both the experimental data of Schäfer et al. (1998) and the computational steady-state modeling results of the present study allow a detailed comparison of the impeller flow field agitated by the pitched-blade impeller. Figure 11 shows the secondary flow field for the computation with the medium grid (125,440 CVs) for different blade angles ϕ. In this figure the blades have to be considered as moving into the page away from the reader. The predicted results were interpolated to a uniform grid (in cylindrical coordinates) of mesh size $\Delta z = 1$ mm, $\Delta r = 1$ mm and $\Delta\phi = 1°$. The interpolation was performed in order to increase the quality of the visualization of the results because the original distribution of the grid points is non-uniform. In the $\phi = 1°$ plane (Fig. 11(*a*)), the flow around the blade under consideration is directed mainly outwards at the top (behind the blade), whereas that near the bottom (in front of the blade) is directed inwards, towards the axis, which is in good agreement with the experimental results. The trailing vortex is the circulation centered around $r/T = 0.165$ and $z/T = 0.34$. Whereas the axial position is the same as reported by experiments, the radial position of the predicted trailing vortex is about $0.01T$ larger than in the experiment. A small circulating motion centred around $r/T = 0.17$ and $z/T = 0.24$ indicates the presence of the trailing vortex from the preceding blade which is still evident 90° after that blade has crossed this plane. In the $\phi = 8°$ plane (Fig. 11(*b*)), the trailing vortex significantly moved downwards and is located at approximately $z/T = 0.325$. Taking into account the vectors at $\phi = 30°$

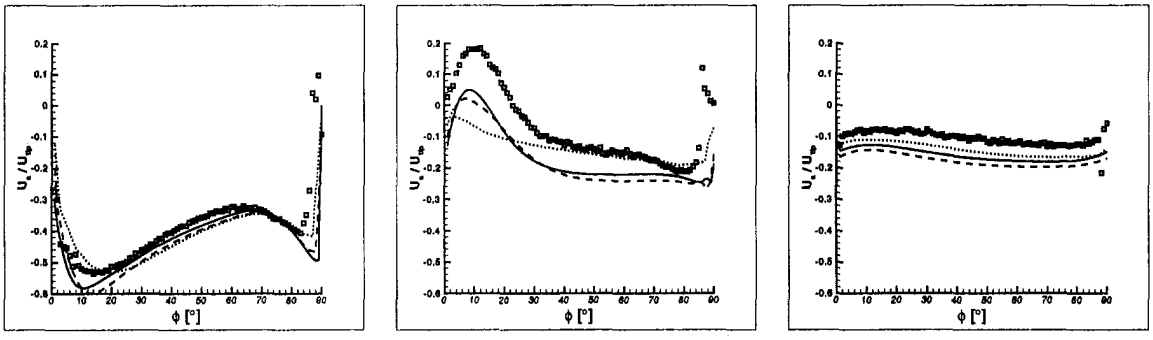

Fig. 12 Circumferential profiles of normalized axial velocity U_a/U_{tip} at three different radial positions (sketched in Fig. 3) in axial mid-impeller plane ($z/T = 0.329$: (*a*) $r/T = 0.118$; (*b*) $r/T = 0.171$; (*c*) $r/T = 0.197$. Symbols and lines as in Fig. 6.

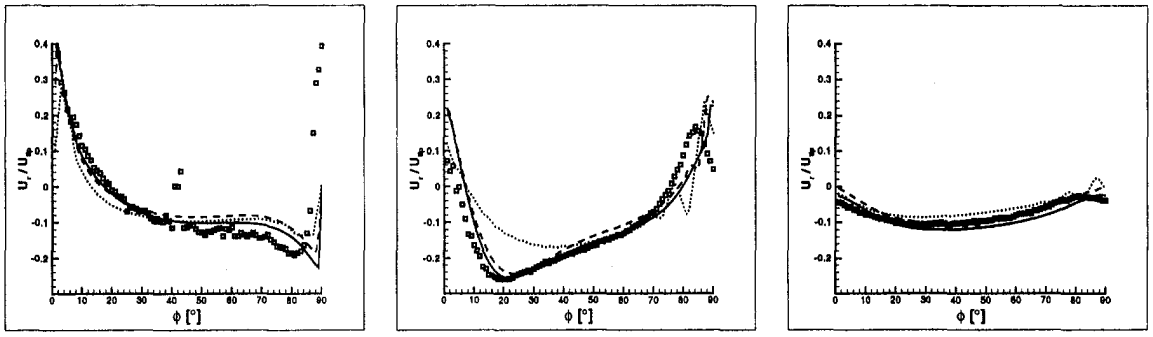

Fig. 13 Circumferential profiles of normalized radial velocity U_r/U_{tip} at three different radial positions (sketched in Fig. 3) in axial mid-impeller plane ($z/T = 0.329$: (*a*) $r/T = 0.118$; (*b*) $r/T = 0.171$; (*c*) $r/T = 0.197$. Symbols and lines as in Fig. 6.

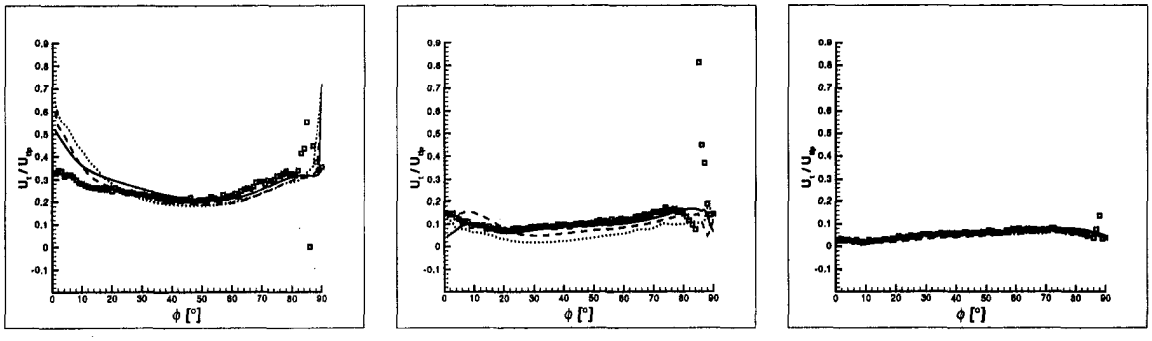

Fig. 14 Circumferential profiles of normalized tangential velocity U_t/U_{tip} at three different radial positions (sketched in Fig. 3) in axial mid-impeller plane ($z/T = 0.329$: (*a*) $r/T = 0.118$; (*b*) $r/T = 0.171$; (*c*) $r/T = 0.197$. Symbols and lines as in Fig. 6.

and $\phi = 60°$, an inclination of the vortex axis of 22° with respect to the horizontal can be extracted. Although this value is slightly higher than the experimental value of 20° reported by Schäfer et al. (1998), the results of the prediction are very encouraging because all flow features reported by the experiments can mainly be reproduced without modifications in the standard k-ϵ turbulence model.

Again, in order to validate the predictions in more detail, normalized mean flow velocity components and normalized turbulent kinetic energy were directly compared with the experimental data of Schäfer et al. (1998). In the case of the impeller flow, circumferential profiles of three different radial positions (see Fig. 3) in the axial mid-impeller plane ($z/T = 0.329$) were chosen. The experimental results are plotted in combination with the results of the steady-state computations on all grid levels, thus allowing grid sensitivity analysis of the predicted results also for the impeller flow field. Figures 12–15 show results for normalized axial, radial and tangential velocity components and normalized turbulent kinetic energy at three different radial positions. Circumferential profiles of the normalized axial velocity U_a/U_{tip} at three different radial positions are plotted in Fig. 12. Figure 12(*a*) shows good agreement of experimental results and fine grid predictions for $\phi > 20°$, whereas the small difference in the peak near $\phi = 10°$ is a result of the finite blade thickness (in contrast to computations with zero thickness of the blades). Outside the impeller swept

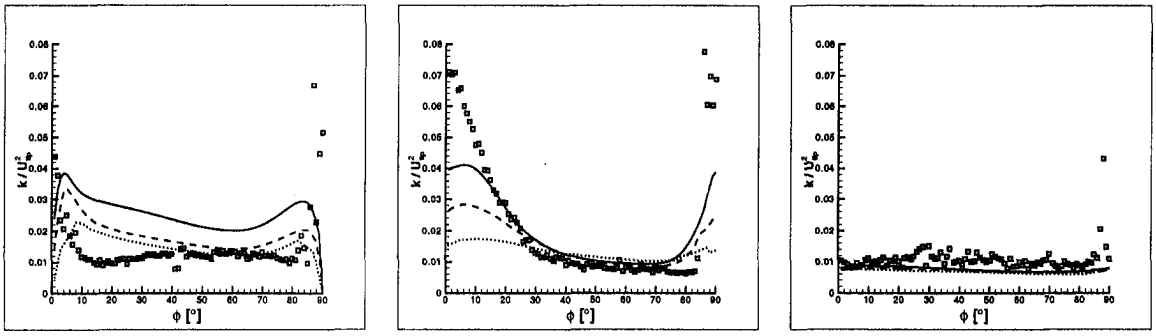

Fig. 15 Circumferential profiles of normalized turbulent kinetic energy k/U_{tip}^2 at three different radial positions (sketched in Fig. 3) in axial mid-impeller plane ($z/T = 0.329$: (*a*) $r/T = 0.118$; (*b*) $r/T = 0.171$; (*c*) $r/T = 0.197$. Symbols and lines as in Fig. 6.

region (Fig. 12(*b–c*)), some quantitative discrepancies can be detected. However, qualitative agreement can be achieved especially for the fine grid solution. Similar conclusions can be drawn for the normalized radial velocity plotted in Fig. 13(*a–c*): very good results were obtained for $r/T = 0.118$. At $r/T = 0.171$ (Fig. 13(*b*)), the relative shape of the profiles is almost identical. Solutions of the medium and fine grids agree very well, suggesting satisfactory grid convergence. At $r/T = 0.197$, the normalized radial velocity is accurately predicted. Almost identical quality and behavior of the results can be reported for the normalized tangential velocity in Fig. 14(*a–c*) and will not be discussed further. The circumferential profiles of the normalized turbulent kinetic energy in the impeller region are very interesting since this quantity has not been compared with comprehensive experimental data in previous papers. Inside the impeller swept region (Fig. 15(*a*)), a high sensitivity of the k/U_{tip}^2 to the grid resolution can be observed. Unfortunately, the experimental values of k/U_{tip}^2 fit best the coarse grid solution for this case. This illustrates the necessity to check the prediction of turbulence models by successive grid refinement studies, since looking only at one (coarse) grid solution could lead to wrong conclusions. Slightly outside the impeller swept region at $r/T = 0.171$ in Fig. 15(*b*), the necessity to perform successive grid refinement is demonstrated again. While the coarse grid solution cannot predict the high turbulence level of the impeller discharge flow for $\phi < 25°$, the medium and fine grid solutions show the right trend. However, the maximum value on this profile of $k/U_{tip}^2 \approx 0.7$ is missed by a factor of almost two even for the fine grid solution. Unfortunately, at this point, it cannot be decided which maximum level of k/U_{tip}^2 will be predicted by the model. At $r/T = 0.197$ (Fig. 15(*c*)), k/U_{tip}^2 is underpredicted, but the experimental results also show large scatter.

6 Conclusion

The 3-D turbulent flow field generated by a pitched-blade impeller with four 45° inclined blades in a baffled stirred tank (Re = 7280) was examined by means of computational fluid dynamics (CFD). Mean flow and turbulence characteristics were computed by solving the Reynolds averaged Navier-Stokes equations combined with the standard k-ϵ turbulence model. High-performance parallel vector computers were applied to allow grid sensitivity studies in order to isolate errors resulting from deficiencies of the turbulence model and those resulting from insufficient grid resolution. The grid sensitivity studies were performed at a higher Reynolds number of Re = 29,000 in order not to violate the range of validity of the wall functions at solid surfaces on the fine grid. Two different modeling approaches were applied and evaluated for the simulations. First, computational results were obtained by a steady-state modeling approach of the impeller motion which is not dependent on the specification of experimentally determined boundary conditions. Nevertheless, the whole geometry of both the impeller and the vessel is considered, which permits detailed prediction of the flow field even inside the impeller swept region. The results of the predictions were compared with the most comprehensive data set of the mean flow and turbulence field in a vessel stirred by an axial flow impeller available to date. It has been shown that grid sensitivity analysis of the computational results, which was done for the first time for an axial flow impeller in turbulent operation, is unconditionally necessary for a correct evaluation of turbulence models. Furthermore, the results of the steady-state modeling approach were tested against a second approach based on fully time-dependent unsteady computations taking the time-dependent change of the underlying solution domain by clicking grids into account. Encouraging agreement between steady-state and unsteady computations was found, and steady-state computations require only a fraction of the time and expense for the stirred vessel configuration under consideration. Hence, steady-state modeling approaches such as that presented here promise to become very helpful CFD tools for mixing process design.

Acknowledgments

Financial support by the Commission of the European Union under the BRITE EURAM Programme, Contract number BRPR-CT96-0185, is gratefully acknowledged. The simulations were carried out on the Fujitsu VPP 700 machine at the Leibniz Computing Centre, Munich. This support is also gratefully acknowledged.

References

Ali, A., H. Yuan, Dickey, D., and Tatterson, G., 1981, "Liquid Dispersion Mechanisms in Agitated Tanks: Part 1. Pitched Blade Turbine," *Chemical Engineering Communications,* Vol. 10, pp. 204–213.

Arnal, M., Lauer, O., Lilek, Z., and Perić, P., 1992, "Prediction of Three-Dimensional Unsteady Lid-Driven Cavity Flow," *Notes on Numerical Fluid Mechanics,* Vol. 36, pp. 13–24, Vieweg, Braunschweig.

Bakker, A., Laroche, R. D., Wang, M. H., and Calabrese, R. V., 1997, "Sliding Mesh Simulation of Laminar Flow in Stirred Tanks," *Transactions of the Institution of Chemical Engineers,* Vol. 75(A), pp. 42–44.

Bakker, A., Myers, K. J., Ward, R. W., and Lee, C. K., 1996, "The Laminar and Turbulent Flow Pattern of a Pitched Blade Turbine," *Transactions of the Institution of Chemical Engineers,* Vol. 74(A), pp. 485–491.

Bakker, A., and H. E. A. Van Den Akker, 1994, "Single-Phase Flow in Stirred Reactors," *Transactions of the Institution of Chemical Engineers,* Vol. 72(A), pp. 583–593.

Durst, F., and M. Schäfer, 1996, "A Parallel Block-Structured Multigrid Method for the Prediction of Incompressible Flows," *International Journal of Numerical Methods in Fluids,* Vol. 22, pp. 549–565.

Durst, F. Schäfer, M., and Wechsler, K. 1996, "Efficient Simulation of Incompressible Viscous Flows on Parallel Computer," *Flow Simulation with High-Performance Computers II,* Notes on Numerical Fluid Mechanics, Vol. 52, pp. 87–101. Vieweg, Braunschweig.

Harvey, A. D., Lee, C. K., and Rogers, S. E., 1995, "Steady-State Modeling and

Experimental Measurement of a Baffled Impeller Stirred Tank," *American Institute of Chemical Engineers Journal,* Vol. 41, No. 10, pp. 2177–2186.

Harvey, A. D., and Rogers, 1996, "Steady and Unsteady Computation of Impeller Stirred Reactors," *American Institute of Chemical Engineers Journal,* Vol. 42, No. 10, pp. 2701–2712.

Harvey, A. D., Wood, S. P., and Leng, D. E., 1997, "Experimental and Computational Study of Multiple Impeller Flows," *Chemical Engineering Science,* Vol. 52, No. 9, pp. 1479–1492.

Harvey, P. S., and Greaves, M., 1982, "Turbulent Flow in Agitating Vessel. Part I: A Predictive Model," *Transactions of the Institution of Chemical Engineers,* Vol. 60, pp. *195–200.*

Jones, W., and Launder, B., 1972, "The Prediction of Laminarization with a Two-Equation Model of Turbulence," *International Journal of Heat and Mass Transfer,* Vol. 15, pp. 301–314.

Ju, S. Y., Mulvahill, T. M., and Pike, R. W., 1990, "Three-Dimensional Turbulent Flow in Agitated Vessels with a Nonisotropic Viscosity Turbulence Model," *Canadian Journal of Chemical Engineering,* Vol. 68, pp. 3–16.

Kresta, S. M., and Wood, P. E., 1991, "Prediction of the Three-Dimensional Turbulent Flow in Stirred Tanks," *American Institute of Chemical Engineers Journal,* Vol. 37, No. 3, pp. 448–460.

Launder, B., and Spalding, D., 1974, "The Numerical Computation of Turbulent Flows," *Computer Methods in Applied Mechanics and Engineering,* Vol. 3, pp. 269–289.

Launder, B. E., and Sharma, B. I., 1974, "Application of the Energy Dissipation Model of Turbulence to Calculation of Flow Near a Spinning Disc," *Letters on Heat and Mass Transfer,* Vol. 15, pp. 301–314.

Leister, H.-J., and Perić, M., 1993, "Vectorized Strongly Implicit Solving Procedure for a Seven-Diagonal Coefficient Matrix," *International Journal of Heat and Fluid Flow,* Vol. 4, pp. 159–172.

Luo, J. Y., Gosman, A. D., Issa, R. I., Middleton, J. C., and Fitzgerald, M. K., 1993, "Full Flow Field Mixing Computation of Mixing in Baffled Stirred Vessels," *1993 Institution of Chemical Engineers Research Event,* Birmingham, UK, 6–7 Jan., pp. 657–659, Institution of Chemical Engineers, London.

Middleton, J. C., Pierce, F., and Lynch, P. M., 1986, "Computations of Flow Fields and Complex Reaction Yield in Turbulent Stirred Reactors, and Comparison with Experimental Data," *Chemical Engineering Research and Design,* Vol. 64, pp. 18–22.

Patankar, S., and Spalding, D., 1972, "A Calculation Procedure for Heat, Mass and Momentum Transfer in Three Dimensional Parabolic Flows," *International Journal of Heat and Mass Transfer,* Vol. 15, pp. 1787–1806.

Pericleous, K. A., and Patel, M. K., 1987, "The Source-Sink Approach in the Modelling of Stirred Reactors," *PhysicoChemical Hydrodynamics,* Vol. 9, pp. 279–297.

Perng, C.-Y., and Murthy, J. Y., 1993, "A Sliding-Mesh Technique for Simulation of Flow in Mixing Tanks," ASME Winter Annual Meeting, New Orleans, LA, Nov. 28–Dec. 3, pp. 1–9.

Ranade, V. V., Bourne, J. R., and Joshi, J. B., 1991, "Fluid Mechanics and Blending in Agitated Tanks," *Chemical Engineering Science,* Vol. 46, No. 8, pp. 1883–1893.

Ranade, V. V., and Dommeti, S. M. S., 1996, "Computational Snapshot of Flow Generated by Axial Impellers in Baffled Stirred Vessels," *Transactions of the Institution of Chemical Engineers,* Vol. 74(A), pp. 476–484.

Ranade, V. V., and Joshi, J. B., 1990, "Flow Generated by a Disc Turbine, Part II: Mathematical Modelling and Comparison with Experimental Data," *Transactions of the Institution of Chemical Engineers,* Vol. 68(A), pp. 34–50.

Ranade, V. V., Joshi, J. B., and Marathe, A. G., 1989, "Flow Generated by Pitched Blade Turbines, II: Simulation Using k-ϵ Model," *Chemical Engineering Communication,* Vol. 81, pp. 225–248.

Rhie, C., and Chow, W., 1983, "Numerical Study of the Turbulent flow Past an Airfoil With Trailing Edge Separation," *American Institute of Aeronautics and Astronautics Journal,* Vol. 21, pp. 1525–1532.

Rutherford, K., Mahmoudi, S. M. S., Lee, K. C., and Yianneskis, M., 1996, "The Influence of Rusthon Impeller Blade and Disk Thickness on the Mixing Characteristics of Stirred Vessel," *Transactions of the Institution of Chemical Engineers,* Vol. 74(A), pp. 369–378.

Sahu, A. K., and Joshi, J. B., 1995, "Simulation of Flow in Stirred Vessels with Axial Flow Impellers: Effects of Various Numerical Schemes and Turbulence Model Parameters," *Industrial and Engineering Chemistry Research,* Vol. 34, pp. 626–639.

Schäfer, M., Yianneskis, M., Wächter, P., and Durst, F., 1998, "On the Trailing Vorticies Around a 45° Pitched Blade Turbine," *American Institute of Chemical Engineers Journal,* Vol. 44, No. 6, pp. 1233–1246.

Stone, H., 1968, "Iterative Solution of Implicit Approximations of Multidimensional Partial Differential Equations," *Society for Industrial and Applied Mathematics (SIAM) Journal of Numerical Analysis,* Vol. 5, pp. 530–557.

Tatterson, G. B., Brodkey, R., and Calabrese, R. V., 1991, "Move Mixing Technology into the 21st Century," *Chemical Engineering Progress,* Vol. 6, pp. 45–48.

Xu, Y., and McGrath, G., 1996, "CFD Predictions of Stirred Tank Flows," *Transactions of the Institution of Chemical Engineers,* Vol. 74(A), pp. 471–475.

Predictable Model for Characteristics of One-Dimensional Solid-Gas-Liquid Three-Phase Mixtures Flow Along a Vertical Pipeline With an Abrupt Enlargement in Diameter

Natsuo Hatta
Professor.

Masaaki Omodaka
Graduate Student. Presently, Nippon Steel Corporation

Fumitaka Nakajima
Graduate Student.

Takahiro Takatsu
Undergraduate Student. Presently, Engineer, NKK Corporation

Hitoshi Fujimoto
Instructor.

Hirohiko Takuda
Assistant Professor.

Department of Energy Science and Technology, Graduate School of Energy Science, Kyoto University, Sakyo-ku, Kyoto 606-8501, Japan

This paper treats the numerical analysis of the rising process of a solid-gas-liquid three-phase mixture along a vertical pipeline with an abrupt enlargement in diameter. The system of governing equations used is based upon the one-dimensional multifluid model and the transitions of gas flow pattern are taken into account in the system of governing equations. For the case of a sudden enlargement in diameter in a coaxial pipeline, the procedure of the numerical calculation to obtain the flow characteristics in the pipeline section after a sudden change in diameter has been established here. Furthermore, in order to confirm the validity of the present theoretical model by the comparison between the calculated and experimental values, the experiments have been made using four kinds of lifting pipes, including the straight one. Thereby, it has been found that the numerical model proposed here gives good fit to the prediction of the flow rates of lifted water and solid particles against that of air supplied for the case of a sudden change in diameter. In addition, the flowing process for each phase has been investigated from a photographic point of view. As a result, we found that the moving process of the solid particles depends strongly upon the volumetric flux of gas-phase as well as the submergence ratio.

1 Introduction

This paper is concerned with the theoretical analysis of the steady-state flow characteristics of multiphase mixtures flowing upward in a vertical pipeline with an abrupt enlargement in a cross-sectional area. In general, it is very difficult to exactly predict the flow characteristics of the case where two or three different phases, among solid-, gas- and liquid-phases, interact with each other and such two- or three-phase mixtures flow upward in a vertical pipe. The air-lift pump, which was originally imagined to be applicable only for a few simple uses like pumping water, has been utilized as a means of lifting explosive/poisonous liquid in chemical industries and conveying slurries in mining. More recently, it has been reported (Kamata and Ito, 1995) that in the steel-making process, although the principle of the gas-lift pump is currently applied to an RH degasser to circulate molten steel, the simplicity of the equipment can make it applicable to transport molten iron or steel between different refining processes. Their experimental study has been performed using Wood's metal instead of a molten steel to investigate the transportation characteristics of the pump. Also, it is well-known that there is a vast amount of marine mineral resources like manganese nodules at the deep-sea bed of 4000 m to 6000 m in depth of water. For lifting such mineral ores from the deep-sea bed to the sea surface, the utilization of the air-lift pump is anticipated and examined from a practical point of view.

Contributed by the Fluids Engineering Division for publication in the JOURNAL OF FLUIDS ENGINEERING. Manuscript received by the Fluids Engineering Division February 9, 1998; revised manuscript received February 8, 1999. Associate Technical Editor: M. Sommerfeld.

Experimental studies so far made in this area are those of Kawashima et al. (1975), Weber and Dedegil (1976), Usami et al. (1986), and Yoshinaga and Sato (1990, 1996). Kawashima et al. (1975) have investigated the relationship between the volumetric fluxes of air supplied and the solid particles discharged with changing the volumetric concentration of the particles. Weber and Dedegil (1976) have made an experimental study with a large and tall air-lift pump which transports gravel. Although their data are very valuable to be analyzed, the upriser length, suction height, volumetric concentration of the particles discharged, and the submergence ratio (the ratio of the distance between the water surface and the gas injector to that between the top end of pipe and the injector) were different from run to run. Usami et al. (1986) have made an experiment on the air-lift pump which conveys simulated manganese nodules. In their experiment, the submergence ratio was fixed at 0.82. Yoshinaga and Sato (1990, 1996) made an investigation with either uniform spherical particles or non-uniform spherical particles. In their experiment, the diameter of the upriser, the diameter of particles, and the submergence ratio were changed systematically. They proposed a model for predicting the steady-state operation performance by applying the momentum conservation law to a control volume bounded by the wall, the top and bottom cross sections of the lifting pipe. They compared the predicted results obtained by the model with the experimental data measured by other investigators and their own experimental data, and confirmed the validity. However, the external forces introduced to their model are only the friction force, the weight of the mixture, and the pressure force of the surrounding water acting on the bottom section of the lifting pipe. The interaction between different phases is neglected in their model. It is unbelievable that

their model is omnipotent due to the fact that the idea which underlies their model is too simple. In fact, they themselves (1990) recognized that for a gas-liquid two-phase flow, the volumetric flux of water against that of supplied air reduced to the atmospheric state which was predicted on the basis of their model are lower by 30% at maximum than the measured data.

More recently, the present authors (1998) proposed a theoretical model to predict the steady-state flow characteristics of the air-lift pump for the case where a transition from the solid-liquid two-phase flow to the solid-gas-liquid three-phase flow occurs by injecting gas-phase into a vertical pipe through a gas-injector. The system of governing equations is based upon the one-dimensional multifluid model on the premise that the solid particles are distributed uniformly in a liquid-phase. The transitions of the gas flow pattern are taken into consideration in the system of equations governing the solid-gas-liquid three-phase flow in a vertical and straight pipe. Then, in order to confirm the validity of the system of governing equations accounting for the gas-phase transition, the results calculated on the basis of our theoretical model were compared to the experimental results measured by several other researchers (Kawashima et al., 1975, Weber and Dedegil 1976, Usami et al., 1986, Saito et al., 1986, Yoshinaga et al., 1990 and Yoshinaga and Sato, 1996). Fortunately, we found that our model gives best-fit to the prediction of the operation performance of an air-lift pump.

In the present paper, the theoretical analysis of the steady-state flow characteristics of the solid-gas-liquid three-phase mixture flow will be examined for the case of a sudden enlargement in diameter along a vertical pipeline. The presence of the sudden expansion has an important aspect of the design of such devices. As the gas expands with the distance from the gas injection, the flow velocities increase, and so do the pressure drops owing to the friction force between the mixture and the inner wall of pipe. In this sense, it is significant to increase the pipe cross section in order to improve the pump efficiency, as the pipe length becomes large. So far as we know, we have seen almost no papers treating the flow characteristics of the solid-gas-liquid three-phase mixture moving upward in a vertical pipe with an abrupt change in diameter from an analytical point of view. In this case, it is very important how the calculation is performed to obtain the characteristics of the steady-state solid-gas-liquid three-phase mixture flow in a vertical pipe with an abrupt change in diameter. In particular, what is of most importance is to establish the numerical procedure to evaluate the flow characteristics in the pipeline section after a sudden change in cross-sectional area. Here, the numerical treatment is proposed to predict the flow characteristics of three-phase mixtures flowing upward along a vertical pipe with a sudden enlargement in diameter. The theoretical model used is based upon the one-dimensional multifluid model and is almost the same as that proposed in our above-mentioned paper. Furthermore, we have performed experiments on the operation performance of gas-lift pump using vertical pipelines made from some combinations of pipe diameters. It has been found that the calculated results agree fairly well with the experimental data from a qualitative and quantitative point of view.

Apart from the above-mentioned problems, the flowing process for each phase is discussed from a photographic point of view. Interesting photographs taken by a high speed video camera are demonstrated on various conditions. It has been found that the moving process of the solid particles depends strongly upon the volumetric flux of gas-phase as well as the submergence ratio.

2 Governing Equations

There is a velocity slip between the solid- and liquid-phases, because the velocity of the solid-phase is slower than that of the liquid-phase. In so doing, the solid particles may reach the gas/liquid interface. Some cases are considered to occur where the solid particles are pulled upward due to the surface tension effect at the interface with the same velocity as that at the top of a gas slug or where the particles fall, ascend and stop in a gas slug through the interface. At any rate, such complicated phenomena must occur at the interface. However, the system of equations governing the solid-gas-liquid three-phase mixture flow is based upon the one-dimensional multifluid model on the premise that the solid particles are distributed uniformly in a liquid-phase. In our

Nomenclature

A = cross-sectional area of pipe (m^2)
A_1, A_2, A_3 = see Eq. (48)
a_i = interfacial area concentration (1/m)
B_1, B_2, B_3 = see Eq. (48)
C_1, C_2 = see Eq. (48)
C_D = interfacial drag coefficient (—)
C_{DG0} = drag coefficient of single bubble in stagnant liquid (—)
C_{DGb}, C_{DGs}, C_{DGc} = drag coefficient of bubble flow, slug flow and churn flow (—)
D = pipe diameter (m)
D_1, D_2 = see Fig. 1 (m)
d_S = particle diameter (m)
d_{sm} = sauter mean diameter of small bubbles (m)
E_0 = Eötvös number (—)
F_g = body force (N/m^3)
F_i = drag force (N/m^3)
F_v = virtual mass force (N/m^3)
F_w = friction force (N/m^3)
g = gravity acceleration (m/s^2)
j_k = volumetric flux for k-phase (m/s)
k_{vG} = virtual mass coefficient for gas-phase (—)
k_{vS} = virtual mass coefficient for solid-phase (—)
L = pipe length (m)
L_g, L_s, L_1, L_2 = see Fig. 1 (m)
M = Morton number (—)
M_k = mass flow rate for k-phase (kg/s)
P = pressure (Pa)
R = gas constant ($m^2/(s^2 \cdot K)$)
Re = Reynolds number (—)
r = weight factor (—)
T = absolute temperature (K)
u_k = velocity for k-phase (m/s)
u_m = superficial mixture velocity (m/s)
γ = submergence ratio (—)
ϵ_k = volumetric fraction for k-phase (—)
ϵ_b = see Eq. (24) (—)
ϵ_{Gs} = average void fraction in liquid slug (—)
λ = friction factor (—)
μ = viscosity (Pa · s)
ν = kinematic viscosity (m^2/s)
ρ = density (kg/m^3)
ρ_m = superficial mixture density (kg/m^3)
σ = surface tension (N/m)

Subscripts

a = top end of pipe
G = gas-phase
L = liquid-phase
m = mixture
S = solid-phase
0 = bottom end of pipe
1 = just before gas-injector
2 = just after gas-injector
3 = just before abrupt enlargement in diameter
4 = just after abrupt enlargement in diameter

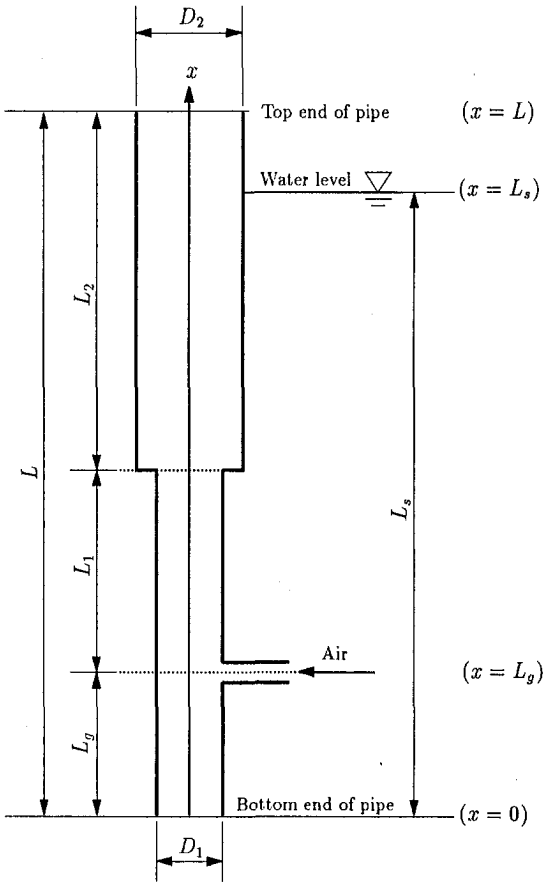

Fig. 1 Coordinate system along a vertical pipe adopted

previous work (1998), the case was treated where the multiphase mixture flows upward in a vertical pipe with a uniform cross-sectional area. Here, the flow field of the three-phase mixture in a vertical pipe with a sudden enlargement in diameter is examined. However, the governing equations are basically the same as those proposed in the previous work. Therefore, the system of equations will be mentioned below as briefly as possible.

First of all, let us define the coordinate system along a vertical lifting pipe. Figure 1 indicates the outline of the mixture flow system. x denotes the distance from the bottom end of the suction pipe ($x = 0$). The position of the top end of the upriser is denoted by $x = L$. The distance from the bottom end to the water surface level is denoted by $x = L_s(<L)$. The position of gas injection is set at $x = L_g$. The pipe length from the gas injector to the position of a sudden enlargement from D_1 to D_2 ($>D_1$) in pipe diameter is represented by L_1 and the length from this position ($x = L_g + L_1$) to the top end of the upriser ($x = L$) is denoted by L_2.

The general conservation equations of mass and momentum which govern each phase in the solid-gas-liquid three-phase flow field are given by

$$\frac{\partial(\rho_G\epsilon_G)}{\partial t} + \frac{\partial(\rho_G\epsilon_G u_G)}{\partial x} = 0 \tag{1}$$

$$\frac{\partial(\rho_L\epsilon_L)}{\partial t} + \frac{\partial(\rho_L\epsilon_L u_L)}{\partial x} = 0 \tag{2}$$

$$\frac{\partial(\rho_S\epsilon_S)}{\partial t} + \frac{\partial(\rho_S\epsilon_S u_S)}{\partial x} = 0 \tag{3}$$

$$\frac{\partial(\rho_G\epsilon_G u_G)}{\partial t} + \frac{\partial(\rho_G\epsilon_G u_G^2)}{\partial x} = -\left(F_{iG} + F_{wG} + F_{gG} + F_{vG} + \epsilon_G\frac{\partial P}{\partial x}\right) \tag{4}$$

$$\frac{\partial(\rho_L\epsilon_L u_L)}{\partial t} + \frac{\partial(\rho_L\epsilon_L u_L^2)}{\partial x} = -\left(F_{iL} + F_{wL} + F_{gL} + F_{vL} + \epsilon_L\frac{\partial P}{\partial x}\right) \tag{5}$$

$$\frac{\partial(\rho_S\epsilon_S u_S)}{\partial t} + \frac{\partial(\rho_S\epsilon_S u_S^2)}{\partial x} = -\left(F_{iS} + F_{wS} + F_{gS} + F_{vS} + \epsilon_S\frac{\partial P}{\partial x}\right) \tag{6}$$

in which t is the time. u, ϵ, ρ and P denote the velocity, volumetric fraction, density and pressure, respectively. Also, the subscripts G, L, and S denote the gas-, liquid-, and solid-phases, respectively. $F_{ik}(k = G, L, S)$ appearing in the momentum conservation equations denotes the drag force transferred to phase k (per unit volume) due to the interaction between phases. F_{wk} is the friction force transferred from pipe wall to phase k. F_{gk} is the gravity force exerted to phase k and F_{vk} is the virtual mass force acting to phase k in accelerating multiphase flow.

And the following relations,

$$P = \rho_G RT \tag{7}$$

$$\epsilon_G + \epsilon_L + \epsilon_S = 1 \tag{8}$$

must be satisfied. Here, R is the gas constant and T is the absolute temperature of gas-phase. T is regarded as constant, because the mixture flow field is assumed to be in a thermal equilibrium between phases and the temperature gradient is neglected along the lifting pipe. Since the volumetric fraction of solid-phase is very small compared with that of gas-phase, the interaction will be neglected between solid- and gas-phases.

Also, in order to practically evaluate the flow characteristics of the mixture flow, it is needed to formulate the external forces acting to phase k (F_{ik}, F_{wk}, F_{gk} and F_{vk}) appearing in Eqs. (4) to (6). Furthermore, the key issue in the accurate modelling of multiphase flow is to specify the constitutive terms, which include the phase interaction terms. The closure relationship used in the present theoretical model will be described in the next section.

3 Formulation of External Forces and Interactive Effects

3.1 Drag Force. First, the drag force F_{iG} transferred from liquid-phase to gas-phase is commonly defined by

$$F_{iG} = \tfrac{1}{8}\rho_L a_{iG} C_{DG}|u_G - u_L|(u_G - u_L) \tag{9}$$

where a_{iG} and C_{DG} denote the interfacial area concentration and drag coefficient, respectively. It is generally accepted that these depend strongly upon the flow pattern of gas-phase. Since the interfacial area concentration is a parameter which characterizes the flow structure, its mechanistic modelling is based upon the geometrical factors, gas volumetric fraction and flow pattern. The interfacial area per unit volume, which is proposed by Ishii et al. (1982), is given in a form of

$$a_{iG} = a_{iGb} = \frac{6\epsilon_G}{d_{sm}} \tag{10}$$

in the bubble flow regime and

$$a_{iG} = a_{iGs} = \frac{4.5}{D}\frac{\epsilon_G - \epsilon_{Gs}}{1 - \epsilon_{Gs}} + \frac{6\epsilon_{Gs}}{d_{sm}}\frac{1 - \epsilon_G}{1 - \epsilon_{Gs}} \tag{11}$$

in the slug flow regime. The interfacial area concentration a_{iGc} in the churn-turbulent flow regime is also evaluated by Eq. (11) in the calculation to be mentioned later. Here, D is the pipe diameter, ϵ_{Gs} and d_{sm} denote the average gas volumetric fraction in the liquid slug and the sauter mean diameter of the small bubbles in the liquid slug, respectively. Again, the following expression for ϵ_{Gs} proposed by Kurul and Podowski (1991),

$$\epsilon_{Gs} = \begin{cases} \epsilon_G & (0 < \epsilon_G < 0.25) \\ 0.3929 - 0.5714\epsilon_G & (0.25 \le \epsilon_G < 0.6) \\ 0.05 & (0.6 \le \epsilon_G < 1) \end{cases} \quad (12)$$

is introduced to the later calculation. According to this, the interfacial area concentration calculated by Eq. (11) agrees with the expression of Eq. (10) in the region of $0 < \epsilon_G < 0.25$ and it is suggested that the flow pattern corresponds to the bubble flow regime.

Furthermore, the following expression,

$$d_{sm} = 1.06\left(\frac{\sigma}{\rho_L^{1/3}}\right)^{1/3}\left\{\frac{\epsilon_G(1-\epsilon_G)D^2}{j(-dP/dx)}\right\}^{2/9} \quad (13)$$

is given by Kocamustafaogullari et al. (1994). Here, σ is the surface tension and j is the superficial velocity which is represented by the sum of the respective volumetric fluxes of solid-, gas- and liquid-phases ($j = j_G + j_L + j_S$).

Denoting the gas volumetric fraction by ϵ_1 when the transition from the bubble to slug flows begins to occur and by ϵ_2 when the transition to the slug flow reaches completion, we assume that

$$\epsilon_1 = 0.25 - 0.05 \quad (14)$$

$$\epsilon_2 = 0.25 + 0.05 \quad (15)$$

Also, indicating the volumetric fraction by ϵ_1 when the slug-churn transition begins to occur and by ϵ_2 when the transition to the churn flow just ends, it is assumed that

$$\epsilon_1 = 0.7415 - 0.05 \quad (16)$$

$$\epsilon_2 = 0.7415 + 0.05 \quad (17)$$

The above value, 0.7415, is determined by setting the drag coefficient of the slug flow to be equal to that of the churn flow, since the drag coefficient is given as a function of the gas volumetric fraction in the two regimes. In the transitional regions from the bubble to slug flows and the slug to churn flows, the following weight factor

$$r = \frac{1}{2}\left[1 + \sin\left\{\frac{\pi}{2}\left(\frac{2\epsilon_G - \epsilon_1 - \epsilon_2}{\epsilon_2 - \epsilon_1}\right)\right\}\right] \quad (18)$$

is introduced to the interpolation of the interfacial area concentration. For the transition ranges from the bubble to slug flows as well as from the slug to churn flows, the following relations,

$$\left.\begin{aligned} a_{iG} &= (1-r)a_{iGb} + ra_{iGs} \\ a_{iG} &= (1-r)a_{iGs} + ra_{iGc} \end{aligned}\right\} \quad (19)$$

are introduced. So that, the transition of the gas flow pattern does not discontinuously occur, but it continuously occurs.

Next, the interfacial drag coefficient of gas-phase differs depending upon the gas flow pattern. The drag coefficient, C_{DGb}, for a swarm of bubbles,

$$\left.\begin{aligned} C_{DGb} &= \frac{C_{DG0}}{\sqrt{\epsilon_L}} \\ C_{DG0} &= \max\left[\min\left[\frac{24}{Re_G}(1 + 0.15Re_G^{0.687}), \frac{72}{Re_G}\right], \frac{8}{3}\frac{E_0}{E_0+4}\right] \end{aligned}\right\} \quad (20)$$

is used to the calculation to be mentioned later (Tomiyama et al., 1995a, b). Here, Re_G and E_0 denote the bubble Reynolds number and the Eötvös number, respectively, and are defined by

$$\left.\begin{aligned} Re_G &= \frac{d_G|u_G - u_L|\rho_L}{\mu_L} \\ E_0 &= \frac{g(\rho_L - \rho_G)d_G^2}{\sigma} \end{aligned}\right\} \quad (21)$$

in which d_G is assumed to be d_{sm} (see Eq. (13)). Also, Eq. (20) is applicable on conditions that $10^{-3} < Re_G < 10^5$, $10^{-2} < E_0 < 10^3$ and $10^{-14} < M < 10^7$, where M is the Morton number defined by

$$\mathrm{M} = \frac{g\mu_L^4(\rho_L - \rho_G)}{\rho_L^2\sigma^3} \quad (22)$$

in which g is the acceleration due to the gravity and μ_L is the liquid-phase viscosity.

Furthermore, the interfacial drag coefficient of the slug flow C_{DGs} and that of the churn flow C_{DGc} are given by Ishii et al. (1982) as follows;

$$\left.\begin{aligned} C_{DGs} &= 9.8(1-\epsilon_b)^3 \\ C_{DGc} &= \tfrac{8}{3}(1-\epsilon_b)^2 \end{aligned}\right\} \quad (23)$$

respectively, in which

$$\epsilon_b = \frac{\epsilon_G - \epsilon_{Gs}}{1 - \epsilon_{Gs}} \quad (24)$$

In the present theoretical model, for the transition ranges from the bubble to slug flows as well as from the slug to churn flows, the following relations,

$$\left.\begin{aligned} C_{DG} &= (1-r)C_{DGb} + rC_{DGs} \\ C_{DG} &= (1-r)C_{DGs} + rC_{DGc} \end{aligned}\right\} \quad (25)$$

are introduced, where the weight factor r is the same as that defined in Eq. (18).

Next, since the solid particles to be lifted in the experiment to be mentioned later are incompressible and spherical in shape, the interfacial area concentration a_{is} is given by

$$a_{is} = \frac{6\epsilon_S}{d_S} \quad (26)$$

in which d_S is the diameter of solid spherical particles. Therefore, the interfacial drag force per unit volume exerted to the solid particles by the liquid-phase is given by

$$F_{iS} = \frac{3}{4}\frac{\epsilon_S}{d_S}\rho_L C_{Ds}|u_S - u_L|(u_S - u_L) \quad (27)$$

Also, the drag coefficient of solid particles is evaluated as a function of the particle Reynolds number Re_S by

$$C_{DS} = \begin{cases} \dfrac{24}{Re_S}(1 + 0.15Re_S^{0.687}) \\ \quad \left(Re_S = \dfrac{d_S|u_S - u_L|\rho_L}{\mu_L} \le 700\right) \\ \left\{\sqrt{\dfrac{24}{Re_S}} + 0.34\left(Re_S^{0.06} + \dfrac{1}{1.72 + 0.018Re_S}\right)\right\}^2 \\ \quad (700 < Re_S < 1.5 \times 10^5) \end{cases} \quad (28)$$

The interfacial drags F_{iG} and F_{iS} exerted to the gas- and solid-phases, respectively are based upon the interaction with the liquid-phase. Accordingly, the following relation

$$F_{iG} + F_{iL} + F_{iS} = 0 \quad (29)$$

holds between different phases.

3.2 Friction Force Between Mixture and Pipe Wall. The pressure drop occurs owing to interfacial friction between the

mixture and the pipe wall. Here, only the liquid-pipe wall interaction is taken into consideration, neglecting the gas-pipe wall and the solid particles-pipe wall friction. Therefore, the friction forces $F_{wk}(k = G, L, S)$ appearing in Eqs. (4) to (6) are evaluated by

$$\left.\begin{aligned} F_{wG} &= 0 \\ F_{wL} &= \frac{dP_f}{dx} = \frac{1}{2}\lambda\rho_m u_m^2 \frac{1}{D} \\ F_{wS} &= 0 \end{aligned}\right\} \tag{30}$$

in which P_f is the pressure loss. ρ_m is the mixture density given by

$$\left.\begin{aligned} \rho_m &= \epsilon_L\rho_L + \epsilon_S\rho_S \\ \rho_m &= \epsilon_G\rho_G + \epsilon_L\rho_L + \epsilon_S\rho_S \end{aligned}\right\} \tag{31}$$

in the two-phase and three-phase mixture flow regions, respectively, and u_m denotes the superficial mixture velocity given by

$$\left.\begin{aligned} u_m &= \epsilon_L u_L + \epsilon_S u_S \\ u_m &= \epsilon_G u_G + \epsilon_L u_L + \epsilon_S u_S \end{aligned}\right\} \tag{32}$$

in the two-phase and three-phase mixture flow regions, respectively. The friction factor λ needed in estimating the friction force is expressed by the Blasius-type equation based upon the superficial mixture velocity u_m and the liquid kinematic viscosity ν_L in the following form of

$$\lambda = C\left(\frac{u_m D}{\nu_L}\right)^{-n} \tag{33}$$

in which C and n are taken to be as 0.45 and 0.18 $\sim$ 0.22, respectively, in the calculation to be compared with experimental data, as will be mentioned later.

3.3 Body Force. The body force terms $F_{gk}(k = G, L, S)$ appearing in Eqs. (4) to (6) are given simply by

$$\left.\begin{aligned} F_{gG} &= \epsilon_G\rho_G g \\ F_{gL} &= \epsilon_L\rho_L g \\ F_{gS} &= \epsilon_S\rho_S g \end{aligned}\right\} \tag{34}$$

where g denotes the gravitational acceleration.

3.4 Virtual Mass Force. When one phase is accelerating relative to the other, the virtual mass force comes in play. The most general form of the one-dimensional and steady-state virtual mass acceleration is given by

$$a_{vm} = u_G\frac{d[u_G - u_L]}{dx} + (u_G - u_L)\left\{(\lambda_v - 2)\frac{du_G}{dx} + (1 - \lambda_v)\frac{du_L}{dx}\right\} \tag{35}$$

for the gas-phase in two-phase flow (Drew et al., 1979). Here, λ_v is the arbitrary parameter to be determined experimentally. Lahey et al. (1980) confirmed from the results of numerical nozzle/diffuser experiments for vertical co-current and counter-current flows that for the general a_{vm} case, with $\lambda_v = 1$ and $\lambda_v = 2$, very little difference in the calculated gas velocity u_G is evident, and that the answer is approximately unchanged, even when the virtual mass force is set to zero. From such a point of view, it is controversial whether or not the virtual mass force term need be introduced to the momentum conservation equations for each phase. Then, the following virtual mass terms for gas-phase and solid-phase,

$$F_{vG} = \epsilon_G\rho_L k_{vG}\left(u_G\frac{du_G}{dx} - u_G\frac{du_L}{dx}\right) \tag{36}$$

$$F_{vS} = \epsilon_S\rho_L k_{vS}\left(u_S\frac{du_S}{dx} - u_L\frac{du_L}{dx}\right) \tag{37}$$

are introduced in the later calculations. Here, k_{vG} and k_{vS} denote the virtual mass coefficient for gas- and solid-phases, respectively, and are given by Ransam (1981) as follows;

$$k_{vG} = \begin{cases} \frac{1}{2}\cdot\frac{1 + 2\epsilon_G}{1 - \epsilon_G} & (0 \le \epsilon_G < 0.5) \\ \frac{1}{2}\cdot\frac{3 - 2\epsilon_G}{\epsilon_G} & (0.5 \le \epsilon_G < 1) \end{cases} \tag{38}$$

and

$$k_{vS} = 0.5 \tag{39}$$

Again, since the virtual mass forces F_{vG} and F_{vS} exerted to the gas- and solid-phases, respectively, are based upon the interaction with the liquid-phase, the following balance law,

$$F_{vG} + F_{vS} + F_{vL} = 0 \tag{40}$$

holds between different phases.

By the way, we have examined the effect of the terms on the numerical results from various points of view. As a result, it has been confirmed that the results are almost unchanged in the calculations to be compared to the experimental data, as will be mentioned later, even though both F_{vG} and F_{vS} are set to be zero. However, one should bear in mind that Eqs. (36) and (37) are introduced in the calculations mentioned later.

3.5 Pressure Loss at the Sudden Enlargement of Cross Section. The pressure loss due to a sudden enlargement in diameter along a vertical pipeline is taken into consideration. Generally, the flow separates from the pipe wall, as it passes through the obstructing pipe fitting, resulting in the generation of eddies in the flow, with consequent pressure loss for the case of a sudden enlargement. In the calculation to be mentioned later, the pressure loss ΔP owing to a sudden expansion is given by

$$\Delta P = (P_4 - P_3) = \rho_{m3}u_{m3}^2\left(\frac{D_1}{D_2}\right)^2\left\{1 - \left(\frac{D_1}{D_2}\right)^2\right\} \tag{41}$$

in which the subscripts 3 and 4 denote quantities just before and after a sudden enlargement in pipe diameter, respectively. Also, ρ_m and u_m are defined by Eqs. (31) and (32), respectively.

4 Procedure of Numerical Calculation

The numerical calculation on the steady-state condition is based upon the numerical procedure mentioned in our previous works (Hatta et al., 1996; Fujimoto et al., 1997; and Hatta et al., 1998). In the present investigation, the case is treated where the solid-gas-liquid three-phase mixture flows upward in a vertical pipeline with a sudden enlargement from D_1 to D_2 in diameter, while in the previous works, the mixture flow field in a vertical pipeline with a uniform cross sectional area was numerically analyzed. Therefore, the present calculations of flow characteristics are performed by dividing an entire pipeline into the two parts. The flow characteristics of the mixture are calculated in the pipeline section of D_1 in diameter and then in the section after a sudden enlargement of D_2 in diameter. Figure 2 indicates a flow chart to obtain the numerical flow characteristics.

First, for a given gas volumetric flux j_{G2} $(= \epsilon_{G2}u_{G2})$, the gas and solid volumetric fractions ϵ_{G2}, ϵ_{S2} just after a gas-injector and the liquid and solid volumetric fluxes j_L and j_S are given tentatively and appropriately, where the subscripts 1 and 2 denote the state/condition just before and after the gas-injector, respectively. As a result, all the flow characteristics in the solid-liquid two-phase mixture flow region can be determined, even though these numerical results are tentative, as follows:

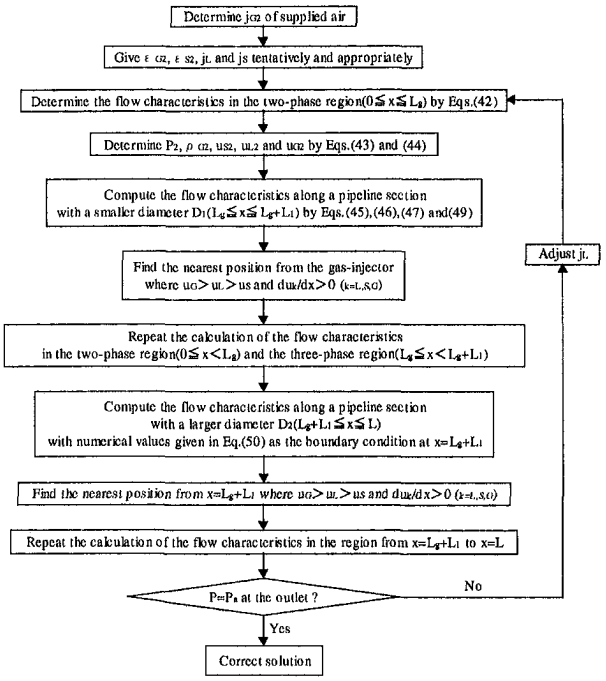

Fig. 2 A flow chart of iteration process

$$\left.\begin{aligned} \epsilon_{L2} &= 1 - \epsilon_{G2} - \epsilon_{S2} \\ \epsilon_{L1} &= \frac{\epsilon_{L2}}{1 - \epsilon_{G2}} \\ \epsilon_{S1} &= 1 - \epsilon_{L1} \\ u_{L1} &= \frac{j_L}{\epsilon_{L1}} \\ u_{S1} &= \frac{j_S}{\epsilon_{S1}} \end{aligned}\right\} \tag{42}$$

At this stage, all the flow characteristics in the solid-liquid two-phase mixture flow region have been obtained and therefore the static pressure and the gas density at the gas injector can be determined by

$$\left.\begin{aligned} P_2 &= P_0 - \rho_{m1} g L_g - \frac{1}{2}\lambda \rho_{m1}(j_L + j_S)^2 \frac{L_g}{D_1} \\ \rho_{G2} &= \frac{P_2}{RT} \end{aligned}\right\} \tag{43}$$

where P_0 is the static pressure at the bottom end of the suction pipe at $x = 0$. And the rising velocity for each phase just after the gas-injector is given by

$$\left.\begin{aligned} u_{S2} &= \frac{u_{S1}}{1 - \epsilon_{G2}} \\ u_{L2} &= \frac{u_{L1}}{1 - \epsilon_{G2}} \\ u_{G2} &= \frac{j_{G2}}{\epsilon_{G2}} \end{aligned}\right\} \tag{44}$$

At any rate, the eight flow characteristics (ϵ_{G2}, ϵ_{L2}, ϵ_{S2}), (u_{G2}, u_{L2}, u_{S2}), P_2 and ρ_{G2} have been determined at this stage. In this sense, it is obvious that the system of equations governing the solid-gas-liquid three-phase mixture flow field can be solved numerically with the above eight flow characteristics as the boundary condition at $x = L_g$. As mentioned already, emphasis is placed upon obtaining the steady-state flow characteristics of the solid-gas-liquid three-phase mixture as a function of x only, along a vertical pipe. Therefore, Eqs. (1) to (6) are independent of the time t. Also, since the virtual mass force terms are described in a form of differential equation, as shown in Eqs. (36) and (37), these equations need be incorporated into the momentum equations. Accordingly, Eqs. (4) to (6) can be rewritten into the following form of

$$\frac{dP}{dx} = C_1 + C_2 \frac{du_G}{dx} \tag{45}$$

$$\frac{du_L}{dx} = (A_1 + A_3 C_1) + (A_2 + A_3 C_2)\frac{du_G}{dx} \tag{46}$$

$$\frac{du_S}{dx} = \{B_1 + B_2 A_1 + (B_3 + B_2 A_3)C_1\} + \{B_2 A_2 + (B_3 + B_2 A_3)C_2\}\frac{du_G}{dx} \tag{47}$$

in which

$$\left.\begin{aligned} A_1 &= \frac{F_{iG} + F_{gG}}{k_{vG}\epsilon_G \rho_L u_G} \\ A_2 &= \frac{\rho_G u_G + k_{vG}\rho_L u_G}{k_{vG}\rho_L u_G} \\ A_3 &= \frac{1}{k_{vG}\rho_L u_G} \\ B_1 &= -\frac{F_{iS} + F_{gS}}{\epsilon_S u_S(k_{vS}\rho_L + \rho_S)} \\ B_2 &= \frac{k_{vS}\rho_L u_L}{u_S(k_{vS}\rho_L + \rho_S)} \\ B_3 &= -\frac{1}{u_S(k_{vS}\rho_L + \rho_S)} \\ C_1 &= -\frac{F_{wL} + F_{gG} + F_{gL} + F_{gS} + \frac{M_L}{A}A_1 + \frac{M_S}{A}(B_1 + B_2 A_1)}{1 + \frac{M_L}{A}A_3 + \frac{M_S}{A}(B_3 + B_2 A_3)} \\ C_2 &= -\frac{\frac{M_G}{A} + \frac{M_L}{A}A_2 + \frac{M_S}{A}B_2 A_2}{1 + \frac{M_L}{A}A_3 + \frac{M_S}{A}(B_3 + B_2 A_3)} \end{aligned}\right\} \tag{48}$$

where M_k ($k = G, L, S$) is the mass flow rate and A is the cross sectional area of pipe.

In order to compute the flow characteristics along a pipeline with a smaller diameter D_1, the computational region from $x = L_g$ to $x = L_g + L_1$ (substantially to $x = L$) is divided into numerous small parts and the above momentum equations are solved in the order of Eqs. (45), (46), and (47) by utilizing one of some numerical solution techniques for the initial value problem of ordinary differential equations. In the calculations to be mentioned later, the explicit Euler scheme is adopted. As a result of these numerical solutions, we have the numerical values for P, ρ_G ($=P/RT$), u_L and u_S at every nodal point. The distance between two neighbouring nodal points is taken to be 10^{-4} m throughout the entire pipe length. Thus, we have automatically the following values,

$$\left.\begin{aligned} \epsilon_L &= \frac{j_L}{u_L} \\ \epsilon_S &= \frac{j_S}{u_S} \\ \epsilon_G &= 1 - \epsilon_L - \epsilon_S \\ u_G &= \frac{\rho_{G2} j_{G2}}{\epsilon_G \rho_G} \end{aligned}\right\} \tag{49}$$

By the way, these numerical results must be unreasonable rather than reasonable, because the numerical calculation is performed with the tentative flow characteristics as the boundary condition at the gas-injector. Concretely speaking, the physically justifiable conditions that the velocity of the individual phase is in the order

of $u_G > u_L > u_S$, and that the axial velocity gradient for each phase is positive ($du_k/dx > 0$, $k = G, L, S$) are not always satisfied in the entire range from $x = L_g$ to $x = L_g + L_1$ (substantially to $x = L$).

Then, one must specify the nearest position from the gas-injector where the axial velocities for each phase are arranged in the order of $u_G > u_L > u_S$ and the velocity gradient is positive for each phase. By so doing, the recalculation can be performed by using ϵ_G and ϵ_S at this point instead of the previous ones. This operation must be repeated until ϵ_{G2} and ϵ_{S2} reach a constant value.

Secondly, the calculation must be continued along a pipeline section after a sudden enlargement in diameter. However, the creation of the boundary condition at the position of a sudden change in diameter (at $x = L_g + L_1$) is a little tedious at the start of the numerical calculation. The calculated flow characteristics just before the sudden change need be connected to the determination of the boundary condition in an appropriate form. Then, as a first step, the following flow characteristics,

$$\left.\begin{aligned} u_{L4} &= \left(\frac{D_1}{D_2}\right)^2 u_{L3} \\ u_{G4} &= \left(\frac{D_1}{D_2}\right)^2 u_{G3} \\ u_{S4} &= \left(\frac{D_1}{D_2}\right)^2 u_{S3} \\ \epsilon_{L4} &= \epsilon_{L3} \\ \epsilon_{S4} &= \epsilon_{S3} \\ \epsilon_{G4} &= 1 - \epsilon_{L4} - \epsilon_{S4} \\ P_4 &= P_3 + \rho_{m3} u_{m3}^2 \left(\frac{D_1}{D_2}\right)^2 \left\{1 - \left(\frac{D_1}{D_2}\right)^2\right\} \\ \rho_{G4} &= \frac{P_4}{RT} \end{aligned}\right\} \quad (50)$$

are given tentatively and imposed on the boundary condition at the position of the sudden change. Here, the subscripts 3 and 4 denote the state/condition just before and after the abrupt change in diameter. Thus, we can numerically solve the system of governing equations and obtain all of the flow characteristics P, ρ_G, u_L, u_S, ϵ_L ($=j_L/u_L$), ϵ_S ($=j_S/u_S$), ϵ_G and u_G at every nodal point in the entire range from the position of a sudden change ($x = L_g + L_1$) to the outlet of the upriser ($x = L$). However, the numerical flow characteristics except P_4 and ρ_{G4} can be also unreasonable rather than reasonable, since the numerical solutions are obtained with the tentative flow characteristics as the boundary condition at $x = L_g + L_1$. That is to say, the axial velocity gradient for each phase is not always guaranteed to be positive in entire range from $x = L_g + L_1$ to $x = L$. Then, we specify the nearest position from the cross section of the abrupt enlargement where the axial velocity gradient is positive for each phase and using the volumetric fractions for each phase at this position, the following values

$$\left.\begin{aligned} u_{L4} &= \frac{j_L}{\epsilon_{L4}} \\ u_{S4} &= \frac{j_S}{\epsilon_{S4}} \\ u_{G4} &= \frac{\rho_{G2} j_{G2} D_1^2}{\rho_{G4} \epsilon_{G4} D_2^2} \end{aligned}\right\} \quad (51)$$

can be obtained. So, the recalculation is performable. The above numerical process is repeated for the establishment of the boundary condition at $x = L_g + L_1$.

Next, attention must be paid to whether the pressure at the outlet section of the upriser reaches the atmospheric pressure ($P = P_a$ at $x = L$), where the subscript a denotes the atmospheric state. If P is different from P_a at $x = L$, the recalculation must be performed from the start by adjusting the volumetric flux j_L of liquid-phase. At any rate, the three conditions that

1 $u_G > u_L > u_S$
2 $du_k/dx \geq 0$ ($k = G, L, S$)
3 $P = P_a$ at $x = L$

must be satisfied. The above-mentioned numerical procedure is repeated in such a way as to obtain the numerical flow characteristics satisfying these conditions.

5 Experiments

In order to confirm the applicability of the above-mentioned system of governing equations to the prediction of the characteristics of the solid-gas-liquid three-phase mixture flow as well as the validity of the above procedure of the numerical calculation, it is indispensable to compare the flow characteristics calculated on the basis of the present model with experimental data. Then, the experiments have been performed using glass spheres as the solid particles, and air and water as the working fluids. In these experiments, the ratio of the small pipe diameter D_1 to the large pipe diameter D_2, the ratio of the pipe length L_1 of D_1 in diameter to the one L_2 of D_2 in diameter and the submergence ratio have been changed systematically.

Figure 3(a) indicates the schematic view of our experimental apparatus. The body of the air-lift pump consists of two parts. One of which is a suction pipe of L_g in length. The other is an upriser of $(L_1 + L_2)$ in length and the diameter of the upriser is abruptly changed from D_1 to D_2 ($>D_1$) at $x = L_g + L_1$. Also, the experiments have been performed using a vertical and straight pipe with a uniform cross-sectional area ($D_1 = D_2$) to be compared with the case of $D_1 < D_2$. A suction box, where the bottom end of the suction pipe is gas-tightly inserted, is connected to a water reservoir through a sufficiently large pipe of 146 mm in diameter. The water surface level in the reservoir can be adjusted by discharging water from a pipe jointed to the hole of the side wall of the reservoir, where several holes are bored at appropriate levels to examine the effect of the submergence ratio γ defined by

$$\gamma = \frac{L_s - L_g}{L - L_g} \quad (52)$$

on the operation performance of air-lift pump. A pumping action is caused by injecting air into the bottom of the upriser through an air-injector.

Also, the solid particles, which fall down through the pipe by gravity from the piston-type particle feeder to the semicircular trough attached to the bottom end of suction pipe in the suction box, are sucked into the lifting pipe along with the water. The trough diameter is taken to be equal to that of the suction pipe. A lot of holes smaller than the particle size are drilled on the trough side. The water flows into the trough through both ends of it and these small holes. Therefore, the solid particles are designed to be sucked automatically into the suction pipe owing to the stream of water.

The air-lift pump is confirmed to be steadily operated by supplying air and solid particles at a fixed flow rate and keeping the water level in the water reservoir constant. The air-injector consists of two circular nozzles of 5.0 mm in inner diameter and they are fixed opposite to each other, as shown in Fig. 3(b). The injected air is merged into the solid-water two-phase mixture lifting in the suction pipe through the air-injector. The solid-gas-liquid three-phase mixture flows upward through first the smaller diameter part and then the larger diameter part of the upriser and is discharged into an air separator. The air is released into the atmosphere and the solid-water mixture is transported to a particle-water separator.

In order to measure the respective flow rates of the water and the particles, the water is led to a sampling tank and the particles are led to a scale. Also, the air flow rate is measured by the flow meter and the pressure gauge.

The same experiments have been repeated ten times or more and the respective flow rates of water and particles have been measured each time to determine the average rate for every run. The scatter bands of the measured values of solid particles and the water

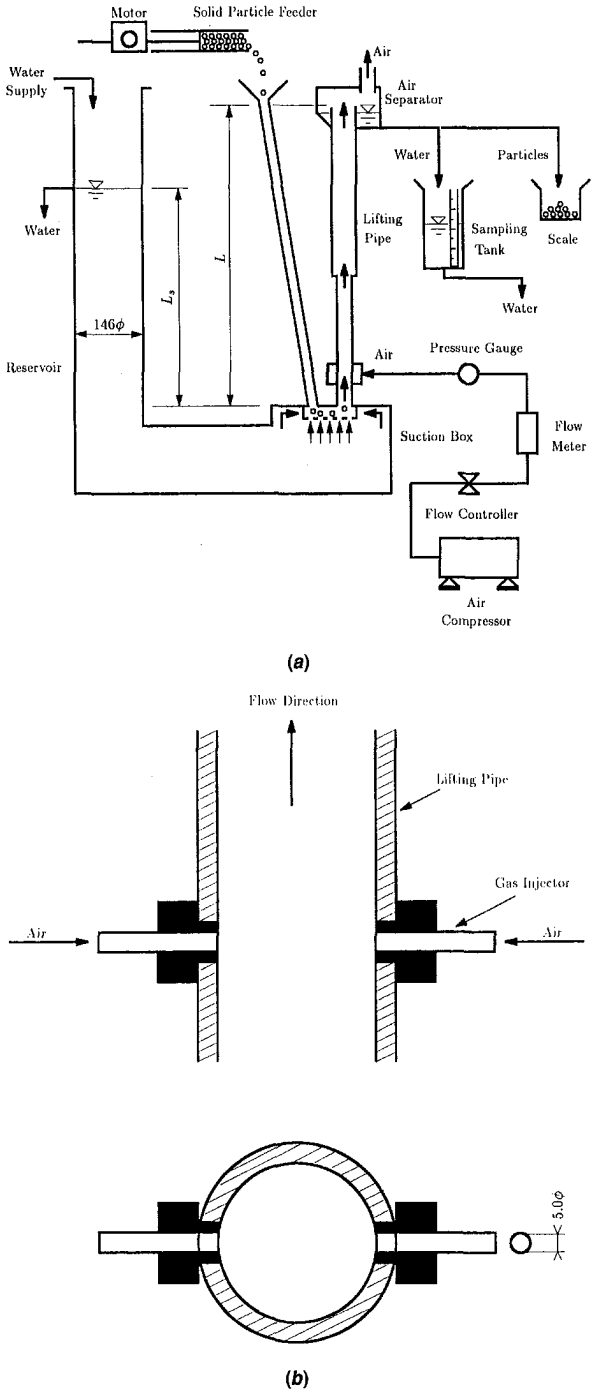

Fig. 3 Schematic view of experimental apparatus (*a*) and arrangement of gas injector attached to a vertical pipe (*b*)

discharged from the top of the upriser have been within ±5% and ±3%, respectively. The error for the flow rate of supplied air has been confirmed to be in the range within ±2%.

6 Results and Discussion

In order to examine the applicability of the present theoretical model built up based upon the multifluid model to the case where the solid-gas-liquid three-phase mixture flows upward in a vertical pipe with a sudden change in diameter, the calculated results obtained by this model have been compared with the data measured using the above-mentioned experimental apparatus. Here, the correspondence of the predicted values to the measured ones will be discussed from a qualitative and quantitative point of view.

Table 1 List of the common numerical values introduced into the calculation

d_S	=	0.0052	(m)
ρ_S	=	2500	(kg/m^3)
L	=	3.0	(m)
P_a	=	1.0×10^5	(Pa)
T	=	293	(K)
R	=	287	(m^2/(s^2 · K))
ρ_L	=	1000	(kg/m^3)
ν_L	=	1.0×10^{-6}	(m^2/s)
g	=	9.8	(m/s^2)
σ	=	7.2×10^{-2}	(N/m)

Table 1 indicates the common numerical values introduced into the calculation. It is added to note that $P_0 = P_a + \rho_L g L_s$.

Table 2 shows the dimensions of four kinds of lifting pipes utilized in the present experiments and the experimental conditions. The total length L ($=L_g + L_1 + L_2$) is fixed at 3000 mm and the length L_g of the suction pipe is 170 mm long for every lifting pipe. Also, in order to see the effect of the submergence ratio γ on the operation performance of air-lift pump, three kinds of ratios have been taken at $\gamma = 0.537, 0.650, 0.795$.

Figures 4(*a*) to (*c*) demonstrate the comparisons of the numerical results calculated on the basis of the present theoretical model with the experimental results obtained using the No. 1 pipe whose diameter is kept constant in the entire range of the lifting pipe. Figures (*a*), (*b*), and (*c*) correspond to the cases where $\gamma = 0.537$, 0.650 and 0.795, respectively. These figures indicate the variation of volumetric flux j_L of liquid-phase against the volumetric flux j_{Ga} of supplied air reduced to the atmospheric state with the volumetric flux j_S of solid-phase as a parameter. The calculated values shown by solid line can be seen to give qualitatively and quantitatively good fit to the experimental results shown by solid and empty circle. The solid circles indicate the case of $j_S = 0$. Also, the increase in the submergence ratio γ shows a tendency to raise j_L and j_S. But when γ is kept too small, it seems to be difficult to convey the solid particles upward owing to decreasing the bottom pressure P_0. In addition, these figures show that as j_{Ga} is increased, j_L first increases in a fairly sharp state, reaches a maximum and then decreases gradually. This is considered to be basis of the fact that the increase in supplied air makes the flow velocities for each phase high and so do the pressure drops more remarkably due to the friction between the mixture and the inner wall of pipe.

Figures 5(*a*) to (*c*) exhibit the comparison between the calculated and experimental results. This is the case of a sudden enlargement from $D_1 \doteq 18$ mm to $D_2 = 22$ mm in diameter at $x =$

Table 2 List of dimensions of lifting pipes used and experimental conditions

Number of pipe	Diameter (mm) D_1	Diameter (mm) D_2	Length of pipe (mm) L_g	Length of pipe (mm) L_1	Length of pipe (mm) L_2	Submergence ratio γ	Solid volumetric flux j_s (m/s)		
1	18	18	170	2830	-	0.537	0		
						0.650	0	0.017	
						0.795	0	0.027	
2	18	22	170	1830	1000	0.537	0	0.009	
						0.650	0	0.015	
						0.795	0	0.017	
3	18	22	170	830	2000	0.537	0	0.009	0.016
						0.650	0	0.009	0.019
						0.795	0	0.010	0.019
4	20	28	170	830	2000	0.537	0	0.008	0.015
						0.650	0	0.008	0.015
						0.795	0	0.008	0.015

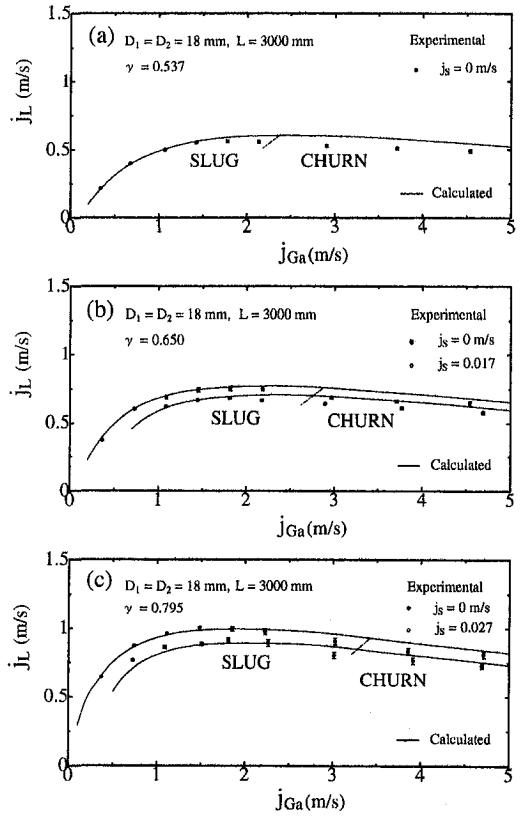

Fig. 4 Comparison between numerical and experimental results for D_1 = D_2 = 18 mm, L_1 = 2830 mm (L_2 = 0 mm), L = 3000 mm, γ = 0.537 (*a*), 0.650 (*b*) and 0.795 (*c*)

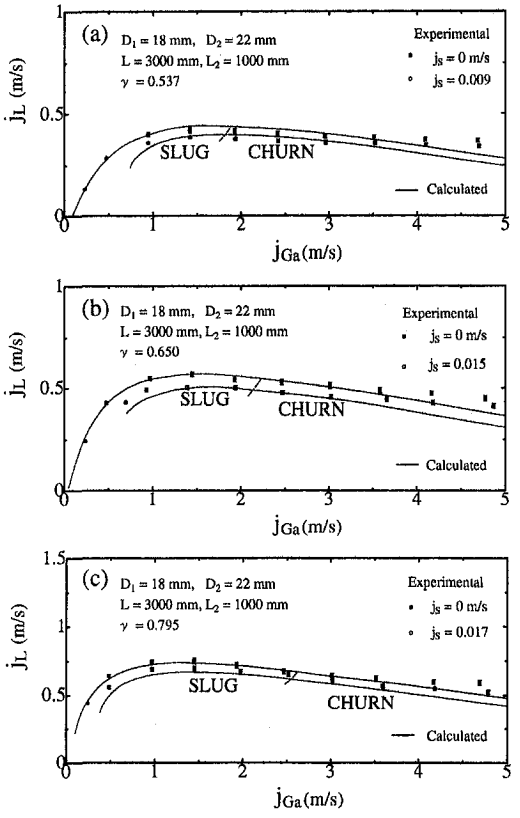

Fig. 5 Comparison between numerical and experimental results for D_1 = 18 mm, D_2 = 22 mm, L_1 = 1830 mm, L = 3000 mm, γ = 0.537 (*a*), 0.650 (*b*) and 0.795 (*c*)

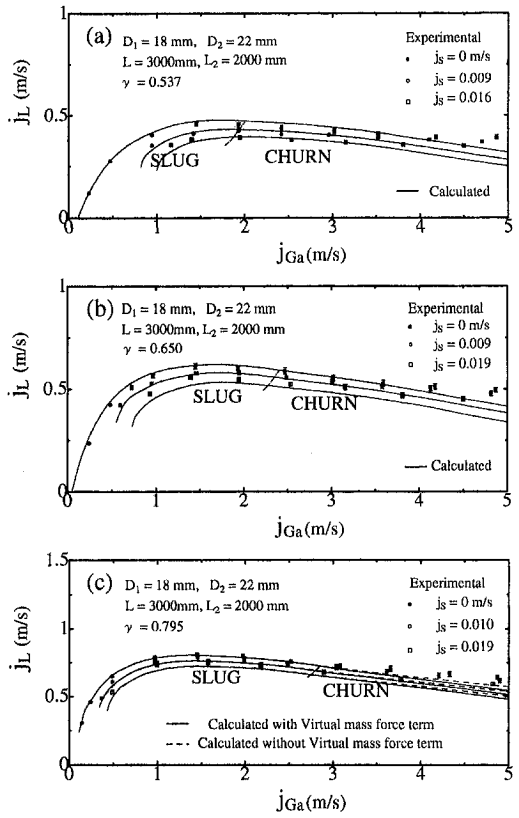

Fig. 6 Comparison between numerical and experimental results for D_1 = 18 mm, D_2 = 22 mm, L_1 = 830 mm, L = 3000 mm, γ = 0.537 (*a*), 0.650 (*b*) and 0.795 (*c*)

2000 mm. j_{Ga}, j_L and j_S are represented by the values of the large diameter part of the upriser, although the respective volumetric fluxes have the difference between the smaller and larger diameter parts of the upriser. The results calculated on the basis of the present theoretical model are seen to give sufficiently good fit to the experimental ones for every submergence ratio.

Figures 6(*a*) to (*c*) give the relation between the experimental data and the calculated value for γ = 0.537, 0.650 and 0.795, respectively. The experiments have been made using the lifting pipe of No. 3 shown in Table 2. Although each diameter of the smaller and larger pipes is the same as the case of the No. 2 lifting pipe, the length of the larger pipe is different from that of the No. 2. The numerical results calculated on the basis of the present theoretical model can be regarded to agree with the experimental data from a qualitative and quantitative point of view. By the way, the dotted lines indicate the numerical value calculated neglecting the virtual mass force terms for gas- and solid-phases. Although a little effect of these terms on the calculated values appears with the increase in j_{Ga}, the difference between the two seems negligibly small.

Figures 7(*a*) to (*c*) demonstrate the comparisons of the calculated results with the experimental data for the lifting pipe of No. 4 shown in Table 2. The respective diameters of the smaller and larger pipes are different from the previous experimental cases. It may be accepted from these figures that the numerical results obtained on the basis of the present numerical model give good agreement with the experimental data for γ = 0.537, 0.650, and 0.795, respectively.

Here we wish to slightly discuss the efficiency of solid collection using Figure 7(*c*). The dotted lines drawn in this figure indicate the predicted evolution of j_L against j_{Ga} with j_S as a parameter for γ = 0.795. It can be understood that j_L becomes lower at a certain j_{Ga} with increasing j_S. Also, this figure shows that no solution can exist under the chain line. The width where the

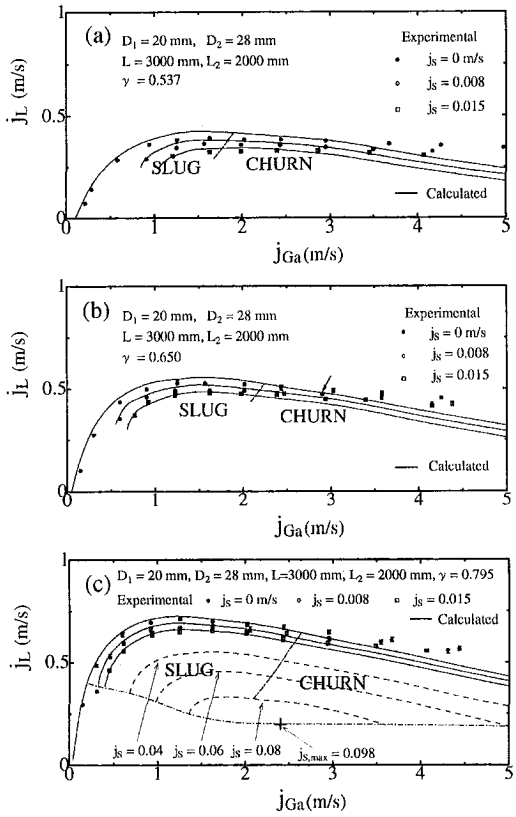

Fig. 7 Comparison between numerical and experimental results for D_1 = 20 mm, D_2 = 28 mm, L_1 = 830 mm, L = 3000 mm, γ = 0.537 (*a*), 0.650 (*b*) and 0.795 (*c*)

volumetric flux j_{Ga} of supplied air can exist becomes smaller as j_S is increased. For example, j_{Ga} is limited in the region from 1.36 m/s to 3.60 m/s for j_S = 0.08 m/s. As j_S is further increased, j_{Ga} approaches an unique value. When j_S reaches the maximum value $j_{S,\max}$, both j_L and j_{Ga} take a unique value. In the present situation, the point shown by plus sign + on the chain line corresponds to $j_{S,\max}$ = 0.098 m/s. In this case, the solution of j_L = 0.198 m/s and j_{Ga} = 2.40 m/s is obtainable.

Figures 8(*a*) to (*c*) demonstrate the numerical flow characteristics calculated on condition that γ = 0.650, j_S = 0.008 m/s and j_{Ga} = 2.91 m/s. This corresponds to the experimental results obtained using the No. 4 pipe, shown in Table 2. This is the result of the case where the gas volumetric fraction ϵ_G is remarkably large. Since $\epsilon_G \simeq 0.8$, the gas flow pattern seems to belong to the churn flow. Also, the velocity for each phase jumps discontinuously at the position of the sudden change in diameter. ϵ_G drops while ϵ_L jumps discontinuously at the position of the abrupt enlargement in diameter and the pressure gradient is seen to drop in an almost linear manner along a pipeline. Again, the pressure gradient changes a little more gradually after the gas-injector than before it, and the pressure jumps discontinuously at the position of the sudden expansion.

Next, the flowing process for each phase will be discussed from a photographic point of view. Concretely speaking, there is a velocity difference between the solid- and liquid-phases and consequentially it comes into question whether the solid particles fall, rise or stop in a gas slug through the gas/liquid interface, or the particles are distributed uniformly in the liquid phase.

Then, in order to examine the solid particle behavior visually, the moving process of the solid particles is recorded by using a high speed video camera (PHOTRON, FASTCAM-hvc-1). The solid particles moving in a vertical pipe of 22 mm in inner diameter have been photographed in the range from x = 1388 mm to x = 1410 mm in height. The view is 22 mm × 22 mm and taken to be equal to the inner diameter of pipe.

Figures 9(*a*) to (*d*) are a sequence of photographs showing the moving process of two solid particles in a gas slug for j_{Ga} = 0.702 m/s (ϵ_G = 0.570), j_L = 0.307 m/s, and j_S = 0.005 m/s. The submergence ratio is fixed at γ = 0.537. Here, it should be noted that only ϵ_G is the calculated value at a corresponding position. These photographs are output by the video printer at regular time intervals of 5/120 s. The two solid particles observed in Figure 9(*a*) are confirmed to once rise, as shown in Fig. 9(*b*). But, they are observed to fall down along with some small liquid droplets after a while. Finally, they go out of view and another solid particle in the upper part comes into view, as shown in Fig. 9(*d*).

Figures 10(*a*) to (*d*) show the moving process of a solid particle near the top of a gas slug on condition that j_{Ga} = 3.78 m/s (ϵ_G = 0.853), j_L = 0.365 m/s, j_S = 0.013 m/s and γ = 0.537. These photographs are output at regular time intervals of 1/120 s. This time interval corresponds to one fifth of the previous case. This is because the particle is rapidly changeable in this experimental situation. It can be observed in every photograph that the solid particle rises along with many small and large droplets even in a gas slug. These droplets are considered to be produced when the solid particles pass through the gas/liquid interface. Also, it is characteristic that there are many small gas bubbles in a liquid film. At any rate, all of the particles have been observed to rise along a pipeline also in other consecutive photographs taken on this condition. The flow is, however, very chaotic, frothy and disordered.

Figures 11(*a*) to (*d*) are a consequence of photographs showing the moving process of some solid particles in a gas bubble on condition that j_{Ga} = 0.748 m/s (ϵ_G = 0.451), j_L = 0.684 m/s, j_S = 0.013 m/s and γ = 0.795. These photographs are output at regular time intervals of 1/120 s. All the particles appearing in these photographs are observed to rise along with some liquid droplets in the gas slug. Also, it is noticeable that there are small

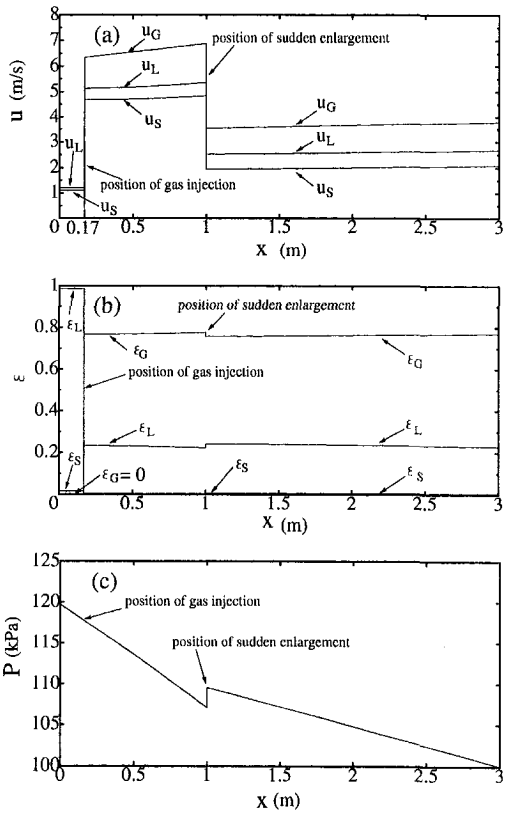

Fig. 8 Velocity distributions for each phase (*a*), volumetric fractions for each phase (*b*) and pressure (*c*) along a vertical pipeline of D_1 = 20 mm, D_2 = 28 mm, L_1 = 830 mm and L = 3000 mm for j_{Ga} = 2.91 m/s, j_S = 0.008 m/s and γ = 0.650. Note that this corresponds to the experimental results shown by the arrow in Fig. 7(*b*)

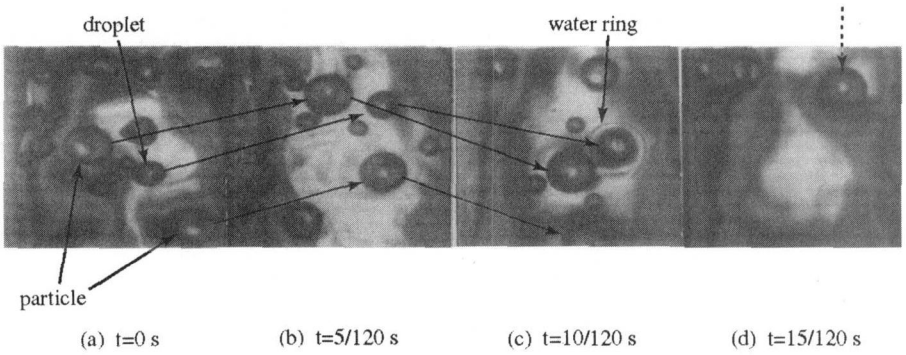

Fig. 9 A sequence of photographs showing moving process of two solid particles in a gas slug for j_{Ga} = 0.702 m/s, j_L = 0.307 m/s, j_S = 0.005 m/s and γ = 0.537

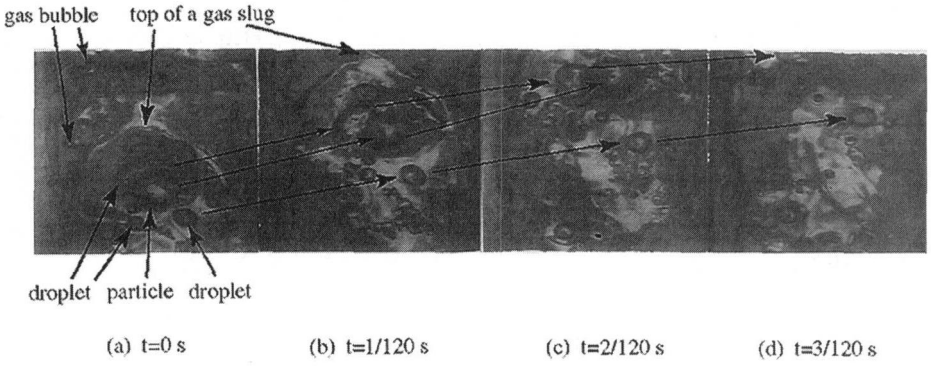

Fig. 10 A sequence of photographs showing moving process of a solid particle near the top of gas slug for j_{Ga} = 3.78 m/s, j_L = 0.365 m/s, j_S = 0.013 m/s and γ = 0.537

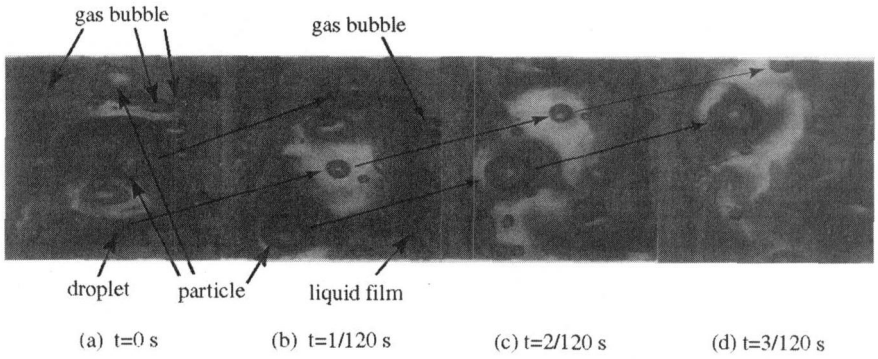

Fig. 11 A sequence of photographs showing moving process of some solid particles in a gas bubble for j_{Ga} = 0.748 m/s, j_L = 0.684 m/s, j_S = 0.013 m/s and γ = 0.795

gas bubbles in the liquid slug and film. It can be imagined that the particles in a gas slug are caught up with the chasing gas/liquid interface and then move in a liquid slug, since the rising velocity of the solid particles is considerably smaller than that of gas-phase. Thereby, the solid particles continue to rise owing to the momentum transferred from the liquid phase. As the momentum becomes larger with increasing the submergence ratio, the particles are apt to move upward in this situation compared with the case of Fig. 9.

Figures 12(*a*) to (*d*) demonstrate the moving process of a particle on condition j_{Ga} = 3.97 m/s (ϵ_G = 0.802), j_L = 0.625 m/s and j_S = 0.014 m/s. The submergence ratio is set at γ = 0.795. The photographs are output at regular time intervals of 1/120 s. A particle located at a lower position in Fig. 12(*a*) can no longer be seen in Fig. 12(*d*). Since ϵ_G is relatively large, the gas slug appearing in Fig. 12(*c*) and (*d*) is quite chaotic and distorted and a large numbers of small gas bubbles are seen in liquid slug. At any rate, the particles are conveyed upward very rapidly.

It has been found that the moving process of solid particles is governed strongly by the volumetric flux of gas-phase and the submergence ratio. First, the particles are apt to rise in a vertical pipe with increasing the submergence ratio. Second, the particles are easier to move upward when the flow field in a vertical pipe is more chaotic, frothy and disordered by increasing the volumetric flux of gas-phase.

In reality, there is a velocity slip between the solid- and liquid-phases and it seems reasonable to consider that the velocity of the solid particles are slower than that of the liquid-phase. Then, it follows that the solid particles possibly reach the gas/liquid interface. However, the moving process of such particles seems to be complicated at the interface. The solid particles, in some cases, can be pulled upward due to the surface tension with almost the same velocity as that at the top of the gas slug. Furthermore, as shown in the above figures, some cases can be observed where the solid-particles fall, ascend and/or stop. Regardless of such a com-

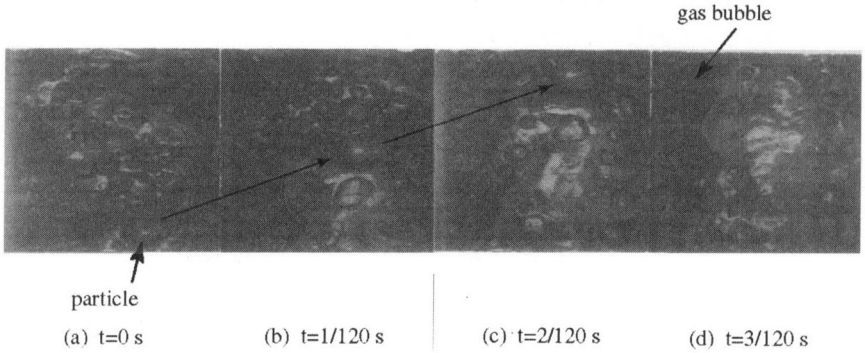

Fig. 12 A sequence of photographs showing moving process of a solid particle for j_{Ga} = 3.97 m/s, j_L = 0.625 m/s, j_S = 0.014 m/s and γ = 0.795

plicated moving process of the solid particles, the present numerical model has been built up on the premise that the particles are distributed uniformly in a liquid phase. As a result, it has been found that the present model gives sufficiently accurate prediction of the flow rates of lifted water and solid particles against that of air supplied. Finally, we believe that the model is valid, at least, for the prediction of global parameters like flow rates or volumetric fluxes. However, it should be added to note that the respective parameters such as the pressure, the moving velocities or the volumetric fractions for each phase along the pipe must be random and oscillatory around a mean value and the numerical flow characteristics calculated on the basis of the present model provide the mean value.

7 Conclusion

This paper has treated the numerical analysis of flow characteristics of the solid-gas-liquid three-phase mixture moving upward along a vertical pipeline with a sudden expansion in the cross sectional area. The system of governing equations is built up based upon the one-dimensional multifluid model, taken into account the transitions of gas flow pattern. For the case of an abrupt change in diameter in the coaxial pipeline, the calculation for the steady-state operation performance of the air-lift pump has been performed by dividing the total pipeline into the two sections. First, the flow characteristics in the smaller diameter pipeline section have been calculated on the basis of the above-mentioned theoretical model. Next, the flow characteristics in the larger diameter pipeline section have been evaluated on the basis of the numerical procedure proposed here. In order to verify the validity of the system of governing equations as well as the procedure of the numerical calculation, the experiments have been made for obtaining the measured data using four kinds of lifting pipes. The comparisons between the calculated and experimental values have been attempted. As a result, it has been found that the present theoretical model gives sufficiently accurate prediction of the flow rates of lifted water and solid particles against that of air supplied for the case of a sudden enlargement in diameter. Also, it has been confirmed that it is very significant to abruptly expand the cross sectional area in order to improve the pump efficiency, as will be encountered in a very large-scale air lift pump to convey the marine mineral resources like manganese nodules at the deep-sea bed of about 5000 m in depth of water. Additionally, it has been demonstrated that the maximum solid/liquid volumetric flux can be predicted on the basis of the present model (see Fig. 7(*c*)).

Furthermore, the flowing process for each phase has been investigated from a photographic point of view. It has been found that the moving process of solid particles is governed strongly by the volumetric flux of gas-phase and the submergence ratio. First, the solid particles are apt to rise in a vertical pipe as the submergence ratio becomes larger. Second, the particles show a stronger rising tendency as the mixture flow field in a vertical pipe becomes more chaotic, frothy and disordered by increasing the volumetric flux of gas-phase.

Here, the emphasis has been placed upon predicting the steady-state flow characteristics. We wish to add to note that the system of equations can be extended to grasping the transitional numerical solutions, although it is difficult to establish the transitional situation of the multiphase flow in a vertical pipe. Again, we would like to propose an optimal logical design such that the gas flow pattern can be controlled for the solid-gas-liquid three-phase mixture lifting along a vertical pipeline. In particular, for a large-scale air-lift pump, it is inevitably important where and how the abrupt enlargement in pipe diameter should be made along a long vertical pipeline.

References

Drew, D., Cheng, L., and Lahey, Jr. R. T., 1979, "The Analysis of Virtual Mass Effects in Two-Phase Flow," *International Journal of Multiphase Flow,* Vol. 5, pp. 233–242.

Fujimoto, H., Isobe, M., Fukui, T., and Hatta, N., 1997, "Effect of Pressure Drop owing to Friction between Pipe Inner Wall and Water on Non-Equilibrium Flow Fields in an Air-Lifting Pipe-4th report," (in Japanese), *Shigen-to-Sozai,* Vol. 113, pp. 133–139.

Griffith, P., and Wallis, G. B., 1961, "Two-Phase Slug Flow," ASME *Journal of Heat Transfer,* Vol. 83, pp. 307–320.

Hatta, N., and Fujimoto, H., 1996, "Theoretical Analysis for Non-Equilibrium Flow Fields with Transitional Process from Two-Phase to Three-Phase Mixtures by Injecting Air Halfway into a Lifting Pipe-3rd report," (in Japanese), *Shigen-to-Sozai,* Vol. 112, pp. 81–88.

Hatta, N., Fujimoto, H., Isobe, M., and Kang, J.-S., 1998, "Theoretical Analysis of Flow Characteristics of Multiphase Mixtures in a Vertical Pipe," *International Journal of Multiphase Flow,* Vol. 24, pp. 539–561.

Hewitt, G. F., and Hall-Taylor, N. S., 1970, Annular Two-Phase Flow, Pergamon Press.

Ishii, M., Mishima, K., Kataoka, I., and Kocamustafaogullari, G., 1982, "Two-Fluid Model an Importance of the Interfacial Area in Two-Phase Flow Analysis," *Proc. 9th U.S. National Congress of Applied Mechanics,* Ithaca, New York, pp. 73–80.

Kamata, C., and Ito, K., 1995, "Cold Model Experiments on the Application of Gas Lift Pump to the Transportation of Molten Metal," *ISIJ International,* Vol. 35, pp. 859–865.

Kawashima, T., Noda, K., Masuyama, T., and Oda, S., 1975, "Hydraulic Transport of Solids by Air Lift Pump," (in Japanese), *Journal of the Mining and Metallugical Institute of Japan,* Vol. 91, pp. 765–772.

Kocamustafaogullari, G., Huang, W. D., and Razi, J., 1994, "Measurement and modeling of average void fraction, bubble size and interfacial area," *Nuclear Engineering and Design,* Vol. 148, pp. 437–453.

Kurul, N., and Podowski, M. Z., 1991, *ANS Proc. 1991,* National Heat Transfer Conference, Minneapolis.

Lahey, R. T., Cheng, L. Y., Drew, D. A., and Flaherty, J. E., 1980, "The Effect of Virtual Mass on the Numerical Stability of Accelerating Two-Phase Flows," *International Journal of Multiphase Flow,* Vol. 6, pp. 281–294.

Ransam, V. H., et al., 1981, *RELAP 5/MOD 1 Code Manual,* Vol. 1, *System Models and Numerical Methods,* NUREG/CR-1826.

Saito, T., Tomishima, Y., Yamasaki, T., Usami, T., Yokokawa, A., and Shimizu, Y., 1986, "Lifting Characteristics of Manganese Nodules by Air Lift Pump Under Steady Conditions—1st Report, Fundamental Results of 200 m Test Plant," (in Japanese), *Saiko-to-Hoan,* Vol. 32, pp. 540–551.

Taitel, Y., Bornea, D., and Dukler, A. E., 1980, "Modeling Flow Pattern Transitions for Steady Upward Gas-Liquid Flow in Vertical Tubes," *AIChE Journal,* Vol. 26, pp. 345–354.

Tomiyama, A., Kataoka, I., and Sakaguchi, T., 1995, "Drag Coefficients of Bubbles—1st Report, Drag Coefficients of a Single Bubble in a Stagnant Liquid," *JSME Journal of Fluid Engineering,* Vol. 61, pp. 2357–2364.

Tomiyama, A., Kataoka, I., and Sakaguchi, T., 1995, "Drag Coefficients of Bubbles—2nd Report, Drag Coefficients for a Swarm of Bubbles and its Applicability to Transient Flow," *JSME Journal of Fluid Engineering,* Vol. 61, pp. 2810–2817.

Usami, T., and Saito, T., 1986, "Studies on the hydraulic Lifting of Solids by Air-Lift Pump," (in Japanese), Report of the National Research Institute for Pollution and Resources, pp. 1–104.

Weber, M., and Dedegil, Y., 1976, *Hydrotransport,* Vol. 4, H1-1–H1-23.

Yoshinaga, T., Sato, Y., and Sadatomi, M., 1990, "Characteristics of Air-Lift Pump for Conveying Solid Particles," (in Japanese), *Japanese Journal of Multiphase Flow,* Vol. 4, pp. 174–191.

Yoshinaga, T., and Sato, Y., 1996, "Performance of an Air-Lift Pump for Conveying Coarse Particles," *International Journal of Multiphase Flow,* Vol. 22, pp. 223–238.

A Domain Decomposition Approach for Incompressible Flows Past Multiple Objects

Hwar-Ching Ku
Professional Senior Engineer,
Johns Hopkins Applied Physics Laboratory,
Johns Hopkins Road, Laurel, MD
20723-6099

Bala Ramaswamy
Associate Professor,
Department of Mechanical and
Environmental Engineering,
University of California at Santa Barbara,
Santa Barbara, CA 93106-5070
e-mail: BALA@engineering.ucsb.edu

A domain decomposition approach has been developed to solve for flow around multiple objects. The method combines features of mask and multigrid algorithm implemented within the general framework of a primitive variable, pseudospectral elements formulation of fluid flow problems. The computational domain consists of a global rectangular domain, which covers the entire flow domain, and local subdomains associated with each object, which are fully overlapped with the rectangular domain. There are two key steps involved in calculating flow past multiple objects. The first step approximately solves the flow field by the mask method on the Cartesian grid alone, including on those grid points falling inside an object (a fuzzy boundary between the fluid-object interface), but with the restriction that the velocity on grid points within and on the surface of an object should be small or zero. The second step corrects the approximate flow field predicted from the first step by taking account of the object surface, i.e., solving the flow field on the local body-fitted (curvilinear) grid surrounding each object. A smooth data communication between the global and local grids can be implemented by the multigrid method when the Schwarz Alternating Procedure (SAP) is used for the iterative solution between the two overlapping grids. Numerical results for two-dimensional test problems for flow past elliptic cylinders are presented in the paper. An interesting phenomenon is found that when the second elliptic cylinder is placed in the wake of the first elliptic cylinder a traction force (a negative drag coefficient) acting on the second one may occur during the vortex formation in the wake area of the first one.

Introduction

The motive to develop the multigrid-mask method is to remedy the drawback of grid generation, which often results in a tremendous effort to achieve the desired layout of grid points for flow past multiple objects. As expected, it becomes even more difficult to generate a single grid system when the objects are close to each other or randomly moving. The situation occurs in many physical problems, such as cross flow in shell-tube heat exchangers, two-phase flow in multiple particle sedimentation, flow over a submarine or an automobile, and flow of blood cells in arterioles, capillaries, and venules (Stokes flow).

The conventional numerical simulation of Navier-Stokes flow with multiobject systems falls into two main categories: (I) distinguishable and (II) indistinguishable fluid-object interface. In category I a distinct boundary between an object and fluid is defined, and exact boundary conditions, velocity, and force can be prescribed on the surface of each object. Actually, in this category the entire flow domain is partitioned into two heterogeneous systems: objects (may or may not have fluid inside) and fluid system. It is capable of providing highly accurate details of flow interaction among objects but is computationally intensive. Ingber (1989) and Tran-Cong and Phan-Thien (1989) use the boundary element method for suspensions of rigid particles in Stokes flow.

In category II it is implied that a fuzzy boundary exists between an object and fluid, namely, there is no distinct boundary between an object and fluid. Therefore, a homogeneous system can be adequately applied to the entire domain. As a result, a single set of fluid dynamics equations holds on all grid points (usually a Cartesian grid) of the domain and no internal boundaries are necessarily defined. If any force exerts on the fluid-object interface, it will become a source term in the Navier-Stokes equations. Despite its simplicity, a sharp discontinuity for the velocity field (or other variables) between the fluid-object interface should be preserved in conformity with the original problem. In order to maintain a sharp front between the fluid-object interface, the fuzzy boundary should be restricted to within a few mesh distances; the less the mesh distance, the better the resolution of fluid-object interface. A variety of means to achieve the desired sharp fluid-object interface are suggested by many investigators Unverdi and Tryggvason (1992), Briscolini and Santangelo (1989), and Peskin (1977). Basically, the solution of flow field is discretized by the finite difference approximation on a global Cartesian grid to cover the entire flow domain.

For the applications in category II, Briscolini and Santangelo (1989) proposed the spectral method to solve the incompressible unsteady flow over a circular cylinder by introducing a strip zone (or equivalent to boundary layers) control within a few meshes. A narrow mask (Gaussian) function with a few meshes wide, defined as zero inside an object and one elsewhere along with a smooth connection between these two values within the strip zone, is applied to the velocity field. Peskin (1977) adopted the immersed boundary method for numerical simulation of blood flow in the human heart. His idea is very similar to the framework of the mask method except a separate body-fitted grid is added to trace the heart wall movement. As for the data communication between the global Cartesian grid and the local body-fitted grid, Peskin (1977) suggests an approximation to the delta-function to define the interpolation of velocity and force transferred between the fluid-object system. Goldstein et al. (1993) and Saiki and Biringen (1996) further extend Peskin's immersed boundary method to simulate flow over a circular cylinder by imposing the no-slip boundary of

Contributed by the Fluids Engineering Division for publication in the JOURNAL OF FLUIDS ENGINEERING. Manuscript received by the Fluids Engineering Division July 21, 1997; revised manuscript received July 8, 1998. Associate Technical Editor: P. M. Sockol.

the object surface with a feedback forcing function added to the momentum equations. This feedback forcing function can bring the fluid velocity to zero on those Cartesian grid points which define the object surface.

The objective of this paper is to develop a numerical method which combines the desired features of both categories I and II and to accurately simulate the flow interaction among multiple objects. In practice, it includes two major steps: (1) apply a Cartesian grid to obtain a fast solution covering the entire domain, which is similar to category II but differs in some respects (it is hereafter called a mask method), and (2) generate a local body-fitted grid literally wrapped around each object, which is similar to category I, by exactly capturing the object surface. The purpose of step (2) is to correct the approximate flow field predicted from step (1) by prescribing exact boundary conditions on the surface of each object.

To illustrate flow over multiple objects, one can regard that the local body-fitted grid (referred to the object domain) fully overlaps with the global Cartesian grid (referred to the entire domain). The iterative solution between the local and global grids can be implemented by the Schwarz Alternating Procedure (SAP) Ku (1995), Ku and Ramaswamy (1995), Ku et al. (1989). The role of the multigrid method during the SAP iterative process is to ensure a smooth data interpolation between the global and local grids without introducing any high-frequency error Ku and Ramaswamy (1995).

The solution of the Navier-Stokes equations is implemented by the pseudospectral element method, which is an extension of the global pseudospectral method to the element-type method by requiring that the function continuity c^0 be continuous across the interface between two adjacent elements when calculating the derivatives of a function.

Briefly, a procedure to implement the multigrid-mask method for flow past multiple objects is described as follows: the solution on the global Cartesian grid is first solved by the mask method, and the solution on the local body-fitted grid is next solved with the prescribed boundary conditions. The multigrid method is employed to reduce the data communication error when the iterative solution between the global and local grids is implemented by the SAP technique.

Section 2 derives the primitive variable form of the Navier-Stokes equations and their direct (or iterative) solution. Section 3 discusses the multigrid-mask SAP domain decomposition method. Section 4 presents numerical results of 2-D problems, and Section 5 provides the conclusions.

The proposed method in this paper is somewhat similar to the popular Chimera's overset grid method, whose applications are mostly implemented in aerodynamics (Steger et al., 1983; Dougherty et al., 1985; Meakin and Suhs, 1989; Meakin, 1992; Meakin, 1995; Lijewski and Suhs, 1994; Atwood, 1994; Sahu and Nietubicz, 1994). The approach involves a number of geometrically simple overlapping component grids, i.e., body-fitted component (local) grids overlapped with the background (global) Cartesian grid. The difference between our proposed method and the Chimera method lies in the background Cartesian grid. In the Chimera method, the Cartesian grid does not extend into the interior of local objects, instead, extends into the outer boundary of body-fitted component grids. Such overset grid device creates a hole region for which data transfer between the component and background grids can be easily performed.

Primitive Variable Formulation

Navier-Stokes Equations. In tensor notation, the time-dependent Navier-Stokes equations in dimensionless form can be described as

$$\frac{\partial u_i}{\partial x_i} = 0. \tag{1}$$

Here u_i is the velocity component and Re is the Reynolds number.

The method applied to solve the Navier-Stokes equations is Chorin's (1968) splitting technique. According to this technique, the equations of motion are written in the form

$$\frac{\partial u_i}{\partial t} + \frac{\partial p}{\partial x_i} = F_i \tag{2}$$

where $F_i = -u_j \partial u_i / \partial x_j + 1/\mathrm{Re}\, \partial^2 u_i / \partial x_j^2$.

The first step is to split the velocity into a sum of predicted and corrected values. The predicted velocity is determined by time integration of the momentum equations without the pressure term

$$\bar{u}_i^{n+1} = u_i^n + \Delta t F_i^n. \tag{3}$$

The second step is to determine the pressure and corrected velocity fields that satisfy the continuity equation by using the relationships

$$u_i^{n+1} = \bar{u}_i^{n+1} - \Delta t \frac{\partial p}{\partial x_i} \tag{4a}$$

$$\frac{\partial u_i^{n+1}}{\partial x_i} 0. \tag{4b}$$

Here the superscript n denotes the nth time step.

An equation for the pressure can be obtained by taking divergence of Eq. (4a). In view of Eq. (4b), it gives

$$\frac{\partial^2 p}{\partial x_i^2} = \frac{1}{\Delta t} \frac{\partial \bar{u}_i}{\partial x_i}. \tag{5}$$

Note that when solving Eq. (5) the relationship of Eq. (4a) on the boundaries should be utilized to absorb the given boundary conditions of the velocity components.

If p satisfies Eq. (5), then $\mathbf{u}^{n+1}$ automatically satisfies Eq. (4b). The solution of the pressure equation, Eq. (5), is the most computationally expensive step. Note that in Cartesian coordinates it can be directly solved by separation of variables using the method proposed by Ku et al. (1989). Equation (5) is of the general form,

$$Lp = S \tag{6}$$

For the approximate solution of Eq. (6), the properties of the operator L depend on the methods chosen to represent the fields and their derivatives.

In general, the operator L arising in the curvilinear coordinate system contains nonconstant metric coefficients, for which there is no direct solution. Thus, we solve a complementary problem whose solution can be easily related to that of the original problem. This technique is called preconditioning. We have adapted the Generalized Conjugate Residual (GCR) method proposed by Wong et al. (1986) to our problem as follows. Instead of Eq. (6) we solve

$$L_{ap}^{-1} Lp = L_{ap}^{-1} S, \tag{7}$$

where the preconditioner L_{ap}, a separable operator which allows a fast solution (see detail in Ku and Ramaswamy, 1995, Ku, 1995) by the eigenfunction expansion technique, can be chosen and constructed from the original operator L by linearizing all nonconstant metric coefficients.

Domain Decomposition With Multigrid-Mask Method

As mentioned in the Introduction, two major steps are involved for the calculation of flow past multiple objects: solution of flow field on the global Cartesian grid as well as on the local

body-fitted grid. A smooth data communication between the global and local grids can be achieved by the multigrid method when the SAP technique is implemented for the iterative solution between the two grids with inter-overlapping area. Each step is addressed in detail as follows:

First Step—Global Grid. A single coordinate system (a global Cartesian grid) is used to first produce the solution of flow field covering the entire domain, irrespective of a fuzzy boundary existed between the fluid-object interface. Usually, several Cartesian grid points fall inside an object. The solution for this step is sometimes called the mask method, and is analogous to that proposed by Briscolini and Santangelo (1989), Peskin (1977), Goldstein et al. (1993), and Saiki and Biringen (1996). It permits flow into those Cartesian grid points falling inside an object without explicitly defining the fluid-object interface. The merit of such a single grid system enables us to take advantage of the fast solution on the Cartesian grid points. The other approach one could use using fictitious domain method proposed by Glowinski et al. (1994, 1995).

The flow field on those Cartesian grid points falling inside or on the surface of the object should be restricted in order to comply with the original problem, i.e., no flow or small velocity should be allowed inside each object, including on the surface as well. Such a requirement, equivalent to finding the predicted velocity $\bar{\mathbf{u}}^{n+1}$ on those Cartesian grid points falling inside an object, can be met by solving the following equation

$$\bar{u}_i^{n+1} = u_i^p + \Delta t \frac{\partial p}{\partial x_i} \tag{8}$$

together with Eq. (5). Here superscript p refers to the prescribed velocity, certainly zero for a nonmoving object and nonzero for a moving object. Due to the nonsmooth flow field exhibited near the fluid-object interface, simply choosing the predicted velocity $\bar{\mathbf{u}}^{n+1}$ to be zero or a constant does not guarantee that the corrected velocity $\mathbf{u}^{n+1}$ on those Cartesian grid points (falling inside an object) obtained from Eq. (4*a*) be $\mathbf{u}^p$ after solving Eq. (5). Adversely, the undetermined predicted velocity $\bar{\mathbf{u}}^{n+1}$ on those Cartesian grid points can be found by repeatedly solving Eqs. (5) and (8) with given $\mathbf{u}^p$ and pressure gradient. Usually, only 1 to 2 iterations are required to ensure that $\|\mathbf{u}^{n+1} - \mathbf{u}^p\| < 10^{-4}$ on those grid points after a few hundred time steps.

Second Step—Local Grid. Despite its simplicity, the mask method only provides an approximate flow field due to the incomplete representation of the object surface. The object surface is also a vital boundary condition for the determination of the flow. Generally, there are few, if any, Cartesian grid points falling on the object surface, and hence the object surface is not sufficiently represented.

In order to correct the approximate flow field predicted from the first step by the mask method, next the object surface should be precisely defined by the local body-fitted grid associated with each object. Since the first step does not define a distinct boundary between the fluid and object, except a fuzzy interface falls within a few meshes, such a distinct fluid-object interface can be retrieved by this step. Importantly, the boundary conditions on the object surface can be exactly imposed without any difficulty.

In view of the domain decomposition approach for flow past multiple objects, one can regard that the local body-fitted grid (referred to the object domain) fully overlaps the global Cartesian grid (referred to the entire domain). The layout of two grid systems for flow past two elliptic cylinders is depicted in Fig. 1. Each grid has its own coordinate system, and in some areas they overlap each other. The iterative solution between the two grid systems with inter-overlapping area can be efficiently implemented by the SAP technique. During the SAP iterative process, the global Cartesian grid provides the outer boundary information for the local body-fitted grid, and in turn the local body-fitted grid corrects the flow field near an object by imposing exact boundary conditions on the object surface.

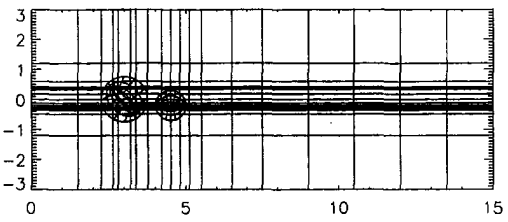

Fig. 1 Element layout for flow past elliptic cylinders

The success of the SAP technique applied to the incompressible flow lies in the unique use of the continuity as the pressure boundary condition (high-order gradient) in the overlapping area (the more the overlapping area, the faster the convergence). The convergence rate can be measured by the residual (l_2 norm) of the flow field, the velocity difference between two grid systems in the overlapping area or Eq. (13). In most cases for conforming grids (grid points coincided with each other), it takes four SAP iterations to sufficiently mark down the residual index to $O(10^{-4}) \sim O(10^{-5})$.

Due to the different orientation and resolution of each grid system, simply performing a global-to-local grid interpolation in the overlapping area will produce the high frequency error, and the results, accordingly, will be polluted throughout the entire computational domain. The technique of filtering the high-frequency noise is also known as the multigrid method. The multigrid method has long been used with the finite-difference methods (Brandt, 1977, Hackbusch, 1985). On the same computational domain, a sequence of uniform grids is employed to accelerate the convergence of iterative methods. The work rests on the "standard coarsening," i.e., doubling the mesh in each direction from one grid to the next coarsest grid and also smoothing the residual to the next coarsest (restriction). The problem is solved on the coarse-grid (low frequency) domain and the coarse-grid correction for the variable transfers the correction back (prolongation) to the fine grid (high frequency) domain to gain rapid convergence. The coarse-grid correction process is also applied here for the data communication (mainly flow components) between the global and local grids. Following a similar approach proposed by Ku and Ramaswamy (1995), the coupled pressure and velocity field between the two overlapping grids can be expressed as

$$\nabla_c \cdot \mathbf{u}_c - \nabla_c \cdot (I_c^f \mathbf{u}_f) = I_c^f (r_f - \nabla_f \cdot \mathbf{u}_f). \tag{9}$$

Here $\nabla_c \cdot$ represents the operator of divergence on the global-grid domain, I_c^f is an interpolation operator from the local-grid domain "f" to the global-grid domain "c", $\mathbf{u}$ is the velocity, r_f is the divergence of the velocity field on the local-grid domain, and it is not known a priori. How to choose r_f will be addressed next. The left-hand side of Eq. (9) is the difference between the global-grid operator acting on the global-grid domain and the global-grid operator acting on the interpolated local-grid subdomain (which is held fixed).

Intrinsically, the continuity equation in the interior of overlapping area (r_f on the local-grid or $\nabla_c \cdot (I_c^f \mathbf{u}_f)$ on the global-grid domain) will not be exactly equal to zero and is determined by the layout of grid points as well as the stiffness of field variables. The continuity equation outside the overlapping area, $\nabla_c \cdot (I_c^f \mathbf{u}_f)$ should naturally set to zero on the global-grid domain. Substituting $\mathbf{u}_c$ and $\mathbf{u}_f$ in terms of pressure gradient from Eq. (4*a*), Eq. (9) becomes

$$\nabla_c \cdot \bar{\mathbf{u}}_c - \Delta t \nabla^2 p_c - \nabla_c \cdot (I_c^f \mathbf{u}_f) = I_c^f (r_f - \nabla_f \cdot \bar{\mathbf{u}}_f + \Delta t \nabla^2 p_f) \tag{10}$$

where $\bar{\mathbf{u}}_c$, $\bar{\mathbf{u}}_f$ are the predicted velocity on the global-grid and local-grid domain, respectively.

It is apparent that Eq. (9) implicitly functions as a coupled equation between the pressure and velocity field; not only the residual of the right-hand side of Eq. (9) should be zero, but also the velocity field during the SAP iteration is unchanged.

For the nonconforming grids (grid points not coincided with each other in the overlapping area), r_f cannot be predetermined and needs to be adjusted at each SAP iteration until the velocity field, $\mathbf{u}_c = \bar{\mathbf{u}}_c - \Delta t \nabla p_c$, $\mathbf{u}_f = \bar{\mathbf{u}}_f - \Delta t \nabla p_f$, generated from the pressure equations

$$\nabla_c \cdot \bar{\mathbf{u}}_c - \Delta t \nabla^2 p_c = \nabla_c \cdot (I_c^f \mathbf{u}_f) + I_c^f (r_f - \nabla_f \cdot \bar{\mathbf{u}}_f + \Delta t \nabla^2 p_f) \quad (11a)$$

$$\nabla_f \cdot \bar{\mathbf{u}}_f - \Delta t \nabla^2 p_f = r_f \quad (11b)$$

satisfies

$$\mathbf{u}_c = I_c^f \mathbf{u}_f \quad (12)$$

as required for convergence. The projection for the residual from the local-grid domain to the global-grid domain has been included as the second term of the right hand side of Eq. (11a). Notice that during the SAP iterative process r_f is always set to zero at the first SAP iteration. Whenever $\mathbf{u}_c \neq I_c^f \mathbf{u}_f$, Eq. (9) acts as a coarse-grid correction process to transfer the correction of the velocity field back to the local-grid domain, i.e.,

$$\mathbf{u}_f^{\text{new}} = \mathbf{u}_f^{\text{old}} + I_f^c(\mathbf{u}_c - I_c^f \mathbf{u}_f^{\text{old}}). \quad (13)$$

This is vital for the success of the scheme. Changes in the velocity field are transferred back to the local-grid domain rather than the velocity field itself. Here the superscripts "old" and "new" simply stand for the SAP iteration count. Both the prolongation I_f^c, which denotes a global-to-local interpolation, and the restriction I_c^f, which denotes a local-to-global interpolation, can be separately constructed by the Chebyshev polynomials for each grid system.

With $\mathbf{u}_f^{\text{new}}$ provided from Eq. (13), r_f can be adequately adjusted (instead of zero at the first SAP iteration) and chosen as

$$r_f = \nabla_f \cdot \mathbf{u}_f^{\text{new}} \quad (14)$$

Continue to update the right hand side of Eqs. (11) with $\mathbf{u}_f^{\text{new}}$ and solve the pressure equations until the convergence criterion $\mathbf{u}_c = I_c^f \mathbf{u}_f$ is met.

For the case of conforming grids, the interpolation operator I_c^f in Eq. (9) becomes a unitary matrix. With $\mathbf{u}_c = \mathbf{u}_f$ it is not difficult to prove that r_f will remain zero all the time if r_f is set to zero at the first SAP iteration.

The multigrid-mask SAP iterative solution of the incompressible Navier-Stokes equations in primitive variable form for flow past multiple objects (also shown in Fig. 1) is summarized by the following algorithm:

1. $\mathbf{u}^{n+1}$ on the outer boundary of an object is first specified through the interpolated solution of flow field on the global-grid domain.
2. Solve the pressure equation on the local-grid or "O" grid ("O" grid is a body-fitted grid surrounding a slender object) domain employing the continuity equation as the pressure boundary conditions on the inner and outer surfaces of an object. The solution of pressure equation, Eq. (11b), is obtained by the preconditioned General Conjugate Residual (GCR) method.
3. With the solution of $\mathbf{u}_f^{n+1}$ on the local-grid domain from step (2), perform the local-to-global interpolation of $I_c^f \mathbf{u}_f$ and the residual of Eq. (11b) in the overlapping area. Solve the pressure equation on the global-grid domain, Eq. (11a), by the mask method with the eigenfunction expansion technique.
4. Update $\mathbf{u}_f^{n+1}$ on the local-grid domain by the coarse-grid correction process, Eq. (13), as well as r_f in Eq. (14).
5. Repeat steps (2) to (4) until the velocity $\mathbf{u}^{n+1}$ in the overlapping area satisfies the convergence criterion of Eq. (12).

Notice that at each time step the solution of the velocity field on the global-grid domain needs to be computed first, and then the SAP iterative procedure is performed as above mentioned.

It is worthwhile to emphasize that even with strong discontinuity exhibited for the velocity (on the global-grid domain) immediately outside an object the multigrid-mask method indeed restricts small prescribed velocity on those Cartesian grid points falling inside an object and satisfies Eq. (12), too.

As for the adaptive composite grids, the solution of velocity field in coarse-grid domain needs first to compute and then repeats the same iterative procedure as above mentioned. In order to guarantee that consistent values of velocity (or pressure gradient) be generated in the overlapping domains, satisfying Eq. (9), the divergence of velocity field $\nabla \cdot \mathbf{u}$ needs to be actually computed in whichever domain is counted. Since $\mathbf{u}$ on fine-grid domains is not known a priori, the divergence of velocity field is only set to zero at the first SAP iteration for step (2). It indicates that any lines acted as the boundary of one domain, the divergence of velocity field along those lines which are also interior lines of neighboring domains, should be satisfied only by its neighboring domains. Outside the inter-overlapping zone, the continuity equation is exactly satisfied in each decomposed subdomains.

Two main issues occurring in the overlapping area between the fine-grid and coarse-grid subdomains one might often encounter are how to (1) efficiently implement the data interpolation; and (2) explicitly impose the global mass conservation for inflow-outflow problems. Each will be addressed separately.

Data Interpolation. Finding the image (ξ, η), $-1 \leq \xi \leq 1$, $-1 \leq \eta \leq 1$, of a collocation point (x, y) from the fine-grid subdomain II mapped onto the coarse-grid subdomain I (or vice versa) is first determined by using the two-dimensional Lagrange interpolation to seek its corresponding position falling into an element on the coarse-grid subdomain which contains $(M + 1) \times (N + 1)$ collocations points, $\xi_i = \cos \pi i/M$ ($i = 0, \ldots, M$), $\eta_j = \cos \pi j/N$ ($j = 0, \ldots, N$), such that

$$x = \sum_{m=0}^{M} \sum_{n=0}^{N} a_{mn} T_m(\xi) T_n(\eta) \quad (15a)$$

$$y = \sum_{m=0}^{M} \sum_{n=0}^{N} b_{mn} T_m(\xi) T_n(\eta) \quad (15b)$$

where T_m denotes the mth order Chebyshev polynomials. Unknown expansion coefficients, a_{mn}, b_{mn}, can be easily obtained by the prescribed points (x, y) on the coarse-grid subdomain I through

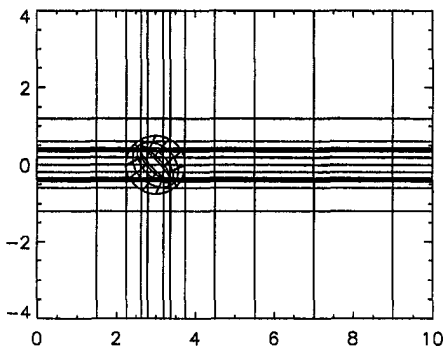

Fig. 2 Element layout for flow past an elliptic cylinder

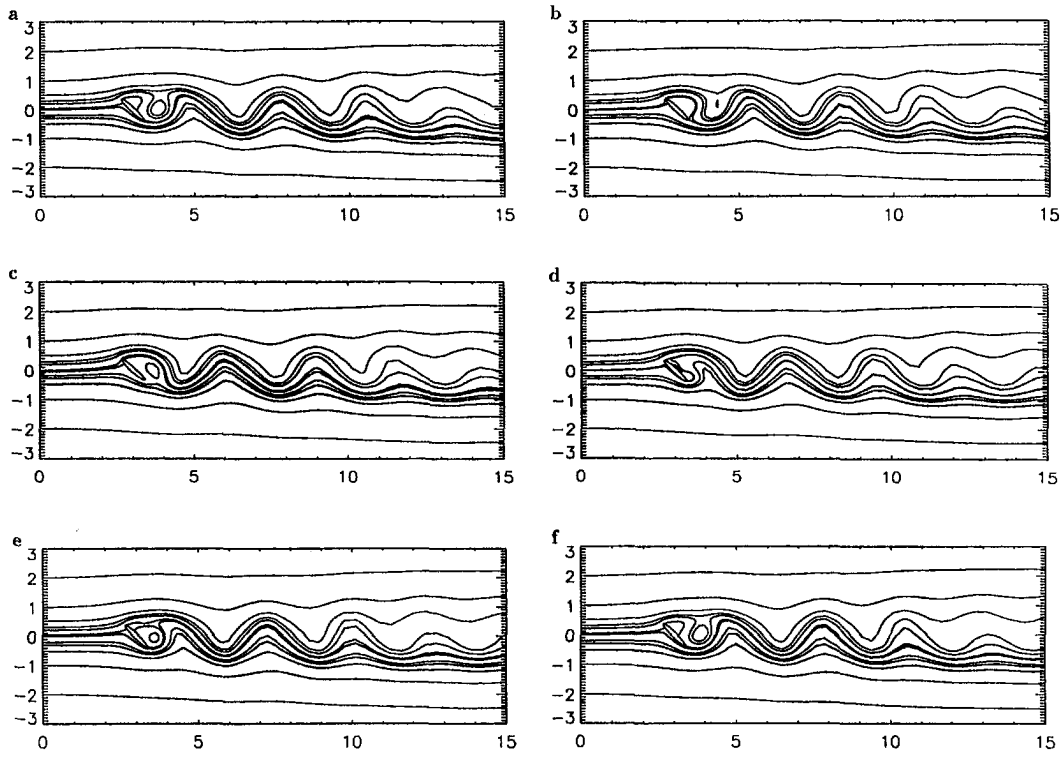

Fig. 3 Full-cycle time history of streamline plots for Re = 200 at time (*a*) $t = 0$, (*b*) $t = 0.2$ T, (*c*) $t = 0.4$ T, (*d*) $t = 0.6$ T, (*e*) $t = 0.8$ T, (*f*) $t = T$

$$x(\xi_i, \eta_j) = \sum_{m=0}^{M} \sum_{n=0}^{N} a_{mn} T_m(\xi_i) T_n(\eta_j) \tag{16a}$$

$$y(\xi_i, \eta_j) = \sum_{m=0}^{M} \sum_{n=0}^{N} b_{mn} T_m(\xi_i) T_n(\eta_j) \tag{16b}$$

With a given point (x, y) in the physical space of fine-grid subdomain II, its image (ξ, η) on the coarse-grid subdomain I can be iteratively solved by the Newton-Raphson method. Once the one-to-one correspondence between the fine-grid and coarse-grid subdomains has been established, the equation required to generate a function $\phi^f(x, y)$ on the fine-grid subdomain interpolated from the coarse-grid subdomain, now becomes

$$\phi^f(x, y) = \sum_{i=0}^{M} \sum_{j=0}^{N} N_i(\xi) N_j(\eta) \phi^c(\xi_i, \eta_j) \tag{17}$$

where $\phi^c(\xi_i, \eta_j)$ denotes the function value at the collocation point (ξ_i, η_j) on the coarse-grid subdomain, and $N_i(\xi)$, $N_j(\eta)$ are the shape functions defining the geometry of the element on the coarse-grid subdomain.

Notice that it requires much less effort to perform the data interpolation if the one-to-one correspondence for the shape functions between subdomains can be permanently stored (once for all). Also the cost for such additional memory is negligible compared to that declared by a single variable.

Global Flow Rate. For the inflow-outflow problems, due to the grids along the inter-overlapping interfaces not intersected at each other (nonconforming grids), the coarse-grid velocity field interpolated from the fine-grid subdomain along the boundary lines, or vice versa, may not exactly satisfy the global mass conservation, and thus a slight adjustment to the velocity field along boundary lines is recommended. A commonly-used formula like the following will meet such a requirement:

$$u_i^{\text{new}} = u_i^{\text{old}} \frac{\int \mathbf{u}^{\text{exact}} \cdot dA}{\int \mathbf{u}^{\text{old}} \cdot dA} \tag{18}$$

Results and Discussion

Four SAP iterations are employed for all the test problems, and the convergence criterion of Eq. (12) is satisfied by the requirement $\|\mathbf{u}_c - I_c^f \mathbf{u}_f\| \leq 2.5 \times 10^{-4}$. The radiation boundary condition is applied on the truncated downstream to give the least influence upon the upstream flow development.

An incoming uniform flow past a slender elliptic cylinder of thickness ratio (minor to major axis) 1:6.66 at 45 deg incidence is studied. Reynolds number is chosen to be Re = 200 (based on the chord length, which is twice the major axis), and the aspect ratio (the channel width over the chord length) is 20. The number of elements allocated for the global domain is 14 $\times$ 16 elements (6 points per element) in the x and y directions and 14 $\times$ 4 elements are adopted for the local domain. The detailed element layout is sketched in Fig. 2.

A benchmark comparison is first made for flow past an elliptic cylinder with the thickness ratio of 0 deg angle and Reynolds number 100, and it gives the drag coefficient $C_D = 0.496$, which is in good agreement with 0.486 obtained from the streamfunction vorticity formulation Rosenfeld and Wolfshtein (1984). When the attack angle becomes 45 deg and Reynolds number is at Re = 200, a well-known Kármán vortex street develops. At time $t = 4.42$, equivalent to $t = 8.84$ of Rosenfeld and Wolfshtein (1984) due to different length scale, streamline plots (not shown here) reproduce a similar pattern of Lugt and Haussling (1974), an immediate separation behind the top tip of elliptic cylinder as well as a primary vortex behind the body. With the separation occurring at the rear (upper) side of the cylinder, the pressure at the upper side is higher than that at the lower side, so the lift becomes more negative. The streamline plots shown in Fig. 3 illustrate the time history of separation behind the elliptic cylinder within a cycle. If one regards the

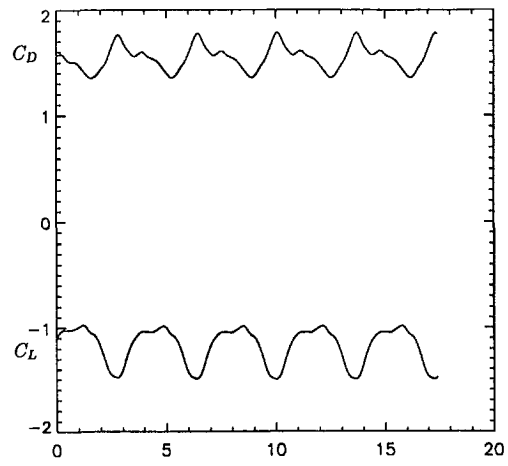

Fig. 4 Time history of drag C_D and C_L coefficients for flow past an elliptic cylinder at Re = 200

separation starting from the leading edge as seen in Fig. 3(*a*), the time evolution of separation is described as follows: the separation region continues to increase toward the trailing edge (Fig. 3(*b*)), and up to the trailing edge where the maximal lift holds. After the separation breaks down (Fig. 3(*c*)), it restarts from the trailing edge (Fig. 3(*d*)) and then gradually extends to the region toward the top tip (Fig. 3(*e*)) where the minimal lift occurs. The separation also splits into two parts, one located immediately behind the ellipse, another formed as a vortex behind the body (Fig. 3(*f*)).

After a few cycles of time elapse, the drag and lift coefficients tend to settle down within the range, $-0.985 \leq C_L \leq -1.500$, $1.355 \leq C_D \leq 1.781$ (as seen in Fig. 4), which are qualitatively similar to the case with thickness ratio of 1:10 in Lugt and Haussling (1974). The Strouhal number is 0.275 in contrast with 0.25 in the case of thickness ratio 1:10.

To demonstrate the capability of multigrid-mask method in simulating the interaction among multiple objects, we add another elliptic cylinder with thickness ratio 1:4 (chord length is 60 percent of the first one) in the direction of incoming flow. The element layout is also sketched in Fig. 1 and the position is placed in the wake of the first elliptic cylinder. It is very common for us to experience the traction force when we park a car and another high speed car passes by from us, or a small plane flying into the wake of a big plane can crash with the big one due to the resulting suction force.

In order to prove the traction force acting on the second elliptic cylinder induced by the wake effect from the front one, it is rational to plot the time history of drag coefficient at the rear one. If any negative value of drag coefficient exists, it supports the evidence. In Fig. 5, the drag and lift coefficients of both elliptic cylinders appear in the same plot. Apparently, the negative drag coefficient occurring at the second one indeed points out that a traction force sometimes does exist on the rear elliptic cylinder. Meanwhile, the drag and lift coefficients for the front elliptic cylinder also change within the range, $1.30 \leq C_D \leq 1.828$, $-0.82 \leq C_L \leq -1.39$, due to the existence of the rear one. Strikingly, the Stouhal number is reduced to 0.208 which is the same as that of the rear elliptic cylinder (resonant effect), whose drag and lift coefficients are $-0.139 \leq C_D \leq 0.360$, $-0.939 \leq C_L \leq 0.911$, respectively.

The streamline plots as seen in Fig. 6 will give a detailed description of the aforementioned traction effect. The phenomena of the front elliptic cylinder is very similar to the single case; separation starts from the leading edge and grows up to the trailing edge where the separation breaks down, then separation restarts from the trailing edge and extends toward the leading edge where it splits into two parts: one is on the surface and another is formed in the wake region. The traction force acting on the second elliptic cylinder can be justified in terms of the vortex formation in the wake region of the first one. Whenever the vortex forms and the wake area extends to occupy the front surface of the second one, the drag coefficient becomes negative and is clearly indicated in Fig. 6(*c*). The negative value persists during the time period (Fig. 6(*c*)–Fig. 6(*e*)) when the separation on the surface of the front elliptic cylinder breaks down at the tail and then restarts from the bottom and extends toward the tip. The intensity of traction force turns out to be the strongest when the wake zone behind the first elliptic cylinder occupying the front surface of the second one becomes the largest (Fig. 6(*d*)).

Conclusions

The solution of the Navier-Stokes equations in primitive variable form has been obtained by the pseudospectral element method via the multigrid-mask SAP domain decomposition technique. The solution procedure for flow past multiple (or single) objects includes two basic steps: solution of flow field on the global Cartesian grid and on the local body-fitted grid. The solution of flow field on the global Cartesian grid is first solved by the mask method, then on the local body-fitted grid. The iterative solution between the global (referred to the entire domain) and local (referred to the object domain) is performed by the SAP technique through the multigrid method.

The first step permits flow into those Cartesian grid points falling inside in an object without knowing the fluid-object interface but subject to the restriction that flow inside or on the surface of an object should be zero or small. The merit of the mask method is its simplicity to provide an approximate flow field by the fast eigenfunction solver. The implementation of the second step is used to correct the flow field predicted from the first step by imposing exact boundary conditions on the object surface.

From the solution point of view, the problem can be interpreted as the local body-fitted grid (referred to the object domain) fully overlapped with the global Cartesian grid (referred to the entire domain). The SAP technique is used for the iterative solution between the two overlapping grids. During the data exchange between the global and the local grids, the coarse-grid correction technique is used to eliminate the high-frequency error caused by the global-to-local grid interpolation.

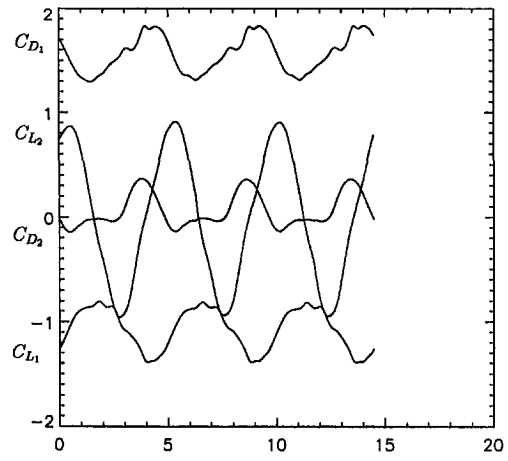

Fig. 5 Time history of drag C_D and lift C_L coefficients for flow past elliptic cylinders at Re = 200

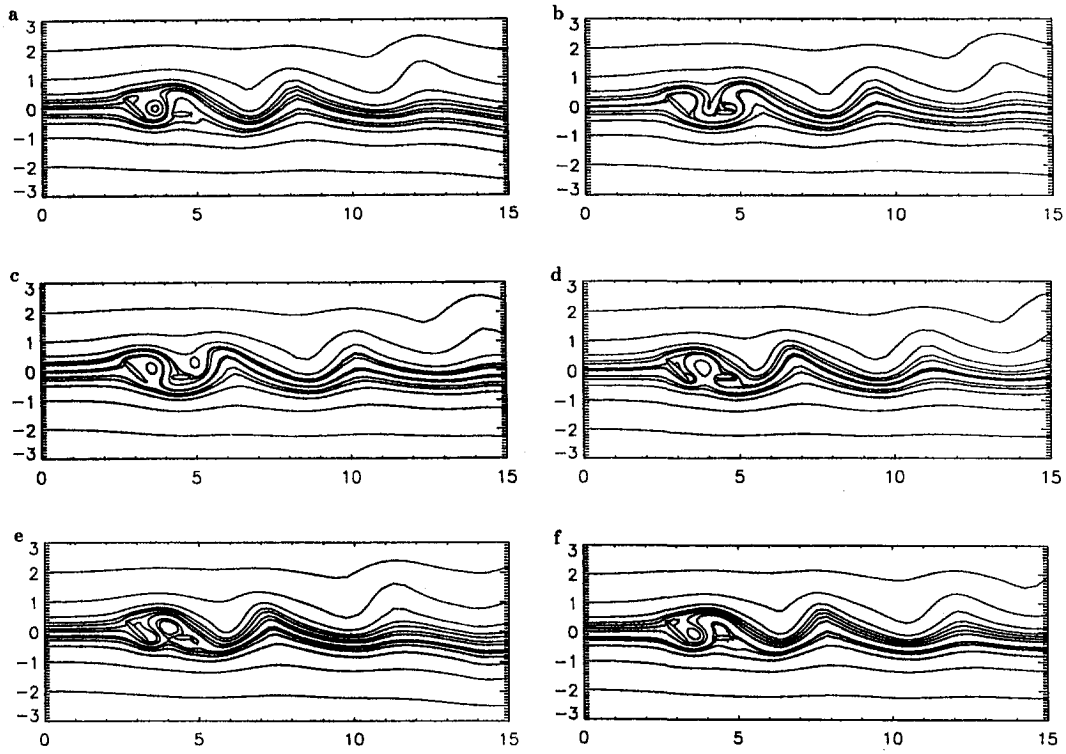

Fig. 6 Time history of streamline plots for Re = 200 at time (*a*) $t = 0$, (*b*) $t = 0.27$ T, (*c*) $t = 0.46$ T, (*d*) $t = 0.67$ T, (*e*) $t = 0.77$ T, (*f*) $t = 0.91$ T

Test problems demonstrate the versatility of the proposed multigrid-mask method. Future research will concentrate on solution of flow in the three-dimensional geometries.

Acknowledgments

The work of the first author was partially supported by the Department of the Navy, Space and Naval Warfare Systems Command, under Contract Number N00039-95-C-0002 and to the second author by the U.S. National Science Foundation, Contract Number DMS-9408151. Furthermore, the authors are in debt to the reviewers for their many suggestions.

References

Lijewski, L., and Suhs, N., 1994, "Time-Accurate Computational Fluid Dynamics Approach to Transonic Store-Separation Trajectory Prediction," American Institute for Aeronautics and Astronautics *Journal of Aircraft,* Vol. 31, pp. 886–891.

Brandt, A., 1977, "Multi-Level Adaptive Solutions to Boundary-Value Problems," *Mathematics and Computation,* Vol. 31, pp. 333–390.

Briscolini, M., and Santangelo, P., 1989, "Development of the Mask Method for Incompressible Unsteady Flow," *Journal of Computational Physics,* Vol. 84, pp. 57–75.

Chorin, A. J., 1968, "Numerical solution of the Navier-Stokes Equation," *Mathematics and Computation,* Vol. 22, pp. 745–762.

Dougherty, F. C., Benek, J., and Steger, J., 1988, "On Applications of Chimera Grid Schemes to Store Separation," NASA TM-88193.

Glowinski, R., Pan, T. W., and Periaux, J., 1994, "A Fictitious Domain Method for External Incompressible Viscous Flow Modeled by Navier-Stokes equations," *Computer Methods in Applied Mechanics and Engineering,* Vol. 112, pp. 133–148.

Glowinski, R., Pan, T. W., Kearsley, A. J., and Periaux, J., 1995, "Numerical Simulation and Optimal Shape for Viscous Flow by a Fictitious Domain Method," *International Journal for Numerical Methods in Fluids,* Vol. 20, pp. 695–711.

Glowinski, R., A. J. Kearsley, A. J., T. W. Pan, T. W., and J. Periaux, J., 1995, "Fictitious Domain Method for Viscous Flow Simulation," *Computational Fluid Dynamics Review 1995,* M. Hafez and K. Oshima, eds., Wiley, Chichester, pp. 357–381.

Goldstein, D., Handler, R., and Sirovich, L., 1993, "Modelong a No-Slip Flow Boundary with an External Force Field," *Journal of Computational Physics,* Vol. 105, pp. 354–366.

Gregoire, J. P., Benque, J. P., Lasbleiz, P., and Goussibaile, J., 1985, *Proceedings of Ninth Conference on Numerical Methods in Fluid Dynamics,* Soubbaramayer and J. P. Boujot, eds., Springer-Verlag.

Hackbusch, W., 1985, *Multi-Grid Methods and Applications,* Springer-Verlag, Berlin.

Ingber, M., 1989, "Dynamic Simulation of the Hydrodynamics Interaction Among Immersed Particles," *International Journal for Numerical Methods in Fluids,* Vol. 9, pp. 263–275.

Ku, H. C., Hirsh, R. S., and Taylor, T. D., 1987, "A Pseudospectral Method for Solution of the Three Dimensional Incompressible Navier-Stokes Equations," *Journal of Computational Physics,* Vol. 70, pp. 439–462.

Ku, H. C., Hirsh, R. S., Taylor, T. D., and Rosenberg, A. P., 1989, "A Pseudospectral Matrix Element Method for Solution of three-Dimensional Incompressible Flows and its Parallel Implementation," *Journal of Computational Physics,* Vol. 83, pp. 260–291.

Ku, H. C., 1995, "Solution of Flow in Complex Geometries by the Pseudospectral Element Method," *Journal of Computational Physics,* Vol. 117, pp. 215–227.

Ku, H. C., and Ramaswamy, B., 1995, "Multi-Grid Domain Decomposition Approach for Solution of Navier-Stokes Equations in Primitive Variable Form," *International Journal for Numerical Methods in Engineering,* Vol. 38, pp. 667–683.

Lijewski, L., and Suhs, N., 1994, "Time-Accurate Computational Fluid Dynamics Approach to Transonic Store-Separation Trajectory Prediction," AIAA *Journal of Aircraft,* Vol. 31, pp. 886–891.

Lugt, H. J., and Haussling, H. J., 1974, "Laminar Flow Past an Abruptly Accelerated Elliptic Cylinder at 45° Incidence," *Journal of Fluid Mechanics,* Vol. 65, pp. 711–734.

Meakin, R. L., 1995, "The Chimera Method of Simulation for Unsteady Three-Dimensional Viscous Flow," *Computational Fluid Dynamics Review 1995,* M. Hafez and K. Oshima, eds., Wiley, Chichester, pp. 70–86.

Meakin, R., and Suhs, N., 1989, "Unsteady Aerodynamic simulation of multiple bodies in relative motion," AIAA Paper 89-1996-CP, 9th CFD Conf., pp. 643–657.

Meakin, R., 1992, "Computations of the Unsteady Flow About a Generic Wing/Pylon/Finned-Store Configuration," AIAA Paper 92-4568-CP, AFM Cong., pp. 564–580.

Peskin, C. S., 1977, "Numerical Analysis of Blood Flow in the Heart," *Journal of Computational Physics,* Vol. 25, pp. 220–252.

Rosenfeld, M., and Kwak, D., 1989, "Numerical Simulation of Unsteady Incompressible Viscous Flows in Generalized Coordinate Systems," *Lecture Notes in Physics,* Vol. 323, pp. 506–509, Springer, New York.

Sahu, J., and Nietubicz, C., 1994, "Application of Chimera Technique to Projectiles in Relative Motion," AIAA Paper 93-3632-CP, AFM Conf., pp. 167–176.

Saiki, E. M., and Biringen, S., 1996, "Numerical Simulation of a Cylinder in Uniform Flow: Application of a Virtual Boundary Method," *Journal of Computational Physics,* Vol. 123, pp. 450–465.

Steger, J., Dougherty, F. C., and Benek, J., 1983, "A Chimera Grid Scheme," *Advances in Grid Generation,* K. N. Ghia and U. Ghia, eds., ASME, Fluids Engineering Division, Vol. 5, pp. 59–69.

Tran-Cong, T., and Phan-Thien, N., 1989, "Stokes Problems of Multiparticle Systems: A Numerical Method for Arbitrary Flow," *Physics of Fluids,* Vol. A 1, pp. 453–461.

Unverdi, S. O., and Tryggvason, G., 1992, "A Front-Tracking Method for Viscous, Incompressible, Unsteady Flow," *Journal of Computational Physics,* Vol. 100, pp. 25–37.

Wong, Y. S., Zang, T. A., and Hussaini, M. Y., 1986, "Preconditioned Conjugate Residual Methods for the Solution of Spectral Methods," *Computers and Fluids,* Vol. 14, pp. 85–89.

Monotonic Convergence Property of Turbulent Flow Solution With Central Difference and QUICK Schemes

Toshiyuki Hayase
Associate Professor,
Institute of Fluid Science,
Tohoku University,
Sendai, 980-8577, Japan
e-mail: HAYASE@ifs.tohoku.ac.jp

Monotonic convergence of numerical solutions with the computational grid refinement is an essential requirement in estimating the grid-dependent uncertainty of computational fluid dynamics. If the convergence is not monotonic, the solution could be erroneously regarded as convergent at the local extremum with respect to some measure of the error. On the other hand, if the convergence is exactly monotonic, estimation methods such as Richardson extrapolation properly evaluate the uncertainty of numerical solutions. This paper deals with the characterization of numerical schemes based on the property of the monotonic convergence of numerical solutions. Two typical discretization schemes of convective terms were considered; the second-order central difference scheme and the third-order Leonard's QUICK scheme. A fully developed turbulent flow through a square duct was calculated via a SIMPLER based finite volume method without a turbulence model. The convergence of the numerical solution with the grid refinement was investigated for the mean flow property as well as fluctuations. The comparison of convergence process between the discretization schemes has revealed that the QUICK scheme results in preferable monotonic convergence, while the second-order central difference scheme undergoes non-monotonic convergence. The latter possibly misleads the determination of convergence with the grid refinement, or causes trouble in applying the Richardson extrapolation procedure to estimate the numerical uncertainty.

1 Introduction

Recent development in the computer capability has enabled us to apply computational fluid dynamics to practically important flow problems. At the same time, the uncertainty assessment of numerical solutions has became an unavoidable task (Freitas, 1993). Several classes are distinguished in the uncertainty of numerical results (Demuren and Wilson, 1994); the truncation error in numerical schemes, the discretization error, the boundary condition, the iterative convergence, and so on. Among these categories the grid dependency of numerical solutions is of fundamental concern to many researchers. Roache (1994) introduced Grid Convergence Index (GCI) as a measure of the grid independency of numerical solutions, which is based on the generalized Richardson Extrapolation. Recently, Celik and Karatekin (1997) examined the applicability of GCI to nonuniform grids. A fundamental requirement in grid-dependency analysis is the monotonic convergence of the numerical solution with the grid refinement. The Richardson Extrapolation including GCI application assumes this property as the basic assumption (Roache, 1994). If the convergence is not monotonic, the solution could be erroneously regarded as convergent at the local extremum in evaluating some measure of the error. A natural question then arises; is there any class of discretization schemes which may result in non-monotonic convergence? The odd- and the even-order difference schemes in convective terms possibly show different behavior from the viewpoint of monotonic convergence. It is well known that even-order central difference schemes do not have any dissipative error term with the leading error term of dispersion error. Odd-order upwind discretization schemes, on the other hand, have dissipative error as the leading error term. Although none of the former studies on steady laminar flow problems has mentioned the possibility of the non-monotonic convergence of the central difference schemes, time-dependent turbulent flow solutions may possibly undergo the non-monotonic convergence due to the dispersion error in the schemes.

The present paper deals with a fully developed turbulent flow through a square duct. A SIMPLER based finite volume method is employed with the second-order central difference scheme and the third-order Leonard's QUICK scheme for the convective terms. The turbulent flow through a square duct represents an excellent test case for evaluating numerical schemes to reproduce anisotropic characteristics of turbulence. A specific feature of the turbulent flow in the noncircular duct is the occurrence of the secondary flow on the plane perpendicular to the main flow direction (Schlichting, 1979). Although the secondary flow velocity is only of the order of 2–3% of the mean axial velocity, its effect on the flow characteristics is not negligible; it transports fluid of large momentum toward each corner of the duct, resulting in a distortion of the mean axial velocity profile. It is well known that the standard $\kappa - \epsilon$ model fails to predict the secondary flow motion. Considering anisotropic characteristics of the turbulence, the secondary flow in a square duct was properly predicted (Demuren and Rodi, 1984). Recently, the detailed structure of the turbulent flow in a square duct was investigated with the large eddy simulation (Madabhushi and Vanka, 1991, Su and Friedrich, 1994), the anisotropic $\kappa - \epsilon$ model (Myong and Kobayashi, 1991), and the direct numerical simulation (Huser and Biringen, 1993).

In this paper the monotonic convergence of the numerical solution with the second-order central difference and the QUICK scheme is investigated for the turbulent flow in a square duct. Section 2 of the paper describes the fundamental equations and the boundary conditions. A summary of the numerical procedure is also given. Calculated results are presented and discussed in Section 3. The convergence of the numerical solution with the time step is first studied for different grid resolutions and discretization

Contributed by the Fluids Engineering Division for publication in the JOURNAL OF FLUIDS ENGINEERING. Manuscript received by the Fluids Engineering Division April 2, 1998; revised manuscript received February 3, 1999. Associate Technical Editor: J. A. C. Humphrey.

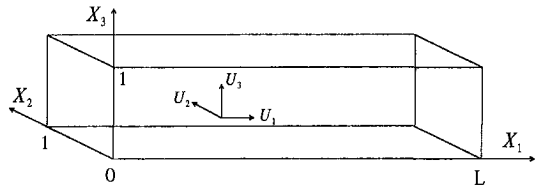

Fig. 1 Geometry and coordinate system

schemes. Using time-step independent solutions, the convergence with the grid refinement is then investigated. The above mentioned DNS solution is used as the reference. Section 4 presents the conclusion of this work.

2 Numerical Procedure

The geometry shown in Fig. 1 is described by the Cartesian coordinate system (X_1, X_2, X_3) with the corresponding velocity components (U_1, U_2, U_3). Pertinent equations for incompressible fluid flow are the equation of continuity:

$$\text{div } \mathbf{U} = 0, \tag{1}$$

and the Navier-Stokes equation:

$$\frac{\partial \mathbf{U}}{\partial T} + (\mathbf{U} \cdot \text{grad})\mathbf{U} = -\text{grad } P + \frac{1}{R_{e0}} \nabla^2 \mathbf{U}, \tag{2}$$

where R_{e0} is the Reynolds number defined as

$$R_{e0} = \tilde{U}_{m0}\tilde{b}/\tilde{\nu}, \tag{3}$$

and the standard mean bulk velocity $\tilde{U}_{m0}$ is given as

$$\tilde{U}_{m0} = \sqrt{2\Delta\tilde{P}/\lambda L\tilde{\rho}}, \tag{4}$$

assuming the Blasius' formula

$$\lambda = 2\Delta P/L = 0.316 R_{e0}^{-1/4}. \tag{5}$$

Dimensionless variables are defined using the standard mean bulk velocity $\tilde{U}_{m0}$, the width $\tilde{b}$ of the square duct and the density $\tilde{\rho}$ of the fluid. Throughout the paper dimensional values are denoted with $\sim$. As to the boundary condition, the no-slip condition is applied on the side walls, while the periodicity L in the X_1 coordinate direction is assumed for the velocity field. A constant pressure difference ΔP is applied between the upstream and the downstream boundaries in the X_1 direction.

A brief description of the solution procedure is given here. A uniformly spaced staggered grid system is defined in each coordinate direction. The discretized representations of the relevant equations are obtained through the control volume method, and are solved by an iterative algorithm similar to the SIMPLER method due to Patankar (1980). A specific feature of the present solution procedure (Hayase et al., 1990) is summarized in the following.

By reference to Fig. 2, values of an arbitrary quantity ϕ at the control volume boundaries in convective terms are expressed with the third-order Leonard's QUICK scheme (hereafter abbreviated as "QUICK scheme") or the second-order central difference scheme (abbreviated as "CENTRAL scheme") as,

Nomenclature

$\tilde{b}$ = width of the square duct
e = tolerance for the numerical solution dependent on the time step
E_1 = energy spectrum of U_1-velocity perturbation in wave number domain
$E[*]_{N_d}$ = averaging over N_d samples
h_T = computational time step
h_T^* = computational time step for the specified error tolerance
h_1, h_2, h_3 = grid spacing in the X_1, X_2, X_3 coordinate direction, respectively
h_{mean} = $= \sqrt[3]{h_1 h_2 h_3}$ = mean grid size
L = periodicity of the flow field in the X_1 direction
M_d = number of time series data
N_d = number of averaging data
N_1, N_2, N_3 = number of computational cells in the X_1, X_2, X_3 direction, respectively
p = order of discretization scheme
$P = \tilde{P}/(\tilde{\rho}\tilde{U}_{m0}^2)$ = pressure
r = grid refinement ratio
$R_{e0} = \tilde{U}_{m0}\tilde{b}/\tilde{\nu}$ = Reynolds number based on the mean bulk velocity evaluated with Blasius' formula
$R_{e\tau} = \tilde{U}_\tau \tilde{b}/\tilde{\nu}$ = Reynolds number based on the mean friction velocity
S_1 = energy spectrum of U_1-velocity perturbation in frequency domain
$T = \tilde{T}/(\tilde{b}/\tilde{U}_{m0})$ = time
$\mathbf{U} = (U_1, U_2, U_3)$ = velocity vector in (X_1, X_2, X_3) coordinate system
$U_\tau = \tilde{U}_\tau/\tilde{U}_{m0}$ = mean friction velocity
$U_c = \tilde{U}_c/\tilde{U}_{m0}$ = mean streamwise velocity at the center of cross section
$U_m = \tilde{U}_m/\tilde{U}_{m0}$ = mean bulk velocity
$\tilde{U}_{m0}$ = mean bulk velocity evaluated with Blasius' formula
(X_1, X_2, X_3) = Cartesian coordinate system (Fig. 1)
y = distance from the wall
y^+ = distance from the wall in wall unit
α = streamwise wave number of perturbation
α_B = bandwidth of energy spectrum
ΔP = pressure difference imposed between the upstream and the downstream boundaries
$\tilde{\epsilon}$ = dissipation rate per unit mass
$\eta = \tilde{\eta}/\tilde{b}$ = Kolmogorov length scale
$\lambda = 2\Delta P/L$ = resistance coefficient
$\tilde{\nu}$ = kinematic viscosity
$\tilde{\rho}$ = density of fluid
τ = Kolmogorov time scale
ϕ = arbitrary quantity
ω = circular frequency

Superscripts

m = index to discretized time
$\sim$ = dimensional value
$\overline{}$ = value averaged in time
$'$ = fluctuation from the mean value

Subscripts

0 = standard values based on Blasius' formula (Eq. (5))
I, II = quantity for fine and coarse grid system in GCI calculation, respectively
m = index to discretized time
n = index to discretized frequency

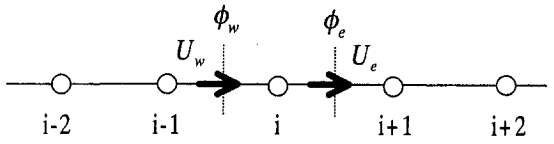

Fig. 2 One-dimensional staggered grid system for the control volume method

QUICK:

$$\phi_e = \phi_i + \underline{1/8(-\phi_{i-1} - 2\phi_i + 3\phi_{i+1})} \quad (U_e > 0)$$
$$= \phi_{i+1} + \underline{1/8(3\phi_i - 2\phi_{i+1} - \phi_{i+2})} \quad (U_e \le 0) \qquad (6)$$

CENTRAL:

$$\phi_e = \phi_i + \underline{1/2(-\phi_i + \phi_{i+1})} \quad (U_e > 0)$$
$$= \phi_{i+1} + \underline{1/2(\phi_i - \phi_{i+1})} \quad (U_e \le 0) \qquad (7)$$

In the expressions, underlined terms are evaluated as source terms in iteration process. These formulations for QUICK and CENTRAL schemes satisfy four rules necessary to the physically consistent numerical scheme due to Patankar (1980), and significantly improves the numerical stability (Hayase et al., 1992).

The MSI method of Schneider and Zedan (1981) is used to solve the linearized pentadiagonal matrix equations. For discretizing time derivative terms, the second-order accurate three-time-level implicit scheme is employed (Fletcher, 1988).

$$\left.\frac{d\phi_i}{dt}\right|^m = \frac{1}{h_T}\left(\frac{3}{2}\phi_i^m - 2\phi_i^{m-1} + \frac{1}{2}\phi_i^{m-2}\right) \qquad (8)$$

Three-dimensional and time-dependent calculation is performed without a turbulence model in order to examine the fundamental relation between the monotonic convergence property and the discretization schemes of convective terms.

3 Results and Discussion

Calculations were carried out on the Cray C916 at the Institute of Fluid Science, Tohoku University. Computational conditions are summarized in Table 1. In previous studies a periodicity L in the X_1 direction was assumed as 4 (Su and Friedrich, 1994), 6.4 (Huser and Biringen, 1993), or 6.3 (Madabhushi and Vanka, 1991) to ensure a sufficiently small two-point correlation for velocity fluctuations. The periodical length L is fixed to 4 in this study. It is noted that the effect of the periodicity on the solution is dependent on the computational grid resolution. This point is discussed later. Computation was performed with three grid systems of different grid resolution. An appropriate time step was first determined for each grid system. Nondimensional pressure difference ΔP corresponding to the Reynolds number of $R_{e0} = 9000$ is specified. Although the nondimensional mean bulk velocity $U_m = \tilde{U}_m/\tilde{U}_{m0}$ is not identical to unity for relatively coarse grid systems, it converges to 1 with improving the grid resolution.

The initial condition of the time-dependent calculation is obtained by interpolating the result of the former study (Hayase et al., 1991). In each grid system preliminary computation was performed until a statistically steady solution was obtained. The mean flow field and the statistical values of perturbations were then computed with the proceeding computational results.

Table 1 Computational conditions

		Present			DNS (Huser and Biringen)	
Grid system		Grid (A)	Grid (B)	Grid (C)	DNS (A)	DNS (B)
Grid points $N_1 \times N_2 \times N_3$		20×10^2	40×20^2	80×40^2	64×81^2	96×100^2
Grid spacing $h_1 \times h_2 \times h_3$		0.2×0.1^2	0.1×0.05^2	0.05×0.025^2	$0.1\times(0.004$ $-0.021)^2$	$0.1\times(0.003$ $-0.017)^2$
Mean grid size $h_{mean} = \sqrt[3]{h_1h_2h_3}$		0.126	0.063	0.032	0.011-0.035	0.010-0.030
Time step h_T (h_T* for 5% error torelance in U_m)	QUICK	0.1 (0.094)	0.05 (0.044)	0.025 (0.027)	0.0157	0.0126
	CENTRAL	0.05 (0.042)	0.025 (0.030)	0.01 (0.017)		
Convective term discretization		3rd-order QUICK or 2nd-order central			5th-order upwind	
Time derivative term discretization		2nd-order 3-time-level implicit			4th-order Runge-Kutta	
Total residual at convergence		0.01	0.01	0.015	-	-
CPU time [s] for one time step		2	15	100	-	-
Periodical length L		4			6.4	
Pressure difference ΔP		0.0649			0.1025	
Standard Reynolds number R_{e0} ($R_{e\tau}$)		9000 (573)			9484 (600)	

3.1 Effect of Time Step. The effect of the computational time step is crucial for the turbulent flow calculation since the flow contains a wide range of the frequency component in its fluctuation. Computation was performed with several values of the time step for each grid system and discretization scheme. Results are plotted in Fig. 3 for the mean bulk velocity obtained by averaging over nondimensional time period of 100. Each result tends to its convergent value with decreasing the time step. The rate of variation is larger for the finer grid, and that of CENTRAL scheme is larger than that of QUICK scheme for the same grid system. This implies that the finer spatial grid requires the smaller time step, and CENTRAL scheme also does than QUICK scheme.

Choi et al. (1994) made a study on the effect of the computa-

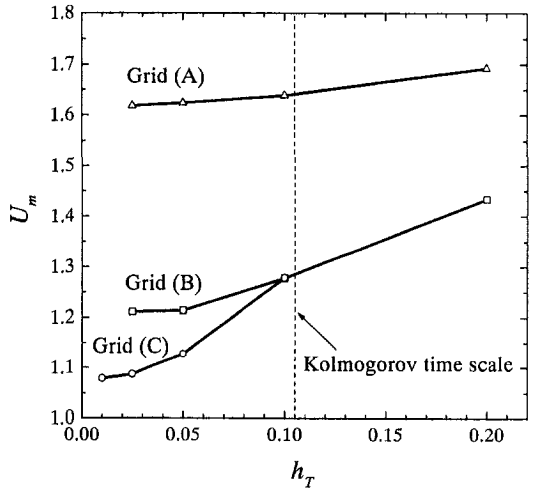

Fig. 3(*a*) QUICK

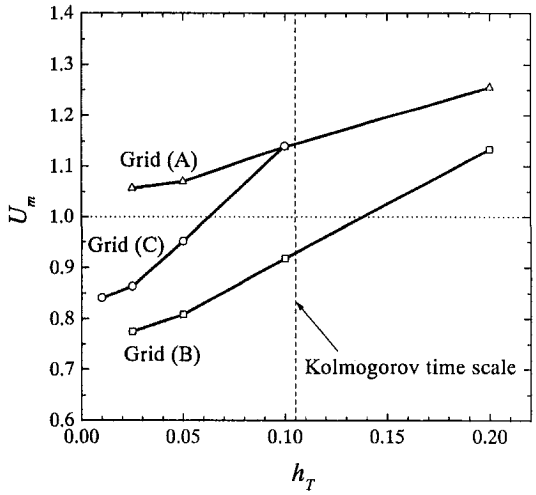

Fig. 3(*b*) CENTRAL

Fig. 3 Variation of the mean bulk velocity with the computational time step

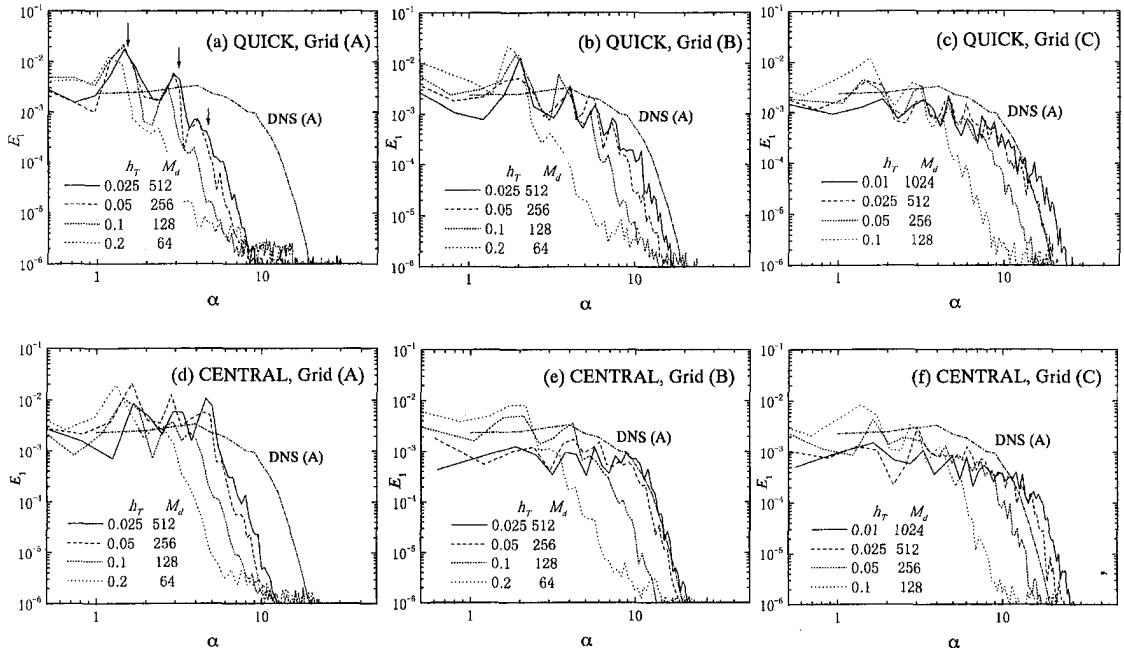

Fig. 4 Comparison of energy spectra for the U_1-velocity perturbation at the center of cross section

tional time step for a fully implicit method in the case of the turbulent flow through a two-dimensional channel. They concluded that the turbulent fluctuations can only be sustained if the computational time step is appreciably less than the Kolmogorov time scale defined as

$$\tau = \sqrt{\tilde{\nu}/\tilde{\epsilon}}(\tilde{U}_{m0}/\tilde{b}). \tag{9}$$

In the present condition, the Kolmogorov time scale is evaluated as $\tau = 0.105$. In Fig. 3 the present results for the grid systems (A) and (B) with QUICK and CENTRAL schemes reproduce the equivalent of turbulent perturbation for the time step larger than the Kolmogorov time scale. In the present semi-implicit solution procedure, Kolmogorov time scale does not necessarily determine the minimum computational time step required to preserve turbulent fluctuations. It is noted that the insensitivity of flow characteristics, e.g., laminar or turbulent, to variation of the time step is a favorable property for numerical procedures since such a numerical solution provides qualitatively correct result even with an insufficient temporal resolution.

The energy spectrum of the U_1-velocity perturbation at the center of a cross section is calculated by the following formula

$$S_1(\omega_n) = \mathbf{E}\left[\frac{h_T}{M_d}\left|\sum_{m=1}^{M_d} U_1'(t_m)\exp(-j\omega_n t_m)\right|^2\right]_{N_d}$$
$$(n=1, \ldots, M_d), \tag{10}$$

where $\omega_n = 2\pi n/(h_T M_d)$ is the nondimensional circular frequency, M_d the number of time series data, and $E[*]_{Nd}$ denotes the averaging over N_d samples.

In the following the energy spectrum is converted into that in the wave number domain as,

$$\mathbf{E}_1(\alpha_n) = \mathbf{U}_c\mathbf{S}_1(\omega_n) \tag{11}$$

where $\alpha_n = \omega_n/\mathbf{U}_c$ is the wave number. Figures 4(*a*)–(*f*) show convergence of the energy spectra with decreasing the time step for three spatial grid systems and for QUICK and CENTRAL schemes. All of the results are obtained from numerical solutions over the same nondimensional time interval of 102.4. The DNS result (Huser and Biringen, 1993) is plotted in each figure as the reference. In each figure the energy increases in a large wave number region with decreasing the time step and the profile of the spectrum converges to the different one depending on the spatial grid resolution and also on the discretization scheme. It is noted that the energy spectra for coarse grid systems have noticeable peaks in their profiles. These peaks represent the dominant wave modes whose wavelengths are nearly given as L/k ($k = 1, 2, 3, \ldots$), where L is the periodical length of the duct. Several wave numbers corresponding to these modes are indicated in Fig. 4(*a*).

The bandwidth of the energy spectra α_B is defined here as the wave number at which the energy spectrum curve crosses the threshold value of 10^{-4}. Figure 5 shows the variation of the bandwidth with the computational time step for three grid systems and QUICK and CENTRAL schemes. It is noted that the bandwidth is more sensitive to the time step than the mean bulk velocity (see Fig. 3). The DNS result (Huser and Biringen, 1993) is also plotted in the figure for reference.

The time step required for a specified error tolerance is evaluated here with the following formula.

$$h_T^* = \Delta\phi\,\frac{|h_{T2} - h_{T1}|}{|\phi_2 - \phi_1|}, \tag{12}$$

where ϕ_1 and ϕ_2 represent characteristic quantities of the solution, such as mean bulk velocity or bandwidth mentioned above, for the time step h_{T1} and h_{T2}, respectively, and $\Delta\phi$ denotes the specified tolerance for the quantity. The formula (12) assumes the linearly proportional relationship between the variation of the characteristic quantity and the time step. Figure 6 shows the values of h_T^* calculated for the tolerance of 5% of the reference values for the mean bulk velocity and the bandwidth with the mean spatial grid size defined as

$$h_{\text{mean}} = \sqrt[3]{h_1 h_2 h_3}. \tag{13}$$

This figure implies the computational time step should be decreased almost linearly proportional to the mean spatial grid size. It is also noted that the time step necessary to obtain an accurate energy spectrum should be smaller than that for the mean bulk velocity by a factor of 0.2, and the time step for CENTRAL scheme must be about half of that for QUICK scheme. The actual time step h_T used in the calculation was determined for each grid

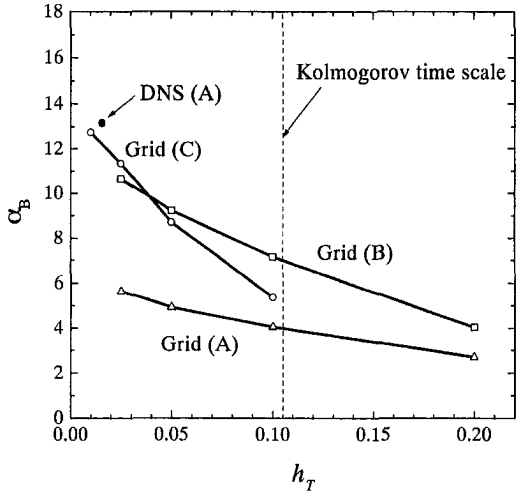

Fig. 5(*a*) QUICK

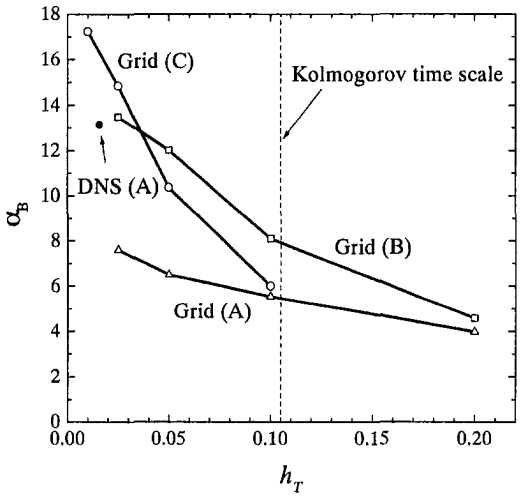

Fig. 5(*b*) CENTRAL

Fig. 5 Variation of the bandwidth of the energy spectrum with the time step

system and discretization scheme considering the value of h_T^* for the mean bulk velocity (see Table 1).

3.2 Effect of Spatial Grid Resolution. Convergence of the numerical solution with the spatial grid refinement is discussed in this section using the former solutions with the appropriate time steps for the grid resolution and the discretization scheme. Figure 7 shows the comparison of the convergence processes of the mean streamwise velocity profile along the wall bisector with QUICK and CENTRAL schemes. The velocity is normalized here by the nondimensional mean friction velocity $U_\tau = \sqrt{\Delta P/(4L)}$, and the distance from the wall is measured in wall unit $y^+ = U_\tau R_{e0} y$. Results of DNS (Huser and Biringen, 1993) and the linear profile $\bar{U}_1/U_\tau = y^+$ are also plotted in the figure as reference. In the case of QUICK scheme in Fig. 7(*a*), the coarse grid (A) gives a rather poor result, but the profile monotonically converges to the DNS results as the grid is refined to (B) or (C). The convergence process of CENTRAL scheme in Fig. 7(*b*) is different from the former case. The coarse grid (A) shows unexpectedly good agreement with the DNS results. The velocity profile, however, diverges from those of DNS with the refined grid (B), and again converges with further refinement to the grid (C).

Convergence processes of the energy spectra with the grid refinement for QUICK and CENTRAL schemes are compared in Fig. 8. Variation of the spectrum profile for QUICK in Fig. 8(*a*) is

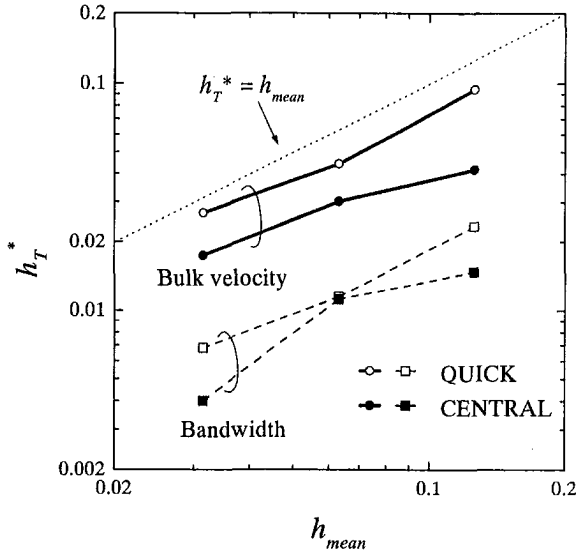

Fig. 6 Computational time step required for 5% error tolerance with the mean spatial grid size

characterized by a monotonic increase in a region of large wave number and small change in that of small wave number. The result of CENTRAL scheme reveals rather complex convergence pro-

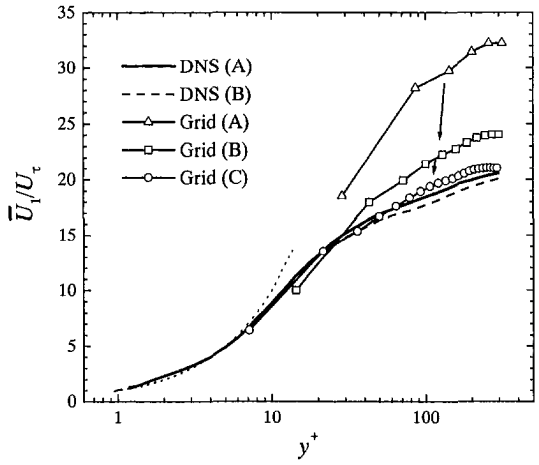

Fig. 7(*a*) QUICK

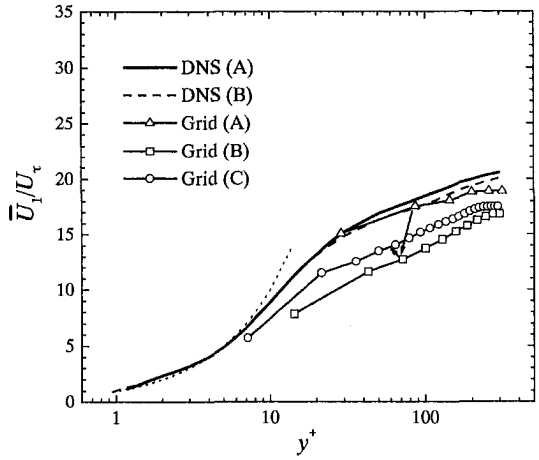

Fig. 7(*b*) CENTRAL

Fig. 7 Convergence of the mean U_1-velocity profile with spatial grid refinement

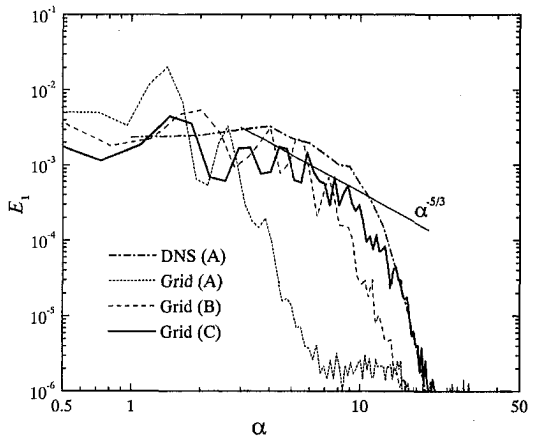

Fig. 8(*a*) QUICK

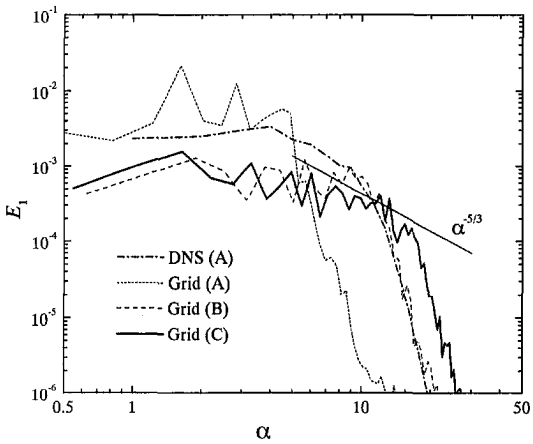

Fig. 8(*b*) CENTRAL

Fig. 8 Convergence of the energy spectrum with spatial grid refinement

cess; the energy spectrum increases for large wave numbers but decreases for small ones. It is noted that the inertial subrange with the slope of $\alpha^{-5/3}$ appears in both the solutions for QUICK and CENTRAL schemes with the fine grid (C).

Monotonic convergence with the grid refinement is evaluated for the mean bulk velocity and the bandwidth in Fig. 9. Variation of the mean bulk velocity with the mean grid size in Fig. 9(*a*) shows a good contrast between the monotonic convergence of QUICK scheme and the non-monotonic one of CENTRAL scheme. At the mean grid size of $h_{mean} = 0.126$ corresponding to the coarse grid (A), the result for QUICK scheme gives the 60% larger estimation for the mean bulk velocity, but it converges monotonically toward the exact value of unity with decreasing the mean grid size. The result for CENTRAL scheme, on the other hand, gives a fairly good result of the only 8% excess mean flow at $h_{mean} = 0.126$, but it decreases below the exact value to the minimum point and again increases to converge to 1 rather slowly with decreasing the mean grid size. This non-monotonic convergence of CENTRAL scheme has essential shortcomings. First, an improvement of the grid resolution does not necessarily result in an improvement of the accuracy of the solution. For example, the error for $h_{mean} = 0.063$ is worse than that of $h_{mean} = 0.126$ in the figure. Second, a non-convergent solution may behave as the convergent one. The variation of the mean bulk velocity with the change of the grid resolution becomes very small around the extremum point near $h_{mean} = 0.063$, satisfying the necessary condition of the convergence. The monotonic behavior of QUICK scheme, which enables us to properly estimate the exact result from solutions with rather coarse grid systems, is preferable to the more complex convergent behavior of CENTRAL scheme.

In the present section the time step for QUICK is set twice as large as that of CENTRAL scheme for each grid system to keep the error of solutions in the same order of magnitude between the discretization schemes (see Table 1). The other result for QUICK with the same time step as CENTRAL scheme for each grid system is plotted in Fig. 9(*a*) with a broken line. The both QUICK results are very close, confirming the computational time steps are chosen appropriately. The result of the DNS (Huser and Biringen, 1993) is plotted in the figure. The error bar denotes the extent of the mean grid size due to the non-uniform grid spacing. Kolmogorov length scale in the buffer region near the wall is estimated as,

$$\eta = \frac{(\tilde{\nu}^3/\tilde{\epsilon})^{1/4}}{\tilde{b}} = \frac{\tilde{\nu}^{3/4}}{\tilde{b}(0.01\tilde{U}_{m0}^3/\tilde{b})^{1/4}} \tag{14}$$

The smallest grid spacing of the DNS (B) near the wall is compatible to the Kolmogorov length scale, and the largest spacing at the center of the cross section is almost the same as that of the present fine grid (C). It is interesting the mean bulk velocity of DNS (B) is nearly the same as the present QUICK result with the

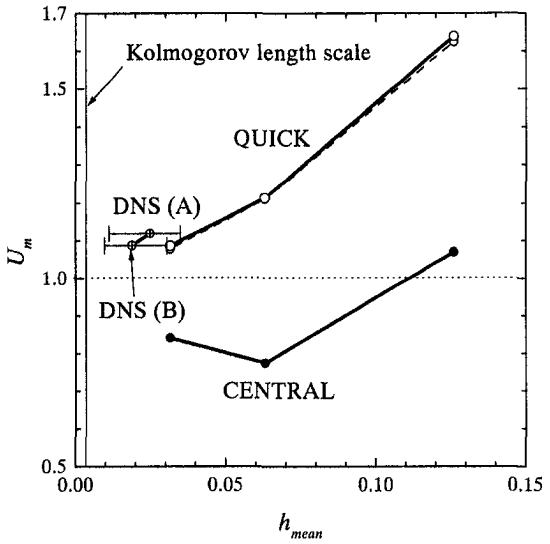

Fig. 9(*a*) Mean bulk velocity

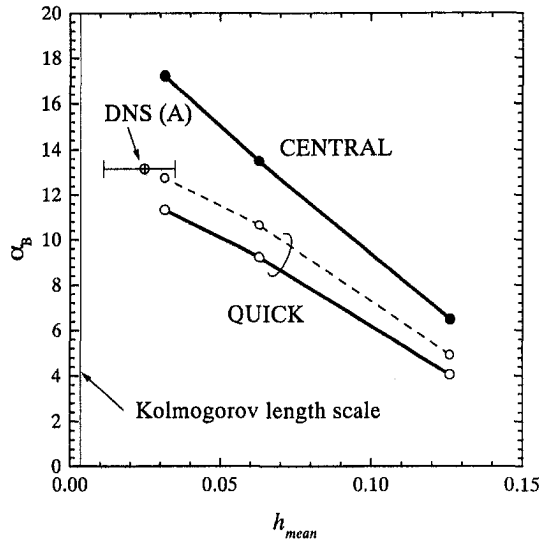

Fig. 9(*b*) Bandwidth of energy spectrum

Fig. 9 Convergence of characteristic quantities with spatial grid refinement

Table 2 Grid Convergence Index (GCI) for the mean bulk velocity

Scheme	Grid	Error (%)	GCI_I (%)	GCI_{II} (%)
QUICK ($p = 3$)	A	64	-	120
	B	21	15	40
	C	9	5	-
CENTRAL ($p = 2$)	A	7	-	150
	B	23	38	32
	C	16	8	-

uniformly spaced grid (C), implying additional grid points of DNS (B) near the wall make little improvement in the accuracy of the mean bulk velocity.

Solid lines in Fig. 9(*b*) show the comparison between variations of the bandwidth with the mean grid size for QUICK and CENTRAL schemes. Reliability of the results is again estimated by the QUICK result with the broken line which is obtained with the smaller time step of CENTRAL scheme. The DNS result is available only for the coarse grid in this case (Huser and Biringen, 1993), and it is difficult to specify the exact value for the bandwidth. Although there is no evidence of the non-monotonic convergence of CENTRAL scheme, the comparison of these results suggests that the CENTRAL result somewhat decreases to converge to the exact value as the grid spacing is further reduced.

Grid Convergence Index (GCI) has been proposed by Roache (1994) to estimate the grid-dependent error of numerical solutions with two computational grid systems as,

$$GCI_I = \frac{3}{r^p - 1}\left|\frac{\phi_{II} - \phi_I}{\phi_I}\right|$$

$$GCI_{II} = \frac{3r^p}{r^p - 1}\left|\frac{\phi_{II} - \phi_I}{\phi_I}\right| \qquad (15)$$

where the subscript I and II denotes the fine and the coarse grid, respectively, $r = h_{II}/h_I$ is the grid refinement ratio, p the order of the discretization scheme, and ϕ denotes an arbitrary quantity of solutions. These indices are derived on the Richardson extrapolation assuming the monotonic convergence of the numerical method (Roache, 1994). GCI values are obtained with grids (A) and (B), or grids (B) and (C) for the mean bulk velocity in Fig. 9(*a*). The results are compared with the actual errors of the solutions in Table 2. GCI values monotonically decreases with the grid refinement for both QUICK and CENTRAL schemes, properly estimating the actual errors of the solutions except for the deceivingly small error of the CENTRAL scheme result on grid (A). It is also noted that GCI value for the CENTRAL scheme with grid (C) gives the estimation of half the real error, but GCI value can be smaller for another computational condition. The difference of the quantity ϕ in Eq. (15) may become very small if the other grid is chosen between grid (A) and (B) resulting in the mean bulk velocity very close to that of grid (C) (see Fig. 9(*a*)).

Averaging the velocity field in time over the nondimensional time period of 100 and in space assuming the rotational symmetry, we obtained the mean velocity and the perturbation velocity fields. Results for three grid systems and QUICK and CENTRAL schemes are shown in Fig. 10. Each figure consists of the mean U_1-velocity contours (upper left), the mean transverse velocity vectors (lower left), contours of the RMS value of the U_1-velocity fluctuation (upper right), and the Reynolds stress (lower right). A result of DNS (Huser and Biringen, 1993) is also given in Fig. 11 for reference. Contours of the U_1-velocity component reproduces characteristic concave contour lines in the grids (B) and (C) for QUICK, and in the grid (C) for CENTRAL. The secondary flow motion appears in all of the lower left results. In relatively coarse grids (A) and (B) intensity of the secondary flow vortices for CENTRAL scheme is smaller than that for QUICK. Locations of the center of vortices are almost the same between the grid (B) for QUICK and the grid (C) for CENTRAL, but the vortex shifts

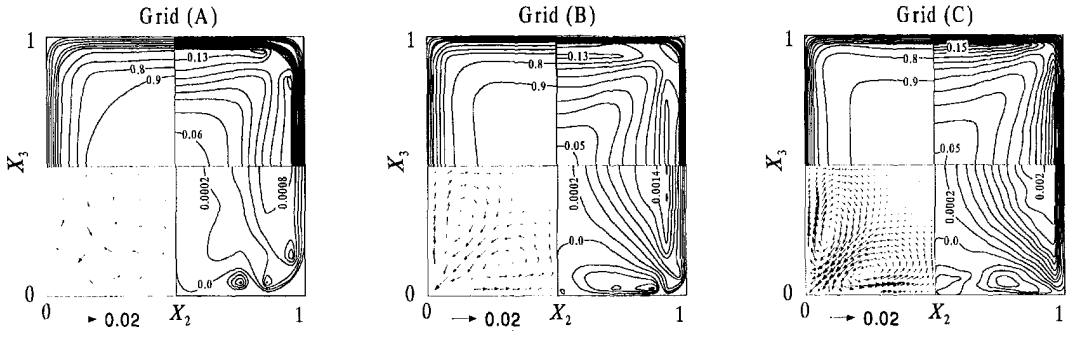

Fig. 10(*a*) QUICK

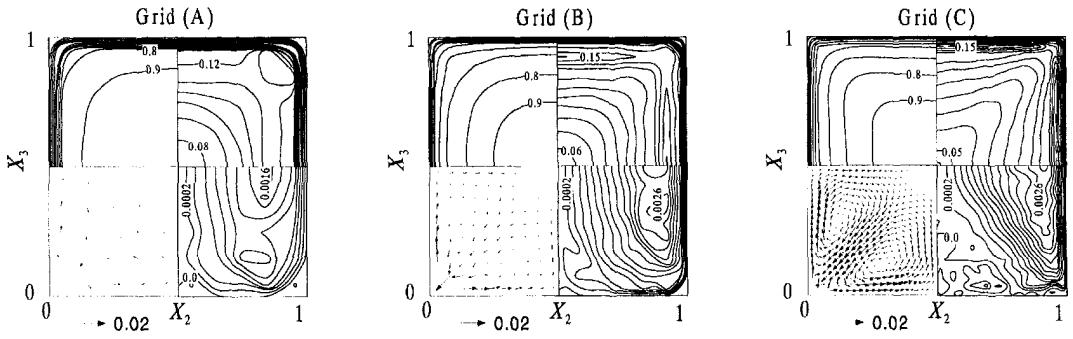

Fig. 10(*b*) CENTRAL

Fig. 10 Comparison of the flow structure between grid systems and discretization schemes. Upper left: mean U_1-velocity contours, U_1/U_c; lower left: mean transverse velocity vectors, $(U_2, U_3)/U_c$; upper right: contours of RMS value of U_1-velocity fluctuation, $(\overline{U_1^2})^{1/2}/U_c$; lower right: contours of the Reynolds stress, $\overline{U_1U_2}/U_c^2$

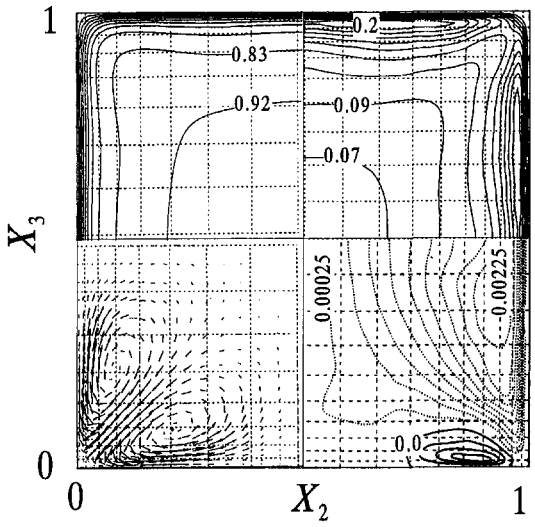

Fig. 11 Flow structure of DNS result (Huser and Biringen, 1993). Upper left and lower left: DNS (A), upper right and lower right: DNS (B), also see key in Fig. 10.

toward the corner in the grid (C) for QUICK, showing a good agreement with the DNS result in Fig. 11. Distributions of the RMS value of the U_1-velocity fluctuation and the Reynolds stress in grid (C) for QUICK agrees well with the DNS result, and the other results even in coarse grid systems also have qualitatively the same structure.

4 Conclusions

This paper has dealt with the characterization of the discretization schemes for the convective terms from the viewpoint of the monotonic convergence of the solutions with the grid refinement. Two typical discretization schemes of the second-order central difference scheme and the third-order Leonard's QUICK scheme were considered. A fully developed turbulent flow through a square duct was calculated via a SIMPLER based finite volume method without a turbulence model. Convergence of the numerical solution with the grid refinement was investigated for the mean flow and the perturbation properties. Comparison between the behaviors of the discretization schemes has revealed that the QUICK scheme results in the preferable monotonic convergence, while the second-order central difference scheme undergoes the non-monotonic convergence. The latter may mislead the determination of the convergence with the grid refinement or may cause trouble in applying the Richardson extrapolation procedure to estimate the numerical uncertainty.

Acknowledgments

The computer code ROTFLO2 used in this study is developed in University of California at Berkeley by T. Hayase, J. A. C. Humphrey, and R. Greif. The author gratefully acknowledges the support received from Grant-in-aid for Scientific Research (#05240202). The calculations were performed on the Cray C-916 in the Institute of Fluid Science, Tohoku University.

References

Celik, I., and Karatekin, O., 1997, "Numerical Experiments on Application of Richardson Extrapolation with Nonuniform Grids," ASME JOURNAL OF FLUIDS ENGINEERING, Vol. 119, pp. 584–590.

Choi, H., and Moin, P., 1994, "Effects of the Computational Time Step on Numerical Solutions of Turbulent Flow," *Journal of Computational Physics,* Vol. 113, pp. 1–4.

Demuren, A. O., and Rodi, W., 1984, "Calculation of Turbulence-Driven Secondary Motion in Non-Circular Ducts," *Journal of Fluid Mechanics,* Vol. 140, pp. 189–222.

Demuren, A. O., and Wilson, R. V., 1994, "Estimating Uncertainty in Computations of Two-Dimensional Separated Flows," ASME JOURNAL OF FLUIDS ENGINEERING, Vol. 116, pp. 216–220.

Fletcher, C. A. J., 1988, *Computational Techniques for Fluid Dynamics,* Springer-Verlag, Vol. 1, p. 302.

Freitas, C. J., 1993, "Policy Statement on the Control of Numerical Accuracy," ASME JOURNAL OF FLUIDS ENGINEERING, Vol. 115, pp. 339–340.

Hayase, T., Humphrey, J. A. C., and Greif, R., 1990, "Mini Manual for ROTFLO2," Department of Mechanical Engineering Report, #FM-90-1, University of California at Berkeley.

Hayase, T., and Suematsu, Y., 1991, "Direct Numerical Simulation of Turbulent Flow in a Square Pipe," *Proceedings of 3rd Triennial International Symposium on Fluid Control, Measurement and Visualization,* San Francisco, W. C. Yang and R. L. Woods, eds., ASME, pp. 99–106.

Hayase, T., Humphrey, J. A. C., and Greif, R., 1992, "A Consistently Formulated QUICK Scheme for Fast and Stable Convergence Using Finite-Volume Iterative Calculation Procedures," *Journal of Computational Physics,* Vol. 98, pp. 108–118.

Huser, A., and Biringen, S., 1993, "Direct Numerical Simulation of Turbulent Flow in a Square Duct," *Journal of Fluid Mechanics,* Vol. 257, pp. 65–95.

Leonard, B. P., 1979, "A Stable and Accurate Convective Modeling Procedure Based on Quadratic Interpolation," *Computational Methods in Applied Mechanics and Engineering,* Vol. 19, pp. 59–98.

Madabhushi, R., and Vanka, S., 1991, "Large Eddy Simulation of Turbulence-Driven Secondary Flow in a Square Duct," *Physics of Fluids A,* Vol. 3, pp. 2734–2745.

Myong, H. K., and Kobayashi, T., 1991, "Prediction of Three-Dimensional Developing Turbulent Flow in a Square Duct with an Anisotropic Low-Reynolds-Number k-e Model," ASME JOURNAL OF FLUIDS ENGINEERING, Vol. 113, pp. 608–615.

Patankar, S. V., 1980, *Numerical Heat Transfer and Fluid Flow,* Hemisphere, Washington, DC/New York.

Roache, P. J., 1994, "Perspective: A Method for Uniform Reporting of Grid Refinement Studies," ASME JOURNAL OF FLUIDS ENGINEERING, Vol. 116, pp. 405–413.

Schlichting, H., 1979, *Boundary-Layer Theory,* 7th English Ed., McGraw-Hill, p. 612.

Schneider, G. E., and Zedan, M., 1981, "A Modified Strongly Implicit Procedure for the Numerical Solution of Field Problems," *Numerical Heat Transfer,* Vol. 4, pp. 1–19.

Su, M., and Friedrich, R., 1994, "Investigation of Fully Developed Turbulent Flow in a Straight Duct with Large Eddy Simulation," ASME JOURNAL OF FLUIDS ENGINEERING, Vol. 116, pp. 677–684.

The Effects of Secondary Flow and Passive Injection on the Motion of Solid Particles Entrained in Flow Through a Curved Converging Channel

James J. Ventresca
Physical Scientist,
National Exposure Research Laboratory,
United States Environmental Protection Agency,
Las Vegas, NV 89118

Wilfred T. Rouleau
Professor of Mechanical Engineering,
Department of Mechanical Engineering,
Carnegie Mellon University,
Pittsburgh, PA 15213

The three-dimensional effects of secondary flow, passive injection, and particle size on the motion of solid particles entrained in a laminar, incompressible flow through a curved, converging, rectangular passage were numerically investigated. Emphasis was placed on observing the physical mechanisms that cause particles 5 μm and smaller in diameter to deposit on passage surfaces and to concentrate near the endwalls and mid-span at the passage exit. Particle trajectories were calculated for 5, 30, and 300 μm diameter solid particles. It was observed that the paths of 5 μm particles were similar to the streamlines of the three-dimensional flow in the channel until the particles encountered the boundary layers on the blade surfaces and endwalls, where they would graze the surfaces (contributing to particle deposition) and concentrate at the exit of the channel. Particles of 30 μm diameter, however, were only slightly affected by secondary flows, but were affected enough to be made to concentrate at the exit near the endwall and mid-span surfaces. Particles of 300 μm diameter were not affected by secondary flows at all. The particle trajectories showed that the passage secondary flow convected particles across endwalls toward the pressure and suction surface boundary layers of the blades. It was observed that small particles were made to decelerate and/or concentrate in the boundary layers near the passage exit. It was found that this concentration of particles along the suction surface and endwalls could be significantly reduced by means of passive injection. (Passive injection is a method of inducing the flow of jets in the curved portion of an airfoil shaped surface due to the pressure difference on opposing sides. This is accomplished by means of holes or slots that have been drilled through the surface at strategic locations.)

Introduction

Due to an increased interest from the U.S. government and industries for the use of coal as an alternative energy source, the study of erosion in coal-fired gas turbines has been an area of important research. Dirty fuels such as coal, containing large amounts of mineral particles, cause erosion of expensive turbine blades. However, with new technological advancements in methods for fluidized bed combustion, gasification and particle separation, coal now offers great promise in meeting the requirements of a gas turbine power plant. But even though the power gas can be sent through these cleaning devices, particles with mean diameters of 10 μm or less may still remain in the gas flow and cause an unacceptable reduction of the life of turbine blades through erosion. Also, blade erosion on another scale has been a significant problem in the aircraft industry and in military applications where operations take place in extremely dusty environments, such as the desert. For example, in the operation of a gas turbine engine in a dusty environment, dust clouds can be generated which contain particles as large as 200 μm in diameter. It has been shown that the damage to a 1000 hp engine, typical for helicopters, can limit the blade life to only 10 hours. This damage is caused by the erosion of the compressor blading through the pitting and cutting back of leading edges and the thinning of trailing edges. Air filtration and coatings can be used; however, they reduce the payload capacity and performance of the engine. Also, it was found that blade coatings cannot be applied in a thickness adequate for developing full effectiveness (Grant, 1973).

In the past, in order to study this small-particle erosion phenomenon, it was shown by using patched flow models (Ulke and Rouleau, 1976) that particles with mean diameters of 10 μm or less are likely to concentrate in the boundary layers of the blade passages due to the action of secondary flows that convect them towards the endwalls and blade surfaces. Thus, the passage wake would contain a high concentration of particles that could cause localized erosion damage in a following blade cascade. On the other hand, large particles are not affected by secondary flows, so that erosion is somewhat uniform over the leading and trailing edges of the blades.

Also, passage vortices, which are always generated when a viscous fluid flows through a curved passage bounded by endwalls, have been implicated as the mechanism that magnifies the erosive tendency of small particles. Therefore, passive injection was proposed by Tal et al. (1982) as a means of reducing the strength of the passage vortices, thereby mitigating erosion. This method utilizes the pressure difference that exists between the two sides of a curved blade to produce jets of fluid by means of holes or slots that have been drilled through the blade, near the endwalls, at strategic locations. Tal, Lee and Rouleau conjectured that these fluid jets would reduce the strength of the passage vortices. However, it was found in the present research that the injection jets have only slight effects on the reduction of secondary flow, but that

Contributed by the Fluids Engineering Division for publication in the JOURNAL OF FLUIDS ENGINEERING. Manuscript received by the Fluids Engineering Division April 15, 1996; revised manuscript received August 5, 1998. The long delay until publication is due mostly to the JFE Editorial Board. Associate Technical Editor: D. Stock.

the great potential effects come from the redirection of particles near the suction surface and endwall boundary layer, so that the particles will not concentrate at the passage exit and deposit on the corresponding surfaces.

An analytical or numerical approach to the problem of erosion reduction (especially by particles less than 10 μm) must stem from an accurate three-dimensional flow model based on the Navier-Stokes equations for fluid flowing in the blade passage, because the no-slip condition on endwalls and blade surfaces, which creates boundary layers, is fundamental to the formation of passage vortices. Particle trajectories can then be determined in order to quantify the effect of passive injection and to estimate the erosion rate from particle impact dynamics based on experimental correlations, e.g., Grant (1973).

Past analysis of erosion in blade passages has been very approximate because the complexity and computational requirements of modeling viscous flow in an actual blade passage could not be handled satisfactorily. For example, Ulke and Rouleau (1976) superimposed boundary layers and secondary flows onto through-flow models based on potential flow. These "patched" flow models are inaccurate for very small particles (less than 10 μm) that follow streamlines more closely than larger particles, since the paths of larger particles are affected more by inertia than are the smaller particles. Hamed and Kuhn (1993) investigated the trajectories of 150 μm diameter sand particles using a laser Doppler anemometer, and formulated statistical correlations for particle restitution ratios to be used in particle tracking programs. Grant (1973) also formulated correlations for material removal and restitution ratios, but made no calculations for particles less than 20 μm. Wenglarz (1987) has studied experimental models for testing turbine blade passages in coal-fired turbines in the interest of studying particle erosion and deposition due to particles greater than 2 μm. Also, El-Sayed (1986), using experimental velocity data for the flow through a converging blade passage, has estimated the erosion due to 1–5 μm particles.

With the availability of a modern supercomputer, CRAY YMP-C90, and a three-dimensional Navier-Stokes code, FDNS3D, this present research concentrated on accurately modeling flow through a curved, rectangular, converging, thin-blade passage, with the passage modeled using a mean camber-line profile. In order to model the pressure difference across the blades, which is necessary for passive injection, the boundary conditions were modeled as if the passage was situated in a blade cascade. The models and numerical solutions were then validated and compared with experimental data. The feasibility of passive injection was studied by modifying FDNS3D to create the injection jets as an active boundary condition. The injection geometries were then modified through an external input file, which facilitated optimization with respect to the reduction of secondary flow.

With the above models, the major goals of this research were to first obtain numerical simulations of the three-dimensional flow through this simple flow passage and to calculate particle trajectories with and without passive injection being applied. Then, passive injection was to be optimized as much as possible, with respect to the reduction of the motion of particles towards the blade surfaces and endwalls, by observing the resulting particle paths over a selected range of injection geometries. (It should be noted that the authors could not find any earlier analysis where any type of particle motion or erosion calculations were made with consideration of secondary flow or passive injection.) The effects of secondary flow, passive injection and particle size on the paths of 5, 30, and 300 μm diameter solid particles were to be analyzed with special attention given regarding the resulting location of particles at the exit of the passage, where a concentration of particles near the inner endwall in a plane perpendicular to the blade surface would (in actual turboexpanders) cause excessive localized erosion to a following rotating blade cascade. Calculations for material removal, based on the results from particle trajectories and semi-empirical correlations, were to be made along with observations with respect to the possible deposition of 5 μm particles on the passage surfaces due to the effects of secondary flows.

Governing Equations

Flowfield Solution and Particle Trajectories. The solution of the steady-state, laminar, incompressible, three-dimensional flowfield was obtained using FDNS3D, which solved the finite difference form of the conservation of momentum and mass equations with constant properties:

$$\rho \mathbf{g} - \nabla p + \mu \nabla^2 \mathbf{V} = 0 \tag{1}$$

$$\nabla \cdot \mathbf{V} = 0 \tag{2}$$

where ρ is the fluid density, $\mathbf{V}$ is the fluid velocity vector, μ is the fluid dynamic viscosity, $\mathbf{g}$ is the gravity vector and p is the fluid pressure.

A particle tracking program was written, based on an analytical solution (fourth-order power series) to the equations of motion for a solid particle in a rotating and nonrotating frame of reference. The program was validated first by substituting the solutions back into the equations of motion, and then by checking the initial and final angle of impacts on all passage surfaces for several test grids (passages). Trajectories for 5 μm diameter solid particles were also compared with streamlines calculated using "TECPLOT V," since these very small particles closely follow streamlines (until an impact on a passage wall occurs).

The motion of a solid particle suspended in a fluid is determined by Newton's second law of motion:

$$\mathbf{F}_D = m_p \ddot{\mathbf{X}} \tag{3}$$

where $\mathbf{F}_D$ is the external force vector acting on a particle (drag force), m_p is the mass of the particle and $\ddot{\mathbf{X}}$ is the resulting acceleration vector of the particle.

In the formulation of the equations of motion, certain assumptions have to be made in order to reduce the numerous complexities. It was assumed that solid spherical sand particles are suspended in air which has a much lower density. Magnus, buoyant, gravitational forces and forces due to pressure gradients were assumed to be small with respect to drag forces. Also neglected were the apparent mass and wall effects. The apparent mass effect is important only if the density of the fluid is comparable to that of the particle and accounts for the additional force required to accelerate a portion of the fluid surrounding the particle. The "Basset force," which takes into account the effect of the deviation in the flow pattern from steady state, was also neglected. This is an instantaneous flow resistance that becomes substantial when particles are accelerated at high rates (Putnam, 1957 and Soo, 1967).

Drag Coefficients. Drag on a solid particle is caused by surface friction and pressure forces that result from flow separation. Drag can't, in general, be accurately modeled by an analytical equation (except for $\mathrm{Re}_p \ll 1$) mainly due to unknown flow separation. It is therefore necessary to calculate the drag force based on empirical equations. The accuracy of these equations in a particular flow is dependent on that flowfield and how much it differs from the flow used to formulate the empirical correlations (turbulence, unsteadiness, etc.).

In a recent paper by Kladas and Georgiou (1993), the relative accuracies of 19 Drag $-$ Re_p relationships were investigated. Particles were subjected to two types of flowfields: swirling flow and crossflow over a cylinder. The results of these experiments were compared and the relative accuracy of each equation was assessed. From this work, four sets of equations valid over different ranges of particle Reynolds numbers, were obtained and used in a particle tracking program. The equations that were chosen fit the form: $C_D = A + B\,\mathrm{Re}_p^m$, where C_D is the drag coefficient, Re_p is the Reynolds number based on particle diameter, and A, B, and

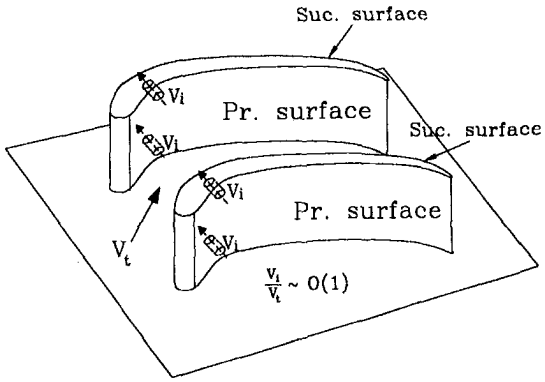

Fig. 1 Passive injection applied to blade passage near endwalls

m are selected from a table based on the value of Re_p (see Kladas, 1993 and Ventresca, 1994).

Numerical Scheme and Boundary Conditions

Flowfield Solution. FDNS3D solves the three-dimensional finite difference form of the Navier-Stokes equations using primitive variables in a general coordinate mesh system. It can solve reacting and non-reacting, compressible, incompressible, laminar or turbulent flows based on a pressure based predictor/multicorrector solution algorithm. Adaptive second-order central differencing schemes and fourth-order dissipation terms are used to model convective terms. Second-order central differencing schemes are used for the viscous and source terms and a first-order upwind scheme is employed for all scalar transport equations. The pressure based predictor/multicorrector solution procedure is used to ensure velocity-pressure coupling and divergence-free flowfield solutions at the end of each time marching step. For the pressure based multi-corrector algorithm, the pressure correction equation used in the code was derived from approximate, discretized momentum and continuity equations. The velocity and density fields are perturbed and expanded in the continuity equation. By neglecting higher order terms and utilizing the velocity correction relation, a predictor-corrector equation for compressible/incompressible flows is obtained.

Passive Injection. Since the source of the actual flow through holes in the blade is the boundary layer on the pressure surface of the blade, an approximate flow analysis must be made on the basis of the energy equation. With no heat transfer or shaft work, and by neglecting changes in thermal and potential energy, the following expression is obtained for a control surface surrounding the fluid in the boundary layer that enters an injection hole:

$$\frac{p_p}{\rho g} + \frac{V_1^2}{2g} = \frac{p_s}{\rho g} + \frac{V_2^2}{2g} + h_v, \tag{4}$$

where p_p is the pressure on the pressure surface, p_s is the pressure on the suction surface and ρ is the density of the gas. It is then assumed that the viscous work term, h_v, and the entrance velocity, V_1, are negligible. Constraining the jets to flow normal to the blade surface (by accounting for the shape of the blade), leads directly to the final expressions for the components of the injection jets, V_2, at the node on the blade suction surface. The pressure difference is simulated using an offset in the pressure surface nodes which are calculated from the geometry of the passage. Here the pressures are taken at the very next nodes normal to the surface, above the "holes," as an approximation, since the actual nodal points representing the inlet surface of the control volume are unknown. This approximation has been validated with the experimental data for injection velocities given by Madden (1984) (Fig. 1). The passive injection "holes" were implemented in various subroutines of FDNS3D that initialize the injection velocity expressions, based on the injection data file and blade shape data obtained from the grid file. The expressions were then evaluated using the solution for the pressure difference across the blades using the main flowfield solution.

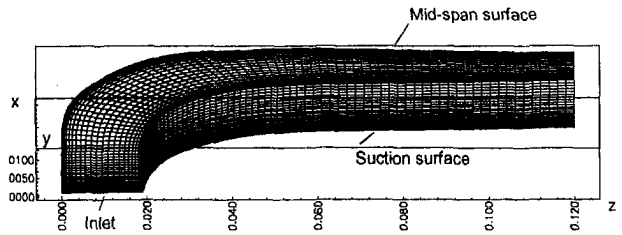

Fig. 2 The 3D computational grid showing inlet, suction and mid-span surfaces

Particle Trajectories. "Ptrack," a particle tracking program, was written by the authors on the basis of an analytical solution (series solutions and a direct analytical solution for the axial position) to the nonlinear three-dimensional equations of motion for a solid particle in a non-rotating and rotating frame of reference. The program was used to trace multiple solid particles through the three-dimensional, rectangular, converging blade passage. "Ptrack" accepts data for the initial particle location, velocity and density, along with the angular velocity of the blade passage about an axis located at a specified radial distance. The user also selects the density and dynamic viscosity of the fluid entraining the eroding particles.

The program proceeds by 1) searching for the particle's cell location 2) searching the flowfield to calculate the gas velocity at that point (based on the weighted average of surrounding nodal velocities) 3) calculating the Reynolds number based on particle diameter and relative velocity 4) calculating the drag coefficient using one of four empirical equations 5) calculating a time step that will keep the maximum distance traveled no more than 25% of the cell's smallest dimension 6) determining if the particle's new position implies that an impact with a boundary has occurred and 7) determining the new particle position and velocity vector based on either rebound equations or the series solution of the equations of motion. The algorithm proceeds until all particles have exited the blade passage or have obtained a zero velocity.

Computational Mesh. A three-dimensional, nonorthogonal, structured grid was used to model the blade passage in the analysis and was obtained from the model of a converging blade passage used in experiments by Lasser (1982) and Madden (1984) (Fig. 2). In order to make direct comparisons with their experimental results for the through-flow and secondary velocity components, the computational grid was constrained to contain nodes on the same cross sections[1] used by Lasser and Madden. The clustering of nodes in shear layers (needed to insure that steep velocity gradients are resolved) and insuring that nodal placements adjacent to the boundaries were orthogonal (needed to help correctly implement boundary conditions), served as additional constraints.

The final grid nodal spacing ($i_{max} = 67$, $j_{max} = 27$, $k_{max} = 23$) and nodal clustering was arrived at by an iterative process. Computational meshes were constructed using a two boundary transfinite interpolation code GRID3D/2D. The passage was split into two zones, separate grids were constructed and then patched together. This extra work was necessary in order to obtain a grid satisfying the above constraints since nodal clustering around the bend tended to create skewed cross sections.[2] The Jacobians of the entire grid's metric coefficients, along with the resulting smooth-

[1] This geometry was obtained by Lasser, modeled after a commercial turboexpander.

[2] Note that the grid was generally nonorthogonal, and that its cross-sections were constrained to be nearly planar, in order to compare with experimental data.

ness of nodal distributions, were checked throughout the iteration process in order to help insure that geometrically induced errors were minimized. Grid independence was demonstrated by comparing solutions of four successive grids and showing that the difference from the chosen grid did not vary by more than an estimated 1.1% from a grid with dimension 73% larger.

Boundary Conditions. At the inlet of the blade passage, the velocity profile was specified. In order to make comparisons with experimental data, a best-fit was made of Lasser's velocity data at the inlet (Lasser, 1982), only taking into account the endwall boundary layer (the presence of an inlet endwall endwall boundary layer is important to model since it directly affects the passage secondary flow).[3] Also at the inlet, pressure was extrapolated upstream. For all solid surfaces, the no-slip condition was specified in the momentum equations. The flowfield was assumed to be a mirror image about the midspan surface, so that a symmetry boundary condition could be used. Here, zero normal gradients for all scalar quantities were satisfied using a second order backward differencing scheme. Velocity vectors were insured to have zero mass flux and flux gradients across the plane of symmetry. Pressure conditions along the walls were extrapolated using zero normal gradients. At the exit plane, global mass conservation was used to supply FDNS3D with velocities to be used in the corrector equations. Finally, passive injection was applied in the manner stated in the above section.

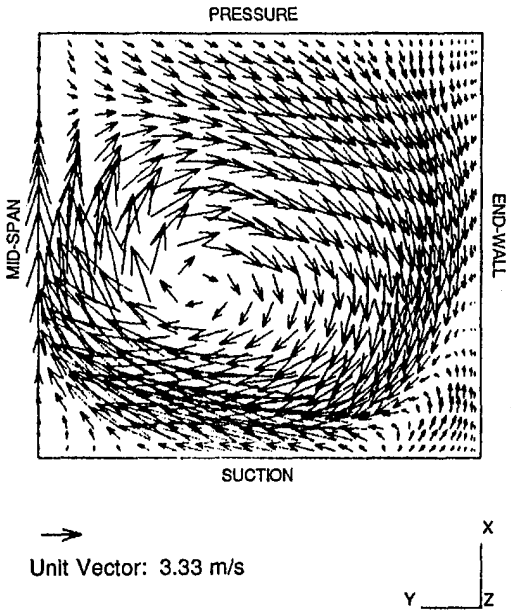

Fig. 3 Velocity vectors and contours at a cross-section at the exit of passage showing passage vortex (units are m/s)

Computational Analysis

In order to assess the feasibility of passive injection and to observe the effects of secondary flow and passive injection on the motion of particles entrained in a flow through a converging blade passage, several laminar flowfield solutions were obtained using a Cray-YMP 2/216 and a Cray-YMP C90. Data from the flowfield solutions was used in order to estimate the reduction in secondary flow and erosion as a result of the application of passive injection. Next, numerical results were compared with experimental data obtained by Lasser (1982) and Madden (1984). The magnitudes of primary and secondary velocity components were compared throughout the passage. A series of flows at a higher Reynolds number were calculated in order to observe the effects of a substantial injection flow rate. Passive injection was implemented for each of the flows using several geometric configurations in order to compare the reduction in secondary flows and the differences in particle trajectories. Velocity and pressure data in the bend were used to facilitate the optimization of this process.

It was decided to place injection holes in the form of slot-jets on the blades near the leading edge and through the bend (blade-to-blade pressure gradient is the highest there), creating the highest injection velocities in the main region responsible for creating the passage vortex. This location was chosen by analyzing earlier solutions for pressure distributions and velocity vector projections at several cross-sections throughout the passage. Final optimization was obtained by varying the width of the slot-jet. The resulting particle trajectories, with and without the application of passive injection, were then computed.

Particle trajectories were calculated from specified initial positions at the passage inlet. In each case, 16 particles were evenly spaced over the inlet. Spherical particles of 5, 30 and 300 μm diameters were assumed with a density of 1550 kg/m^3 (SiO_2) and an initial velocity equal to the average inlet velocity of the gas flow. Thus, it would be possible to observe the effects of secondary flow on particle size and to estimate erosion patterns and material removal. A conservative time step size was used (5×10^{-7} s) for accuracy, since a Cray-YMP C90 was available. Solutions were obtained in a few CPU minutes (calculating 16 particles at a time). The number of impacts for each particle along with its position and velocity were recorded at the end of each run, and then separate particle paths were downloaded onto an 80486-DX microcomputer using "PCSlip." The passage grid file was combined with particle paths to create particle trajectory plots using "TECPLOT."

By comparing data from particle trajectories with and without passive injection, the feasibility of passive injection was assessed with respect to reducing the percentage of concentrated particles at the passage exit along the endwall surfaces. After observing particle trajectories and then comparing them with each other for the different passive injection geometries, the reduction of erosion could be judged.

Results and Conclusions

The numerical results were directly compared with experiments made by Lasser (1982) and Madden (1984). When results were compared with Lasser's experiments, his experimental values of primary flow velocity components are at most 5% higher (some error exists in modeling the estimated inlet conditions from experiments, and it should also be noted that since laminar flow models were used for simplicity, there exists some error in comparison, since the experimental flows were probably slightly turbulent, $Re_{Dh} = 7{,}700$, although no turbulence measurements were made). Predicted secondary flow patterns are similar to the experimental results, except that a slightly stronger cross-flow along the endwall, in the bend, was calculated by the numerical model. In later runs with passive injection applied with evenly spaced holes, the percentage difference in primary and secondary velocity components between Madden's experiments and these numerical results is estimated to be approximately 7% over the passage.

A qualitative analysis was made concerning the possibility of using passive injection to reduce localized concentration of particles at the passage exit. Also, a revealing investigation into the structure of the fluid flowfield (secondary flow and pressure distribution) resulted in some insights as to the way in which passive injection was to be optimized (Fig. 3). Attempts at optimization were made using 0.5 mm and 3.0 mm wide slot-jets located in the bend portion of the passage, near the endwalls. Other passive injection configurations were made using 6 and 8, 0.8 mm holes spaced evenly throughout passage, near the endwalls. It was observed that passive injection had negligible effects on the velocity profiles for the through flow near surfaces throughout the passage. Thus it may be assumed that shear losses are not appreciably changed by passive injection.

[3] There was a negligible velocity defect in the blade-to-blade direction.

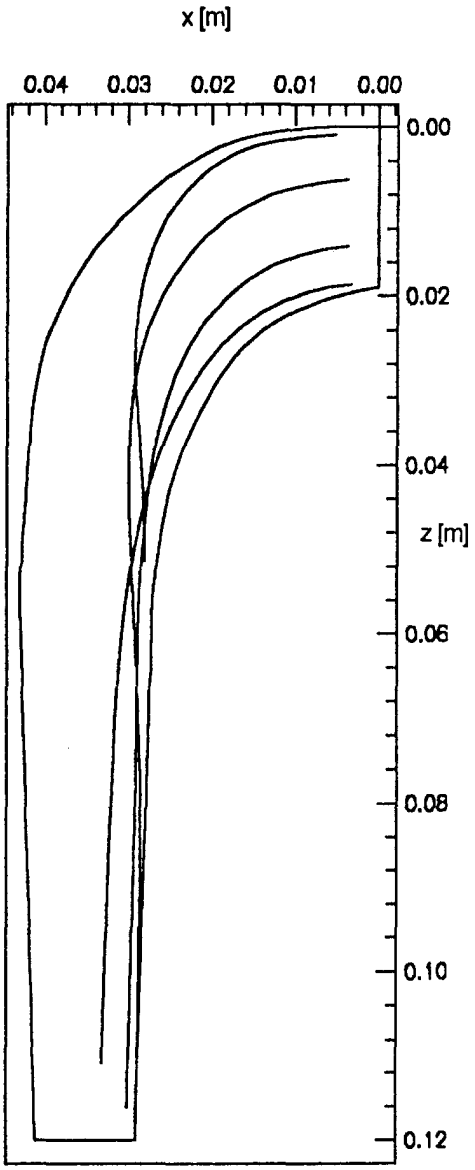

Fig. 4 Particle trajectories with no passive injection (5 μm diameter, silicon dioxide, 36 m/s inlet velocity)

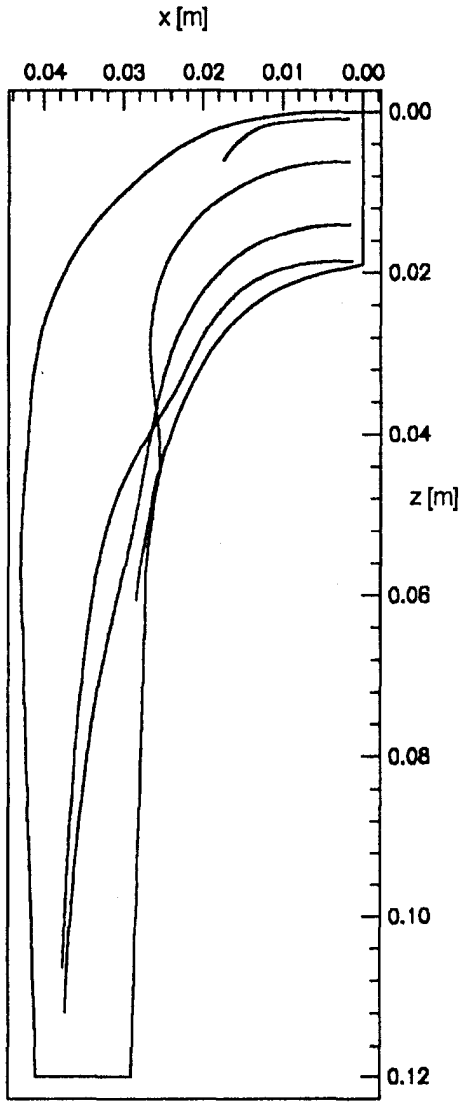

Fig. 5 Particle trajectories with passive injection applied as slot-jet near endwalls in curved portion of channel (5 μm diameter, silicon dioxide, 36 m/s inlet velocity)

Particle trajectories were calculated for each of the above flows in order to observe the effects of passive injection and particle size on particle trajectories (particles were injected evenly over the inlet of the passage). This helped to optimize the passive injection process with respect to the reduction of the motion of particles towards boundary layers, and the magnitude of secondary flow. The effectiveness and feasibility of passive injection was then determined (Figs. 4, 5).

Effects of Secondary Flow. It was observed that the developing passage vortices convect very small particles (5 μm diameter) towards boundary layers and across the endwalls, where they usually decelerate and/or concentrate near the midspan or endwalls, at the passage exit. This phenomenon has been seen in coal-fired turbomachinery, where high concentrations of particles near the inner endwall of the stator blade passages are responsible for excessive erosion at the roots of the following rotor blades.

Small particles that enter the blade passage close to an endwall, are convected towards the suction blade surface by the passage vortices, where they tend to remain in the blade boundary layer, increasing the local particle concentration. At the passage midspan, small particles (5 μm diameter) just entering the passage, are convected towards the pressure surface by the developing passage vortex. Once these small particles entered the boundary layers, their residence time increased drastically.

Effects of Particle Size

From the results of calculations with particle diameters of 5, 30 and 300 μm, it was verified that increases in the size of a particle increase the drag force ($\propto r^2$); however, it is the increase in the spherical particle's mass ($\propto r^3$) that has a greater effect on the trajectories, i.e., larger particles are subjected to much smaller accelerations caused by drag forces.

After viewing the numerical results, it is evident that large particles (30 μm in mean diameter and larger) are not affected by the secondary flows, as smaller particles are (Fig. 6). The larger particles move in straighter paths and impinge on the surfaces at larger angles of attack. Also, larger particles do not become trapped or decelerated in the boundary layers as smaller particles do, and do not concentrate near the endwalls and blade surfaces.

Optimization of Passage Injection

A geometrical optimization of passive injection, with respect to the minimization of passage secondary flow and particle concen-

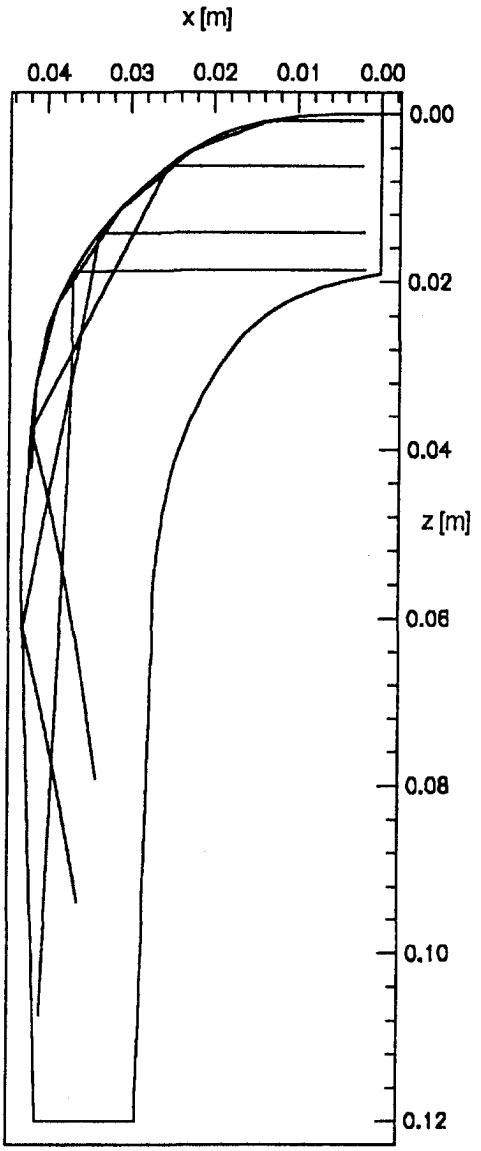

Fig. 6 Particle trajectories with no passive injection (300 μm diameter, silicon dioxide, 36 m/s inlet velocity)

tration, was attempted. Optimizing passive injection increases the injection mass flow rate and usually reduces the secondary flow percentage, although never eliminates it. It was observed, by implementing injection in the form of slots, that the secondary flow could be reduced approximately an average of 20% over the passage (for these incompressible, laminar flows). It was also found that the injection jets can be used to convect particles away from the suction blade surface and to help reduce the concentration of particles along the endwalls, which would otherwise lead to high localized erosion and possibly particle deposition and flow obstruction (depending on the nature of the particles). It was estimated that at least a 6% reduction in the concentration of particles along the endwall was possible.

It was observed that placing injection holes after the curved portion of the passage had no benefits, because there is no longer a strong blade-to-blade pressure gradient that is needed to create jets with sufficient flow rate to have any useful effect. It should be noted that too much mass flow from the injection jets in particular locations may adversely alter secondary flow patterns (adding additional vortices) and may increase passage profile losses. The results show that it is possible to manipulate particle trajectories, so that by carefully placing injection holes throughout the curved portion of the passage, particles can be kept away from the blade surfaces and boundary layers.

References

Azim, A. F. Abdel, and Rouleau, W. T., 1983, "Secondary Flow Effect on Erosion Damage of a Stationary Cascade," 6th International Conference on Erosion by Liquid and Solid Impacts (ELSI VI), Cambridge University, Sept.

Ekerle, W. A., and Langston, L. S., 1987, "Horseshoe Vortex Formation Around a Cylinder," ASME *Journal of Engineering for Gas Turbines and Power,* Vol. 109, Apr., pp. 278–284.

El-Sayed, A. F., Lasser, R., and Rouleau, W. T., 1986, "Effects of Secondary Flow on Particle Motion and Erosion in a Stationary Cascade," *International Journal of Heat and Fluid Flow,* Vol. 7, No. 2, June.

Finnie, I., and Kabil, Y. H., 1968, "On the Formation of Surface Ripples During Erosion," *Wear,* Vol. 8, pp. 5–21.

Grant, George K., 1973, "A Model to Predict Erosion in Turbomachinery Due to Solid Particles in a Particulated Flow," UMI Dissertation Services, Apr.

Hah, C., 1984, "A Navier Stokes Analysis of Three-Dimensional Turbulent Flows Inside Turbine Blade Rows at Design and Off-Design Conditions," ASME *Journal of Engineering for Gas Turbines and Power,* Vol. 106, Apr., pp. 421–428.

Hamed, A., and Kuhn, T. P., 1993, "Effects of Variational Particle Restitution Characteristics on Turbomachinery Erosion," *International Gas Turbine and Aero-engine Congress and Exposition,* Cincinnati, Ohio, May.

Kawai, T., Hinoki, S., and Adachi, T., 1989, "Secondary Flow Control and Loss Reduction in a Turbine Cascade Using Endwall Fences," *JSME International Journal,* Series II, Vol. 32, No. 3, pp. 375–385.

Kladas, D. D., and Georgiou, D. P., 1993, "A Relative Examination of C_D – Re Relationships Used in Particle Trajectory Calculations," ASME JOURNAL OF FLUIDS ENGINEERING, Vol. 115, Mar., pp. 162–165.

Kozlu, H., Louis, and Jean F., 1987, "Particle Transport Across the Transpired Turbulent Boundary Layer," *Gas Turbine Conference and Exhibition,* Anaheim, CA, May.

Lasser, R., 1982, "The Effects of Secondary Flows in an Arbitrarily Curved Blade Passage of Converging Cross Section and in the Wake Downstream of a Cascade of Airfoils," Ph.D. dissertation, Carnegie Mellon University.

Madden, M., 1984, "Secondary Flow Control by Passive Injection," Master's thesis, Carnegie Mellon University.

Putnam, A. A., et al., 1957, "Injection and Combustion of Liquid Fuels," WADC TR 56-344, Batelle Memorial Institute, Mar.

Soo, S. L., 1967, *Fluid Dynamics of Multiphase Systems,* Blaisdell Publishing, Waltham, MA.

Tal, R., Lee, D. N., and Rouleau, W. T., 1982, "Secondary Flow Control by Passive Injection," Internal Report, Mechanical Engineering Department, Carnegie Mellon University.

Ulke, A., 1975, *An Approximate Analysis of the Effect of Secondary Flows on the Motion of Particulates in an Axial Flow Gas Turbine,* Ph.D. dissertation, Carnegie Mellon University.

Ulke, A., and Rouleau, W. T., 1976, "The Effects of Secondary Flow on Turbine Blade Erosion," ASME Paper No. 76-GT-74.

Ventresca, James J., 1994, *The Effects of Secondary Flow and Passive Injection on the Motion of Solid Particles Through a Curved Converging Channel,* Ph.D. dissertation, Carnegie Mellon University.

Wenglarz, Richard A., 1987, "Turbine Deposition, Erosion and Corrosion Evaluations Using a Simplified Test Approach," *Gas Turbine Conference and Exhibition,* Anaheim, CA, May.

Theoretical Modeling of Central Air-Jet Pump Performance for Pneumatic Transportation of Bulk Solids

D. Wang[1]
Research Associate.
e-mail: dmwang@wordly.com

P. W. Wypych
Associate Professor.

Department of Mechanical Engineering,
University of Wollongong,
Northfields Avenue, Wollongong, NSW 2522,
Australia

A mathematical model to predict the air-solids performance of central air-jet pumps has been developed based on the fundamentals of fluid and particle mechanics. The influence of throat entry configuration on performance has been incorporated into the analytical model by introducing a throat entry function and suction area ratio. Nondimensional parameters to represent air-solids jet pump performance has been defined and used in the analytical procedure. The performance predictions obtained by this model show good agreement with experimental results.

1 Introduction

Central air-jet pumps (also called venturi eductors, ejectors, syphons, injectors, etc.) as shown in Fig. 1, consist of a nozzle, mixing tube (also called throat tube), suction chamber, throat entry, and diffuser. These pumps are becoming more popular in a wide range of industries for the pneumatic conveying of bulk solids, because of their considerable advantages such as reliability, no moving parts, low capital cost and convenience for maintenance (Fox, 1984, 1992; Keys and Chamber, 1990; Pogorelov, 1990; Nazarov et al., 1990). Understanding the relationship between motive, suction and discharge flows in an air-jet pump is vital to designing and operating a reliable and energy-effective air-jet pump conveying system. Hence, this topic has attracted considerable investigations both experimentally and theoretically over the past two decades, with some of the major ones listed below.

Bohnet (1978, 1982, 1983, 1985) derived a mathematical model using continuity and conservation of momentum to calculate the variation of static pressure along the jet pump based on the solids to air mass flow rate ratio, the velocity of particles at constant solids flow rate, the assumption that the particles are accelerated in an air jet of constant mean velocity and the measurements of solids velocity profile inside the jet pump. Experimental data obtained on a jet pump of 33.3 mm in throat diameter for a few different products were used to determine pressure transformation efficiencies of the diffuser, throat and throat entry section (e.g., from suction port to throat inlet). Design diagrams were presented by means of some simplifications to this model. Due to the limitation of experimental data used to determine those pressure transformation efficiencies that contribute to calculating results (the maximum motive pressure used in the experiments was about 20 kPag), the application of this model is very limited. Also, although he noted that the location of the nozzle had a significant influence on the performance of jet pump, Bohnet (1978, 1982, 1983, 1985) did not incorporate this factor into his model.

Chellappan and Ramaiyan (1986) carried out experimental investigations into the effect of geometrical parameters on the performance of gas-solid jet pumps. While there were no analytical design guides, useful trends in graphical form to illustrate the influence of geometrical parameters were reported. The effect of design and operating parameters on the performance of gas-solid jet pumps also was investigated experimentally by Dawson et al. (1989) and Davies et al. (1990). The principal difference between these two experimental works is that the first used a fixed geometry conveying system and a larger particle (wheat, average particle diameter d_p = 3814 μm, particle density = 1328 kgm^{-3}) and that the latter artificially induced a back pressure in their experiments and used a smaller particle (sand, d_p = 186 μm, particle density = 2631 kgm^{-3}; casein, d_p = 315 μm, particle density = 1255 kgm^{-3}).

Fox (1984) presented data collected from the actual performance of proprietary design venturi eductors of industrial installations with pulverized and coarse coal, plastic pellets and talc. These data were condensed into a graph that permitted reasonably simple and accurate prediction of airflow rate and pressure requirements of a given conveying installation. A step-by-step procedure in selecting an adequate air-solids jet pump using this graph was presented. Several case studies also were given where typical problems with existing systems were solved by the introduction of an air-solids jet pump (Fox et al., 1992).

Pittman and Mason (1986) presented some graphical information on the flow rate of product against the volumetric flow rate of air supplied for different bulk materials and pipe lengths, and illustrated some of the many different configurations of air-solids jet pump.

Kmiec (1987) continued Bohnet's work and presented velocity profiles for mixed particle size and showed that the smaller the particle, the faster they were accelerated. However, his main conclusion was that the overall efficiency of pressure transformation in the jet pump depended on the expansion of the motive jet only and that the higher the inlet gas velocity, the lower the efficiency of pressure transformation.

Westaway (1987) reported comprehensive sets of experimental data encompassing a wide range of operating conditions (different conveying pipeline diameters and length) with many different products.

Despite the above investigations, the development of a reliable theoretical model has been hindered by the complexities of two-phase (gas-solid) flow. Trial and error and empiricism still are used in design practice. In this paper, a mathematical model to predict the air-solids performance of central air-jet pumps has been developed based on the fundamentals of fluid mechanics and verified by using experimental results.

[1] Currently, Dura Products International, 60 Carrier Drive, M9W 5R1, Toronto, Canada.

Contributed by the Fluids Engineering Division for publication in the JOURNAL OF FLUIDS ENGINEERING. Manuscript received by the Fluids Engineering Division March 27, 1996; revised manuscript received August 11, 1998. The long delay until publication is due mostly to the JFE Editorial Board. Associate Technical Editor: D. Stock.

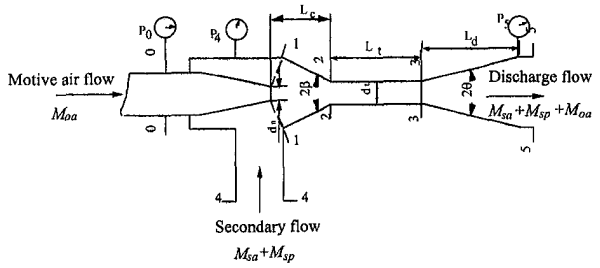

Fig. 1 General configuration of central air-jet pump

2 Performance Representation

Air-solids jet pump performance can be represented by either dimensional or non-dimensional performance plot for a given jet pump configuration. The former shows the variation of suction solid mass flow rate M_{sp} with pressures difference $\bar{p}_5 - \bar{p}_4$, where total pressures $\bar{p}_4$ and $\bar{p}_5$ are defined as

$$\bar{p}_4 = p_4 + \frac{\rho_{s4} v_{s4}^2}{2} \tag{1}$$

and

$$\bar{p}_5 = p_5 + \frac{\rho_{m5} v_5^2}{2} \tag{2}$$

Nondimensional pump performance is presented using a pressure ratio h via mass flow rate ratio x plot for a given air-jet pump configuration (represented by area ratio m). These nondimensional parameters are defined as:

$$m = A_2/A_n \tag{3}$$

$$x = \frac{M_{sa} + M_{sp}}{M_{oa}} = \frac{\rho_{sa}}{\rho_{o1}} q_a = \frac{\rho_p}{\rho_{o1}} q_p \tag{4}$$

where $q_p = Q_{sp}/Q_{o1}$ and $q_a = Q_{sa}/Q_{o1}$

$$h = (\bar{p}_5 - \bar{p}_4)/(\bar{p}_0 - \bar{p}_4) \tag{5}$$

where $\bar{p}_0 = p_0 + \rho_{a0} v_0^2/2$

For a jet pump operating under a given operating condition, p_0 and p_4 are given. The dimensional performance plot can be converted from nondimensional characteristic parameters if the dependence of h on x is known for specific jet pump geometry. From Eqs. (4) and (5), the conversion relations for a given jet pump configuration are:

$$\bar{p}_5 - \bar{p}_4 = h(\bar{p}_0 - \bar{p}_4) \tag{6}$$

$$M_{sp} = xM_{oa} \tag{7}$$

where M_{oa} can be calculated using the equations given by Wang and Wypych (1995). The performance modeling work presented in this paper concentrates on the nondimensional format.

3 Performance Modeling

3.1 Properties of Air-Solids Two-Phase Flow. In an air-jet pump used for bulk solids conveying, the secondary flow from section 4-4 to section 1-1 and the combined flow from section 1-1 to section 5-5 (refer to Fig. 1) should be considered as air-solids two-phase flow. Some properties of the secondary air-solids two-phase flow pertinent to performance modeling are defined below: *Volumetric concentration* is defined as the ratio of volume occupied by particles to total volume. For secondary flow between sections 4-4 and 1-1, this parameter can be expressed by

$$c_{vs} = \frac{V_{sp}}{V_{sp} + V_{sa}} = \frac{q_p}{q_p + q_a} \tag{8}$$

Volumetric concentration can also be represented by the densities of gas, particle and bulk solids. Considering mass conservation of the secondary bulk solids flow,

$$\rho_b V_{sb} - \rho_p V_{sp} = \rho_{4a} V_{sa} \tag{9}$$

According to Eq. (8), $V_{sp} = c_{vs} V_{sb}$ and $V_{sa} = (1 - c_{vs}) V_{sb}$. Therefore,

$$c_{vs} = \frac{\rho_b - \rho_a}{\rho_p - \rho_a}. \tag{10}$$

If $\rho_a/\rho_p \approx 0$ and $\rho_a/\rho_b \approx 0$, then

$$c_{vs} \approx \rho_b/\rho_p \tag{11}$$

Void fraction is defined as the ratio of volume occupied by gas to total volume. For secondary air-solids flow,

$$\varepsilon_s = 1 - c_{vs} \tag{12}$$

Nomenclature

A = cross-sectional area, m^2
C = area ratio of suction
c = concentration
d = diameter, m
h = pressure ratio
k = constant related to friction loss
L = length, m
m = area ratio of throat cross-section to nozzle outlet
M = mass flow rate, kg s^{-1}
p = static pressure, Pa abs
$\bar{p}$ = total pressure, Pa abs
q = volumetric flow rate ratio
Q = volumetric flow rate, m^3 s^{-1}
S = velocity ratio of gas to particle at suction port
v = velocity, m s^{-1}
V = volume, m^3
x = mass flow rate ratio of secondary flow to motive flow
z = dynamic pressure of motive jet flow, Pa
α = throat entry function defined in Eq. (30)
δ = allowed calculation error
ψ = mass flows ratio of solids to air
ρ = density, kg m^{-3}
λ = friction factor
β = half conic angle of throat entry, °
ζ = momentum correction coefficient due to the variation of motive air-jet profile
θ = half conical angle of diffuser, °
σ = ratio of diffuser outlet area to inlet area
μ = momentum correction coefficient due to nonuniform velocity distribution
ξ_d = coefficient related to friction in diffuser

Subscripts

0-5 = locations shown in Fig. 1
a = air
b = bulk solid
c = nozzle to throat gap
d = diffuser
m = mixture
n = outlet of nozzle
o = motive fluid
p = particles
s = secondary flow
t = throat
u = shut-off
v = volumetric

Density of air-solids mixture can be expressed by volumetric concentration or void fraction. For secondary air-solids flow, the mixture density is expressed by volumetric concentration as:

$$\rho_{s4} = \rho_p c_{vs} + \rho_{4a}(1 - c_{vs}) \tag{13}$$

or expressed by void fraction as

$$\rho_{s4} = \rho_p(1 - \varepsilon_s) + \rho_{4a}\varepsilon_s \tag{14}$$

3.2 Determination of Suction Air Mass Flow Rate. As an air-jet pump operates to convey bulk solids from an open feeding hopper to a pipeline, air may be sucked in with the bulk solids or blown out depending on the operating conditions. However, if the motive air blows out, the air-jet pump does not work properly and the pumping effect deteriorates. Therefore, only the case of suction air should be considered in modelling air-jet pump performance.

The density of secondary air-solids two-phase flow can also be expressed by

$$\rho_{s4} = \rho_p \frac{q_p}{q_p + q_a} + \rho_{4a}\left(1 - \frac{q_p}{q_p + q_a}\right) \tag{15}$$

If there is no slip between the solids and air, $\rho_{s4} = \rho_b$. Comparing with Eq. (13), $c_{vs} = q_p/(q_a + q_p)$. That is,

$$q_a = \left(\frac{1 - c_{vs}}{c_{vs}}\right) q_p \quad (0 < c_{vs} < 1) \tag{16}$$

From Eq. (4),

$$q_p = \frac{1}{\rho_p}(\rho_{o1}x - \rho_{4a}q_a) \tag{17}$$

Substituting Eq. (17) into Eq. (16) results in

$$q_a = \frac{(1 - c_{vs})\dfrac{\rho_{o1}}{\rho_p}x}{c_{vs} + (1 - c_{vs})\dfrac{\rho_{4a}}{\rho_p}} \tag{18}$$

If there is slip between the solids and air at the suction port, then by considering the mass conservation of secondary flow and assuming the ratio of velocities to be constant:

$$\rho_p c_{vs} v_{4p} A_4 + \rho_{4a}(1 - c_{vs}) v_{4a} A_4 = \rho_{s4}(c_{vs} v_{4p} + (1 - c_{vs}) v_{4a}) A_4 \tag{19}$$

This equation can be rearranged as

$$\rho_{s4} = \rho_p \frac{c_{vs}}{c_{vs} + (1 - c_{vs})S} + \rho_{4a}\frac{(1 - c_{vs})S}{c_{vs} + (1 - c_{vvs})S} \tag{20}$$

where $S = v_{4a}/v_{4p}$ is the velocity slip ratio. Comparing Eq. (20) with Eq. (15) results in

$$q_a = \left(\frac{1 - c_{vs}}{c_{vs}}\right) S q_p \quad (0 < c_{vs} < 1) \tag{21}$$

Substituting Eq. (17) for q_p in Eq. (21) yields

$$q_a = \frac{(1 - c_{vs})S\dfrac{\rho_{o1}}{\rho_p}x}{c_{vs} + (1 - c_{vs})S\dfrac{\rho_{4a}}{\rho_p}} \tag{22}$$

It can be seen by comparing Eqs. (18) and (22) that the suction air mass flow rate depends on the volumetric concentration, velocity slip ratio and solid mass flow rate for a given motive mass flow rate. If there is no or little velocity slip ($S \approx 1$), Eq. (22) reduces to Eq. (18).

3.3 Fundamental Equations of Air-Solids Jet Pumps. Assuming that the air jet operates isothermally and under steady-state conditions, application of the macroscopic mass and energy balance for the motive air flow through the nozzle leads to

$$p_1 \ln\left(\frac{p_0}{p_1}\right) = (1 + k_{01})z \tag{23}$$

where $z = \rho_{o1}v_{o1}^2/2$. Note that for sonic flow at the nozzle throat, p_1 can be determined by using the corresponding equations given by Wang and Wypych (1995).

Application of the macroscopic mass and energy balance approaches to the secondary air-solid two-phase flow between the suction port (section 4-4) and the inlet of the throat entry (section 1-1), as shown in Fig. 1, results in

$$\frac{\bar{p}_4 - p_1}{z} = (1 + k_{41})\frac{C^2\left(q_a\dfrac{p_4}{p_1} + q_p\right)^2}{(m - 1)^2}\frac{\rho_{s1}}{\rho_{o1}} \tag{24}$$

where $C = (A_3 - A_n)/A_{s1}$ is defined as the suction area ratio.

The suction area ratio C is a ratio of the flow area occupied by the secondary flow at section 3-3 to the flow area of secondary flow at section 1-1. For the jet pump shown in Fig. 1, based on the geometrical relationship, the following expression to determine the suction area ratio can be obtained:

$$C = \frac{m - a_n^2}{\left(\dfrac{2L_c}{d_n}\tan\beta + \sqrt{m} - a_n\right)\cos\beta\left[2a_n + \left(\dfrac{2L_c}{d_n}\tan\beta + \sqrt{m} - a_n\right)\cos^2\beta\right]} \tag{25}$$

where $a_n = d_w/d_n$ is a coefficient to take into consideration the thickness of nozzle outlet and d_w is the external diameter of the nozzle outlet.

Using the energy balance approach for the motive and secondary streams between the throat entry inlet section 1-1 and throat inlet section 2-2 shown in Fig. 1, by means of some substitutions and calculations, it can be found that

$$\frac{p_2 - p_1}{z} = \frac{(m - 1)^2 + x^2\left(q_a\dfrac{p_4}{p_1} + q_p\right)C^2 - (1 + k_{12})\left\{\zeta_{o2}(m - 1)^2 + x^2\left(q_a\dfrac{p_4}{p_2} + q_p\right)\zeta_{s2}\right\}}{(1 + x)(m - 1)^2} \tag{26}$$

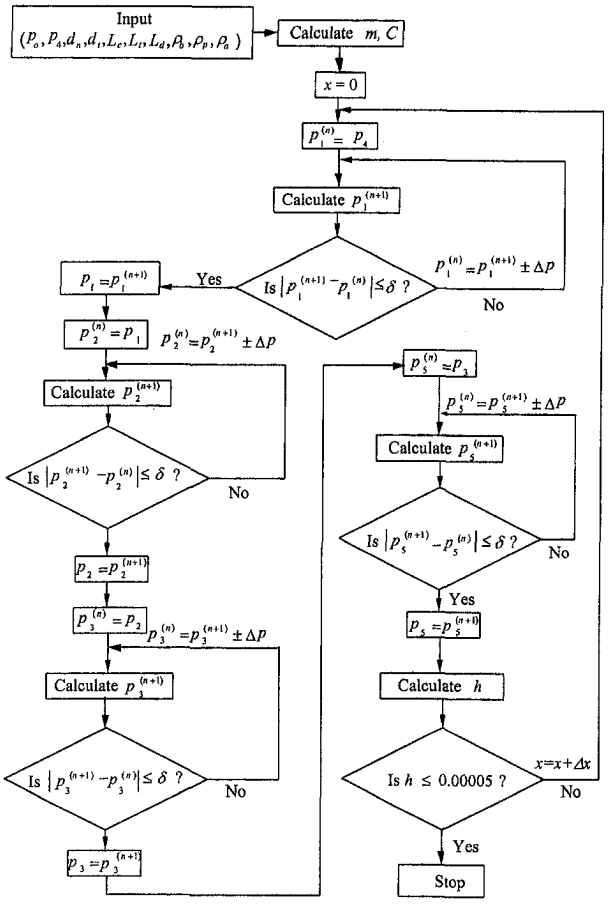

Fig. 2 Outline of performance prediction model solving procedure

The application of mass and momentum balances for the motive and secondary mixture between the throat inlet and outlet results in

$$\frac{p_3 - p_2}{z} = \frac{2x\left(q_p + q_a\frac{p_4}{p_2}\right)\zeta_{s2}}{m(m-1)} + \frac{2\zeta_{o2}}{m} - \frac{(1+x)\left(\frac{p_1}{p_3} + q_a\frac{p_4}{p_3} + q_p\right)(2\mu_3 + k_{23})}{m^2} \quad (27)$$

Application of the macroscopic mass and energy balance for the air-solids mixture flow between the diffuser inlet and outlet and introducing the mass conservation relationship and substituting for velocity result in

$$\frac{\bar{p}_5 - p_3}{z} = \frac{(1-k_{35})(1+x)}{m^2}\left(\frac{p_1}{p_3} + q_a\frac{p_4}{p_3} + q_p\right) \quad (28)$$

3.4 Determination of Coefficients. Coefficients k_{01}, k_{12}, k_{41}, k_{23} and k_{35} are involved in the performance modelling to account for the influence of the friction and variation of flow area on performance. By introducing ψ to represent the mass flow ratio of particle to gas in the jet pump,

$$\psi = \frac{M_p}{M_a} = \frac{q_p\rho_p/\rho_{o1}}{1 + q_a p_4/p_1} \quad (29)$$

Considering that the momentum or energy losses due to friction expressed in terms of coefficient k_{12}, k_{23} and k_{35}, and that expressed by using λ_a and λ_p should be equal results in the following expressions:

$$k_{12} = \frac{(\lambda_a + \psi\lambda_p)\frac{L_c}{d_n}\left(1 + q_a\frac{p_4}{p_1}\right)^2(1+x)}{\zeta_{o2}(m-1)^2 + \zeta_{o2}^2 x^2\left(q_p + q_a\frac{p_4}{p_2}\right)} \quad (30)$$

$$k_{23} = \frac{(\lambda_a + \psi\lambda_p)L_t/d_t}{\left(1 + \frac{\rho_p q_p/\rho_{o1}}{1 + \rho_p q_a/\rho_{o1}}\right)\left(1 + \frac{q_p}{q_a p_4/p_3 + p_1/p_3}\right)} \quad (31)$$

$$k_{35} = \frac{\xi_d}{\left(1 + \frac{\rho_p q_p/\rho_{o1}}{1 + \rho_p q_a/\rho_{o1}}\right)\left(1 + \frac{q_p}{q_a p_4/p_3 + p_1/p_3}\right)} \quad (32)$$

where

$$\xi_d = \left\{\frac{\lambda_a + \psi\lambda_p}{8\tan(\theta)} + \frac{m_d - 1}{m_d + 1}\sin(2\theta)\right\}\left(1 - \frac{1}{m_d^2}\right) \quad (33)$$

which has been based on previous work (Aggarwal et al., 1986) but modified for two-phase flow. Hence, k_{12}, k_{23} and k_{35} are related to air friction λ_a and particle friction λ_p. Air friction factor is available in common reference books, such as (Blenvens, 1984), and experimental data on particle friction factor λ_p of various product flows in pipe are available in the literature (Weber, 1981, 1982). Although there is some difference between the friction in the pipe and that in the jet pump, this kind of difference is negligible when the readily available pipe friction factor is applied to the very short length of throat tube.

Coefficient k_{01} is introduced to allow for pressure loss due to viscous friction, turbulence and boundary variations while motive air flows through the nozzle. For a convergent nozzle with straight-tip, k_{01} = 0.06 to 0.11 (Blevens, 1984). Other investigators recommend k_{01} = 0.03 to 0.05 (Grupping et al., 1988) and k_{01} = 0.1 (Hatzlavramldls, 1991). Coefficient k_{41} is introduced to account for the pressure loss for secondary flow from the suction port (section 4-4) to section 1-1 shown in Fig. 1. This coefficient can be determined approximately by treating the flow passage as a combining tee (i.e., one stream of fluid flowing straight into the tee and the other flowing into the tee at right angles to the straight-flowing fluid, and the two combined flowing out of the tee in the direction of the straight-flowing fluid). Coefficients ζ_{o2}, ζ_{s2}, and μ_3 are introduced to account for the effects of a non-uniform velocity distribution over the controlling sections. Assuming that the average motive jet velocity is maintained between the nozzle outlet and the throat inlet, the momentum modification coefficients due to the variation of motive air-jet profile and velocity distribution from

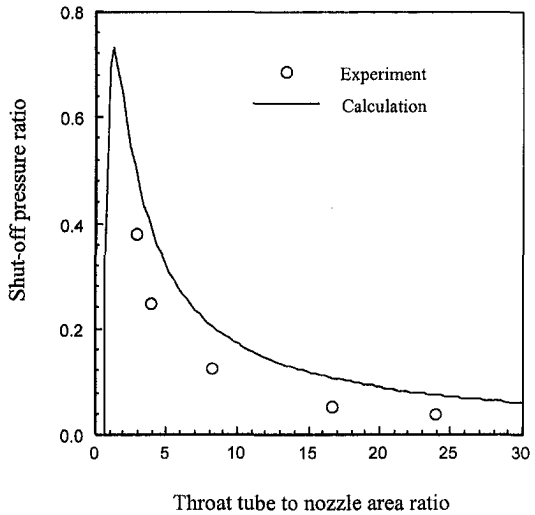

Fig. 3 Variation of shut-off pressure ratio with area ratio

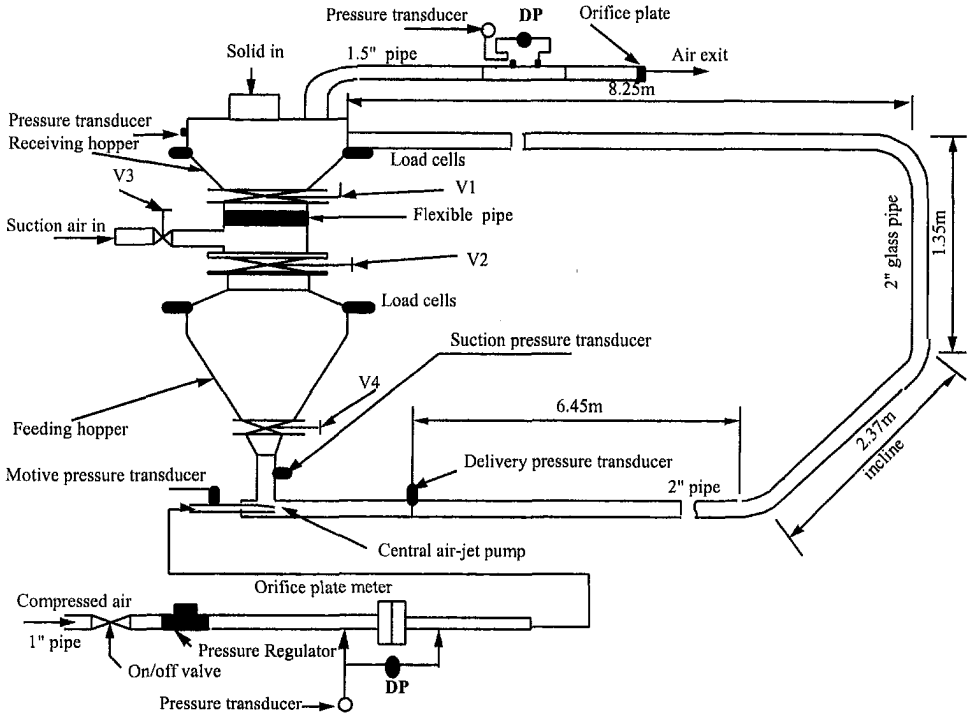

Fig. 4 General layout of test rig

nozzle outlet to throat inlet become unity, i.e. $\zeta_{o2} = 1$, $\zeta_{s2} = 1$. With the assumption that the motive and secondary fluids are perfectly mixed at the throat tube exit, the momentum modification coefficient due to velocity slip between particles and air at throat outlet (section 3-3) becomes unity, i.e., $\mu_3 = 1$.

3.5 Outline of Solution Method. By using the macroscopic energy balance approach between the suction port and the inlet of throat entry, p_1 can be expressed by $\bar{p}_4$, and Eq. (23) may be transformed into

$$\left(\bar{p}_4 - (1 + k_{41})\frac{\rho_{s1}v_{s1}^2}{2}\right)\ln\left(\frac{p_0}{p_1}\right) = (1 + k_{01})\frac{\rho_{o1}v_{o1}^2}{2} \quad (34)$$

By introducing a throat entry function defined as

$$\alpha = \frac{\dfrac{\bar{p}_4}{\bar{p}_0 - \bar{p}_4}\ln\left(\dfrac{p_0}{p_1}\right)}{1 + \ln\left(\dfrac{p_0}{p_1}\right)\dfrac{C^2(q_a p_4/p_1 + q_p)^2(1 + k_{41})\rho_{s1}/\rho_{o1}}{(m-1)^2(1 + k_{01})}} \quad (35)$$

Equation (34) can be transformed to

$$v_{01} = \frac{1}{\sqrt{1 + k_{01}}}\sqrt{\frac{2(\bar{p}_0 - \bar{p}_4)\alpha}{\rho_{o1}}} \quad (36)$$

Combining Eq. (5) with Eq. (36), the pressure ratio can be expressed by the throat entry function as

$$h = \frac{\alpha(\bar{p}_5 - \bar{p}_4)}{(1 + k_{01})z} \quad (37)$$

Equation (37) can be rearranged as

$$h = \frac{\alpha}{(1 + k_{01})}\left(\frac{\bar{p}_5 - p_3}{z} + \frac{p_3 - p_2}{z} + \frac{p_2 - p_1}{z} + \frac{p_1 - \bar{p}_4}{z}\right) \quad (38)$$

The solution to Eq. (38), showing the variation of pressure ratio h with mass flow rate ratio x can be obtained by combining Eq. (38) with Eqs. (24) to (28) and expressed using the following general form:

$$h = f(m, x, C, \rho_{o1}, \rho_p, \rho_b, \rho_{4a}, p_0, p_4, p_5) \quad (39)$$

It can be seen from Eq. (39) that the characteristics of an air-solids jet pump is determined by the geometric parameters m and C, and also related to the operating conditions expressed by x, ρ_p, ρ_b, ρ_{4a}, ρ_{o1}, p_0, p_4 and p_5. Therefore, to obtain the relationship between h and x for a jet pump with fixed geometry and operating under a given motive pressure, the performance prediction model expressed by Eqs. (22) to (35) and (38) must be solved simultaneously. This equation set is nonlinear transcendental and can be solved iteratively for specific motive and suction pressures. The calculation procedure is outlined in Fig. 2.

4 Shut-Off Pressure Ratio

Shut-off pressure ratio is referred as the pressure ratio at which secondary flow ceases. In this case, the motive air jet is impinging on a moving column of fluid in the throat tube, and there is ideally no other fluid entering or leaving the moving fluid column. Hence, this situation is basically single-phase flow with sudden expansion and $p_4 = p_1 = p_2$. Applying the momentum approach and neglecting frictional losses between section 1-1 and section 2-2, it can be obtained that

$$h_u = \frac{2\alpha}{m(1 + k_{01})}\left(1 - \frac{1 + k_{35} + \lambda_a L_t/d_t}{2m}\right) \quad (40)$$

The value of area ratio corresponding to the maximum shut-off pressure ratio can be determined by:

$$\frac{\partial h_u}{\partial m} = 0 \quad (41)$$

Combining Eqs. (40) and (41) leads to

$$m_u = 1 + k_{35} + \lambda_a L_t/d_t \quad (42)$$

Table 1 Properties of products tested

Name	Bulk density (kg m^{-3})	Particle density (kg m^{-3})	Particle diameter (mm)
Wheat	793	1424	3.6
Sorghum	772	1370	3.8
Plastic pellets	530	893	3.7

The graphical expression of Eq. (40) for $k_{35} = 0.1$, $\lambda_a = 0.025$ and $L_t/d_t = 5.6$ is shown in Fig. 3. It can be seen from this figure that the maximum shut-off pressure ratio can be reached if the area ratio is around 2. It should be noted from Eq. (42) that the area ratio corresponding to the maximum shut-off pressure ratio is related to friction losses that depend on the geometry of jet pump. It can also be seen clearly from Fig. 3 that shut-off pressure ratio decreases quite rapidly as the area ratio increases up to approximately 25 and that a further increase in area ratio will have little influence on the shut-off ratio. Therefore, an effective area ratio should be selected in the range of 2 and 25. Experimental data also have been plotted in this figure for comparison with the predictions by using Eq. (40). It can be seen clearly that the trend of shut-off pressure ratio varying with area ratio is well modeled by Eq. (40). The over-evaluation of the shut-off pressure ratio might arise from an under-evaluation of the pressure loss across the jet pump.

5 Experimental Investigations

In order to demonstrate the performance prediction model, a test rig depicted in Fig. 4 was designed and fabricated to monitor the performance of an air-jet pump with different geometry and subjected to different motive pressure, back pressure and nozzle geometry. Detailed description of the test rig, testing procedure, instrumentation and data acquisition can be found elsewhere (Wang and Wypych, 1995). Properties of the materials used for the test program are given in Table 1. The general configuration of the air-jet pump tested is shown in Fig. 1. This jet pump was designed to provide easy changing of the nozzle configuration and/or nozzle geometry. Table 2 provides the detailed dimensions of five jet pump geometries tested.

6 Comparison Between Theory and Experimental Results

For a given m and C, the solution to the performance prediction model of an air-solids jet pump can be obtained. This solution provides dimensionless air-solids jet pump characteristics and can be illustrated by a graph of h versus x for different m. A comparison between predicted and experimental results is made to demonstrate the validity of the performance prediction model developed in Section 3 for different jet pump geometries (represented by area ratio), operating conditions (represented by motive and delivery pressures) and bulk solids (i.e., plastic pellets, wheat, sorghum—see Table 1).

Figures 5 to 10 provide the comparisons between theoretical predictions (using the theoretical model developed in Section 3) and experimental results for different area ratios. It can be seen from these figures that the nondimensional characteristic curve

Table 2 Dimensions of air-jet pumps

Area ratio	Diameter of nozzle outlet (mm)	Diameter of mixing tube (mm)	Nozzle-throat gap (mm)
2.86	14.01	23.68	30, 50, 70, 87
3.96	11.95	23.68	30, 50, 70, 87
8.14	8.30	23.68	30, 50, 70, 87
16.67	5.80	23.68	30, 50, 70, 87
23.84	4.85	23.68	30, 50, 70, 87

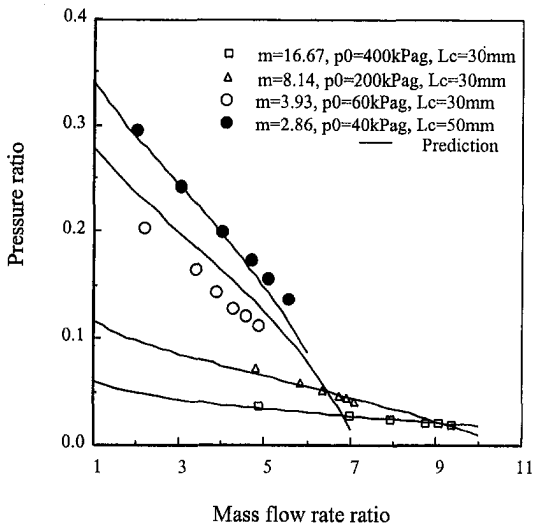

Fig. 5 Comparison between predicted and experimental results for plastic pellets

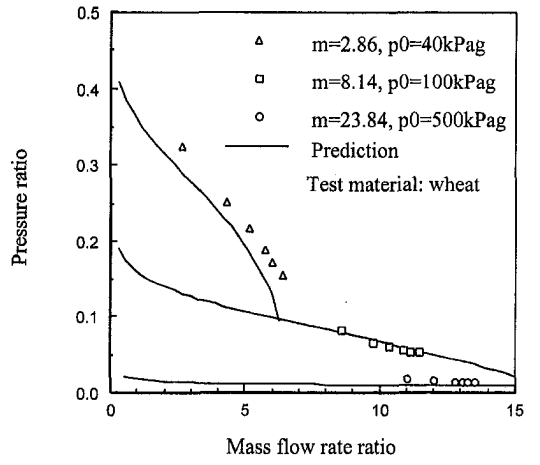

Fig. 6 Comparison between predicted and experimental results for wheat

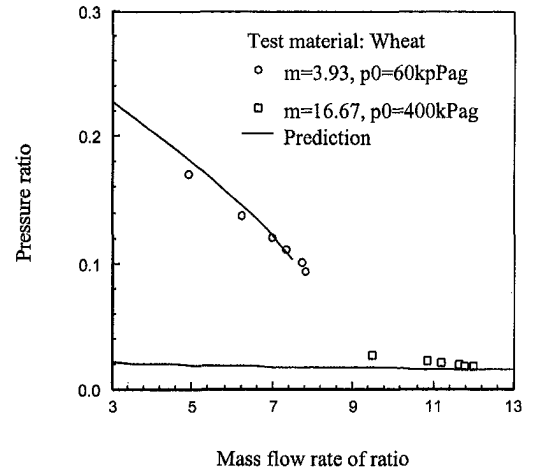

Fig. 7 Comparison between predicted and experimental results for wheat

becomes flatter as m increases. This suggests that the larger area ratio jet pump suits the application condition of lower back pressure and larger mass flow rate of product, and vice versa.

Comparisons between theoretical calculations of nondimen-

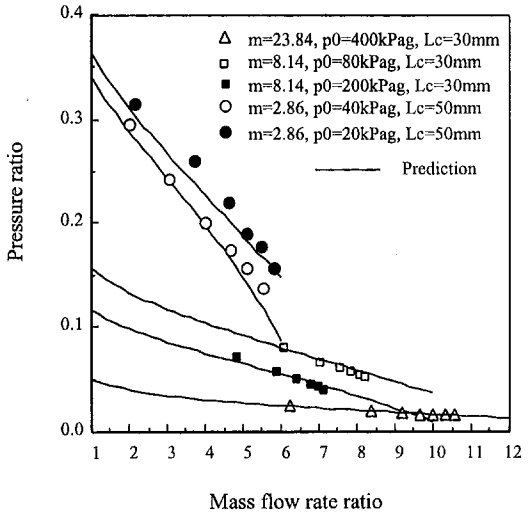

Fig. 8 Comparison between predicted and experimental results for plastic pellets

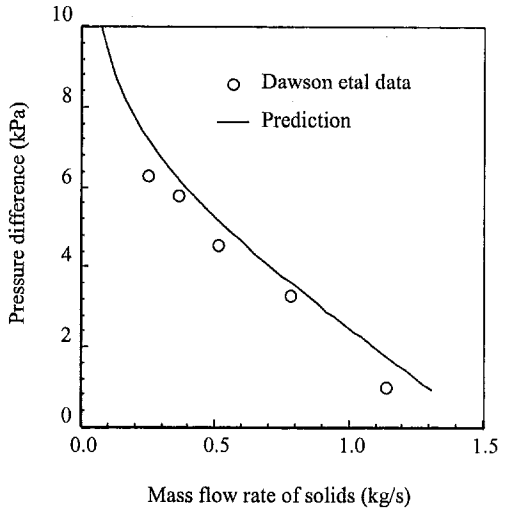

Fig. 11 Comparison between predicted dimensional performance and Dawson et al. experimental data (d_t = 76 mm, d_n = 21 mm, L_t/d_t = 3, Sand: ρ_b = 1350 kg/m^3, ρ_p = 2631 kg/m^3, p_0 = 168 kPa)

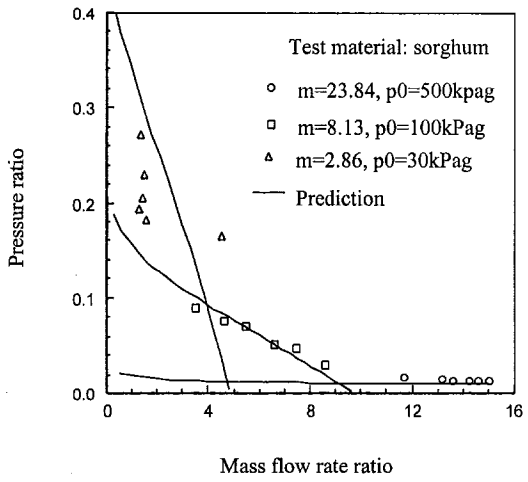

Fig. 9 Comparison between predicted and experimental results for sorghum

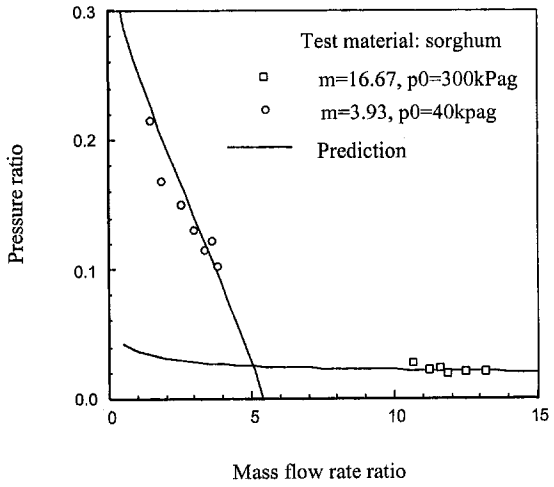

Fig. 10 Comparison between predicted and experimental results for sorghum

sional pump performance for the jet pump with area ratios of 2.86, 8.14, and 23.84 and experimental results for different motive pressures are included in Fig. 8. It can be seen that for a given area ratio, the performance line corresponding to the higher motive pressure is always underneath that for the lower motive pressure.

Note three kinds of material have been used to demonstrate the performance prediction model. Experimental data on sand reported by Dawson et al. also have been used to verify the performance prediction model, refer to Fig. 11.

It can be seen from all the comparisons shown in Figs. 5 to 11 that the predicted results are in good agreement with the experimental data, except for the case for $m = 2.86$ in Fig. 9. The scatter shown here may be due to material deposition, because the motive pressure may have been too low to ensure proper dilute-phase flow. Small dures/slugs of material actually were observed during these experiments.

7 Conclusions

By employing the fundamental principles of fluid dynamics and particle mechanics, a mathematical model is developed to predict air-solids jet pump performance.

This model predicts well the performance characteristics of five different jet pump geometries subjected to four different products and a wide range of operating conditions. The experimental results also demonstrate the importance of jet pump geometry (e.g., area ratio) and operating conditions (e.g., motive and delivery pressure) on pump performance.

References

Aggarwal, D. K., Gupta, R. S. and Vasandani, V. P., 1986, "Optimum Design of Jet Pumps," *Journal, Institution of Engineers* (India), Vol. 66, No. ME6, pp. 139–144.

Blevens, R. D., 1984, *Applied Fluid Dynamics Handbook,* Section 6.3, "Straight Uniform Pipes and Ducts," Van Nostrand Reinhold, pp. 50–54.

Bohnet, M., and Wagenknecht, U., 1978, "Investigations on Flow Conditions in Gas/Solid Injectors," *German Chemical Engineering,* No. 1, pp. 298–304.

Bohnet, M., 1982, "Aerodynamic Calculation of Gas/Solid Injectors," *Pneumatech 1,* International Conference on Pneumatic Conveying Technology, Stratford Upon-Avon, 3–5 May.

Bohnet, M., and Teifke, J., 1985, "New Results on the Efficiency of Energy Transformation in Gas/Solid Injectors," Reliable Flow of Particulate Solids, Bergen, Norway, 20–22 Aug.

Bohnet, M., 1983, "Design of Gas-Solids Injectors," Chapter 30, *Handbook of Fluids in Motion,* Nichocas, P. et al., eds., Ann Arbor Science, pp. 785–805.

Chellappan, S., and Ramaiyan, G., 1986, "Experimental Study of Design Parameters of Gas/Solid Injector Feeder," *Powder Technology,* Vol. 48, pp. 141–144.

Davies, C. E., Dawson, S. G. B and Hartley, M., 1990, "Venturi Feeders for Pneumatic Conveying Characteristics of Different Feeder Types," CHEMECA '90,

18th Australian Chemical Engineering Conference, Auckland, New Zealand, 27–30 Aug.

Dawson, S. G. B., Harris, B. J., and Davies, C. E., 1989, "Characteristics of Venturi Feeders for Powders," CHEMECA '89, 17th Australian Chemical Engineering Conference, Broadbeach, Quinsland, 23–25 Aug.

Fox, L. S., Campbell, K., and Irwin, K., 1992, "Fox venturi eductors replace airlocks in highly abrasive furnace slag application," *Powder Handling and Processing,* Vol. 4, No. 3, pp. 326–327.

Fox, L. S., 1984, "Venturi Eductors in Pneumatic Conveying Systems—Particularly for Reducing Rotary Valve Wear," *Powder and Bulk Solids Handling and Processing,* Rosemont, IL, *Proceedings,* pp. 544–556.

Grupping, A. W., Coppes, J. L. R., and Groot, J. G., 1988, "Fundamentals of Oil Well Jet-Pumping," *SPE Production Engineering,* Feb., pp. 9–14.

Hatzlavramldls, D. T., 1991, "Modeling and Design of Jet Pumps," *SPE Production Engineering,* Nov., pp. 413–419.

Keys, S., and Chambers, A. J., 1990, "Pneumatic Conveying of Copper Strip," *Bulk Solids Handling,* Vol. 10, No. 2, pp. 155–158.

Kmiec, A., 1987, "An Analytical Study of Flows in Gas/Solid Injectors," Pneumatech 3, 3rd International Conference on Pneumatic Conveying Technology, Jetsey, CI, 24–26 Mar., *Proceedings,* pp. 169–197.

Nazarov, V. D., Mamontov, V. I., Snitivker, G. A., Chasnyk, S. M., and Panin, O. K., 1990, "System for Pneumatic Transport of Dust," Translated from *Metallurgy,* No. 11, pp. 25–26, Nov., 1989, Plenum Publishing.

Pittman, A. N., and Mason, J. S., 1986, "Pneumatic Conveying of Bulk Solids Using a Vacuum Aerated Feed Nozzle," 11th Annual Powder & Bulk Solids Conference, Rosemont, IL, 13–15 May, pp. 188–202.

Pogorelov, V. I., 1990, "Theory of Ejectors Designed for Transporting Tows," *Machines and Apparatus,* Translated from Khimicheskie Volokna No. 1, pp. 39–42, January–Feb.

Wang, D., and Wypych, P. W., 1995, "Air-Only Performance of Central Air-Jet Pumps for the Transportation of Bulk Solids in Pipelines," *Powder Handling and Processing,* Vol. 7, No. 2, pp. 111–118.

Wang, D., and Wypych, P. W., 1995, "Central Air-Jet Pump Performance for the Pneumatic Transport of Bulk Solids," *Powder Handling & Processing,* Vol. 7, No. 3, pp. 213–218.

Weber, M., 1982, "Correlation Analysis in the Design of Pneumatic Transport Plant," *Bulk Solids Handling,* Vol. 2, pp. 231–233.

Weber, M., 1981, "Principles of Hydraulic and Pneumatic Conveying in Pipes," *Bulk Solids Handling,* Vol. 1, pp. 57–63.

Westway, S. F., 1987, "An Investigation Into the Performance of Venturi Eductors for the Transport of Solids Particlesin Pipelines," ME thesis, Thomas Polytechnic.

M. J. Findlay
Post-Doctoral Fellow.

M. Salcudean
Professor.

I. S. Gartshore
Professor.

Department of Mechanical Engineering,
University of British Columbia,
Vancouver, BC, Canada, V6T 1Z4

Jets in a Crossflow: Effects of Geometry and Blowing Ratio

The flow field characteristics of three different geometries of square jets in a crossflow at various blowing ratios are examined. The geometries considered are: perpendicular, streamwise-inclined, and spanwise-inclined jets. The inclined jets are at a 30 deg angle to the wind tunnel floor. Mean velocity and turbulence measurements along with film cooling effectiveness and scalar transport data were obtained. Jet-to-crossflow blowing ratios of 1.5, 1.0 and 0.5 are used with a density ratio of 1. It is shown that the flow field at the jet exit is strongly influenced by the crossflow as well as by the inlet conditions at the entrance to the jet orifice. The strong streamline curvature which is present in the perpendicular and spanwise injection cases appears to result in the greatest turbulence anisotropy. The film cooling effectiveness is best at the lowest blowing ratios as the jet is deflected strongly towards the floor of the wind tunnel, although the improvement is more significant for the streamwise injection case.

Introduction

Jets in a crossflow are found in many applications ranging from smokestack pollution dispersion to V/STOL aircraft control to film cooling in gas turbine engines. Although similar characteristics can be found in all these flow fields, the details can be quite different depending primarily on the jet-to-crossflow momentum ratio (I) (Holdeman and Walker, 1977). For film cooling applications, the momentum ratio is typically fairly low, around 1.0 or lower, reflecting a trade-off between the heat transfer and the aerodynamics of the turbine blade, as well as considerations of power output.

Early studies on jets in a crossflow as applied to the film cooling process focussed primarily on measuring the adiabatic film cooling effectiveness (η) along the surface downstream of the slot or jets. Measurements of the flow field were not common, as seen in the review paper by Goldstein (1971).

Andreopoulos and Rodi (1984) made one of the first detailed flow field studies using a three-sensor hot-wire probe. They investigated the flow produced by a single round jet perpendicular to the crossflow at low velocity ratios of $R = 0.5, 1.0, 2.0$. Many of the features found in the single jet case are also present in a row of jets. At low R the momentum of the injected fluid is insufficient to penetrate beyond the boundary layer into the mainstream flow and remains close to the wall. As the velocity ratio is increased the jet eventually penetrates beyond the boundary layer and is deflected in the direction of the crossflow. In addition, two counter-rotating vortices form inside the jet.

The jet spacing-to-diameter ratio, s/D, is an important parameter in the study of a row of jets in a crossflow. For square jets, the limiting case of $s/D = 1$ corresponds to a two-dimensional slot which has the greatest penetration into the crossflow. As s/D increases to between 3 and 5, the jet penetration is reduced as the free-stream fluid is entrained in the jet, enhancing deflection. As the spacing is increased further the jet penetration increases again due to the presence of the free-stream fluid flowing between adjacent jets which tends to increase the pressure on the downstream side of the jets (Sterland and Hollingsworth, 1975). Ligrani et al. (1994a) found a similar trend in the adiabatic film cooling effectiveness from a single row of holes with a compound (streamwise and spanwise) angle orientation. For $s/D = 6$, the spanwise-averaged effectiveness is 20 to 39 percent higher than when a spacing of $s/D = 7.8$ is used, suggesting greater jet penetration into the crossflow as s/D increases.

The use of round holes in jet in crossflow studies is far more common than square or rectangular jets. Detailed studies of a turbulent free square jet were undertaken by Quinn and Militzer (1988) and Quinn (1992). Comparisons were made with data for a circular jet with the same upstream conditions and exit area. These studies showed that a square jet spreads faster than a circular jet in the near flow field. If the spreading of a turbulent free jet is viewed as the result of entrainment of the ambient fluid, then a square jet entrains fluid faster than an equivalent circular jet in the near field. By 20 "equivalent jet diameters" downstream (defined as the diameter of a circular jet with the same exit plane area as the square jet), the jet is fully axisymmetric. Recent work by Haven and Kurosaka (1997) indicates that square jets do not penetrate as far into the crossflow as do round jets. However, implications of improved film cooling for square jets are not clear due to the increased mixing with the crossflow.

Studies on inclined jets where the flow field has been measured are less common than for perpendicular jets, although this trend has been changing over recent years. Papers on streamwise-inclined jets (Kadotani and Goldstein, 1979; Lee et al., 1994; Pietrzyk et al., 1989; Kohli and Bogard, 1995) are discussed in more detail in a previous paper (Findlay et al., 1996). Of particular interest is the study by Pietrzyk et al. (1989) which used a short entry length ($L/D = 3.5$) in order to more closely simulate the conditions typical in film cooling applications. Their data suggested the presence of a separation bubble from the sharp entrance to the jet orifice; a conclusion which was supported by later computational studies (Leylek and Zerkle, 1994; Findlay et al., 1996).

Honami et al. (1994) investigated the thermal and velocity fields for 30° spanwise-inclined jets with $s/D = 5$ and velocity ratios of $R = 0.5, 0.85, 1.2$. Surface temperature data was obtained using an encapsulated thermotropic liquid crystal. The authors found that the jet flow was asymmetric with a large vortex on one side. The asymmetry was increased with the velocity ratio which resulted in low film cooling effectiveness. Recent work by Berger and Liburdy (1998) investigates the influence of hole geometry and compound-angle injection for a row of 35 deg inclined jets. The lateral and vertical mean velocity components were measured using a PIV system and jet penetration and spreading was inferred from the distribution of seed particles in the flow. The study shows the degradation of the counter-rotating vortex pair structure into a single vortex as the compound angle is increased from streamwise to spanwise injection.

Contributed by the Fluids Engineering Division for publication in the JOURNAL OF FLUIDS ENGINEERING. Manuscript received by the Fluids Engineering Division August 27, 1998; revised manuscript received March 15, 1999. Associate Technical Editor: P. W. Bearman.

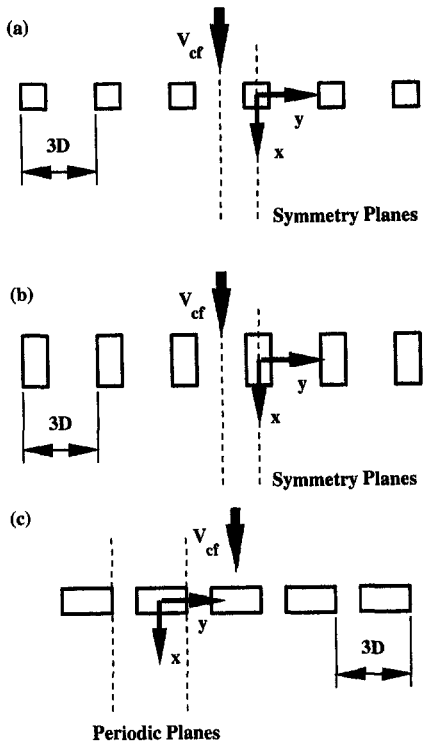

Fig. 1 Coordinate definitions for (*a*) perpendicular, (*b*) streamwise, (*c*) spanwise jets. The *z*-axis points out of the page.

Ligrani et al. (1992, 1994a, 1994b), Ligrani and Ramsey (1995) have investigated the effects of hole orientation on the film cooling performance for one and two rows of injection holes with various s/D and blowing ratios on flat plates. Film cooling effectiveness over curved surfaces with various hole geometries has been examined by Ou and Han (1994), Mehendale and Han (1992), and Salcudean et al. (1994), among others, which are more typical of turbine blade geometries. The intent of this paper is to combine detailed flow field measurements with film cooling effectiveness and jet penetration/spreading data in order to provide a comprehensive data set for validation of CFD codes predicting flow over flat plates.

Experimental Apparatus and Method

The experiments were performed in an open circuit, subsonic wind tunnel. A boundary layer trip wire, 2.4 mm in diameter, was attached at the entrance to the test section to ensure that the boundary layer upstream of the jet holes was turbulent for all blowing ratios used in the experiments. A more detailed description of the wind tunnel, flowmeters and settling chamber may be found in Ajersch et al. (1997).

The tunnel coordinate systems for each case are shown in Fig. 1. The coordinate axes are located on the jet which was used for the experiments. In each case the row of jet holes was aligned across the test section so that the row was perpendicular to the crossflow. The streamwise and spanwise jets were inclined at a 30 deg angle to the test section floor. The jet holes were square in all cases. The hole length-to-diameter ratio (L/D) was 6 for the perpendicular jets and 4 for the streamwise and spanwise jets. The perpendicular jets blow in the positive z-direction, the streamwise jets blow in the positive x-direction and the spanwise jets blow in the negative y-direction.

For the perpendicular and streamwise-inclined jets, symmetry of the flow field was assumed along the plane through the centre of the jet and along the plane half way between adjacent jets, as indicated in Fig. 1. For the selection of the appropriate spanwise jet, the film cooling effectiveness was measured downstream of several of the jets to determine the periodicity of the flow from jet-to-jet. The velocity fields along the planes of periodicity shown in Fig. 1 were compared to ensure that the flow field above the floor level was periodic as well.

As mentioned previously, the momentum flux ratio (I) is an important parameter in determining the flow field characteristics for jets in a crossflow. In this study no temperature difference was introduced between the jets and the crossflow and since the velocities involved in these experiments were low the relevant parameter becomes the velocity or blowing ratio, R. Three velocity ratios were considered: $R = 1.5$, 1.0, and 0.5 ($I = 2.25$, 1.0, and 0.25 respectively.) The jet bulk velocity V_j was fixed for all cases and the crossflow velocity V_∞ was adjusted to obtain the desired R. For all geometries and blowing ratios the jet Reynolds number $\mathrm{Re}_j = V_j D/\nu$ was fixed at approximately 5000 and the upstream boundary layer thickness was approximately $2.0D$.

Instrumentation. A three-component laser Doppler velocimetry (LDV) system was used to measure the flowfield for these experiments. The TSI LDV system used here is the same as that described by Ajersch et al. (1997) and will only be summarized here. The LDV system consists of two probes (six beams) connected to the beam separator and signal processors via fiber optic cables. The probes were mounted at 90 deg to each other and at a small ($\approx$6 deg) angle to the test section floor to allow measurements to be taken at the jet exit in the plane of the floor. A TSI software package controlled the acquisition and storage of the raw data.

Seed particles for the flow were obtained from two smoke generators, one at the wind tunnel inlet for the crossflow and one in-line with the compressed air supply for the jets. The LDV system was operated in coincidence mode which allows the turbulence characteristics of the flow to be determined. More details on the alignment and operation of the system may be found in Findley (1998).

A flame ionization detector (FID) was used to measure the film cooling effectiveness and jet spreading/penetration. A small amount of propane was added to the air supply for the jets which was sampled through a "rake" of eleven fine tubes (0.5 mm OD) spanning $3D$. More details on the FID apparatus may be found in Salcudean et al. (1994).

The uncertainty in the LDV measurements was calculated using the standardized method of Kline and McClintock (1953). A more complete description of the analysis can be found in Ajersch et al. (1997). The uncertainty in the alignment angles was $\pm$0.15 deg and the uncertainty in the measurement position was $\pm$0.1 mm. The uncer-

Nomenclature

D = jet diameter (= jet width)
I = jet-to-crossflow momentum flux ratio $= (\rho V^2)_j/(\rho V^2)_\infty$
M = jet-to-crossflow mass flux ratio $= (\rho V)_j/(\rho V)_\infty$
R = jet-to-crossflow velocity ratio $= V_j/V_\infty$
Re = Reynolds number
U, V, W = mean velocity components
V_∞ = crossflow velocity
V_j = bulk jet velocity
k = turbulence kinetic energy $= \frac{1}{2}(\overline{uu} + \overline{vv} + \overline{ww})$
s = jet spacing
u', v', w' = turbulent normal stresses
x, y, z = axes of the tunnel coordinate system
ν = kinematic viscosity
ρ = density
η = film cooling effectiveness

tainty in the mean velocity is $\pm 0.01 V_j$ and the uncertainties in the turbulent normal and shear stresses are $\pm 0.001 V_j^2$ and $\pm 0.0002 V_j^2$, respectively. The uncertainty values for the LDV measurements may be higher in regions of high turbulence due to the velocity bias which is introduced by the turbulent nature of the flow which cannot be corrected by any bias correction scheme (Fuchs et al. 1994). The uncertainty in the FID measurements was ± 0.02.

Results and Discussion

Measurements of the velocity were taken five jet diameters upstream of the centre of the jet ($x/D = -5$) for all geometries. Boundary layer thickness was found to be approximately $2.0D$ for all cases and velocity ratios. The free-stream turbulence kinetic energy (k) ranges from 3% of V_∞ for $R = 1.5$ down to 1% for $R = 0.5$. The normalized turbulence kinetic energy $\sqrt{k}/V_\infty$) increases to between 8–10% near the wall. The data for perpendicular jets was reported earlier by Ajersch et al. (1997); selected data is included here for comparison with the new geometries.

Jet Exit. The flow field at the jet exit ($z/D = 0$) depends on the jet-to-crossflow velocity ratio, R. The jet exit velocity profiles for the perpendicular and streamwise-inclined ($L/D = 8$) are not shown here due to space limitations but may be found in Ajersch et al. (1997) and Findlay et al. (1996), respectively. In the case of the perpendicular jet holes, as R is reduced (V_∞ is increased) the jet exit flow is skewed towards the downstream edge of the jet hole, as expected. For the streamwise-inclined jets, as R is reduced the jet exit profile becomes more uniform due to the velocity bias towards the upstream side of the jet hole which is produced by the sharp-edged entrance to the jet hole (Pietrzyk et al., 1989). The

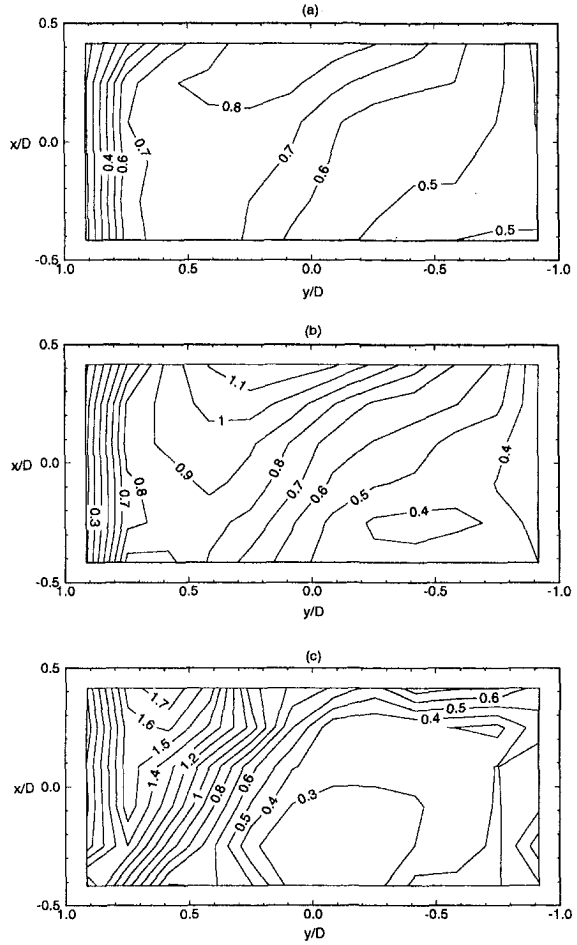

Fig. 2 Spanwise jet exit (W/V_j) contours (*a*) $R = 1.5$, (*b*) $R = 1.0$, (*c*) $R = 0.5$

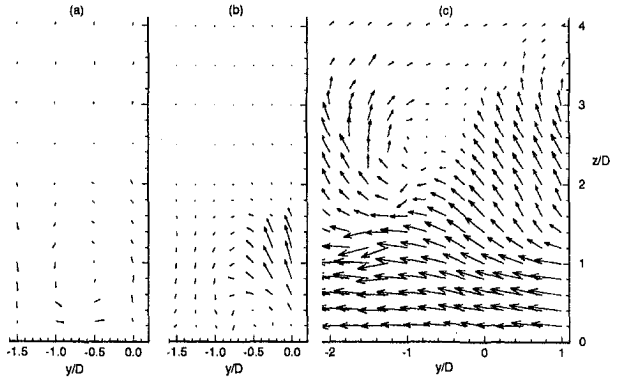

Fig. 3 Normalized *V*, *W* velocity vectors at $x/D = 3$, $R = 1.5$ for (*a*) perpendicular, (*b*) streamwise, (*c*) spanwise jets

streamwise-inclined jets used in these experiments had a shorter entry length ($L/D = 4$) than those referenced previously, but the exit profiles are essentially the same. The primary difference is that the maximum vertical velocity in the jet exit plane is higher (by about 18%) for the shorter entry length jets due to the stronger "jetting effect" which is present. The location of the maximum velocity region is the same.

The flow field at the jet exit for the spanwise-inclined jets is shown in Fig. 2 at $R = 1.5, 1.0, 0.5$. Note that the coordinate system boxes in Fig. 2 correspond to the edges of the jet opening and the contours are of the normalized vertical component of velocity, W/V_j. Of particular interest here is the shift in the region of maximum vertical velocity. At $R = 1.5$ the high-velocity region is skewed slightly in the positive y-direction due to the jetting effect produced by the sharp-edged inlet. The flow is also pushed toward the downstream edge of the jet by the crossflow. As the crossflow velocity is increased the maximum vertical velocity increases and the region shifts towards the positive y-direction to a greater extent. This trend differs from velocity profiles at the jet exit which were assumed as boundary conditions in earlier computational studies (Sathyamurthy and Patankar, 1990; Zhou, 1993).

Mean Velocity Field. The V- and W-components of velocity, normalized by the bulk jet velocity (V_j), at the $x/D = 3$ plane are shown for all three geometries at $R = 1.5, 1.0, 0.5$ in Fig. 3, 4, and 5, respectively. At $R = 1.5$ for the perpendicular jet a clear vortex forms at a height of $z/D = 0.9$. In the case of the streamwise-inclined jet a weak vortex may be discerned at $z/D = 0.4$. For the spanwise-inclined jet there is evidence of a vortex at $x/D = 3$ but this disappears by $x/D = 5$. As the crossflow velocity is increased, the vortices present in the perpendicular and streamwise cases are pushed closer to the tunnel floor and become weaker due to the presence of the floor. The spanwise jet still shows

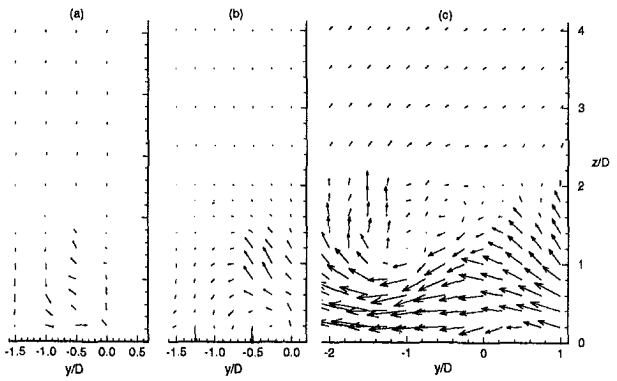

Fig. 4 Normalized *V*, *W* velocity vectors at $x/D = 3$, $R = 1.0$ for (*a*) perpendicular, (*b*) streamwise, (*c*) spanwise jets

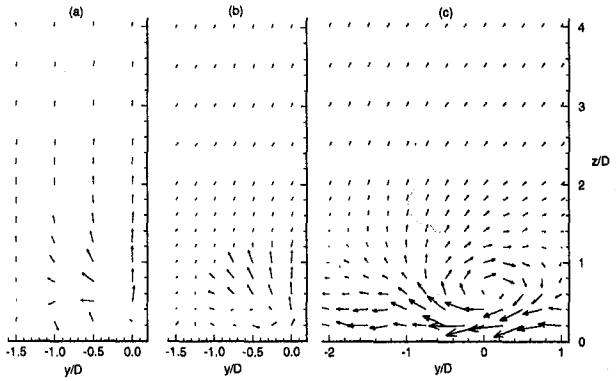

Fig. 5 Normalized V, W velocity vectors at $x/D = 3$, $R = 0.5$ for (*a*) perpendicular, (*b*) streamwise, (*c*) spanwise jets

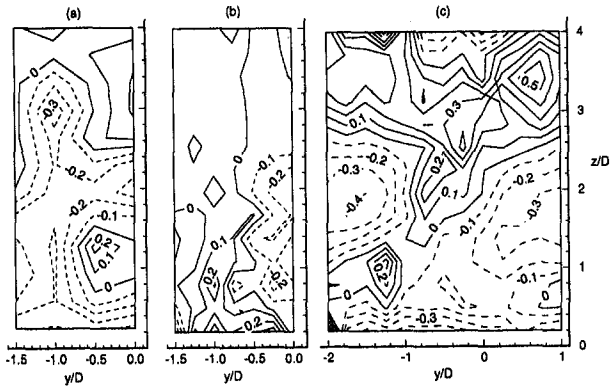

Fig. 7 Contours of w'-ratio at $x/D = 3$, $R = 1.5$ for (*a*) perpendicular, (*b*) streamwise, (*c*) spanwise jets.

indications of vortex formation, but again this disappears by $x/D = 5$. Finally, at $R = 0.5$ the perpendicular and streamwise-inclined jets produce only a very weak vortex. However, a vortex does form for the spanwise-inclined jets. This result appears to contradict the results of Honami et al. (1994) which found stronger vortices as R was increased. The discrepancy arises due to the proximity of the jets. In this case the close spacing ($s/D = 3$) causes the flow from adjacent jets to interact and prevent the flow from curling around to form a vortex. The data of Berger and Liburdy (1998) show a clear vortex at $R = 1.25$ for spanwise injection, but s/D is not specified. In the $R = 0.5$ case, the jet flow is swept downstream quickly enough to prevent the interaction.

Figure 6 shows the normalized streamwise velocity (U/V_j) for $R = 1.5$ at the $x/D = 3$ plane. As expected, the blockage created by the perpendicular and spanwise-inclined jets is much greater than in the streamwise-inclined case. It was expected that the streamwise case with a shorter entry length ($L/D = 4$ compared with $L/D = 8$ (Findlay et al., 1996) would result in a lower-velocity region (or possibly backflow) in the near-hole region due to the nearer proximity of the separation at the sharp-edged entrance to the jet orifice. This does not seem to be the case and the jet penetration is essentially unchanged. It seems that the sharp edge at the downstream side of the jet exit does not have an effect on the already separated flow from the short entry length. In the case of a longer entry length, the flow within the jet hole may reattach within the hole but separate again from the downstream edge of the jet which results in greater penetration of the jet into the crossflow.

In all cases, as the velocity ratio is decreased to $R = 0.5$ the jets are not able to penetrate beyond the boundary layer and the jet flow remains close to the wall.

Turbulence Anisotropy. The use of a three-component LDV system operating in coincidence mode allowed all of the turbulent Reynolds stresses to be measured in these experiments. Due to space constraints, only a measure of the turbulence anisotropy will be presented here. One of the normal stress ratios used by Ajersch et al. (1997) will be used, called the w'-ratio, which is defined as

$$\frac{w' - u'}{u'} \tag{1}$$

where u' and w' are the square roots of the turbulent normal stresses in the x- and z-directions, respectively. A value of zero indicates that the turbulence is isotropic in the z-direction and a value of 0.5, for example, indicates that w' is 50% higher than u'. The w'-ratio at $R = 1.5$ and $x/D = 3$ for all three geometries is shown in Fig. 7. The perpendicular and spanwise jets show the greatest anisotropy. This reflects the stronger interaction between the jet and crossflow for these two geometries.

Film Cooling Effectiveness. At low velocity ratios, determination of jet spreading and penetration becomes difficult (Findlay et al., 1996). Near $R = 1.0$ the boundaries of the jet are difficult to discern from contours of streamwise velocity due to the similarity in V_j and V_∞. At $R = 0.5$ many of the features of the flow are smeared out in the turbulence of the boundary layer. Measurements of the concentration of propane in the jet flow give an excellent indication of mixing between the jet and crossflow and the penetration of the jet. Contours of concentration are shown Fig. 8 and Fig. 9 at $x/D = 3$ for the streamwise and spanwise cases at $R = 1.5$, 0.5, respectively. At $R = 1.5$ the contours are in close agreement with those of Fig. 6. The periodicity of the flow in the spanwise injection case can be seen as well. Cross-stream fluid has been entrained in the jet and drawn towards the floor in the

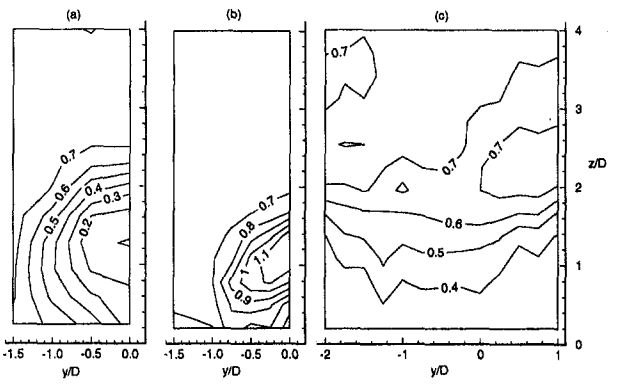

Fig. 6 Contours of streamwise velocity (U/V_j) at $x/D = 3$, $R = 1.5$ for (*a*) perpendicular, (*b*) streamwise, (*c*) spanwise jets

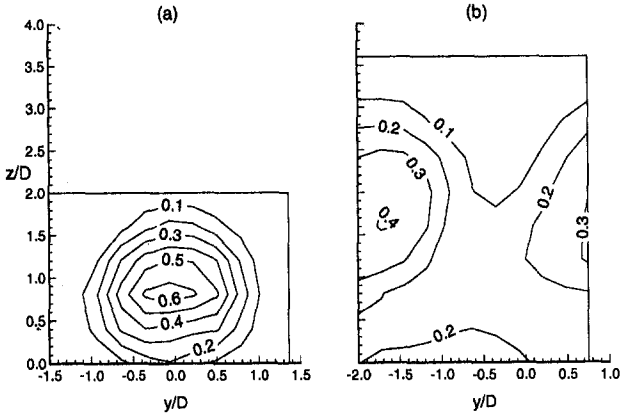

Fig. 8 Concentration contours (0 = crossflow, 1 = Jet) at $x/D = 3$, $R = 1.5$ for (*a*) streamwise, (*b*) spanwise jets

spanwise case. However, comparison with Fig. 3 indicates that no strong vortex has formed at $R = 1.5$ resulting in very little flow toward the floor. The cross-stream fluid is entering at the space between adjacent jets and is trapped between the core jet flow and the floor. With streamwise injection, the counter-rotating vortices which are formed at $R = 1.5$ bring the cross-stream fluid towards the floor relatively quickly which results in a large area of the floor being exposed to the free-stream fluid.

At $R = 0.5$ it is apparent that there has been less mixing between the jet and the crossflow in the streamwise case, which is consistent with the fact that there is no vortex formation. The jet flow has also spread laterally along the floor to a greater extent than in the $R = 1.5$ case. In the spanwise case the vortex which has formed appears to draw free-stream fluid towards the floor but it also serves to spread the jet fluid along the floor to a greater extent.

The spanwise-averaged film cooling effectiveness (η) is shown in Fig. 10 comparing the streamwise and spanwise injection cases at $R = 1.5$ and $R = 0.5$. In the streamwise case the value of η drops rapidly at $R = 1.5$ as x/D increases due to the large area of the floor which is exposed to the crossflow. At $R = 0.5$ the effectiveness is much better as the jet does not penetrate beyond the boundary layer and spreads laterally.

In the spanwise case η is typically better than in the streamwise case. Again, there is a sharp drop in η as x/D increases. An interesting feature of the graph is that η increases between $x/D = 5$ and 8 at $R = 1.5$. The cross-stream fluid which is trapped between the jet flow and the floor has mixed with the jet fluid to a greater extent by $x/D = 8$. In contrast to the streamwise injection, there is little improvement in η as R is reduced because of the increased mixing between the jet and cross-stream fluid produced by the vortex which is formed.

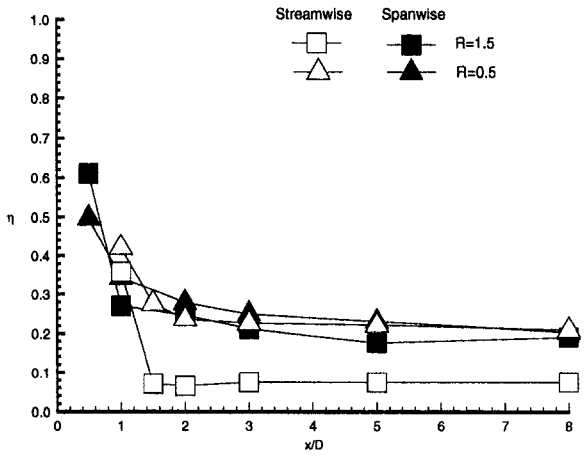

Fig. 10 Spanwise-averaged film cooling effectiveness (η) for streamwise and spanwise jets

Conclusions

Detailed measurements of the flow field produced by a row of square jets injecting fluid perpendicular, streamwise-inclined at 30 deg, and spanwise-inclined at 30 deg into a crossflow have been made using a three-component LDV system and flame ionization detector (FID). Jet-to-crossflow velocity ratios of $R = 1.5$, 1.0, 0.5 were used, with the jet Reynolds number fixed at approximately 5000.

The inclination of the jet holes in the streamwise and spanwise cases creates a nonuniform velocity profile at the jet exit. For spanwise injection the flow field becomes skewed toward one corner of the jet exit hole as the crossflow velocity increases. This result differs from assumed velocity profiles used in previous literature on the numerical simulation of this flow field and again stresses the need for simulations to include the flow at the jet hole inlet.

As expected, the streamwise-inclined jets produced less blockage to the cross-stream flow than the perpendicular and spanwise-inclined cases. The proximity of the jets ($s/D = 3$) in the spanwise case results in the interaction of adjacent jets at higher blowing ratios which prevents the formation of the vortices which are present with larger jet spacing. The increased blockage which results in an increase in streamline curvature in the perpendicular and spanwise cases results in stronger turbulence anisotropy. In addition, the endwall vorticity from within the injection tube, observed by Haven and Kurosaka (1997) results in unsteadiness along the edges of the jet flow.

Measurements of jet penetration and film cooling effectiveness (η) indicate that none of the jets penetrate beyond the boundary layer at $R = 0.5$. Spanwise-averaged film cooling effectiveness is typically better at the lower blowing ratios due to better lateral spreading of the jet fluid along the floor. In the spanwise case the improvement in η as R decreases is less apparent than in the streamwise case due to the increased mixing between the jet and the crossflow produced by the vortex which is formed. Evidence that fluid from the crossflow is trapped between the floor and the jet flow in the spanwise case is found at $R = 1.5$ resulting in a lower η.

Clearly, at low velocity ratios (R) there is little difference between the streamwise and spanwise injection cases as far as η is concerned. However, the blockage produced by the spanwise injection is much greater than for the streamwise injection which has implications for turbine performance. Practical considerations may not allow the use of a low blowing ratio. At higher blowing ratios, spanwise injection provides better film cooling protection. The differences shown in the behaviour of the various geometries at different blowing ratios, as well as manufacturing constraints, point to the need for careful consideration of these factors in the selection of the most appropriate geometry and blowing ratio for a given film cooling application.

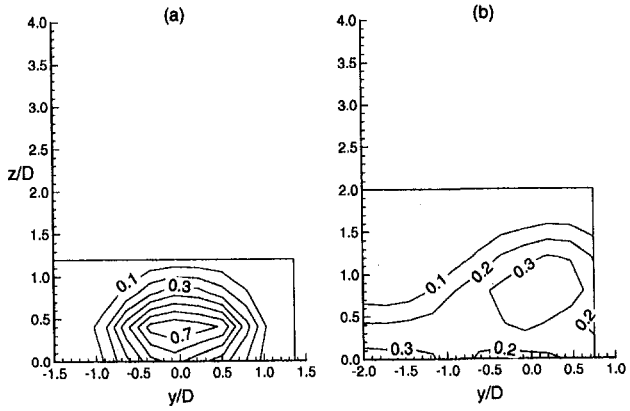

Fig. 9 Concentration contours (0 = Crossflow, 1 = Jet) at $x/D = 3$, $R = 0.5$ for (*a*) streamwise, (*b*) spanwise jets

Acknowledgments

This work was supported by the Natural Sciences and Engineering Research Council of Canada and by Pratt and Whitney Canada.

References

Ajersch, P., Zhou, J-M., Ketler, S., Salcudean, M., and Gartshore, I. S., 1997, "Multiple Jets in a Crossflow: Detailed Measurements and Numerical Simulations," ASME JOURNAL OF TURBOMACHINERY, Vol. 119, No. 2, pp. 330–342.

Andreopoulos, J., and Rodi, W., 1984, "Experimental Investigation of Jets in a Crossflow," *Journal of Fluid Mechanics*, Vol. 138, pp. 92–127.

Berger, P. A., and Liburdy, J. A., 1998, "A Near-Field Investigation into the Effects of Geometry and Compound Angle on the Flowfield of a Row of Film Cooling Holes," ASME Paper 98-GT-279, IGTI, June 2–5, Stockholm, Sweden.

Findlay, M. J., He, P., Salcudean, M., and Gartshore, I. S., 1996, "A Row of Streamwise-Inclined Jets in Crossflow: Measurements and Calculations," ASME

Paper 96-GT-167, presented at the International Gas Turbine and Aeroengine Congress & Exhibition, Birmingham, UK, June 10–13.

Findlay, M. J., 1998, "Experimental and Computational Investigation of Inclined Jets in a Crossflow," Ph.D. thesis, University of British Columbia, Vancouver, Canada.

Fuchs, W., Nobach, H., and Tropea, C., 1994, "Laser Doppler Anemometry Data Simulation: Application to Investigate the Accuracy of Statistical Estimators," *AIAA Journal,* Vol. 32, No. 9, pp. 1883–1889.

Goldstein, R. J., 1971, "Film Cooling," *Advances in Heat Transfer,* Vol. 7, pp. 321–379.

Haven, B., and Kurosaka, M., 1997, "Kidney and Anti-Kidney Vortices in Crossflow Jets," *Journal of Fluid Mechanics,* Vol. 352, pp. 27–64.

Holdeman, J. D., and Walker, R. E., 1977, "Mixing of a Row of Jets with a Confined Crossflow," *AIAA Journal,* Vol. 15, pp. 243–249.

Honami, S., Shizawa, T., and Uchiyama, A., 1994, "Behavior of the Laterally Injected Jet in Film Cooling: Measurements of Surface Temperature and Velocity/Tempera-ture Field Within the Jet," ASME *Journal of Turbomachinery,* Vol. 116, pp. 106–112.

Kadotani, K., and Goldstein, R. J., 1979, "On the Nature of Jets Entering a Turbulent Flow," ASME *Journal of Engineering for Power,* Vol. 101, pp. 459–465.

Kline, S. J., and McClintock, F. A., 1953, "Describing Uncertainties in Single-Sample Experiments," *Mechanical Engineering,* Vol. 77, No. 4, pp. 3–8.

Kohli, A., and Bogard, D. G., 1995, "Adiabatic Effectiveness, Thermal Fields, and Velocity Fields for Film Cooling with Large Angle Injection," ASME *Journal of Turbomachinery,* Vol. 119, No. 2, pp. 352–358.

Lee, S. W., Lee, J. S., and Ro, S. T., 1994, "Experimental Study on the Flow Characteristics of Streamwise Inclined Jets in Crossflow on Flat Plate," ASME *Journal of Turbomachinery,* Vol. 116, pp. 97–105.

Leylek, J. H., and Zerkle, R. D., 1994, "Discrete-Jet Film Cooling: A Comparison of Computational Results with Experiments," ASME *Journal of Turbomachinery,* Vol. 116, pp. 358–368.

Ligrani, P. M., Ciriello, S., and Bishop, D., 1992, "Heat Transfer, Adiabatic Effectiveness, and Injectant Distributions Downstream of a Single Row and Two Staggered Rows of Compound-Angle Film-Cooling Holes," ASME *Journal of Turbomachinery,* Vol. 114, pp. 687–700.

Ligrani, P. M., Wigle, J. M., and Jackson, S. W., 1994a, "Film-Cooling From Holes With Compound Angle Orientations: Part 2—Results Downstream of a Single Row of Holes With 6*d* Spanwise Spacing," ASME *Journal of Heat Transfer,* Vol. 116, pp. 353–362.

Ligrani, P. M., Wigle, J. M., Ciriello, S., and Jackson, S. M., 1994b, "Film-Cooling From Holes With Compound Angle Orientations: Part 1—Results Downstream of Two Staggered Rows of Holes With 3*d* Spanwise Spacing," ASME *Journal of Heat Transfer,* Vol. 116, pp. 341–352.

Ligrani, P. M., and Ramsey, A. E., 1995, "Film Cooling From Spanwise Oriented Holes in Two Staggered Rows," ASME *Journal of Turbomachinery,* Vol. 119, No. 3, pp. 562.

Mehendale, A. B., and Han, J. C., 1992, "Influence of High Mainstream Turbulence on Leading Edge Film Cooling Heat Transfer," ASME *Journal of Turbomachinery,* Vol. 114, pp. 707–715.

Ou, S., and Han, J. C., 1994, "Leading Edge Film Cooling Heat Transfer Through One Row of Inclined Film Slots and Holes Including Mainstream Turbulence Effects," ASME *Journal of Heat Transfer,* Vol. 116, pp. 561–569.

Pietrzyk, J. R., Bogard, D. G., and Crawford, M. E., 1989, "Hydrodynamic Measurements of Jets in Crossflow for Gas Turbine Film Cooling Applications," ASME *Journal of Turbomachinery,* Vol. 111, pp. 139–145.

Quinn, W., and Militzer, J., 1988, "Experimental and Numerical Study of a Turbulent Free Square Jet," *Physics of Fluids,* Vol. 31, No. 5, pp. 1017–1025.

Quinn, W., 1992, "Streamwise Evolution of a Square Jet Cross Section," *AIAA Journal,* Vol. 30, No. 12, pp. 2852–2857.

Salcudean, M., Gartshore, I., Zhang, K., and McLean, I., 1994, "An Experimental Study of Film Cooling Effectiveness Near the Leading Edge of a Turbine Blade," ASME *Journal of Turbomachinery,* Vol. 116, pp. 71–79.

Sathyamurthy, P., and Patankar, S. V., 1990, "Prediction of Film Cooling with Lateral Injection," Conference Proceedings, *Heat Transfer in Turbulent Flows,* Vol. 138, pp. 61–70.

Sterland, P. R., and Hollingsworth, M. A., 1975, "An Experimental Study of Multiple Jets Directed Normally to a Crossflow," *Journal of Mechanical Engineering Science,* Vol. 17, No. 3, pp. 117–124.

Zhou, J.-M., 1993, "A Computational and Experimental Investigation of Gas Turbine Blade Film Cooling," Ph.D. thesis, University of British Columbia, Vancouver, Canada.

S. X. Shi
Professor.

D. G. Xi
Professor.

J. R. Qin
Research Assistant.

N. Liu
Associate Professor.

National Engine Combustion Laboratory,
Tianjin University,
Tianjin 300072,
P. R. China

G. C. Shu
Graduate Student,
Department of Mechanical Engineering,
Louisiana State University,
Baton Rouge, LA 70802

Unstable Asymmetric Modes of a Liquid Jet

This paper reports the results of a linear instability analysis for a viscous liquid jet injecting into a quiescent inviscid gas medium with three-dimensional disturbances. A dispersion equation that accounts for the growth of asymmetric waves is derived, and the maximum rates of growth of various modes are calculated. The asymmetric breakup phenomenon of the jet and its structures at different modes is also studied by using a high-speed multi-frame holographic system. The theoretical predictions agree well with the experimental observations. The results of this study thus confirm the existence and even domination of unstable asymmetric modes under certain physical conditions in the breakup process.

1 Introduction

Most previous studies on breakup of liquid jets were based on the assumption that disturbances grow symmetrically (Bogy, 1979; Reitz and Bracco, 1982; Lin and Kang, 1987). However, recent theoretical investigations revealed the possibility of existence and even domination of asymmetric unstable modes in the breakup process of a liquid jet (Yang, 1992; Li and Kelly, 1992; Schetz et al., 1980; Stockman and Bejan, 1982; Li, 1995; Qin, 1995). The latest investigation was conducted by Li (1995). The result showed that at least the first order mode has a higher growth rate than axisymmetric one under certain physical conditions. This conclusion is important and it could not be reached if the liquid viscosity is ignored. However, this does not mean that the first order asymmetric mode will certainly dominate the liquid jet. The dominating mode, in the sense of the linear instability, should be one possessing the highest growth rate of all the modes and in the entire range of wavenumber from 0 to ∞.

The questions to be answered here are whether or not every single unstable mode has the possibility to become a dominant mode and under what physical conditions an asymmetric mode may become dominant in a liquid jet. Further, according to L. Rayleigh (Drazin and Reid, 1981), a dominating mode can be observed in practice. Another question thus arises as to whether a jet dominated by an asymmetric mode could be observed in experiments under the theoretically predicted conditions. In the present investigation, attempts have been made to clarify the problems mentioned above.

2 Theoretical Study

2.1 Dispersion Relationship of a Viscous Liquid Jet. Consider a viscous liquid jet discharging with velocity U from a nozzle of radius a into an infinitely large quiescent inviscid and incompressible gas medium. The system is subjected to an initial disturbance of an infinitesimal magnitude, with velocity $\vec{v}$ and pressure p. The flow motion is governed by the Navier-Stokes equations in the dimensionless form (Batchelor, 1970):

$$(\partial_t - \delta_{i1}\partial_r)\vec{v}_i = -\nabla p_i/(\delta_{i1} + \delta_{i2}Q) + (\delta_{i1}/\mathrm{Re})\nabla^2\vec{v}_i \quad (1)$$

$$\nabla \cdot \vec{v}_i = 0 \quad (2)$$

where subscript $i = 1, 2$ denotes the liquid and the gas respectively; $\delta_{ij} = \begin{cases} 0 & i \neq j \\ 1 & i = j \end{cases}$; $Q = \rho_2/\rho_1$ is the density ratio of gas to liquid; $\mathrm{Re} = Ua/\gamma$ is the Reynolds number, in which γ is the kinematic viscosity of the liquid; t is time; (r, θ, x) are the cylindrical coordinates; $\vec{v}_i = (u_i, v_i, w_i)$. In the above equations, the length, velocity, and time are dimensionless. The reference length and velocity are a and U, respectively.

The dimensionless dynamic and kinematic boundary conditions are

$$p_1 - p_2 = (2/\mathrm{Re})\partial_r u_1 - \mathrm{We}(1 + \partial_{xx} + \partial_{\theta\theta})\eta \quad (3)$$

$$\partial_\theta u_1 + r\partial_r v_1 - v_1 = 0 \quad (4)$$

$$\partial_x u_1 + \partial_r w_1 = 0 \quad (5)$$

$$u_i = (\partial_t + \delta_{i1}\partial_x)\eta \quad (6)$$

where $\eta = \eta_0 \exp[st + i(kx + n\theta)]$ is the perturbed displacement of surface in the liquid and the gas; $\mathrm{We} = \sigma/(aU^2\rho_1)$ is Weber number; σ is the surface tension.

The governing equations (1) (2) and boundary conditions (3) through (6) are same as those used by Li (1995). A different method of derivation is here used to obtain its dispersion relation. In the following derivation, two functions φ and ψ are employed to simplify the solving procedure.

By taking the divergence of Eq. (1) and from continuity Eq. (2), we have,

$$\nabla^2 p_i = 0 \quad (7)$$

By introducing the normal modes

$$P_i = \hat{P}_i \exp[st + i(kx + n\theta)] \quad (8)$$

Contributed by the Fluids Engineering Division for publication in the JOURNAL OF FLUIDS ENGINEERING. Manuscript received by the Fluids Engineering Division March 20, 1997; revised manuscript received December 21, 1998. Associate Technical Editor: M. Triantafyllou.

$$\vec{v}_i = \vec{\hat{v}}_i \exp[st + i(kx + n\theta)] \quad (9)$$

then,

$$\hat{p}_1 = BIn(kr) \quad (10)$$

$$\hat{p}_2 = AKn(kr) \quad (11)$$

where $In(kr)$ and $Kn(kr)$ are the nth-order modified Bessel function of the first and the second kinds; A and B are constants. Substituting Eq. (10) into Eq. (1), the velocity of gas can be obtained:

$$\vec{\hat{v}} = A[-(k/sQ)K'n(kr),\ -(in/sQr)Kn(kr),\ -(ik/sQ)Kn(kr)] \quad (12)$$

For the liquid, let

$$\vec{v}_1 = \vec{v}_v + B[(k/\epsilon)I'n(kr),\ (in/\epsilon r)In(kr),\ (ik/\epsilon)In(kr)] \times \exp[st + i(kx + n\theta)] \quad (13)$$

where $\epsilon = -(s + ik)$ and $\vec{v}_v = (u_v, v_v, w_v)$, which can be further expressed as:

$$u_v = \partial_r\varphi - (1/r)\partial_\theta\psi \quad (14)$$

$$v_v = (1/r)\partial_\theta\varphi + \partial_r\psi \quad (15)$$

$$w_v = CIn(lr) \exp[st + i(kx + n\vartheta)] \quad (16)$$

in which $l^2 = k^2 - \epsilon$ Re; φ, ψ are functions with third order derivatives. Substituting Eq. (12)–Eq. (15) into Eq. (1)–Eq. (2), we have

$$\hat{u}_v = -C(ik/l)In(lr) - D(in/r)In(lr) \quad (17)$$

$$\hat{v}_v = C(kn/l^2r)In(lr) + DlI'n(lr) \quad (18)$$

where, $\vec{\hat{v}} = (\hat{u}, \hat{v}, \hat{w})$. Substituting Eq. (10) through Eq. (18) into boundary conditions Eq. (3) through Eq. (6), the dispersion relationship can be finally obtained:

$$|a_{ij}| = 0 \quad (19)$$

where

$$a_{11} = (k/\epsilon)I'n(k);\ a_{12} = (s + ik)k/(s^2Q)K'n(k);$$

$$a_{13} = -(ik/l)In(l);\ a_{14} = -inIn(l);$$

$$a_{21} = (2k/\epsilon\ \mathrm{Re})In'(k) - [2(k^2 + n^2)/\epsilon\ \mathrm{Re} + 1]In(k);$$

$$a_{22} = -Kn(k) + \mathrm{We}(k^2 + n^2 - 1)/(Qs^2)K'n(k);$$

$$a_{23} = (2ik/\mathrm{Re})I'n(l);$$

$$a_{31} = (2ik^2/\epsilon)I'n(k);\ a_{32} = 0;$$

$$a_{33} = (k^2/l)In(l) + lIn'(l);\ a_{34} = nkIn(l);$$

$$a_{41} = (2ink/\epsilon)I'n(k) - (2in/\epsilon)In(k);\ a_{42} = 0;$$

$$a_{43} = (kn/l)I'n(l) + (nk/l - 2kn/l^2)In(l);$$

$$a_{44} = -2lI'n(l) + (l^2 + 2n^2)In(l).$$

The rest of a_{ij} are zero.

It can be verified that the dispersion relation given by Eq. (19) is identical to that given in Li's paper (1995) although its form of presentation is quite different. This is due to the different methods of derivation employed and due to the fact that the Weber number used here was defined by Yang (1992) which is the reciprocal of that given in Li's paper. Equation (19) has to be solved numerically. Li has given some numerical results in his paper. These results show that the first order mode may be more unstable than zero order mode. However, to prove that asymmetric modes may become dominant and to find out the corresponding physical conditions, a great deal of numerical calculation has to be carried out.

2.2 Conditions for Occurrence of Unstable Asymmetric Modes. Generally, the mode that can be observed in experiment has the highest growth rate. The maximum growth rate of disturbances for various modes can be calculated with Eq. (19). By summarizing the numerical solutions for all the cases, a distribution diagram of the dominating modes in Re-We plane was obtained.

Figure 1 gives the distribution of dominant modes from the first to fourth order when the density ratio $Q = 1.1 \times 10^{-3}$. Both horizontal and vertical coordinates are in logarithmic scales. The numbers in the circles indicate the order of the modes.

It is noteworthy that the dominant modes numbered are located in sequence according to their respective number of order. Such a regularity of sequence should be kept the same for modes higher than 4th. The results shown in Fig. 1 also indicate that every asymmetric mode may become dominant as long as the required physical conditions are satisfied. This means that every asymmetric mode has the possibility to be observed in practice.

It is also interesting to note that in Fig. 1 there is a reversed 'S-curve'—a curve in the shape of a reversed 'S' which divides the Re-We plane into two parts. In the right part, the symmetric mode is dominant, whilst in the left part, asymmetric modes are dominant. Results of further study give the distribution of regions for various asymmetric dominant modes, as shown in the left side of S-curve.

When physical parameters of jets keep constant, Weber number We will vary linearly with Re in the logarithmic coordinate diagram. The oblique lines in Fig. 1 denote the relationship between

Nomenclature

U = velocity of liquid jet discharging from a nozzle
a = radius of undisturbed jet
$\vec{v} = (u, v, w)$, perturbation velocity of
$\vec{\hat{v}} = \vec{v} = \vec{\hat{v}} \exp(st + i(kx + n\theta)$
p = perturbation pressure
$\hat{p} = p = \hat{p} \exp(st + i(kx + n\theta)$
γ = kinematic viscosity of liquid
t = time
(r, θ, x) = cylindrical coordinates
$\mathrm{Re} = Ua/\gamma$ = Reynolds number
η = perturbed displacement of jet surface
σ = surface tension
ρ = density
$\mathrm{We} = \sigma/(aU^2\rho_1)$ = Weber number
s = complex frequency
k = axial wavenumber
n = mode order
In = nth-order modified Bessel function of first kind
Kn = nth-order modified Bessel function of second kind
A, B, C, D = arbitrary constants
$\epsilon = -(s + ik)$
$l = l^2 = k^2 - \epsilon$ Re
φ, ψ = functions with third derivatives
a_{ij} = elements of coefficient matrix
Q = density ratio of gas to liquid

Subscript

$i = 1$ = for liquid
$i = 2$ = for gas

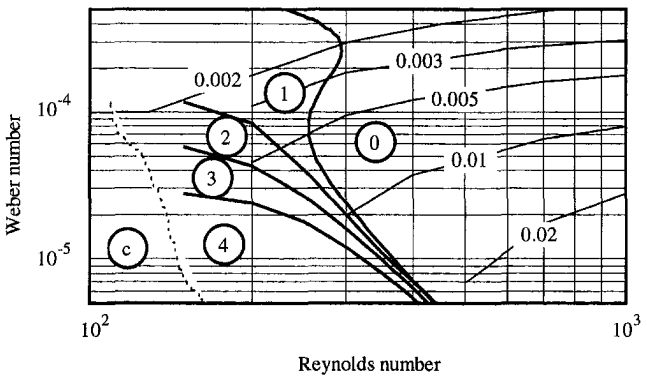

Fig. 1 The distribution of dominant modes

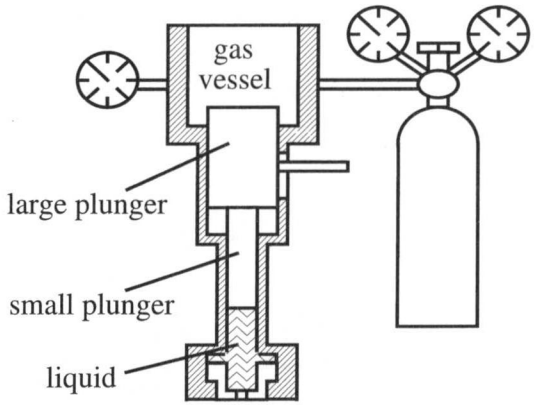

Fig. 3 Experimental apparatus

Re and We for different liquids, each of these lines crosses several regions. This implies that the jet structures may become different for the same liquid by changing injection conditions.

There is a region 'c' on the left side of dotted curve in Fig. 1. In this region, the instability of jet becomes more complicated. The numerical results show that symmetric mode has the highest growth rate in this region.

The numerical results also show that when the density ratio Q changes, all the regions numbered in Fig. 1 simply move horizontally towards left when Q increases, and toward right when Q decreases. It is also interesting to note that when Re $\rightarrow \infty$ and We $\rightarrow 0$, the boundaries of various regions will converge into one curve. This indicates that all modes have almost the same maximum growth rate under the conditions of atomization.

The figures with decimals in Fig. 1 denote the constant maximum growth rates of axial-symmetric modes on their respective curves. In Fig. 1, the asymmetric dominant modes are so distributed that the difference in the disturbance growth rate between two adjacent modes is small. The theoretical separating curve between two adjacent regions is not sharply defined. It is most likely that not only the dominant unstable wave but also its adjacent modes may be observed on the jet surface. The real jet surface may be considered as a superposition of waves with more than one mode. It is, therefore, much more difficult to observe an asymmetric dominant mode than a symmetric one.

Figure 2 shows the disturbed surfaces of jets for different dominant modes. Each of these disturbed surfaces is obtained by superposing η (displacement of jet surface) on the undisturbed surfaces and then by the help of a surface constructing. These theoretical jet patterns shown are used to identify asymmetric modes observed in experiments by direct comparison.

3 Experimental Observation

3.1 Experiment Setup. The experimental apparatus for producing high-speed liquid jets is shown schematically in Fig. 3. When the compressed N_2 from a compressed nitrogen bottle pushes the small plunger down, the plunger in turn compresses the liquid so that the liquid is injected through the nozzle into a chamber with a pressure of one atmosphere. In this way, a high-speed liquid jet is formed. In order to avoid nonlinear disturbances, the nozzle must be machined with high degree of accuracy and smoothness. Figure 4(a) shows the cross-section of the nozzle employed in the present experiment and the laser diffraction photograph of the nozzle hole. The hole was carefully bored with a precision machine. Figure 4(b) shows a liquid jet at a low speed to demonstrate that the nozzle imperfections do not introduce significant nonlinear disturbances. The diameter and length of the nozzle hole are 0.4 mm and 1.2 mm, respectively. Its length to diameter ratio $l/d = 3$. These parameters are within the range usually used for diesel engines.

Figure 5 illustrates the schematic diagram of the multi-frame high-speed holographic system. This system consists of a ruby laser, a multi-frame controller, electron-optic switches and so on. The photographic principle of this system is similar to that of the off-axis holography (Chigier, 1991), but it has three reference beams which reach the recording plate successively with an interval of 20 μs (Xi et al., 1996). The object beam is separated from the reference beams by a Glan-Foucault polarizing prism and then passes through the jet to the recording plate. The exposure time of every event is about 30 ns. In order to observe the surface waves clearly, besides the background illuminating light, a foreground beam is arranged to illuminate the jet directly. From the photographs obtained by this optical system one can not only identify

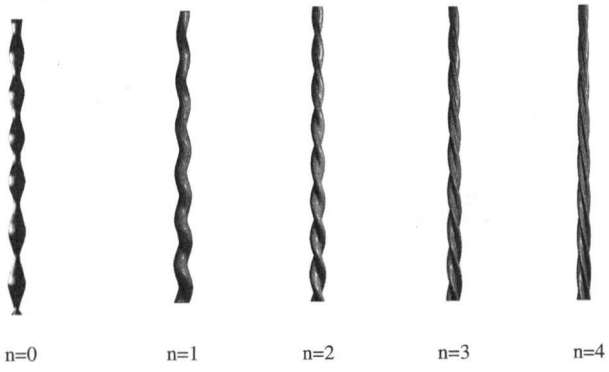

Fig. 2 The structure of jets dominated by different modes

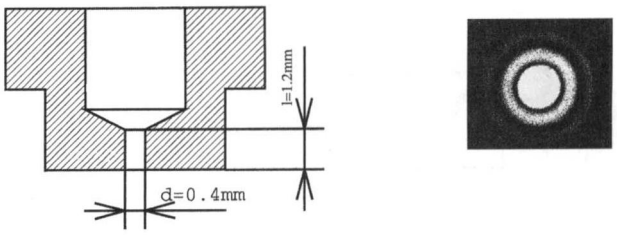

Fig. 4 (a) The cross-section of the nozzle and laser diffraction photograph of the nozzle hole

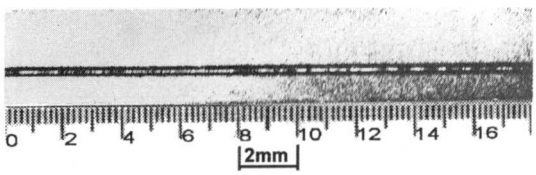

Fig. 4 (b) A liquid jet at a low speed

Table 1 Physical properties of liquids used

Liquids used	1	2	3
Ratio of glycerin to water (by volume)	3	4.3	5.9
Kinematic viscosity (10^{-6} m^2/s)	65	96	125
Density (10^3 kg/m^3)	1.2	1.21	1.22
Surface tension (10^{-3} N/m)	66	65	64

the spatial structure of a liquid jet, but also can accurately determine its moving speed.

3.2 Experimental Results. Three kinds of liquid are employed in the experiments. They are mixtures of glycerin and water with different volume proportions. Their physical properties are listed in Table 1. When the physical parameters of the liquid of the jet are unchanged, We of the jet varies linearly with Re in the logarithmic coordinate diagram. These three liquids correspond to the three straight oblique lines in Fig. 6. The reason why these three liquids are selected is that the three oblique lines can cross different regions in the Re-We diagram so that the variation of jet structure due to the variation of injection conditions can be observed.

Since glycerol is very hygroscopic, the mixture of glycerol and water was kept in a bottle sealed by a rubber plug and the experiments were carried out in an air-conditioned room.

Figures 7, 8, and 9 show the jet structures of the three liquids under different injection conditions respectively. These pictures are taken from the reconstruction image of the holograms taken in experiments. During the process of reconstruction, some original noise (speckles) is unavoidable. In order to remove the noise in the background region (outside of the liquid jets), these pictures are treated simply with a computer. The holographic pictures observed are much clearer than the photographs given in this paper.

4 Discussion

Figure 1 was obtained with linear instability theory. The Re-We plane in this figure is divided into a series of regions, each of which is occupied by a dominant unstable mode. The regions are separated by the curves with equal growth rates of disturbances between two adjacent regions. This confirms theoretically the existence and domination of asymmetric modes in the breakup process of a liquid jet and gives the conditions for the occurrence of such modes and the tendency of their variations. However, it should be pointed out that the separating curve is not a sharp division line between the two adjacent regions. At points along and near the separating curve, the growth rates of disturbances for the two most unstable modes are about the same.

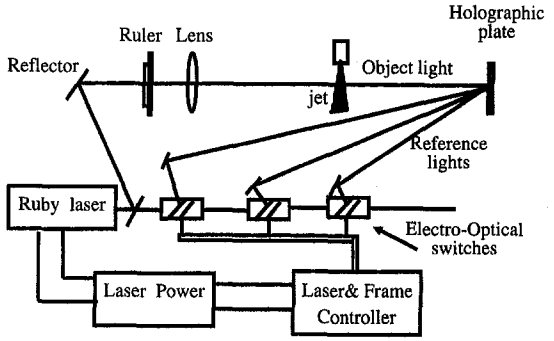

Fig. 5 Sketch of multi-frame high-speed holographic system

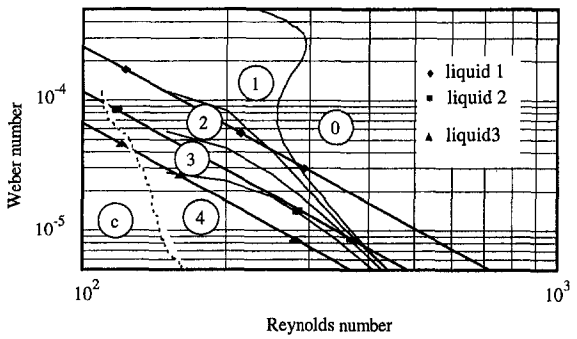

Fig. 6 Relationship between Re & We for 3 different liquids

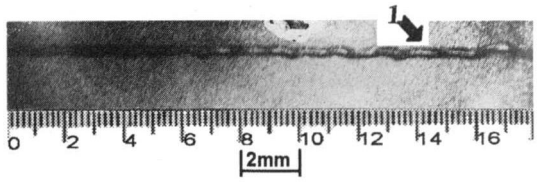

Fig. 7 (*a*) Re = 123, We = 1.7 × 10^{-4}, U = 40m/s

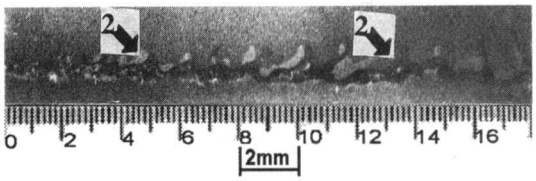

Fig. 7 (*b*) Re =215, We = 5.6 × 10^{-5}, U =70m/s

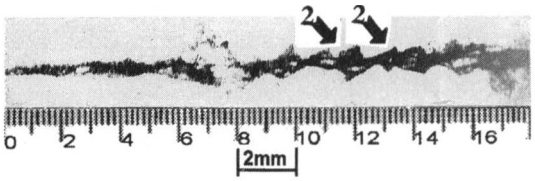

Fig 7. (*c*) Re = 292, We = 3 × 10^{-5}, U = 95m/s

Fig. 7 Jet structures of liquid 1

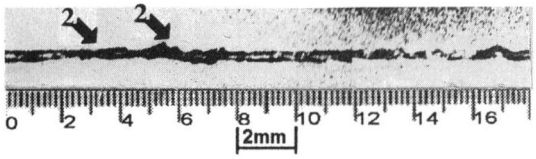

Fig. 8 (*a*) Re = 118, We = 8.4 × 10^{-6}, U = 57m/s

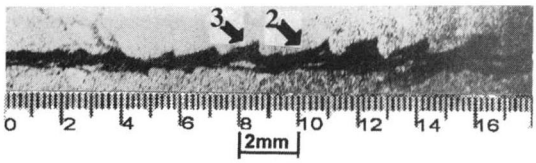

Fig. 8 (*b*) Re = 283, We = 1.4 × 10^{-5}, U = 136m/s

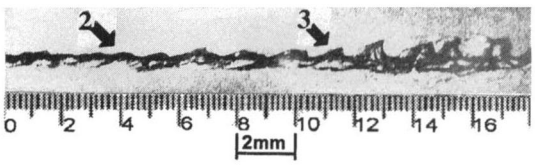

Fig. 8 (*c*) Re = 369, We = 8.6 × 10^{-6}, U = 177m/s

Fig. 8 Jet structures of liquid 2

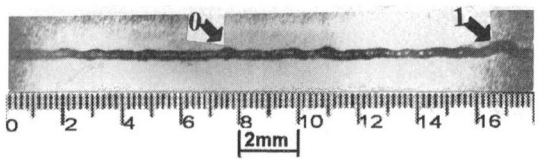

Fig. 9 (*a*) Re = 121, We = 4.6 × 10^{-5}, U = 40m/s

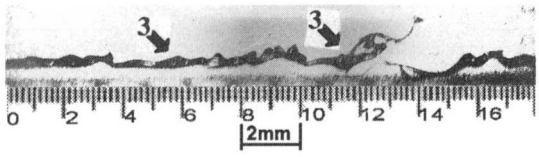

Fig. 9 (*b*) Re = 160, We = 2.6 × 10^{-5}, U = 100m/s

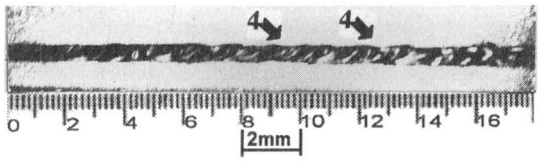

Fig. 9 (*c*) Re = 280, We = 8.5 × 10^{-6}, U = 175m/s

Fig. 9 Jet structures of liquid 3

According to the Re-We diagram given in Fig. 1 as well as the theoretical structures shown in Fig. 2, the experimental results shown in Figs. 7, 8, and 9 can be explained.

First, consider liquid 1. According to Fig. 6, from low-speed to high-speed, the variation tendency of the most unstable modes is from low order mode to high order mode. The jet structures at the experimental points should be characterized by the first order and the second order modes. Although the pictures shown here have lost the stereoscopic effect of hologram, the characteristics of the jet structures can still be identified. For example, the jet structure in Fig. 7(*a*) is distinctly characterized by the first mode and those in Figs. 7(*b*) and (*c*) have distinctive characteristics of the second mode. These results agree fairly well with the theoretical results given in Fig. 6. The location pointed by an arrow head shows distinct features of a specific mode. The number at the arrow denotes the order of the mode.

The criterion for identifying a mode is the shape of the jet cross-section. However, the cross-section of a jet can not be observed directly in experiments since all the photos taken in this paper (such as Figs. 7, 8) show the side views of jets injecting downwards. The only way to discern the structure of a mode is to compare the pattern on the jet surface with the theoretical patterns of various modes given in Fig. 2. Each of these surface patterns has a corresponding cross-section shape. It should be pointed out that these white-black photos of jet surfaces taken from their holographic reconstructed images have lost some information about their structures. Therefore, it's a better way to identify the structures by directly observing their holographic reconstructed images.

Now consider liquid 2, the jet structures at the three experimental points should have the characteristics of the second and the third modes. Figures 8(*a*), (*b*), and (*c*) show the results of experimental observation. In (*a*), because the growth rate of disturbances is very low, the mode characteristics are not well developed. Only at specific location (pointed by the arrow), the second order mode characteristics can be observed. The jet structures in (*b*) and (*c*) are dominated by the third order mode. However, the second mode characteristics can also be found at the same time. The arrow marked number 3 pointing to the location showing the third-order mode characteristics and that marked 2 pointing to those having the second order mode characteristics. No mode other than the second order and the third order modes can be found in the two jet structures.

Figure 9 is the experimental results of liquid 3. The jet structure in (*a*) has distinctively symmetric characteristics. It located at the region 'C'. This is consistent with the theoretical result. The jet structures shown in the figures (*b*) and (*c*) have, respectively, the 3rd order mode and the 4th order mode characteristics.

5 Conclusion

1. The results of both the theoretical study and the experiment work confirm the existence of the unstable asymmetric modes, which under certain conditions may dominate the breakup process of a viscous liquid jet. It is for the first time that the domination of the asymmetric modes is observed in experiments in accordance with theoretical predictions.
2. The maximum growth rates of disturbances for all modes (including symmetric and asymmetric) are almost the same at low Weber numbers.
3. The main geometric features of the theoretical modes agree fairly well with those observed in the experiments.
4. The conditions for the occurrence of asymmetric modes and the tendency of their variations can be theoretically predicted and controlled.

References

Batchelor, G. K., 1970, *An Introduction to Fluid Dynamics,* Cambridge University Press, p. 147.

Bogy, D. B., 1979, "Drop Formation in a Circular Liquid Jet," *Annual Review of Fluid Mechanics,* Vol. 11, p. 207.

Chigier, N., 1991, "Optical Imaging of Sprays," *Progress in Energy Combustion Science,* Vol. 17, p. 211.

Li, H. S., and Kelly, R. E., 1992, "The Instability of a Liquid Jet in a Compressible Airstream," *Physics of Fluids A4,* Vol. 10, p. 2162.

Li, X. G., 1995, "Mechanism of Atomization of a Liquid Jet," *Atomization and Spray,* Vol. 5, p. 89.

Lin, S. P., and Kang, D. J., 1987, "Atomization of a Liquid Jet," *Physics of Fluids,* Vol. 30(7), p. 2000.

Qin, J. R., 1995, "Asymmetric Instability of a Liquid Jet," Master thesis, Tianjin University.

Reitz, R. D., and Bracco, F. V., 1982, "Mechanism of Atomization of a Liquid Jet," *Physics of Fluids,* Vol. 25(10), p. 1730.

Schetz, J. A., Kush Jr., E. A., and Joshi, P. B., 1980, "Wave Phenomena in Liquid Jet Breakup in a Supersonic Crossflow," *AIAA Journal,* Vol. 18(7), p. 774.

Stockman, M. G., and Bejan, A., 1982, "The Nonaxisymmetric (Buckling) Flow Regime of Fast Capillary Jets," *Physics of Fluids,* Vol. 25(a), p. 1506.

Xi, D. G., et al., 1996, "Time-Based Multi-Frame Holography and its Application," *Journal of Combustion Science and Technology,* Vol. 4, p. 400.

Yang, H. Q., 1992, "Asymmetric Instability of a Liquid Jet," *Physics of Fluids,* Vol. A4(4), p. 681.

Near Surface Characterization of an Impinging Elliptic Jet Array

Simona C. Arjocu[1]
Post-Doctoral Research Fellow.

James A. Liburdy[2]

Department of Mechanical Engineering,
Clemson University,
Clemson, SC 29634
e-mail: liburdy@engr.orst.edu

In this study naturally occurring large-scale structures and some turbulence characteristics within an impinging jet array are investigated. The dynamics of a three-by-three elliptic jet array are analyzed relative to the flow structures within the array. With applications to electronic component cooling, low Reynolds number conditions, Re = 300 to 1500, are presented. Two jet aspect ratios are used, 2 and 3, with identical jet hydraulic diameters and jet-to-jet space. The effects of impinging distance are studied in the range of one to six jet hydraulic diameters. Flow visualization and PIV are used for the identification of structures and quantitative analysis. These results are used to evaluate the integrated surface layer vorticity, Γ^*, which is shown to depend on the jet aspect ratio and impingement distance. Also, a transport coefficient is presented, based on a turbulence velocity and length scales. This coefficient is shown to experience a maximum value versus impingement distance that coincides with the location of axis switching.

Introduction

Impinging jets have been widely studied since they have a wide range of applications, in part due to high rates of heat and mass transport associated with relatively low required work, or driving pressure. It is not fully clear what mechanisms of the jet flow development are responsible for the transport properties, and to what degree. It has been shown by several researchers that large scale structures develop within the jet shear layer. These may be important in enhancing the heat transfer between the jet and an impingement surface. Experimentally, Yule (1978) has shown that a free axisymmetric jet is characterized by two types of structures: (i) a vortex ring which develops in the transition region, and is characterized by continuous, concentrated and coherent vorticity distribution and (ii) large eddies with inherent three dimensionality with embedded small scale turbulence content. The larger scale eddies have a wide range of length scales and spatial trajectories and are not axisymmetric. Based on the results of Melander and Hussain (1993), a coherent structure embedded in a turbulent, isotropic and homogeneous background generates a local shear layer that could sustain turbulent fluctuations by shear production. Incoherent vortical structures swirl azimuthally around the coherent structure. When a jet impinges on a flat surface, a feedback loop may be formed, as shown by Ho and Nosseir (1981). In this process the downstream convected coherent structures are influenced by the upstream propagating pressure waves generated by impingement of the coherent structures on the surface. These events may phase lock at the nozzle lip at resonant frequencies determined by the impingement distance.

The numerical simulation of a vortex ring impinging on a flat surface, by Orlandi and Verzico (1993), showed that, for Reynolds numbers between 564 and 3000, a thin layer of vorticity is generated at the plate by the induction of a primary ring. This layer rolls up and forms a second ring that merges with the initial ring. Additional vortex rings occur when the azimuthal vorticity becomes important, at Reynolds number near 1000. Experimentally, using flow visualization and Particle Image Velocimetry, Landreth and Adrian (1990) noticed the presence of primary vortices in the jet shear layer. These vortices were found to spread radial near the impingement surface. Secondary vortices formed in the wall boundary layer that interacted with the primary vortices.

In co-flowing jets or jet arrays, jet interaction changes the generation and both spatial and temporal evolution of the large scale structures. Villermaux and Hopfinger (1994) noticed that for a large number of planar coflowing interacting jets, there is a merging length where the jet diameter reaches the size of jet spacing. At this point the mean velocity appears essentially uniform. Before merging, recirculation cavities are formed between the jets, which maintain a permanent back flow to the jet nozzle. The potential core length of a jet within an array is smaller than that of a single jet, and decreases with increased nozzle spacing, as determined by Moustafa and Rathakrishnan (1993). In addition, entrainment and mixing are greater for a jet array compared to a single jet.

Single elliptical shaped orifice jets have been shown to exhibit unique characteristics. Hussain and Husain (1989) experimentally compared the flow structures developed with various initial conditions, for excited and unexcited jets. The elliptical shape results in different radii of curvature in the major and minor planes which imply different advection velocities in these planes. The elliptic flow structure generated by the shear layer switches axis before breakdown, or rolls up at the end of the potential core. The nonuniform exit momentum thickness in the case of contoured jets strongly influences the shear layer instability and determines different locations of the axis switching. In the case of sharp edged elliptic jets, due to the vena contracta phenomenon, axis switching takes place closer to the jet exit plane. The switching location increases linearly with aspect ratio. Husain and Hussain (1991) showed that pairing of two elliptical structures is caused by self and mutual induction of the neighboring structures, which results in significant contributions to flow entrainment and transport phenomena. Ho and Gutmark (1987) state that the mass entrainment of an elliptic contoured jet is three to eight times higher than that of a planar or circular jet.

For a jet array with a Reynolds number less than 1500, with a confining jet plate, Arjocu and Liburdy (1997a and 1997b) classified the flow field structures into categories based on their formation and the region where they reside: (i) large scale structures developed by impingement, and (ii) shear layer structures induced by both the shear layer instability and the return flow. The structures size and location change with Reynolds number and impinge-

[1] Presently: Dept. of Surgery, MUSC, Charleston, SC 29403.
[2] Presently: James R. Welty Professor of Mechanical Engineering, Oregon State University, Corvallis, OR 97331.

Contributed by the Fluids Engineering Division for publication in the JOURNAL OF FLUIDS ENGINEERING. Manuscript received by the Fluids Engineering Division August 4, 1998; revised manuscript received February 23, 1999. Associate Technical Editor: D. R. Williams.

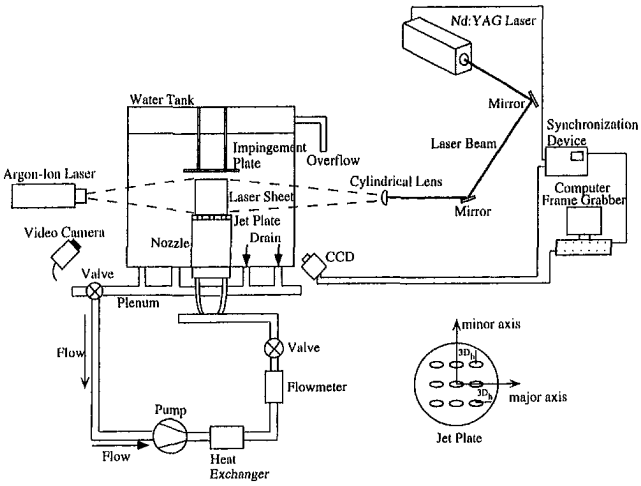

Fig. 1 Experimental flow facility

ment distance and, in some cases, are periodic. Axis switching, similar to that observed with a single elliptic jet, was shown to occur for all jets within the array when the ratio of the impingement distance to the jet diameter, H, was in the range of three to four. At impingement distances greater than that necessary for axis switching, several events were observed. Jet column instability was found to be Reynolds number dependent, with relative low velocity fluid, or small scale turbulent structures penetrating the jet column. Jet swaying was also observed with greater amplitude and frequency with increasing impingement distance and Reynolds number. The occurrence of small scale shear layer structures which penetrate into the impingement region increases with impingement distance and Reynolds number.

The aforementioned studies emphasize the complex flow structure dynamics associated with single elliptic jets and jet arrays. In the present study a confined submerged elliptic jet array impinging on a flat surface is investigated relative to the flow development and the influence of hydrodynamics conditions on the dynamics of the flow structures. Attention is focused on the central jet in the array, which is considered a typical internal jet. A primary goal is to determine how the elliptic jet flow characteristics are influenced by the interaction and dynamics within the array. Also of interest is the identification of a quantitative measure that relates to the overall transport properties of the flow. The flow characteristics were studied using flow visualization, Particle Image Velocimetry (PIV) and hot film anemometry.

Experimental Conditions and Methods

In this study experimental evidence of the large scale structures and some measures of turbulence within a three-by-three submerged impinging elliptic jet array are presented. The jet orifice aspect ratios for this study are, $r = 2$ and 3, (ratio of the semi-major and semi-minor axes) with an orifice thickness of approximately 3.2 mm. This implies a thin uniform exit momentum thickness. Therefore, the hydraulic diameter, $D_h = 9$ mm, was used as the length scale. The jet center-to-center spacing, normalized by the jet hydraulic diameter, was equal to three for both aspect ratios. The dimensionless impingement distance, $H = h/D_h$, was varied between 1 and 5. The jets were unforced, with jet Reynolds numbers between 300 and 1500.

A schematic representation of the experimental set-up along with details of the jet plate are presented in Fig. 1. The facility contained a constant head water tank with the jet array and the impingement surface submerged. The flow was pump driven in a closed loop, through a calibrated rotameter and a nozzle assembly, where a series of screens assured uniform pressure at the jet exit, and removed flow disturbances. The fluid temperature was controlled using a water-water heat exchanger to maintain the temperature within ±0.5°C of the hot film calibration temperature. The impingement surface could be raised or lowered to achieve the desired impingement distances.

The flow visualization used a 1 mm thin argon-ion laser sheet to illuminate the region of interest. The laser sheet was positioned in three different planes. Two planes were aligned with the major and minor jet axis. The third was parallel with the jet plate, 1 mm from the impingement surface. The flow was seeded with glass microparticles, 60 μm in diameter, which were essentially neutrally buoyant. Images were recorded using a 30 frames per second video camera positioned normal to the laser sheet plane. The recorded images were interrogated frame by frame, tracking individual particles.

Time series data were obtained at selected locations within the flow field using a hot film anemometer system. These locations are shown in Fig. 2: (1) the centerline of the jet exit plane, (2) the stagnation point, (3) $0.5D_h$ from the jet exit plane in the shear layer, and (4) 2 mm away from the impingement surface at the return flow separation point. Details of the probe and its calibration are provided by Arjocu and Liburdy (1997a).

For the PIV measurements the flow was seeded with fluorescent micro-beads, with an average diameter of 27 μm. The flow was illuminated by a series of Nd:YAG 6 nanoseconds laser light pulses, with an adjustable time delay between 2 and 6 ms, based on the flow conditions. The images were processed, for velocity data, within a 32 × 32 pixel sub-region, with a CCD camera synchronized with the laser. Seed density was adjusted to yield approximately 4–8 particle pairs per sub-region. The field of view spanned the centerlines of adjacent jets and a distance of one jet hydraulic diameter from the impingement surface. The resolution was approximately 45 μm/pixel. For each test condition a series of five instantaneous data sets were collected and analyzed. For this study it was not intended to determine statistical averages from the PIV data, but rather to obtain instantaneous measures of the vorticity field near the impingement surface.

The estimated uncertainty (95% confidence level) of the velocity data is less than 4% for the hot film results. The PIV velocity data have a wide range of uncertainties depending on the magnitude of the velocity. Near the maximum velocity, the uncertainty is approximately 1.5%. But this increases to near 50% at the very low velocities within the return flow regions, but this region is not of interest here and does not contribute to the vorticity magnitude to any significant extent.

Results

The presentation of results includes interpretation of the flow visualization, vorticity field data based on the PIV velocity data, and statistical measures from time series data using hot film anemometry at selected points. These data are used to interpret the effect of impingement distance on the flow structures, and how this affects the transport characteristics of the impingement process.

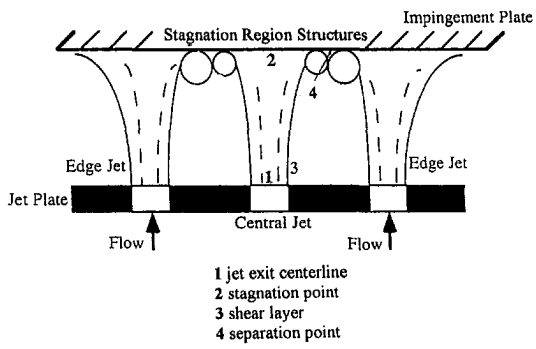

Fig. 2 Location of hot film data collection

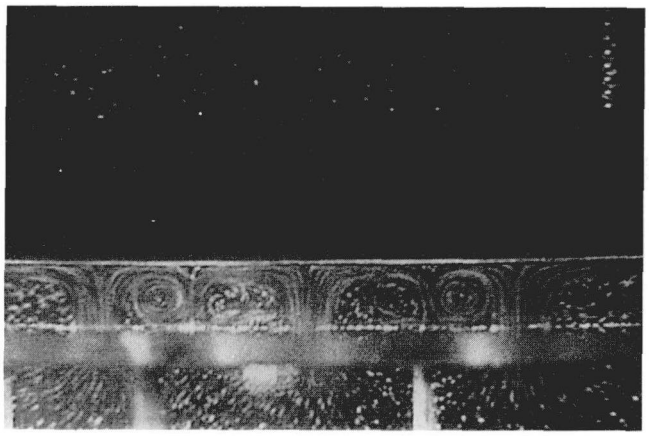

Fig. 3(*a*)

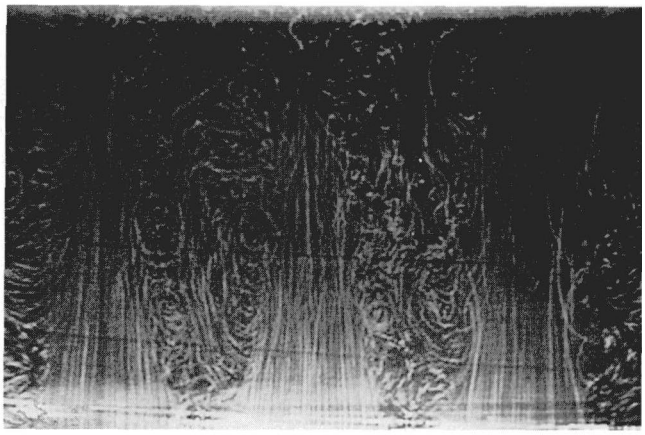

Fig. 3(*d*)

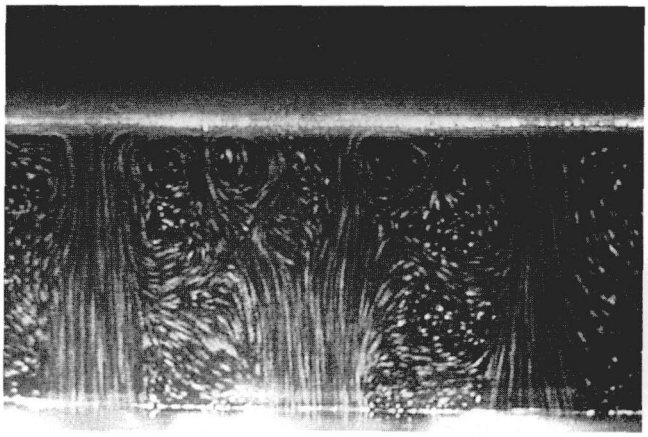

Fig. 3(*b*)

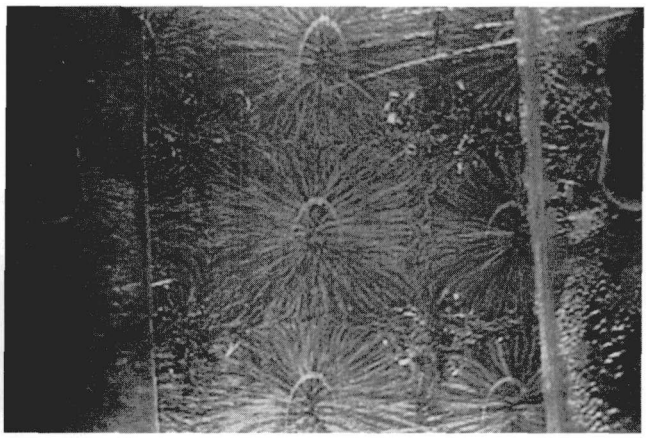

Fig. 3(*e*)

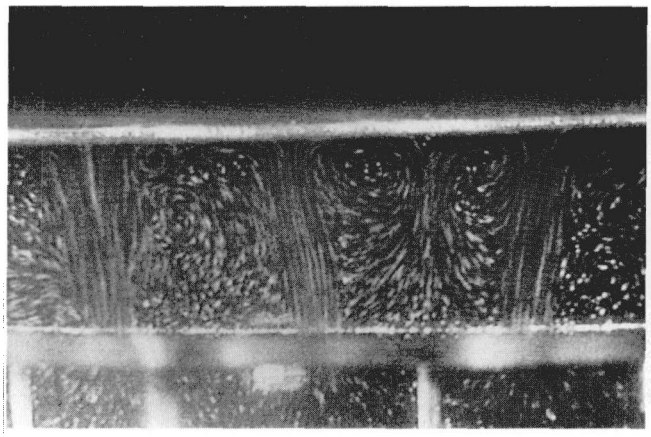

Fig. 3(*c*)

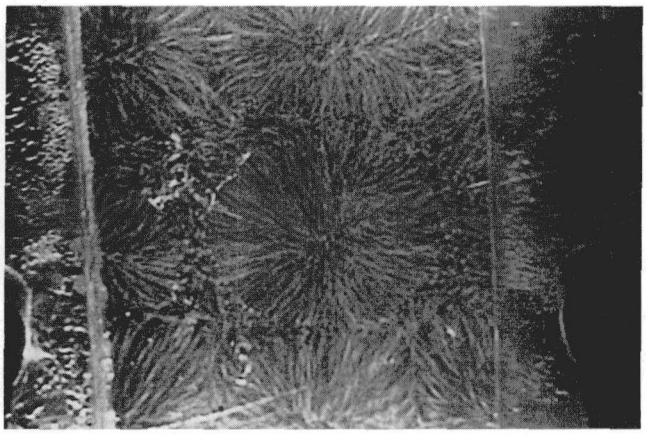

Fig. 3(*f*)

Fig. 3 Flow visualization, photographs taken from video recordings used to identify large scale flow characteristics. (*a*) $H = 1$, major axis, Re = 300, $r = 2$, (*b*) $H = 4$, major axis, Re = 300, $r = 2$, (*c*) $H = 3$, minor axis, Re = 300, $r = 3$, (*d*) $H = 5$, major axis, Re = 1500, $r = 3$, (*e*) $H = 1$, Re = 300, $r = 2$, (*f*) $H = 3$, Re = 300, $r = 2$.

Flow Structure Description. Basic flow structures were identified in both the major and minor planes based on how they formed and the region in which they evolved. The structures formed around the central jet in the impingement region, are identified as "central structures." The analogous adjacent structures formed by the edge jets are called "outer structures." The central and outer structures interact to varying degrees based on their size, Reynolds number and impingement distance. Additional structures occurred in the shear layer of the jet development region and also in the return flow towards the jet exit plane. These were most apparent at larger impingement distances and are referred to as "shear layer structures" and "return flow structures," respectively. Significant interaction was observed between the shear layer and return flow, but these are limited to the single jet spacing used in this study. It should be noted that in the minor plane there was a slight tilting or inclination of the outer structures towards the outside of the array. Because of this it might be presumed that the center jet of a much larger array may have slightly different characteristics than that observed in the three-by-three array.

Figure 3 presents a series of photographs of the flow visualiza-

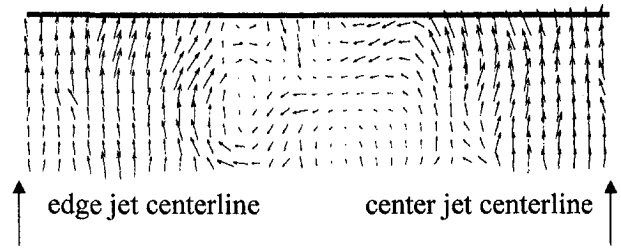

Fig. 4(*a*)

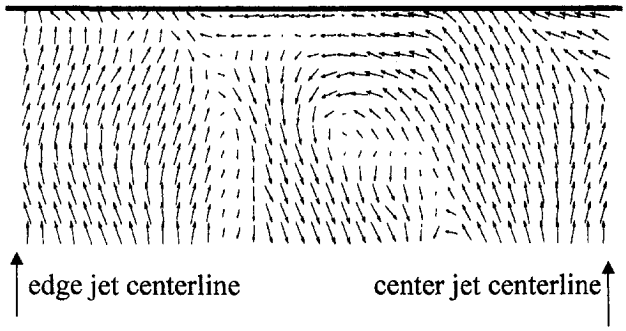

Fig. 4(*b*)

Fig. 4 PIV velocity vector data sets. (*a*) $H = 1$, major axis, Re = 1500, $r = 2$, (*b*) $H = 4$, major plane, Re = 300, $r = 2$. Uncertainty estimates for (*a*) is +/−1.5% and for (*b*) is +/−4%.

tion for two Reynolds numbers. At low impingement distances, Fig. 3(*a*), the outer structures are stable and fill the channel formed by the jet plate and impingement surface, with a characteristic size of $1D_h$. Only for the higher Reynolds number case, at $H = 1$, is a weak central structure be seen, with characteristic size of $0.5D_h$. Rather than being attached to the impingement surface, its center of rotation is closer to the jet exit plane. A typical PIV result, for low Reynolds number and $H = 1$, shown in Fig. 4(*a*), indicates well defined outer structures, which are observable in both the major and minor planes. However, in the minor plane, there is a noticeable reduction of the velocity of the returned flow. This is because of the larger effective distance between the edges of adjacent jets in the minor plane. This difference in return flow characteristics weakens the interaction with the shear layer.

At higher impingement distances, Fig. 3(*b*) shows obvious convergence of the jet streamlines in the major plane, and spreading in the minor plane. This is consistent with a single elliptic jet as it goes through axis switching. The central structure has a characteristic size of approximately $0.5D_h$ to $0.8D_h$, with larger sizes occurring in the minor plane where there is less flow confinement. These structures display a variation of strength with time, while being localized near the impingement surface. Evidence of this variation is contained in the PIV data, with one instantaneous field in Fig. 4(*b*) showing that there are not continuous, well defined central structures.

The size dependence of the central structures on Reynolds number and impingement distance is similar for the two jet aspect ratios and is the same for both major and minor planes. For H beyond three there is strong evidence of jet swaying, Fig. 3(*c*). It should be noted that swaying is not as strong in the major plane. This is most likely a result of the return flow being stronger in this plane and the jet is more stable to variations in the lateral forces generated by the return flow.

Flow visualization for $H = 5$, Fig. 3(*d*), illustrates the interaction between the return flow and the shear layer and the corresponding development of shear layer structures. At this impingement distance there is jet swaying as well as periodic entrainment of large volumes of surrounding fluid. These shear layer structures, in contrast to those in the surface layer, have a finite life and are readily convected in the flow. The downstream convection feeds these smaller structures into the more stationary central and outer structures. However, some of the structures do not reach the impingement region and are washed away by the returning flow, or appear to dissipate. The shear layer structures increase in total number with impingement distance.

The plane parallel with the impingement surface was viewed from below to detect axis switching for a range of impingement distances. Axis switching occurs over a finite distance and examples of the changing flow pattern are shown in Figs. 3(*e*) and 3(*f*). The outer jets experienced axis switching at, or near, $H = 3$, and the center jet close to $H = 4$. This difference may be a result of the center jet being more confined to lateral flow, necessary for axis switching in a single jet.

Surface Layer Vorticity. The PIV velocity fields were used to calculate the vorticity distribution using a filtered central difference method. The main interest is the larger scale vortical structures. Since velocity vector spacing was approximately 0.72 mm ($0.08D_h$) very small velocity derivatives were not resolved. The sign of vorticity is not of concern so the spatial distribution of the square of the vorticity is presented. Based on viscous stagnation flow theory, the near surface boundary layer thickness at the impingement surface decreases with increasing Reynolds number, and for these flow conditions ranges from $0.15D_h$, at Re = 300, to $0.067D_h$, at Re = 1500. The vorticity distribution along the surface, evaluated at this viscous boundary layer edge, has an order of magnitude increase from Re = 300 to Re = 1500. Details of the vorticity distribution can be found in Arjocu and Liburdy (1997b).

The squared vorticity was integrated across the impingement surface in the major and minor planes for two different layer thicknesses, $0.23D_h$ and $0.5D_h$. This integral value, Γ^*, is used to quantify the surface layer vorticity magnitude. Γ^* was scaled using the characteristic length of D_h, a velocity scale based on the jet exit velocity, U_e, and the integration area A, which was equal to the surface layer thickness times the length of the region from the center jet centerline to the edge jet centerline (the jet spacing). The nondimensional parameter representing the integrated surface vorticity becomes $\Gamma^* D_h^2 / A U_e^2$. Consequently, the vorticity scaling is based on large scale velocity gradients on the order of D_h.

Results of the integrated vorticity versus H are presented in Fig. 5. Significant differences occur between the lower and higher aspect ratio jets. For aspect ratio of 3 there is only a slight variation with impingement distance but the magnitudes are as much as four to eight times lower when compared to jets with an aspect ratio of two. These results suggest that the higher aspect ratio elliptical jet does not generate as strong vorticity in either plane of the jet. This may be because the higher aspect ratio jet behaves more like a slot jet and the elliptical nature of the large scale structures are weak or broken apart more easily by the return flow. Also, it is known that axis switching for single higher aspect ratio jets occur further downstream. It is not conclusive from these data if that is true for the jet array. At the higher Reynolds number the results are fairly constant between $H = 2$ and $H = 4$, with a large decrease for $H = 5$. At the lower Reynolds number there is a well defined peak at $H = 3$. Based on this it is suggested that increased vorticity is generated within the flow as axis switching occurs. At the higher Reynolds number the switching is further complicated by additional turbulence generation which also contributes to the measured vorticity.

Comparison of the results in Figs. 5(*a*) and 5(*b*) indicates that the proper scaling is not used for Γ^*, since there is a difference of approximately a factor of three between the two Reynolds number cases. Since the vorticity generally increases with Reynolds number, especially at the smaller scales, the vorticity scaling, U_e/D_h, does not adequately account for the variation in the vorticity spectrum. An alternative scaling of the vorticity, to help account for the changing turbulence spectrum, is the root mean square velocity, u_{rms}. However, this raises the question of where, within the flow, u_{rms} should be evaluated. Since the shear layer convects large scale structures into the impingement region, the stagnation

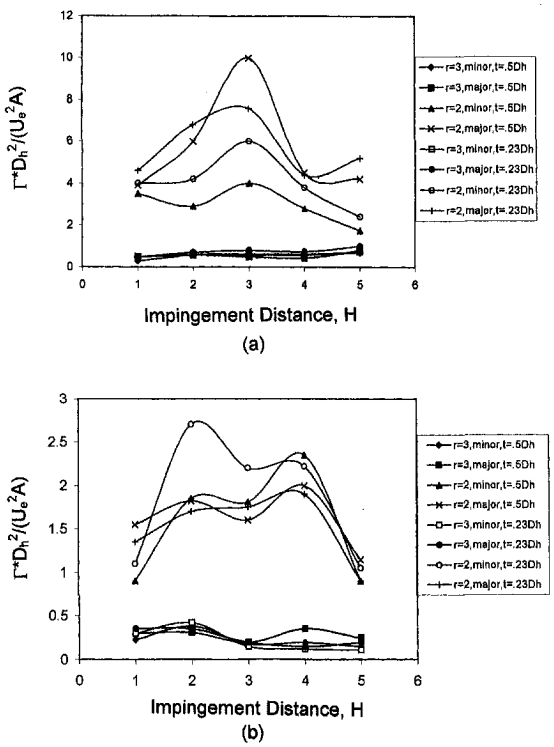

Fig. 5 Integrated vorticity, Γ*, versus *H* in both the major and minor planes. (*a*) Re = 300, (*b*) Re = 1500. Uncertainty estimates for (*a*) is +/−8% and for (*b*) is +/−4%.

point rms value is a candidate for a representative scaling. This results in a nondimensional surface layer vorticity expressed as $\Gamma^* D_h^2/Au_{\text{rms}}^2$. For a given Reynolds number, this parameter is relatively constant from $H = 3$ to $H = 5$. However, comparing the higher and lower Reynolds number, $\Gamma^* D_h^2/Au_{\text{rms}}^2$ is three times larger for the higher Reynolds number. At lower H values the turbulence does not develop before impingement and the rms values are very low, see Fig. 8. Therefore, at low H the surface vorticity needs an alternative scaling. Further work needs to be done using a larger data set of vorticity measurements over a wider range of Reynolds numbers to determine if the surface layer vorticity can be properly scaled with the flow conditions. Despite the lack of a proper generalized scaling, the current results indicate that the integrated surface vorticity is enhanced when the impingement distance, H, is approximately three to four for an array of elliptic jets with an aspect ratio of two.

The PIV velocity data were further analyzed to determine a measure of the length scales, and in particular to identify the large scale structures near the surface. The instantaneous power spectrum density (PSD) of the square velocity spatial distribution was used to identify these length scales. Peaks in the spectrum are associated with the amplitude, or energy, and the associated spatial frequency of dominant flow structures. The spatial frequency associated with an individual peak represents the inverse of a measure of the length scale. Length scales in the directions parallel with the impingement plate and perpendicular to the surface within each major and minor plane were evaluated. It was found that the scales in each direction are essentially the same. Figure 6 shows an example of a PSD evaluated in the major plane for $H = 2$ and Re = 300. All spectra had this same general trend of distinct peaks but with variation of the frequencies at which the peaks occurred. The highest amplitude peak for each case is associated with a length scale on the order of the jet hydraulic diameter, regardless of Reynolds number, aspect ratio or impingement distance. This peak is at a spatial frequency of 0.11 mm^{-1}, and has been filtered from the signal. The secondary peaks, at higher frequencies, have associated length scales varying in a relative narrow band, from

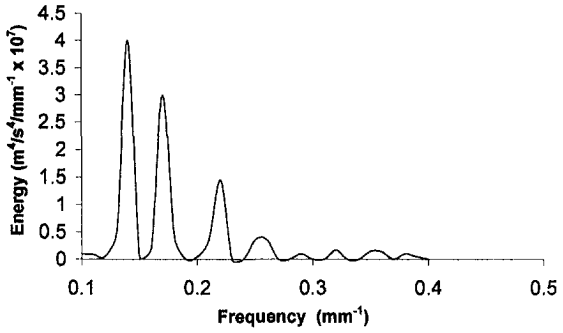

Fig. 6 Power spectral density of the squared velocity calculated from the PIV data, aspect ratio of 2, major plane, *H* = 2, Re = 300

7.2 mm to 4.8 mm, which represent sizes of $0.8D_h$ to $0.5D_h$, respectively. Increasing the impingement distance causes the energy to be distributed over a larger number of discrete length scales, such that higher spatial frequencies (smaller length scales) occur. These results are consistent with estimates of flow structure sizes made from the flow visualization.

The relatively strength of secondary structures within the flow was evaluated by using the ratio of the energy of the primary peak to the secondary peak. The energy ratio of the first two peaks in the spectrum, averaged over the major and minor planes and the two jet aspect ratios, is presented in Fig. 7. There is an increase of concentrated energy at the larger scale as the impingement distance increases. A maximum energy of the large scales is encountered where the center jet experiences axis switching. At this location the peak energy is twice as large as the next largest scale. At still larger impingement distances the energy is distributed over a larger number of length scales. Therefore, the largest scales loose their energy, but only at impingement distances greater than that required for axis switching. The large scale structures apparently maintain their energy content, and even concentrate their energy levels, as the flow develops during the first axis switching process. Beyond this distance the larger structures tend to break down and a broader spectrum of scales exist with less concentrated energy.

Turbulence Scales. The hot film data were used to develop a better understanding of the total transport process associated with the impingement process. Turbulence data were taken in the form

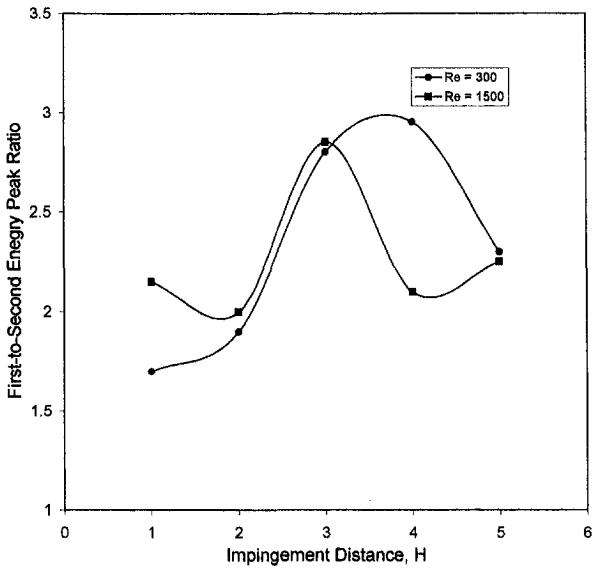

Fig. 7 Ratio of the first to second peak of the power spectral density, aspect ratio = 2. Uncertainty estimate is +/−10%.

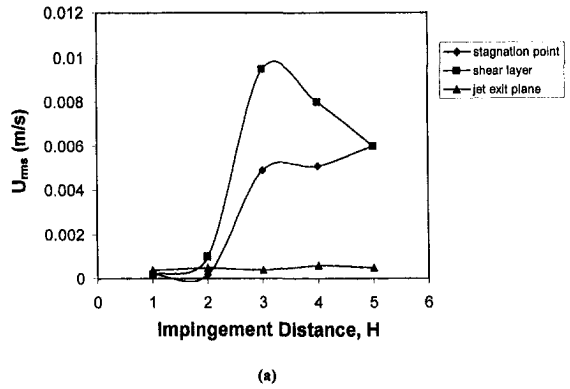

(a)

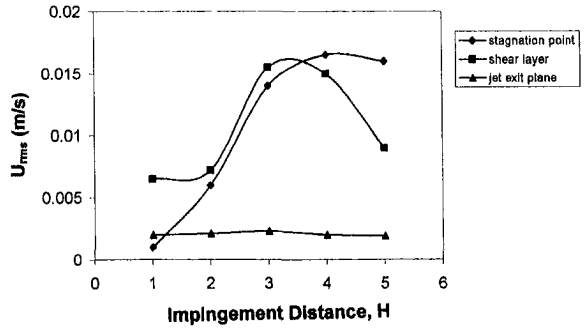

(b)

Fig. 8 Root mean square velocity from hot film data, aspect ratio = 2, at the exit plane, shear layer and stagnation points shown in Fig. 2. (*a*) Re = 300, (*b*) Re = 1500. Uncertainty estimate is +/−4%.

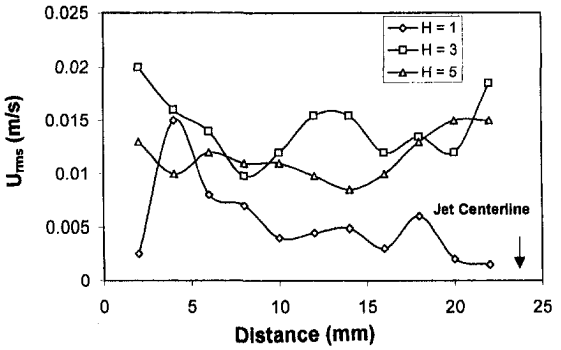

Fig. 9 (*a*)

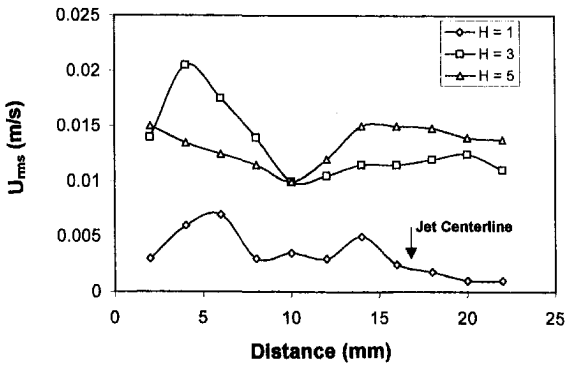

Fig. 9 (*b*)

Fig. 9 Root mean square velocity from hot film data 2 mm from the impingement surface, Re = 1500, distance is measure from the edge of the outside jet which is closest to the center jet, $r = 2$. (*a*) Minor plane, (*b*) major plane. Uncertainty estimate is +/−4%.

of time series data and used to determine rms velocity and integral time scales at the locations indicated in Fig. 2. Note that the location within the shear layer is in the minor axis. The rms values versus H for the two Reynolds numbers are indicated in Fig. 8. When the impingement distance is equal to, or greater than three, the stagnation region and shear layer rms level increase significantly. Based on the flow visualization, this increase of rms with H in the stagnation region coincides with jet instability, swaying motion and increased dynamic characteristics of the central structure. As the stagnation point rms level increases with H so does the rms level in the shear layer. There is a decrease of rms in the shear layer beyond $H = 4$, which does not occur at the stagnation point. This decrease may be influenced by changes in the nature of the return flow towards the shear layer. When H increases to three there is a large increase in turbulence levels in the stagnation region. As this flow recirculates back towards the jet exit plane it may act to increase the rms levels in the shear layer. Beyond $H = 4$, however, the return flow is weakened and there is greater time for turbulence decay in the return flow and the feedback of turbulence to the shear layer is reduced.

The near surface variation of the rms level was measured in the region between adjacent jets a distance of 2 mm from the impingement surface. The probe was traversed from the edge jet towards the center jet beginning at the edge of the projection of the inside part of the jet orifice in both the major and minor planes. Results are shown in Fig. 9 for an aspect ratio of two. The trends are similar in both planes. For the high Reynolds number case, there is essentially no decay of turbulence along the surface as the flow spreads towards the separation region. Increasing H results in increased turbulence levels in both planes. For $H = 1$ the turbulence level is seen to grow towards the separation region. This is mostly likely because the turbulence does not develop significantly in the jet prior to impingement and is still undergoing development along the impingement surface.

The integral time scales associated with the selected locations within the flow are shown in Fig. 10. For the lower Reynolds number there is no significant variation with H. The higher Reynolds number case has its largest time scale between $H = 3$ and 4. The stagnation point experiences its peak at a lower H than the shear layer. Since the rms level also increases with H, the larger

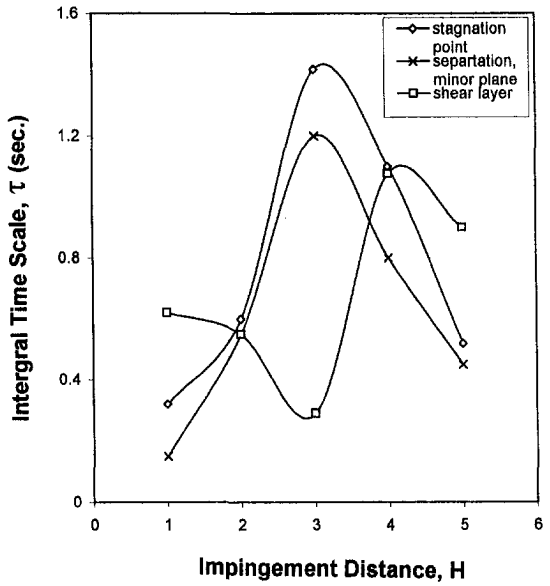

Fig. 10 Integral time scale versus *H* at selected locations shown in Fig. 2, $r = 2$. Uncertainty estimate is from +/−1% for the higher values to +/−5% for the lower values.

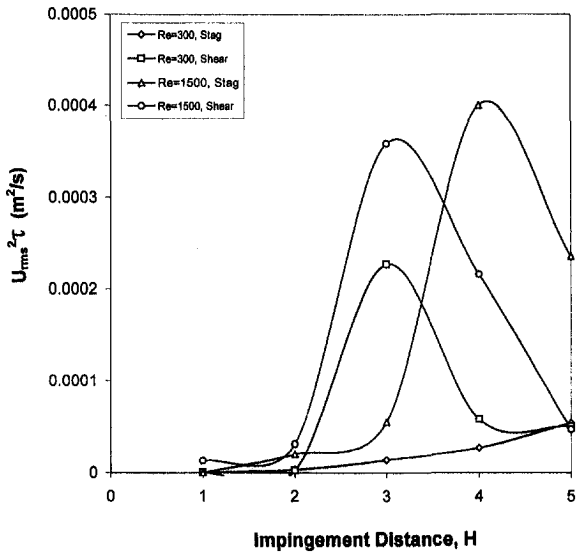

Fig. 11 Transport parameter, ($u_{rms}^2\tau$), versus H at the stagnation point and shear layer, Re = 1500

scale structures may become more organized in the sense that they increase their relative amplitude and increase the integral time scale. The integral time scales then decrease by $H = 5$ which is consistent with the notion that smaller scales are generated within the flow and that a broader spectrum of scales exist. The existence of larger scales for $H = 3$ at the separation point in the minor plane indicates that the spreading flow carries the large scale structures into this region. The shear layer has a peak at $H = 4$ which may be a result of feedback from the return flow. This feedback concept is reinforced by the fact that the return flow weakens at greater impingement distances and the shear layer also experiences a similar reduction.

To determine a measure of the transport capabilities of the jet array, a transport parameter is defined as follows. Assuming a transport property consistent with a gradient transport assumption used in turbulence modeling, a transport coefficient can be constructed using an appropriate velocity and length scale. In this simple approach the rms level, u_{rms}, is used as the velocity scale and the length scale is based on the product of the integral time scale, τ, and the velocity scale. This results in a transport coefficient proportional to ($u_{rms}^2\tau$). This is plotted versus H in Fig. 11, at the stagnation region and the shear layer. Assuming any other multiplicative parameters required in the definition of the transport coefficient are not functions of location, it is possible to use the trends of ($u_{rms}^2\tau$) to relate the transport coefficient to H. The results indicate an increasing transport coefficient with H in both the stagnation region and the jet shear layer. In the shear layer the feedback process from the impingement flow seems to enhance the transport coefficient near $H = 3$. The decrease beyond this point is attributed to the previous argument for the peak of the time scales at $H = 3$. The stagnation region also experiences a peak value, but this is closer to $H = 4$. It is interesting to note that the shear layer for the lower Reynolds number also experiences this peak but the stagnation region does not. This would indicate that the shear layer is not influenced by the stagnation region turbulence level. Rather, the shear layer experiences an increased shear level caused by the return flow, which tends to increase the local the rms level. However, it does not occur for low H, where very low levels of turbulence were measured in the shear layer largely because the return flow is contained in a fairly stationary large scale flow structure that nearly fills the region.

Conclusions

The flow visualization of the elliptic jet array illustrates the presence of two primary flow structure categories within the central jet region of a three-by-three elliptic jet array: (i) central and outer structures near the impingement surface that are generated by the stagnation flow and jet-jet interaction and (ii) shear layer generated flow structures that are convected towards the surface. Both of these types of structures influence the turbulence with evidence of interaction between structures. The return flow interacts with the shear layer and this interaction is most significant near $H = 3$, which is also the downstream distance where axis switching occurs. By estimating the instantaneous surface layer vorticity distribution, an integral parameter, Γ^*, is shown to depend on the jet aspect ratio and reaches a peak near $H = 3$. Interestingly, the lower aspect ratio jets yields the higher values of Γ^*. This may be a consequence of the break down of the large scale flow structures for the high aspect ratio jet. Turbulence data indicate a feedback process between the stagnation region and the jet shear layer, which acts through the return flow. This process seems to be maximized when the impingement surface is at the distance close to where axis switching occurs. A transport parameter, based on the rms velocity and integral time scale, is shown to reach a maximum near the region of axis switching. This parameter also experiences a peak in the shear layer, again at an impingement distance consistent with axis switching. There is evidence that the large scale events associated with axis switching may contribute to an overall increase in surface transport properties within an impinging elliptic jet array.

References

Arjocu, S. C., and Liburdy, J. A., 1997a, "Flow Structures in an Impinging Elliptic Jet Array," *Proceedings of ASME-Fluids Div. Annual Summer Meeting,* Vancouver, BC, Canada.

Arjocu, S. C., and Liburdy, J. A., 1997b, "Analysis of Flow Structures Occurring in Impingement of Elliptic Jet Arrays," *Proceedings of 20th. AIAA Fluid Dynamics Conference,* Snowmass, CO.

Ho, C. M., and Gutmark, E., 1987, "Vortex Induction and Mass Entrainment in a Small Aspect Ratio Elliptic Jet," *Journal of Fluid Mechanics,* Vol. 179, pp. 383–405.

Ho, C. M., and Nosseir, N. S., 1981, "Dynamics of an Impinging Jet. Part 1. The Feedback Phenomenon," *Journal of Fluid Mechanics,* Vol. 105, pp. 119–142.

Husain, H., and Hussain, F., 1991, "Elliptic Jets. Part 2. Dynamics of Coherent Structures: Pairing," *Journal of Fluid Mechanics,* Vol. 23, pp. 439–482.

Hussain, F., and Husain, H., 1989, "Elliptic Jets. Part 1. Characteristics of Unexcited and Excited Jets," *Journal of Fluid Mechanics,* Vol. 208, pp. 257–320.

Landreth, C. C., and Adrian, R. J., 1990, "Impingement of a Low Reynolds Number Turbulent Circular Jet Onto a Flat Plate at Normal Incidence," *Experiments in Fluids,* Vol. 9, pp. 74–84.

Melander, M. V., and Hussain, F., 1993, "Coupling Between a Coherent Structure and Fine Scale Turbulence," *Physical Review E,* Vol. 48, No. 4, pp. 2669–2689.

Moustafa, G. H., and Rathakrishnan, E., 1993, "Studies on the Flow Field of Multijet with Square Configuration," *AIAA Journal,* Vol. 31, No. 7, pp. 1189–1190.

Orlandi, P., and Verzico, R., 1993, "Vortex Rings Impinging on Walls: Axisymmetric and Three Dimensional Simulations," *Journal of Fluid Mechanics,* Vol. 256, pp. 615–646.

Villermaux, E., and Hopfinger, E. J., 1994, "Periodically Arranged Co-Flowing Jets," *Journal of Fluid Mechanics,* Vol. 263, pp. 63–92.

Yule, A. J., 1978, "Large-Scale Structure in the Mixing Layer of a Round Jet," *Journal of Fluid Mechanics,* Vol. 89, No. 3, pp. 413–432.

B. J. Sun
Associate Professor.
e-mail: sunbj@sunctr.hdpu.edu.cn

D. C. Yan
Professor.

Department of Mechanics,
Peking University,
Beijing, Peoples Republic of China 100871

Energy Concentrated and Self-Resonating Mini-Extended Jet Nozzle Used for Jet Drilling

Theoretical, experimental, and field test studies of the self-resonating pulsating jet have been carried out. The interaction mechanism of vortices and outlet wall is described. On the basis of theoretical calculations and experimental data, a new mini-extended and energy concentrated self-resonating pulsating jet nozzle can be recommended. Hydrodynamic experiments, rock erosion tests, and field tests in a drilling engineering environment were carried out using the new nozzle. The results show that the new nozzle has stronger erosion capability than the cone-type or conventional organ-pipe self-resonating nozzle jet. The field test results in drilling engineering show that the outlets of the newly designed nozzles have strong anti-scouring ability. The new exit design of the nozzle can increase its life span.

1 Introduction

Jet drilling is a kind of drilling technology in which the hydraulic energy of a high-pressure water jet is applied to fracture rocks and clean out cuttings in the bottom of the oil well. This practice can reduce the probability of refracturing of the rock debris by the drill bit, as well as to increase the drilling speed. Engineers are therefore paying more and more attention to the newly developed jet drilling technology and its theory. Mini-extended nozzles are developed in order to reduce velocity attenuation and enhance the energy of the jet at the bottom of the well. They convert hydraulic pressure to kinetic fluid-flow energy with a minimum of flow disturbance, thereby focussing the stream of fluid against the floor of the formation and across the cutting face of the bit (Smith, 1987; Chia et al., 1986). Field results from the North Sea indicate that use of these nozzles increases the penetration rate up to 50%, and at an average of 16% (Peschel et al., 1985). Another new kind of highly efficient jet for erosion and cleaning is the self-resonating pulsating jet, whose high velocity stream fluctuates as it flows through the nozzle (Garner, 1980; Johnson et al., 1982, 1984). It has a higher pulsating velocity and transient impact force in comparison with the common jet. It was found that a pulsating nozzle installed on drilling bits could generate a more highly efficient jet flow often needed to fracture rock and clean cuttings. There are two common types of pulsating nozzles. The Helmholtz self-resonating pulsating nozzle is more complicated in structure and has not been widely used due to problems in life-span, details of manufacture, and other problems. The organ-pipe self-resonating pulsating nozzle is the subject of this paper. It has a simpler configuration and easier operation in drilling engineering. The fundamental geometry of this nozzle is schematically shown in Fig. 1. Experimental results (Johnson, 1982) show that the organ pipe pulsating nozzle mounted on Smith F2-CE bits can enhance drilling speed by about 10~30 percent over a conventional nozzle. However, the walls of the outlets of nozzles are more easily eroded by high-speed fluid flow. One can increase the anti-scouring ability of the outlet of organ pipe nozzles by thickening the outlet part of the nozzle; this will reduce the pulsating velocity and decrease the erosion characteristic of the jet (Sun et al., 1994, Shen et al., 1987). Preliminary results indicate that the average life span of organ-pipe self-resonating nozzles will not usually exceed 80 hours (Shen et al., 1991) due to scouring problem in the nozzle exit. Moreover, organ pipe pulsating nozzles have a section with sudden diameter reduction, which may create vortices at the exit and increase energy loss (Gerhart and Gross, 1985).

This paper introduces a new type pulsating nozzle that is developed on the basis of a series of theoretical analysis and experimental research. The new nozzle jet has less energy loss and stronger erosion ability for rock. The experimental results from the laboratory and drilling engineering tests show that this kind of pulsating nozzle has a life of 120 hours, increased drilling speed, and can reduce the cost of drilling operations in comparison with the conventional nozzle under the same conditions.

2 Theory and the Design of the Nozzle

The Organ-Pipe Self-Resonating Pulsating Nozzle. The theory of the self-resonating system is based on transient flow and passive acoustic oscillating theory (Crow and Champagne, 1971; Johnson et al., 1982). A jet nozzle is fed from a supply system that has a natural acoustic frequency equal to the preferred-mode frequency in the power spectrum of the turbulence jet flow. The jet flow passing through the self-resonating nozzle generates a fluctuating pressure which will feed back to the resonator of the nozzle with acoustic speed and enhance the upstream velocity fluctuations. The jet nozzle must be shaped to feed back the pressure oscillations in the supply system associated with the formation of ring vortices in the pulsating jet. The feedback mechanism creates the resonance in the supply chamber, which in turn further excites the jet until an equilibrium to be reached by damping. In this case, the jets induce large shedding vortices and form the pulsating jet flow.

Johnson (1980, 1984) gave the approximate formula used for estimating the length of the organ pipe based on acoustic analyses and experimentation:

$$\frac{L_p}{d_1} = \frac{k_n}{MS_d}, \tag{1}$$

where k_n is the mode parameter, given by

$$k_n = F(n,D_s,D_1,d_1) = \begin{cases} (2n-1)/4 & \text{for} \left(\frac{D_s}{D_1}\right)^2 \text{and} \left(\frac{D_1}{d_1}\right)^2 \gg 1 \\ n/2 & \text{for} \left(\frac{D_s}{D_1}\right)^2 \gg 1 \text{ and} \left(\frac{D_1}{d_1}\right)^2 \ll 4 \end{cases} \tag{2}$$

where S_d is critical Strouhal number, M is the Mach number, d_1 is the nozzle diameter, and n is the mode number of the organ pipe. Figure 1 defines the dimensional parameters.

Contributed by the Fluids Engineering Division for publication in the JOURNAL OF FLUIDS ENGINEERING. Manuscript received by the Fluids Engineering Division October 14, 1997; revised manuscript received January 6, 1999. Associate Technical Editor: S. Banerjee.

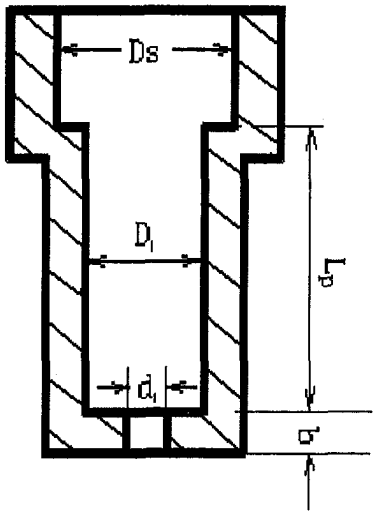

Fig. 1 Diagram of conventional organ-pipe self-resonating nozzle

The Design of a New Mini-Extended and Energy Concentrated Self-Resonating Pulsating Nozzle. The erosion effect for rock of jet depends on mean impact pressure, and the peak and amplitude value of the pressure fluctuation. The mean nozzle life span depends on the thickness b of the exit. However, the conventional organ-pipe pulsating nozzle is composed of an upstream reduction section with a ratio of $(D_s/D_1)^2$, and a downstream section with $(D_1/d_1)^2$. Such a ration change would lead to large energy losses and would not make the outlet of these nozzles strong enough, which can be seen from the following analysis. On the principle of fluid mechanics, the energy loss can be represented by head loss

$$h_l = k\frac{v^2}{2g} \tag{3}$$

where k is the loss coefficient, and v is the velocity of the nozzle exit. An empirical equation for the loss coefficient for a sudden diameter reduction is (Philip and Gerhart, 1985)

$$k \approx 0.42\left[1 - \left(\frac{d_1}{D}\right)^2\right] \tag{4}$$

Based on our practical case, let $d_1 = 10$ mm, $D = 16$ mm, then $k = 0.26$. If flow rate $Q = 7.2$l/s, then the head loss $h_l = 111.6$ m, which is nearly 10 percent of the total pump head.

For a smooth contoured reduction, we can obtain the loss coefficient based on the data given by Gerhart et al. (1985, p. 489), so when $d_1/D = 0.6$, the value of k for an abrupt reduction is 7 times more than that for smooth contoured reduction. From this datum, if we use smooth contoured reductions design, the nozzle energy loss may be deduced.

A large number of experiments have been conducted in order to study the influence of the outlet thickness on the erosion of organ-pipe nozzles (Sun et al., 1994, Shen et al., 1987). The results indicate that the erosion capability of the jet spray from an organ-pipe nozzle becomes greater with decreasing exit thickness. This decrease, of course, will also decrease the strength of the nozzle exit.

In order to increase the anti-scouring capability of the nozzle outlet and decrease the energy loss of the jet flow, the upstream reduction is designed as an exponent surface that can generate fluctuating pressure efficiently. The downstream reduction is designed as a streamlined surface which can feed back turbulent pressure and make the jet self-resonate efficiently, as demonstrated by experiment (Sun et al., 1993). The coordinate of streamline is calculated by в и т С и н С и й equation (Shen, 1997)

$$r_1 = r_c \Big/ \sqrt{1 - \left(1 - \frac{r_c^2}{r_0^2}\right)\left(1 - \frac{x_1^2}{l^2}\right)^2 \Big/ \left(1 + \frac{x_1^2}{3l^2}\right)^2} \tag{5}$$

Here x is an axial coordinate corresponding to the radius r of the stream line pipe, and r_0, and r_c are the up and down radii of the stream line reduction part, respectively. In our design $r_0 = D/2$, $r_c = d_1/2$, and l is the total length of streamline reduction. The value of r_0, r_c and l can vary with different nozzles. Due to the complexity of turbulent flow we cannot design the new nozzle by a purely theoretical equation alone. Acoustic analyses and experimental study together give the following equation to estimate the length of the organ-pipe (Sun, 1993):

$$L_p = \frac{Hnd_1}{MS_{d1}}, \tag{6}$$

where $H = 0.5 \sim 0.55$ is a constant, n is the mode number of the organ pipe, $S_{d1} = fd_1/V$ is the Strouhal number, and M is the Mach number. This new configuration design makes the jet core become longer, and can generate a preferable pulsating jet (Sun, 1993). The gradual reduction configuration makes the nozzle exit stronger and more able to withstand the scouring of jet flow.

Design of the Profile of the External Expanding Part of the Nozzle Outlet. The profile of the external expanding part of the nozzle plays a very important role in creating the self-resonating pulsation feature of the jet. Experimental results indicate that the jet pulsation becomes larger and the jet erosion capability becomes stronger if the thickness of the nozzle outlet is less. Suppose there is a large number of axi-symmetrical vortices in the jet flow, whose axial positions may be distributed at random, and whose vorticities concentrated in the central region around the axis, neglecting the interferences among vortices. The vorticity equation in polar coordinates, which applies to a single axisymmetric moving vortex associated with the moving vortex, can be obtained on Navier-Stokes equation (Shen et al., 1992)

$$\frac{\partial \Omega}{\partial t} + \frac{1}{R^2 \sin\theta}\left[-\frac{\partial \varphi}{\partial \theta}\left(\frac{\partial \Omega}{\partial R} - \frac{\Omega}{R}\right) + \frac{\partial \varphi}{\partial R}\left(\frac{\partial \Omega}{\partial \theta} - \cot\theta\Omega\right)\right] = \nu\left[\frac{1}{R^2 \partial R}\left(R^2 \frac{\partial \Omega}{\partial R}\right) + \frac{1}{R^2 \sin\theta}\frac{\partial}{\partial \theta}\left(\sin\theta \frac{\partial \Omega}{\partial \theta}\right) - \frac{\Omega}{R^2 \sin^2\theta}\right], \tag{7}$$

where Ω is vorticity, φ is the velocity potential, ν is kinematic viscosity, and t is time, By assuming b to be the radius of a vortex ring, and U the velocity of the vortex, we can obtain from (7):

$$b = \sqrt{5.02\nu t}, \tag{8}$$

$$U = \frac{C}{t^{1.5}}. \tag{9}$$

The results show that the radius of the vortex ring becomes larger with $t^{0.5}$ law. If the radius of the vortex ring increases, a large pulsed velocity can be produced. Figure 2 shows that the discrete vortex shedding has been formed at the end of organ-pipe resonator and gets larger along the wall of nozzle outlet. For an outlet of a nozzle such as shown in Fig. 2, some vortices will be destroyed due to the "absorption" of the nozzle outlet wall. The case may be even worse with a thick nozzle outlet. But the thinner nozzle outlet can not bear strong scouring of jet. In order to prevent the vortex from breaking down at the nozzle outlet due to "absorption," we design the profile of the nozzle outlet as a quarter circular arc, as shown in Fig. 3. Another benefit of this design is to overcome the head loss due to sudden enlargement of the organ-pipe exit (Gerhart et al., 1985). It is easy to see this from Fig. 2. When the high-velocity jet spray leaves the exit, there is a large velocity difference between the jet and ambient fluid, it must cause acute

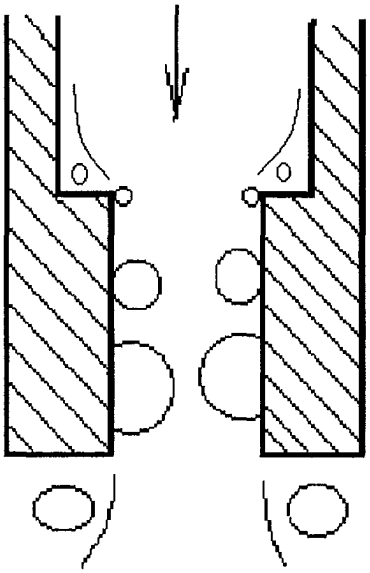

Fig. 2 Interaction Model of vortices and outlet wall of nozzle

fluid momentum exchange and vortex movement, all of which must consume the energy of the jet.

All in all, our purpose in design the new nozzle was to reduce the jet head loss and prolong the nozzle life span, which would be demonstrated by the jet erosion efficiency for rock and increased real drilling time of the new nozzle in engineering uses.

3 Experimental Results in Laboratory

Experimental Facilities. The test equipment we used is shown in the paper of Shen et al. (1991) and Sun et al. (1993). A triplex pump whose pressure head could be varied from 8 MPa to 30 MPa, and flow rate adjusted from 2 LPs to 10 LPs provides high-pressure fluid flow. The test chamber is a plexiglas cell that is used to simulate a submerged environment like a well bore. The liquid is tap water. All tests are conducted to simulate well bore just under atmospheric pressure and normal temperature. The flow rate is measured by a volumetric method in our experiments. On the top of the frame was an electrical device that is used to raise or lower the nozzle. A rock specimen box can be mounted on the chassis in the erosion experiments. Mini-extended conventional cone and organ-pipe self-resonating nozzles are tested simultaneously with the newly designed mini-extended and energy concentrated self-resonating nozzle. The diameter of all tested nozzles are $d_1 = 10$ mm. The thickness of the organ-pipe nozzle exit b is 6.5 mm, which coincides with the actual engineering size.

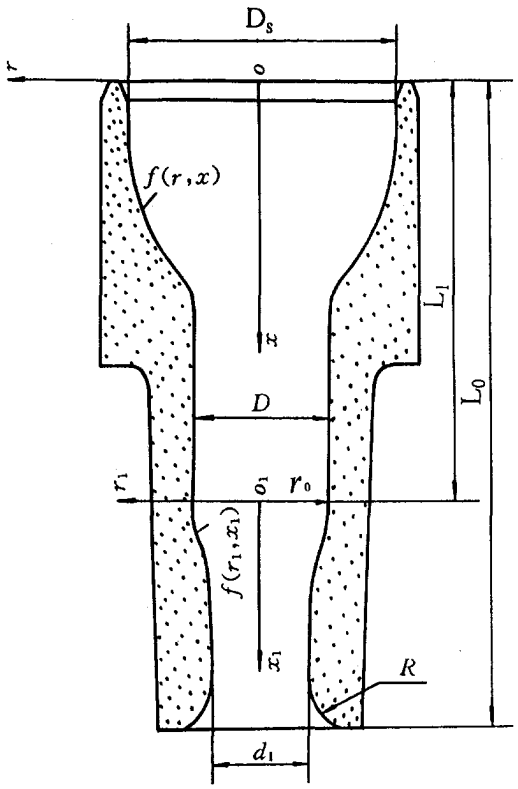

Fig. 3 Diagram of new designed nozzle

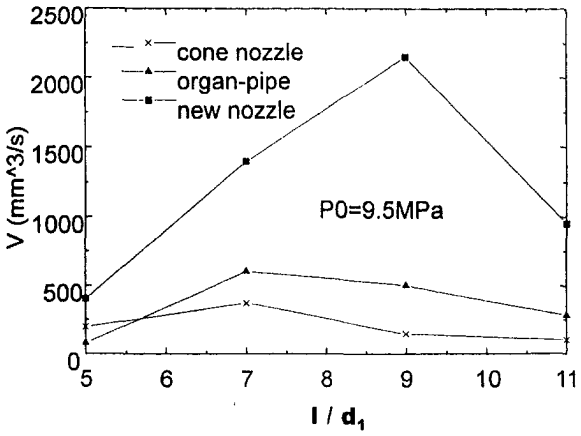

Fig. 4 The comparison of erosion volume rate of three nozzles

The Results of Rock Specimen Erosion Experiments. For the purpose of comparison, we conducted all tests under the same pump pressure conditions. There was a little difference among their flow rates. Under the condition of pump pressure $P = 9.5$ Mpa, the flow rate for the organ-pipe nozzle was 7.2 l/s, cone nozzle was 7.17 l/s, and that of the new nozzle was 7.32 l/s. Figures 4 and 5 are the results of rock specimen erosion with the same pump pressure. Two parameters are adopted to compare jet erosion capability. One is the volume erosion rate V, which is the erosion volume per second. We used a liquid injection method to measure the volume of the removal rate, before measurement, by dipping the tested rock sample in water until it becomes saturated, then taking it out from the water, and removing the water on the surface of the rock simple, and finally injecting liquid into the

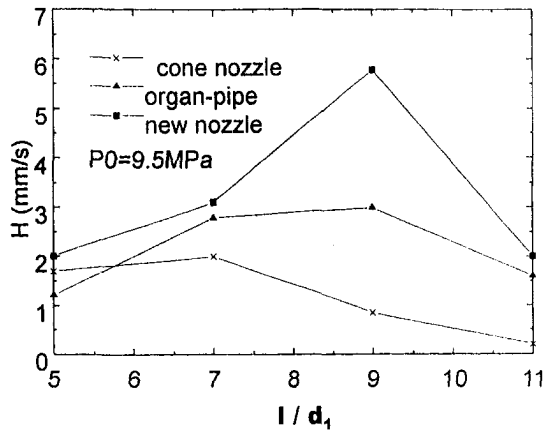

Fig. 5 The comparison of erosion depth rate of three nozzles

Table 1 The physical characteristics of the isotropic natural Zibo sandstone

density	porosity	elasticity modulus	hardness	tensile strength	compressive strength	Poisson's ratio	grain-size
2.0 g/cm^3	15%	5×10^7 N/m^2	5.1 N/m^2	0.025 N/m^2	0.545 N/m^2	0.34	0.05~0.3 mm

erosion pit until it is full of liquid. We consider the liquid consumed as the total volume of erosion created by the jet. The second method is the depth erosion rate H that comes from the average erosion depth per second. The rock specimen used was isotropic natural Zibo sandstone. Its physical characteristics measured before the experiments are shown in Table 1. All erosion tests have been repeated three times under the same conditions for precision of measurement. The erosion experiment results are showed in Figs. 4 and 5. The results show that the volume erosion rate of the new nozzle jet is 3.2 times greater than that of the organ-pipe nozzle jet and 5.5 times greater than that of the cone nozzle jet. Similarly, it was demonstrated that the average depth erosion rate of the new nozzle is almost 100% greater than that of the organ-pipe nozzle jet and 1.8 times greater than that of the cone nozzle jet at their optimizing dimensionless stand-off distances. From Figs. 4 and 5 we can find that the best erosion dimensionless stand-off distance of the new nozzle jet is 9, and the other two nozzle jets are 7~9. These results are in agreement with Sheng et al. (1991). The results mentioned above show that the new self-resonating pulsating nozzle jet has the strongest erosion ability among the three tested nozzles.

4 Preliminary Test Results Under Field Drill Engineering Conditions and Discussion

All nozzles used in drilling engineering are made with carbide. Table 2 shows probation results of the newly-designed nozzle jets mounted on J22 drilling bits at the Dagong oil field in 1996. All listed results are compared with the conventional mini-extended nozzle jet under very similar conditions. The bits from number 1 to number 10 are fixed with new mini-extended and power concentrated self-resonating pulsating nozzles. Every bit is mounted with three nozzles. The bits from contrast 1 to contrast 10 are fixed with conventional mini-extended nozzles whose lengths are equal to the new designed nozzles. The results show that nine tenths of the new nozzles can enhance the drilling speed with an average 31.68 percent, except for two peculiar results, which may be caused by unusual formation conditions, see No. 6 and No. 8 in Table 2. Moreover, their life test results show all tested nozzles can exceed 120 working hours accumulatively, and they are still in good working order. All of them can work for the same time as the cone nozzle, which is very important for its application in engineering. Under very similar conditions, the average life-span of the organ type self-resonating nozzles is 78.82 hours (Shen et al., 1991). These preliminary field test results demonstrate that the gradual reduction configuration makes the newly designed nozzle exit stronger and more able to withstand the scouring of jet flow.

The mechanism that caused the erosion rate of pulsating jet improvement under atmospheric condition has been discussed by other authors (Johnson, 1982,, 1984; Shen et al., 1991; Garner, 1980, Sun et al., 1994). Self-resonating pulsating jet afford at least three preferable advantage over the cone nozzle jet: (1) more cavitation erosion; (2) improved chip cleaning effect; (3) greater transient impact pressure for breaking up. That may be true in the case of the beginning of an oil well drilling. At a large depth well, the ambient pressure becomes high, and the probability of cavitation due to jet impact pressure fluctuation and vortices movement maybe reduce (Hammitt, 1980). We haven't found a systematic study on cavitation in a large depth hole bottom till now.

For our study, first, the newly designed nozzle jet has less head loss, which is benefit to rock breaking up and chip cleaning out. Second, the new nozzle pulsating jet form a series of ring vortices that across the hole bottom generates a substantial pressure fluctuation at this surface. These pulsation of negative pressure should overcome most normal hold-down pressure, and thus lift the chips previously created by the mechanical bit, even at depths where cavitation is suppressed (Shen et al., 1991). Finally, the big peak pressure of the jet pressure fluctuation affords greater erosion capability in some incompact stratum.

5 Conclusions

The experimental data and field test results in drilling engineering indicate that the new mini-extended and energy concentrated

Table 2 Preliminary test results of new designed nozzles used in drilling engineering

Serial number	layers	drill time (hr)	drilling speed (m/hr)	improve rate of drilling speed	fluid flow rate (l/s)	Pump Pressure MPa	Drilling depth (m)		Bits	
							from	to	model	diameter size (mm)
1	s3	45	3.69	40%	27.8	20	3259	3425		
contrast 1	s3	49.9	2.70		27.6	20	3352	3485		
2	s2	63.1	2.96	40%	27.85	19	3062	3249		
contrast 2	s2	70	2.16		28.0	20	3084	3235		
3	s3	28.3	8.17	52%	33.3	20	2085	2317		
contrast 3	s3	26.5	5.38		33.4	21	2108	2251		
4	Ed	19.83	7.06	14%	30.5	19	2430	2570		
contrast 4	Ed	45.40	6.21		30.4	19	2400	2682		
5	s2	67.8	7.06	36%	26	17	2570	3048	J22	216
contrast 5	s2	64.25	5.17		27.2	19	2520	2852		
6	s1	36.42	9.18	111%	27.5	17	2215	2553		
contrast 6	s1	71.83	4.36		27.2	17	2210	2523		
7	s2	56.25	6.34	23%	26	17	2609	2966		
contrast 7	s2	64.25	5.17		25.8	17	2520	2851.9		
8	Ng	35.00	12.26	−29%	29.4	16	1585	2014		
contrast 8	Ng	34.00	15.76		29.7	17	1400	1936		
9	Ed	48.67	3.99	18%	26.8	16	2014	2208		
contrast 9	Ed	92.75	3.39		27	17	1936	2250		
10	s2	31.50	4.06	11.8%	26.2	16	2862	2990		
contrast 10	s2	54.50	3.63		26.2	17	2816	3014		

self-resonating pulsating nozzle can generate less energy loss and has a stronger erosion capability in comparison with the mini-extended cone nozzle and conventional organ-pipe self-resonating nozzle. Results indicate that the new design of the nozzle has successfully overcome the short life-span shortcoming of the conventional organ-pipe self-resonating nozzle.

References

Crow, S. C., and Champagne, F. H., 1971, "Orderly Structure in Jet Turbulence," *Journal of Fluid Mechanics,* Vol. 48, pp. 547–591.

Garner, 1980, "Rock Bit Combination to Enhance Cutting Removal," U.S. Patent 4,187,921.

Johnson, V. E., et al., 1982, "The Development of Structured Cavitating Jets for Deep-hole Bits," SPE 11060.

Johnson, V. E., 1984, "Enhance Liquid Jet Erosion" U.S. Patent 4,474,251.

Hammitt, Frederick, G., 1980, *Cavitation and Multiphase Flow Phenomena,* McGraw-Hill.

Peschel, E., et al., 1985, "Economical Drilling with Rock Bits Equipped with Extended Nozzles: Field Experiences in North Sea," SPE/IADC 13461, pp. 331–340.

Gerhart, Philip, M., and Gross, Richard, J., 1985, *Fundamental of Fluid Mechanics,* Addison-Wesley Publishing Company, Inc.

Shen, Zhonghou, et al., 1992, "Theory of Vortex and Design of Self-resonating Jet Nozzles," The Third Pacific Rim International Conference on Water Jet Technology, pp. 255–264.

Shen, Zhonghou, et al., 1991, "New Jet Theory and Prospects of Its Application in Drilling Engineering," *Proceedings of the Thirteen World Petroleum Congress,* Buenos Aires, pp. 397–405.

Shen, Zhonghou, Li, Gensheng, and Zhou, Changshan, 1991, "Experimental Study on Self-excited Resonant Pulse Jet Nozzle for Roller Bit," *Journal of the University of Petroleum,* China, Vol. 15, No. 3, pp. 36–43.

Shen, Zhonghou, et al., 1987, "Experimental Study on Rock Erosion by Self-resonating Cavitating Jets," *International Water Jet Symposium,* Beijing, China, pp. 2-35~2-43.

Shen, Zhonghou, et al., 1997, *Water Jet Theory and Technology,* Petroleum University Press, China.

Smith, R. D., et al., 1987, "Crossflow Rotary Cone Rock Bit with Extended Nozzle," U.S. Patent 4,687,067.

Sun, Baojiang, 1993, "Discussion on High Efficient Pulse Jet Nozzle Used for Jet Drilling," *Oil Drilling and Production Technology,* Vol. 15, pp. 13–19.

Sun, Baojiang, Wang, Ruyuan and Shen, Zhonghou, 1994, "Design of a New Type of Self-Resonating Pulsating Nozzle," *Journal of the University of Petroleum,* China, Vol. 18, No. 3, pp. 31–34.

Investigations of 3D Turbulent Flow Inside and Around a Water-Jet Intake Duct Under Different Operating Conditions

Peixin Hu
Research Fellow.

Mehrdad Zangeneh
Lecturer.

Department of Mechanical Engineering,
University College London,
Torrington Place,
London WC1E 7JE, United Kingdom

In this paper the flow field in the intake duct of a model water-jet unit is studied by using a commercial 3D CFD code. In order to model the intake duct/hull interaction, the computational domain includes a large section of the hull in the vicinity of the intake duct opening. Appropriate boundary conditions are used on the far upstream and downstream of the duct inlet in order to minimize the effect of the domain boundaries on the flow field in the vicinity of the intake duct. Computations are performed for different boat speeds and flowrates. In addition, the effects of the impeller shaft, shaft rotation, boat trim as well as the traverse flow across the hull are investigated. The results of the computations are compared with some preliminary experimental results obtained from model self-propulsion tests in a towing tank. Good correlation is obtained between the predictions and the experimental results.

1 Introduction

Marine water-jets have a number of advantages both in terms of propulsive efficiency and manoeuvrability over conventional propellers at speeds in excess of 30 knots. Despite these advantages their utilization in marine propulsion has been relatively slow due to a lack of proper understanding of the flow phenomena in water-jets. An area where further studies are required is the detailed flow in the intake duct under different boat operating conditions. With these further studies we can estimate the energy loss through the intake duct and the degree of nonuniformity near the inlet of pump and investigate the cavitation caused by the separation near the intake duct lip.

Previous experimental work in this area has been mainly limited to the measurement of the static pressure along the ramp and the lip wall, see for example Okamoto et al. (1993), as well as measurement of the exit flow field from the duct, see Aartojarvi (1995). Due to the complexity of the problem and the difficulty and costs of model tests, more detailed experimental measurements have not been made. Also in the development of water-jets, the design of the intake duct has an important effect on the thrust produced as well as the performance of the pump and the overall noise and vibrations. Many manufacturers in fact use off-the-shelf components for the pump and nozzles, but use custom designs for the intake duct.

Developments in Computational Fluid Dynamics make it possible to predict the detailed 3D turbulent flow in the intake duct. The purpose of the present study is to investigate the validity of such an approach for evaluation of the detailed flow field in the water-jet intake duct under different boat speeds and operating conditions. A number of numerical investigation of the flow field in the duct have been reported in the literature, in which either potential flow or 2D viscous flow assumption is used. For example, Pylkkanen (1994, b, c) and Latorre and Kawamura (1995) performed the 2D numerical study of the water-jet inlet pressure distribution. Szantyr and Bugaski (1995) and Van Terwisga (1996) investigated the 3D potential flow inside and around the intake duct of the water-jet. Recently, Seil et al. (1995) and Thurnock and Hughes (1997) have computed the 3D viscous flow inside the intake duct, but their computations did not include the effect of the impeller shaft.

In this study, the computations are based on the intake duct of a model water-jet, designed by British Maritime Technology Ltd. Some preliminary test results obtained from the self-propulsion tests in the Haslar Hydrodynamic Testing Centre, will be used to validate the computational results. The computation domain includes a large region of the hull around the intake duct inlet, in order to model the interaction between the duct and the hull. The flow in the duct is computed both with and without shaft in order to investigate the effect of the shaft on the exit flow field from the duct. In addition, the effect of shaft rotation and the traverse flow across the hull on the duct flow field is investigated.

2 Numerical Technique

The commercial general CFD package Fluent (see Fluent, 1996) is used in all computations performed in this paper. In the code Fluent the 'SIMPLE' algorithm, which uses the finite volume method, see Patankar (1981), is used to discretize the momentum equation, the continuity equation and the turbulent equations. Then these discretized equations are solved iteratively. Body-fitted coordinate system is adapted and nonstaggered grid is used in the computation. In this paper, the high Reynolds number turbulent k-ϵ model, see Launder and Sharma (1974), is used in all cases in the investigations. In the region near wall the wall function, logarithmic law of the velocity, is used when $y^+ > 11.2$ and the laminar stress-strain relationship is used when $y^+ \leq 11.2$, see Fluent (1996).

The schematic diagram of the water-jet intake duct is shown in Fig. 1. The duct geometry is that of an existing water-jet model, designed and tested by British Maritime Technology Ltd. The duct has a rectangular cross-section at inlet which is changed to a circular cross-section at the exit. The geometry of this intake duct is symmetric. When the impeller shaft is stationary, all the boundary conditions are symmetric. Therefore, at first in the investigations in this paper the computational domain is taken to be a half of the intake duct. In simulating the cases with rotating shaft and when there is a traverse flow across the boat, the computational domain includes the whole intake duct. The quasi-cuboid below the intake duct is an artificial domain which is taken from the vicinity around the inlet of the intake duct in order to model the

Contributed by the Fluids Engineering Division for publication in the JOURNAL OF FLUIDS ENGINEERING. Manuscript received by the Fluids Engineering Division June 2, 1998; revised manuscript received March 18, 1999. Associate Technical Editor: P. M. Sockol.

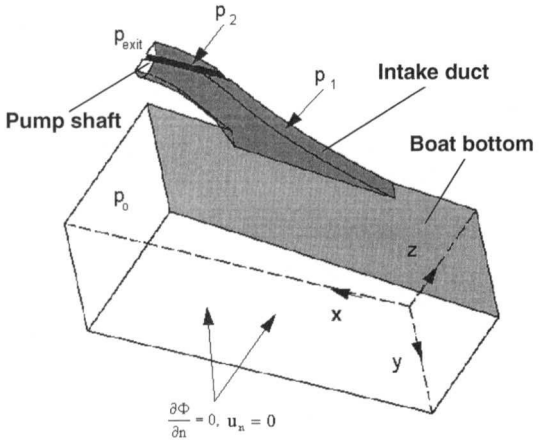

Fig. 1 Schematic diagram of the computational domain for the intake duct of the water-jet

interaction of the hull with the water-jet. Each side of this quasi-cuboid except the top side and the symmetric plane is taken far away from the inlet of the duct so that the artificial boundary conditions on the sides of the quasi-cuboid do not influence the results of the solution. Typically, the height and the width of this quasi-cuboid are about 4 times and 6.8 times of the width of the intake duct inlet, respectively. On the bottom side and the side opposite to the central plane the normal component of the fluid velocity, u_n, and the normal derivatives of other components of the fluid velocity and the scalar parameters of the fluid, $\partial\phi/\partial n$, are set to be zero, see Fig. 1. At the duct exit the static pressure, p_{exit}, is specified. The static pressure, p_o, is specified downstream of the quasi-cuboid as well. Upstream of quasi-cuboid, the static pressure is specified when the boat is at bollard pull and the velocity of the fluid is specified when the boat is moving. The boundary layer thickness and the maximum velocity of the fluid upstream of the inlet are specified according to the experimental data. The iterations in all the computations in this paper have stopped until further iteration of computation has no effect on the results. When the computational domain can be considered to be symmetric, a typical grid for the half computational domain, which is used in the computations when there is an impeller shaft, is 32 × 90 × 45 or 129600 cells. After this grid is mirrored to another half domain, the grid on the wall of the intake duct and the bottom of the boat is shown in Fig. 2. A grid 47 × 125 × 61 (or 358375 cells) which has as more than twice of cell number as the grid shown in Fig. 2 is used in the investigation of grid dependency. Both power-law scheme and blended second-order upwind/central difference scheme, see Leonard (1979), are used in the computations. The contours of velocity magnitude of fluid at the central plane of the intake duct obtained by using the grid 32 × 90 × 45 and power-law scheme, the grid 32 × 90 × 45 and second-order upwind scheme and the grid 47 × 125 × 61 and second-order upwind scheme are shown in Figs. 3(*a*), 3(*b*) and 3(*c*), respectively. By comparing Fig. 3(*a*) where the power-law scheme is used with Fig. 3(*b*) where the second-order upwind scheme is used, it is found that the patterns in both figures are similar but the details of contour, especially near the junction of the shaft and the duct, have some differences. It is observed that the contours of velocity magnitude of fluid presented in Fig. 3(*c*) where the cell number used in the computation is as twice as that used in Fig. 3(*b*) are quite similar to that shown in Fig. 3(*b*). Therefore, for the cases investigated in the following, when the domain can be considered to be symmetric, the grid, as shown in Fig. 2, is used. When the shaft is rotating or there is a traverse flow across the hull, the condition of symmetry is no longer valid and therefore a mesh

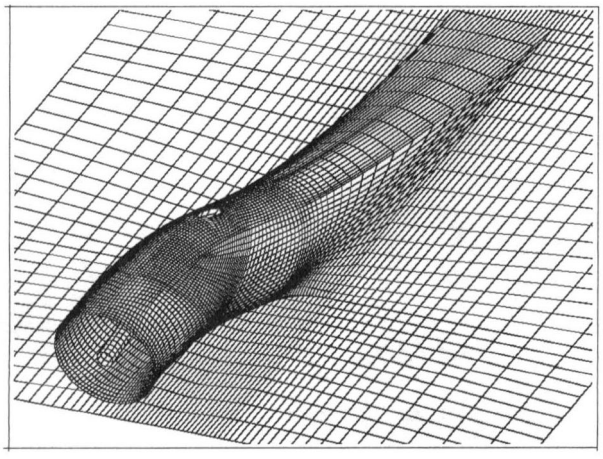

Fig. 2 Typical grid on the wall of the water-jet intake duct and the impeller shaft, 32 × 90 × 45 after mirroring the mesh to another half of computational domain

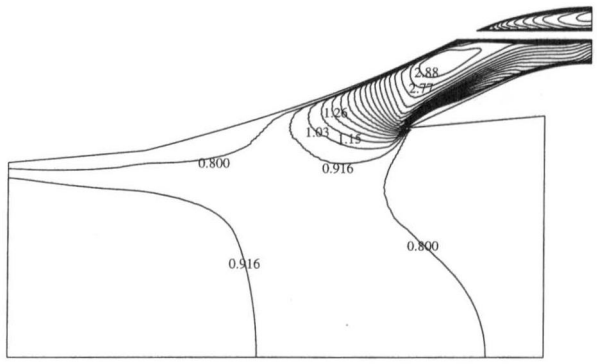

Fig. 3(*a*) Grid 32 × 90 × 45 and first-order scheme

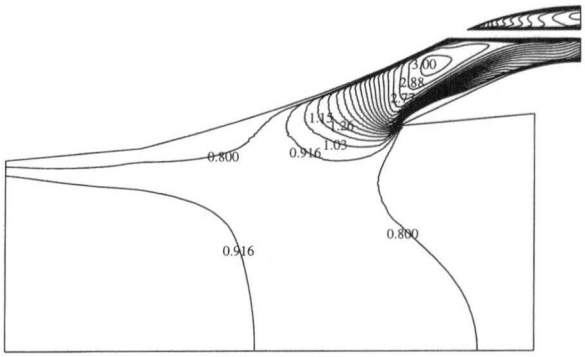

Fig. 3(*b*) Grid 32 × 90 × 45 and second-order upwind scheme

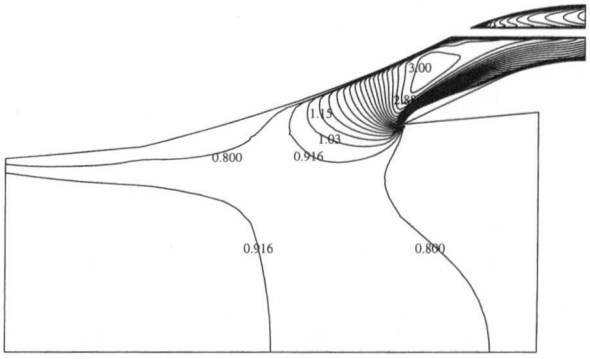

Fig. 3(*c*) Grid 47 × 125 × 61 and second-order upwind scheme

Fig. 3 Fluid velocity at the central plane of the intake duct predicted by different grid and scheme

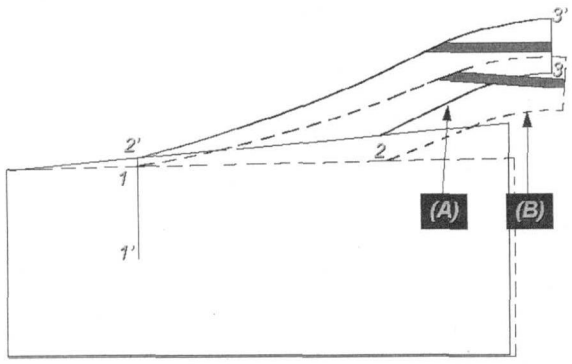

Fig. 4 Outline geometry of the intake duct (A) originally designed by BMT and (B) trim: 4°

including the whole intake duct is used. For this purpose a 64 × 105 × 55 grid (or 369600 cells) was used. The blended second-order upwind/central difference scheme is used in all cases in the following as well.

The outline geometry at the central plane of the intake duct with an impeller shaft is shown in Fig. 4 and is labelled (A). Also shown in the figure is the geometry of duct (A) after taking into account of 4° of trim, labelled (B).

3 Computations Without Shaft

The 3D turbulent flow inside and around the intake duct without an impeller shaft under the different boat speeds was investigated. In the following only typical results when the boat speed is 1 m/s at IVR = 2.2 and the boat is under self-propulsion are presented. IVR is the inlet velocity ratio which is defined as the ratio of the fluid velocity u_r at the cross-section normal to the internal flow at the aft of the duct lip to the boat speed u_b, i.e., u_r/u_b.

The velocity vectors of the fluid near the duct lip is shown in Fig. 5(*a*) and the *u*-component (axial) contours of the fluid velocity at the exit of the intake duct is presented in Fig. 5(*b*). No separated flow near the duct lip is found in the investigations when the computation does not include the shaft.

4 Computations With Stationary Shaft

When there is a stationary shaft the computations have been performed for the boat speed, 0 m/s, 1 m/s, 2 m/s, 3 m/s, and 3 m/s with a trim of 4°, corresponding Froude numbers (Fr in short) are 0, 0.2, 0.4, 0.7, and 0.7, respectively. The cavitation usually occurs near the duct lip and the shaft will change the flow pattern near the duct exit. Therefore, we will concentrate the discussion on the fluid flow near the duct lip and in the vicinity of the duct exit in the following.

4.1 Separated Flow Near to the Inlet Lip. The velocity vectors of the fluid near to the duct lip obtained in the computations when the boat is at bollard pull, IVR = 2.2 and IVR = 0.9 for the geometry (A) are presented in Figs. 6(*a*), 6(*b*), and 6(*c*), respectively. Clearly there is a separation near to the duct lip in Figs. 6(*a*) and 6(*b*) when the boat is at the bollard pull and IVR = 2.2. Comparing the flow pattern near the duct lip in Fig. 6(*b*) where there is a shaft with that in Fig. 5(*a*) where there is no shaft it is observed that the shaft has an important effect on the flow field even far upstream of its location. Therefore, even in the investigations into the flow field near the duct lip it is also important to include the shaft in the computational model. In addition, it is observed that the separation near the duct lip will lead to the formation of the low pressure zone near the lip and then possible cavitation. When the boat speed is increased from 0 m/s (at the bollard pull) to 1 m/s (IVR = 2.2), the size of the separation near to the lip, see Fig. 6(*b*), is reduced to about a half of that in Fig. 6(*a*). When the boat speed is increased further to 2 m/s and 3 m/s, or the inlet velocity ratio (IVR) is reduced to 0.9, the separation near to the duct lip disappears, for example see Fig. 6(*c*). It is observed that when the boat speed is increased from the bollard pull the stagnation point is moved from the bottom of the duct lip to the upside of the duct lip and simultaneously the separated flow near the duct lip is reduced and then disappears. Similar results were found by Seil et al. (1995). The geometry (A) in the vicinity of the duct lip presented in Fig. 4 is quite similar to the one used in the experiment performed by Matsumoto et al. (1993). They also observed that when IVR is large there is a separated flow near the duct lip and when IVR is small there is no separated flow in that region.

4.2 Flow Field at the Duct Exit Plane. The velocity vectors of the fluid at the duct exit are shown in Figs. 7(*a*) and 7(*b*) when the boat speed is 3 m/s (Fr = 0.7) with hull pitch of 0° (IVR = 0.9) and 4° (IVR = 0.9), respectively. The results show the presence of the region of the secondary flows above the shaft at the duct exit. These twin secondary flows make the fluid spiral along the shaft and into the pump. The area of the secondary flows is very sensitive to the boat pitch angle. With the increase of the boat pitch angle, the area of the secondary flows is increased, see Fig. 7(*b*).

The *u*-component contours of the fluid velocity for IVR = 2.2, IVR = 0.9 with the trim of 0° and IVR = 0.9 with the trim of 4°

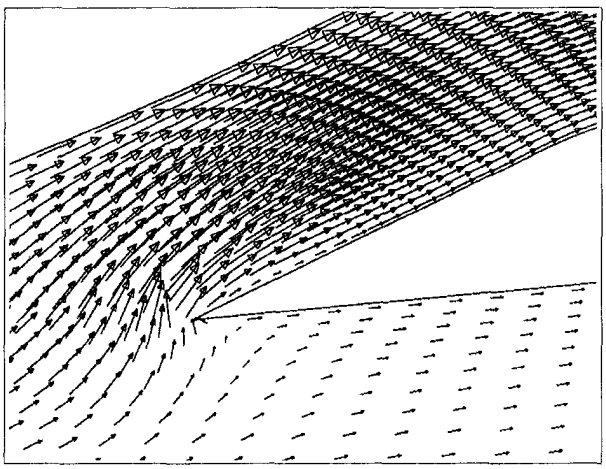

Fig. 5(*a*) Velocity vectors of the fluid near the duct lip

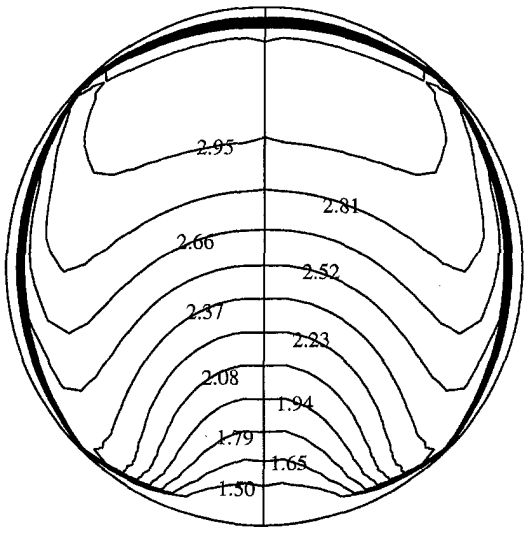

Fig. 5(*b*) The *u*-component contours of the fluid velocity at the exit of the intake duct

Fig. 5 Turbulent flow inside and around the intake duct without an impeller shaft. IVR = 2.2.

are presented in Figs. 8(*a*), 8(*b*), and 8(*c*), respectively. The patterns of the contours presented in Figs. 8(*a*) and 8(*b*) is quite similar to that obtained in the experiment performed by Aartojarvi (1995). With the decrease of IVR, or the increase of the boat speed, the flow field at the duct exit (impeller inlet) becomes more uniform. Also significant is the fact that once the actual experimentally measured pitch angle is taken into account at 3 m/s, the duct exit flow becomes more uniform.

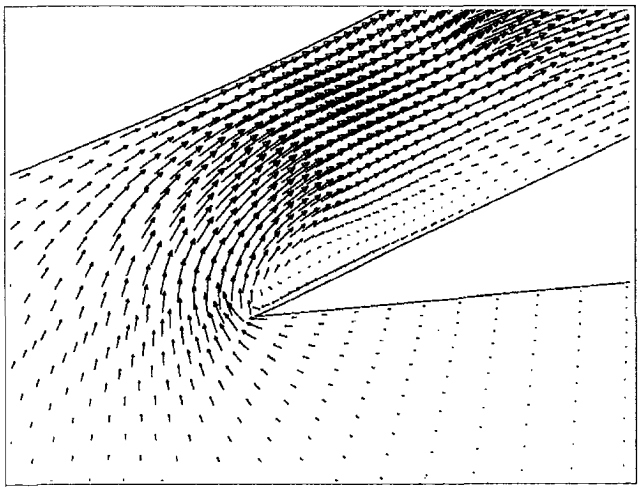

Fig. 6(*a*) At bollard pull

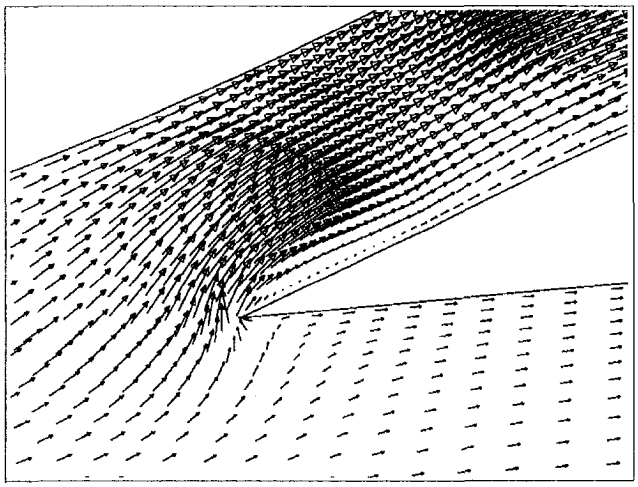

Fig. 6(*b*) IVR = 2.2

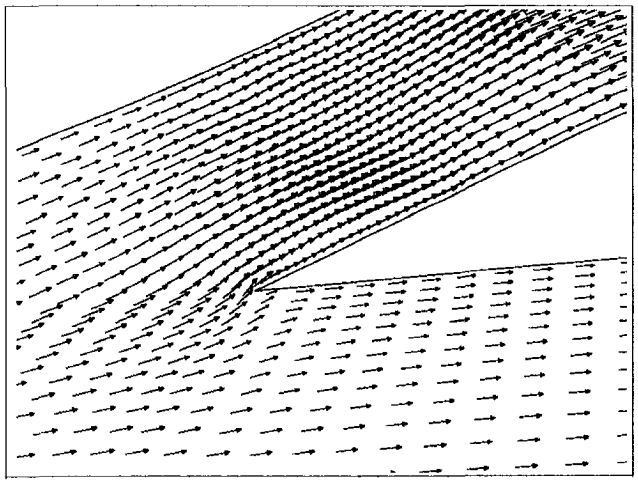

Fig. 6(*c*) IVR = 0.9

Fig. 6 Velocity vector of the fluid near the duct lip

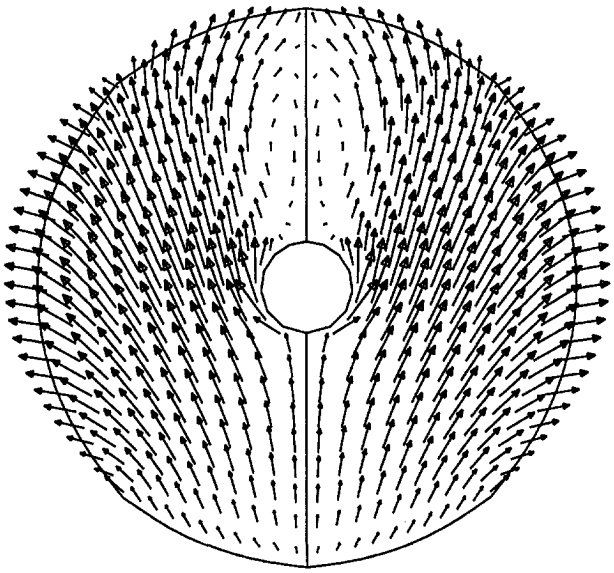

Fig. 7(*a*) Trim: 0°

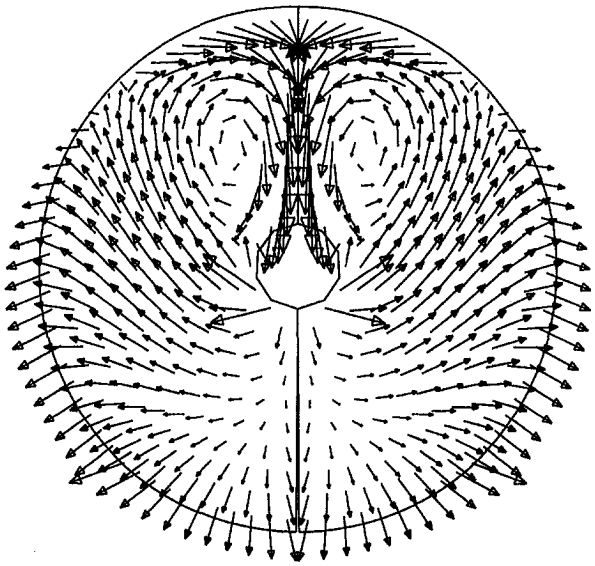

Fig. 7(*b*) Trim: 4°

Fig. 7 Velocity vectors of the fluid at the exit of the intake duct. IVR = 0.9.

5 Computations With Rotating Shaft

In most of the practical situation the impeller shaft has no protected cover. In this section we will investigate the effect of shaft rotation on the flow pattern in the duct by the change of Reynolds number. The effect of the rotating shaft is mainly related to the viscous effect of the fluid and therefore Reynolds number is used in this section. In the computations the shaft rotation is taken as 4400 rpm based on the experimental data and Froude number is 0.2. When Reynolds number based on the diameter and the fluid velocity at the duct exit is 2×10^5 (corresponding IVR is 2.1) the velocity vectors of the fluid and the u-component contours of the fluid velocity at the duct exit are presented in Figs. 9(*a*) and 9(*c*), respectively. It is found from Figs. 9(*a*) and 9(*c*) that the flow field both for the vector and u-component contours of the fluid velocity is generally symmetric. Only a very small region of the flow field

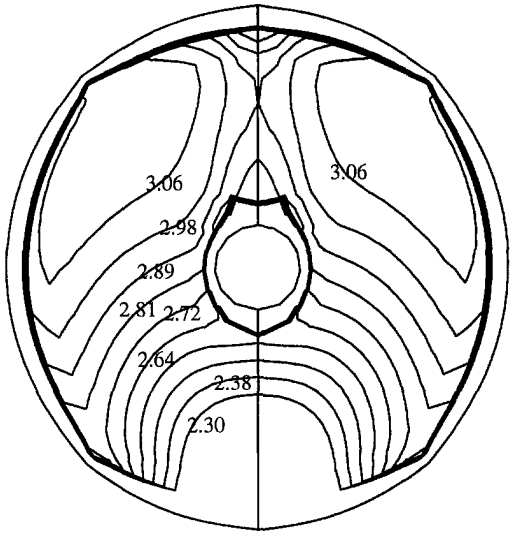

Fig. 8(*a*) IVR = 2.2 and trim: 0°

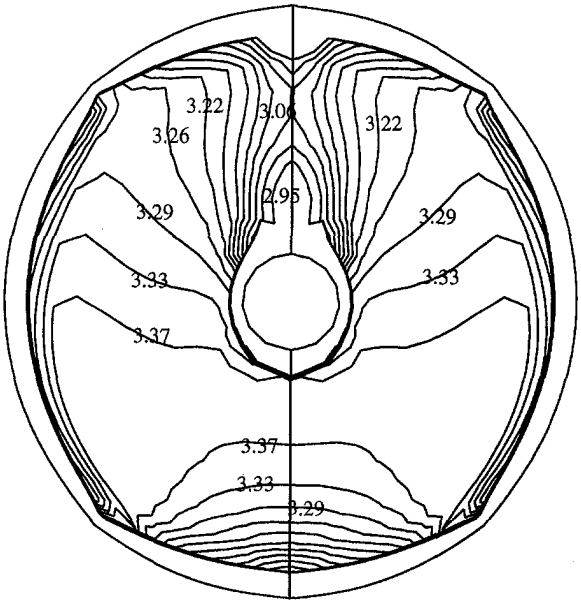

Fig. 8(*b*) IVR = 0.9 and trim: 0°

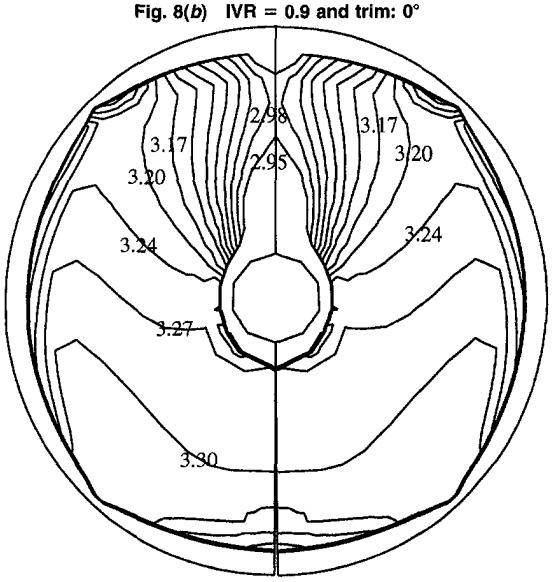

Fig. 8(*c*) IVR = 0.9 and trim: 4°

Fig. 8 The *u*-component contours at the duct exit

near to the shaft is influenced by the rotating shaft. To investigate the effect of Reynolds number on the results, the rotational speed of the shaft and boat speed (or Froude number) were kept constant. When Reynolds number is reduced to 1.1×10^5 (corresponding IVR is 1.3), the resulting vectors and the u-component contours of the fluid velocity are presented in Figs. 9(*b*) and 9(*d*), respectively. The secondary flows above the impeller shaft, see Fig. 9(*b*), and the u-component contours of the fluid velocity, see Fig. 9(*d*), are now twisted because of the rotating shaft. Therefore, the effect of the rotating shaft on the output flow of the intake duct is large when Reynolds number is small but with the increase of Reynolds number this effect becomes small.

6 Computations With Traverse Flow Across the Hull

Sometimes the vessel needs to move in the direction that has an angle with the central plane of the vessel, that is, there is a traverse flow across the vessel. In the investigation of this situation it is assumed that there is an angle of 10 deg between the moving direction and the central plane of the boat and Froude number is 0.2. We will investigate the effect of a traverse flow across the boat by the change of Reynolds number as well. The vectors and the u-component contours of the fluid velocity at the duct exit when $\mathrm{Re} = 2.1 \times 10^5$ (IVR = 2.3) are presented in Figs. 10(*a*) and 10(*c*), respectively. It is found that the spiral flows above the impeller shaft are twisted because the traverse flow across the inlet of the intake duct and there is another large secondary flow below the shaft and in the left-hand side as well. The resulting velocity contours, for the u-component, is not symmetric, see Fig. 10(*c*). This increases the flow nonuniformity at the pump inlet and therefore noise and vibration. When Re is reduced to 9.8×10^4 (IVR = 1.0), the flow at exit of the duct becomes even more nonuniform, see Figs. 10(*b*) and 10(*d*).

7 Pressure Loss Through the Intake Duct

The pressure loss is calculated by evaluating the difference in mass-averaged total pressure between a given point in the duct exit 3-3′ and the point in the duct inlet, 2-2′, see Fig. 4. The duct loss of the total pressure for the boat speed 0 m/s, 1 m/s, 2 m/s and 3 m/s (or Fr 0, 0.2, 0.4, 0.7) in the normal operating conditions are shown in Fig. 11. It is observed that at the low speed of the boat, for example 1 m/s, the total pressure loss increases quickly with the increase of the flowrate through the water-jet. A maximum total pressure loss happens when the boat is at bollard pull in the investigation. In the range of the high flowrate through intake duct, the total pressure loss is smaller at the high boat speed than that at the low boat speed. This confirms the conclusion that the water-jet efficiency increases with the boat speed.

8 Effect of Shaft on the Flow Field

As discussed in Section 4.1, a separated flow occurs near the duct lip when IVR is greater than 2.2 for the case when the shaft is present. Also the secondary flows, which spiral along the shaft, appears above the shaft, see discussions in Section 4.2. Pressure coefficients along the intake duct both when the computational domain includes an impeller shaft and does not are presented in Fig. 12. The pressure coefficient here is defined as

$$\frac{p_o - p}{\frac{1}{2}\rho u_b^2} \tag{1}$$

where p is the static pressure, p_o is the pressure at the reference point which is set at downstream of the quasi-cuboid domain, see Fig. 1, ρ is the density of the water and u_b is the boat speed. In Fig. 12 the horizontal coordinate, s/D, is a length along the intake duct to the exit which is normalized by the diameter, D, at the exit of the intake duct. The junction points of the ramp, and the lip, and the bottom of the boat, respectively, are set as an origin of the coordinate. It is observed that the pressure coefficient along the ramp in the vicinity of the inlet of the intake duct when including a shaft is similar to the one obtained in the absence of the shaft.

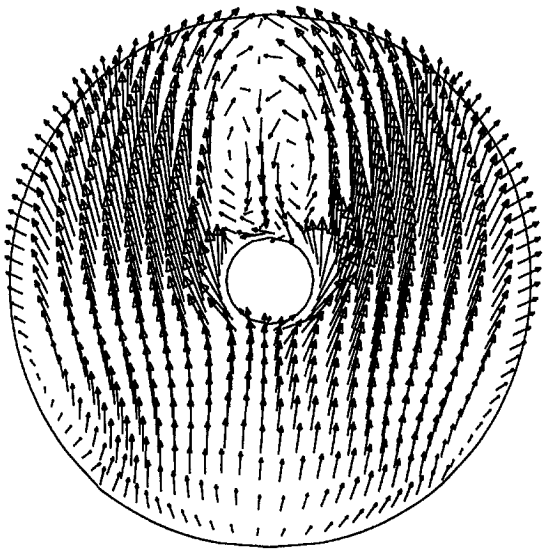

Fig. 9(*a*) Re = 2 × 10^5

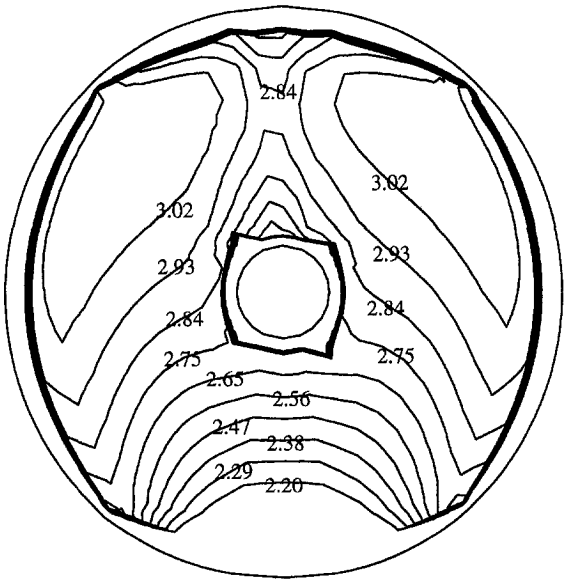

Fig. 9(*c*) Re = 2 × 10^5

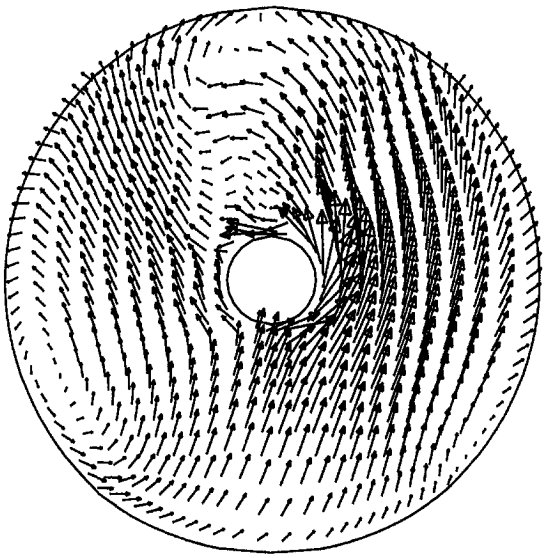

Fig. 9(*b*) Re = 1.1 × 10^5

Velocity vectors of the fluid

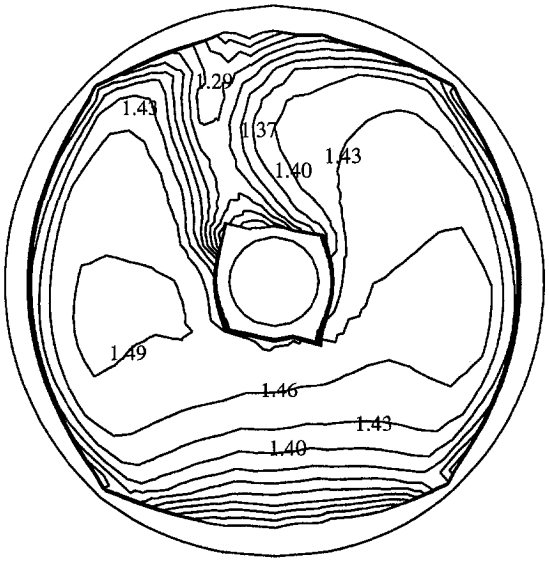

Fig. 9(*d*) Re = 1.1 × 10^5

The *u*-component contours of the fluid velocity.

Fig. 9 Flow field at the duct exit when the shaft rotates. Rotating rate = 4400 rpm and boat speed = 1 m/s (Fr = 0.2).

Near the duct lip the pressure coefficient when including the shaft is slightly different from the one obtained in the absence of the shaft. This is because there is separated flow near the duct lip when the shaft is included. The most significant effect of the shaft on the pressure is only found in the vicinity of the shaft.

9 Shape of the Stream Tube Entering the Intake

In practice, the thrust delivered by the water-jet is usually predicted by calculating the momentum change between the stream tube inlet and the exit of the water-jet. The inlet of this stream tube which is used for the control volume to predict the thrust is at the cross-section below the ramp tangency point, see for example Van Terwisga (1996). The shape of the stream tube inlet is usually assumed to be rectangular or elliptic. The dimensions of the rectangle (or the ellipse) are unknown. One dimension of the rectangle (or ellipse) is usually assumed and then another dimension is determined by the flowrate through the water-jet. In this study the predicted results were used to estimate the shape of the inlet stream tube. To do this, streamline starting at different depths from the hull on section 1-1, see Fig. 4, was traced and at the given value of the width (y) the limiting depth z of the streamline entering the duct was obtained. The process was then repeated across the width and then a series of coordinates (y, z) were obtained. By repeating this exercise for different operating conditions a range of values was obtained which are presented in Fig. 13(a). The predicted stream tube shapes are almost half elliptical

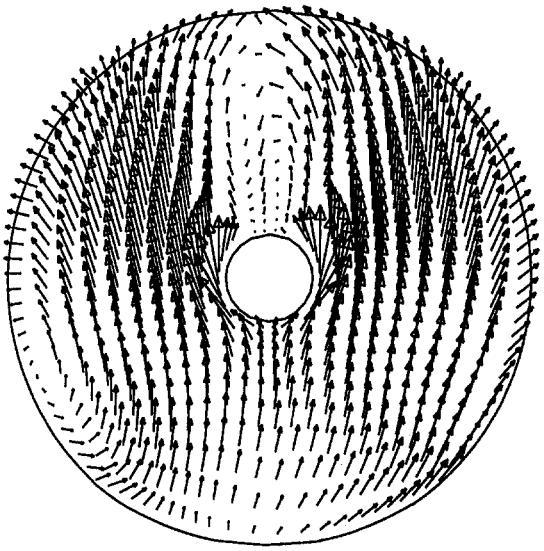

Fig. 10(*a*) Re = 2.1 × 10^5

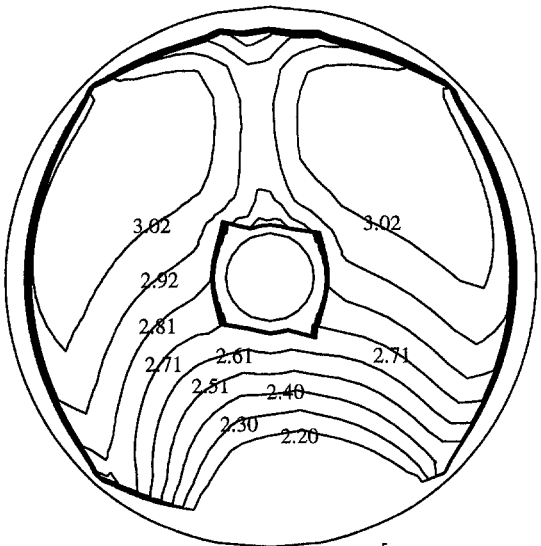

Fig. 10(*c*) Re = 2.1 × 10^5

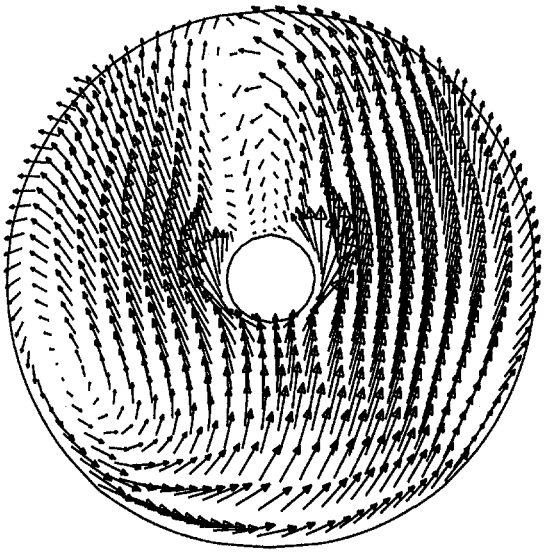

Fig. 10(*b*) Re = 9.8 × 10^4

Velocity vectors of the fluid

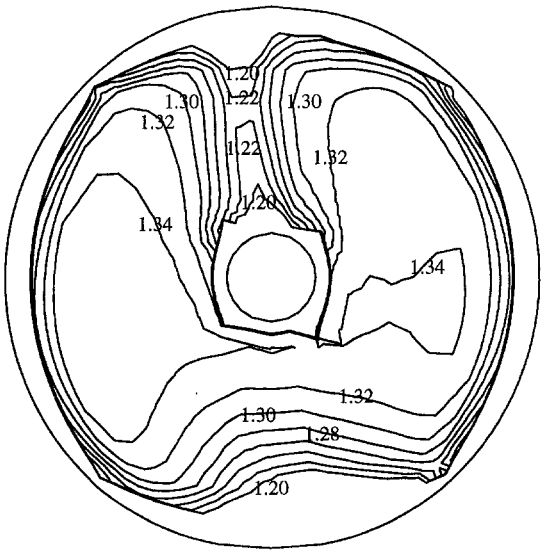

Fig. 10(*d*) Re = 9.8 × 10^4

The *u*-component contours of the fluid velocity

Fig. 10 The flow field at the duct exit when there is a traverse flow. Boat speed = 1 m/s (Fr = 0.2).

in shape. At IVR = 1, the inlet stream tube width is found to be about 1.2 times duct inlet width. Generally the depth and width of the inlet stream tube increase with increase in IVR, see Fig. 13(*b*), in which the variation is shown by a cubic fit with equation. Therefore, the depth and width of the inlet stream tube increase with the increase of the flowrate through the intake duct and decrease with the increase of the fluid velocity upstream of the intake inlet (or the boat speed).

10 Comparison With the Experimental Data

In this section, the computation results will be compared with the data from the preliminary measurements made by British Marine Technology Ltd at Haslar Hydrodynamic Testing Centre in UK. In these measurements the volume flowrate was measured by using a pitot-static tube in the nozzle. In addition, the impeller rotational speed, torque and thrust were measured. Also the static pressure at locations, p_1 and p_2, see Fig. 1, was measured.

Now we define the pressure difference coefficient, *Cp*, which is similar to expression (1). $P_o - P$ in the expression (1) is replaced by the pressure difference between the duct static 1 and 2, that is,

$$c_p = \frac{p_1 - p_2}{\frac{1}{2}\rho u_b^2} \tag{2}$$

The pressure difference coefficient, *Cp*, against the inlet velocity ratio, IVR, obtained from both the experiment and the computations for the different boat speed is shown in Fig. 14. It is found that the pressure difference coefficient for the different boat speed obtained from the computation is now on the same line of the profile. The change in the pressure difference coefficient, *Cp*, with

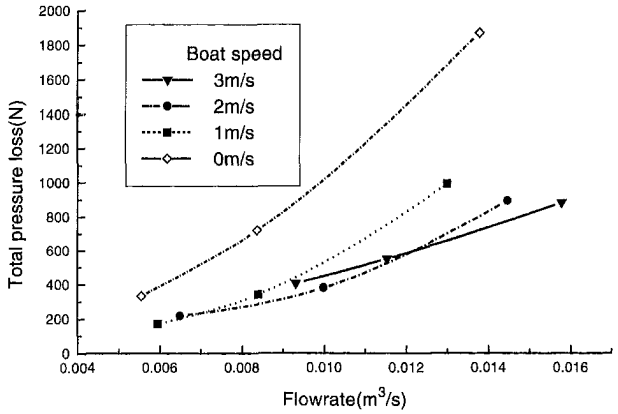

Fig. 11 Total pressure loss through the duct for the different boat speed

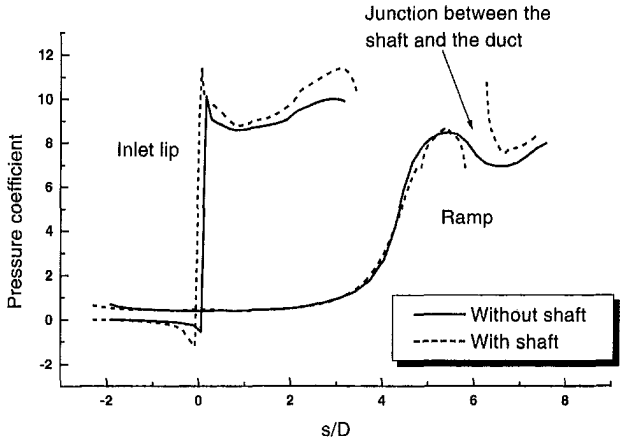

Fig. 12 Pressure coefficient along the intake duct. IVR = 2.2

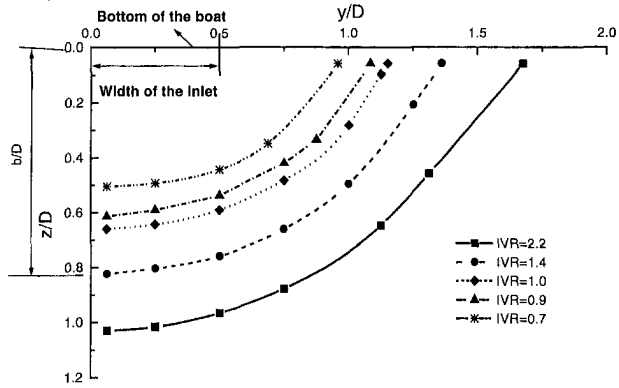

Fig. 13(*a*) Stream tube inlet

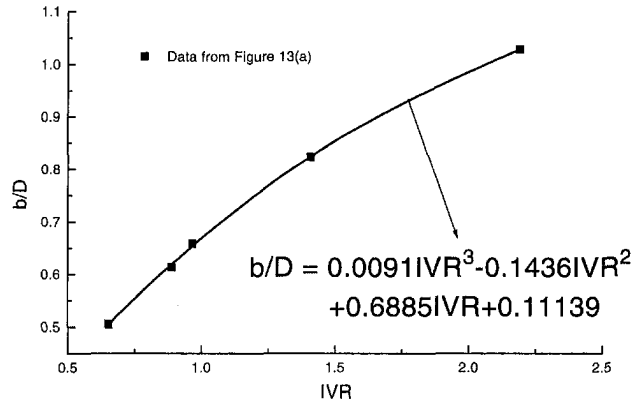

Fig. 13(*b*) Depth, *b/D*, of the stream tube inlet against IVR

Fig. 13 Shape of the stream tube inlet

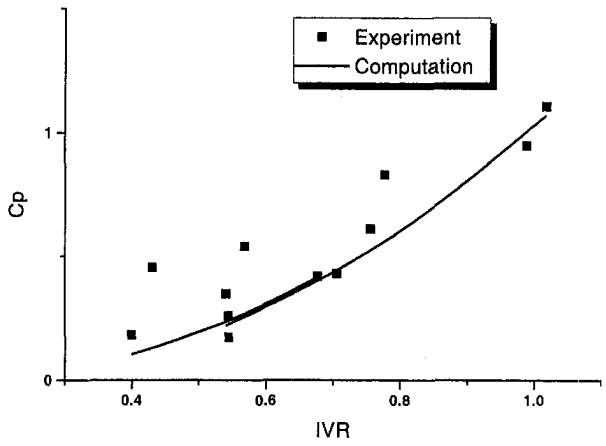

Fig. 14 Comparison between the numerical results and experimental data. *Cp:* pressure difference coefficient

IVR, as obtained from the experiment is consistent with the one obtained in the computations. This confirms the validity of the predictions used in this study.

12 Conclusions

Comparison of the predictions obtained by the 3D viscous flow solver and the experimental results shows good correlation. The following conclusions can be drawn from the computational studies:

- The presence of the shaft, even when stationary, has an important effect on the flow field in the duct, especially near the lip region and at duct exit.
- Shaft rotation and traverse flow across the hull have an important effect on the exit flow field from the duct only at low Reynolds numbers.
- The flow field at exit from the duct, i.e., impeller inlet, becomes more uniform as the IVR is reduced.
- The boat trim (or pitch angle) has an important effect on the flow field near to the duct exit.
- The inlet shape of the stream tube entering the intake can be assumed to be a half ellipse and the dimensions of this ellipse only depends on IVR. Correlation has been derived defining the variation of stream tube depth with IVR.

Acknowledgment

This study is sponsored by EPSRC, grant No. GR/L11618, as part of the FASTCRAFT program managed by Dr. Johnathan Williams of Marintech South Ltd. Additional support is provided by BAe SEMA, DERA, Lloyds Register, US Office of Naval Research and Vosper Thornycroft. The authors are grateful to Dr. Ian Dand of BMT Ltd (UK) for providing the duct geometry and the experimental data used in this paper.

References

Aartojavi, K., 1995, "Noise From Waterjet Propulsion," *Proceedings of the 3rd Int. Conf. on Fast Sea Transportation,* Lubeck-Travemunde, Germany, C. Kruppa, ed., pp. 1157–1166.

Dai, C., Kerr, C., Nguyen, R., and Wang, H. C., 1995, "A Novel Flush Inlet Design Methodology for Waterjet Propulsion," *Proceedings of the 3rd Int. Conf. on Fast Sea Transportation,* Lubeck-Travemunde, Germany, C. Kruppa, ed., pp. 1367–1378.

Fluent, 1996, *Manual, User's Guide,* Fluent Incorporated, Lebanon, NH.

Latorre, R., and Kawamura, T., 1995, "Numerical Study of Waterjet Inlet Pressure Distribution," *Naval Engineers Journal,* Sept., pp. 67–78.

Launder, B. E., and Sharma, B. I., 1974, "Application of the Energy-Dissipation Model of Turbulence to the Calculation of Flow Near a Spinning Disc," *Letters in Heat and Mass Transfer,* Vol. 1, pp. 131–138.

Leonard, B. P., 1979, "A Stable and Accurate Convective Modelling Procedure Based on Quadratic Upstream Interpolation," *Computer Methods in Applied Mechanics and Engineering,* Vol. 19, pp. 59–98.

Matsumota, K., Tanaka, H., and Qzowa, H., 1993, "Optimization of Design Parameters of Water-Jet Propulsion System," *Proceedings of the 2nd Int. Conf. on Fast Sea Transportation,* K. Sukai et al., ed., Tokyo, Japan, pp. 1489–1498.

Okamoto, Y., Sugioka, H., and Kitamura, Y., 1993, "On the Pressure Distribution of a Waterjet Intake Duct in Self Propulsion Conditions," *Proceedings of the 2nd Int. Conf. on Fast Sea Transportation,* K. Sukai et al., ed., Tokyo, Japan, pp. 855–866.

Patankar, S. V., 1981, *Numerical Heat Transfer and Fluid Flow,* Hemisphere Publishing Corporation, New York, ISBN 0-89116-522-3.

Pylkkanen, J. V., 1994a, "Test Cases of Application of CFD Code to Predict Waterjet Inlet Flows," Technical Report VALB 11, VTT Manufacturing Technology, Finland, June.

Pylkkanen, J. V., 1994b, "Design of Waterjet Inlet: Selection of Main Dimensions and Two-Dimensional Diffuser and Lips Section Ships," Technical Report VALB 29, VTT Manufacturing Technology, Finland, October.

Pylkkanen, J. V., 1994c, "CFD Analysis and Iterative Design of Waterjet Inlet," Int. Conf. on Ship and Marine Research (NAV 94), CETENA, Rome, Italy, Oct., pp. 1–9.

Seil, G. J., Fletcher, C. A. J., and Doctors, L. J., 1995, "The Application of Computational Fluid Dynamics to Practical Water-Jet Propulsion System Design and Analysis," *Proceedings of the 3rd Int. Conf. on Fast Sea Transportation,* Lubeck-Travemunde, Germany, C. Kruppa, ed., pp. 1379–1390.

Steen, S., and Minsaas, K. J., 1995, "Experiences From Design and Testing of Water-Jet Inlets for High Speed Craft," *Proceedings of the 3rd Int. Conf. on Fast Sea Transportation,* Lubeck-Travemunde, Germany, C. Kruppa, ed., pp. 1255–1270.

Szantyr, J. A., and Bugalski, T., 1995, "A Numerical Method for Hydrodynamics Analysis of Waterjets," *Proceedings of the 3rd Int. Conf. on Fast Sea Transportation,* Lubeck-Travemunde, Germany, C. Kruppa, ed., pp. 1271–1282.

Turnock, S. R., and Huges, A. W., 1997, "Evaluation of a CFD Code for Investigating Hull-Water-Jet Flow Interaction," Int. Conf. Power, Performance & Operability of Small Craft, Sept., Southampton, UK.

Van Terwisga, T., 1996, "Waterjet-Hull Interaction," Ph.D thesis, MARIN Wageningen, The Netherlands, 1996—ISBN 90-75757-01-8.

Wilson, M. B., 1971, "A Survey of Propulsion-Vehicle Interactions on High-Performance Marine Craft," *Proceedings of 18th ATTC,* pp. 23–25.

Krzysztof Cieslicki
Professor,
Institute of Automatic Control & Robotics,
Warsaw University of Technology,
Chodkiewicza 8, Warsaw, Poland;

Department of Physics of Flow,
Strata Mechanics Research Institute,
Polish Academy of Science,
Reymonta 27, Krakow, Poland
e-mail: cieslick@mp.pw.edu.pl

Anna Lasowska
Assistant Professor,
Department of Physics of Flow
Strata Mechanics Research Institute,
Polish Academy of Science,
Reymonta 27, Krakow, Poland

Experimental Investigations of Steady Flow in a Tube With Circumferential Wall Cavity

The problem of an axisymmetrical laminar flow past a square cavity was treated experimentally. The cavity flow patterns obtained in flow visualization were of a special interest. Some geometrical features of dividing streamline like coordinates of separate and reattachment points as well as the coordinates of the vortex center were measured for a range of Re numbers and compared with the numerical results obtained by Stevenson. The detected flow patterns were also related to the global pressure-flow characteristic. Two zones of laminar flow characterized by the different nonlinear corrections to Darcy's law were distinguished.

1 Introduction

Stevenson (1973) considered steady laminar flow of a viscous, incompressible liquid through a channel formed by a tube of radius R_1 with a circumferential wall cavity of depth R_3 and length $L_3 - L_2 = R_3$ (Fig. 1). In his analysis he set the ratio of cavity depth to the tube radius to be equal to $R_3/R_1 = 1.333$. His calculations used the Finite Differences Method with the classical assumption of nonslip boundary condition on walls and parabolic velocity profile sufficiently far upstream of the cavity. He carried out calculations for three values of Reynolds numbers Re: 0 (Stokes flow), 50, and 200.

A characteristic feature of the considered flow is its partition by a separation surface into a core or an axial mainstream responsible for the flow rate and a single large vortex filling the cavity (Friedman, 1970). The separation surface intersects the channel wall along twin closed curves which are seen in an axial cross-section as the separation point and the reattachment point (Fig. 1). Results of Stevenson's calculations show that the flow separation appears for Re = 0 and continues to exist throughout the range of Re numbers considered. Stokes flow (Re = 0) is a singular limiting form of the flow.

Flows with cavity and separation are studied in numerous research centers and concern a wide range of applications, e.g., in botany, flows at very low Reynolds numbers (Re < 1) are investigated with ecological purposes in view. Structural constitution of plant nutritional vessels is modeled by axisymmetric channels with periodically distributed cavities, which are suitable for the study of physiological liquid transport phenomena (Jeje and Zimmermann, 1979; Butterfield and Meyland, 1980; Jeje, 1985; Zimmermann, 1983; Juritza, 1987; Schulte et al., 1989).

Moreover, flows with Re of the order of some hundred are used for studying the initial stages of clot formation in blood flow. Thrombogenesis study was carried out using flow chambers connected across an outside-body shunt in dogs (Stevenson, 1973). Periodically nonuniform capillary tubes are also frequently applied in modeling of inertial effects present in flow through granular porous media (Dullien and Azzam, 1973, Lymberopuulos and Payatakes, 1992). An additional objective of such experiments is to find an appropriate nonlinear correction to Darcy's law at low Reynolds numbers (Cieslicki and Lasowska, 1995, Firdaouss et al., 1997).

The existence of vortices in the neighborhood of protruding and reentrant corners in Stokes' plane flow was theoretically predicted by Moffat (1964). They are related to imaginary eigenvalues of the biharmonic operator in the Stokes' equation. In spite of this early theoretical work an analytical description of axisymmetric flow, even for creeping flow (Re close to zero), presents such difficulties (Takematsu, 1966, Tutty, 1988) that numerical solutions are considered best appropriate. For example, Friedman (1970) calculated streamlines of an axisymmetric flow with a single square cavity, with a constant inlet velocity profile. O'Brien (1972) studied the influence of the type of inlet velocity profile for a square cavity on cavity flow streamline patterns in plane flow, the shape of the separation surface being of foremost interest.

The flow considered was also studied experimentally. Because of difficulties in visualizing axisymmetric flows most experimental work was done on plane models e.g., Taneda (1979). The scarce work done on axisymmetric models as Jeje (1985), Lasowska (1986), and Schönberger (1992) had a rather qualitative character.

Stevenson's numerical solutions are unique since his rendering of streamline patterns is of high precision when compared to those in papers mentioned above and taken from such authors as: Stark (1972), O'Brien (1972), Payatakes and Neira (1977), Lahbabi and Chang (1986). The main purpose of this paper is therefore to produce an experimental verification of Stevenson's numerical calculations. Cavity flow over a similar range of Reynolds numbers has been produced and such features as positions (R_{S2}, R_{S3}) of separation and reattachment points and also of the vortex center (R_C, L_C) were compared to those found by Stevenson (1973).

The next objective of this work was to answer the question: "Does the character of the inlet velocity profile influence the recirculation flow streamlines patterns in steady states, or presumably not?". Accordingly, research has been undertaken for two inlet velocity profiles: a parabolic and a flattened one.

Additionally, a pressure-flow relation of an axisymmetric channel composed of a number of alternate narrow and wide segments with respective diameter d, D and lengths l_n, l_w, was measured. The cavity dimensions were similar to those in the Stevenson's numerical model. The main contribution of our experiments was to correlate pressure-flow relation with the detected cavity flow patterns. A detailed description of the experimental conditions is in Section 2, while the results are presented and explained in Section 3 and 4.

Contributed by the Fluids Engineering Division for publication in the JOURNAL OF FLUIDS ENGINEERING. Manuscript received by the Fluids Engineering Division November 17, 1997; revised manuscript received February 3, 1999. Associate Technical Editor: S. Banerjee.

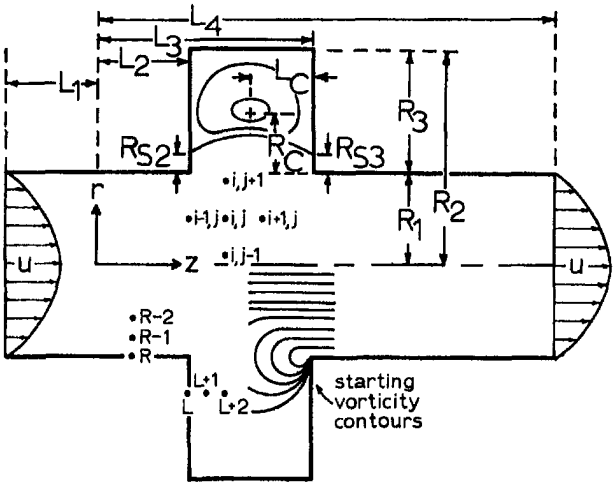

Fig. 1 Definition sketch

2 Description of the Experiment

A hydraulic outlay of the experiments is shown in Fig. 2(*a*) and its optical outlay in Fig. 2(*b*).

The flow of liquid in models of dimensions: tube diameter $d = 2R_1 = 8$ mm, cavity depth $H = R_3 = 10.6$ mm, cavity length $L = L_3 - L_2 = 10.6$ mm was hydrostatically induced. Constant pressure drop was maintained and adjusted by means of a pair of small overflow reservoirs provided at both far ends of the model (Fig. 2(*a*). The mass flow rate ρQ was measured by weighing the mass of liquid which left the model within a given time interval. Also recorded was liquid temperature at both ends of the model. The volume rate of flow Q supplied the Reynolds number: $\mathrm{Re} = 4Q/\pi d\nu$.

Immersion liquids with refractive indexes equal to that of the model material (Plexiglas) were used in experiments. (It came out that the liquid had to be made optically homogeneous to the model walls with an accuracy of four decimal places in the refractive index, if optical distortions in the flow images were to be eliminated.) The liquids were water solutions of glycerin with addition of ammonium rhodanate. They had a refractive index of $n_d = 1.4589$, coefficients of dynamic viscosity $\eta = 10$ or 40 mPas, and density $\rho = 1.208$ g/cm^3. Höppler viscometer was used to measure viscosity with accuracy of 0.5 percent. Rheological investigation of the properties of the immersion liquids showed their Newtonian character.

Flow visualization by marker particles was applied in the research (Fig. 2(*b*)) The method consists in taking photos (on photographic plates) of the traces of particles dispersed in the flowing liquid when they fell within a 0.4 mm thick laser luminous sheet along the axial plane of the model. Epoxy resin particles of 40 μm in diameter served as markers and their density was made equal to that of the surrounding liquid to an accuracy of 0.001 g/cm^3, as verified by a very precise buoyancy test. Particle traces follow liquid streamlines in stationary flow.

The experiments were performed in isothermal conditions thus avoiding variation of optical and mechanical parameters of the liquid and any thermal convection. Constant temperature was maintained within the ± 0.2°C interval.

Photographs were taken with an exposure time depending on the value of Re number and on the concentration of marker particles. The series of flow images obtained from the experiments for a given value of Re, were analyzed in detail. Coordinate values R_{S1}, R_{S2}, R_C, L_C were read off from pictures taken in steady flow at a 25 times magnification. Uncertainties in experimental measurements and results are indicated in figures.

Steady flow was assumed to have been established when successive measurements showed:

—reproducible flow rate,
—unchanged positions of the points of separation, reattachment and vortex center.

Steady-state vortex patterns were observed for all Re number values below 330 when the first symptoms of instability onset could be detected. For $\mathrm{Re} < 330$ no evidence of periodic or aperiodic streamline pattern variations were observed.

In order to study how the type of inlet velocity profile affects the cavity flow streamline pattern, the experiments were carried out on two near identical models differing only in their inlet segment shapes. Stevenson's assumptions could be reproduced exactly on the first model (Fig. 3(*a*)). Both upstream and downstream of the cavity there were suitably selected lengths of tube. Developed laminar flow with a parabolic velocity profile was obtained in an

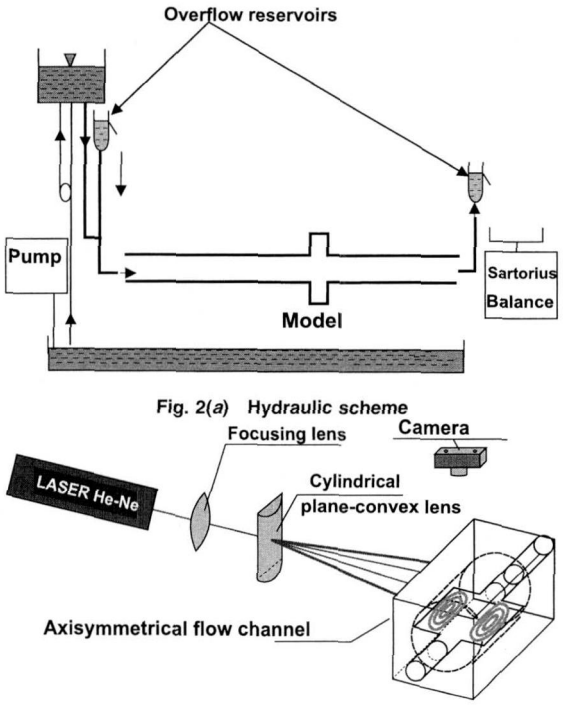

Fig. 2(*a*) Hydraulic scheme

Fig. 2(*b*) Optic scheme

Fig. 2 Schematic diagram of experimental apparatus

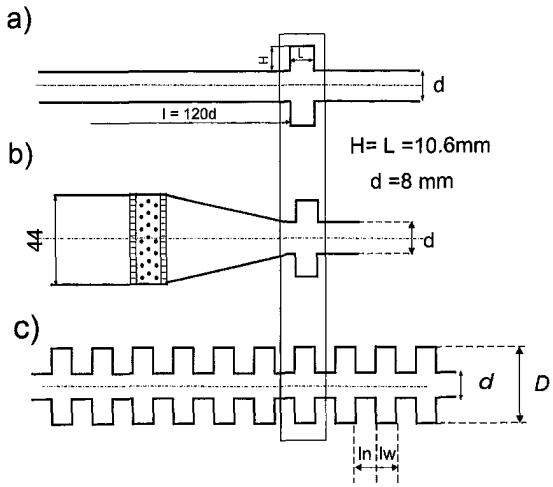

Fig. 3 Schematic diagram of models used in experiments. (*a*) Stevenson's model with the parabolic inlet velocity profile; (*b*) model with a filter and nozzle to obtain the flattened inlet velocity profile; (*c*) periodical model.

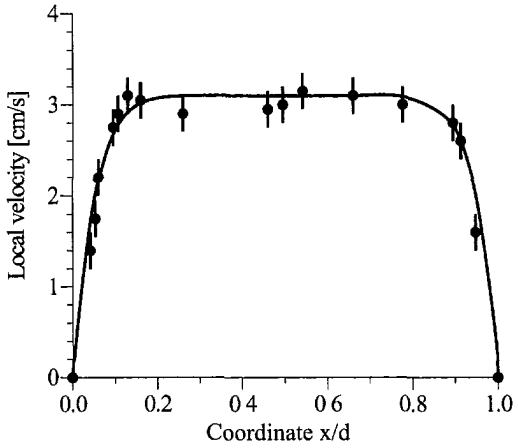

Fig. 4 A typical flattened velocity profile (Re = 50). Uncertainty in local velocity measurement is estimated to be ±0.2 cm/s.

inlet tube of length $l = 120d$ over the whole range of Reynolds numbers in the experiment. The second model (Fig. 3(*b*)) was provided with a filter and a nozzle so as to obtain a flattened shape of the inlet velocity profile at the cavity mouth. A short, 2 mm, piece of tube was inserted between the nozzle and the cavity to produce parallel inflow into the model.

The model with spatial periodicity (Fig. 3(*c*)) comprised 64 segments, alternatively narrow and wide. Their respective diameter and length were: $d = 3$ mm, $l_n = 10$ mm and $D = 7$ mm, $l_w = 2$ mm. Measurements of the flow characteristics on this model were performed as described in Cieslicki (1986) and Lasowska (1996). The pressure drop in the model was measured with a Fischer and Porter pressure difference converter with an accuracy of 0.05 mm H_2O (~0.5 Pa).

3 Results of Experiments

In Fig. 4 a typical, flattened velocity profile, determined at the nozzle end in model (3b) for Re = 50, is shown. It was obtained from the measurements on photographs of the length of particle traces for fixed exposure times.

The flattened profile was approximated by a power formula (1):

$$V(r) = V_{\max}\left[1 - \left(\frac{r}{R_1}\right)^n\right] \tag{1}$$

For the presented profile, the value $n = 7.4$ is constant within the range of investigated values of Re. The value of the exponent n in the laminar flow regime depends mainly on the convergence angle of the nozzle applied.

In Fig. 5(*a, b*) the images of cavity flow streamlines in models with parabolic and flattened inlet velocity profiles and for comparable values of Re are put together.

In Fig. 6 the streamline patterns obtained from the Stevenson's calculation and from the above-described experiments are compiled. The dependence of coordinates of the vortex center R_C, L_C and of the position of the separation and reattachment points R_{S1}, R_{S2} on Re numbers as obtained for both the models, and calculated by Stevenson (1973) are shown in Fig. 7(*a, b, c*).

In Fig. 8(*a*) the pressure - flow relation of periodical model is plotted in a coordinate system J/Q versus Re, where $J = \Delta H/L_t$, (ΔH - piezometric head, L_t - the whole model length). In Fig. 8(*b*) only a part of this characteristic for Re < 50 is shown. It also correlates the low Re numbers range of flow characteristic with the geometric flow patterns of cavity streamlines.

4 Discussion of Results

The cavity streamline patterns in steady flow when the inlet velocity profile is either parabolic or flattened do not show any

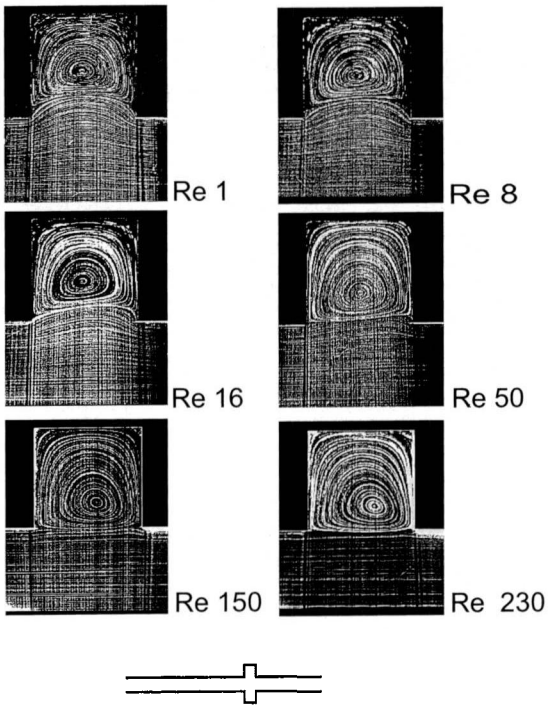

Fig. 5(*a*) Parabolic inlet velocity profile

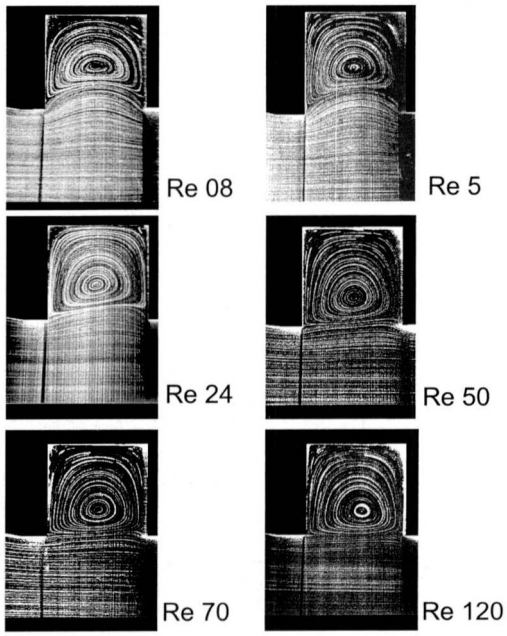

Fig. 5(*b*) Flattened inlet velocity profile

Fig. 5 Cavity flow patterns in stationary flow of various Re number. Uncertainty in Re is estimated to be ±2.5 percent.

significant discrepancy at respectively the same Re numbers within the range of 0.2 to 300. The only small difference occurred for very slow Stokes flow (Re < 1) when the shape of the separation line for the flattened profile was slightly more bulging toward the outside cavity wall. This confirms the calculations of O'Brien (1972).

The cavity streamline patterns calculated by Stevenson (1973) and those obtained by experiment agree very well. An increase of

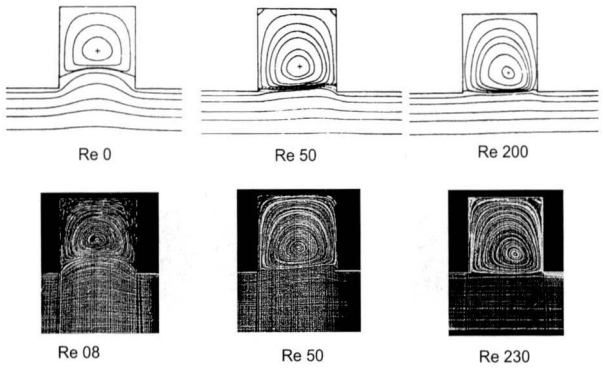

Fig. 6 Flow patterns obtained from Stevenson's numerical calculation and from experiments

Re number causes only a small change in the geometrical shape of streamlines such as displacement of the separation and reattachment points toward the protruding corners of the cavity and some "straightening" of separation lines. As a result, the main flow practically fails to penetrate the cavity region and bears close resemblance to parallel pipe flow. At the same time, the vortex center is displaced to the right along the channel axis, which is the

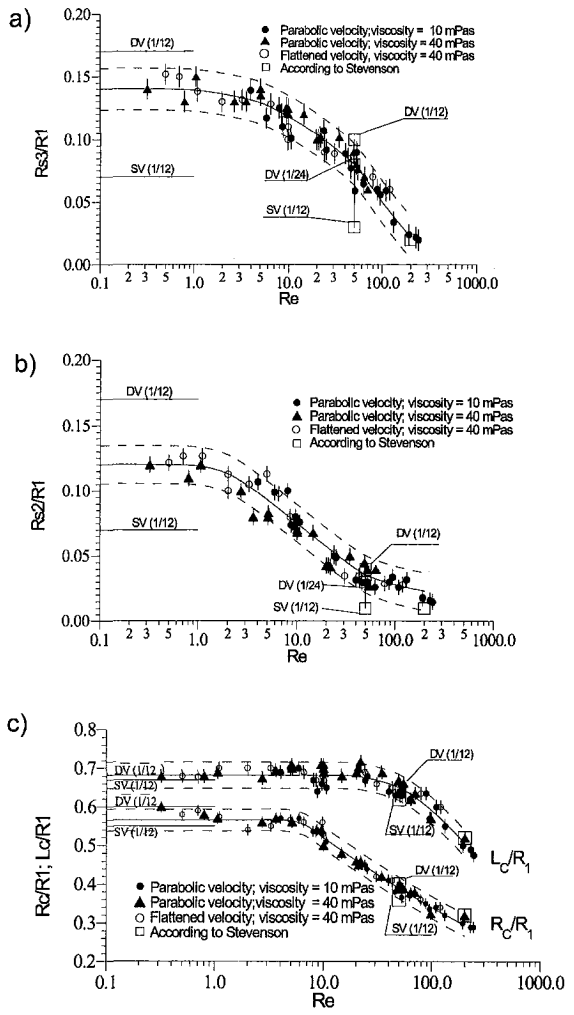

Fig. 7 Characteristic geometrical parameters of cavity flow against Re in models 3a and 3b. (*a*) Position of reattachment point. Uncertainty in R_{S3}/R_1 is ±0.006; (*b*) position of separation point. Uncertainty in R_{S2}/R_1 is ±0.008; (*c*) coordinates of vortex center. Uncertainty in L_C/R_1 is ±0.0175, in R_C/R_1 is ±0.014.

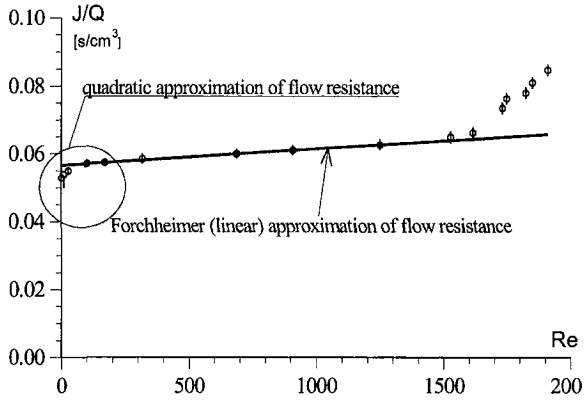

Fig. 8(*a*) The whole flow characteristic. Uncertainty in *J/Q* in Forschheimer zone is estimated to be ±0.017 s/cm³.

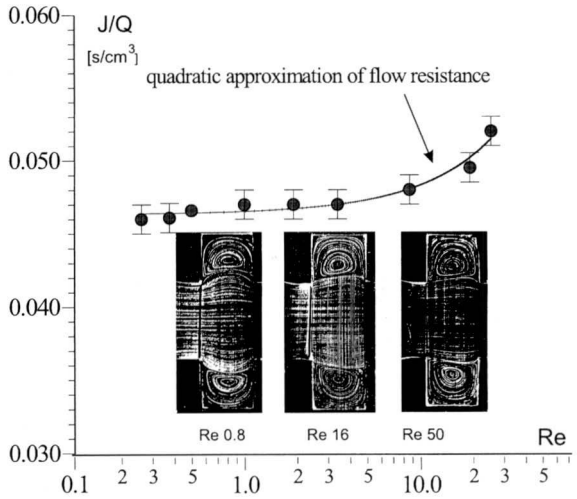

Fig. 8(*b*) Low Re numbers range. Uncertainty in *J/Q* in parabolic zone is estimated to be ±0.01 s/cm³.

Fig. 8 Resistance to flow of spatially periodic model against Re

flow direction. Plots of the positions of stationary vortex center, separation and reattachment points against Re numbers quantitatively confirm this observation. No significant difference of behavior was detected for the two velocity profiles.

The positions of the separation and reattachment points strongly depend on Re values. With Re increasing from Re ≈ 1 their gradual shift towards the cavity edges was observed. The Stokes approximation is thus valid below the limiting value Re ≈ 1. The third point i.e., the vortex center undergoes some lesser displacement above Re = 7. All three points become fixed when Re > 200.

The results of Stevenson's (1973) numerical calculation shown additionally in Fig. 7 (because of the applied logarithmic scale, numerical values corresponding to Re = 0 are shown as horizontal lines) had been obtained by various methods, so at a Re value there is more than one value of the magnitudes considered. Stevenson calculated velocity fields in the neighborhood of flow singularities, namely, protruding corners, for different numerical schemes: (SV and DV), and for different mesh sizes (1/12 and 1/24). SV stands for a single-valued vorticity boundary condition whereas DV stands for double-valued one. Values calculated according to the first scheme (SV) are lower, while those corresponding to the second scheme DV are higher. Coordinates of separation and reattachment points of the separation line for lower values of Re (equal to 0 and 50) proved to be particularly sensitive to the method of calculation. For Re = 200 results obtained for both schemes were the same. The experimental points lie between the values obtained numerically according to both schemes, but they are somewhat closer to those of the DV scheme. As it might be

expected, for smaller Re, the greater is the calculation accuracy by virtue of a decrease in mesh size, the closer is the agreement of the calculated results with those of the experiment. It should be stress, that a scatter of points due to experimental errors, particularly for low Re values, remains well below the discrepancy of numerical results obtained from both schemes.

As seen from Fig. 8(*a*) there is a linear dependence on Re of hydraulic resistance J/Q in the spatial periodicity model. This occurs within almost the whole laminar flow zone, so the well known Forchheimer Equation (FE) can be used to approximate it:

$$\frac{J}{Q} = A_1 + B_1 Q \tag{2}$$

Flow visualization experiments had shown that in the range of FE validity the streamline pattern in the mainstream is parallel within close limits (Cieslicki, 1988).

At low Re values a very small deviation from FE was observed and this correlates with relatively larger changes in the streamline patterns in the cavity. It results from the latest papers, either theoretical (Mei and Auriault, 1991, Firdaouss et al., 1997) or experimental (Cieslicki and Lasowska, 1995) that, within this Re range, the hydraulic resistance of spatial periodicity models increases quadratically with flow rate (or Re) according to Eq. (3):

$$\frac{J}{Q} = A_0 + B_0 Q^2 \tag{3}$$

This formula loses validity when the main flow fails to encroach on the cavity, that is for $\mathrm{Re} > 100$.

5 Conclusions

The results of the experiments performed fully confirm Stevenson's numerical results. The partition of the flow into the main core and the vortex filling the cavity was observed from the lowest Re number of 0.2 upwards. The major consequence of flow partition is the absence of mass exchange between the mainstream and the annular vortex over a wide range of Re numbers.

Characteristic geometrical features of the cavity flow such as positions of separation and reattachment points and of the vortex center as measured and calculated, show very good agreement. In the range below $\mathrm{Re} \approx 50$ results of the calculation scheme DV (as compared to SV) seemed to yield results which were somewhat closer to those of the experiment. Within the range $\mathrm{Re} \leq 1$ geometrical parameters of cavity flow patterns do not change, so Stokes approximation can be used for its numerical calculation.

When increasing the average flow velocity, the cavity volume occupied by the stationary vortex expanded by a small amount. These changes are particularly pronounced within the range of velocities corresponding to the Re numbers from near zero up to about 50. A quadratic correction to Darcy's law could be applied within this flow range in the spatial periodicity model. With a further velocity increase (up to the point of stability loss) the main and recirculatory flow volume changes insignificantly and the hydraulic resistance increases linearly (Eq.(2)), so that FE is applicable.

The inlet velocity profile at the cavity mouth does not significantly affect the geometric patterns of streamlines in the steady-state flow conditions. So the character of the studied flow is dominated by the cavity dimension ratio only.

To the best of our knowledge, during twenty five years since the publication of Stevenson's (1973) work none of the numerical calculations presented by other authors were as close to experimental results as his are. Therefore, we feel obliged to give prominence to the great precision of Stevenson's calculations and to the correctness of his choice of boundary conditions.

References

Butterfield B. G., and Meyland B. A., 1980, *Three-Dimensional Structure of Wood,* Chapman and Hall, London, New York.

Cieslicki K., and Lasowska A., 1986, "Flow of Water in Models of Porous Space in the Light of the Forchheimer Equation," *Archives of Mining Science,* Vol. 31, pp. 63–75. (in Polish)

Cieslicki K., 1988, "Nonlinear Fluid Flow through Periodic Models of Porous Space, Part I. Theoretical Considerations, Part II. Experimental Results," *Bulletin of the Polish Academy of Sciences, Technical Sciences,* Vol. 36, pp. 3–27.

Cieslicki, K., and Lasowska, A., 1995, "The Effect of Inertia on Flows in Tubes with Periodic Step Changes in Diameter," *Bulletin of the Polish Academy of Sciences, Technical Sciences,* Vol. 43, pp. 423–438.

Dullien F. A., and Azzam M. I., 1973, "Flow Rate–-Pressure Gradient Measurements in Periodically Nonuniform Capillary Tubes," *AIChE Journal,* Vol.19, pp. 222–229.

Firdaouss M., Guermond J. L., and Le Quere P., 1997, "Nonlinear Corrections to Darcy's Law at Low Reynolds Numbers," *Journal of Fluid Mechanics,* Vol. 343, pp. 331–350.

Friedman F., 1970, "Flow in a Circular Pipe with Recessed Walls," *ASME Journal of Applied Mechanics,* Vol. 37, pp. 5–8.

Jeje A. A., 1985, "Flow Models of Microcapillaries of Living Plants," *Physical Hydrodynamics*, Vol. 115, pp. 15–26.

Jeje A. A., and Zimmerman M. H., 1979, "Resistance to Water Flow in Xylem Vessels," *Journal of Experimental Botany,* Vol. 30, pp. 817–823.

Juritza G., 1987, "Anatomie der Samenpflanzen," Thieme, Stuttgart.

Lahbabi A., and Chang H. CH., 1986, "Flow in Periodically Constricted Tubes: Transition to Inertial and Non steady Flows," *Chemical Engineering Science*, Vol. 41, pp. 2487–2505.

Lasowska A., 1996, "Experimental Investigations of Flow Through Porous Media and Selected Models of the Porous Space," PhD thesis, Polish Academy of Science, Strata Mechanics Research Inst. Krakow.

Lymberopuulos D. P., and Payatakes A. C., 1992, "Derivation of Topological, Geometrical and Correlational Properties of Porous Media from Pore Chart Analysis of Several Section Data," *Journal of Colloid and Interface Science,* Vol. 150, pp. 61–80.

Mei C. C., and Auriault J. L., 1991, "The Effect of Weak Inertia on Flow through a Porous Medium," *Journal of Fluid Mechanics,* Vol. 222, pp. 647–663.

Moffat H. K., 1964, "Viscous and Resistive Eddies Near a Sharp Corner," *Journal of Fluid Mechanics,* Vol. 18., pp. 1–18.

O'Brien V., 1972 "Closed Streamlines Associated with Channel Flow over a Cavity," *Physics of Fluids*, Vol. 15, pp. 2089–2097.

Payatakes A. C., and Neira M. A., 1977, "Model of the Constricted Unit Cell Type for Isotropic Granular Porous Media," *AIChE Journal,* Vol. 23, pp. 922–931.

Schönberger Ch., 1992 "Experimentelle Untersuchungen über schleichende Strömungen durch ein Rohr mit ringförmen Wandstrukturen," *Diplomarbeit,* Max-Planck-Institut für Strömungsforschung, Göttingen.

Schulte P. J., Gibson A. C., and Nobel P.S., 1989, "Water Flow in Vessels with Simple or Compound Perforation Plates," *Annals of Botany*, Vol. 64, pp. 171–180.

Stark K. P., 1972, "Numerical Study of the Nonlinear Laminar Regime Flow in an Idealized Porous Media," *International Association for Hydraulic Research*, Vol. 18, pp. 86–102

Stevenson J. F., 1973, "Flow in a Tube with Circumferential Wall Cavity," *ASME Journal of Applied Mechanics,* Vol. 40, pp. 355–360.

Taneda S., 1979, "Visualization of Separating Stokes Flow," *Journal of Physical Society of Japan*, Vol. 46, pp. 1935–1942.

Takematsu M., 1966, "Slow Viscous Flow past a Cavity," *Journal of Physical Society of Japan*, Vol. 21, No. 9, pp. 1816–1821.

Tutty O. R., 1988, "Flow in a Tube with a Small Side Branch," *Journal of Fluid Mechanics,* Vol. 191, pp. 79–109.

Zimmermann M. H., 1983, *Xylem Structure and Ascent of Sap,* Springer, Berlin, Heidelberg, New York, Tokyo.

Flow Measurements in a Fishtail Diffuser With Strong Curvature

M. I. Yaras
Associate Professor,
Department of Mechanical and
Aerospace Engineering,
Carleton University,
Ottawa, Ontario,
Canada K1S 5B6
e-mail: Metin_yaras@carleton.ca

The paper presents detailed measurements of the incompressible flow development in a large-scale 90 deg curved diffuser with strong curvature and significant streamwise variation in cross-sectional aspect ratio. The flow path approximates the so-called fishtail diffuser utilized on small gas turbine engines for the transition between the centrifugal impeller and the combustion chamber. Two variations of the inlet flow, differing in boundary layer thickness and turbulence intensity, are considered. Measurements consist of three components of velocity, static pressure and total pressure distributions at several cross-sectional planes throughout the diffusing bend. The development and mutual interaction of multiple pairs of streamwise vortices, redistribution of the streamwise flow under the influence of these vortices, the resultant streamwise variations in mass-averaged total-pressure and static pressure, and the effect of inlet conditions on these aspects of the flow are examined. The strengths of the vortical structures are found to be sensitive to the inlet flow conditions, with the inlet flow comprising a thinner boundary layer and lower turbulence intensity yielding stronger secondary flows. For both inlet conditions a pair of streamwise vortices develop rapidly within the bend, reaching their peak strength at about 30 deg into the bend. The development of a second pair of vortices commences downstream of this location and continues for the remainder of the bend. Little evidence of the first vortex pair remains at the exit of the diffusing bend. The mass-averaged total pressure loss is found to be insensitive to the range of inlet-flow variations considered herein. However, the rate of generation of this loss along the length of the diffusing bend differs between the two test cases. For the case with the thinner inlet boundary layer, stronger secondary flows result in larger distortion of the streamwise velocity field. Consequently, the static pressure recovery is somewhat lower for this test case. The difference between the streamwise distributions of measured and ideal static pressure is found to be primarily due to total pressure loss in the case of the thick inlet boundary layer. For the thin inlet boundary layer case, however, total pressure loss and flow distortion are observed to influence the pressure recovery by comparable amounts.

Introduction

Diffusing bends are used in a diverse range of industrial applications. One particular application, comprising the focus of the present investigation, is the case of small gas-turbine engines utilizing a centrifugal impeller as the last compressor stage. In this instance, the high-kinetic-energy radial flow at the impeller exit is to be efficiently diffused and redirected into a combustion chamber. In the pipe diffuser and fishtail diffuser configurations this task is accomplished by a series of diffusing passages wrapped around a radial-to-axial turn (Kenny, 1968; Reeves 1977; Blair and Russo, 1980). The diffusion and redirection must be achieved over the shortest possible length to avoid penalties in terms of engine diameter and weight. At the same time, it is essential to minimize total pressure losses and maintain minimal flow distortion at the diffuser exit, the latter constraint being imposed by the desire to maximize the static pressure recovery during diffusion and the combustion efficiency in the combustion chamber. Some current fishtail diffuser designs incorporate straightening vanes near the diffuser exit in an attempt to reduce the cross flows in the discharging flow at the expense of extra weight and manufacturing difficulties.

Despite the difficulty in establishing an optimum trade-off between the conflicting requirements of aerodynamic efficiency, compactness, and discharge conditions suitable for efficient combustion, very few studies have been conducted on the fundamental physics of the flow evolving in such geometries. The nature of the flow through straight diffusers is well understood and detailed performance charts for such configurations have been established (e.g., Dolan and Runstadler, 1973). Likewise, the development of streamwise vorticity and the associated redistribution of the streamwise flow as well as generation of losses in constant-area bends have been investigated fairly extensively for developed as well as developing flows (e.g., Rowe, 1970; Agrawal et al., 1978; Humphrey et al., 1981; Taylor et al., 1982). In contrast, relatively few studies have considered the case of simultaneous diffusion and turning of flows. Among them are the works of Fox and Kline (1962), Sagi and Johnston (1967), Parsons and Hill (1973), McMillan (1982), and Wellborn et al. (1992). However, none of these studies considered strong curvature or substantial streamwise variation in the cross-sectional aspect ratio, both of which are characteristics of fishtail diffusers. The work of Blair and Russo (1980) is one study that investigated such geometries. In that study, however, the extent of the measurements did not allow for a detailed account of the flow development. The first phase of the present investigation (Yaras, 1996) consisted of measurements at the inlet and exit of a scaled up fishtail diffuser typical of those utilized on small aero-engines. Those measurements quantified the extent of three-dimensionality of the flow discharging from the diffuser, the overall total pressure loss, the static pressure recovery, as well as the effects of inlet mean-flow nonuniformities on these aspects of the flow. However, absence of measurements within the diffuser prevented identification of the flow phenomena responsi-

Contributed by the Fluids Engineering Division for publication in the JOURNAL OF FLUIDS ENGINEERING. Manuscript received by the Fluids Engineering Division September 15, 1998; revised manuscript received February 11, 1999. Associate Technical Editor: D. R. Williams.

ble for some of the observed trends. The present work consists of detailed measurements at several cross sections throughout the diffuser, providing a clear account of the flow evolution.

Flows with substantial streamline curvature and secondary flows developing under the influence of cross-stream pressure gradients continue to defy precise numerical simulation, primarily due to the limitations of current Reynolds-stress models. In addition to providing the basis for understanding the physics of the flow in fishtail diffusers, by virtue of its detail and accuracy, the present set of measurements forms a reliable test case for future numerical simulation efforts.

Fishtail diffusers on gas-turbine engines experience compressible and unsteady inlet flow conditions with highly nonuniform spatial distributions of velocity and elevated levels of turbulence. The present work examines the effect of spatial distribution of the inlet velocity and to some extent that of the inlet turbulence intensity on the development of the flow in the diffuser. Investigation of the effects of compressibility and unsteadiness is envisaged in subsequent phases of this project.

Experimental Apparatus

Diffuser Test Section. Measurements were carried out in the test rig shown schematically in Fig. 1. Longitudinally, the diffusing part of the rig consists of four sections, with each section further partitioned into symmetric upper and lower halves. The first section provides a conical flow path with an inlet diameter of 193.7 mm and an included angle of 6.15 degrees. In the subsequent three sections the flow path turns by 90 degrees along a centerline with a radius that is 4.36 times the inlet diameter of the diffuser. In these sections, the cross section of the flow path becomes increasingly more oblong with downstream distance while the cross-sectional area continues to increase linearly until it reaches a size that is 3.42 times the inlet area of the diffuser. Beyond the 90 deg diffusing bend, the cross section of the flow path remains unchanged through the tail duct. Pertinent geometric information on the flow path is summarized in Fig. 2(*b*). This geometry approximates a scaled-up version of typical fishtail diffuser geometries utilized in small gas-turbine engines, with the inlet of the test rig corresponding to the throat of these in-service diffusers. Further details on the design and manufacturing of the test rig are given by Yaras (1996).

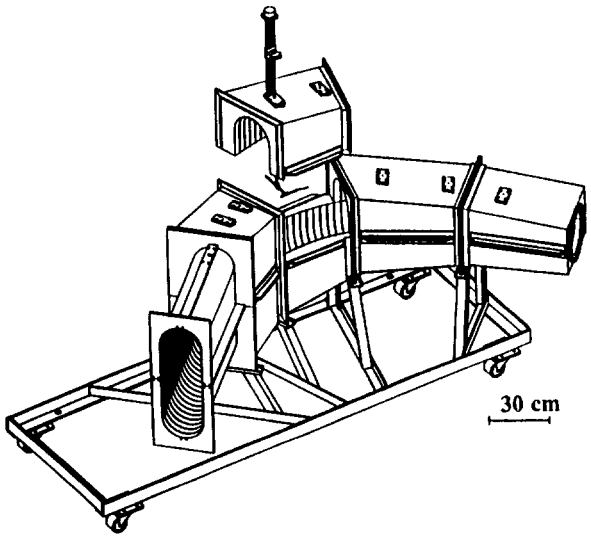

Fig. 1 Schematic of the fishtail diffuser test section

An open-circuit wind tunnel is used as the wind source for the diffuser rig. A variable-speed centrifugal fan draws in ambient air and delivers it through a honeycomb into a circular settling chamber containing three screens. At the exit of the settling chamber the air passes through two contractions of 9:1 and 4.4:1 contraction ratios followed by a PVC pipe of 7.87 length-to-diameter ratio that leads to the inlet of the diffuser test rig. For the test case with thicker boundary layer at the diffuser inlet, a trip ring ($\Delta r_t/r_A = 0.125$, $\Delta x_t/\Delta r_t = 0.8$) was installed at the inlet of the pipe.

Instrumentation. All pressures were measured with capacitive-type pressure transducers. The transducer outputs were converted to digital form with 12-bit resolution. A motorized traversing gear mounted on the inlet pipe allowed radial traverse of the diffuser inlet flow. This measurement plane (Plane A) is located sufficiently upstream of the diffuser inlet to avoid any influence of the diffuser on the local static pressure profile. Radial distribution of the velocity was measured at twelve evenly-spaced

Nomenclature

A = local cross-sectional area
B = blockage factor = $1 - (\bar{V}/V_{CL})_A$
C_P = $(P - P_A)/\frac{1}{2}\rho V_{CLA}^2$ = static pressure coefficient
$\tilde{C}_P$ = $(\tilde{P} - P_A)/\frac{1}{2}\rho\alpha_A\bar{V}_A^2$ = mass-averaged static pressure coefficient
C_{PO} = $[(P_O)_{CLA} - P_O]/\frac{1}{2}\rho V_{CLA}^2$ = total pressure coefficient
$\tilde{C}_{PO}$ = $[(P_O)_{CLA} - \tilde{P}_O]/\frac{1}{2}\rho\alpha_A\bar{V}_A^2$ = mass-averaged total pressure coefficient
$\tilde{C}_{qs}$ = $\frac{1}{2}\rho(\tilde{V}_y^2 + \tilde{V}_z^2)/\frac{1}{2}\rho\alpha_A\bar{V}_A^2$ = mass-averaged secondary kinetic energy coefficient
h = half-height of the diffuser side walls; refer to Fig. 2(*a*)
L = diffuser centerline length
P = static pressure
P_O = stagnation pressure
r = radius of the upper and lower walls; refer to Fig. 2(*a*)
Tu = turbulence intensity
V = velocity
x, y, z = orthogonal curvilinear coordinates; x axis is tangent to the centerline of the flow path with $x = 0$ at the inlet of the diffuser; refer to Fig. 2(*a*)
α = $(1/A\bar{V}_x^3)\int V^2V_x dA$ = kinetic energy factor
α_p = $(1/A\bar{V}_x^3)\int V_x^3 dA$ = primary-flow kinetic energy factor
α_{xy}, α_{xz} = flow direction in the x-y and x-z planes, respectively
Δr_t = height of the trip ring
Δx_t = thickness of the trip ring
δ = boundary layer thickness
δ^* = $\int_{r_A}^{r_A-\delta}(1 - V/V_e)dr$ = boundary layer displacement thickness
θ = $\int_{r_A}^{r_A-\delta}(1 - V/V_e)V/V_e dr$ = boundary layer momentum thickness; also used for the turning angle of the diffuser centerline; refer to Fig. 2(*a*)
ρ = density
φ = circumferential coordinate; refer to Fig. 2(*a*)
ω = vorticity, nondimensionalized by the radius and V_{CL} of Plane A

Subscripts

CL = centerline
e = boundary-layer edge value
x, y, z = components in the x, y and z directions
A, B = cross-sectional measurement Planes A and B; refer to Table 1

Superscripts

$\bar{}$ = area-averaged quantity
$\tilde{}$ = mass-averaged quantity

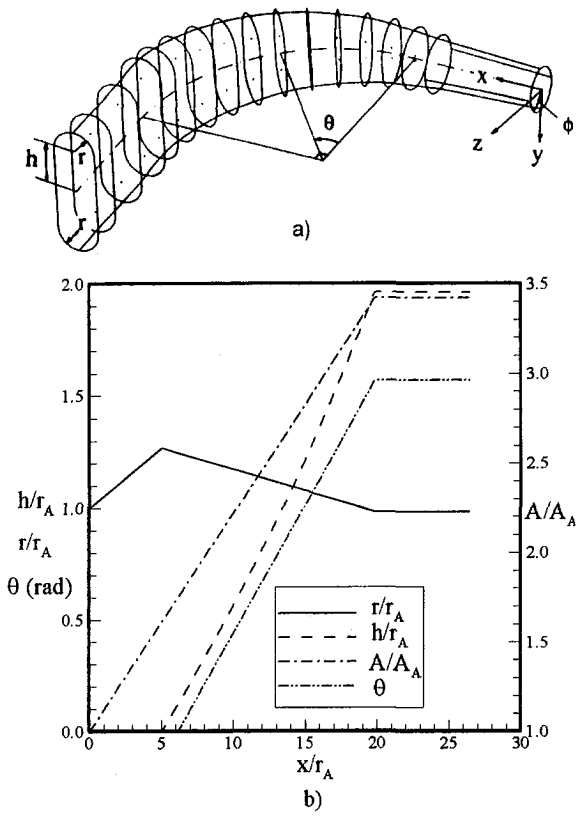

Fig. 2 Geometry of the diffuser flow path

circumferential positions. A pitot probe of 0.5 mm tip diameter was used for these measurements. The static pressure was obtained from a pressure tap on the pipe wall located at the same streamwise position.

Measurements of total pressure, static pressure, and three components of velocity were carried out at four cross-sectional planes within the diffuser using a miniature seven-hole pressure probe in non-nulling mode. The probe tip diameter is 2.1 mm and is of conical geometry with an included angle of 60 degrees. The probe pressures were measured through a scanning valve. The locations of the measurement planes are listed in Table 1. The number of data points in these planes varied from about 700 points in Plane B to about 1100 points in Plane E, providing very detailed resolution of the flow. It would have been sufficient to document one half of each cross-sectional plane since the diffuser geometry is symmetric with respect to the x-z plane (Fig. 2) and the inlet flow was fairly axisymmetric for both of the test cases considered. However, preliminary analysis of the results showed slightly larger discrepancy between the mass-flow rates of Planes A to E when the integration was performed over only one half of each plane. The discrepancy was more noticeable for Case II, the test case with relatively larger circumferential nonuniformity in Plane A. This would have increased the uncertainty in the mass-averaged flow parameters presented herein, overshadowing some of the real trends in these quantities. Therefore, complete measurement of each cross-sectional plane was opted for, yielding integrated mass-flow rates for Planes A to E that remained within one percent of each other.

The seven-hole probe was calibrated in 3 deg steps up to 27 degrees of flow misalignment and in 5 deg steps from 25 to 50 degrees of flow misalignment. The calibration was checked regularly during the experiments. The calibration was performed at a Reynolds number corresponding to the mean velocity in Plane D of the diffuser. Tests on the variation of the probe calibration with Reynolds number showed only small sensitivity.

An uncertainty analysis, as described by Moffat (1982), was performed to establish the error estimates for the dynamic and total pressures and the local flow direction measured with the seven-hole probe. In this analysis, first the uncertainty in the seven pressures of the probe was evaluated. This step accounted for repeatability errors for the measurements in the diffuser test rig as well as for propagation of uncertainties such as those associated with the pressure-transducer calibration curves. The corresponding error estimates in the measured flow variables were then combined with the errors introduced by the biquadratic interpolation scheme used in conjunction with the calibration curves of the probe. Based on this analysis, the velocity and total pressure extracted from the probe are estimated to be accurate to within one percent of the diffuser-inlet centerline velocity and dynamic pressure, respectively. Outside the stalled region of the diffuser flow, the error in the measured flow direction is estimated to be within ± 0.9 degrees.

The design of the test rig allows for motorized traverse of the probe in the y or z directions. For instance, with the traversing gear mounted as shown in Fig. 1, motorized traverses are performed in the y direction. For traversing a complete cross-sectional plane in this configuration, the probe is repositioned manually along the z direction after each motorized traverse in the y direction. Multiple mounting ports for the traversing gear, distributed along the length of the diffuser, allow probe access to cross-sectional planes throughout the diffuser. Similar mounting ports exist on the outer wall of the lower half of each section, providing for motorized traverse in the z direction. When not in use, the probe stem and pressure tubing access holes, each of 6.4 mm diameter, are sealed from the inside with thin adhesive tape. The seven-hole probe data presented in this paper were obtained with motorized probe motion in the y direction.

Once the traversing gear is mounted at the appropriate port, fine adjustment of the probe tip position in the streamwise (x) direction is accomplished by sliding the probe in its holder relative to the probe stem. For motorized traverses in the y direction, manual positioning along the z axis is performed with the aid of an alignment/positioning device designed for use on this test rig (Saroch, 1996). This device also provides for referencing the probe position in the y direction and establishing its orientation relative to the curvilinear reference axes shown in Fig. 2(a). The probe position and its orientation relative to the reference axes are estimated to be accurate to within ± 0.20 mm and ± 0.1 degrees, respectively.

Experimental Results and Discussion

Diffuser Inlet Flow. All measurements were performed at a Reynolds number of $7.25 \pm 0.1 \times 10^5$ based on the diameter and the spatially-averaged velocity at the diffuser inlet. The corresponding Mach number was less than 0.2.

The flow development through the diffuser was measured for two variations of the inlet boundary layer thickness ($B = 0.89$, 0.94). These configurations were among the five test cases for which the diffuser exit flow was measured (Yaras, 1996). In that study, distinct variations in the streamwise and secondary flow pattern of the discharging flow was observed particularly between these two configurations, hence their selection for the present investigation. The integral boundary layer parameters extracted from pitot-probe measurements in Plane A are given in Fig. 3. The

Table 1 Location of the measurement planes

	x/L	θ
Plane A	−0.076	0.0°
Plane B	0.190	0.0°
Plane C	0.416	31.7°
Plane D	0.599	63.5°
Plane E	0.752	90.0°

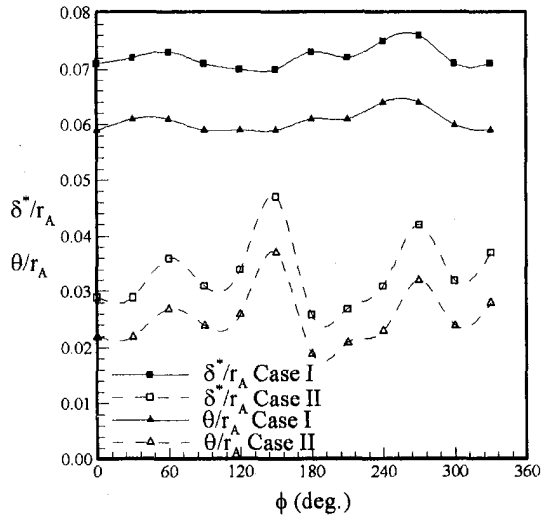

Fig. 3 Integral boundary-layer parameters in Plane A (uncertainty in $\delta^*/r_A = \mp 0.002$ and in $\theta/r_A = \mp 0.002$)

circumferential distributions of the displacement and momentum thicknesses in Case II are not as uniform as those in Case I. This variation is the result of a small asymmetric step that existed at the joint of the contraction and the approach pipe in Case II. The boundary-layer shape factor, δ^*/θ, is within the range of 1.2 to 1.35 for both test cases. The velocity profiles shown in Fig. 4 are typical of the profiles measured at all circumferential positions. The velocity distribution outside the boundary layer is seen to be essentially uniform, although the extent of this inviscid core is evidently quite small for Case I. Spatial variations in the core-velocity magnitude of Case II remained within ±0.5 percent of the centerline velocity, V_{CL}. Seven-hole probe measurements in the same measurement plane confirmed that the velocity distribution remained uniaxial for both test cases.

Significantly higher levels of turbulence intensity is observed in Fig. 4 for the case with a trip ring installed at the pipe entrance. These distributions of turbulence intensity were measured with a single-hot-wire probe. Increased turbulence at the inlet of straight diffusers is known to enhance static pressure recovery (Cutler and Johnston, 1981; Klein, 1981). Augmented mixing caused by increased freestream turbulence would tend to delay separation and reduce blockage at the outlet, thereby yielding improved pressure recovery. In curved diffusers this effect of turbulence is likely to be diminished since secondary flows caused by the flow turning would have a significant influence on the boundary layer development along the diffuser walls. On the other hand, the flow path on the present test rig is of straight, conical geometry prior to the diffusing bend. Changes in the turbulence intensity of the incoming flow may therefore influence the flow in the diffusing bend through its effect on the boundary layer development in the conical section.

Flow Development in the Diffuser. In this section the development of the diffuser flow is discussed through examination of several flow quantities. Figures 5(*a*) and 6(*a*) illustrate the streamwise and cross-stream velocity distributions at four cross-sectional planes for each of the test cases. The streamwise (x) velocity distributions are nondimensionalized by the spatially averaged value of the streamwise velocity within the corresponding measurement planes. Reference vectors for these mean velocities are also given in the figure to provide a sense for the relative magnitudes of the secondary velocities, i.e. flow angularity, as well as the overall streamwise deceleration through the diffusing bend. Corresponding streamwise vorticity distributions, extracted from the velocity data, are presented in Figs. 5(*b*) and 6(*b*). The vorticity is nondimensionalized by the radius and centerline velocity of Plane A. In order to clearly illustrate the distribution of vorticity for the bulk of the flow in each plane, the range of the vorticity scale for Plane B was chosen to be twice as large as that of the remaining planes. For the same reason, these ranges were selected to exclude the considerably larger magnitudes of streamwise vorticity associated with the thin boundary layer along the walls. The peak magnitude of the nondimensional streamwise vorticity in this layer was roughly 1, 15, 10 and 1 for planes B to E respectively. Finally, distributions of the total pressure coefficient are presented in Fig. 5(*c*) and 6(*c*).

Plane B. The diffuser flow path is of conical shape up to Plane B. Comparison of the axial velocity distributions for the two test cases in this measurement plane reveals somewhat higher circumferential nonuniformity for Case II. This is consistent with the corresponding circumferential distributions of the boundary layer thickness in Plane A. Relatively higher axial velocity is evident in the vicinity of the wall for Case I. This is due to augmented momentum exchange between the fluid near the wall and the remainder of the flow caused by higher levels of turbulence in this test case (Fig. 4).

Deviation of the velocity vectors from the axial direction would be expected in keeping with the conical flow path preceding this measurement plane. However, the observed secondary velocity distribution does not follow an axisymmetric pattern, exhibiting some upstream influence of the cross-stream pressure gradients developing in the 90-degree bend which commences slightly downstream of Plane B. This effect is also evident in the vorticity plots where streamwise vorticity of opposite sign is observed along the upper and lower portions of the diffuser wall. In any event, the flow angularity in this measurement plane is quite small, with the flow remaining within three degrees of the axial direction.

The total pressure distribution in Plane B shows a significant region of loss-free fluid for Case II. For Case I, however, an inviscid core is no longer present due to the thicker boundary layer at the diffuser entrance and enhanced mixing between the core and the boundary-layer fluid induced by relatively high levels of turbulence.

Plane C. Strong secondary flows associated with a pair of streamwise vortices of opposite sense of rotation is evident in Plane C. The formation of such vortices is well known from studies in constant-area bends (e.g., Rowe, 1970, Agrawal et al., 1978). Comparison of the cross flows or the streamwise vorticity for the two test cases indicates notably stronger vortices for Case II, the case with a thinner boundary layer at the diffuser inlet

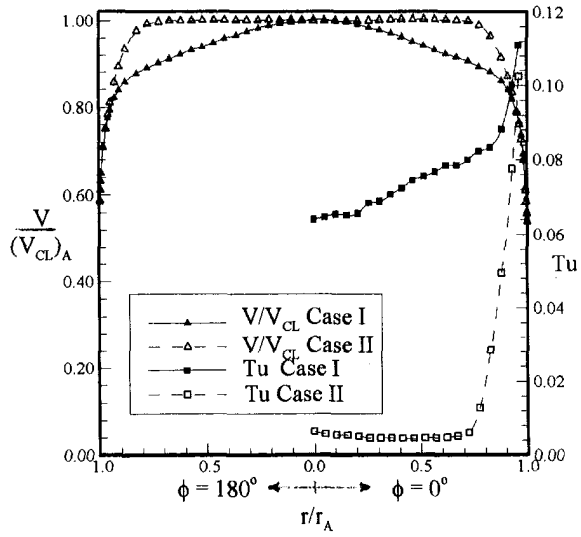

Fig. 4 Velocity and turbulence profiles in Plane A (uncertainty in $V/V_{CL,A} = \mp 0.007$, and in turbulence intensity ±5 percent)

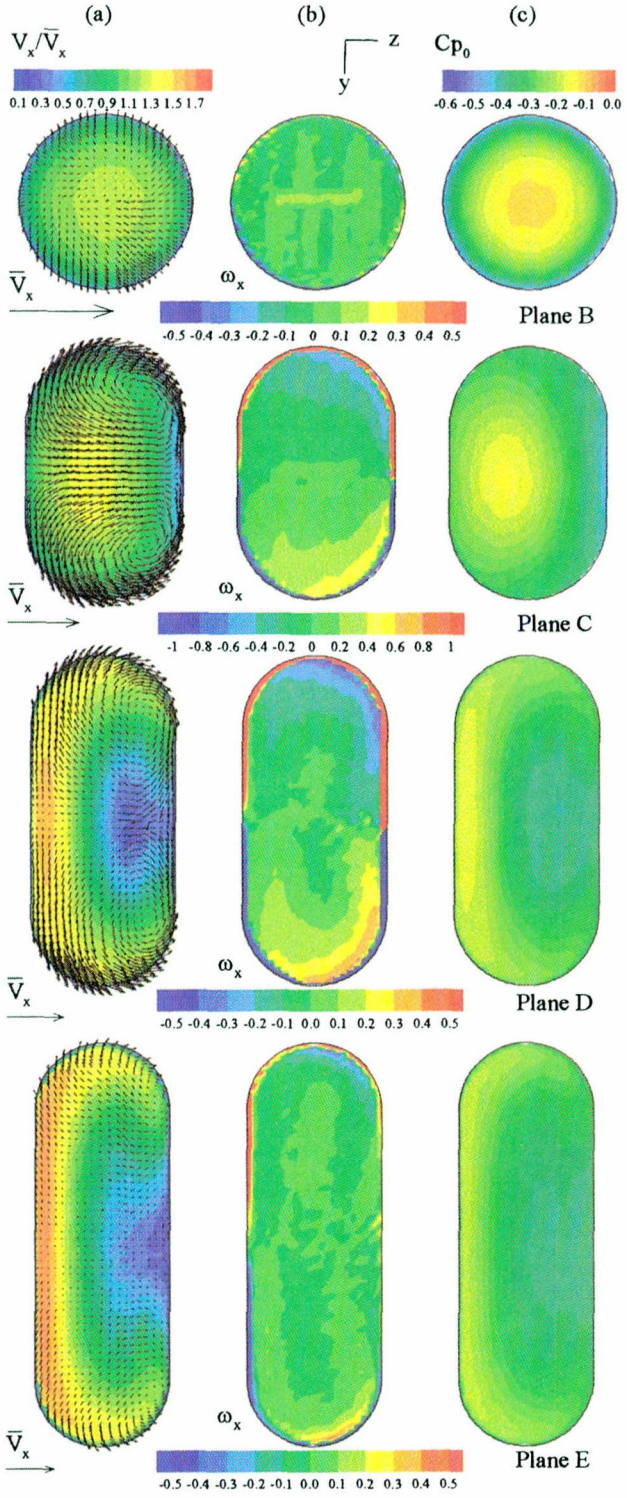

Fig. 5 Distributions of the streamwise and secondary velocity components (*a*), streamwise vorticity (*b*) and total-pressure coefficient (*c*) for Case I (uncertainties: $V/V_{CL\,A} = \mp 0.01$; outside the stalled region, α_{xy}, $\alpha_{xz} = \mp 0.9°$; $\omega_x = \mp 0.05$; $C_{PO} = \mp 0.01(\frac{1}{2}\rho V^2_{CL\,A})$)

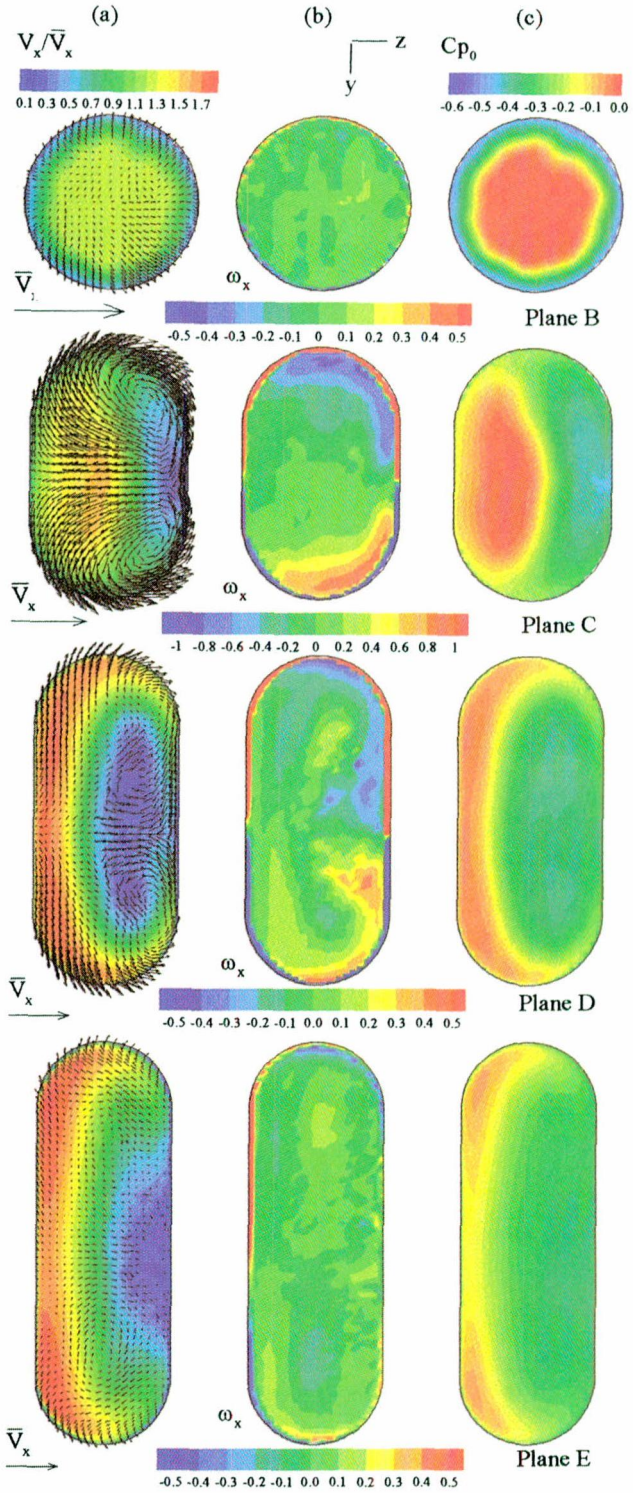

Fig. 6 Distributions of the streamwise and secondary velocity components (*a*), streamwise vorticity (*b*) and total-pressure coefficient (*c*) for Case II (uncertainties: $V/V_{CL\,A} = \mp 0.01$; outside the stalled region, α_{xy}, $\alpha_{xz} = \mp 0.9°$; $\omega_x = \mp 0.05$; $C_{PO} = \mp 0.01(\frac{1}{2}\rho V^2_{CL\,A})$)

(Plane A). In contrast, the work of Taylor et al. (1982) on constant-area bends showed the strength of these vortices to increase with increasing boundary layer thickness at the inlet. The initial development of streamwise vorticity in a bend is due to the vortex lines within the inlet boundary layer developing a streamwise component. In the present diffusing bend, the segments of the circumferential vortex lines lying in the plane of the bend, i.e., along the upper and lower walls, are expected to rotate during the initial portion of the bend resulting in the development of streamwise vorticity. Through inviscid flow theory, the magnitude of this streamwise vorticity can be related to the flow turning and the amount of vorticity contained within the inlet boundary layer in the plane of the bend (e.g., Squire and Winter, 1951; Hawthorne, 1951). The overall circulation within the boundary layer in Plane

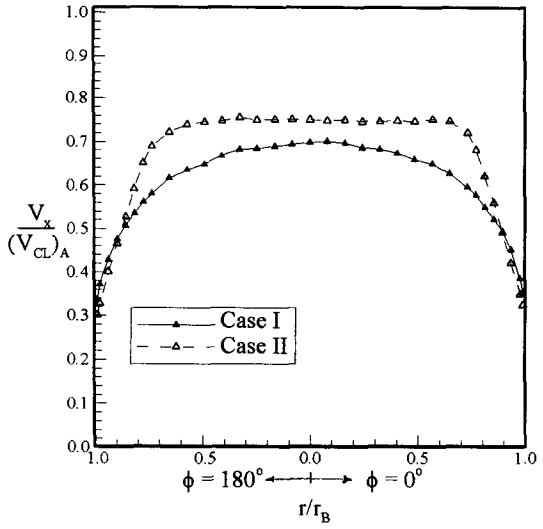

Fig. 7 Velocity profiles at $\varphi = 0°$ and $\varphi = 180°$ in Plane B (uncertainty in $V/V_{CL_A} = \mp 0.01$)

A is dictated by the core velocity. However, the magnitude of this circulation is altered by the adverse streamwise pressure gradient experienced by the flow as it passes through the conical portion of the diffuser preceding the 90-degree bend. The axial velocity profiles given in Fig. 7 indicate that the bulk of the flow has decelerated to a larger extent in Case I due to the fuller boundary layer velocity profile in this test case. Thus, a larger portion of the vorticity contained within the boundary layer of Plane A is destructed between Planes A and B in Case I compared to Case II. The lower levels of streamwise vorticity associated with the vortex pair in Case I may thus be attributed to this difference in the overall vorticity contained in the boundary layer just upstream of the bend.

Considerable redistribution of the streamwise flow is evident under the influence of the cross flows induced by the pair of vortices. Cross-stream pressure gradients set up by this redistribution result in substantial streamwise vorticity production within a thin layer of fluid along the walls. This vorticity sheet is clearly visible in Figs. 5(*b*) and 6(*b*) and, as was noted earlier, the vorticity levels in this sheet are significantly larger than the limits of the vorticity scales given on these figures. In each symmetric half of the measurement plane, interaction between this vorticity sheet and the adjacent vortex comprising vorticity of opposite sign is likely one of the mechanisms influencing the overall circulation of this vortex as it evolves in the streamwise direction. In fact, this interaction may help explain the trend of increasing vortex strength with increasing inlet boundary layer thickness observed by Taylor et al. (1982). Provided the overall vorticity of the inlet boundary layer is maintained, increasing the thickness of the boundary layer would merely spread the vorticity lines within the boundary layer. It is plausible that this would lead to reduced interaction between these vorticity lines (once they develop streamwise components) and the aforementioned vorticity sheet developing along the walls of the bend. In the present study, this effect appears to be more than offset by the differing circulation within the boundary layer upstream of the bend between the two test cases.

The net radial mass flux associated with the movement of high-momentum fluid towards the outer wall in Case II is seen to have produced a region of fluid with very small streamwise momentum along the inner wall (Fig. 6(*a*)). Such a region of low-momentum fluid is also evident in Case I (Fig. 5(*a*)) but is much thinner due to weaker cross flows and lesser gradients of streamwise momentum in Plane B of this case. Finally, the distributions of the total pressure coefficient in Figs. 5(*c*) and 6(*c*) reveal that the faster moving fluid in the outer half, originating from the core region of Plane B, has experienced very little loss between the two measurement planes.

Plane D. Secondary-flow velocities in Plane D are observed to be considerably smaller than those in Plane C, particularly for Case II. This is consistent with the reduced levels of vorticity contained in the vortex pair compared to the levels in Plane C. As was noted earlier, interaction between the vortex pair and the vorticity sheet along the walls is one mechanism that may contribute to this diminishing strength of the vortex pair. Comparison of the vorticity distributions in Planes C and D indicates that the vorticity attributed to the vortex pair is convected along the inner wall towards the symmetry plane under the influence of the cross flows. This convection is seen to have brought the pair closer to each other, particularly for Case II where the cross flows are stronger. Thus, in this instance mutual interaction of the pair is another possible mechanism for their diminishing strength.

In constant-area ducts with bend radius to hydraulic diameter ratios of 2.3 and 12, Taylor et al. (1982) and Rowe (1970) observed cross flows to reach their peak levels at 60 and 30 degrees into the bend, respectively. On the other hand, in the present diffusing bend, with the bend radius to hydraulic diameter ratio varying from 4.36 at the inlet to 2.36 at the exit, peak secondary flows are seen to occur at about 30 degrees into the bend. Based on these trends, it seems likely that a factor additional to the bend curvature contributed to the vortex pair reaching its peak strength at a notably smaller angular distance into the bend in the current experiments than in the work of Taylor et al. Streamwise deceleration of the flow through the diffusing bend would tend to increase the duration of interaction between regions of fluid of opposite signs of vorticity noted in the previous paragraph. One might expect this effect to reduce the peak strength of the vortex pair and cause this peak to occur at a smaller angular distance into the bend.

In each symmetric half of the measurement plane, there is evidence of a second vortex embedded in the first one, and comprising vorticity with an opposite sense of rotation. Vorticity with this sense of rotation has been observed in previous studies in constant-area bends (e.g., Rowe, 1970; Agrawal et al., 1978; Taylor et al., 1982). While this vorticity is of the same sign as that associated with the thin vorticity sheet along the inner wall, there is no evidence that it is merely the result of fluid within this sheet being convected by the cross flows induced by the first vortex pair. It is more likely due to streamwise vorticity production under the influence of cross-stream pressure gradients. In fact, the pressure distributions in Figs. 5(*c*) and 6(*c*) reveal that such production of vorticity must have started just downstream of Plane C. For instance, the fluid in the upper and lower portions of Plane C for Case II clearly experiences pressure gradients suitable for the production of vorticity with this rotational sense. This second vortex pair would be expected to be somewhat weaker for Case I due to the relatively smaller cross-stream pressure gradients prevailing in this case. Comparison of the vorticity distributions in Plane D for the two test cases confirms this anticipated trend.

Further, redistribution of streamwise momentum by the cross flows between Planes C and D is seen to have caused considerable growth of the low-momentum flow region by the inner wall, especially for Case II. At the same time, fluid of somewhat higher momentum convected by the cross flows has formed a thin layer along the inner wall, effectively lifting the region of low momentum fluid off the wall. Finally, examination of the total pressure distribution in this plane reveals that the high total pressure core fluid in Plane B, now spread along the outer wall, has continued to experience little loss between planes C and D.

Plane E. Vorticity plots for this plane reveal significantly reduced levels of streamwise vorticity for the first vortex pair except for narrow strips along the upper and lower walls. This is consistent with the anticipated destruction of such vorticity under the influence of cross-stream pressure gradients prevailing in this region of the flow. On the other hand, the second pair of vortices,

first observed in Plane D, are now somewhat more established. In accordance with this vorticity distribution, the secondary velocities in Figs. 5(*a*) and 6(*a*) show a flow pattern dominantly influenced by the second pair of vortices, particularly for Case II.

The distribution of streamwise velocity resembles that of Plane D with a notable region of low momentum fluid by the inner wall. A slight reduction in the relative extent of this low-momentum region is evident between these planes, particularly for Case II. The layer of relatively high-momentum fluid by the inner wall that was observed in Plane D is no longer present. This is expected since the secondary flows induced by the first vortex pair that were responsible for this layer have significantly diminished at this streamwise position. In fact, in Case II fluid of high streamwise velocity along the upper and lower walls of Plane D has now been pushed back toward the outer wall by the cross flows of the second vortex pair.

Mass-Averaged Quantities. Applying the conservation of energy principle to the flow between the inlet plane and a cross section inside the diffuser yields

$$P_A + \frac{\rho}{2}\alpha_A \bar{V}_{x_A}^2 = \tilde{P} + \frac{\rho}{2}\alpha \bar{V}_x^2 + (\tilde{P}_{O_A} - \tilde{P}_O) \tag{1}$$

where α is the kinetic energy factor defined as

$$\alpha = \frac{1}{A\bar{V}_x^3}\int V^2 V_x dA \tag{2}$$

Writing Eq. (1) in terms of pressure coefficients yields,

$$\tilde{C}_P = 1 - \frac{\alpha}{\alpha_A}\left(\frac{\bar{V}_x}{\bar{V}_{x_A}}\right)^2 + (\tilde{C}_{P_O} - \tilde{C}_{P_{O_A}}) \tag{3}$$

The kinetic energy factor is an indicator of the excess kinetic energy of a flow compared to a unidirectional plug profile of the same flow rate. Through Eq. (3), stagnation pressure loss and nonuniformity of the velocity field are seen to be the two mechanisms that may be responsible for the less-than-ideal pressure recovery of a diffuser.

Streamwise variation of the mass-averaged total pressure coefficient in Fig. 8(*a*) displays somewhat higher loss generation for Case I within the conical path preceding the bend. This is expected in light of the significantly smaller extent of the inviscid core and elevated levels of turbulence at the diffuser inlet of this case. Within the initial 30 deg portion of the bend, the flow in both test cases experiences the same amount of pressure loss despite the development of stronger cross flows and larger gradients of streamwise velocity in Case II. Possible mechanisms that may contribute to the generation of loss are the development of the boundary layer along the walls and mixing within the bulk of the flow induced by cross flows and gradients of the streamwise velocity. It therefore follows that the development of the boundary layer on the walls of the bend is likely the dominant loss generation mechanism in this instance. In the remaining 60 deg of the bend, the flow in Case II experiences somewhat higher loss. In this portion of the bend, notably higher magnitudes of streamwise velocity are observed along the outer wall in this test case. The resultant higher levels of shear along this wall is likely the primary factor responsible for this difference in the generated loss. Distribution of the mass-averaged secondary kinetic energy coefficient shown in the same figure (scaled up by a factor of 10) suggests that dissipation of the secondary kinetic energy between $x/L = 0.42$ and $x/L = 0.6$, which is higher for Case II, contributes to this difference in losses as well. Interestingly, the excess loss within the last 60 degrees of the bend for Case II appears to offset the excess loss generated in the conical section for Case I, resulting in essentially the same amount of overall pressure loss for both test cases.

Slightly higher pressure recovery is evident throughout the

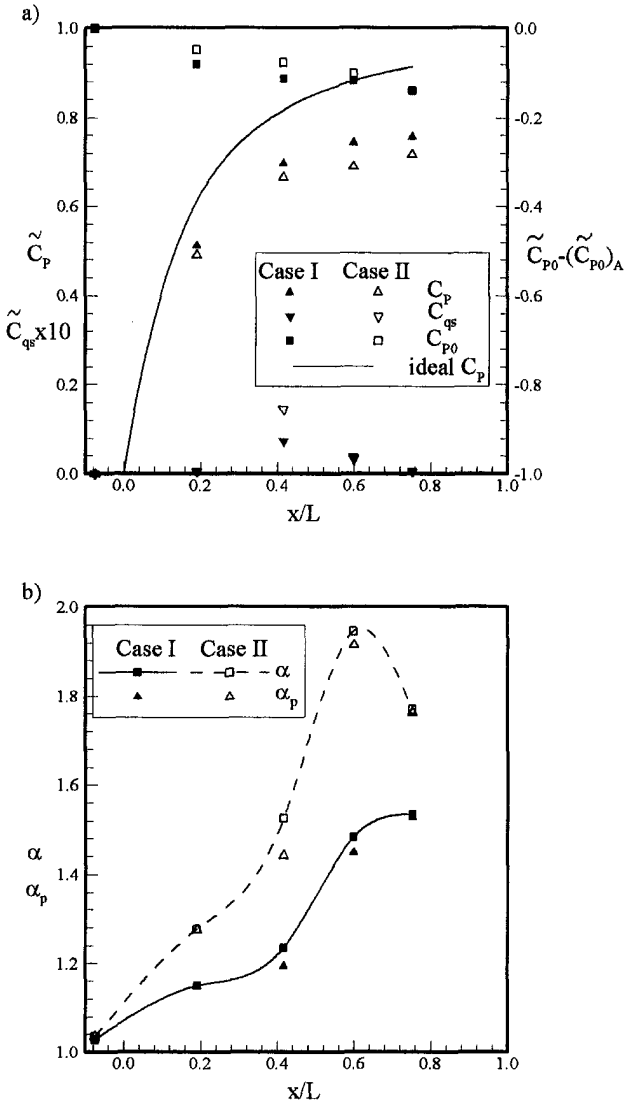

Fig. 8 (*a*) Distributions of mass-averaged quantities (uncertainties: $\tilde{C}_{P_{OA}} = \mp 0.005$, $\tilde{C}_{P_O} = \mp 0.01$, $\tilde{C}_P = \mp 0.005$, $\tilde{C}_{qs} = \mp 0.004$) (*b*) distribution of the kinetic energy factors (uncertainty in α, $\alpha_p = \mp 0.05$)

diffuser for Case I despite the observed trends in total pressure losses. Evidently, considerably larger nonuniformity of the flow in Case II, apparent in the relative values of the kinetic energy factor in Fig. 8(*b*), more than offsets the difference in the net total pressure loss between corresponding measurement planes of the two cases, yielding lower pressure recovery for every measurement plane of Case II.

As indicated by Eq. (3), flow nonuniformity and losses are the two mechanisms that may cause deviation from ideal pressure recovery. For Case I, the deviation of the measured static pressure distribution from the ideal pressure rise curve in Fig. 8(*a*) is seen to be quite close to the corresponding amounts of net total pressure loss shown on the same figure. Thus, total pressure loss is the primary cause of less-than-ideal pressure rise for each measurement plane of this test case. The same comparison for Case II suggests comparable contributions of loss generation and flow distortion to the deficiency in pressure rise for all measurement planes.

In Fig. 8(*b*) a continuous increase in the kinetic energy factor, α, is observed up to about $x/L = 0.6$, with the rate of increase being considerably higher for Case II. Between Planes D and E, the value of α appears to level off for Case I whereas a notable decrease is observed for Case II. These trends in α are consistent with case-

to-case and streamwise variations in the nonuniformity of the axial velocity observed in Figs. 5(*a*) and 6(*a*). Comparison of the trends in the kinetic energy factor associated with this component of velocity, α_p, with those of α (Fig. 8(*b*)) confirms that nonuniform distribution of the axial velocity rather than secondary flows is the primary factor responsible for the observed trends in α.

Conclusions

The general flow pattern within a diffusing bend of strong curvature has been observed to be similar to that occurring in constant-area bends. The dominant vortical structures within the initial portion of the diffusing bend consist of the well-known pair of counter rotating vortices, carrying fluid along the upper and lower walls towards the inner wall. The secondary flows induced by this pair of vortices are observed to reach maximum strength at about 30 degrees into the diffusing bend and are found to be considerably stronger for the case with a thinner boundary layer and lower freestream turbulence intensity at the inlet. This difference in the strength of these vortices is argued to be due to different amounts of vorticity adjustment the boundary layers experience within the conical section preceding the bend. The diffusing nature of the flow appears to result in these vortices reaching their peak strength earlier in the bend than in the case of constant-area bends of similar curvature. Little evidence of these vortices remains at the 90 deg plane. A second pair of vortices embedded within the first pair are observed to develop within the second half of the bend and are generally more pronounced for the thinner inlet boundary layer case. For this test case, stronger secondary flows throughout the bend result in more extensive redistribution of the streamwise flow.

Somewhat higher total-pressure loss is observed within the conical section preceding the diffusing bend for the thick inlet boundary layer case. On the other hand, loss generation within the last 60 degrees of the bend is found to be slightly higher for the thin inlet boundary layer case. These differences appear to offset each other, yielding the same amount of overall loss for both test cases. Despite relatively lower net total pressure loss within the diffusing bend (Planes B, C, and D) for the thin inlet boundary layer case, the mass-averaged static pressure at each measurement plane is lower for this test case. This is due to significantly larger levels of flow distortion observed in this test case.

For the thick inlet boundary layer case, the difference between measured and ideal static pressure distributions along the diffusing bend is found to be primarily due to total pressure losses. For the thin inlet boundary layer case, flow distortion and loss generation influence the streamwise static pressure distribution by comparable amounts.

Acknowledgments

The author gratefully acknowledges the research grant provided by the Natural Sciences and Engineering Research Council of Canada in support of this project.

References

Agrawal, Y., Talbot, L., and Gong, K., 1978, "Laser Anemometry Study of Flow Development in Curved Circular Pipes," *Journal of Fluid Mechanics,* Vol. 85, pp. 497–518.

Blair, L. W., and Russo, C. J., 1980, "Compact Diffusers for Centrifugal Compressors," AIAA-80-1077, presented at the AIAA/SAE/ASME 16th Joint Propulsion Conference.

Cutler, A. D., and Johnston, J. P., 1981, "The Effects of Inlet Conditions on the Performance of Straight-Walled Diffusers at Low Subsonic Mach Numbers—A Review," Stanford University Report PD-26.

Dolan, F. X., and Runstadler, P. W., 1973, "Pressure Recovery Performance of Conical Diffusers at High Subsonic Mach Numbers," NASA Contractor Report 2299.

Fox, R. W., and Kline, S. J., 1962, "Flow Regimes in Curved Subsonic Diffusers," ASME *Journal of Basic Engineering,* Vol. 84, pp. 303–316.

Hawthorne, W. R., 1951, "Secondary Circulation in Fluid Flow," *Proceedings of the Royal Society,* Series A, Vol. 206, pp. 374–387.

Humphrey, J. A. C., Whitelaw, J. H., and Yee, G., 1981, "Turbulent Flow in a Square Duct with Strong Curvature," *Journal of Fluid Mechanics,* Vol. 103, pp. 443–463.

Kenny, D. P., 1968, "A Novel Low Cost Diffuser for High Performance Centrifugal Compressors," ASME 68-GT-38.

Klein, A., 1981, "Review: Effects of Inlet Conditions on Conical-Diffuser Performance," ASME JOURNAL OF FLUIDS ENGINEERING, Vol. 103, pp. 250–257.

McMillan, O. J., 1982, "Mean-Flow Measurements of the Flow Field Diffusing Bend," NASA Contractor Report 3634.

Moffat, R. J., 1982, "Contributions to the Theory of Single-Sample Uncertainty Analysis," ASME JOURNAL OF FLUIDS ENGINEERING, Vol. 104, pp. 250–260.

Parsons, D. J., and Hill, P. G., 1973, "Effects of Curvature on Two-Dimensional Diffuser Flow," ASME JOURNAL OF FLUIDS ENGINEERING, Vol. 95, pp. 349–360.

Reeves, G. B., 1977, "Design and Performance of Selected Pipe-Type Diffusers," ASME 77-GT-104.

Rowe, M., 1970, "Measurements and Computations of Flow in Pipe Bends," *Journal of Fluid Mechanics,* Vol. 43, pp. 771–783.

Sagi, C. J., and Johnston, J. P., 1967, "The Design and Performance of Two-Dimensional, Curved Diffusers," ASME *Journal of Basic Engineering,* Vol. 89, pp. 715–731.

Saroch, M. F., 1996, "Contributions to the Study of Turbomachinery Aerodynamics, Part I: Design of a Fish-Tail Diffuser Test Section, Part II: Computations of the Effects of AVDR on Transonic Turbine Cascades," Masters thesis, Department of Mechanical and Aerospace Engineering, Carleton University.

Squire, H. B., and Winter, K. G., 1951, "The Secondary Flow in a Cascade of Aerofoils in a Nonuniform Stream," *Journal of Aeronautical Sciences,* Vol. 18, pp. 271–277.

Taylor, A. M., Whitelaw, J. H., and Yianneskis, M., 1982, "Curved Ducts With Strong Secondary Motion: Velocity Measurements of Developing Laminar and Turbulent Flow," ASME JOURNAL OF FLUIDS ENGINEERING, Vol. 104, pp. 350–359.

Wellborn, S. R., Reichert, B. A., and Okiishi, T. H., 1992, "An Experimental Investigation of the Flow in a Diffusing S-Duct," AIAA-92-3622 presented at the AIAA/SAE/ASME/ASEE 28th Joint Propulsion Conference.

Yaras, M. I., 1996, "Effects of Inlet Conditions on the Flow in a Fishtail Curved Diffuser With Strong Curvature," ASME JOURNAL OF FLUIDS ENGINEERING, Vol. 118, Dec. pp. 772–778.

F. Morency
Ph.D. Student,
École Polytechnique de Montréal,
Département de génie mécanique,
CP 6079,
Succ. Centre Ville,
Montréal (Québec), H3C 3A7
Canada

J. Lemay
Professor,
Département de génie mécanique,
Université Laval,
Ste-Foy,
Québec, Canada, G1K 7P4
e-mail: jlemay@gnc.ulaval.ca

Singularity Detection in Experimental Data by Means of Wavelet Transform

1 Introduction

When using analog to digital (A/D) converters, it is well known from the sampling criteria that one must filter the analog signal in order to circumvent the aliasing phenomenon. A low-pass filter is generally used with a cut-off frequency set at less than the Nyquist frequency, f_N, defined as $f_N = f_s/2$ where f_s is the sampling frequency. If the anti-aliasing filter has a high roll-off slope, which is usually the case, the filtered signal will exhibit only small differences in the energy level between two consecutive points in the time domain. However, if data points have energy levels much higher or lower than their immediate neighbors, they should be considered as probably erroneous. Such points can be sparse and not very apparent in a large data base.

If the data are adequately filtered, the only possible source of erroneous spikes is the data acquisition system (DAQ). Ideally a well built DAQ should not induce this kind of problem. Unfortunately, some large DAQ systems involving high speeds and simultaneous data sampling on several channels (e.g., such as used in multiple hot-wire measurement) can be susceptible to this problem, unlike many PC mounted systems which have been tested and refined by thousands of users. We would like to present here two, perhaps rare, but concrete examples of erroneous spikes being introduced into data sets due to: 1) analog cross-talk originating from a timing error in the analog multiplexing just before the A/D conversion. 2) digital cross-talk arising from a memory addressing error due to wrong time sequencing in the data transfer. This second problem only occurs in DAQ systems where several A/D converters are sharing a single large memory buffer, which is not very usual.

The principal objective of this paper is to present a way of detecting sparse erroneous data points present in a sampled signal. To illustrate this technique, a discrete random signal is first built with an imposed shape in the frequency domain. A few data points of this discrete signal are modified to simulate erroneous measurements which are then detected using an algorithm based on the wavelet transform. Finally, the results obtained using this technique are compared to those obtained by means of a simple time derivative procedure.

2 Discrete Random Signal

Consider a typical experimental time signal $x(t)$ sampled at N equally spaced points, a distance Δt apart, such that

$$x_n = x(n\Delta t) \quad \text{with} \quad n = 0, 1, 2, \ldots, N-1. \tag{1}$$

The sampling rate of this discrete signal is f_s and the time spacing between two sampled points is $\Delta t = 1/f_s$. For the purpose of the demonstration, a test signal is constructed numerically. A discrete random signal is first created in the frequency domain. The spectrum of the signal is defined by

$$h(f) = \frac{1}{\sqrt{1 + (f/f_c)^8}}, \tag{2}$$

representing the amplitude function of a fourth order Butterworth filter, falling off at -80 dB/decade for large values of f/f_c (f_c = cut-off frequency). In this demonstration, the following dimensional values have been used:

$$f_c = 2.5 \text{ kHz}, \quad f_s = 25.6 \text{ kHz},$$

$$f_N = \frac{f_s}{2} = 12.8 \text{ kHz} \quad \text{and} \quad \Delta t = \frac{1}{25.6} \text{ ms} \tag{3}$$

Since the sampling frequency is $f_s = 25.6$ kHz, the function $h(f)$ is then only used in the range defined by the Nyquist frequency, $-12.8 \text{ kHz} \le f \le 12.8$ kHz. It should be noted that these values have been chosen arbitrarily and that only the ratio f_N/f_c is important (i.e., the present development remains valid for any frequency range). It is also worth mentioning that the imposed spectrum is typical of a broad band random signal which has been adequately filtered and sampled. The use of the Butterworth function with the aforementioned values thus results in a time signal characterized by a low energy level at high frequencies. This gives a signal with small amplitude differences between two consecutive points in the time domain. Let us now consider $X(f_k)$, the discrete Fourier transform of x_n, defined by

$$X(f_k) = \sum_{n=0}^{N-1} x_n e^{-j2\pi kn/N} = X_R(f_k) - jX_I(f_k), \tag{4}$$

with $k = 0, 1, \ldots, N-1$ and $f_k = \pm k/N\Delta t$. The values of X_R and X_I are such that the square of the modulus of X is equal to h at the discrete frequency f_k:

$$h(f_k) = X_R(f_k)^2 + X_I(f_k)^2 = X_R(f_k)^2(1 + (X_I(f_k)/X_R(f_k))^2). \tag{5}$$

If we define $\tan\theta(f_k)$ as $X_I(f_k)/X_R(f_k)$, we can then write X_R as a function of $\theta(f_k)$ and $h(f_k)$:

$$X_R(f_k) = \pm\sqrt{\frac{h(f_k)}{1 + \tan^2\theta(f_k)}} = \pm\sqrt{h(f_k)}\cos\theta(f_k); \tag{6}$$

$$X_I(f_k) = X_R(f_k)\tan\theta(f_k). \tag{7}$$

Contributed by the Fluids Engineering Division for publication in the JOURNAL OF FLUIDS ENGINEERING. Manuscript received by the Fluids Engineering Division August 14, 1997; revised manuscript received March 16, 1999. Associate Technical Editor: J. K. Eaton.

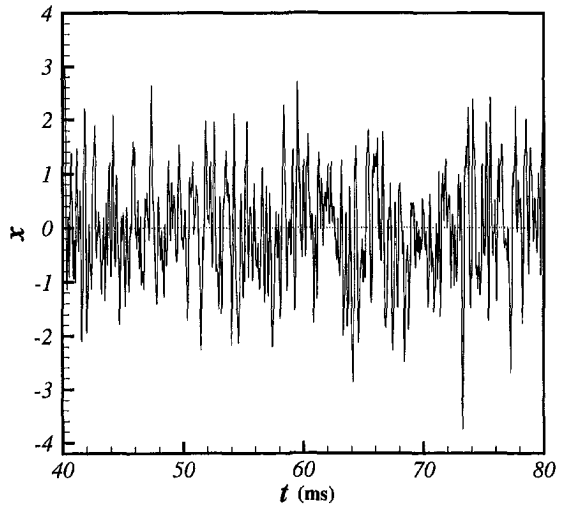

Fig. 1 Random temporal signal $x(t)$ from $t = 40$ ms to $t = 80$ ms

The variable $\theta(f_k)$ is given a random value between $-\pi$ and π for each frequency f_k, except at $f_k = 0$ where $\theta = 0$. The sign of X_R is also randomly selected. Since our goal is to build a time signal $x(t)$ which is a real function, the Fourier transform $X(f)$ must exhibit conjugate symmetry. We thus imposed X_R and X_I to be respectively symmetrical and antisymmetrical about $f_k = 0$. Once the signal has been constructed in the frequency domain, one goes back to the time domain by taking the inverse Fourier transform of $X(f_k)$, with $N = 2^{16}$ points. The real function $x(t)$ is centered and reduced to provide a mean $\mu_x = 0$ and a standard deviation $\sigma_x = 1$. Figure 1 illustrates the temporal signal obtained by the previous procedure.

3 Modification of the Signal

Now that a theoretical signal has been built, some false values are introduced at a few points. Two kinds of modifications are made. These two modifications introduce erroneous discrete signal values that add energy at high frequencies in the spectral domain.

A type 1 error is introduced at the sampling points $n = 500$, 1500, 2500, . . . , 65 500 of the original signal, so that a total of 66 errors are present in the modified signal $x_e(n\Delta t)$. This error is defined by the following relations:

$$x_e(n\Delta t) = x(n\Delta t) + 5\sigma \quad \text{if} \quad x(t) < 1; \tag{8}$$

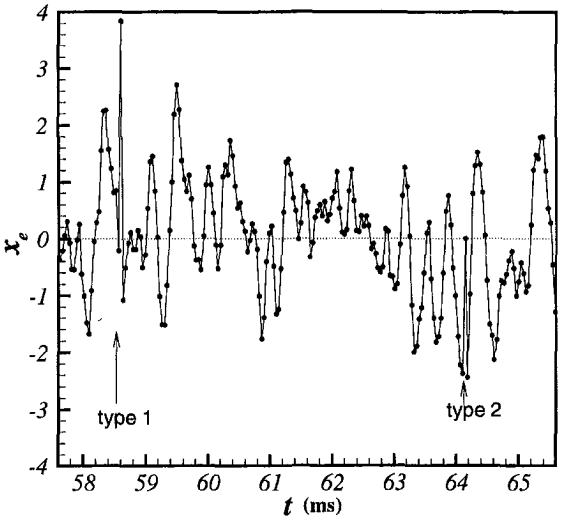

Fig. 2 Modified signal $x_e(n\Delta t)$: type 1 error at time $t = 1500\Delta t$; type 2 error at time $t = 1642\Delta t$

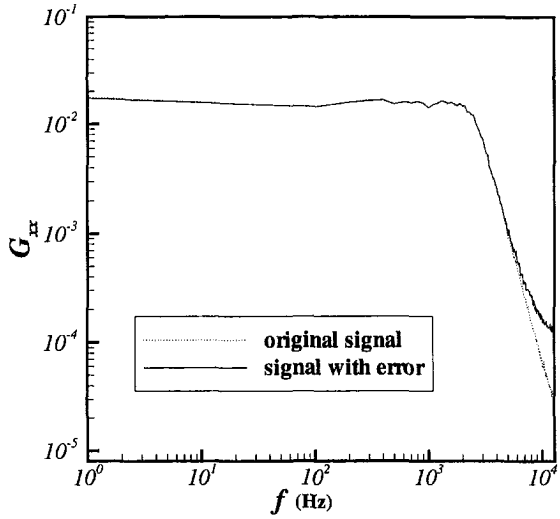

Fig. 3 Auto-spectral density function of the original and modified signal

$$x_e(n\Delta t) = x(n\Delta t) - 5\sigma \quad \text{if} \quad x(t) \geq 1. \tag{9}$$

A type 2 error is introduced around points $n = 650$, 1650, . . . , 64 650 so that 65 errors are present in the modified signal $x_e(n\Delta t)$. The exact point n is selected so that $|x|$ is a local maximum in the range $n - 30 < n < n + 30$. At this particular point n, the signal value is set to $x_e(n\Delta t) = 0$. Figure 2 shows a part of the modified signal $x_e(n\Delta t)$. The standard deviation is now $\sigma_x = 1.016$ and $\mu_x = 0$.

The auto-spectral density function is evaluated by dividing the data record into $n_d = 256$ blocks, each consisting of $N = 256$ data values, with a block length $N\Delta t = 10$ ms. Figure 3 illustrates the one-sided auto-spectral density function, $G_{xx}(f_k)$, obtained for the original and the modified signals. These functions have been adjusted to satisfy the Parseval's identity. One observes that $f_{max} = 12.8$ kHz and $f_c = 2.5$ kHz, as imposed by the function $h(f)$ used to build the random signal. It is also apparent that the discrete errors added to the theoretical signal increase the energy level of the high frequency components.

4 Error Detection

To detect the introduced errors, we used the discrete wavelet transform (DWT) algorithm presented in "Numerical Recipes" (Press et al., 1992) with a Daubechies 4 (DAUB4) wavelet type. The DAUB4 wavelet is the simplest and the most localized member of the Daubechies wavelet family. These characteristics make it very well suited to the purpose of singular error detection. The first step of the DAUB4 wavelet transform is to form the matrix product $\mathbf{A} \times \mathbf{x} = \mathbf{x}_w$:

$$\begin{pmatrix} c_0 & c_1 & c_2 & c_3 & & & & & & & & \\ c_3 & -c_2 & c_1 & -c_0 & & & & & & & & \\ & & c_0 & c_1 & c_2 & c_3 & & & & & & \\ & & c_3 & -c_2 & c_1 & -c_0 & & & & & & \\ & & & & & & \ddots & & & & & \\ & & & & & & & c_0 & c_1 & c_2 & c_3 & \\ & & & & & & & c_3 & -c_2 & c_1 & -c_0 & \\ c_2 & c_3 & & & & & & & & c_0 & c_1 & \\ c_1 & -c_0 & & & & & & & & c_3 & -c_2 & \end{pmatrix} \times \begin{pmatrix} x_1 \\ x_2 \\ x_3 \\ x_4 \\ \vdots \\ x_{N-3} \\ x_{N-2} \\ x_{N-1} \\ x_N \end{pmatrix} = \begin{pmatrix} s_1 \\ d_1 \\ s_2 \\ d_2 \\ \vdots \\ s_{N/2-1} \\ d_{N/2-1} \\ s_{N/2} \\ d_{N/2} \end{pmatrix} \tag{10}$$

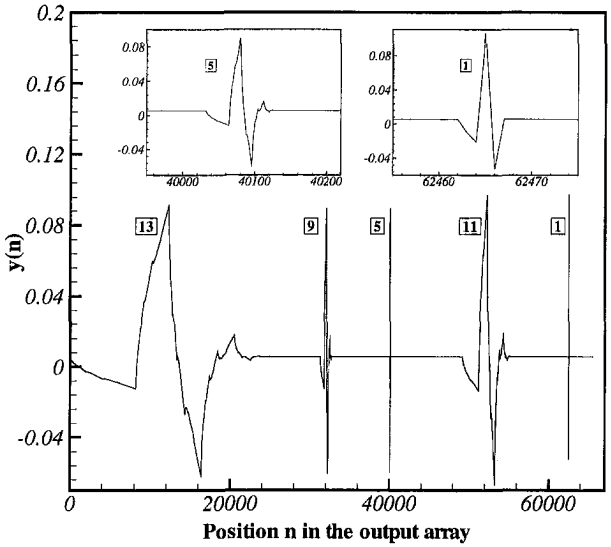

Fig. 4 Some basis functions from the wavelet family DAUB4. The output array consists of N = 65 536 points; this gives 15 wavelet hierarchical levels, the hierarchical level No. 1 corresponding to the 32 768 smallest wavelets. In order to illustrate their shape, five typical wavelets are plotted (one wavelet in each of the hierarchical levels 1, 5, 9, 11, and 13).

where **A** is the matrix of the wavelet filter coefficients, **x** the input signal vector, and $\mathbf{x}_w$ the output vector. As the matrix **A** indicates, the first stage of the wavelet transform consists of two interlaced convolution operations. The odd lines of the matrix act as a low-pass filter (*smoothing filter*) while the even lines act as a high-pass filter (*difference filter*). These two sets of lines are aligned in the matrix, so that the successive sets of outputs, denoted by s and d for "smooth" and "difference," are related to the same input points. The resulting output vector is thus composed of interlaced smooth and difference coefficients ($N/2$ s's and $N/2$ d's). The first stage of the wavelet transform is then completed by permuting the output vector in such a way that the first $N/2$ elements are the s coefficients and the last $N/2$ elements are the d's. The $N/2$ d coefficients, resulting from this first step, are called the wavelet coefficients of the hierarchical level No. 1.

Successive steps of the wavelet transform consist of applying the interlaced convolution on the s coefficients in a hierarchical way. For example, in the second stage, the filter matrix **A** (reduced by half) is applied to the $N/2$ s coefficients. This operation produces an output vector of $N/4$ s's and $N/4$ d's, the latter consisting of the wavelet coefficients of the hierarchical level No. 2. This pyramidal procedure is repeated until one obtains the last hierarchical level consisting of two s and two d coefficients.

The wavelet filter coefficients are chosen in such a way that the transpose matrix of **A** is its inverse matrix: $\mathbf{A}^T = \mathbf{A}^{-1}$. This condition makes the wavelet transform orthogonal and thus invertible.

The wavelet transform gives coefficients that contain frequency information at multiple temporal locations of the transformed signal (Farge, 1992). For example, one can filter the data by putting the coefficients corresponding to a given hierarchical level equal to zero. The filtered signal is obtained by computing the inverse wavelet transform. One can also obtain the basis function of the DAUB4 wavelet family by putting all the d coefficients equal to zero, and those to be observed to one. The basis function is then obtained by computing the inverse wavelet transform of this vector. Figure 4 illustrates some of these basis functions.

The discrete wavelet transform evaluates coefficients of hierarchical level m only at 2^m points of the signal. The wavelet coefficients of the smallest hierarchical level (m = 1) are used because one needs information on high frequency phenomena covering only one time step. With m = 1, we will get a coefficient for every two times steps of the modified signal $x_e(n\Delta t)$ (B.-Morency, 1996).

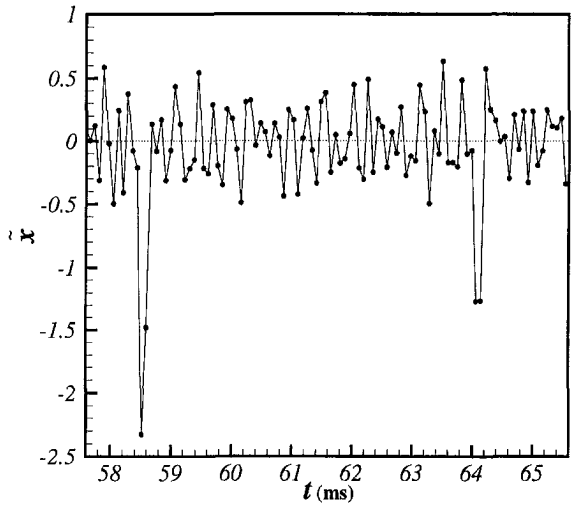

Fig. 5 Wavelet coefficients (hierarchical level No. 1) of the signal $x_e(n\Delta t)$

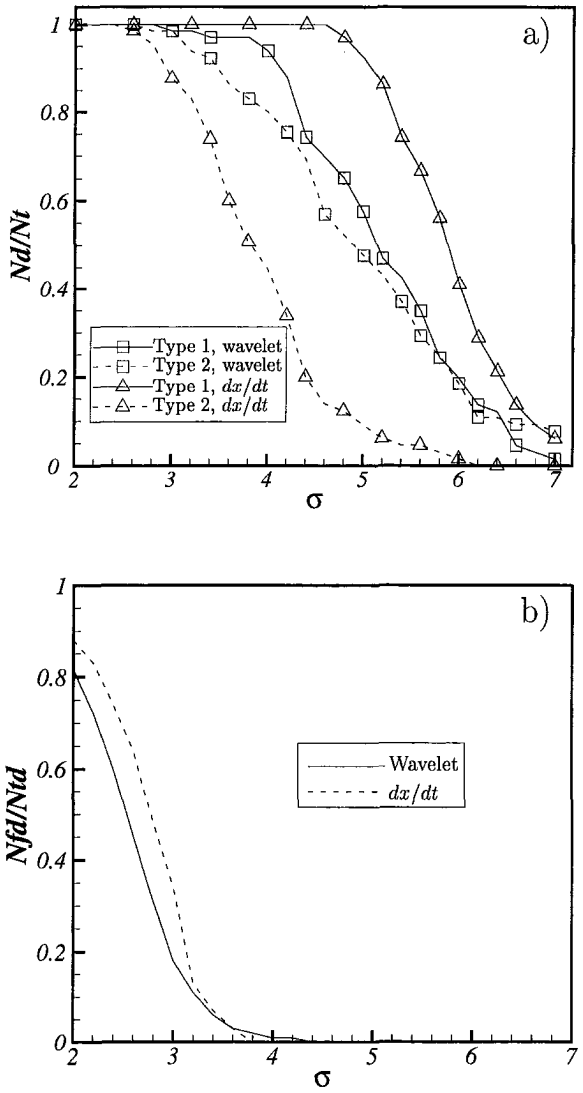

Fig. 6 Comparison between the wavelet and the time derivative results; N_d = number of true detected errors, N_t = total number of errors, N_{fd} = number of falsely detected errors and N_{td} = total number of detected errors. The ratios N_d/N_t (*a*) and N_{fd}/N_{td} (*b*) are plotted as a function of σ, the detection criteria (σ = the standard deviation of either the wavelet coefficients or the time derivative signal).

To detect erroneous points on the signal $x_e(n\Delta t)$, a criterion based on the standard deviation σ_{w1} of the wavelet coefficient of the smallest hierarchical level is established. Whenever the value of a coefficient falls outside the $\pm 3\sigma_{w1}$ range, the surrounding points of the corresponding position on the signal $x_e(n\Delta t)$ must be visually verified. The decision whether or not to correct the signal at this point or at a nearby point is then taken.

An example of the wavelet coefficients corresponding to the part of the modified signal shown in Fig. 2 is presented in Fig. 5. Four wavelet coefficients considerably exceed $\pm 3\sigma_{w1}$ (± 0.9); the first two at times $t = 1498\Delta t$ and $t = 1500\Delta t$, corresponding to a type 1 error imposed at time $t = 1500\Delta t$, the other two at times $t = 1640\Delta t$ and $t = 1642\Delta t$, corresponding to the type 2 error imposed at time $t = 1642\Delta t$. Using the wavelet detection method with the criterion $\pm 3\sigma_{w1}$, all the modified points of the signal $x_e(t)$, and only those points, were found.

5 Performance of the Wavelet Detection Method

To investigate the performance of the present detection technique, the two following parameters are defined: N_d/N_t is the ratio between the number of true detected errors and the total number of imposed errors; N_{fd}/N_{td} is the ratio between the number of falsely detected errors and the total number of detected errors. The latter ratio implies that $N_{fd}/N_{td} = 1 - N_d/N_{td}$, as by definition $N_{fd} + N_d = N_{td}$. The best technique should gives $N_{fd}/N_{td} = 0$ ($N_d = N_{td}$) and $N_d/N_t = 1$, indicating that there is no false detection and that all the imposed errors have been detected.

Figure 6 shows the ratios N_d/N_t and N_{fd}/N_{td} plotted as a function of σ_{w1}, the detection criterion. The performance of the present method is also compared to that of a more classical approach based on the time derivative of the signal. The results indicate that the wavelet approach with the criterion $\pm 3\sigma_{w1}$ is the most efficient technique.

6 Conclusion

The use of the fast wavelet transform enables one to find the points on a signal where occasional high frequency phenomena occur. If the latter are associated with some sparse erroneous sampling, the wavelet transform can help one quickly check and correct the signal. This kind of problem has been observed, for example, in a data base obtained by multiple hot-wire rake measurements in a turbulent mixing layer, where the method presented here has been successfully used to remove erroneous, type 1 data points (B.-Morency, 1996).

References

B.-Morency, F., 1996, "Utilisation de l'estimation stochastique linéaire pour l'analyse d'une couche de mélange plane turbulente," Master's thesis, Université Laval.

Farge, M., 1992, "Wavelet Transforms and Their Applications to Turbulence," *Annual Review of Fluid Mechanics*, Vol. 24, pp. 395–457.

Press, W. H., Teukolsky, S. H., Vetterling, W. T., and Flannery, B., 1992, *Numerical Recipes in FORTRAN (The Art of Scientific Computing)*, 2nd Edition, Cambridge University Press.

Tore Løland[1]
Research Fellow.

Lars R. Sætran
Associate Professor.

Department of Mechanics, Thermo- and Fluiddynamics,
Norwegian University of Science and Technology,
Kolbjørn Hejes vei 2,
N-7034 Trondheim,
Norway

Robert Olsen
Research Scientist.

Inge R. Gran
Research Scientist.

Applied Thermodynamics and Fluid Dynamics,
Sintef Energy Research,
Kolbjørn Hejes vei 1b,
N-7034 Trondheim,
Norway

Reidar Sakariassen
Measurement Specialist,
Statoil, K-lab,
P.O. Box 308,
N-5500 Haugesund,
Norway

Fluid Motion in Ultrasonic Flowmeter Cavities

The ultrasonic flow meter is a newcomer among flow meters for measuring large quantities of natural gas. It has notable advantages compared to traditional meters. The ultrasonic flow meter is much more compact and has a wider dynamic range for flow measurements than the orifice plate meter. When manufactured, the ultrasonic sensors are often set back from the pipe wall in a cavity. When the fluid flows past the cavities, a secondary flow of vortices with characteristic size equal to the cavity width is established inside the cavities. The aim of this study has been to investigate the influence of this secondary flow on the accuracy of the ultrasonic flowmeter. Both measurements and numerical simulations of the cavity flow have been conducted. It has been found from the present work, that the influence of the flow in the cavities on the measurements increases nonlinearly with the pipe flow rate.

1 Introduction

The traditional method for measuring large gas flow rates is the orifice plate meter. For this meter, the flow rate is a function of the pressure difference across the plate, the thermodynamic characteristics of the gas, and the geometry of the orifice plate.

Since this method is described in an international standard, ISO-5167-1, it has been accepted as the basis for sales and allocation metering by the gas companies and the various national authorities. However, the orifice plate has several drawbacks that become apparent when designing and operating modern gas metering stations: It requires a lot of space and has limited flexibility with respect to capacity.

To overcome some of these drawbacks, new types of meters have been installed as an alternative to the orifice plate system. The device attracting the greatest interest today is the multi-path ultrasonic flowmeter. It has the advantage of having no moving parts, and it is also bidirectional. This allows gas to flow in both directions without affecting the accuracy. The main advantage seen from an offshore point of view is that the meter allows construction of compact metering stations with negligible pressure loss.

In short terms, the working principle of an ultrasonic flowmeter is: A piezoelectric element is placed at the bottom of a cavity as shown in Fig. 1. When a pulse is received at B, it switches and sends back the same pulse type to A. For each of the paths, two transit times, t_1 and t_2, are found. t_1 is the time from A to B and t_2 is the time from B to A. By using these times, the pipe velocity, $\bar{V}$, based on the transit time measurements are given as (Sakariassen, 1996)

$$\bar{V} = \frac{L_p^2}{2d}\frac{t_2 - t_1}{t_2 t_1} \tag{1}$$

where L_p and X are given in Fig. 1.

In a multi-path ultrasonic flowmeter, the pipe flow is measured along a multiple number of acoustic paths. An estimate of the mean axial fluid velocity in the pipe cross-section, $\bar{V}_{AV}$, is calculated as

$$\bar{V}_{AV} = \sum_{\forall i} W_i \bar{V}_i \tag{2}$$

where W_i is the weighing factor for acoustic path number i and $\bar{V}_i$ is the average pipe velocity measured along acoustic path i. The weighing factor may be a fixed number different for each of the acoustic paths, or a more complex expression which results in numbers that vary with the ratio between the gas flow velocities from the individual acoustic paths. The ultrasonic flowmeter is a bidirectional flowmeter, and the direction of the pipe flow is indicated by the sign of $(t_2 - t_1)$. If the pipe flow direction changes, $(t_2 - t_1)$ changes sign.

The ultrasonic flowmeter offers valuable additional information about the pipe flow and the velocity of sound. This extra information can partly be used for diagnostics of the "health condition" of

[1] Present address: Statoil, K-lab, P.O. Box 308 N-5500 Haugesund, Norway.

Contributed by the Fluids Engineering Division for publication in the JOURNAL OF FLUIDS ENGINEERING. Manuscript received by the Fluids Engineering Division July 13, 1998; revised manuscript received January 26, 1999. Associate Technical Editor: D. R. Williams.

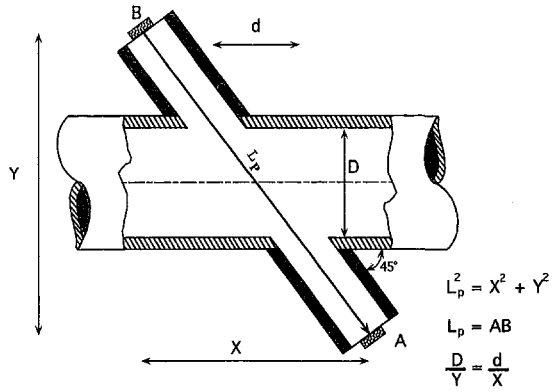

Fig. 1 Geometric parameters for an ultrasonic flowmeter. The arrow on L_p gives the positive direction

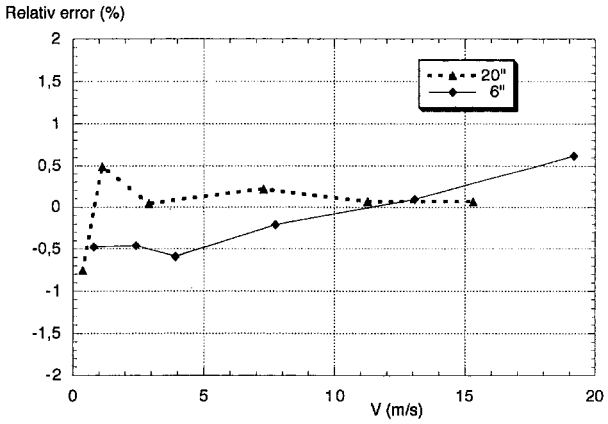

Fig. 2 The calibration curves for a 6 in. and a 20 in. meter (Sakariassen, 1996)

the meter and partly as information about what is going on inside the pipe.

van Bloemendaal and van der Kam (1995) have shown that the ultrasonic flowmeter may be used after 90 and 180 deg bends if certain precautions are taken. They also showed that small step changes in the pipe diameter do not affect the ultrasonic flowmeter. Both Sakariassen (1996) and van Bloemendaal and van der Kam (1995) have reported malfunction of the ultrasonic flowmeter if it is placed near a pressure-reduction valve that produces noise in the same frequency range as the ultrasonic pulse.

Another problem found, is that small meters (e.g., 6 in.) have larger uncertainty in the pipe flow measurements than larger meters, like e.g., 20 in. meters. Sakariassen (1996) has shown that in some cases the relative error depends on the pipe flow, especially for the small meters. This effect is illustrated in Fig. 2.

The difference in accuracy between the larger and the smaller size meter is the background for this investigation. The cavity that is used to house the piezoelectric element has the same size for both the 6 in. meter and the 20 in. meter. This means that the length difference, ΔL, for the two meter types is due to the difference in pipe diameter. The secondary flow in the cavities has a bigger impact on the transit time for the 6 in. meter than for the 20 in. meter.

The cavity flow problem is of interest in many engineering applications, and the ultrasonic flowmeter is one of them. From a fundamental point of view, the cavity flow problem is very interesting. In most flow problems involving separation, e.g., backward facing step flow, visualization becomes difficult, because the vortex structure is unsteady. In cavity flows on the other hand, there is a possibility of obtaining a stationary vortex.

The depth-to-width ratio of the cavity is an important parameter when characterizing the flow in the cavity. If the cavity has a greater depth than width it is called a deep cavity. Rockwell and Naudascher (1978) have made a review article of the flow inside cavities.

There are two main purposes of the present study. One is to investigate two simple two-dimensional model cavities that describe the ultrasonic flowmeter cavities, using both experimental techniques and numerical simulations to determine the flow pattern inside the cavities. The other is to use the results to analyze how the secondary flow in the cavities influences a thin ultrapulse traveling between the two ultrasonic sensors.

A short description of an ultrasonic flowmeter is given in Section 1. Both measurements and numerical simulations have been performed. The different techniques are described in Section 2. In Section 3, the results are given with comparison of measurements and numerical simulations. Section 4 shows the deviation introduced on the ultrasonic flowmeters by the cavity velocities, and the conclusions are given in Section 5.

2 Experimental Setup

2.1 The Water Tunnel. The water tunnel used has a vertical test section of 1 m × 0.14 m × 0.14 m. The capacity of the tunnel is $Q_{max} = 0.027$ m^3/s, which gives a maximum velocity of 1.5 m/s. The walls in the test section are made of glass, which makes the tunnel suitable for LDV measurements and laser-sheet flow visualizations. In this work the depth of the cavity was 105 mm with an angle of 45 deg, and the width of the cavity was 12.5 mm at the opening.

2.2 Measuring Systems. The laser sheet flow visualization system is based on a 5 W Ion Argon laser from LEXEL. It produces green light at 514 nm. A four-sided polygon mirror is used to sweep the laser beam over the visualization area. The rotation speed of the polygon mirror may be changed from 1 rpm to 18,000 rpm. The seeding particles used for the flow visualizations are 12 μm hollow glass spheres coated with silver.

The LDV measurements are performed using a commercial two-component LDV system from TSI. For the LDV measurements 4 μm latex particles were used.

2.3 Numerical Implementation. The mathematical models used have been implemented in a well-documented general-purpose CFD code (Melaaen, 1992b, Melaaen, 1992a).

In the computations presented here, a grid with 195 × 131 nodes is employed. The grid lines are concentrated in the vicinity of the cavity. The standard high-Re k-ϵ model together with law-of-the-wall treatment has been used to account for the turbulence (Melaaen, 1992b, Melaaen, 1992a). Different computational grids have been used to verify that the results presented here are grid independent.

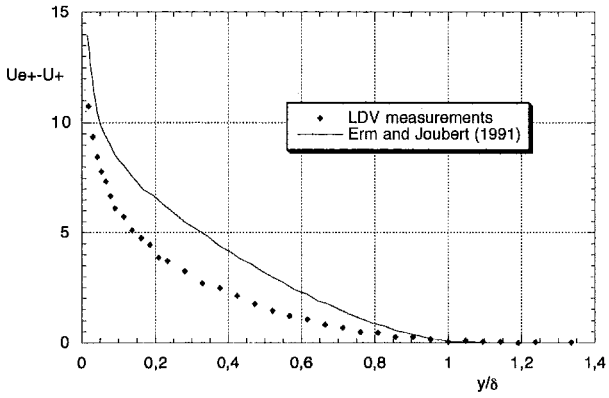

Fig. 3 The measured velocity profile at the front of the cavity given in outer variables compared with zero pressure gradient measurements

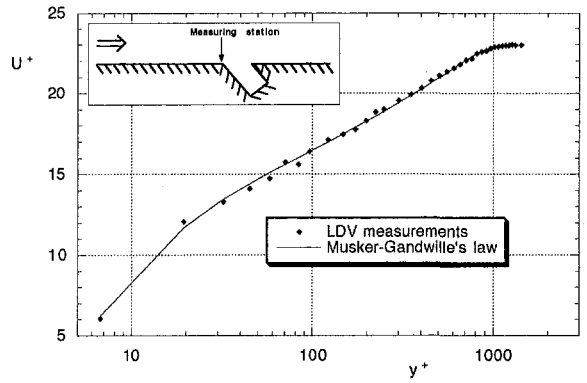

Fig. 4 The measured velocity profile at the front of the cavity given in inner variables compared with the Musker-Grandwill law

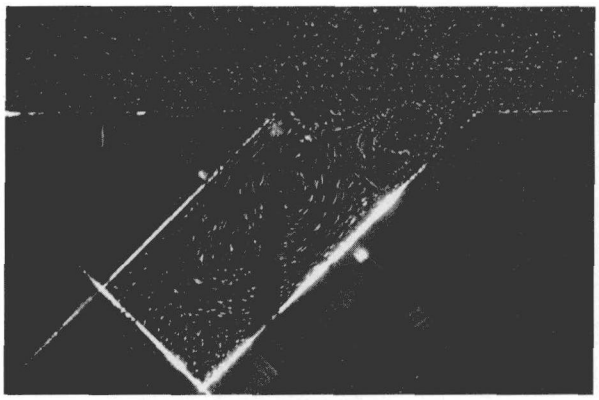

Fig. 6 A picture from the sloping cavity pointing countercurrent. Pipe flow from left to right.

3 Results

3.1 The Boundary Layer Flow. LDV measurements of the boundary-layer flow entering the cavity are shown in Fig. 3. The results are compared with zero-pressure-gradient boundary layer measurements by Erm and Joubert (1991).

The LDV measurements were used to find the Clauser shape parameter, $G = 5.64$, the von Kármán shape parameter, $H = 1.34$, and the wake strength, $\Delta U^+ = 0.31$. All these parameters are lower than for a zero-pressure gradient boundary layer. The velocity defect $U_e^+ - U^+$ is also lower than for zero-pressure boundary layers, and verify that a favorable pressure gradient is present in the boundary layer entering the model cavities.

Figure 4 shows that the boundary layer entering the cavities is a fully developed boundary-layer flow. As seen in the figure, the measurements follow the Musker-Grandwill law (Musker, 1979 and Dean, 1976) for boundary layer flow.

3.2 Cavity Flow. As seen in Fig. 5 there is one vortex in the upper part, and one further inside the cavity. For the other configuration in an ultrasonic flowmeter, the cavity is placed pointing countercurrent. Figure 6 shows a picture taken with this geometry.

The picture shows that the vortex structure is different in this case. There is a small vortex at the downstream corner, and a bigger one is covering the whole cavity width in the lower part of the cavity. Also visible in this picture is the stagnation point in the cavity at the downstream wall.

In Figs. 7 and 8, the results from both measurements and numerical simulations are given for the sloping cavity pointing in the pipe flow direction. In the measurements, only $\overline{u'u'}$ and $\overline{v'v'}$ were measured. The turbulence kinetic energy in the measurement was estimated by assuming $\overline{w'w'} = \frac{1}{2}(\overline{u'u'} + \overline{v'v'})$, such that $k = \frac{3}{4}(\overline{u'u'} + \overline{v'v'})$.

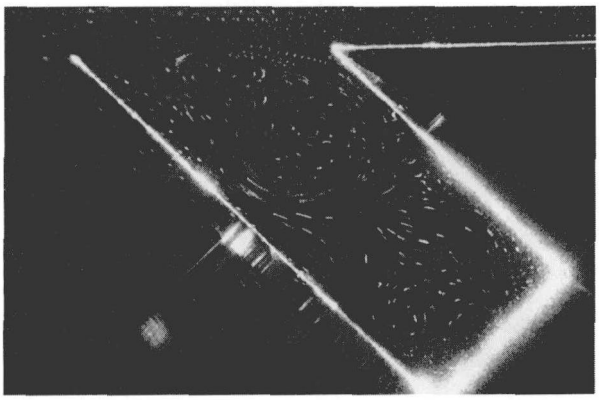

Fig. 5 A picture from the sloping cavity pointing in the pipe flow direction. Pipe flow from left to right.

The figures show that the predicted mean velocity and turbulence kinetic energy agree well with the measurements. This is also the case for other positions, and for the cavity pointing countercurrent.

4 Correction for the Ultrasonic Flowmeter

The ultrapulse is a concentrated beam (like water coming out of a fire hose). This concentrated ultrapulse is influenced by the

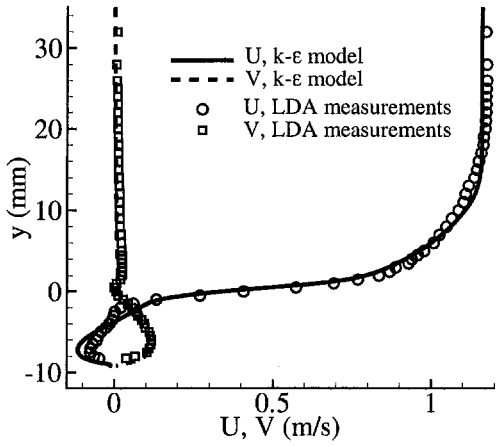

Fig. 7 The mean axial and transverse velocities for a sloping cavity pointing in the pipe flow direction, at one fourth of the cavity opening before the downstream corner

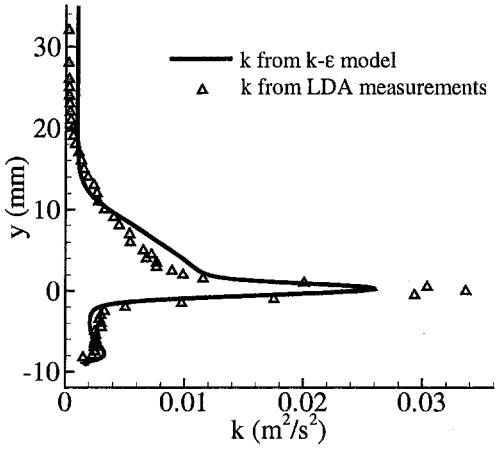

Fig. 8 Turbulence kinetic energy, *k*, for a sloping cavity pointing in the pipe flow direction, at one fourth of the cavity opening before the downstream corner

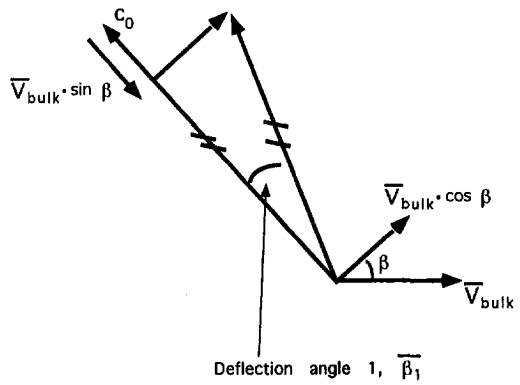

(a) The ultrapulse traveling countercurrent

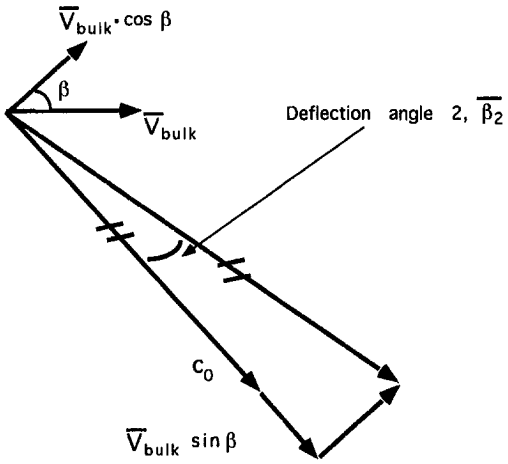

(b) The ultrapulse traveling in the pipe flow direction

Fig. 9 The deflection angle

component of the pipe flow normal to the ultrapulse and the one along the ultrapulse as illustrated in Fig. 9.

This means that it is possible to find relations between the pipe flow and the deflection of the ultrapulse. The ultrapulse is influenced more and more as it travels through the pipe. For simplicity, only the angle found from Fig. 9 is used here. This means that the deflection is given by

$$L_{def,1} = \frac{\bar{V}_{bulk} \tan \bar{\beta}_1}{c_0 - \bar{V}_{bulk} \sin \bar{\beta}_1} D, \quad (3)$$

$$L_{def,2} = \frac{\bar{V}_{bulk} \tan \bar{\beta}_2}{c_0 + \bar{V}_{bulk} \sin \bar{\beta}_2} D, \quad (4)$$

where $L_{def,1}$ and $L_{def,2}$ are illustrated in Fig. 10, and $\bar{V}_{bulk}$ is the bulk velocity in the pipe. It can be seen from Eqs. (3) and (4) that the deflection depends on both the pipe flow and the diameter of the pipe.

The ultrapulse is a concentrated beam that is deflected as it travels through the pipe. Inside the cavities, the ultrapulse travels through a fluid in motion, dominated by vortex structures as illustrated in Figs. 5 and 6. This leads to a hysteresis in the ultrapulse path as shown in Fig. 10.

In the present work, it was found that the vortex structure depends on the orientation of the cavity. This means that the effect of the cavities is different for the ultrapulse traveling in the pipe flow direction, 2, than for the one traveling countercurrent, 1.

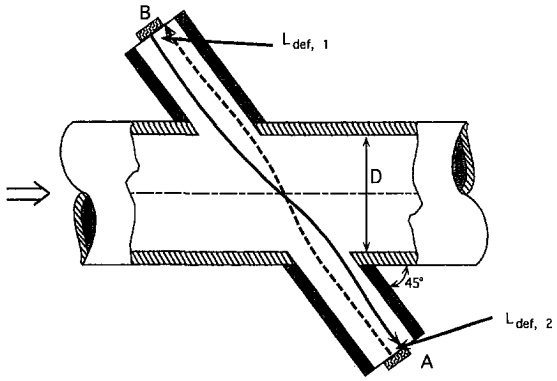

Fig. 10 The hysteresis in the ultrapulses traveling between the sensors

Mean velocities from parts of the cavities were extracted from the numerical simulations, both for the case pointing in the pipe flow direction and the one pointing countercurrent, as illustrated in Figs. 11 and 12.

In the present investigation it is assumed that the width of the ultrapulse is 4 mm. This means that the area as illustrated in Figs. 11 and 12 is 4 mm wide. The mean area is moved according to Eqs. (3) and (4) as the pipe flow increases.

The direction is defined positive out of the cavity pointing countercurrent (B) and positive in to the one pointing in the pipe flow direction (A), as illustrated in Fig. 1.

The numerical simulations show that the cavity field mean velocity in the cavity, as illustrated in Figs. 11 and 12, depends linearly on the flow rate. This is true for all of the cavity field mean velocities influencing the ultrasonic pulse. The results also show that the cavity field mean velocity increases linearly when moving from the cavity centerline and outward to the cavity wall. Figure 5 shows that there is a vortex covering almost the entire cavity width in the case of the cavity pointing in the pipe flow direction. For the cavity pointing countercurrent, there is a small vortex at the downstream corner, and a larger one further down in the cavity. Because of the difference in the vortex structure, the linear dependency between the mean cavity field velocity in the cavity and the distance from the cavity centerline depends on the orientation of the cavity.

These findings were used to correct the formula given in the

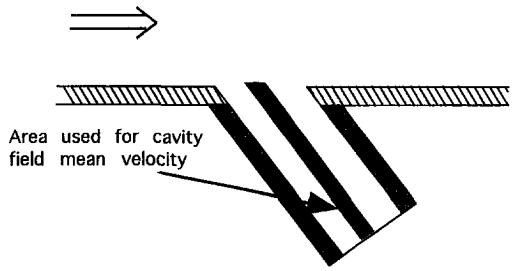

Fig. 11 The area used to find the cavity field mean velocity for the cavity pointing in the pipe flow direction

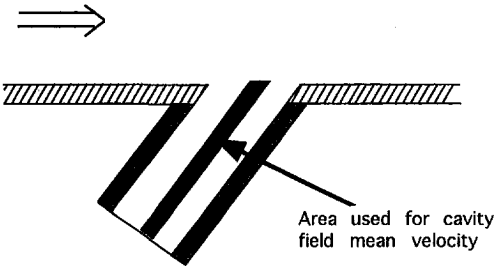

Fig. 12 The area used to find the cavity field mean velocity for the cavity pointing countercurrent

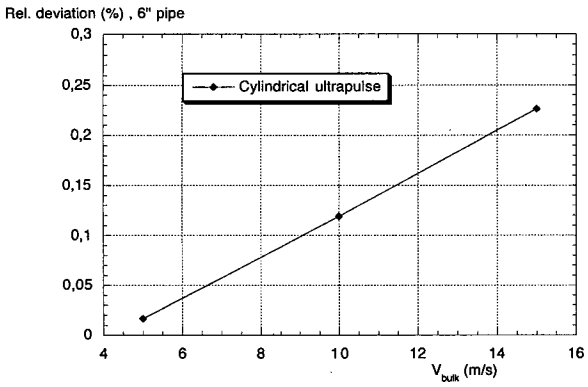

Fig. 13 The relative deviation as a function of the pipe flow

ISO/DTR 12765 "Measurement of Fluid Flow in Closed Conduits—Flow Rate Measurement by Means of Ultrasonic Flowmeters." A correction was made to the integral for the velocity along the path. This correction takes into account both the size of the meter and the velocity inside the pipe.

The original equation defining the pipe flow is given by Eq. (1). In this case the velocity is integrated along the path L_p with the assumption that there is no flow inside the cavity.

$$\int_0^Y v(y)dy = \bar{V}D \tag{5}$$

The new formula with the correction suggested from the present findings is given as

$$\bar{V} = \frac{L_p^2}{2d}\frac{t_2 - t_1}{t_2 t_1} + \frac{1}{4}(\bar{V}_{A_1} + \bar{V}_{B_1} + \bar{V}_{A_2} + \bar{V}_{B_2})\left(\frac{X}{d} - 1\right) \tag{6}$$

where $\bar{V}_{A1}$ and $\bar{V}_{B1}$ are the cavity field mean velocities in the cavity that influence the ultrapulse traveling countercurrent from cavity A to cavity B, as illustrated in Fig. 10. Similarly, $\bar{V}_{A2}$ and $\bar{V}_{B2}$ are the cavity field mean cavity velocities influencing the ultrapulse traveling from B to A.

In this case the integration was done along the path based on the findings from the measurements and numerical simulations of the flow inside the cavities. The integral becomes

$$\int_0^Y v(y)dy = D\left[\bar{V} + (\bar{V}_{A_i} + \bar{V}_{B_i})\left(\frac{X}{2d} - \frac{1}{2}\right)\right] \tag{7}$$

where V_{Ai} is the cavity field mean velocity in the cavity pointing in the flow direction, and V_{Bi} is the cavity field mean velocity in the cavity pointing countercurrent. The number i takes the value 2 for the ultrapulse traveling in the flow direction, and 1 for the ultrapulse traveling countercurrent.

By comparing Eqs. (1) and (6) the influence from the cavity field mean velocities can be expressed in terms of a relative deviation as

$$\text{Rel. deviation} = \frac{\frac{1}{4}(\bar{V}_{A_1} + \bar{V}_{B_1} + \bar{V}_{A_2} + \bar{V}_{B_2})\left(\frac{x}{d} - 1\right)}{\bar{V}_{\text{bulk}}} \tag{8}$$

where $\bar{V}_{\text{bulk}}$ is the actual bulk velocity in the pipe.

By combining the predicted cavity velocity field from the numerical simulations with knowledge about the deflection of the ultrapulse, the relative deviation can be plotted. The result is shown in Fig. 13. The relative deviation increases linearly with the pipe flow rate. This means that the absolute deviation increases quadratically, i.e. as $O(\bar{V}^2_{\text{bulk}})$.

There is a linear dependency between the pipe flow rate and the mean velocity in the cavities. A linear increase in the mean velocity outward from the centerline of the cavity is also found. These two effects together lead to an absolute deviation increasing as $O(\bar{V}^2_{\text{bulk}})$.

The results in Fig. 13 show the influence of the cavity flow on a thin ultrapulse traveling in model cavities. The effect of changing the area used to find the mean velocity will influence the observed effect. In reality, the size of the beam might be 20 mm. The 4 mm pulse used in this case was used to illustrate the flow effect that a thin ultrapulse would experience traveling through the pipe flow including the cavities.

In the present investigation, two-dimensional models were used. This was done to optimize the conditions for the experimental techniques applied. The depth and the angle of the cavities may also affect the secondary flow in the cavities. The effects of changing from two-dimensional cavities to real ultrasonic cavities or varying the cavity depth and angle of the cavity were not considered in the present work.

The present work shows that there is a secondary flow inside the cavities and that the presence of this flow may influence the accuracy of the ultrasonic flowmeter.

5 Conclusion

Results from an investigation of flow inside cavities have been reported. The experimental measuring techniques used are Laser Doppler Velocimetry, LDV, and visualizations of the flow using Laser Sheet Flow Visualizations. Numerical simulations using standard CFD techniques have also been conducted. The experiments and numerical simulations show good agreement. The results from the present investigation have been used to find the influence of the cavity flow on the accuracy of the ultrasonic flowmeter. The investigation shows that there is a hysteresis in the ultrapulse path, which depends on the pipe flow rate. The relative deviation introduced by the cavities on the pipe flow measurements increases linearly with increasing pipe flow rate. The deviation also depends on the size of the meter. The reason for this is that the size of the cavities used to house the ultrasonic sensors in practice is independent of the pipe diameter.

This investigation suggests that the velocities inside the cavities should not be neglected, as is done in the present draft for the ISO technical report on ultrasonic flowmeters.

Acknowledgment

The authors gratefully acknowledge the financial support for this research from the companies Verbundnetz Gas AG, VNG, and STATOIL.

References

Dean, R. B., 1976, "A Single Formula for the Complete Velocity Profile in a Turbulent Boundary Layer," ASME JOURNAL OF FLUIDS ENGINEERING, Vol. 98, p. 723.

Erm, L. P. and Joubert, P. N., 1991, "Low-Reynolds-Number Turbulent Boundary Layer," *Journal of Fluid Mechanics,* Vol. 230, p. 1.

Melaaen, M. C., 1992a, "Calculation of Fluid Flows with Staggered and Nonstaggered Curvilinear Nonorthogonal Grids—A Comparison," *Numerical Heat Transfer, Part B,* Vol. 21, pp. 21–39.

Melaaen, M. C., 1992b, "Calculation of Fluid Flows with Staggered and Nonstaggered Curvilinear Nonorthogonal Grids—The Theory," *Numerical Heat Transfer, Part B,* Vol. 21, pp. 1–19.

Musker, A. J., 1979, "Explicit Expression for the Smooth Wall Velocity Distribution in a Turbulent Boundary Layer," *AIAA Journal,* Vol. 17, p. 655.

Rockwell, D., and Naudascher, E., 1978, "Review—Self-Sustaining Oscillations of Flow Past Cavities," ASME JOURNAL OF FLUIDS ENGINEERING, Vol. 100, p. 152.

Sakariassen, R., 1996, "Real-Life Experience with Multipath Ultrasonic Gas Flow Meters," *International Pipeline Conference—Vol. 2,* p. 1077.

van Bloemendaal, K., and van der Kam, P. M. A., 1995, "Installation Effects on Multi-Path Ultrasonic Flow Meters: The Ultraflow Project," *3rd International Symposium of Flow Measurement,* San Antonio.

A Macroscopic Turbulence Model for Flow in a Porous Medium

A. Nakayama
Professor.
e-mail: tmanaks@eng.shizuoka.acjp

F. Kuwahara
Associate Professor.

Department of Mechanical Engineering,
Shizuoka University,
3-5-1 Johoku, Hamamatsu, 432 Japan

A complete set of macroscopic two-equation turbulence model equations has been established for analyzing turbulent flow and heat transfer within porous media. The volume-averaged transport equations for the mass, momentum, energy, turbulence kinetic energy and its dissipation rate were derived by spatially averaging the Reynolds-averaged set of the governing equations. The additional terms representing production and dissipation of turbulence kinetic energy are modeled introducing two unknown model constants, which are determined from a numerical experiment using a spatially periodic array. In order to investigate the validity of the present macroscopic turbulence model, a macroscopically unidirectional turbulent flow through an infinite array of square rods is considered from both micro- and macroscopic-views. It has been found that the streamwise variations of the turbulence kinetic energy and its dissipation rate predicted by the present macroscopic turbulence model agree well with those obtained from a large scale microscopic computation over an entire field of saturated porous medium.

Introduction

There exist a considerable number of experimental reports such as Mickeley et al. (1965), Kirkham (1967), Macdonald et al. (1979), and Dybbs and Edwards (1984), which confirm the existence of turbulence within a saturated porous medium. According to Dybbs and Edwards (1984) who conducted a flow visualization study, fluid flow in a porous medium exhibits turbulent characteristics when the pore-Reynolds number (based on the pore scale and velocity) becomes above a few hundred.

Rudraiah (1983) introduced the Reynolds decomposition for the macroscopic governing equations to treat turbulent flows in porous media. A comprehensive review on the Reynolds decomposition and turbulence modeling using modified Darcy's equations has been provided by him (Rudraiah, 1988). In his initiative work, however, only zero-equation models based on a gradient diffusion model for closure were investigated, so as to treat comparatively simple free convective turbulent flows in porous media.

Perhaps, Lee and Howell (1987) were the first to introduce a set of transport equations for the turbulence kinetic energy and its rate of dissipation to analyze turbulent flows in porous media. However, no account was taken for possible production and dissipation due to the presence of porous matrix, since they considered only highly porous media.

Recently, two distinct two equation turbulence models have been established for turbulent flows in porous media. Antohe and Lage (1997) chose to carry out the Reynolds averaging over the volume-averaged macroscopic equations to derive two-equation turbulence model equations, whereas Masuoka and Takatsu (1996) derived a macroscopic turbulence transport equation by spatially averaging the turbulence transport equation of the two-equation turbulence model. Antohe and Lage (1997) examined their model equations for the turbulence kinetic energy and its disspation rate, assuming a unidirectional fully-developed flow through an isotropic porous medium. Their model demonstrates that the only possible steady state solution for the case is "zero" macroscopic turbulence kinetic energy. This solution should be re-examined, since the macroscopic turbulence kinetic energy in a forced flow through a porous medium must stay at a certain level, as long as the presence of porous matix keeps on generating it. (The situation is analogous to that of turbulent fully-developed flow in a conduit.) Also, it should be noted that the small eddies must be modelled first, as in the case of LES (Large Eddy Simulation). Thus, we must start with the Reynolds averaged set of the governing equations and integrate them over a representative control volume, to obtain the set of macroscopic turbulence model equations. Therefore, the procedure based on the Reynolds averaging of the spatially averaging continuity and momentum equations is questionable, since the eddies larger than the scale of the porous structure are not likely to survive long enough to be detected. Moreover, none of these models has been verified experimentally.

Our main purpose is to propose a comprehensive set of macroscopic two-equation turbulence model equations which is sufficiently general and capable of simulating most turbulent flows in porous media. The macroscopic transport equations for the turbulence kinetic energy and its dissipation rate are derived by spatially averaging the Reynolds-averaged transport equations along with the k-ϵ turbulence model. For the closure problem, the unknown terms describing the production and dissipation rates inherent in porous matrix are modeled collectively. In order to establish the unknown model constants, we conduct an exhaustive numerical experiment for turbulent flows through a periodic array, directly solving the microscopic governing equations, namely, the Reynolds-averaged set of continuity, Navier-Stokes, turbulence kinetic energy and its dissipation rate equations. The microscopic results obtained from the numerical experiment are integrated spatially over a unit porous structure to determine the unknown model constants.

The macroscopic turbulence model, thus established, is tested for the case of macroscopically unidirectional turbulent flow. The streamwise variations of the turbulence kinetic energy and its dissipation rate predicted by the present macroscopic model are compared against those obtained from a large scale direct computation over an entire field of saturated porous medium, to substantiate the validity of the present macroscopic turbulence model.

Microscopic Governing Equations

Turbulence may become appreciable even in porous media. As long as that the pore Reynolds number is sufficiently high (and that the turbulence length scale is much smaller than the pore scale), any one of reliable turbulence models designed for clear fluid flows (without a porous ma-

Contributed by the Fluids Engineering Division for publication in the JOURNAL OF FLUIDS ENGINEERING. Manuscript received by the Fluids Engineering Division April 29, 1998; revised manuscript received March 12, 1999. Associate Technical Editor: M. N. Dhaubdhadel.

trix) may be used to resolve microscopic details of turbulent flow fields within a microscopic porous structure.

The Reynolds-averaged set of the governing equations in consideration, namely, the continuity equation, Navier-Stokes equation, energy equation, turbulence kinetic energy transport equation, and that of dissipation rate, are given for incompressible flows as follows:

$$\frac{\partial \bar{u}_j}{\partial x_j} = 0 \tag{1}$$

$$\frac{\partial \bar{u}_i}{\partial t} + \frac{\partial \bar{u}_j \bar{u}_i}{\partial x_j} = -\frac{1}{\rho}\frac{\partial \bar{p}}{\partial x_i} + \frac{\partial}{\partial x_j}\left(\nu\left(\frac{\partial \bar{u}_i}{\partial x_j} + \frac{\partial \bar{u}_j}{\partial x_i}\right) - \overline{u_u' u_j'}\right) \tag{2}$$

$$\rho_f c_{pf}\frac{\partial \bar{T}}{\partial t} + \rho_f c_{pf}\frac{\partial \bar{u}_j \bar{T}}{\partial x_j} = \frac{\partial}{\partial x_j}\left(k_f \frac{\partial \bar{T}}{\partial x_j} - \rho_f c_{pf}\overline{T' u_j'}\right) \tag{3}$$

$$\frac{\partial k}{\partial t} + \frac{\partial \bar{u}_j k}{\partial x_j} = \frac{\partial}{\partial x_j}\left(\left(\nu + \frac{\nu_t}{\sigma_k}\right)\frac{\partial k}{\partial x_j}\right) - \overline{u_i' u_j'}\frac{\partial \bar{u}_i}{\partial x_j} - \epsilon \tag{4}$$

$$\frac{\partial \epsilon}{\partial t} + \frac{\partial \bar{u}_j \epsilon}{\partial x_j} = \frac{\partial}{\partial x_j}\left(\left(\nu + \frac{\nu_t}{\sigma_\epsilon}\right)\frac{\partial \epsilon}{\partial x_j}\right) + \left(-c_1 \overline{u_i' u_j'}\frac{\partial \bar{u}_i}{\partial x_j} - c_2 \epsilon\right)\frac{\epsilon}{k} \tag{5}$$

It is assumed that forced convection is dominant such that the body force terms are neglected. The Reynolds stress and turbulent heat flux tensors are given by

$$-\rho_f \overline{u_i' u_j'} = \rho_f \nu_t\left(\frac{\partial \bar{u}_i}{\partial x_j} + \frac{\partial \bar{u}_j}{\partial x_i}\right) - \frac{2}{3}\rho_f k \delta_{ij} \tag{6a}$$

and

$$-\rho_f c_{pf}\overline{T' u_j'} = \rho_f c_{pf}\frac{\nu_t}{\sigma_T}\frac{\partial \bar{T}}{\partial x_j} \tag{6b}$$

respectively. The eddy diffusivity is given by

$$\nu_t = c_D \frac{k^2}{\epsilon} \tag{7}$$

Moreover, for the solid phase, the energy equation runs as

$$\rho_s c_s \frac{\partial T}{\partial t} = \frac{\partial}{\partial x_j}\left(k_s \frac{\partial T}{\partial x_j}\right) \tag{8}$$

In the foregoing expressions, the three values of a repeated index are summed up according to Einstein's summation convention. The barred quantities represent ensemble-averaged components, whereas the primes indicate fluctuating components. The subscripts f and s refer to fluid phase and solid phase, respectively.

It is somewhat controversial, whether or not a simple two-equation turbulence model based on an isotropic eddy diffusivity can be used for such complex turbulent flows as in saturated porous media. In this study, we consider a comparatively simple turbulence model to illustrate a consistent modeling procedure for turbulence in porous media, but believe that the modeling procedure presented here is quite general and valid for any further modifications using more elaborate turbulence models.

Kuwahara et al. (1998) numerically investigated the microscopic turbulence fields within a fluid-saturated periodical array, using both low- and high-Reynolds number versions of the k-ϵ model, and found that the difference in the volume-averaged quantities predicted by both of the models is insignificant. Thus, we choose the standard (high Reynolds number) version of the k-ϵ model along with conventional wall functions to save the number of grid nodes. The model constants and turbulent Prandtl numbers, recommended by Launder and Spalding (1972), are given as follows:

$$c_D = 0.09, \quad c_1 = 1.44, \quad c_2 = 1.92,$$
$$\sigma_k = 1.00, \quad \sigma_\epsilon = 1.30, \quad \sigma_T = 0.90 \tag{9}$$

Macroscopic Continuity, Momemtum and Energy Equations

We integrate the Reynolds averaged equations (1) to (5) over a control volume V, which is much larger than a microscopic (pore structure) characteristic size but much smaller than a macroscopic characteristic size. Then, from (1) and (2), the following macroscopic equations can be obtained:

$$\frac{\partial}{\partial x_j}\langle \bar{u}_j \rangle^f = 0 \tag{10}$$

$$\frac{\partial \langle \bar{u}_i \rangle^f}{\partial t} + \frac{\partial}{\partial x_j}\langle \bar{u}_j \rangle^f \langle \bar{u}_i \rangle^f = -\frac{1}{\rho_f}\frac{\partial}{\partial x_i}\left(\langle \bar{p} \rangle^f + \frac{2}{3}\rho_f \langle k \rangle^f\right) + \frac{\partial}{\partial x_j}\left[(\nu + \nu_t)\left(\frac{\partial \langle \bar{u}_i \rangle^f}{\partial x_j} + \frac{\partial \langle \bar{u}_j \rangle^f}{\partial x_i}\right)\right] + \frac{1}{V_f}\int_{A_{\text{int}}}\left[(\nu + \nu_t)\left(\frac{\partial \bar{u}_i}{\partial x_j} + \frac{\partial \bar{u}_j}{\partial x_i}\right) - \left(\frac{\bar{p}}{\rho_f} + \frac{2}{3}k\right)\delta_{ij}\right] n_j dA - \frac{\partial}{\partial x_j}\langle \overline{u_j'' u_i''} \rangle^f \tag{11}$$

where A_{int} is the total interface between the fluid and solid phases while n_j is the unit vector pointing normally outward from the fluid

Nomenclature

A = surface area
A_{int} = total interface between the fluid and solid
C = Forchheimer constant
c_1, c_2, c_D = turbulence model constants
c_p = specific heat at constant pressure
D = size of square rod
H = size of unit cell
k = turbulence kinetic energy; thermal conductivity
K = permeability
Le = Lewis number
p = pressure
Re_H = Reynolds number
T = temperature
u_i, $\mathbf{u}$ = velocity vector
u, v = velocity components
x, y = Cartesian coordinates
ϵ = dispassion rate of turbulence kinetic energy
ν = kinematic viscosity
ν_t = effective viscosity
σ_k, σ_ϵ = effective Prandtl number
ρ = density

Special symbols

$\bar{a}$ = ensemble mean
a' = turbulent fluctuation
a'' = deviation from intrinsic average
$\langle a \rangle$ = volume average
$\langle a \rangle^{f,s}$ = intrinsic average
$|\alpha|$ = absolute value

Subscripts and Superscripts

dis = dispersion
f = fluid
s = solid
tor = tortuosity

to solid side. V_f is the volume space which the fluid occupies such that

$$\langle a\rangle^f = \frac{1}{V_f}\int_{V_f} a dV \tag{12}$$

denotes the intrinsic average of a, whereas the double prime denotes the deviation from the intrinsic average, such that

$$a'' \equiv a - \langle a\rangle^f \tag{13}$$

In the numerical study of turbulent flow through a periodic array, Kuwahara et al. (1998) concluded that Forchheimer-extended Darcy's law holds even in the turbulent flow regime in porous media. The experimental data, provided by Fand et al. (1987), also support the validity of Forchheimer-extended Darcy's law. Thus, we follow Vafai and Tien (1981) and introduce Forchheimer's modification for the last two terms on the right-hand side, representing the intrinsic volume average of the total surface force (acting onto the fluid inside the pore) and the inertial dispersion, respectively. Thus, we obtain the macroscopic momentum equation as follows:

$$\frac{\partial\langle\bar{u}_i\rangle^f}{\partial t} + \frac{\partial}{\partial x_j}\overline{\langle u_j\rangle^f\langle\bar{u}_i\rangle^f} = -\frac{1}{\rho}\frac{\partial}{\partial x_i}\left(\langle\bar{p}\rangle^f + \frac{2}{3}\rho_f\langle k\rangle^f\right) + \frac{\partial}{\partial x_j}\left[(\nu+\nu_t)\left(\frac{\partial\langle\bar{u}_i\rangle^f}{\partial x_j} + \frac{\partial\langle\bar{u}_j\rangle^f}{\partial x_i}\right)\right] - \phi\left(\frac{\nu}{K} + \frac{\phi C}{\sqrt{K}}(\langle\bar{u}_j\rangle^f\langle\bar{u}_j\rangle^f)^{1/2}\right)\langle\bar{u}_i\rangle^f \tag{14}$$

where the permeability K and Forchheimer constant C are the empirical consatnts which depend on the porosity $\phi = V_f/V$. Similarly, spatial integration of the two microscopic energy equations (3) and (8) yields

$$\rho_f c_{pf}\left(\frac{\partial\langle T\rangle}{\partial t} + \frac{\partial}{\partial x_j}\langle\bar{u}_j\rangle^f\langle\bar{T}\rangle^f\right) = \frac{\partial}{\partial x_j}\left[\left(k_f + \frac{\rho_f c_{pf}\nu_t}{\sigma_T}\right)\frac{\partial\langle\bar{T}\rangle^f}{\partial x_j}\right] + \frac{1}{V_f}\frac{\partial}{\partial x_j}\int_{A_{\text{int}}} k_f\bar{T}n_j dA + \frac{1}{V_f}\int_{A_{\text{int}}}\left[\left(k_f + \frac{\rho_f c_{pf}\nu_t}{\sigma_T}\right)\frac{\partial\bar{T}}{\partial x_j}\right]n_j dA - \frac{\partial}{\partial x_j}[\rho_f c_{pf}\langle\bar{u}_j''\bar{T}''\rangle^f] \tag{15}$$

and

$$\rho_s c_s\frac{\partial\langle\bar{T}\rangle^s}{\partial t} = \frac{\partial}{\partial x_j}k_s\frac{\partial\langle\bar{T}\rangle^s}{\partial x_j} - \frac{1}{V_s}\frac{\partial}{\partial x_j}\int_{A_{\text{int}}} k_s\bar{T}n_j dA - \frac{1}{V_s}\int_{A_{\text{int}}}\left[\left(k_f + \frac{\rho_f c_{pf}\nu_t}{\sigma_T}\right)\frac{\partial\bar{T}}{\partial x_j}\right]n_j dA \tag{16}$$

We shall assume that thermal equilibrium exists between the fluid and solid matrix, namely, $\langle\bar{T}\rangle^f = \langle\bar{T}\rangle^s$. Adding up the foregoing two energy equations, we have

$$[\phi\rho_f c_{pf} + (1-\phi)\rho_s c_s]\frac{\partial\langle\bar{T}\rangle^f}{\partial t} + \phi\rho_f c_{pf}\frac{\partial}{\partial x_j}\langle\bar{u}_j\rangle^f\langle\bar{T}\rangle^f = \frac{\partial}{\partial x_i}\left[\left(k_e + \phi\frac{\rho_f c_{pf}\nu_t}{\sigma}\right)\delta_{ij} + (k_{\text{tor}})_{ij} + (k_{\text{dis}})_{ij}\right]\frac{\partial\langle\bar{T}\rangle^f}{\partial x_j} \tag{17}$$

where

$$k_e \equiv \phi k_f + (1-\phi)k_s \tag{18a}$$

$$\frac{1}{V}\int_{A_{\text{int}}}(k_f - k_s)\bar{T}n_j dA \equiv (k_{\text{tor}})_{ij}\frac{\partial\langle\bar{T}\rangle^f}{\partial x_j} \tag{18b}$$

and

$$-\phi(\rho c_p)_f\langle\bar{u}_j''\bar{T}''\rangle^f \equiv (k_{\text{dis}})_{ij}\frac{\partial\langle\bar{T}\rangle^f}{\partial x_j} \tag{18c}$$

k_e is the stagnant thermal conductivity. The apparent conductivity tensors $(k_{\text{tor}})_{ij}$ and $(k_{\text{dis}})_{ij}$ are introduced to model the tortuosity molecular diffusion term and the thermal dispersion term, respectively. The empirical and theoretical expressions for $(k_{\text{tor}})_{ij}$ and $(k_{\text{dis}})_{ij}$ may be found elsewhere (Kuwahara et al. (1996), Kaviany (1991)). When the Reynolds number is high, both k_e and $(k_{\text{tor}})_{ij}$ may be dropped as compared with the thermal dispersion and turbulent diffusion.

Macroscopic Transport Equations for Turbulence Kinetic Energy and Its Dissipation Rate

For describing the turbulent diffusion, we may recast the eddy diffusivity formula (7) using the intrinsically averaged values of the turbulence quantities as

$$\nu_t = c_D\frac{(\langle k\rangle^f)^2}{\langle\epsilon\rangle^f} \tag{19}$$

The macroscopic transport equations for $\langle k\rangle^f$ and $\langle\epsilon\rangle^f$ may be obtained by integrating the microscopic transport equations (4) and (5) as

$$\frac{\partial\langle k\rangle^f}{\partial t} + \frac{\partial}{\partial x_j}\langle\bar{u}_j\rangle^f\langle k\rangle^f = \frac{\partial}{\partial x_j}\left[\left(\nu + \frac{\nu_t}{\sigma_k}\right)\frac{\partial\langle k\rangle^f}{\partial x_j}\right] + 2\nu_t\langle s_{ij}\rangle^f\langle s_{ij}\rangle^f - \langle\epsilon\rangle^f + 2\nu_t\langle s_{ij}''s_{ij}''\rangle^f + \frac{\nu}{V_f}\int_{A_{\text{int}}}\frac{\partial k}{\partial x_j}n_j dA - \frac{\partial}{\partial x_j}\langle\bar{u}_j''k''\rangle^f \tag{20}$$

and

$$\frac{\partial\langle\epsilon\rangle^f}{\partial t} + \frac{\partial}{\partial x_j}\langle\bar{u}_j\rangle^f\langle\epsilon\rangle^f = \frac{\partial}{\partial x_j}\left[\left(\nu + \frac{\nu_t}{\sigma_\epsilon}\right)\frac{\partial\langle\epsilon\rangle^f}{\partial x_j}\right] + (2c_1\nu_t\langle s_{ij}\rangle^f\langle s_{ij}\rangle^f - c_2\langle\epsilon\rangle^f)\frac{\langle\epsilon\rangle^f}{\langle k\rangle^f} + 2c_1\nu_t\langle s_{ij}''s_{ij}''\rangle^f\frac{\langle\epsilon\rangle^f}{\langle k\rangle^f} + \frac{\nu}{V_f}\int_{A_{\text{int}}}\frac{\partial\epsilon}{\partial x_j}n_j dA - \frac{\partial}{\partial x_j}\langle\bar{u}_j''\epsilon''\rangle^f \tag{21}$$

where

$$s_{ij} = \frac{1}{2}\left(\frac{\partial\bar{u}_i}{\partial x_j} + \frac{\partial\bar{u}_j}{\partial x_i}\right) \tag{22}$$

In the above equations, all triple and high order correlations are dropped. The presence of porous matrix has brought out two additional terms in the turbulence kinetic energy equation (20), namely, the production term $2\nu_t\langle s_{ij}''s_{ij}''\rangle^f$ and the dissipation term $(\nu/V_f)\int_{A_{\text{int}}}(\partial k/\partial x_j)n_j dA$. (Note, it is $2\nu_t\langle s_{ij}''s_{ij}''\rangle^f$ that is solely responsible for the kinetic energy production for the case of macroscopically uniform flow with zero macroscopic mean shear, and also that $(\partial k/\partial x_j)n_j$ in the dissipation term is always negative due to the no-slip requirements. See also the argument on this respect by Masuoka and Takatsu (1996).) The sum of these two terms corresponds to the net-production rate inherent in the presence of porous matrix, which balances with the dissipation rate for the case of fully-developed macroscopically unidirectional flow with zero macroscopic mean shear through a porous medium. Thus, we model these two terms collectively as

$$\epsilon_\infty \equiv 2\nu_t \langle s''_{ij}\, s''_{ij}\rangle^f + \frac{\nu}{V_f}\int_{A_{\text{int}}} \frac{\partial k}{\partial x_j}\, n_j dA \tag{23}$$

A similar argument can be made for the corresponding two terms on the right-hand side of the macroscopic equation for the dissipation rate (21). Thus, we set

$$c_2 \frac{\epsilon_\infty^2}{k_\infty} \equiv 2c_1\nu_t \langle s''_{ij}\, s''_{ij}\rangle^f \frac{\langle\epsilon\rangle^f}{\langle k\rangle^f} + \frac{\nu}{V_f}\int_{A_{\text{int}}} \frac{\partial \epsilon}{\partial x_j}\, n_j dA^f \tag{24}$$

Hence, we obtain the following set of the macroscopic transport equations for $\langle k\rangle^f$ and $\langle\epsilon\rangle^f$:

$$\frac{\partial\langle k\rangle^f}{\partial t} + \frac{\partial}{\partial x_j}\langle\bar u_j\rangle^f\langle k\rangle^f = \frac{\partial}{\partial x_i}\left[\left(\nu + \frac{\nu_t}{\sigma_k}\right)\delta_{ij} + \frac{(k_{\text{dis}})_{ij}}{\text{Le}_k\phi\rho_f c_{pf}}\right]\frac{\partial\langle k\rangle^f}{\partial x_j} + 2\nu_t\langle s_{ij}\rangle^f\langle s_{ij}\rangle^f - \langle\epsilon\rangle^f + \epsilon_\infty \tag{25}$$

and

$$\frac{\partial\langle\epsilon\rangle^f}{\partial t} + \frac{\partial}{\partial x_j}\langle\bar u_j\rangle^f\langle\epsilon\rangle^f = \frac{\partial}{\partial x_i}\left[\left(\nu + \frac{\nu_t}{\sigma_\epsilon}\right)\delta_{ij} + \frac{(k_{\text{dis}})_{ij}}{\text{Le}_\epsilon\phi\rho_f c_{pf}}\right]\frac{\partial\langle\epsilon\rangle^f}{\partial x_j} + \left(2c_1\nu_t\langle s_{ij}\rangle^f\langle s_{ij}\rangle^f - c_2\langle\epsilon\rangle^f\right)\frac{\langle\epsilon\rangle^f}{\langle k\rangle^f} + c_2\frac{\epsilon_\infty^2}{k_\infty} \tag{26}$$

where Le_k and Le_ϵ are the Lewis numbers for the mechanical dispersions. The model constants, namely, ϵ_∞ and k_∞, should be determined from either turbulence measurements or numerical experiments.

Preliminary Consideration for Turbulence Model Constants

Experimental determination of the unknown model constants, namely, ϵ_∞ and k_∞, requires detailed turbulence measurements in a pore-scale, which may not easily be done even for artificially consolidated porous media. Alternatively, we may choose to conduct a numerical experiment to determine them, using the set of microscopic governing equations.

For the macroscopically uniform flow with zero mean shear, the macroscopic model equations (25) and (26) reduce to

$$\langle\bar u\rangle^f\frac{d\langle k\rangle^f}{dx} = -\langle\epsilon\rangle^f + \epsilon_\infty \tag{27}$$

and

$$\langle\bar u\rangle^f\frac{d\langle\epsilon\rangle^f}{dx} = -c_2\frac{(\langle\epsilon\rangle^f)^2}{\langle k\rangle^f} + c_2\frac{\epsilon_\infty^2}{k_\infty} \tag{28}$$

When the flow is periodically fully-developed, the foregoing equations yield

$$\langle k\rangle^f = k_\infty \quad \text{and} \quad \langle\epsilon\rangle^f = \epsilon_\infty \tag{29}$$

Thus, we may determine the unknown model constants, ϵ_∞ and k_∞, from the intrinsic volume average values of the turbulence kinetic energy and its dissipation rate attained in a periodically fully-developed flow through a porous medium.

Kuwahara et al. (1994) and Nakayama et al. (1995) conducted a series of numerical experiments for the laminar flow regime, using various two- and three-dimensional numerical models for porous media, such as arrays of square rods, circular rods, spheres and cubes. They found that all these models lead to almost identical expressions for the permeability, which are in good accord with Ergun's empirical formula (1952). The recent numerical study on thermal dispersion by Kuwahara et al. (1996) also supports the possibility of utilizing the results based a two-dimensional numerical model to estimate the thermal dispersion in packed spheres. These reports prompt us to consider a two-dimensional periodic array of square rods placed in an infinite space, as illustrated in Fig. 1.

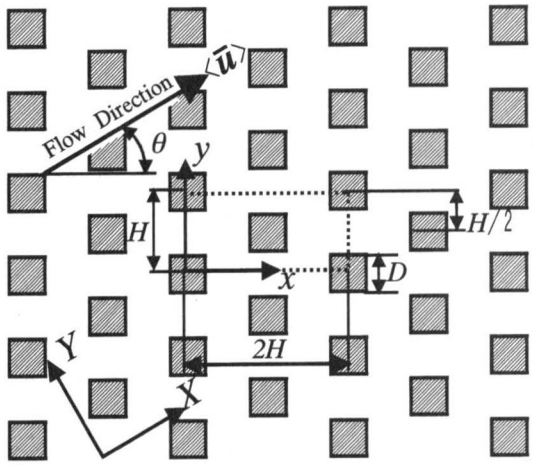

Fig. 1 Physical model and its coordinates

Numerical Procedure

Due to the periodicity of the model, only a one structural unit can be taken as a microscopic calculation domain, as indicated by dashed lines in the figure. On the solid walls, usual wall functions based on the constant stress layer assumption are applied to the grid nodes next to the solid wall to match the interior flow with the required wall conditions, while, on the periodic boundaries, the following compatibility and periodic constraints are imposed:

$$\bar{\mathbf{u}}|_{x=2H} = \bar{\mathbf{u}}|_{x=0},\ \bar{\mathbf{u}}|_{y=H} = \bar{\mathbf{u}}|_{y=0} \tag{30a}$$

$$\int_0^H \bar u dy\bigg|_{x=2H} = \int_0^H \bar u dy\bigg|_{x=0} = H|\langle\bar{\mathbf{u}}\rangle|\cos\theta \tag{30b}$$

$$\int_0^{2H} \bar v dx\bigg|_{y=H} = \int_0^{2H} \bar v dx\bigg|_{y=0} = 2H|\langle\bar{\mathbf{u}}\rangle|\sin\theta \tag{30c}$$

$$k|_{x=0} = k|_{x=2H},\ k|_{y=0} = k|_{y=H} \tag{30d}$$

$$\epsilon|_{x=0} = \epsilon|_{x=2H},\ \epsilon|_{y=0} = \epsilon|_{y=H} \tag{30e}$$

Only the representative cases of $\theta = 0$ are treated in this report. We shall define the Reynolds number based on the Darcian velocity $|\langle\bar{\mathbf{u}}\rangle| = \phi|\langle\bar{\mathbf{u}}\rangle^f|$ and length of structural unit H as $\text{Re}_H = |\langle\bar{\mathbf{u}}\rangle|H/\nu$. Extensive numerical calculations using the microscopic governing equations (1) to (5) are carried out for a wide range of the porosity $\phi = 1 - (D/H)^2$ (0.2 ~ 0.9) and Reynolds number Re_H (10^5 ~ 10^7), so as to investigate their effects on the numerical results.

The governing equations are discretized by integrating them over a grid volume. SIMPLE algorithm for the pressure-velocity coupling, as proposed by Patankar and Spalding (1972) is adopted to correct the pressure and velocity fields. Calculation starts with solving the two momentum equations, and subsequently, the estimated velocity field is corrected by solving the pressure correction equation reformulated from the discretized continuity and momentum equations, such that the velocity field fulfills the continuity principle. Then, the turbulence model equations are solved to find the eddy diffusivity field. This iteration sequence is repeated until convergence is achieved. Further details on this numerical procedure can be found in Patankar (1980) and Nakayama (1995). All computations have been carried out for a one structural unit $2H \times H$ using highly nonuniform grid arrangements with 300×150 nodes. It has been confirmed that the results are independent of the

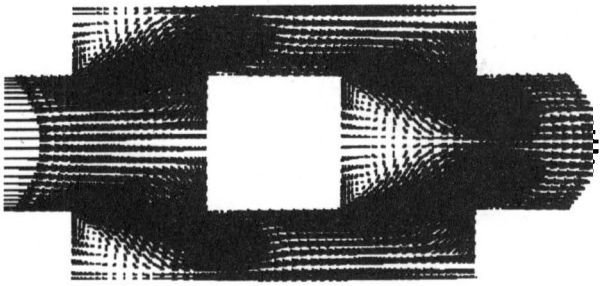

(a) Velocity vectors

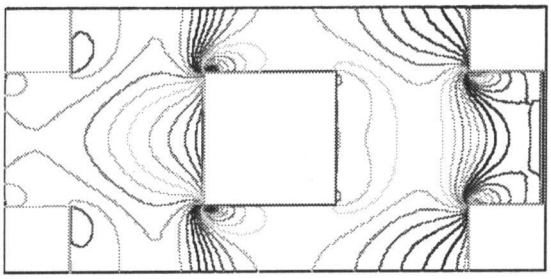

(b) Pressure

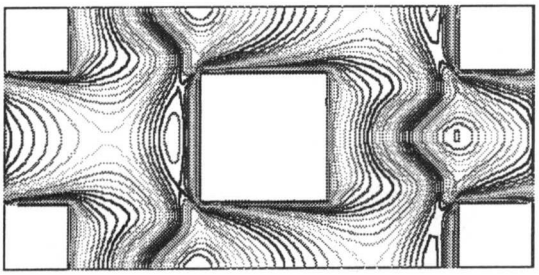

(c) Turbulence kinetic energy

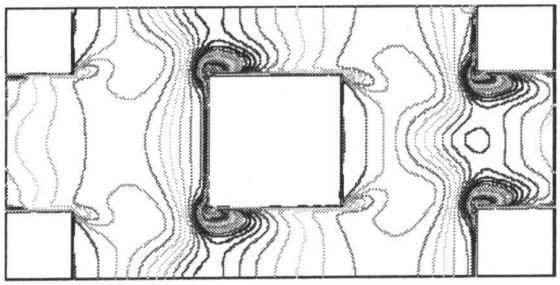

(d) Dissipation rate of turbulence kinetic energy

Fig. 2 Typical microscopic results for $Re_H = 10^5$ and $\phi = 0.75$. (*a*) Velocity vectors; (*b*) pressure; (*c*) turbulence kinetic energy; (*d*) dissipation rate of turbulence kinetic energy.

grid system. All computations were performed using the computer system CONVEX 220 at Shizuoka University Computer Center.

Determination of Turbulence Model Constants

Figures 2(*a*) to (*d*) show typical distributions of velocity vectors, pressure, turbulence kinetic energy and its dissipation rate in a microscopic porous structure, obtained at $Re_H = 10^5$ for the cases of $\phi = 0.75$.

The flow accelerates around the windward corners and separates over the leeward corners to form weak recirculation bubbles as in the case of the backward facing step. The pressure increases at the front stagnation face of the square rod, and decreases drastically around the corner as can be seen from the pressure contours. The macroscopic pressure gradient, obtained by integrating the microscopic pressure results over a structural unit, agrees very well with the existing emprical formula. Such comparison can be found in Nakayama et al. (1995) and Kuwahara et al. (1996). The turbulence kinetic energy is high around the corner where a strong flow acceleration takes place, and subsequently, a strong shear layer is formed downstream of the corner. A series of calculations performed for various sets of porosity and Reynolds number, reveal that the dimensionless quantities are sensitive to the porosity, but fairly insensitive to the Reynolds number.

Having established the microscopic turbulence fields, the intrinsic volume average values can readily be evaluated by integrating the microscopic turbulence quantities over the fluid phase domain within the structural unit. As can be expected from the microscopic results, the effect of the Reynolds number on the intrinsic average quantities, $\langle k \rangle^f = k_\infty$ and $\langle \epsilon \rangle^f = \epsilon_\infty$ is negligibly small, whereas that of the porosity is substantial, as can be seen from Figs. 3(*a*) and (*b*), plotted for k_∞ and ϵ_∞, respectively. These figures suggest the following correlations:

$$k_\infty = 3.7 \frac{1-\phi}{\sqrt{\phi}} |\langle \bar{\mathbf{u}} \rangle|^2 = 3.7(1-\phi)\phi^{3/2} \langle \bar{u}_j \rangle^f \langle \bar{u}_j \rangle^f \quad (31)$$

and

$$\epsilon_\infty = 39 \frac{(1-\phi)^2}{\phi} \frac{|\langle \bar{\mathbf{u}} \rangle|^3}{H}$$

$$= 39\phi^2(1-\phi)^{5/2} \frac{1}{D} (\langle \bar{u}_j \rangle^f \langle \bar{u}_j \rangle^f)^{3/2} \quad (32)$$

Nakayama et al. (1995) and Kuwahara et al. (1996) showed though numerical experiments that the results based a two-dimensional numerical model can be used to estimate the pressure drop and thermal dispersion in packed spheres. Thus, the present

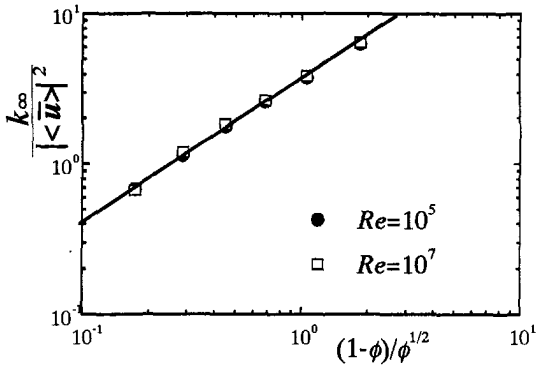

Fig. 3(*a*) Turbulence kinetic energy

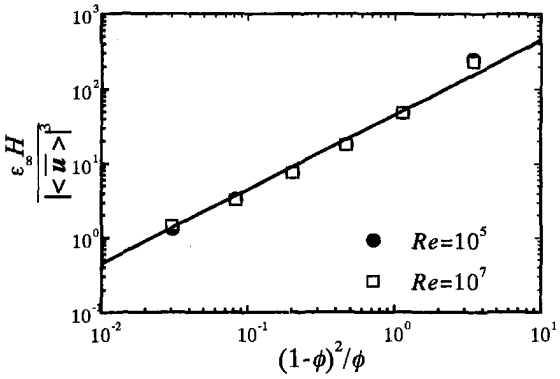

Fig. 3(*b*) Dissipation rate of turbulence kinetic energy.

Fig. 3 Effect of porosity on turbulence

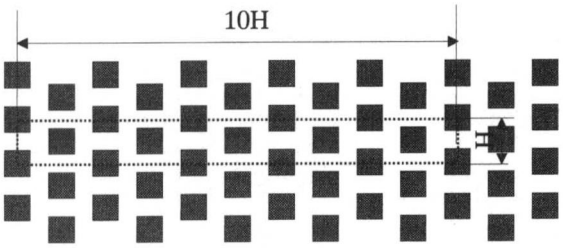

Fig. 4 Physical model for a large scale direct computation

formulas (31) and (32) for the model constants k_∞ and ϵ_∞, determined numerically using the microscopic results based on the square rod array, may be used to investigate the turbulent flow through packed spheres, as the square rod size D is taken for the average diameter of packed spheres.

Assessment of Macroscopic Turbulence Model

In order to assess the present macroscopic turbulence model, we shall investigate a steady unidirectional highly turbulent flow entering into a semi-finite periodic array of square rods, from both microscopic and macroscopic points of view. From the microscopic view, we carry out a large scale direct computation using the set of microscopic equations for a row of the periodic structural units, as shown in Fig. 4, and then integrate the microscopic results of turbulence quantities over every unit, to obtain the macroscopic decay of turbulence. (The periodic boundary conditions are used only for the upper and lower boundaries.) From the macroscopic view, we solve the macroscopic turbulence model equations (25) and (26) with the model constants as given by (31) and (32), to predict the streamwise decay of turbulence, and compare the results against the foregoing results based on the large scale direct computation. In the large scale direct computation, the grid nodes (3000×150) are laid out so that we have the same spatial resolution as in the microscopic calculation within a single unit. In the one-dimensional computation with the macroscopic model equations, we set $\Delta x = H/150$ to have a sufficient resolution. In both microscopic and macroscopic computations, we have carried out the grid refinement tests and confirmed that the grid systems used in the study are quite adequate for the present purpose.

Figures 5(*a*) and (*b*) show the microscopic fields of turbulence kinetic energy and its dissipation rate obtained from the large scale direct computation for the case of $\mathrm{Re}_H = 10^5$, $\phi = 0.75$, the inlet turbulence kinetic energy $\langle k \rangle^f = 10k_\infty$ and its dissipation rate $\langle \epsilon \rangle^f = 30\epsilon_\infty$. It can be seen that the turbulence decays drastically over a short distance from the entrance, and that periodically fully-developed patterns are established as the fluid passes downstream. The streamwise decay of the macroscopic turbulence kinetic energy and that of the dissipation rate predicted by the present macroscopic turbulence model are presented in Figs. 6(*a*) and (*b*) along with the intrinsically averaged values based on the large scale direct computation. Good agreement between the two sets of the results reveals the validity of the present macroscopic turbulence model. The difference between the two sets of the results is

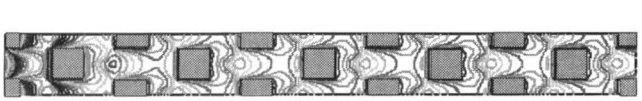

Fig. 5(*a*) Turbulence kinetic energy

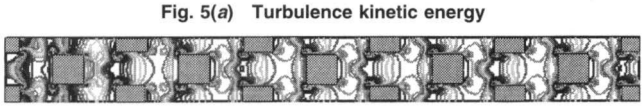

Fig. 5(*b*) Dissipation rate of turbulence kinetic energy

Fig. 5 Microscopic results from a large scale computation

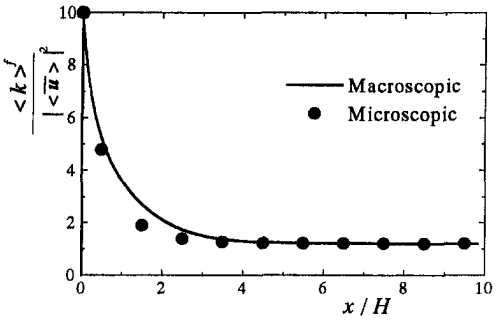

Fig. 6(*a*) Turbulence kinetic energy

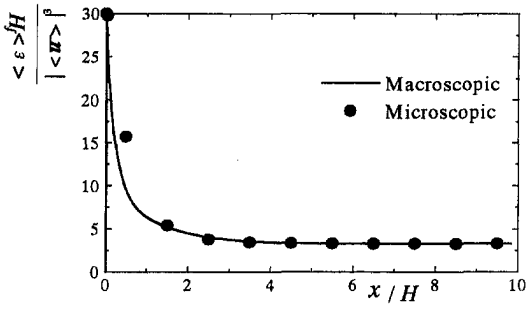

Fig. 6(*b*) Dissipation rate of turbulence kinetic energy

Fig. 6 Decay of turbulence

appreciable near the inlet, where the turbulence kinetic energy decreases drastically. The error, however, is found 30% at most.

Finally, let us estimate the effect of turbulence on the scalar transport as compared with that of the mechanical dispersion. From Eq. (17), the apparent thermal conductivity tensor is given by

$$(k_{\mathrm{app}})_{ij} = \left(k_e + \phi \frac{\rho_f c_{pf} \nu_t}{\sigma} \right) \delta_{ij} + (k_{\mathrm{tor}})_{ij} + (k_{\mathrm{dis}})_{ij} \qquad (33)$$

For the case of high Reynolds number, the molecular diffusion terms are negligible. Hence, we may approximate the apparent thermal conductivity tensor as

$$(k_{\mathrm{app}})_{ij} \approx \phi \frac{\rho_f c_{pf} \nu_t}{\sigma} \delta_{ij} + (k_{\mathrm{dis}})_{ij} \qquad (34)$$

Its transverse component (normal to the macroscopic flow direction) may be estimated as follows:

$$(k_{\mathrm{app}})_{22} \approx \left(0.03 \frac{\phi}{\sigma_T \sqrt{1-\phi}} + 0.05 \sqrt{1-\phi} \right) \phi \rho_f c_{pf} \langle \bar{u} \rangle^f D \qquad (35)$$

Equations (31), (32) and (19) are used to evaluate the fully developed value of ν_t whereas the correlation based on the numerical experiment by Kuwahara et al. (1996) is used to estimate $(k_{\mathrm{dis}})_{22}$. The foregoing equation suggests that the contribution from the turbulent mixing is comparable to that from the mechanical dispersion. It is also interesting to note that, for given mass flow rate $\phi \langle \bar{u} \rangle^f$ and particle size D, the increase in the porosity ϕ enhances turbulent mixing, and at the same time, damps mechanical dispersion within porous media. Thus, even in a sufficiently highly porous medium, where the effect of the mechanical dispersion on the scalar transport is insignificant, that of the turbulence mixing may not be negligible.

Conclusions

A macroscopic two-equation turbulence model has been proposed for analyzing turbulent flow and heat transfer within porous

media. The Reynolds-averaged set of the governing equations in consideration, namely, the continuity equation, Navier-Stokes equation, energy equation, turbulence kinetic energy transport equation, and that of dissipation rate, were integrated over a control volume to obtain the spatially-averaged set of the governing equations. The additional terms representing production and dissipation of turbulence kinetic energy and its dissipation rate have been modeled introducing two unknown model constants, which are determined from a numerical experiment using a spatially periodic array. The model has been tested for macroscopically unidirectional flow through a porous medium. Further investigation is needed to find out the applicability of the present model to more general cases of turbulent flows in porous media.

References

Antohe, B. V. and Lage, J. L., 1997, "A General Two-Equation Macroscopic Turbulence Model for Incompressible Flow in Porous Media," *International Journal of Heat and Mass Transfer,* Vol. 13, pp. 3013–3024.

Dybbs, A. and Edwards, R. V., 1984, "A New Look at Porous Media Fluid Mechanics-Darcy to Turbulent," *Fundamentals of Transport Phenomena in Porous Media,* Bear and Corapcioglu, eds., Martinus Nijhoff Publishers, pp. 199–254.

Ergun, S., 1952, "Fluid Flow Through Packed Columns," *Chemical Engineering Progress,* Vol. 48, pp. 89–94.

Fand, R. M., Kim, B. Y. K., Lam, A. C. C., and Phan, R. T., 1987, "Resistance to Flow of Fluids Through Simple and Complex Porous Media Whose Matrices are Composed of Randomly Packed Spheres," ASME JOURNAL OF FLUIDS ENGINEERING, Vol. 109, pp. 268–274.

Kaviany, M., 1991, *Principles of Heat Transfer in Porous Media,* Springer-Verlag, New York, pp. 42–49.

Kirkham, C. E., 1967, "Turbulent Flow in Porous Media-An Analytical and Experimental Study," Dept. of Civil Engng., Univ. of Melbourne, Australia, Feb.

Kuwahara, F., Kameyama, Y., Yamashita, S., and Nakayama, A., 1998, "Numerical Modeling of Turbulent Flow in Porous Media Using a Spatially Periodic Array," *Journal of Porous Media,* Vol. 1, pp. 47–55.

Kuwahara, F., Nakayama, A., and Koyama, H., 1994, "Numerical Modelling of Heat and Fluid Flow in Porous Medium," *Proc. the 10th Int. Heat Transfer Conf.,* Vol. 5, pp. 309–314.

Kuwahara, F., Nakayama, A., and Koyama, H., 1996, "A Numerical Study of Thermal Dispersion in Porous Media," ASME *Journal of Heat Transfer,* Vol. 118, pp. 756–761.

Launder, B. E. and Spalding, D. B., 1972, *Mathematical Models of Turbulence,* Academic Press.

Lee, K., and Howell, J. R., 1987, "Forced Convective and Radiative Transfer Within a Highly Porous Layer Exposed to a Turbulent External Flow Field," *Proc. 2nd ASME/JSME Thermal Engng. Joint Conf.,* Vol. 2, pp. 377–386.

Macdonald, I. F., El-Sayed, M. S., Mow, K., and Dullien, F. A. L., 1979, "Flow Through Porous Media-Ergun Equation Revisited," *Industrial Engineering Chemical Fundamentals,* Vol. 18, pp. 199–208.

Masuoka, T. and Takatsu, Y., 1996, "Turbulence Model for Flow Through Porous Media," *International Journal of Heat and Mass Transfer,* Vol. 39, pp. 2803–2809.

Mickeley, H. S., Smith, K. A., and Korchak, E. I., 1965, "Fluid Flow in Packed Beds," *Chemical Engineering Science,* Vol. 23, pp. 237–246.

Nakayama, A., 1995, *PC-Aided Numerical Heat Transfer and Convective Flow,* CRC Press, Boca Raton.

Nakayama, A., Kuwahara, F., Kawamura, Y., and Koyama, H., 1995, "Three-Dimensional Numerical Simulation of Flow Through a Microscopic Porous Structure," ASME/JSME Thermal Engineering Conf., Vol. 3, pp. 313–318.

Patankar, S. V., 1980, *Numerical Heat Transfer and Fluid Flow,* Hemisphere, Washington, D.C..

Patankar, S. V. and Spalding, D. B., 1972, "A Calculation Procedure for Heat, Mass and Momentum Transfer in Three-Dimensional Parabolic Flows," *International Journal of Heat and Mass Transfer,* Vol. 15, pp. 1787–1806.

Rudraiah, N., 1983, "Turbulent Convection in a Porous Medium Using Spectral Method," *Proc. II Asian Cong. Fluid Mech., Science Press,* Beijing, China, pp. 1021–1027.

Rudraiah, N., 1988, "Turbulent Convection in Porous Media with Non-Darcy Effects," ASME HTD (Heat Transfer Division), Vol. 96, pp. 747–754.

Vafai, K. and Tien, C. L., 1981, "Boundary and Inertia Effects on Flow and Heat Transfer in Porous Media," *International Journal of Heat and Mass Transfer,* Vol. 24, pp. 195–203.

High-Lift Optimization Design Using Neural Networks on a Multi-Element Airfoil

Roxana M. Greenman
Aerospace Engineer.
rgreenman@mail.arc.nasa.gov

Karlin R. Roth
Aerospace Engineer.

NASA Ames Research Center,
Moffett Field, CA 94035

The high-lift performance of a multi-element airfoil was optimized by using neural-net predictions that were trained using a computational data set. The numerical data was generated using a two-dimensional, incompressible, Navier-Stokes algorithm with the Spalart-Allmaras turbulence model. Because it is difficult to predict maximum lift for high-lift systems, an empirically-based maximum lift criteria was used in this study to determine both the maximum lift and the angle of attack at which it occurs. Multiple input, single output networks were trained using the NASA Ames variation of the Levenberg-Marquardt algorithm for each of the aerodynamic coefficients (lift, drag, and moment). The artificial neural networks were integrated with a gradient-based optimizer. Using independent numerical simulations and experimental data for this high-lift configuration, it was shown that this design process successfully optimized flap deflection, gap, overlap, and angle of attack to maximize lift. Once the neural networks were trained and integrated with the optimizer, minimal additional computer resources were required to perform optimization runs with different initial conditions and parameters. Applying the neural networks within the high-lift rigging optimization process reduced the amount of computational time and resources by 83% compared with traditional gradient-based optimization procedures for multiple optimization runs.

Introduction

The design of an aircraft's high-lift system is a crucial part of the design phase of commercial and military airplanes since this system controls the takeoff and landing performance. A well designed high-lift system can lead to increased payloads and increase the operational flexibility by extending ranges and by decreasing take-off and landing distances. Traditionally, high-lift designs have been accomplished through extensive wind tunnel and flight test programs which are expensive and difficult due to the complex flow interactions. Recently, computational fluid dynamics (CFD) has been incorporated in high-lift design (Ying, 1996). For high-lift applications, CFD can also be expensive because the entire design space is large, grids must be generated around geometrically-complex high-lift devices, and complex flow phenomena must be resolved. In order to achieve optimum, rapid designs, new tools for speedy and efficient analysis of high-lift configurations are required.

Artificial neural networks are a collection (or network) of simple computational devices used to calculate nonlinear data. The ability of neural networks to accurately learn and predict nonlinear multiple input and output relationships makes them a promising technique in modeling nonlinear aerodynamic data. Computational fluid dynamics in conjunction with neural networks and optimization may help reduce the time and resources needed to accurately define the optimal aerodynamics of an aircraft including high-lift. Essentially, the neural networks will reduce the amount of data required to define the aerodynamic characteristics of an aircraft while the optimizer will allow the design space to be easily searched for extrema.

Recently, neural networks have been applied to a wide range of problems in the aerospace industry. One study demonstrated that application of neural networks to rotor blade design reduced the time required to optimize the blades (LaMarsh et al., 1992). Faller and Schreck (1995) used neural networks to predict real-time three-dimensional unsteady separated flowfields and aerodynamic coefficients of a pitching wing. It has also been shown that neural networks trained with measured data predict with sufficient accuracy to enable identification of instrumentation system degradation (McMillen et al., 1995). Steck and Rokhsaz (1997) have trained neural networks to predict aerodynamic forces with sufficient accuracy for design and modeling. As a final example, Rai and Madavan (1998) demonstrated the feasibility of applying neural networks to aerodynamic design of turbomachinery airfoils.

Neural networks have been used at NASA Ames Research Center to minimize the amount of data required to define the aerodynamic performance characteristics of a wind tunnel model (Jorgensen and Ross, 1997 and Ross et al., 1997). It was shown that when only 50% of the data acquired from the wind tunnel test was used to train neural nets, the results had the same predictive accuracy as the experimental measurements. The success of the NASA Ames neural network application for wind-tunnel data prompted this current study (Greenman, 1998) to use optimization with neural networks to optimize high-lift aerodynamics of a multi-element airfoil.

This paper describes a process which allows CFD to impact high-lift design. This process has three phases: 1) generation of the training database using CFD; 2) training of the neural networks; and 3) integration of the trained neural networks with an optimizer to capture and search the high-lift design space. In this study, an incompressible two-dimensional Navier-Stokes solver is used to compute the flowfield about the three-element airfoil shown in Fig. 1. The selected airfoil is a cross-section of the Flap-Edge model (Storms, 1997) that was tested in the 7- by 10-Foot Wind Tunnel No. 1 at the NASA Ames Research Center (detailed analysis comparing CFD results to experimental data is presented by Greenman (1998)). The CFD database for this flap optimization problem contains 27 different flap riggings (refer to Fig. 1(*b*)) which are each computed at ten different angles of attack. The neural networks are trained by using the flap riggings and angles of attack as the inputs and the aerodynamic forces as the outputs. The neural networks are defined to be successfully trained to predict the aerodynamic coefficients when given a set of inputs that are not

Contributed by the Fluids Engineering Division for publication in the JOURNAL OF FLUIDS ENGINEERING. Manuscript received by the Fluids Engineering Division May 19, 1998; revised manuscript received January 25, 1999. Associate Technical Editor: D. Williams.

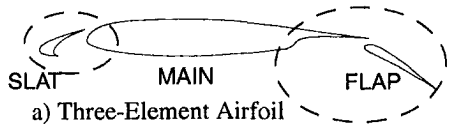

a) Three-Element Airfoil

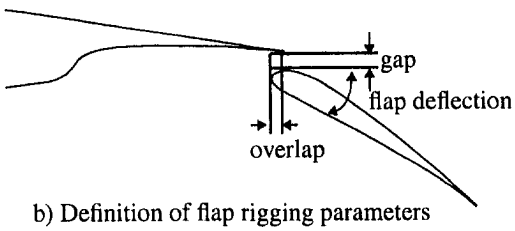

b) Definition of flap rigging parameters

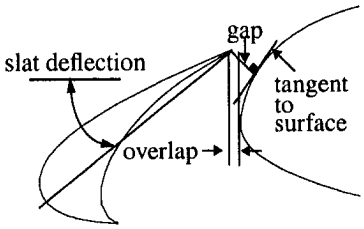

c) Definition of slat rigging parameters

Fig. 1 Three-element airfoil

in the training set, the outputs are predicted within the experimental error. The experimental error of the total lift coefficient (C_l) is ± 0.02 for $C_l \leq 0.95 C_{l_{max}}$ and ± 0.06 for $C_l \geq 0.95 C_{l_{max}}$. Finally, the trained neural networks are integrated with the optimizer to allow the design space to be easily searched for points of interest. It will be shown that this enhanced design process minimizes the cost and time required to accurately optimize the high-lift flap rigging. To date, this is the first study that used trained neural networks on a CFD database integrated with a gradient optimizer to optimize the high-lift rigging on a multi-element airfoil.

A brief description of the training set generation is presented in the next section, including grid generation, the governing equations, maximum lift criteria, and the flow solver. Next, the neural network training is discussed followed by the optimization process. The results are then presented, from which the effectiveness of optimization with neural networks as a tool to reduce resources required in aerodynamic design is discussed.

Training Set Generation

Geometry Definition. Extensive wind-tunnel investigations (Storms, 1997) have been carried out for the Flap-Edge geometry shown in Fig. 1. The model is a three-element airfoil consisting of a 12%c LB-546 slat, NACA 63_2-215 Mod B main element and a 30%c Fowler flap where c is the chord of the cruise wing. Two-different slat deflection angles are computed, six and twenty-six degrees. Each slat has a gap of $gap_s = 2.0\%c$ and an overlap of $ol_s = -0.05\%c$. In this present study, only the results of the six-degree slat deflection data set are presented (refer to Greenman (1998) for detailed $\delta_s = 26.0°$ results). For the computational data base, 27 different flap riggings are created for each slat configuration. The flap riggings are combinations of the following flap deflection, gap, and overlap defined in Fig. 1(*b*). The flap deflection angles are $\delta_f = 25.0°$, 29.0°, and 38.5°. The three gap settings are $gap_f = 1.50$, 2.10, and 2.70%c whereas the overlap settings are $ol_f = 0.40$, 1.00, and 1.50%c. All gap and overlap values in this paper are expressed in terms of percent clean chord, %c. In this study, $\mathrm{Re}_c = 3.7$ million and the angle of attack varies from $0.0° \leq \alpha \leq 22.0°$.

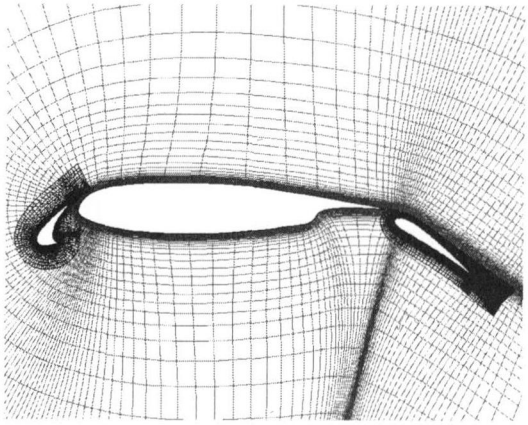

Fig. 2 Grid around three-element airfoil (every other point shown for clarity)

Grid Generation. The grids around the three-element airfoil are generated using OVERMAGG (Rogers, 1997) which is an automated script system used to perform overset multi-element airfoil grid generation. OVERMAGG takes as input the surface definition of the individual elements of the airfoil. Then it creates a surface grid for each individual element by generating and redistributing points from the given surface definition. It calls the HYPGEN code (Chan et al., 1993) to generate volume grids about each element. OVERMAGG also automatically calls the PEGSUS code (Suhs and Tramel, 1991) to unite the individual meshes into an overset grid system which is the final output of OVERMAGG.

Figure 2 shows the grid system used. A grid resolution study (Greenman, 1998) is conducted to determine the grid density required to solve the physical flow features. As a result, a total of 121,154 grid points are used consisting of a 242 × 81 C-grid around the slat; a 451 × 131 C-grid around the main; and a 351 × 121 embedded grid around the flap which is used to help resolve the merging wake in this region. The normal wall spacing for all grids is 5×10^{-6} chords and $\mathrm{Re}_c = 3.7$ million.

Nomenclature

C_d = drag coefficient, $C_d \equiv D/(q_\infty S)$
C_l = lift coefficient, $C_l \equiv L/(q_\infty S)$
C_m = moment coefficient, $C_m \equiv M/(q_\infty S c)$
C_p = pressure coefficient, $C_p \equiv (P - P_\infty)/q_\infty$
c = chord, $c = 0.761$ m
D = drag force
L = lift force
M = pitching moment
ol = overlap
p = pressure
q_∞ = freestream dynamic pressure, $q_\infty \equiv \frac{1}{2}\rho_\infty V_\infty^2$
rms = root-mean-square
Re_c = Reynolds number, $\mathrm{Re}_c = \rho_\infty V_\infty c/\mu_\infty$
S = wing area
V = freestream velocity
α = angle of attack
δ = deflection angle
μ = coefficient of viscosity
ρ = density

Subscripts

f = flap
max = maximum
s = slat
∞ = freestream value

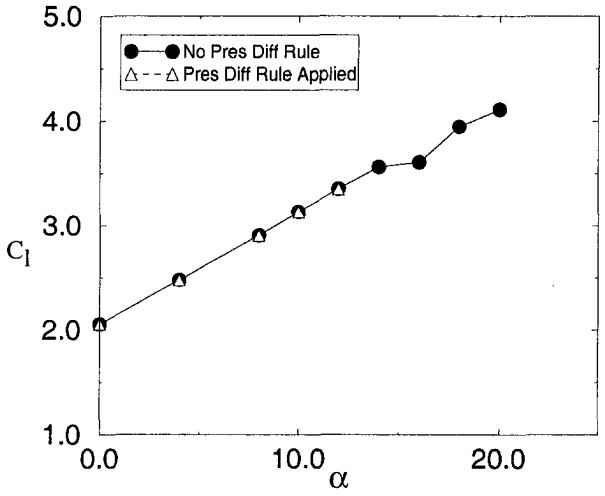

Fig. 3 Computational lift coefficient versus angle of attack for $\delta_S = 6.0°$, $gap_s = 2.0\%c$, $ol_s = -0.05\%c$, $\delta_f = 38.5°$, $gap_f = 2.7\%c$, $ol_f = 0.4\%c$

Numerical Methods. In order to generate the necessary computational training data, each high-lift configuration is analyzed at ten different angles of attack. The incompressible Navier-Stokes equations in two-dimensional generalized coordinates are solved using INS2D-UP (Rogers and Kwak, 1990, 1991) flow solver. This code has been used extensively to predict high-lift multi-element airfoil flows. INS2D-UP uses an artificial compressibility approach to couple the mass and momentum equations. The convective terms are differenced using a third-order accurate upwind biased flux-splitting. The equations are solved using a generalized minimum residual implicit scheme. Since the flow is turbulent, the Spalart-Allmaras (Spalart and Allmaras, 1992) turbulence model is used in this study for closure. The Spalart-Allmaras turbulence model has been successfully used to compute flowfields associated with high-lift multi-element airfoils (Rogers, 1993 and Dominik, 1994).

Maximum Lift Criteria. The determination of maximum lift is one of the most important results of any high-lift wing design study. Figure 3 shows the computed lift coefficient versus angle of attack for one high-lift setting. The solid symbols show that the computational curve continues to increase and thus does not accurately predict maximum lift.

Valarezo and Chin (1994) reported a hybrid method that couples cost-effective computational fluid dynamics technology with empirically-observed phenomenon in order to predict maximum lift ($C_{l_{max}}$) for complex multi-element wing geometries. Their semi-empirical $C_{l_{max}}$ criteria for multi-element airfoils or wings, designated the "pressure difference rule" (PDR), states that for a given Reynolds and Mach number combination, there exists a certain difference between the peak suction pressure coefficient and the trailing edge pressure coefficient, $\Delta C_{p_{diff}} = C_{p_{peak}} - C_{p_{te}}$ at the maximum lift condition. For the flow conditions of this study, the pressure difference value is -13.0. The rule is applied to each element of the airfoil. The slat is the element that has pressure differences greater than the acceptable value, thus this is the critical element in determining the maximum lift. By applying the pressure difference rule to the training data set, it is then reduced to include only the data points that are at or below the maximum lift (open triangles in Fig. 3). Although this particular configuration was not tested in the wind-tunnel, the angle where maximum lift is predicted is near where the expected experimental value would be by observations of similar configurations.

The neural networks are trained with the entire data set for the six-degree slat and then also with the processed data set that includes only data up to and containing maximum lift to compare the prediction accuracy. For the outputs, C_l, C_d, and C_m, the rms (root-mean-square) error is much lower when the pressure difference rule is applied (Greenman, 1998).

Neural Network Training

The architecture of the neural networks in this study is a multilayer network with tangent hyperbolic activation functions in hidden layer units, and a linear transfer function in the output unit. Individual 4-input, 1-output networks are used to model each of the desired aerodynamic coefficients. A NASA Ames variation of the Levenberg-Marquardt training scheme is used because it provides better accuracy than the other schemes tested including the back-propagation training method (Jorgensen and Ross, 1997 and Norgaard et al., 1997). The single output networks for each of the aerodynamic coefficients yield more precise modeling than multiple-output networks (McMillen et al., 1995 and Ross et al., 1997). The neural network contains 15 nodes in the hidden layer and Fig. 4 shows a sketch of the architecture.

The four independent input variables are flap deflection, gap, overlap, and angle of attack (α) as illustrated in Fig. 4. The outputs are lift, drag and moment coefficients (C_l, C_d, and C_m), and the pressure difference, $C_{p_{diff}}$. Thus, four different networks are used to train each of the outputs. However, only the results from the neural network that predict the lift coefficient and the pressure difference are presented in this paper.

Optimization With Neural Networks

Optimization Procedure. The problem addressed in this study is to optimize the high-lift riggings to maximize the lift coefficient. The design variables are flap deflection, gap, overlap and the angle of attack. The objective function which is defined to be the value or function that is being driven to the optimal maximum (or minimum) is the lift coefficient. In this study, the optimizer is integrated with the trained neural networks so that it can calculate the gradient search direction in order to find the maximum objective function. In some instances, a constraint $C_{p_{diff}} \geq -13.0$ is applied to the optimization problem.

The optimization procedure that is used in this study is shown in Fig. 5. There are three different phases in the optimization procedure: generate the training set, train the neural networks, and optimize. The first two phases need only to be performed once in this process. The first phase is to generate the training set as discussed in the previous sections. This data set is then used in phase 2 to train the neural networks to accurately predict the aerodynamic coefficients for any set of inputs that is within the design space.

The trained neural networks are now used in phase three which is an iterative phase. The optimization phase begins with the optimizer generating a baseline objective function from the initial values of the design variables. This is accomplished by inputting

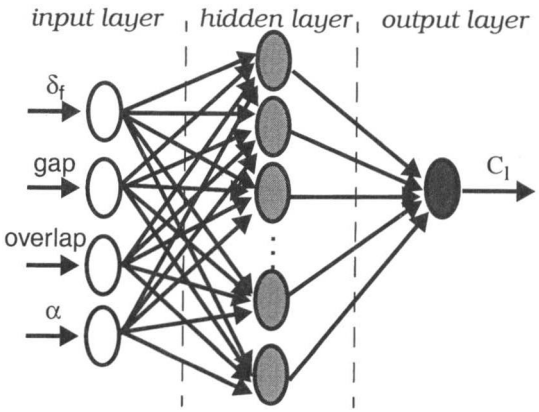

Fig. 4 Neural network architecture with 15 nodes in the hidden layer

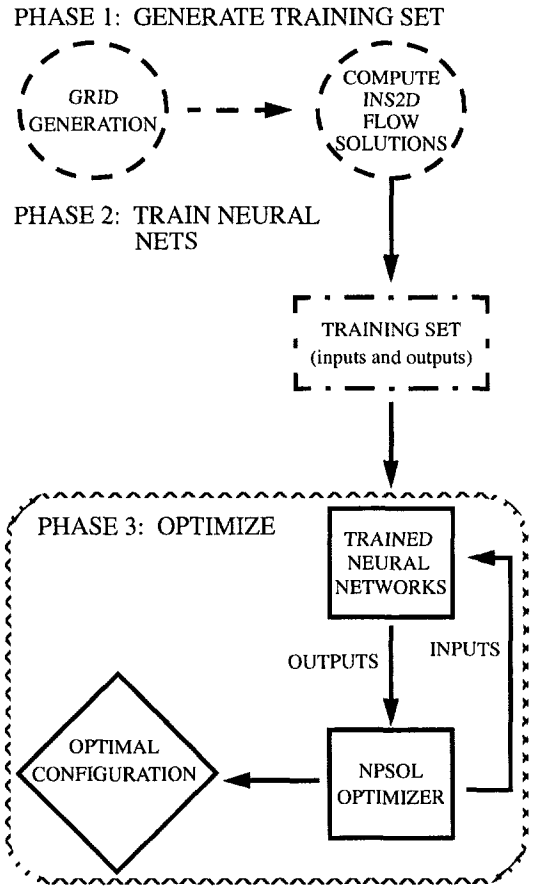

Fig. 5 The three phases of the neural network optimization procedure

the initial values of the design variables into the neural network which then computes the output, that is the lift coefficient, for those sets of design variables. One of the most important advantages of the optimization process is that once the neural networks have been trained, new designs can be rapidly analyzed whereas, the traditional optimization process would require function evaluations using CFD for every new design considered. The next step that the optimizer performs is to perturb each of the design variables to calculate the direction of the gradient using the previously obtained values from the neural net. Figure 6 illustrates the details of phase 3 of the optimization process. Using the neural network,

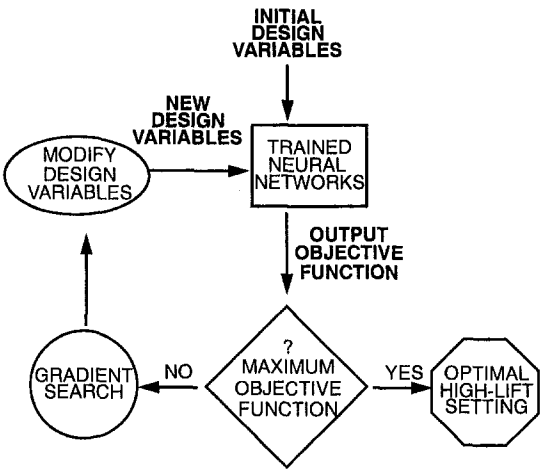

Fig. 6 Phase 3 of optimization process

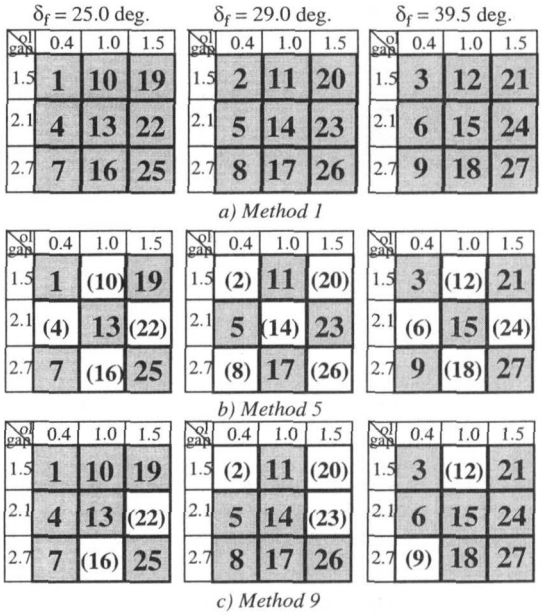

Fig. 7 Computational cases that are used to train the neural networks

the optimizer continues to modify the design variables and search for the correct gradient direction until a set of design variables is found with a maximum objective function which meets all the constraints.

Optimizer. The optimizer that is used in this study is NPSOL (Gill et al., 1994) which is a gradient-based optimizer. NPSOL is chosen as the optimizer because of past experience (Greenman et al., 1998) and its flexibility. In order to locate the maximum of the objective function, the optimizer uses a sequential quadratic programming algorithm. The search direction at each iteration is the solution of a quadratic programming problem.

Results

Minimizing Training Data Samples. The neural networks are trained with computational data consisting of 27 configurations as shown in Fig. 7. The numbers in the shaded boxes represent the case number for that particular flap rigging. A study was conducted to determine the correct number of iterations (the number of times the training data is presented to the neural networks to learn) required to train the neural networks. The results of this learning curve are presented by Greenman (1998). It was determined that 250 iterations were optimal for this study.

Even though the computational database that is used is sparse, a study (Greenman, 1998 and Greenman and Roth, 1999) was conducted to see how much further the training set can be reduced and still allow the neural networks to predict within the acceptable error. Several subsets of the computational data were used to train the neural nets. It was shown that carefully selecting configurations to omit from the training set, neural networks can be trained with only 50–74% of the entire data set to accurately predict the aerodynamic characteristics of a multi-element airfoil (Greenman, 1998 and Greenman and Roth, 1999). Method 1 designates the training set which contains all the computed data (Fig. 7). Figure 7 shows additional training methods that are successful in training the neural networks and that are presented in this paper. Here, the shaded boxes represent the cases that are in the training set whereas the numbers in the white boxes and in the parentheses are the cases that are omitted from the training set.

High-Lift Flap Setting Optimization. The high-lift system is optimized by maximizing the lift coefficient. The design variables in this study are chosen to be the flap deflection, gap, overlap, and

Table 1 Design space for δ_s = 6.0 degrees

Design Variables	Lower Bound	Upper Bound
δ_f	25.0	38.5
gap_f	1.50	2.70
$overlap_f$	0.40	1.50
α	0.0	10.0

angle of attack. The bounds on the design space (shown in Table 1) are chosen to be the same as the design space that are used to train the neural networks with the exception that for optimization cases without constraints, the angle of attack is bounded to $\alpha = 10.0°$ since this is near the range where maximum lift is predicted to occur by the pressure difference rule for most of the configurations. To start the optimization, the initial values of the design variables are arbitrarily chosen.

Method 9. Method 9 is used to train the neural networks which are integrated with the optimizer. Method 9 contains only 74% of the entire configurations in the training set (Fig. 7). Five different optimization runs are shown in Table 2. Each of these runs has different initial or starting values (orig) of the design variables (DV). Gradient based optimizers do not guarantee that the maximum which is found is the global maximum of the design space; it only guarantees an improvement. Thus, different starting values of the design variables are used to search the entire design space. The first optimization run, 9-A, has the initial design variables set to the lower bounds. Whereas, the second run, 9-B, has the initial values set to the upper bounds of the design space. In the third run, 9-C, the initial conditions are set to the average value of the lower and upper bounds. The last two runs have arbitrary initial values to test different regions of the design space. With this optimization procedure, the design space can be easily searched with several optimization runs because each run only requires several seconds of CPU time. A total of 28.6 CPU seconds are used for these five optimization runs.

In this study, the optimizer found 2 different maximums. The smaller of the two maximums is found using the initial design variables of Runs 9-B through 9-E. The modified high-lift rigging is $\delta_f = 38.5°$, $gap_f = 2.04\%c$, $ol_f = 1.50\%c$, and $\alpha = 10.0°$ and has $C_l = 4.11$. The other maximum for this particular study

Table 2 Optimization results with method 9 as the training set

Run	DV	orig	mod	C_l orig NN	C_l orig INS2D	Δ% orig	C_l mod NN	C_l mod INS2D	Δ% mod	ΔC_p diff mod INS2D	CPU (sec)
9-A	δ_f	25.0	38.5	2.04	2.04	0.0	4.13	4.03	2.48	-14.8	6.9
	gap_f	1.50	2.01								
	ol_f	0.40	0.56								
	α	0.0	10.0								
9-B	δ_f	38.5	38.5	3.54	3.56	-0.56	4.11	4.00	2.75	-14.5	3.3
	gap_f	2.70	2.04								
	ol_f	1.50	1.50								
	α	10.0	10.0								
9-C	δ_f	32.0	38.5	3.19	3.20	-0.31	4.11	4.00	2.75	-14.5	6.9
	gap_f	2.10	2.04								
	ol_f	0.95	1.50								
	α	5.0	10.0								
9-D	δ_f	30.0	38.5	3.02	2.96	2.02	4.11	4.00	2.75	-14.5	5.5
	gap_f	1.90	2.04								
	ol_f	0.75	1.50								
	α	4.0	10.0								
9-E	δ_f	27.0	38.5	2.51	2.47	1.62	4.11	4.00	2.75	-14.5	6.0
	gap_f	2.10	2.04								
	ol_f	0.50	1.50								
	α	2.0	10.0								

Table 3 Constrained optimization results for method 9 as the training set

Run	DV	orig	mod	C_l orig NN	C_l orig INS2D	Δ% orig	C_l mod NN	C_l mod INS2D	Δ% mod	ΔC_p diff mod NN	ΔC_p diff mod INS2D	CPU (sec)
9-C-ΔC_p	δ_f	32.0	37.5	3.19	3.20	-0.31	3.94	3.86	2.07	-13.0	-13.0	27.3
	gap_f	2.10	2.08									
	ol_f	0.95	0.40									
	α	5.0	9.0									
9-C-opt	δ_f	32.0	38.5	3.18	3.20	-0.63	3.94	3.92	0.51	-13.0	-13.4	26.1
	gap_f	2.10	1.5									
	ol_f	0.95	0.4									
	α	5.0	8.30									

is just slightly higher at $C_l = 4.13$. The modified values of the design variables for this case are $\delta_f = 38.5°$, $gap_f = 2.01\%c$, $ol_f = 0.56\%c$, and $\alpha = 10.0°$. The flap deflection for both instances is optimal at the upper bound. The modified gaps are free variables (the variable lies between the upper and lower bounds) and close to each other, whereas the overlaps are quite different. The smaller maximum has the overlap at the upper bound whereas the larger maximum has it as a free variable. Both configurations have the angle of attack to be optimal at the upper bound.

The accuracy of the neural network prediction is tested for both the initial and modified configurations by generating the appropriate grid and computing the INS2D solution. Then the predicted and computed C_l are compared and the percent difference (Δ%) is shown in Table 2. The initial configurations have lower errors than the modified configurations. In Run 9-A there is zero error and only one case has an error greater than 2%. Modified configurations have prediction errors greater than 2%. The pressure difference rule is applied to these cases to determine if the modified configurations have a C_{pdiff} less than the acceptable value. Examining the outcome, shows that the pressure difference exceeds the allowable value of $C_{pdiff} = -13.0$. All the pressure differences are equal to or greater than $C_{pdiff} = -14.5$. Some CFD training data may be nonphysical at the upper bound of the angle of attack since the bound on angle of attack is chosen to be an average value of where maximum lift occurs. Consequently, the neural networks are not properly trained to predict the aerodynamics in this range.

Constrained Optimization. In order to test whether the accuracy would get better if the modified configurations were restricted within the empirically predicted pre-stall range, the upper bound on the angle of attack design variable is removed. Instead a constraint is placed on the value of the pressure difference, $C_{pdiff} \geq -13.0$. An additional neural network is trained with flap deflection, gap, overlap, and angle of attack to predict the pressure difference. In this case, the entire training data is used to compute C_{pdiff}, whereas the neural networks that compute the aerodynamic coefficients are trained with data only including pre-stall data that is predicted by the pressure difference rule. The design variables of the optimization runs remain the same as does the objective function. The results of the case that found the best improvement by the optimizer are shown in Table 3 for Run 9-C-ΔC_p. The modified design variables are $\delta_f = 37.5°$, $gap_f = 2.08\%c$, $ol_f = 0.40\%c$, and $\alpha = 9.0°$. The modified angle of attack is lower than in the previous case that specified the upper bound to be $\alpha = 10.0°$. The neural network predicted the pressure difference value to be exactly what is calculated with the INS2D solution and predicted the modified lift coefficient to be higher than 2% the actual INS2D value.

To further reduce the prediction error in the modified lift coefficient, the INS2D data from this optimal case is added to the training data. The neural networks are then re-trained with this additional information in hope that it will improve the accuracy. The optimization runs are again constrained and the best improvement is shown in Table 3 denoted by Run 9-C-opt. The values of the modified design variables are different for the flap deflection, gap, and angle of attack and are the same for the overlap that in the

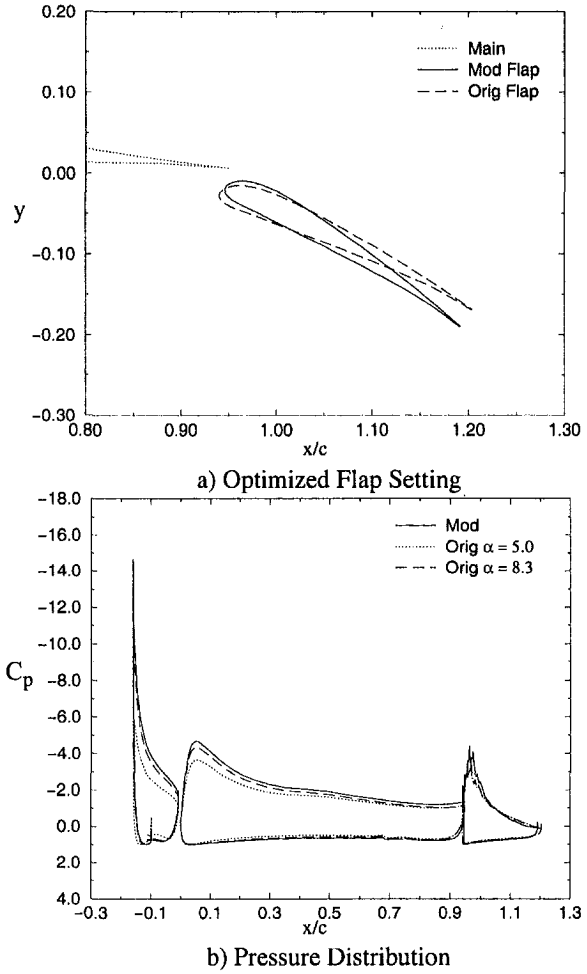

Fig. 8 Optimization results for run 9-C-opt (flap settings denoted in Table 3)

previous case. The modified lift coefficient predicted by the neural network happens to be the same as in the previous optimization run, however, the INS2D value of the modified coefficient is different and the error is reduced to only 0.51%. Thus, by constraining the design space that the optimizer is allowed to search and by adding one data point near maximum lift to the training data, the prediction error is reduced and all constraints are met. The predicted and actual pressure difference are close and differ by only 0.4. It should be noted that the CPU time required to run a constrained optimization run is increased, however, it is still less than 30 seconds as shown in Table 3.

To get a better understanding of the flow physics, the pressure distribution of the modified and original configurations for optimization Run 9-C-opt are examined. Figure 8(*a*) shows the modified and original flap positions in relation to the main element trailing edge. Figure 8(*b*) shows the pressure distribution of the slat, main, and flap elements in a solid line for the modified configuration. The original configuration was initially at $\alpha = 5.0°$ (plotted in a dotted line) but in order to compare the pressure distributions, the original configuration is also plotted at $\alpha = 8.3°$ (in a dashed line). The basic shape of the C_p curves are similar for all elements for both configurations. The flow is attached for all elements. The suction pressure on the modified elements are clearly larger than the original configuration resulting in greater lift. There are interesting features on the original and modified flap elements. The sharp spike at the trailing edge occurs from the sharp point at the trailing edge of the flap geometry. The multiple spikes that are located at the leading-edge of the flap element are associated with the original definition of the geometry. The flap at this region is faceted (refer to Greenman (1998) for detailed explanation of the flow physics).

Benefits of New Process

The aerodynamic design space of a multi-element airfoil is very complex and may have many local maximums and minimums. When a gradient-based optimizer is used to search the design space, many starting points need to be examined in order to find the greatest improvement. This can be very computationally expensive in traditional optimization.

Computational Resources. The advantage of using neural networks in the optimization process versus the traditional optimization process is the turn around time and the CPU time that is saved for many optimization runs. In the traditional optimization process, every time that the design variables are perturbed, the gradient needs to be calculated to determine the search direction. In order to calculate the gradient, a grid needs to be generated and the aerodynamic coefficients must be calculated by solving the flowfield with INS2D. Even though, the traditional optimization method will have shorter turn around time and CPU time when doing one or two optimization runs, there is no guarantee that one or two optimization runs will find the global maximum. On the contrary, the neural networks will have less overall turn around time and CPU time for many optimization runs and there is no major increase in overall turn around or CPU time for additional runs. Once the neural networks are trained, only 5–10 seconds are required for each additional optimization run. The CPU time that is used in this optimization study for the different training methods used is shown in Fig. 9. Also plotted in this figure are the calculated CPU time that would have been used in the traditional optimization process. The CPU time for the traditional method is estimated by using the same number of function calls that is used in the neural network optimization procedure. Then for each iteration it is estimated that the CPU time will consist of 4.3 seconds to generate a grid and 600 seconds (on a Cray C90) for each flow solution. If more than three optimization runs are executed, then the neural network optimization procedure should be used. The neural network optimization procedure curves are nearly flat. Thus, the major contributor to the CPU time in the neural network optimization is training the neural networks to learn and to predict the aerodynamics of the airfoil.

Cost Analysis. Another advantage of using the neural network optimization procedure is reduction of cost. There are many factors contributing to the total cost of a research job including the cost of the engineer support, computer resources, and wall clock turn

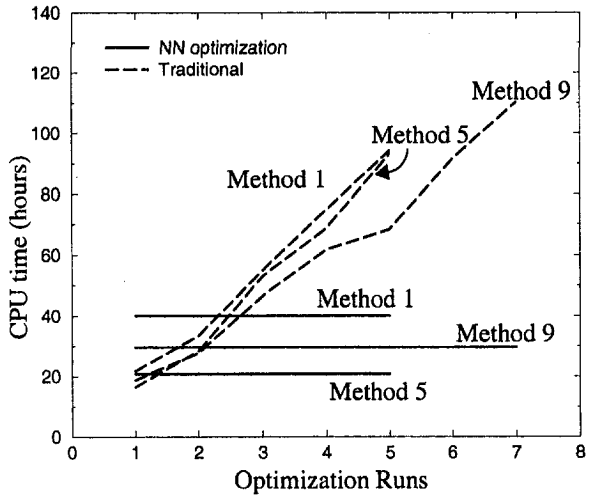

Fig. 9 Comparison of CPU time required for traditional and neural network optimization procedures

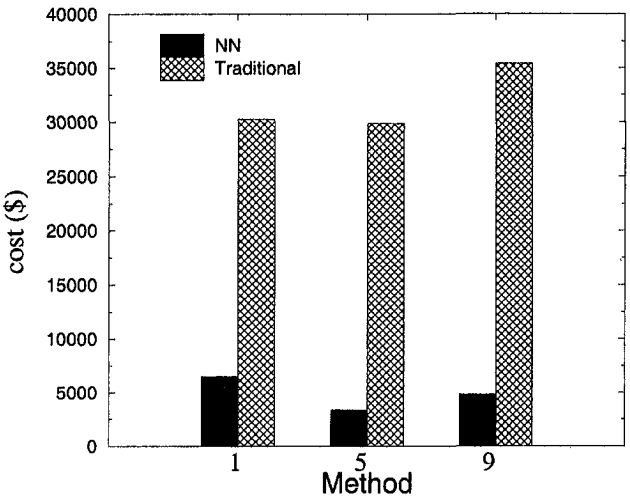

Fig. 10 Comparison of total cost for the neural network and traditional optimization procedure

around time. One of the largest contributors to turn around time is waiting for a computer job to be completed especially if the job executes within a batch queue. The average turn around time for the computers used in this study at the Numerical Aerospace Simulation Facility (NAS) at NASA Ames Research Center is 23.45 hours for an eight-hour queue job.

To calculate the cost that is related to the two types of optimization procedures considered, it is assumed that an experienced engineer is executing both optimization processes. The set-up time is assumed to be equal for both processes. The engineer is a full time equivalent of $200,000 per year and there are 2080 working hours in a year. Thus, there is a charge of $96.15 per hour for an engineer. Another expense which must be considered is computer resources. For this comparison, assume the cost of a computing hour is $39.00.

The total costs are compared in Fig. 10 for the two optimization procedures (refer to Greenman, 1998 for details on calculating costs). For five optimization runs for each training method, the neural network optimization procedure does cost less. Again, if only one or two optimization runs are performed, then the traditional optimization procedure would cost less, however, for multiple runs, the neural network optimization procedure uses less resources, The biggest advantage now is that many more optimization runs can be performed with the neural network optimization procedure while only adding seconds to the CPU time and turn around time.

The neural network optimization procedure should be used for design because several designs with different constraints or design space can be considered without driving the cost and turn around time up. Also, once a design is chosen, the design space can be altered and the optimization procedure can now be performed again with minimum additional cost and turnaround time.

Conclusions

An enhanced design process was developed which integrates neural network and optimizer technologies together with a computational database. The process is modular, allowing insertion of emerging neural network, optimization, and CFD technologies within its framework. This design process was tested for a typical high-lift design problem to optimize flap rigging for maximum lift. Initial studies showed that although optimization could be conducted using a sparse training dataset, unconstrained optimization of the high-lift system produced unacceptably high errors. Due to the complexity of the high-lift flow physics near the maximum lift condition, an empirically based constraint, which identifies configurations at the maximum lift condition within the computational database, was required in order to achieve accurate neural net predictions for this design problem. Using the empirical constraint together with an iterative optimization procedure which re-inserted the optimized configuration into the training database and repeated the optimization produced an optimal configuration with only 0.5% error. A cost analysis was conducted by comparing the optimization with neural networks procedure to the traditional optimization procedure. It was found that the optimization with neural networks procedure resulted in a reduction of turnaround time, CPU time, and cost if more than two optimization runs were conducted. Using the optimization procedure, the average cost reduction is 83%.

Acknowledgments

This work would not have been possible without the helpful discussions and suggestions from Dr. James C. Ross, Dr. Stuart E. Rogers, and Dr. Charles C. Jorgensen at NASA Ames Research Center.

References

Chan, W. M., Chui, I. T., and Buning, P. G., 1993, "User's Manual for the HYPGEN Hyperbolic Grid Generator and the HGUI Graphical User Interface," NASA TM 108791.

Dominik, C., 1994, "Application of the Incompressible Navier-Stokes Equations to High-Lift Flows," AIAA Paper 94-1872.

Faller, W. E., and Schreck, S. J., 1995, "Real-Time Prediction of Unsteady Aerodynamics: Application for Aircraft Control and Maneuverability Enhancement," *IEEE Transactions on Neural Networks,* Vol. 6, No. 6, pp. 1461–1468.

Gill, P. E., Murray, W., Saunders, M. A., and Wright, M. H., 1994, "User's Guide for NPSOL 5.0: A Fortran Package for Nonlinear Programming," Dept. of Operations Research, Stanford University, TR SOL 94, Stanford, CA.

Greenman, R. M., 1998, "Two-Dimensional High-Lift Aerodynamic Optimization Using Neural Networks," Stanford University Ph. D. Dissertation (see also NASA TM 112233).

Greenman, R. M., and Roth, K. R., 1999, "Minimizing Computational Data Requirements For Multi-Element Airfoils Using Neural Networks," AIAA Paper 99-0258.

Greenman, R. M., Cheung, S., and Tu, E. L., 1998, "Coupled Navier-Stokes and Optimizer Analysis of a Transonic Wing," *Journal of Aircraft,* Vol. 35, No. 3, pp. 362–369.

Jorgensen, C. C., and Ross, J. C., "System and Method for Modeling the Flow Performance Features of an Object," U.S. Patent No. 5,649,064, July 1997.

LaMarsh, W. J., Walsh, J. L., and Rogers, J. L., 1992, "Aerodynamic Performance Optimization of a Rotor Blade Using a Neural Network as the Analysis," AIAA Paper 92-4837.

McMillen, R. L., Steck, J. E., and Rokhsaz, K., 1995, "Application of an Artificial Neural Network as a Flight Test Data Estimator," *Journal of Aircraft,* Vol. 32, No. 5, pp. 1088–1094.

Norgaard, M., Jorgensen, C. G., and Ross, J. C., 1997, "Neural-Network Prediction of New Aircraft Design Coefficients," NASA TM 112197.

Rai, M. M., and Madavan, N. K., 1998, "Application of Artificial Neural Networks to the Design of Turbomachinery Airfoils," AIAA Paper 98-1003.

Rogers, S. E., 1993, "Progress in High-Lift Aerodynamic Calculations," AIAA Paper 93-0194.

Rogers, S. E., 1997, "Manual for the OVERMAGG Script System," NASA Ames Research Center.

Rogers, S. E., and Kwak, D., 1990, "An Upwind Differencing Scheme for the Time Accurate Incompressible Navier-Stokes Equations," *AIAA Journal,* Vol. 28, No. 2, pp. 253–262.

Rogers, S. E., and Kwak, D., 1991, "An Upwind Differencing Scheme for the Steady State Incompressible Navier-Stokes Equations," *Journal of Applied Numerical Mathematics,* Vol. 8, pp. 43–64.

Ross, J. C., Jorgenson, C. C., and Norgaard, M., 1997, "Reducing Wind Tunnel Data Requirements Using Neural Networks," NASA TM 112193.

Spalart, P. R., and Allmaras, S. R., 1992, "A One-Equation Turbulence Model for Aerodynamic Flows," AIAA Paper 92-0439.

Steck, J. E., and Rokhsaz, K., 1997, "Some Applications of Artificial Neural Networks in Modeling of Nonlinear Aerodynamics and Flight Dynamics," AIAA Paper 97-0338.

Storms, B., 1997, Private communication.

Suhs, N. E., and Tramel, R. W., 1991, "PEGSUS 4.0 User's Manual," AEDC-TR-91-8.

Valarezo, W. O., and Chin, V. D., 1994, "Method of Prediction of Wing Maximum Lift," *Journal of Aircraft,* Vol. 31, No. 1, pp. 103–109.

Ying, S. X., 1996, "High Lift Challenges and Directions for CFD," *AIAA/NPU AFM Conference Proceedings,* China.

Comparison of Flying-Hot-Wire and Stationary-Hot-Wire Measurements of Flow Over a Backward-Facing Step

O. O. Badran
Assistant Professor,
Al-Balqâ Applied University,
Amman College,
Department of Mechanical Engineering,
Amman 11133, Jordan

H. H. Bruun
Reader in Fluid Dynamics,
Department of Mechanical and
Medical Engineering,
University of Bradford, Bradford,
BD7 1DP, United Kingdom

This paper is concerned with measurements of the flow field in the separated flow region behind a backward-facing step. The main instrument used in this research was Flying X Hot-Wire Anemometry (FHWA). Stationary (single normal) Hot-Wire Anemometry (SHWA) was also used. Comparative measurements between the SHW probe and the FHW system were conducted downstream of the step (step height H = 120 mm) and results are presented for axial locations of 1H and 2H. Two step configurations were considered: (i) a blunt leading edge with flow underneath (Case I) and (ii) a blunt leading edge with no flow underneath (Case II). It is observed from the results presented that the two Hot-Wire methods produce significantly different mean velocity and turbulence results inside the separation bubble. In particular, the SHWA method cannot detect the reverse flow velocity direction, while the Flying Hot-Wire clearly identifies the existing reverse flow. Also, in the shear flow region, the results presented indicate that measurements with a SHW probe must be treated with great caution.

1 Introduction

Until recently, accurate measurements of turbulence data for flow over a backward-facing step (BFS) were difficult to obtain, primarily due to the reverse flow velocities within the separation bubble. The FHWA system has been developed as an accurate instrumentation for measurements in separated flow regions. This technique is therefore very useful in providing experimental input to current generation of turbulence models for flow over, for example, wings, BFS, blades, etc. Other methods developed for measurements in highly turbulent and separated flows are the Pulsed Hot-Wire Anemometer (PHWA) technique and Laser Doppler Anemometer (LDA) technique. Both of these methods have their own limitations, e.g., a conventional PHWA probe cannot be used close to a wall due to its size and the maximum detectable flow velocity is rather low (about 12 ms^{-1}) due to electromagnetic pick-up signal restrictions (Bruun, 1995). The LDA method is now used extensively in both liquid and gas flows containing flow regions with high turbulence or separated flow. However, LDA methods have several restrictions. LDA systems, in particular for multi-component measurements, are costly and bias effects and seeding problems can be significant in near wall regions and in separated flow regions (see for example Durao et al., 1980; Dring, 1982; Stock and Fadeff, 1983; Johnson et al., 1984; Stevenson et al., 1984; Haghgooie et al., 1986; Winter et al., 1991a,b; and Ruck, 1991).

An increasing amount of attention has been devoted to the Flying Hot-Wire Anemometer (FHWA) technique and signal-analysis procedures of moving Hot-Wire probes as described by Bruun (1995).

The basic principle of the FHWA can be explained with reference to Fig. 1. Consider a surface with a (two-dimensional) separated flow region. A space-fixed coordinate system is introduced in which the flow velocity vector, $\vec{V}$, and its velocity components U and V are to be evaluated. Specified by the geometry of the FHWA mechanism the sensors (usually an X-configuration) of the probe will follow a prescribed curve; for example, curve (a) in Fig. 1. At a time t, the probe is assumed to be at a known position (x_p, y_p) and to move with a known probe velocity, $\vec{V}_p$.

The moving Hot-Wire probe is exposed to a relative velocity, $\vec{V}_r$, and this velocity vector is normally measured and evaluated for an X-probe in terms of the velocity components (U_r', V_r') in a probe-stem aligned coordinate system. Provided the orientation of the probe-stem relative to the space-fixed coordinate system is known, the corresponding space-fixed velocity components (U_r, V_r) can be evaluated. Having measured $\vec{V}_p$ and $\vec{V}_r$ the flow vector, $\vec{V}$, is obtained from

$$\vec{V} = \vec{V}_p + \vec{V}_r, \tag{1}$$

as illustrated in Fig. 1. Provided that the magnitude of the probe velocity, $\vec{V}_p$, is greater than the magnitude of the flow velocity, $\vec{V}$, then the relative velocity vector, $\vec{V}_r$, will remain within the approach quadrant of the X-probe, and the Hot-Wire signals can be interpreted uniquely.

Any path can be used which cuts through the separated flow region in such a manner that the relative velocity remains within the approach quadrant of the X-probe. In practice, three different probe paths and related mechanisms have been used. (i) A circular motion (Cantwell, 1976; Wadcock, 1978; Coles and Wadcock, 1979; Cantwell and Coles, 1983; Walker and Maxey, 1985; Sirivat, 1989; Hussein and George, 1989; George et al., 1989b; Hussein, 1990). (ii) A linear motion (Perry, 1982; Watmuff, et al., 1983; Hussein, 1990; and Panchapakesan and Lumley, 1993). Crouch and Saric (1986) have also reported the development of an oscillatory Single Normal (SN) Hot-Wire system. (iii) A curvilinear "bean-shaped" motion (Thompson, 1984, 1987; Thompson and Whitelaw, 1984; Jaju, 1987; Al-Kayiem, 1989; Bruun et al., 1990a; Al-Kayiem and Bruun, 1991; Badran, 1993; Mahmood, 1995). This is the system used in this investigation.

Stationary Hot-Wire Anemometry (SHWA) has been one of the main tools for studying turbulent flow phenomena, in particular for low and moderate turbulence intensity flows. However, one of the main limitations of SHW probes are their inability to measure and correctly interpret the probe signal in high turbulence intensity and recirculating flows.

Nevertheless, SHWA has been applied to a number of such flow

Contributed by the Fluids Engineering Division for publication in the JOURNAL OF FLUIDS ENGINEERING. Manuscript received by the Fluids Engineering Division May 16, 1997; revised manuscript received January 5, 1999. Associate Technical Editor: S. Banerjee.

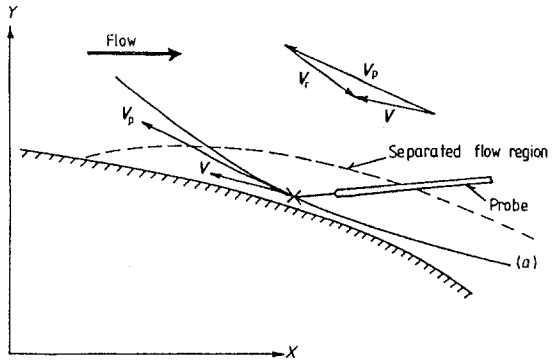

Fig. 1 The principle of measurements with an *X*-configuration Flying Hot-Wire probe

fields. For example, Bradshaw and Wong (1972) and Chandersuda and Bradshaw (1981) used stationary *X*-probes for the measurement of the fluctuating u^2 and v^2 and related shear stress in reattaching flows. Simpson (1976) used SHWA in a separating boundary layer, and Nakayama and Liu (1990) studied the turbulent near wake of a flat plate.

SHWA has also been applied to the backward-facing step configuration investigated in this study, in particular in many of the earlier investigations (Hsu, 1950; Tani et al., 1961; Abbot and Kline, 1962; Kiya, 1978; and Kiya and Sasali, 1983). Most of these authors have discussed the caution with which their results should be treated in high turbulence intensity flow and re-circulating flow regions.

The aim of this paper is two-fold. To demonstrate by FHWA that high quality mean and turbulence intensity data can be obtained for the flow field behind a backward-facing step and to demonstrate by comparative measurements the magnitude of the errors in these quantities if measured by the SHWA technique.

2 Experimental Facilities

The investigation was carried out in a subsonic, variable low-speed, open-loop wind tunnel. The test section was a square of 601 mm × 601 mm cross-section. A pitot static tube was used to measure the free-stream velocity inside the test section of the wind tunnel. The position of the pitot-static tube for the backward-facing step tests and the geometry and notation for the step are shown in Fig. 2. The vertical position Y denotes the distance from the bottom of the step. The experiments were carried out at a Reynolds number of $\mathrm{Re} = 7.9 \times 10^4$, based on step height H.

The FHW assembly was mounted above the wind tunnel on two parallel supporting metal frames, exterior to the wind tunnel bridging the working section and anchored to the ground. First, this prevents vibrations from the wind tunnel structure, caused by the fan and the flow, affecting the Hot-Wire's response. Second, this mounting allows only the flying arm to move inside the wind tunnel. This arrangement is superior to the FHWA of C.I.T. where the major part of the apparatus was mounted inside the wind tunnel, causing severe blockage.

A four-bar mechanism was selected for the FHWA system to provide a "bean shaped" probe path. The schematic diagram in Fig. 3 shows the FHWA mechanism and the resulting probe path corresponding to one complete revolution of the flywheel. The principle of the FHWA system is described in e.g., Bruun (1995), and testing and evaluation of an *X*-probe FHWA system for windtunnel studies is described in Al-Kayiem and Bruun (1991).

A PDP 11/23 computer was used to control the electronic instrumentation for the data acquisition and analysis of the FHWA data. Details of this electronic system are described by Al-Kayiem (1989) and Badran (1993). Details of the current upgraded FHWA system are described by Mahmood (1995). The FHWA velocity measurements were obtained by a *X*-array Hot-Wire probe using two DISA 55M10 constant temperature anemometers.

Also in this investigation a digital microcomputer data acquisition and analysis system was used to digitise, record and process the mean and fluctuation output signal from the SHWA probe.

3 Results and Discussion

In this paper results are presented for two flow cases. For Case I (see Fig. 2(*a*)) there was flow underneath the step configuration, and for Case II (see Fig. 2(*b*)) the passage underneath the step was sealed (no flow condition). Also for both cases the boundary layer

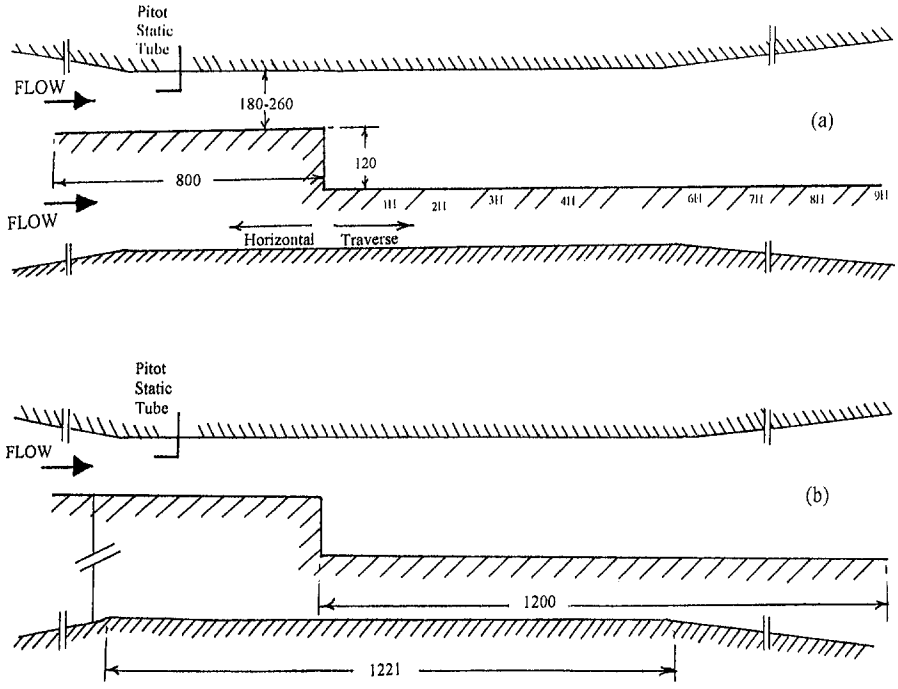

Fig. 2 Backward-facing step model showing upstream and downstream plates. Dimensions in mm. (*a*) Flow underneath step, (*b*) no flow underneath step.

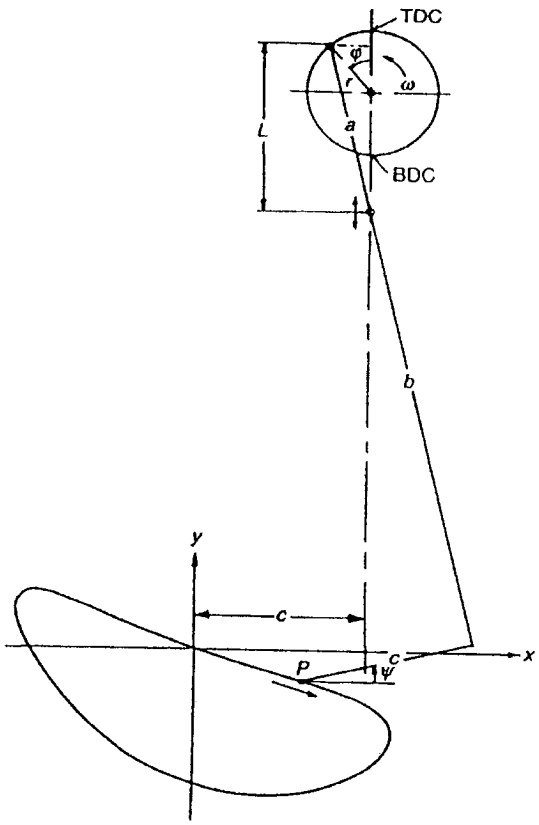

Fig. 3 Four-bar Flying Hot-Wire probe mechanism and notation, showing the top dead center (TDC) and the bottom dead center (BDC). The geometry is that of the Bradford FHA system: r = 60 mm, a = 160 mm, b = 410 mm, and c = 147 mm.

development on the front part of the plate leading to the step was initiated by a blunt leading edge to enhance the boundary layer growth. The FHWA technique used an X-probe and the measured quantities were therefore $\bar{U}$, $\bar{V}$, u^2, v^2 and $\overline{uv}$. However, as this paper contains a comparison with a Stationary single normal (SN) Hot-Wire probe only data for $\bar{U}$ and u^2 are presented.

The comparison will be demonstrated by one set of results for each case. For Case I (flow underneath) data for $\bar{U}$ and u^2 are shown in, respectively, Figs. 4(*a*) and (*b*) for an axial position $X/H = 1$. For Case II (no flow underneath), the corresponding data at $X/H = 2$ are shown in Figs. 5(*a*) and (*b*), respectively.

Several conclusions can be made from these results. First, from the $\bar{U}$ results (Figs. 4(*a*) and 5(*a*)), it is noticed that in the potential flow region outside the shear layer which surrounds the separation bubble both methods give similar results. This is to be expected as the turbulence intensity is low in this region (as confirmed by the results in Figs. 4(*b*) and 5(*b*)). With a step height $H = 120$ mm it is observed that significant differences occur as the probes enter the shear layer region. The maximum values of u^2 (see Figs. 4(*b*) and 5(*b*)) are located in the middle of the shear layer (Y = 100–120 mm) and the SHWA probe is seen to record too high values for $\bar{U}$ as expected due to higher order truncation errors (Kavall et al., 1983; Bruun, 1995). As the probes are moved closer to the wall the SHWA probe will continue to record to high values, and when the turbulence intensity exceeds about 30% rectification problems become significant. This is most clearly demonstrated inside the separation bubble where the SHWA probe fails to identify the existing negative mean flow values.

The u^2 data, Figs. 4(*b*) and 5(*b*), also demonstrate the limitations of the SHWA probe. In the potential flow region. (see e.g., Fig. 4(*b*)) where the turbulence intensity is low (u^2 low, $\bar{U}$ high), both methods give similar results. In the separated flow region near the wall the FHWA measure similar magnitude of values of u^2 as in the potential flow. However, in this region $\bar{U}$ is low (and negative) and substantial flow reversal also occurs. Consequently, the corresponding SHWA data are significantly in error and greatly underestimate the values of u^2 (as discussed in e.g., Bruun, 1995). The data in Fig. 4(*b*) also indicate a significant difference in the vertical position of the peak u^2 value between the SHWA and FHWA methods. Any fixed probe may affect a disturbance-sensitive shear layer and for the case with flow underneath the step such a situation may exist. It is possible that the shear layer was sensitive to a flip-flop spatial position and that the stationary probe and its support influenced the flip-flop behaviour of the shear layer, as also discussed by Bruun et al. (1991). For Case II, without flow underneath the step, the shear layer was more stable and the SHWA probe was not observed to shift the peak value of u^2 relative to the FHWA data as noticed in Fig. 5(*b*). The other comments made related to Fig. 4(*b*) are also seen to apply to the data in Fig. 5(*b*).

4 Experimental Uncertainty

Measurements were carried out with both stationary (SHWA) and flying (FHWA) anemometer probes. For measurements of the longitudinal mean velocity component, assuming a Gaussian turbulent velocity signal and a 98% confidence level, the range of the measured mean velocity $\hat{\bar{U}}$ relative to the real mean velocity $\bar{U}$ will be

$$\frac{\hat{\bar{U}}}{\bar{U}} = 1 \pm 2.33 \frac{1}{\sqrt{N}} \frac{\sigma_u}{\bar{U}} \tag{2}$$

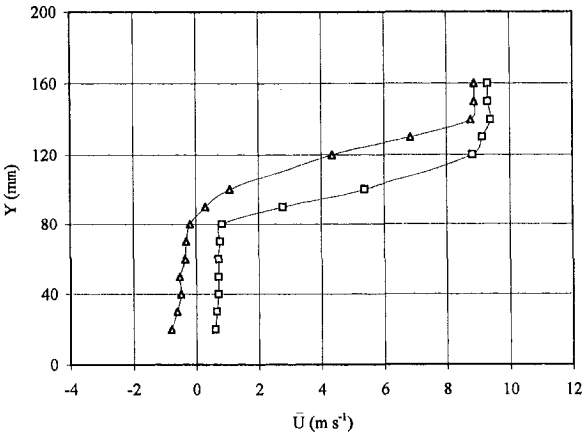

Fig. 4(*a*) Profiles of mean velocity $\bar{U}$ at X/H = 1. Flow underneath step. □: SHWA results; △: FHWA results.

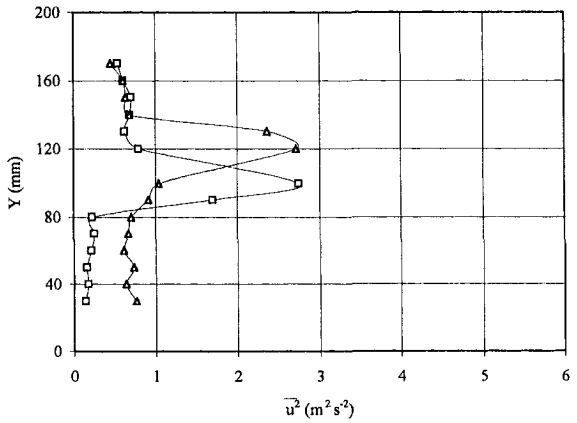

Fig. 4(*b*) Profiles of $\overline{u^2}$ at X/H = 1. Flow underneath step. □: SHWA results; △: FHWA results.

where N is the number of independent samples in the sample record and σ_u is the rms value of the fluctuating component.

For the SHWA each sample record was 2000 samples taken over a period of 20 s. This is a rather low sampling rate and the number of independent samples in the sample record when placed in the free stream and outer part of the shear layer may be taken as being 2000. In parts of the flow where the turbulence intensity is low, say, $\mathrm{Tu} = \sigma_u/\bar{U} = 10\%$ the uncertainty range for the mean value $\hat{\bar{U}}$ is

$$\frac{\hat{\bar{U}}}{\bar{U}} = 1 \pm 2.33 \frac{1}{\sqrt{2000}} 0.1 = 1 \pm 0.005 \qquad (3)$$

The corresponding uncertainty in $u' = (\overline{u^2})^{1/2}$ will be about 5 times higher (see e.g., Bruun, 1995).

However, as the turbulence intensity increases towards 30% and beyond, errors occur due to series expansion truncation and rectification errors. The magnitude of these errors in the shear layer and reversed flow region is demonstrated by the results in Figs. 4(*a*) and 5(*a*).

The Flying Hot-Wire (FHWA) data were obtained by ensemble averaging 200 sweeps with a 10s rest period in between each sweep. Consequently, the number of independent samples N was 200 and the measurement time for each point was about 35 min. As the number of samples for the stationary Hot-Wire was 2000 it follows from Eq. (2) that the SHWA is more accurate than the FHWA in the low turbulence intensity regions.

However, for measurements in the high turbulence intensity and recirculation regions (both contain low mean velocities) the FHWA is clearly superior. The probe velocity $\vec{V}_p$ ensures that no flow reversal is experienced by the X-probe during the measurements and the imparted relatively high probe velocity will also reduce the observed turbulence intensity during measurements thus virtually eliminating the related series expansion errors. Equation (2) can therefore be applied to high turbulent intensity regions, and e.g., for a local turbulence intensity Tu of 50% we get

$$\frac{\hat{\bar{U}}}{\bar{U}} = 1 \pm 2.33 \frac{1}{\sqrt{200}} 0.5 = 1 \pm 0.08 \qquad (4)$$

Furthermore, validation tests were also carried out by Al-Kayiem and Bruun (1991) in the empty windtunnel for both still air and uniform flow conditions. From these tests it was concluded that the effect of probe vibration during measurement sweeps was insignificant.

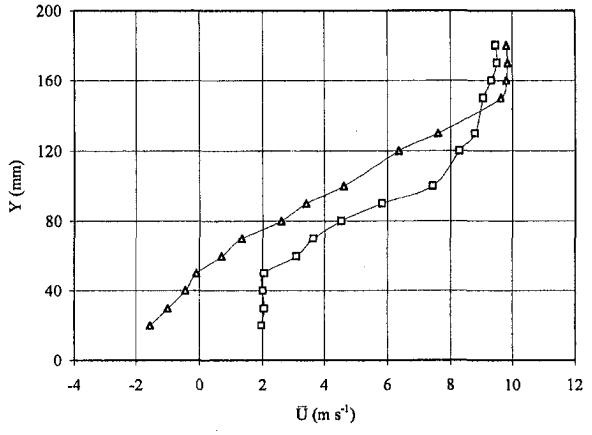

Fig. 5(*a*) Profiles of mean velocity $\bar{U}$ at $/H = 2$. No flow underneath step. □: SHWA results; △: FHWA results.

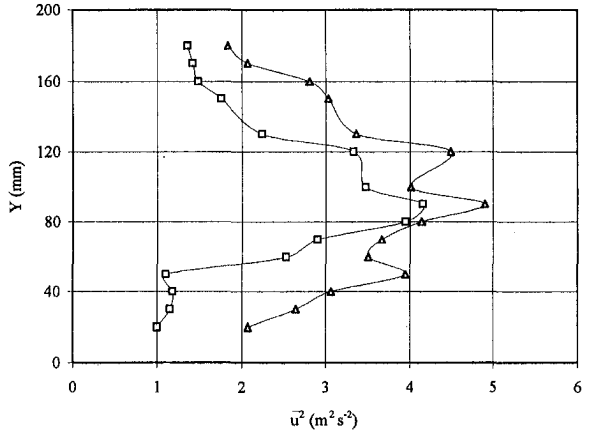

Fig. 5(*b*) Profiles of $\overline{u^2}$ at $X/H = 2$. No flow underneath step. □: SHWA results; △: FHWA results.

Conclusion

This paper has described a comparative investigation of the flow behind a backward-facing step using a Flying Hot-Wire Anemometry (FHWA) technique and a stationary single normal Hot-Wire (SHWA) probe.

As discussed, the Flying Hot-Wire (FHWA) technique is an accurate method for obtaining mean and turbulent quantity measurements in highly turbulent and separated flows. Using the FHWA data as reference the magnitude of the errors introduced by the stationary (SHWA) probe technique in both the shear layer region and separation bubble were demonstrated for both mean and turbulent quantities.

References

Abbot, D. E., and Kline, S. J., 1962, "Experimental Investigation of subsonic turbulent flow over single and double backward facing steps." ASME *Journal of Basic Engineering,* Vol. 84, pp. 317–325.

Al-Kayiem, H. H., 1989, "Separated Flow on a High Lift Wing," Ph.D. thesis, Department of Mechanical and Manufacturing Engineering, University of Bradford.

Al-Kayiem, H. H., and Bruun, H. H., 1991, "Evaluation of a Flying X Hot-Wire Probe System," *Measurement Science and Technology,* Vol. 2, pp. 374–380.

Badran, O. O., 1993, "A Flying Hot-Wire study of separated flows," Ph.D. thesis, Department of Mechanical and Manufacturing Engineering, University of Bradford.

Bradshaw, P., and Wong, F. Y. F., 1972, "The Reattachment and Relaxation of a Turbulent Shear Layer," *Journal of Fluid Mechanics,* Vol. 52, pp. 113–135.

Bruun, H. H., 1995, *Hot-Wire Anemometry,* Oxford University Press, Oxford.

Bruun, H. H., Al-Kayiem, H. H., and Badran, O. O., 1990a, "Flying Hot-Wire anemometry with X-wire probes," ASME, *Proc. on the Heuristics of Thermal Anemometry,* FED, Vol. 97, University of Toronto, pp. 81–86.

Cantwell, B. J., 1976, "A Flying Hot Wire Study of the Turbulent Near Wake of a Circular Cylinder at a Reynolds Number of 140000," Ph.D. thesis, California Institute of Technology.

Cantwell, B. J., and Coles, D. E., 1983, "An Experimental Study of Entrainment and Transport in the Turbulent Near Wake of a Circular Cylinder," *Journal of Fluid Mechanics,* Vol. 136, pp. 321–374.

Chandersuda, C., and Bradshaw, P., 1981, "Turbulence Structure of a Reattaching Mixture Layer," *Journal of Fluid Mechanics,* Vol. 110, pp. 171–179.

Coles, D., and Wadcock, A. J., 1979, "Flying-Hot-Wire Study of Flow Past a NACA 4412 Airfoil at Maximum Lift," *AIAA Journal,* Vol. 17, pp. 321–329.

Crouch, J. D., and Saric, W. S., 1986, "Oscillating Hot-Wire Measurements Above an FX63-137 Airfoil," AIAA 24th Aerospace Sciences Meeting, January 6–9, Nevada, AIAA-86-0012.

Dring, R. P., 1982, "Sizing Criteria for Laser Anemometry Particles," ASME JOURNAL OF FLUIDS ENGINEERING, Vol. 104, pp. 15–17.

George, W. K., Hussein, H. J., and Woodward, S. H., 1989b, "An Evaluation of the Effect of a Fluctuating Convection Velocity on the Validity of Taylor's Hypothesis," *Proc. 10th Australasian Fluid Mechanics Conf.,* Melbourne.

Hussein, H. J., 1990, "Measurements of Turbulent Flows with Flying Hot-Wire Anemometry," ASME, *Proc. Symp. on the Heuristics of Thermal Anemometry,* FED, Vol. 97, University of Toronto, pp. 77–80.

Hussein, H. J., and George, W. K., 1989, "Measurement of Small Scale Turbulence in an Axisymmetric Jet Using Moving Hot-Wires," *Proc. Seventh Symp. on Turbulent Shear Flow,* Stanford University, 30.2.1–30.2.6.

Hsu, H. C., 1950, "Characteristics of Mean Flow and Turbulence at an Abrupt Two-Dimensional Expansion," Ph.D. thesis, Department of Mechanics and Hydraulics, State University of Iowa.

Jaju, A. A. R., 1987, "Development of a Flying Hot-Wire Probe System," M.Phil. thesis, Department of Mechanical and Manufacturing Engineering, University of Bradford.

Johnson, D. A., Modarress, D., and Owen, F. K., 1984, "An Experimental Verifi-

cation of Laser-Velocimeter Sampling Bias and its Correction," ASME JOURNAL OF FLUIDS ENGINEERING, Vol. 106, pp. 5–12.

Kim, J. J., 1978, "Investigation of Separation and Reattachment of a Turbulent Shear Layer: Flow Over a Backward-Facing Step," Ph.D. thesis, Stanford University.

Kiya, M., and Sasaki, K., 1983, "Structure of a Turbulent Separation Bubble," *Journal of Fluid Mechanics,* Vol. 137, pp. 83–113.

Mahmood, Z., 1995, "Turbulent and Separated Flow Over Multi-Element Aerofoils," Ph.D. thesis, Department of Mechanical and Manufacturing Engineering, Bradford University.

Nakayama, A., and Liu, B., 1990, "The Turbulent Near Wake of a Flat Plate at Low Reynolds Number," *Journal of Fluid Mechanics,* Vol. 217, pp. 93–114.

Panchapakesan, N. R., and Lumley, J. L., 1993, "Turbulence Measurements in Axisymmetric Jets of Air and Helium, Part 1, Air Jet," *Journal of Fluid Mechanics,* Vol. 246, pp. 197–223.

Perry, A. E., 1982, *Hot-Wire Anemometry,* Clarendon Press, Oxford.

Ruck, B., 1991, "Distortion of LDA Fringe Pattern by Tracer Particles," *Experiments in Fluids,* Vol. 10, pp. 349–354.

Simpson, R. L., 1976, "Characteristics of a Separating Incompressible Turbulent Boundary Layer," *AIAA Journal,* Vol. 14, pp. 124–126.

Sirivat, A., 1989, "Measurement and Interpretation of Space-Time Correlation Functions and Derivative Statistics from a Rotating Hot Wire in a Grid Turbulence," *Experiments in Fluids,* Vol. 7, pp. 361–370.

Stevenson, W. H., Thompson, H. D., and Craig, R. R., 1984, "Laser Velocimeter Measurements in Highly Turbulent Recirculating Flows," ASME JOURNAL OF FLUIDS ENGINEERING, Vol. 106, pp. 173–180.

Stock, D. E., and Fadeff, K. G., 1983, "Measuring Particle Transverse Velocity Using an LDA," ASME JOURNAL OF FLUIDS ENGINEERING, Vol. 105, pp. 458–460.

Tani, I., Tuchi, M., and Komeda, H., 1963, "Experimental Investigation of Flow Separation Associated with a Step or a Groove," Aeronautical Research Institute, University of Tokyo, Report No. 364, Vol. 27, No. 4, pp. 119–137.

Watmuff, J. H., Perry, A. E., and Chong, M. S., 1983, "A Flying Hot-Wire System," *Experiments in Fluids,* Vol. 1, pp. 63–71.

Winter, A. R., Graham, L. J. W., and Bremhorst, K., 1991a, "Velocity Bias Associated with Laser Doppler Anemometer Controlled Processors," ASME JOURNAL OF FLUIDS ENGINEERING, Vol. 113, pp. 250–255.

Winter, A. R., Graham, L. J. W., and Bremhorst, K., 1991b, "Effects of Time Scales on Velocity Bias in LDA Measurements Using Sample and Hold Processing," *Experiments in Fluids,* Vol. 11, pp. 147–152.

Wadcock, A., 1978, "Flying-Hot-Wire Study of Two-Dimensional Turbulent Separation on an NACA 4412 Airfoil at Maximum Lift," Ph.D. thesis, California Institute of Technology.

Walker, M. D., and Maxey, M. R., 1985, "A Whirling Hot-Wire Anemometer with Optical Data Transmission," *Journal of Physics E: Scientific Instruments,* Vol. 18, pp. 516–521.

A Multiple Disk Probe for Inexpensive and Robust Velocimetry

Sheldon I. Green
Associate Professor.

Steven N. Rogak
Assistant Professor.

Department of Mechanical Engineering
University of British Columbia,
Vancouver, B.C., Canada V6T 1Z4
e-mail: green@mech.ubc.ca

A novel velocimeter consisting of multiple orthogonal disks fitted with pressure transducers has been developed. Dynamic pressure differences are measured between the center of one disk face and the center of the other face, on each of the disks. While previously-developed anemometers based on dynamic pressure differences (such as yaw or three-hole probes) can only measure velocities with a small range of directions, the new disk probe can measure three components of velocity, even in highly three-dimensional flows where the approximate direction of the flow is not known. Wind tunnel tests have shown the velocimeter to be quite accurate; it can measure velocities to ±1.4% and wind directions to ±4 deg. The velocimeter is very robust and therefore can make measurements in environments too harsh for most other velocity transducers.

1 Introduction

Present methods for measuring multiple components of velocity can be divided into two broad classes: accurate, expensive, laboratory-type instruments, and robust (but less accurate), inexpensive, instruments. Into the first class would fall devices such as hot wire anemometers (Comte-Bellot, 1976; Perry, 1982), laser Doppler velocimeters (Drain, 1980); Durst et al., 1981), particle image velocimeters (Adrian, 1991; Grant, 1997), and a host of others. These devices are characterized by excellent accuracy (typically, velocities can be measured to within 1%) but high cost ($10k–$100k+) and comparatively poor durability. Their high cost and poor durability in general limit these devices to use in a controlled environment like a laboratory; they are rarely used in an industrial or field work setting.

The class of robust, inexpensive instruments would include cup, propeller, and vane anemometers (Wyngaard, 1981), claw probes, yaw head probes, and five-hole and seven-hole probes (Rae and Pope, 1984; Chue, 1975; Zilliac, 1993; Everett et al., 1983). In general, these devices are reliable and reasonably accurate (directions to ±1 deg and velocities to ±1%), but can accurately measure only mean flow velocities within ±70 deg of a known flow direction (Chue, 1975; Zilliac, 1993). Recently, Rediniotis and Kinser (1998) have developed a probe using 18 holes over the surface of a sphere. Although this probe is nearly omni-directional (cone angles >90 degrees), and is apparently accurate for the reported conditions, it should be noted that calibration of that device is complex due to the large number of pressure taps and the complex flow regimes around a sphere that occur at various Reynolds numbers.

As there is no device, at present, that will measure robustly and economically 3D velocities in highly 3D flow, there is a need for such a device. The multiple disk probe described here is just such a device. The device has obvious applications in meteorological stations (particularly in a harsh marine environment), in structural aerodynamics, and in industrial aerodynamics.

2 Theory of Operation of a Multiple Disk Probe

A multiple disk probe consists of two or three orthogonal circular disks, situated fairly closely together in space (Green and Rogak, 1997). Each disk is fitted with a pressure transducer, or pressure tap lines, to measure the pressure difference from the center of one side of the disk to the center of the opposite side. Neglecting the (small) effect of fixtures required to hold the disks in place, the pressure difference between one side of the disk and the other side must be a function solely of the disk geometry, the properties of the air, the magnitude of the velocity, and the angle made by the velocity vector relative to the normal vector to the disk.[1] Most significantly, owing to the symmetry of the disk geometry, the pressure difference cannot be a function of the azimuthal orientation of the velocity vector, ϕ (Fig. 1).

The principle of operation of a multiple disk probe is best understood by considering a purely two-dimensional flow (Fig. 2). Let us denote the pressure drop across Disk 1 by $(\Delta p)_1$ and that across Disk 2 by $(\Delta p)_2$. Qualitatively, if $0 < \alpha_1 < \pi/2$, then $(\Delta p)_1$ is positive and so is $(\Delta p)_2$. For $\pi/2 < \alpha_1 < \pi$, $(\Delta p)_1$ is negative and $(\Delta p)_2$ is positive. Similarly, for $\pi < \alpha_1 < 3\pi/2$, $(\Delta p)_1$ is negative and so is $(\Delta p)_2$. Finally, for $3\pi/2 < \alpha_1 < 2\pi$, $(\Delta p)_1$ is positive and $(\Delta p)_2$ is negative. Therefore, it is trivial to distinguish the quadrant of the flow direction. Determining the exact angle of the flow is slightly more involved.

In view of the physical argument made above, $(\Delta p)_1$ is a function of just the disk geometry (which can be characterized by the disk diameter, D) the magnitude of the flow velocity, V, the density of the fluid, ρ, the viscosity of the fluid, μ, and the angle made by the flow to the Disk 1 normal, α_1. In nondimensional form, this information may be expressed as $(c_p)_1 = f(\mathrm{Re}_D, \alpha_1)$, where f is some function, $c_p = \Delta p/(0.5\ \rho V^2)$ is the pressure coefficient, and $\mathrm{Re}_D = \rho VD/\mu$ is the Reynolds number based on disk diameter. Similarly, for the second disk, $(c_p)_2 = f(\mathrm{Re}_D, \alpha_2)$.[2] Now, since $\alpha_2 = (\pi/2) - \alpha_1$, if one measures the two pressure coefficients, one effectively has two equations to solve for the two unknowns: Re_D and α_1. Alternatively, one may consider a flow with some fixed viscosity and density about two disks of the same diameter. Then, $(\Delta p)_1 = g(V, \alpha_1)$ and $(\Delta p)_2 = g(V, (\pi/2) - \alpha_1)$, where g is some function, and again it is clear that by

[1] Variations in the velocity field over length scales comparable to the disk diameter must also be small. The intensity and scale of freestream turbulence may also have some impact on the pressure difference, but owing to the large scale separation (without reattachment) for $|\alpha|$ not too close to 90 deg, we would expect this effect to be small for most α.

[2] We have assumed here that the wake of one disk has negligible impact on the flow about the second disk, which will be the case unless α_1 is nearly ±90 deg. If $\alpha_1 = 90$ deg then the wake of Disk 1 will be quite small, and thus have a small impact on $(\Delta p)_2$. Similarly, if $\alpha_1 = -90$ deg then $(\Delta p)_1 = 0$, a value that is unaffected by the wake of Disk 2, located upstream of it.

Contributed by the Fluids Engineering Division for publication in the JOURNAL OF FLUIDS ENGINEERING. Manuscript received by the Fluids Engineering Division July 27, 1998; revised manuscript received February 2, 1999. Associate Technical Editor: D. P. Telionis.

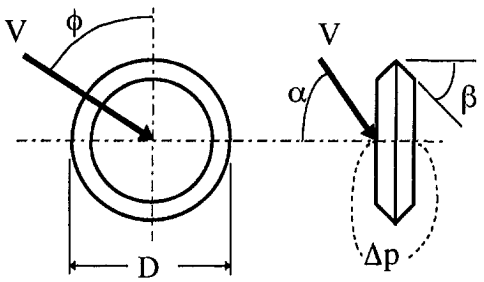

Fig. 1 The geometry of a single disk. Due to symmetry, Δp is not a function of the azimuthal angle ϕ. The disk bevel angle is β.

measuring $(\Delta p)_1$ and $(\Delta p)_2$ one has two equations in the two primitive variables V and α_1.

As will be discussed below, owing to the one-to-one dependence of (c_p) on α_1 and Re_D separately, the two equations described above may be solved readily, and yield a unique solution. In particular,

$$(\Delta p)_1 = \frac{1}{2}\rho \cdot V^2 f(\mathrm{Re}_D, \alpha_1) \tag{1}$$

$$(\Delta p)_2 = \frac{1}{2}\rho \cdot V^2 f\left(\mathrm{Re}_D, \frac{\pi}{2} - \alpha_1\right) \tag{2}$$

Dividing Eq. (1) by Eq. (2) yields a function h that depends on α_1 and Re_D:

$$\frac{(\Delta p)_1}{(\Delta p)_2} = \frac{f(\mathrm{Re}_D, \alpha_1)}{f(\mathrm{Re}_D, (\pi/2) - \alpha_1)} = h(\mathrm{Re}_D, \alpha_1) \tag{3}$$

It turns out that h depends weakly on Re_D and varies almost monotonically with α. Using any reasonable initial guess for Re_D, it is possible to estimate the flow angle by measuring h. Equation (1) or (2) can then be used to determine the airspeed V, which can be used to calculate Re_D. Flow angle and speed are then refined. This procedure converges in one iteration. Extension of this method to three-dimensional flows measured by three orthogonal disks is fairly straightforward because the pressure coefficient for each disk exhibits a "cosine-like" variation with α.

3 Apparatus

A two-dimensional version of the multiple disk probe was mounted on a turntable in a wind tunnel at UBC (Fig. 3). The turntable is fitted with a lead screw that allows one to adjust the turntable angle to an accuracy of 0.1 deg. The two disks, each of 2.54 cm diameter and thickness 0.38 cm, were mounted with centers in the vertical center of the test section but horizontally offset by about 10 cm. The test section of the wind tunnel is 69 cm high and 94 cm in breadth. For the work described here the freestream velocity did not exceed 12 m/s (27 mph), as our focus

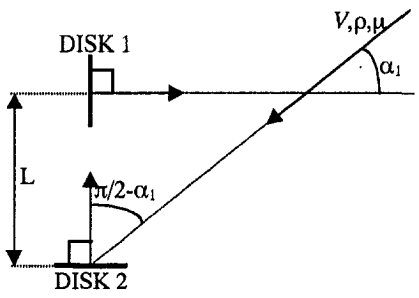

Fig. 2 Determination of 2D velocity using 2 disks. The disk normals are parallel with the x and y axes.

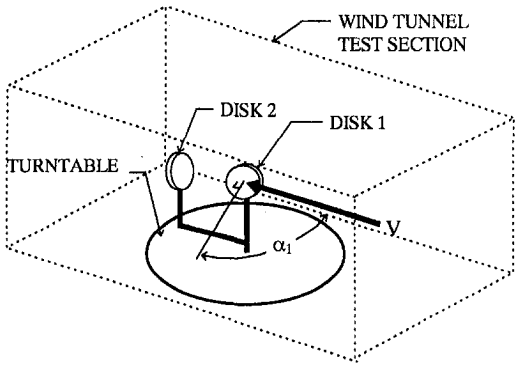

Fig. 3 Wind tunnel tests of multiple disk probe

was on the behavior of the probe in wind conditions that might be encountered in a traffic tunnel. The wind tunnel velocity was measured by a Betz manometer connected to pressure tap rings located at the test section and immediately upstream of the contraction section of the wind tunnel. A pitot-static tube confirmed the accuracy of the Betz manometer velocity measurements.

Initial tests were carried out with just a single disk mounted in the wind tunnel, to explore the influence of disk geometry on disk pressure coefficient. Three different disk geometries were tested in turn: a square edged disk, a disk with both edges bevelled to an angle of 30 deg (β = 30 deg, refer to Fig. 1), and a third disk with edges bevelled at β = 55 deg. Each disk was fitted with two pressure tap lines. Each pressure tap line is connected to one of two thin gauge, flush-mounted tubes (i.e., the tubes do not protrude above the disk surface) that terminate at surface pressure holes. These holes are 1.7 mm in diameter and 1 mm deep and are centered on either side of the disk (Fig. 4). The pressure tap lines on either side of the disk were connected to the two sides of an inexpensive differential pressure transducer (Microswitch model 160PC). The disks were mounted in the wind tunnel by means of long tapered rods of maximum diameter 3.3 mm, which were in turn connected to an aluminum L-beam bolted to the wind tunnel turntable.

4 Results

As discussed in the Theory section, the ideal disk probe would have a pressure coefficient variation with (α_1) such that $h(\alpha_1)$ (refer to Eq. (3)) is not merely one-to-one, but also has a large slope everywhere. Of the three disks studied, the disk with the 55 deg bevel best satisfies these requirements, having the largest mean slope and the least non-monotonic behavior (Fig. 5). Conse-

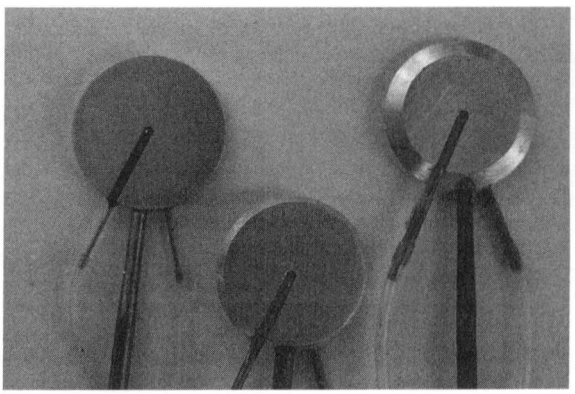

Fig. 4 Photograph of three disk probe geometries. Left: square cut disk. Center: 30 deg bevel disk (β = 30 deg). Right: β = 55 deg disk. Pressure tap lines are recessed in the disk surface and faired flush, but are still visible in the photograph.

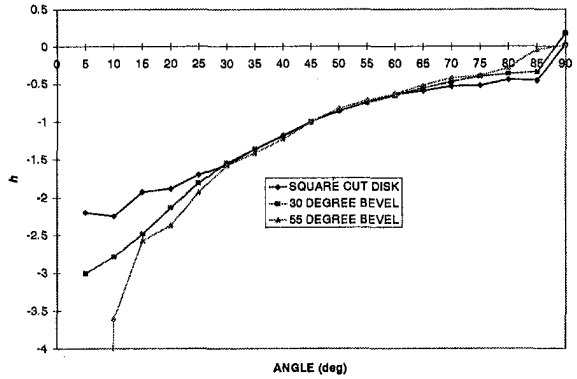

Fig. 5 Dependence of the disk pressure ratio, h, on α and disk geometry. Re = 11900

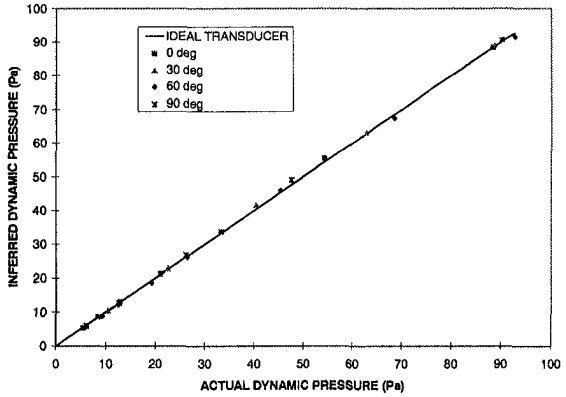

Fig. 8 Accuracy of the disk probe for velocity magnitude determination

quently, in the tests described subsequently, only the 55 deg bevel disk was used. Note that due to symmetry the behavior of a disk is completely characterized by its response to flow angles between 0 and 90 deg.

Figure 6 shows the dependence of the pressure coefficient of a single disk on the Reynolds number, for Reynolds numbers of 6600, 11900, and 20300 (roughly, freestream velocities of 3.9 m/s, 7.1 m/s and 12.1 m/s). When the disk is within 15 deg of perpendicular to the flow, there is no dependence of the pressure coefficient on the Reynolds number. However, when the disk is at a larger angle to the flow, there is a significant pressure coefficient dependence on the Reynolds number (see, for example, Fig. 7). This dependence on Reynolds number causes h to vary from 2 (high Re_D) to 3 (low Re_D) for $\alpha = 20$ deg, at which angle it experiences its greatest percentage variation. In order to measure the flow direction and velocity, it is therefore necessary to use an iterative procedure. An intermediate Reynolds number is assumed, for which there is a prescribed curve of $h(\alpha_1)$. Having measured h one may calculate α_1. Knowing α_1, one then calculates V. This value of V allows one better to estimate the Reynolds number, and one then iterates with a different $h(\alpha_1)$ curve. One iteration results in convergence. In general, data inversion can be done in real time.

If one wishes to use the multiple disk probe for velocimetry, there should be good agreement between the flow velocity and angle measured by the probe, and the true flow velocity and angle. With both disks mounted on the turntable, and the turntable at a prescribed angle, both the flow velocity and direction could be measured by independent means. These independent measurements of the flow are compared against the disk probe measurements in Figs. 8 and 9.

Figure 8 is a graph of the actual dynamic pressure in the wind tunnel airflow plotted against the dynamic pressure inferred from the disk probe pressures, for four different angles α_1 of the flow relative to the disks (0, 30, 60, and 90 deg. Angles between 90 and 360 deg gave identical results, owing to the symmetry of the disk probe). An ideal transducer would be plotted as a line of slope 1; the disk probe plots as a line of slope 1, but with an r.m.s. error of 2.8% (i.e., a velocity error of 1.4%). These errors result from interpolation of the $h(\alpha_1)$ curves and, to a lesser degree, transducer error and probe manufacturing tolerances.

Figure 9 is a plot of the actual angle of the flow versus the angle inferred from the disk probe measurements, for three different flow Reynolds numbers. The disk probe differs from ideal behavior slightly, with an r.m.s. error of 4.1 deg. Virtually all the significant deviations from ideal behavior occur when either face of one of the disks is at an angle of 70 deg to the flow. If one eliminates these data from the error calculations, the r.m.s. angle error is under 2 deg.

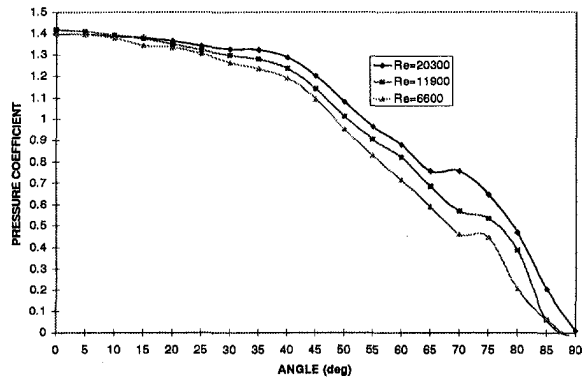

Fig. 6 Dependence of disk pressure coefficient on α and Re. All pressure coefficient curves have a "cosine-like" dependence on α.

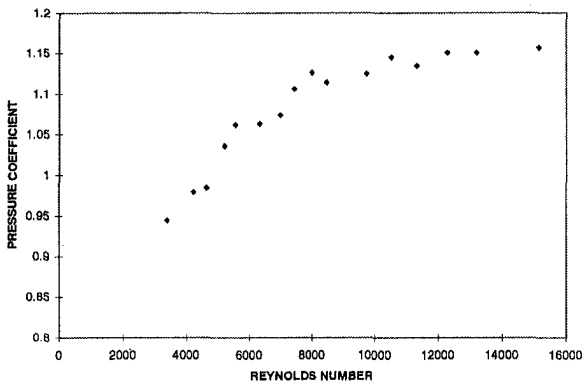

Fig. 7 Dependence of disk pressure coefficient on Re for $\alpha = 45$ deg

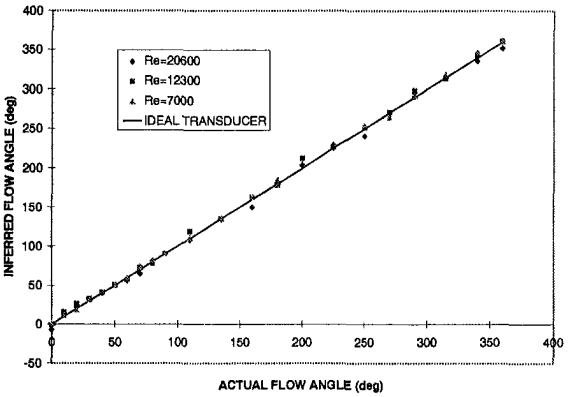

Fig. 9 Accuracy of the disk probe for flow angle determination

5 Discussion

In Fig. 5 we showed that the 55 deg bevel disk has substantially better characteristics than the other two disk geometries tested. The superior behavior is most obvious when the disks are nearly parallel to the flow (i.e., $\alpha \cong 90$ deg), and is believed to be caused by the complex separation and reattachment of the flow when the plane of the disk is nearly aligned with the flow. However, even the 55 deg bevel disk has deficiencies. Figure 6 shows that for 65 deg $< \alpha <$ 75 deg the c_p versus α curve has non-monotonic behavior, which results in the angular determination error described in the Results section. It is possible that a different disk edge geometry would have yielded more reliable measurements. Unfortunately, the judicious selection of a disk geometry requires a knowledge of the complex separation and reattachment characteristics of the three-dimensional flow around a disk at intermediate Reynolds numbers. This knowledge is presently lacking, and may be difficult to attain owing to the Reynolds number dependence of the flow. In this regard, it bears mention that when the disk is perpendicular to the flow ($\alpha = 0$) the flow is Re independent above Re = 7000, but when the disk is oriented at 45 deg to the flow c_p increases with Re for Re $<$ 16000 (Fig. 7). The implication of this Reynolds number dependence is that the probe is generally more accurate at higher flow velocities.

The disk probe has been tested in a steady, uniform flow field. In general, the performance of the probe will deteriorate if the local velocity is different near the different disks. In practice, this will mean that the disk probe will not be suitable for investigating flows with length scales comparable to, or smaller than, the disk spacing L. For similar reasons, we would not expect it to measure accurately unsteady flows with frequencies of the order V/L. Note that for the velocities used in the present work, V/L would be greater than 39 Hz. In fact, the response frequency of the pressure tap lines (also an issue for multi-hole probes) would be much less than this. For higher frequency fluctuations, the probe will average the pressure fluctuations in some sense, but the resulting averaged pressure and inferred velocity would be a biased (to high velocities) measurement of the true mean velocity.

While these limitations would preclude the use of the prototype disk probe in most wind tunnel testing, its performance would be adequate for meteorological monitoring or large-scale industrial aerodynamics. The authors are using the velocimeter in land-based meteorological trials and Environment Canada has expressed interest in the velocimeter for marine meteorological stations (many existing anemometers are susceptible to storm damage to their moving parts).

6 Conclusions

A novel velocimeter comprised of multiple orthogonal disks fitted with pressure transducers has been developed. Wind tunnel tests have shown that in a two-dimensional flow the velocimeter can measure the velocity magnitude with an r.m.s. error of 1.4%, and velocity vector direction with an r.m.s. error of 4 deg. This level of accuracy, combined with the inherent robustness of the multiple disk probe, suggests that it could find application in meteorological stations and in industrial aerodynamics.

Acknowledgment

The authors gratefully acknowledge the financial assistance of NSERC.

References

Adrian, R. J., 1991, "Particle Imaging Techniques for Experimental Fluid Mechanics," *Annual Review of Fluid Mechanics,* Vol. 23, pp. 261–304.

Chue, S. H., 1975, "Pressure Probes for Fluid Measurements," *Progress in Aerospace Science,* Vol. 16, pp. 147–223.

Comte-Bellot, G., 1976, "Hot Wire Anemometry," *Annual Review of Fluid Mechanics,* Vol. 8, pp. 209–231.

Drain, L. E., 1980, *The Laser Doppler Technique,* Wiley, New York.

Durst, F., Melling, A., and Whitelaw, J. H., 1981, *Principles and Practice of Laser-Doppler Velocimetry,* Academic Press, New York.

Everett, K. N., Gerner, A. A., and Durston, D. A., 1983, "Seven-Hole Cone Probes for High Angle Flow Measurement: Theory and Calibration," *AIAA Journal,* Vol. 21, p. 992.

Grant, I., 1997, "Particle Image Velocimetry: A Review," *Journal of Mechanical Engineering Science,* Vol. 211, pp. 55–76.

Green, S. I., and Rogak, S. N., 1997, Disk Probe Velocimeter, patent action commenced.

Rediniotis, O. K., and Kinser, R. E., 1998, "Development of a Nearly Omnidirectional Velocity Measurement Pressure Probe," *AIAA Journal,* Vol. 36, pp. 1854–1860.

Perry, E., 1982, *Hot Wire Anemometry,* Clarendon Press, Oxford, U.K.

Rae, W. H., and Pope, A., 1984, *Low Speed Wind Tunnel Testing,* Wiley, New York.

Wyngaard, J. C., 1981, "Cup, Propeller, Vane, and Sonic Anemometers in Turbulence Research," *Annual Review of Fluid Mechanics,* Vol. 13, pp. 399–423.

Zilliac, G. G., 1993, "Modelling, Calibration, and Error Analysis of Seven Hole Pressure Probes," *Experiments in Fluids,* Vol. 14, pp. 104–120.

M. Sleiman
Senior Engineer.

A. Tam
Senior Engineer.

M. P. Robichaud
CFD Group Leader; Adjunct Professor,
Department of Mechanical Engineering,
Concordia University.

M. F. Peeters
CFD Group Leader.

Numerical Applications Group,
Pratt & Whitney,
Montreal, Quebec, Canada
F4G 1A1

W. G. Habashi
Professor,
Department of Mechanical Engineering,
Concordia University,
Director CFD Laboratory,
Montreal, Quebec, Canada H3G 1M8;
Aerodynamics Consultant, Pratt & Whitney

Multistage Simulation by an Adaptive Finite Element Approach Using Structured Grids

This paper presents the application of a three-dimensional Navier-Stokes finite element code (NS3D) in the context of turbomachinery rotor-stator multistage interaction. A mixing-plane approach is used, in which boundary conditions at a common interface plane between adjacent blade rows are iteratively adjusted to yield a flow satisfying the continuity, momentum, and energy conservation equations, in an average sense. To further improve the solutions, a mesh adaptation technique then redistributes the mesh points of the structured grid within each component, according to an a posteriori edge-based error estimate based on the Hessian of the local flow solution. This matrix of second derivatives controls both the magnitude and direction of the required mesh movement at each node, is then implemented using an edge-based spring analogy. The methodology is demonstrated for two test cases with two types of data: a well-instrumented experimental large-scale rotating rig for a second stage compressor at UTRC and an actual engine. The latter, a two-stage compressor of a turboprop, has been only tested as a single-stage configuration, because of the quality of the experimental data available. All results compare well to the data and demonstrate the utility of the approach. In particular, the mesh adaptation shows large improvements in agreement between the calculations and the experimental data.

1 Introduction

The flow in a turbomachine is three-dimensional, viscous, turbulent, and unsteady. Considerable progress has been made in the last decade in developing appropriate computational fluid dynamics codes capable of predicting flow patterns and other aerodynamic properties of flows in turbomachinery components, in particular blade rows. Analyzing the flow within the passage of a single blade row, without considering the effects of the upstream and/or downstream rows, misses some important information. Thus, to better understand the flow in compressors and turbines, current research is focusing on the flow physics within the passage of a blade row embedded in a multi-stage environment. Accounting for such interaction is expected to yield more realistic performance predictions and to lead to more enlightened design decisions, not least among them is accounting for the influence of the blade rows' axial gaps on performance and wake quenching through clocking of blades of successive rows.

Many issues relating to the numerical simulation and modeling of the flow in multistage turbomachinery have been raised and the models proposed range from simple steady interface ones (Dawes, 1992) and (Giles, 1988), to fully-unsteady ones (Rai, 1989), with the passage-average model (Adamczyk, 1990) somewhere in between. There is no doubt that should large computer resources be readily available, an unsteady solution, with no modeling sacrifices, would be preferred. Computational power constraints in the industry preclude this, except on a demonstration basis.

On the other hand, complexity of the interaction models is no guarantee of their higher fidelity. It is doubtful that the results of sophisticated interaction models can be confidently integrated in the design procedure when even the benchmarking of well-known CFD codes for an isolated rotor, Rotor 37, has proven so far inconclusive at the Hague ASME-IGTI '94 meeting. It is, therefore, our belief that before augmenting the complexity of rotor-stator interaction models, one must pay particular attention to the solver itself and tackle, one by one, the numerical difficulties that may lead to inaccurate answers, not least among them is inappropriately distributed mesh points.

This paper is a step in this direction and illustrates how the application of a general code and a simple interaction model, when coupled with mesh adaptation, can accurately describe the three-dimensional time-averaged flow field of a blade row embedded in a multistage configuration. The 3-D mesh adaptation presented in this paper is applied on structured grids and only involves mesh movement capability.

2 Numerical Method

NS3D solves in conservation form the 3-D compressible, variable property, Navier-Stokes equations, for the conservative variables, $(p, \rho u, \rho v, \rho w)$. A dissipation term, of the form $\lambda \nabla_p^2$, with λ being a small coefficient, is introduced on the right-hand side of the continuity equation to permit the use of equal order interpolation for velocities and pressure. The accuracy of the approach has been proven to be formally second order (Baruzzi, 1995).

An isoparametric finite element approach is used, with both the flow variables $(p, \rho u, \rho v, \rho w)$ and geometry described by trilinear shape functions, except near walls due to the turbulence modeling implementation, as will be described in the next paragraph. The equations are discretized by a weak-Galerkin approach in which the equations are satisfied in a weighted residual sense.

Turbulence is modeled with the well-known high-Reynolds number (k, ε) model. Near walls, a finite element version of wall functions is used, in which elements adjacent to walls incorporate into their shape functions the composite linear-logarithmic behavior of the velocity vector in the direction normal to the wall, while retaining a linear behavior in the other

Contributed by the Fluids Engineering Division for publication in the JOURNAL OF FLUIDS ENGINEERING. Manuscript received by the Fluids Engineering Division November 19, 1996; revised manuscript received March 22, 1999. Associate Technical Editor: M. N. Dhaubhadel.

two directions. Thus, for these elements, the velocity shape function normal to walls is chosen to continuously and unidirectionally represent a viscous sublayer, a transition layer and a logarithmic outer layer, up to the first point off the wall. This can be considered an intermediate approach between wall functions and costly low-Reynolds number models, with the advantage of incorporating in the solution procedure a discretization of the momentum and continuity equations up to the walls. To accurately integrate the large gradients associated with the partially-logarithmic variation in the near-wall element, nine Gaussian points are used in the direction normal to the wall during the assembly of the influence matrices.

A Newton method is then used to linearize the Navier-Stokes and turbulence equations. A highly parallelized preconditioned iterative solver is used for the continuity and momentum equations solved in a fully-coupled way, while the energy, k and ε equations are solved in a sequential way. In light of the sensitivity of iterative methods to matrix conditioning, a time term is introduced in all the equations to enhance diagonal dominance through a mass matrix, $[M]$. Thus, the resulting set of simultaneous linear equations, at each Newton step, for (p, ρu, ρv, ρw) can be written as:

$$\begin{bmatrix} [M]/\Delta t + [K^{\vec{V}}]_{\vec{V}} & [K^{p}]_{\vec{V}} \\ [K^{\vec{V}}]_{p} & [M]/(RT\Delta t) + [K^{p}]_{p} \end{bmatrix} \begin{Bmatrix} \Delta\rho\vec{V} \\ \Delta p \end{Bmatrix} = -\begin{Bmatrix} R_{\vec{V}} \\ R_{p} \end{Bmatrix} \quad (1)$$

where Δ is the change in a variable, V is the velocity vector, p the pressure and R_v and R_p the residuals of the momentum and continuity equations, respectively. For numerical stability at high Reynolds numbers, a streamline diffusion is added to both sides of the momentum equation. This can be represented in the symbolic form:

$$[K(\lambda, \mu_{art})]\begin{Bmatrix} \Delta\rho V \\ \Delta p \end{Bmatrix} = -\begin{Bmatrix} R_{\vec{V}}(\mu_{art}) \\ R_{p}(\lambda) \end{Bmatrix} \quad (2)$$

To improve the convergence robustness of the overall algorithm, a hybrid artificial viscosity approach is used. The iteration matrix $[K]$ is computed with a large initial value for the parameters λ and μ_{art}, referred to as λ^{LHS} and μ_{art}^{LHS}. and these are progressively unloaded but always remain at a higher value than those in the residual, denoted by λ^{RHS} and μ_{art}^{RHS}. The residual, representing the physical solution, is therefore finally converged with the smallest possible values of these control parameters for which the outer Newton iteration converges. The equations for energy, as well as for k and for ε, are handled in a similar manner.

3 Mesh Adaptation Scheme

The solution of turbomachinery CFD problems requires a large number of mesh points to approximate physical features such as shocks, boundary layers and wakes. Problem sizes become even more prohibitive when quasi-steady or unsteady interaction problems are tackled. Emphasis is seldom placed on methods to automatically optimize the mesh. Thus, it is not unexpected that slightly different answers could be obtained by various users of the same code, on the same problem, with approximately the same number of mesh points. In addition, there is no guarantee that the answers obtained are the most accurate possible for the given number of mesh points.

In general, adaptive methods comprise two components: error estimation and an adaptive strategy. A directionally adaptive approach is used in this paper to remove the onus of mesh decisions from the user by coupling mesh and solver to yield stretched and oriented grids capable of capturing the physical phenomena involved, without disproportionate mesh refinements that yield intractable grids. Our approach (Ait-Ali-Yahia, 1997) is to seek solutions on anisotropic meshes where refinement is made along those directions with rapidly changing flow variables. The error estimate as well as the mesh adaptation scheme are edge-based and, hence, equally applicable to finite difference, finite volume or finite element method. The error estimate construction and mesh movement algorithm have been described in detail (Tam, 1998). The question regarding the quality of the representation of the true error by the error estimate is amply answered by considering an exact test case of a known analytical function possessing sharp changes in gradients (Figs. 1 and 2).

4 Rotor-Stator Interaction Approach

In contrast to the passage-averaging approach where there is complete overlap between the grids of the upstream and downstream blade rows to account for body forces and deterministic stresses, in the proposed interaction model the exit plane of an upstream blade row and the inlet plane of the downstream one are located at the same axial position, denoted as the interface plane. An averaging procedure is applied at this plane to extract the "mixed out" flow properties from the solution.

The unknown boundary conditions at the interface between two blade rows are considered part of the numerical solution, with the interaction starting by initializing the flow either from an inviscid through-flow solution or from a common guessed pressure at the components' interface planes. At every iteration, the interface boundary condition is updated by passing the proper information between adjacent blade rows. For example, in a one-stage axial flow compressor one interface plane normal to the engine axis, located between the trailing edge of the rotor and the leading edge of the stator, is required. Circumferentially-averaged radial profiles of absolute total temperature, density, radial velocity, axial velocity and absolute tangential velocity obtained from the solution of the upstream blade row are specified at the inlet plane of the downstream blade row, and the circumferentially "mixed out" static pressure obtained from the solution of the downstream blade row is specified at the exit plane of the upstream blade row. The above procedure is repeated at every iteration until the residuals of the equations are reduced by three orders of magnitude, and the mass flow rate and the circumferentially-averaged radial profiles obtained from the upstream and downstream blade rows are matched within a specified tolerance. The properties exchange at the interface plane is detailed in the next section.

4.1 Thermodynamic Variables Based on Mixing-Plane Approach. In the mixing-plane approach the interface boundary conditions can be defined from circumferentially-averaged quantities at the interface plane, as follows:

$$F_1 = \overline{\rho u}_z = \frac{1}{Pitch}\int_0^{Pitch} \rho u_z d\theta \quad (16a)$$

$$F_2 = \overline{\rho u}_z^2 + \bar{p} = \frac{1}{Pitch}\int_0^{Pitch} (\rho u_z^2 + p) d\theta \quad (16b)$$

$$F_3 = \overline{\rho u}_z \bar{u}_\theta = \frac{1}{Pitch}\int_0^{Pitch} \rho u_z u_\theta d\theta \quad (16c)$$

$$F_4 = \overline{\rho u}_z \bar{u}_r = \frac{1}{Pitch}\int_0^{Pitch} \rho u_z u_r d\theta \quad (16d)$$

$$F_5 = \overline{\rho u}_z \bar{H}_o = \frac{1}{Pitch}\int_0^{Pitch} \rho u_z H_o d\theta \quad (16e)$$

$$\bar{H}_o = \frac{\gamma}{\gamma - 1}\frac{\bar{p}}{\bar{\rho}} + \frac{1}{2}(\bar{u}_r^2 + \bar{u}_\theta^2 + \bar{u}_z^2) \tag{17}$$

Equations (16)–(17) can be solved to obtain the "mixed-out" values of pressure, velocity, and total enthalpy as follows:

$$\bar{p} = \frac{\gamma}{\gamma + 1}(F_2^2 + \sqrt{F_2^2 + (\gamma^2 - 1)(F_2^2 + F_3^2 + F_4^2 - 2F_1F_5)})$$

$$\bar{u}_z = \frac{F_2 - \bar{p}}{F_1}$$

$$\bar{u}_\theta = \frac{F_3}{F_1}$$

$$\bar{u}_r = \frac{F_4}{F_1}$$

$$\bar{H}_o = \frac{F_5}{F_1} \tag{18}$$

Values of all other flow variables such as total pressure, static temperature, Mach number and flow angles can be defined based on these "mixed out" values. An important point to note is that the physical mixing process implied in this procedure will generate viscous losses, and will result in a flow with a higher entropy level, and hence higher measured losses, than the actual.

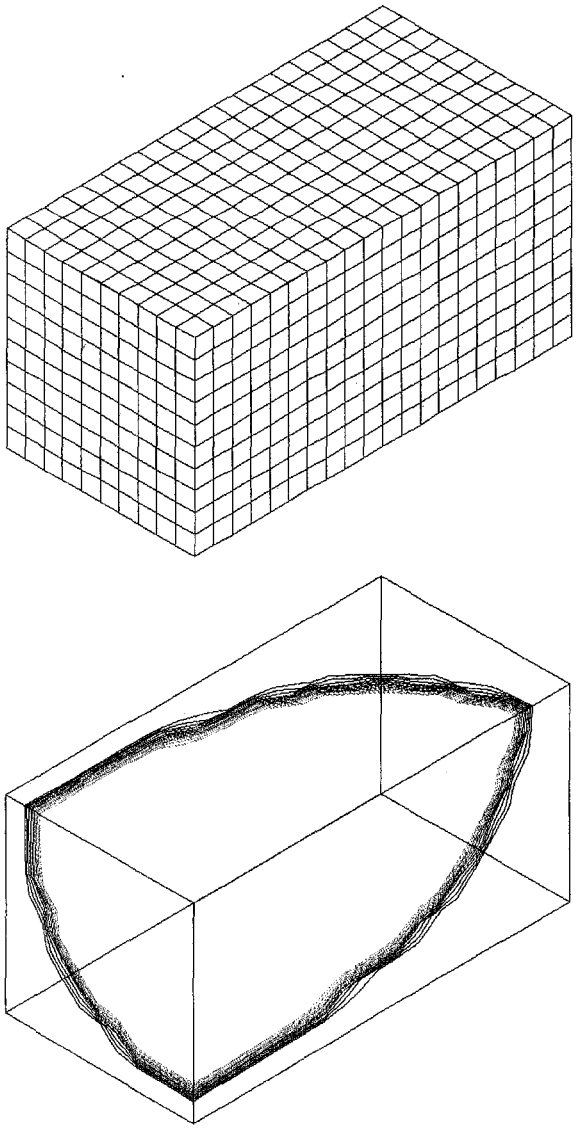

Fig. 1 Initial nonadapted hexahedral grid and corresponding isolines of analytical function

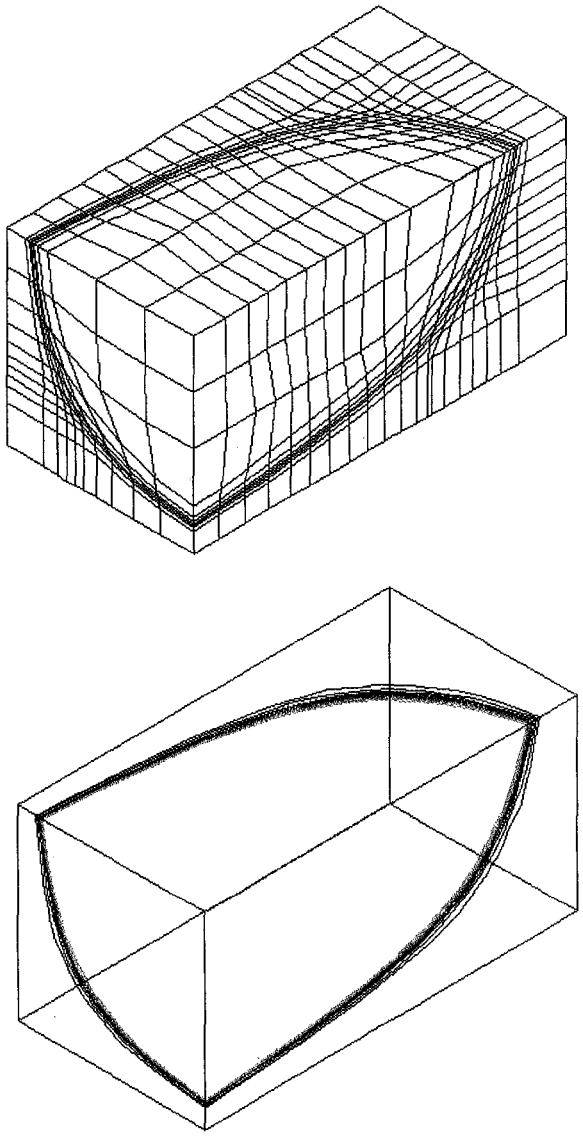

Fig. 2 Adapted hexahedral grid and corresponding isolines of the analytical function

4.2 Multistage Flow Chart. For multistage analysis, the overall procedure carried out is as follows:

1 Inlet boundary conditions (inlet radial distributions of total temperature, To, total pressure, Po, Mach number, M, inlet gas angle, α, cone angle ϕ); and exit boundary conditions (radial distribution of static pressure, p, for each blade row are obtained from a through-flow analysis.
2 An inviscid (Euler) grid for each blade row is generated and the flow field is initialized based on the through-flow results obtained from step 1.
3 A viscous (Navier-Stokes) grid for each blade row is then generated and a viscous flow field initialized, axisymmetrically, based on the solution obtained in step 2.
4 Single-component viscous calculations are carried out using the solutions in step 3 as initial solutions.
5 Multistage computations are then carried out. This step could be combined with 4.

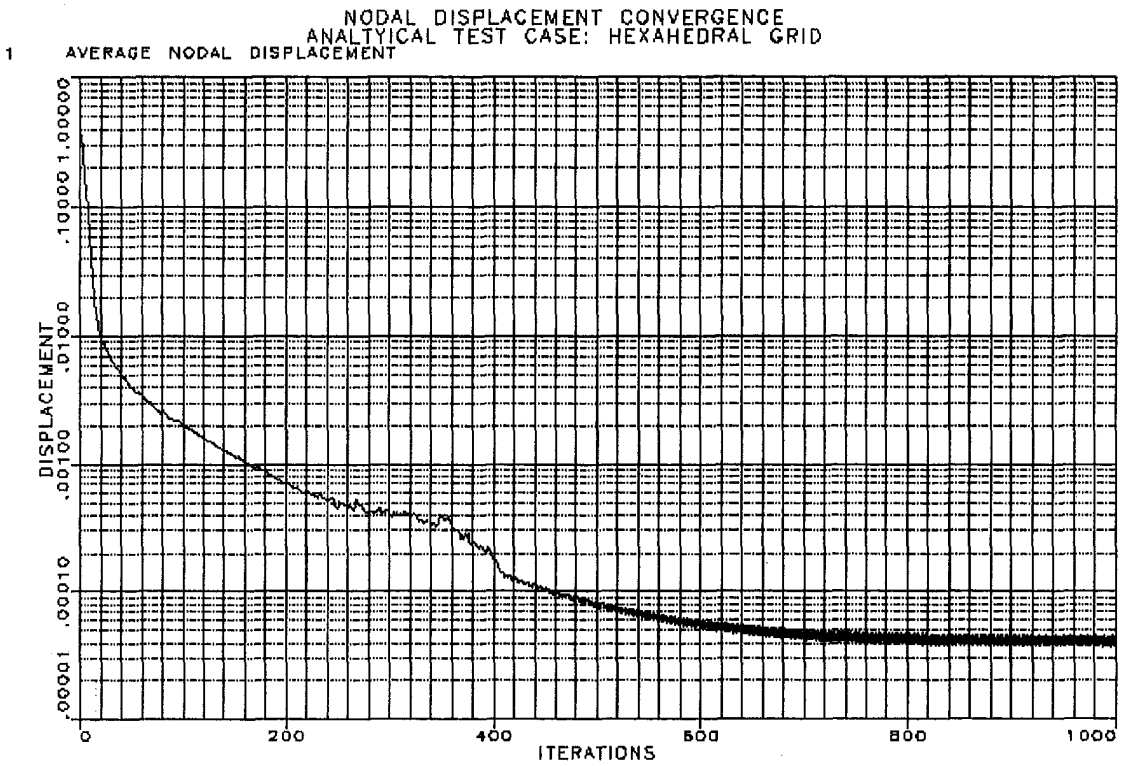

Fig. 3 Convergence of mesh movement scheme for analytical case on hexahedral grid

5 Results

The results first address the accuracy and validity of the adaptive scheme. After this is conclusively established, the multistage calculations are validated and the effect of mesh adaptation on one of the two test cases analyzed.

5.1 Validation of Mesh Adaptation Scheme Through an Analytical Test Case. To investigate the effectiveness of the adaptive procedure on structured grids, an exact test case is first chosen to demonstrate the capability of the mesh movement strategy to equidistribute the interpolation error of a known function over the edges (Tam, 1998). An analytical function f, possessing strong gradients,

$$f(x, y, z) = \arctan\ [1000(x^4y^4z^4 - \tfrac{1}{256})] \qquad (19)$$

has been defined over a $[0, 1] \times [0, 1] \times [0, 2]$ domain which comprises 2541 ($11 \times 11 \times 21$) nodes. The initial and adapted

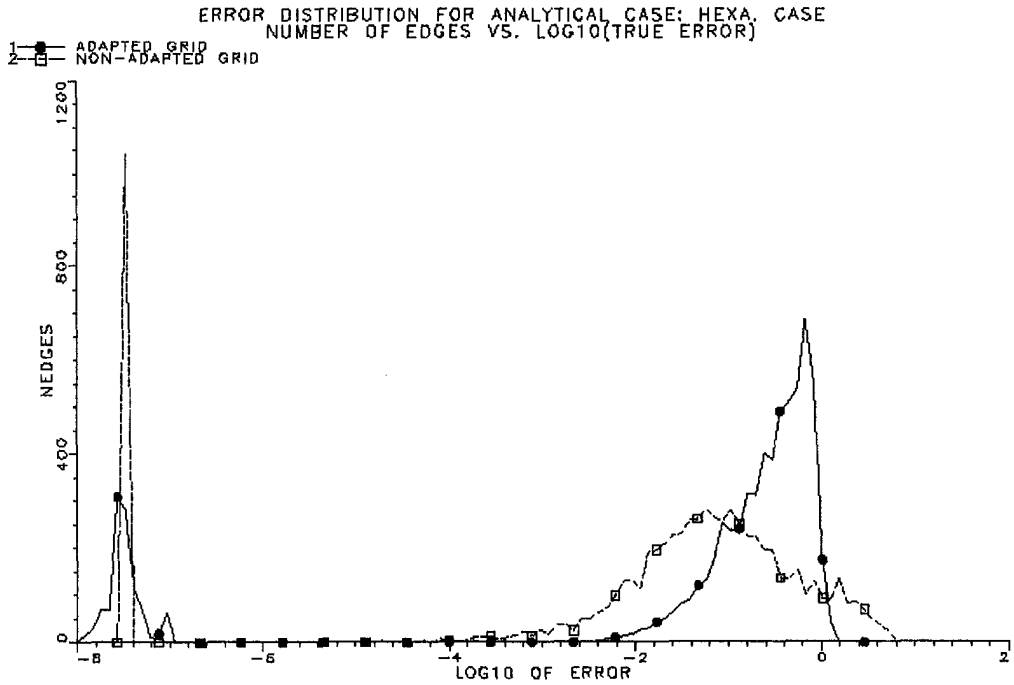

Fig. 4 Analytical case on hexahedral grid: error distribution over edges and adapted grids

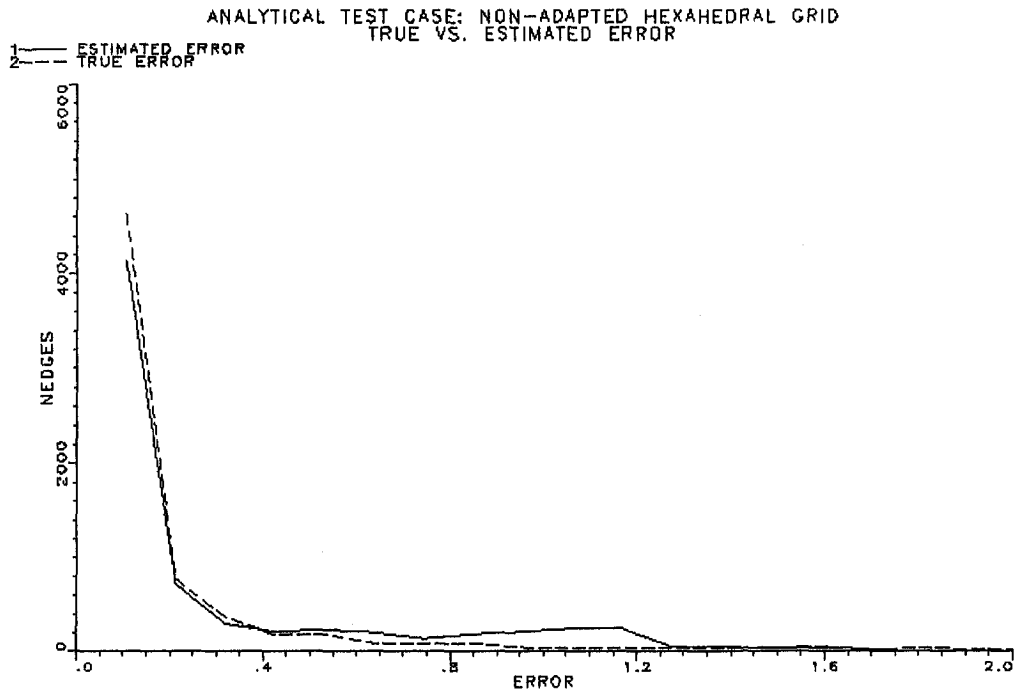

Fig. 5 Plot of true versus estimated error for analytical function on non-adapted hexahedral grid

meshes, along with the corresponding isolines of f are shown in Figs. 1 and 2, respectively. The adapted mesh greatly improves the resolution of the function in regions where large values of the second derivatives of f occur. This grid was obtained after 250 iterations of the mesh movement scheme, using a relaxation factor of 1.0.

In Fig. 3 the convergence history of the nodal displacement algorithm reveals that the average displacement decreased by four orders of magnitude over 700 iterations, beyond which point no important changes in the positions of the vertices are detected.

A distribution of the number of edges versus the exact error over these edges is presented in Fig. 4. In the adapted case, the distribution has shifted toward a near Gaussian one in which the maximum error over an edge has been reduced by four-fold.

Questions regarding the "quality" of the error estimate often arise in grid adaptation investigations, i.e., how does it represent the "real error," were it known. To address this issue, the number of edges versus the exact and estimated error were plotted for both initial and adapted hexahedral grids (Figs. 5 and 6). The exact error over the edges was computed using the exact Hessian matrix of the analytical function whereas the estimated error was determined

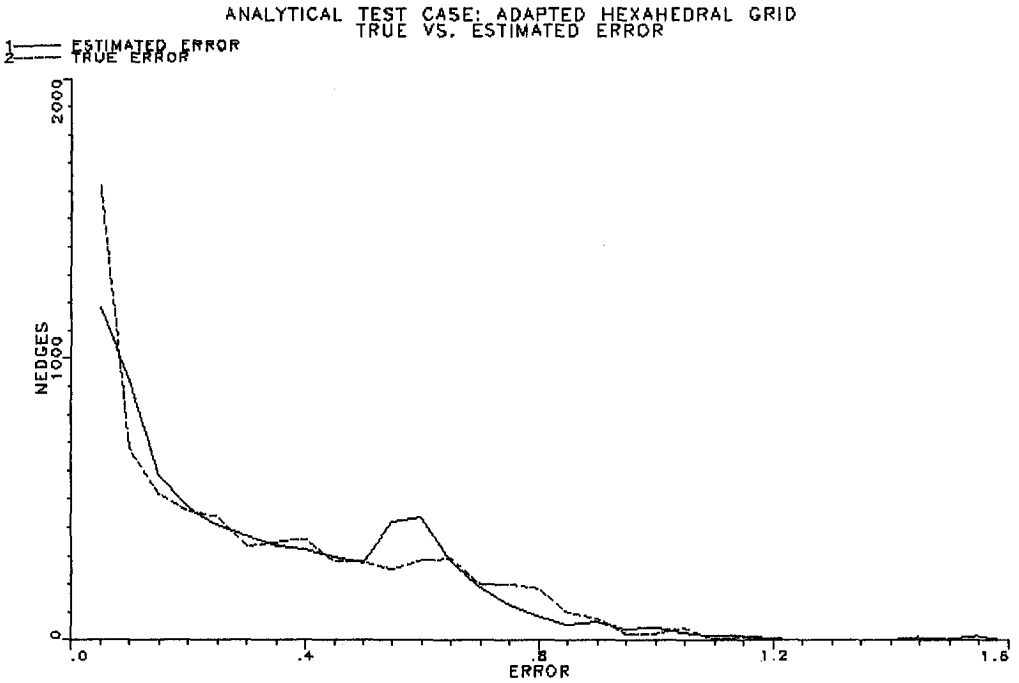

Fig. 6 Plot of true versus estimated error for analytical function on adapted hexahedral grid

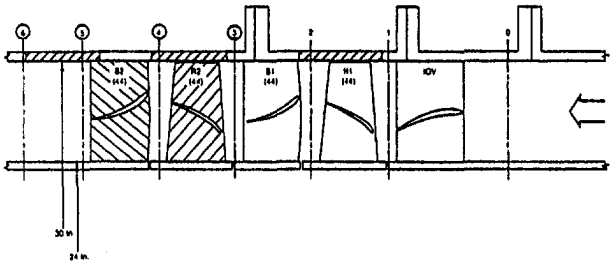

Fig. 7 The 2.5 stage compressor model

using second derivatives recovered through the weak Galerkin formulation (Tam, 1998). The estimated error appears to quite closely follow the exact error for both the initial and adapted cases.

5.2 Multistage Analysis of a Low-Speed Axial-Flow Compressor. The second stage rotor and stator of the UTRC Large Scale Rotating Rig for which detailed experimental data are available (Dring, 1993) has been chosen as the first test case. It is considered a difficult test case because of the low Mach number in the flow field (relative Mach = 0.1) and the presence of corner stalls near the endwalls of the stator. Mesh adaptation is expected to alleviate some of the solver's problems for this particular test case, which could not be made to converge in (Dring, 1986).

The meshes used for all test cases are H-grids. The rotor grid used 25 points upstream of the blade, 55 points on the blade and 12 points downstream of the blade. There were 30 points in the hub to shroud direction and 29 points in the blade-to-blade direction. The stator grid used 14 points upstream of the blade, 57 points on the blade and 15 points downstream of the blade. There were 25 points in the hub to shroud direction and 21 points in the blade-to-blade direction. The rotor tip clearance/chord is 1 percent and the stator hub clearance/chord is 0 percent.

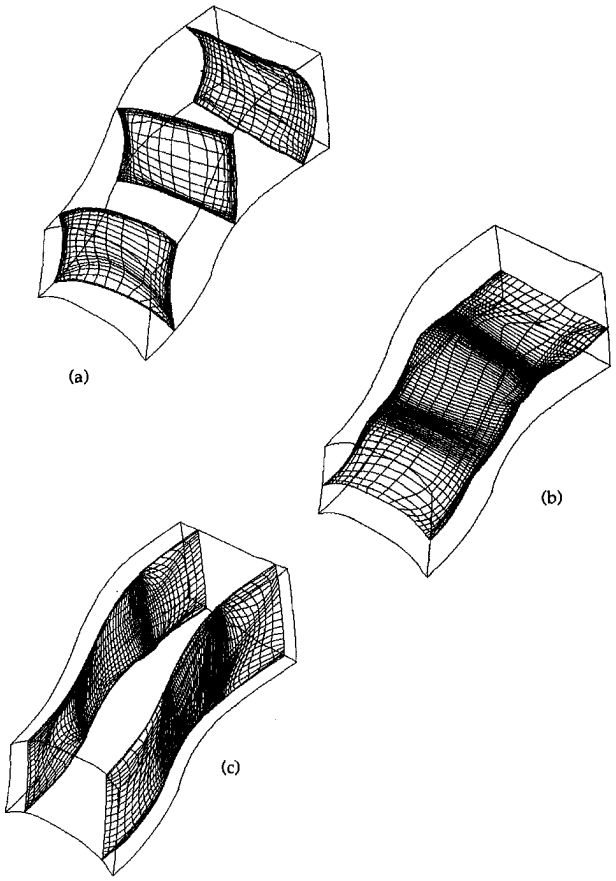

Fig. 8 Various planes of adapted grid of the second stage UTRC stator (*a*) I = 5, 39, 82 planes, (*b*) j = 10 plane, (*c*) k = 9, 18 planes

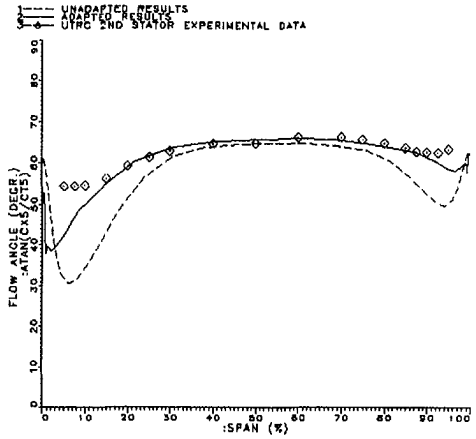

Fig. 9 UTRC 2nd Stator: flow angle at exit versus % span

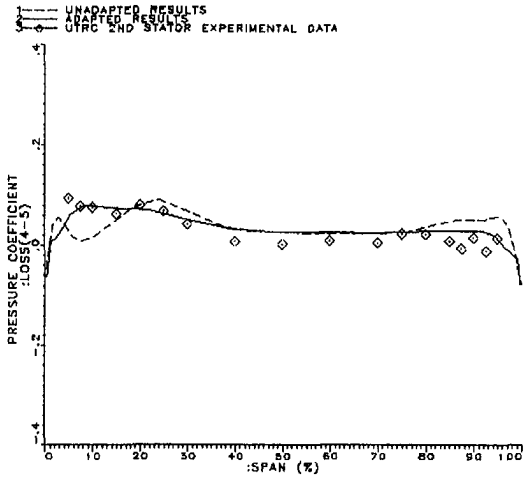

Fig. 10 UTRC 2nd Stator: distribution of loss versus % span

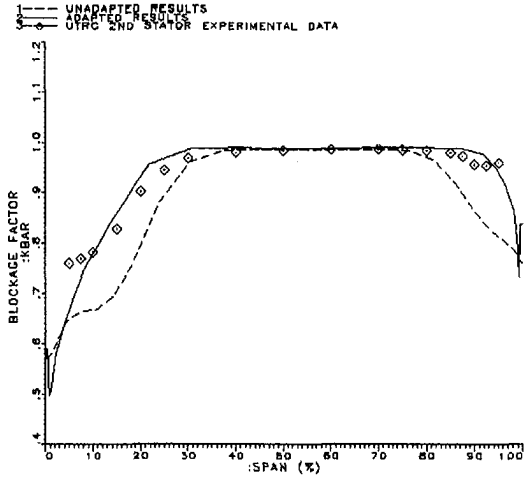

Fig. 11 UTRC 2nd Stator: distribution of blockage versus % span

As shown in Fig. 7, the rotor inlet is located at station 3 and the stator exit is at station 5. Station 4 is considered the interface mixing plane between the rotor and stator. Station 3 is at 24 percent of the rotor axial chord upstream of the rotor leading edge. Station 4 is at 30 percent of the rotor axial chord downstream of the rotor trailing edge and 19 percent of the stator axial chord upstream of the stator leading edge. Station 5 is located at 18

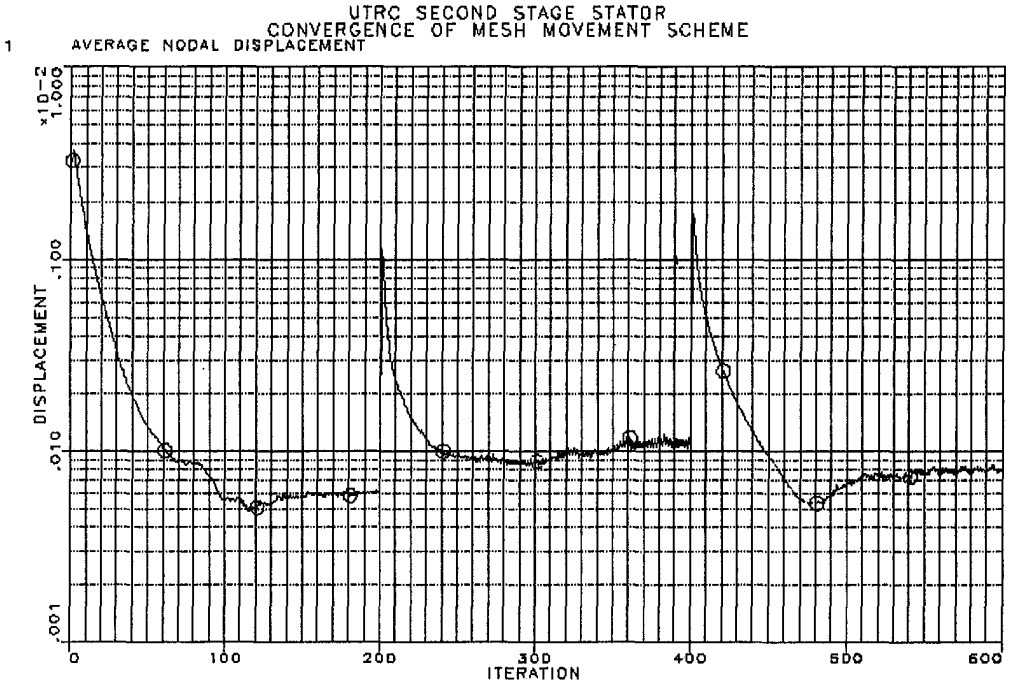

Fig. 12 UTRC 2nd Stator: convergence of nodal displacement scheme

percent of the stator axial chord downstream of the stator trailing edge. The rotor and stator each possess 44 blades.

Two situations have been examined:

(i) Grid adaptation applied to the 2nd stator, solved with inlet and exit boundary conditions imposed from experimental values,

(ii) The adapted numerical solution for the 2nd stator obtained from part (i), above, is then analyzed in a multistage environment whereby the inlet conditions at station 4 (exit of rotor and inlet of stator) are determined iteratively.

The effect of adaptation will be first discussed for situation (i), i.e., the "isolated" second stator. Three cycles of adaptation were required to produce the adapted grid shown in Figs. 8(*a–c*). It should be remarked that in this situation, the degree of nodal movement was severely limited by the fact that no mesh movement was allowed on boundary curves and surfaces. These curves and surfaces were generated by a non-CAD based in-house mesh generation code. In fact, since this was a turbulent case, all eight nodes of the hexahedral wall layer were restricted from moving so as to preserve the original y^+ values. Despite these severe constraints, the adapted numerical results showed noticeable improvement over the nonadapted predictions and responded convincingly toward the experimental data (Figs. 9, 10, 11).

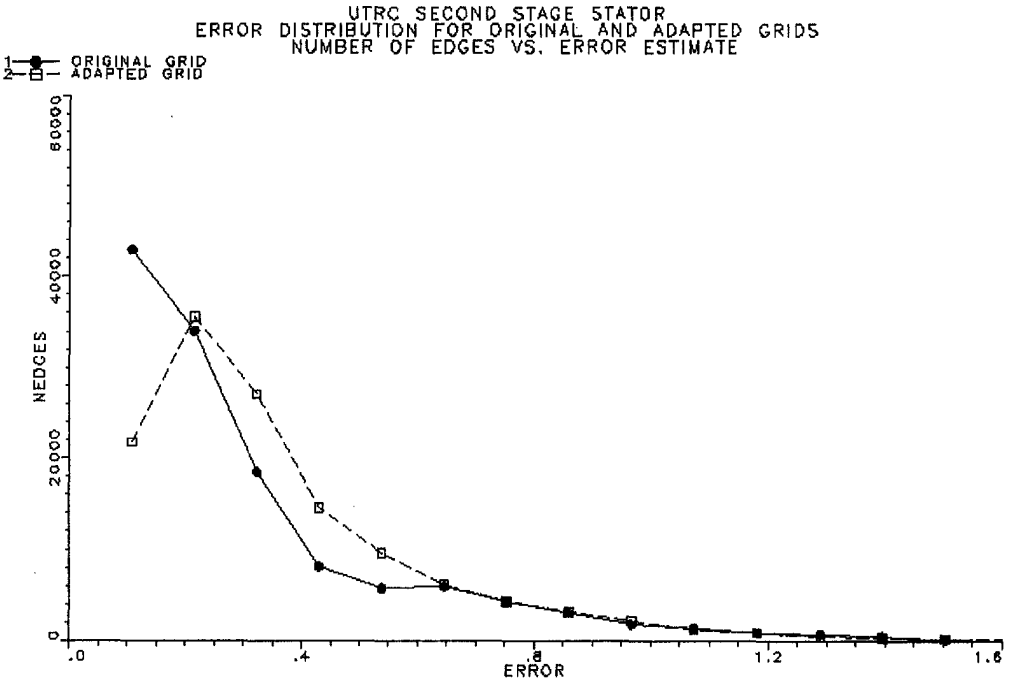

Fig. 13 UTRC 2nd Stator: error distribution over edges for original and adapted grids

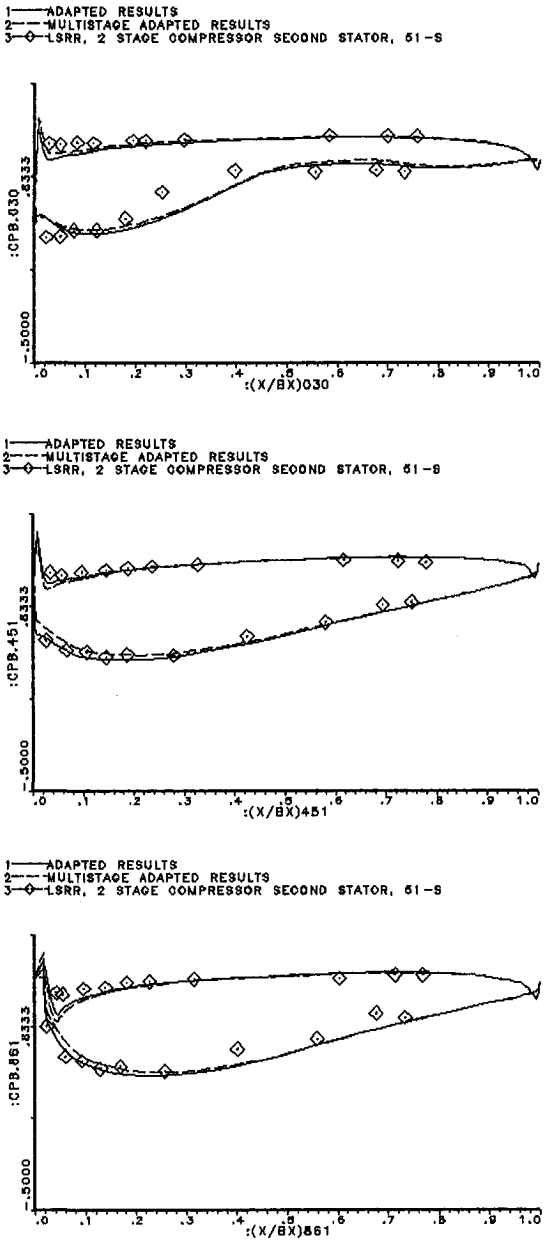

Fig. 14 Pressure coefficient distribution on airfoil sections at 3%, 45.1%, and 86.1%: versus axial location

Figure 9 compares the radial distributions of numerical and experimental values of exit flow angle. The flow angles, after adaptation, are well predicted between 10–90 percent span. The adaptive procedure improves the solution in the regions of 10–40 percent and 70–90 percent span. However, between the hub to 10 percent span and 90 percent span to shroud, the observed discrepancy may be attributed to the fact that the nodes associated with wall elements are not allowed to move.

The spanwise distribution of loss, computed as the difference between total pressure coefficient at inlet and exit, is shown in Fig. 10. The prediction of loss, particularly in the vicinity of the hub and shroud, is much improved with grid adaptation.

A plot of blockage versus percentage span is given in Fig. 11. The blockage factor distribution represents the departure of the actual flow field from axi-symmetry assumed in the through-flow analysis (Dring, 1986). The adapted blockage distribution represents a concrete improvement over the nonadapted results.

The second derivatives of the Mach number solution obtained from the initial unadapted grid is used to build the driving edge-based error estimate in the adaptation case. Other single variables or weighted combinations could also be used in the error estimator but the Mach number was determined to be the most appropriate for this low speed test case. In each of the three adaptive cycles, a given level of artificial dissipation was specified and the L_2-norm of the solution residual was required to decrease by three orders of magnitude before the nodes were displaced 200 times. This number of iterations may seem rather small for a 3-D case but, since the displacement algorithm is applied only to the volume nodes, it was observed that any further increase in the number of sweeps over the nodes would not result in any noticeable change of the nodal positions. As indicated in the convergence history of the mesh movement scheme (Fig. 12), the greatest change in the grid point positions occurred in the first adaptive cycle where the average displacement drops from 3×10^{-3} to 5×10^{-5} over the first 200 iterations. The leveling of the displacement curve in each cycle may be attributed to the low value specified for the allowable maximum edge length. A low limit was necessary to ensure that the resulting hexahedral elements in the adapted grid were not highly skewed. The final adapted solution was obtained using 20 percent less artificial dissipation than in the nonadapted case. A

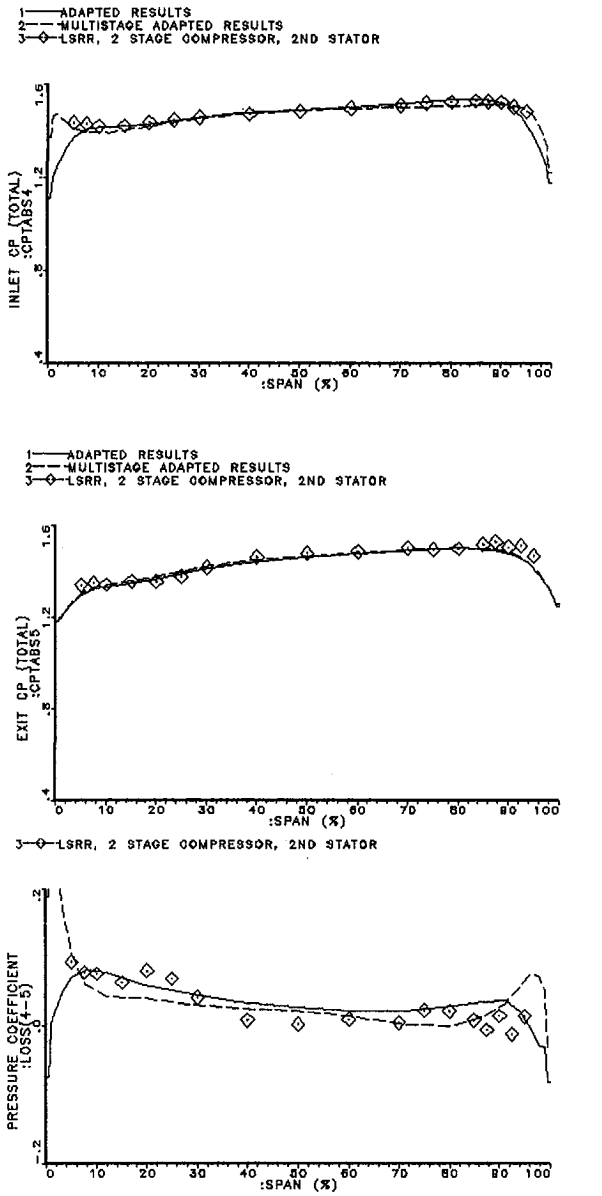

Fig. 15 Total pressure coefficient at stator inlet (station 4) and exit (station 5), and absolute total pressure loss versus % span

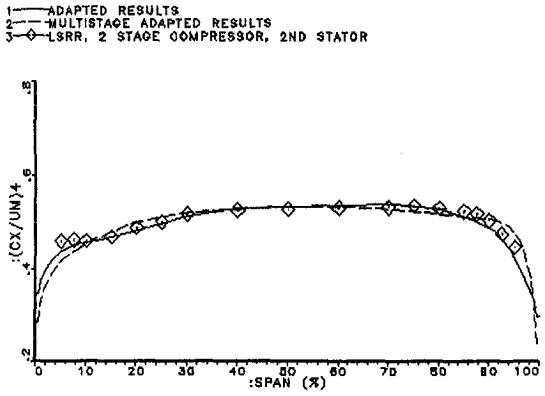

Fig. 16 Normalized axial velocity at stator inlet (station 4) versus % span

relaxation factor of 0.9 was employed in the movement scheme in all three cycles. Figure 13 provides the error distribution over the edges for the nonadapted and adapted grids. It is clear that the error is more equi-distributed over the edges of the adapted grid.

For case (ii) we analyze the entire 2nd stage. The stator grid used was the adapted grid from part (i). Each component is first converged, separately, in terms of mass. Interaction then begins between the components. The proper mixed-out quantities from Eqs. (16) are calculated at the planes corresponding to the interface, from each side, and properties in Eq. (17) determined. The new inlet (rothalpy, components of mass flux-scaled to correspond to the inlet mass flow rate in the far upstream component, turbulent quantities) and exit (static pressure) values are obtained by suitably under-relaxing the change at the nodal values from the previous iteration. This interaction then continues at each Newton iteration.

In Fig. 14 comparison between the measured and computed stator pressure distributions for case (ii) are made at 3, 45.1, and 86.1 percent span. The comparison is good from hub to tip, with the numerical solution clearly indicating the region of separation on the suction side at the 3 percent span section. Results at the other sections are also good, with the adapted solution invariably getting closer to the experimental values.

Figure 15 shows the spanwise distributions of total pressure coefficients at stations 4 and 5, and the spanwise loss distribution. All are well predicted and the adaptive solution captures better the loss distributions near the end walls. It should be noted that this is achieved despite of the small pressure ratio of the case, which gives little variation in the total pressure profiles, leading to some inaccuracy in being able to define the loss.

Finally, Fig. 16 shows the radial profile of the axial velocity at station 4 (stator inlet), normalized with respect to wheel speed. It is well predicted, even near the end walls.

5.3 Single-Stage Analysis of a Turboprop First Stage. An analysis of a turboprop first high pressure (HP) axial compressor

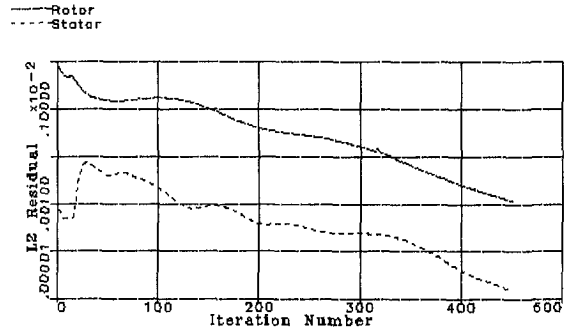

Fig. 17 Convergence history of the Navier-Stokes equations for the 1st stage of the turboprop

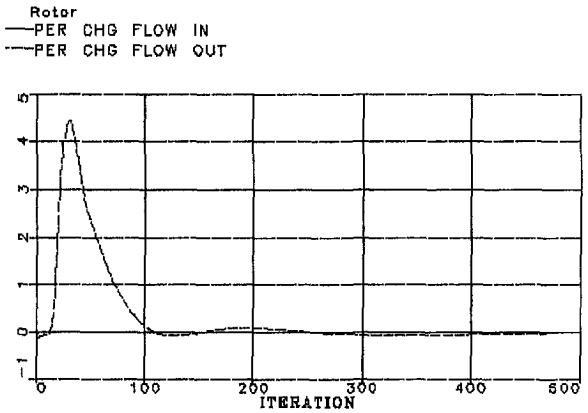

Fig. 18 Percentage change in mass flow versus iteration number at the inlet and exit planes of the 1st rotor in the 1st stage of the turboprop

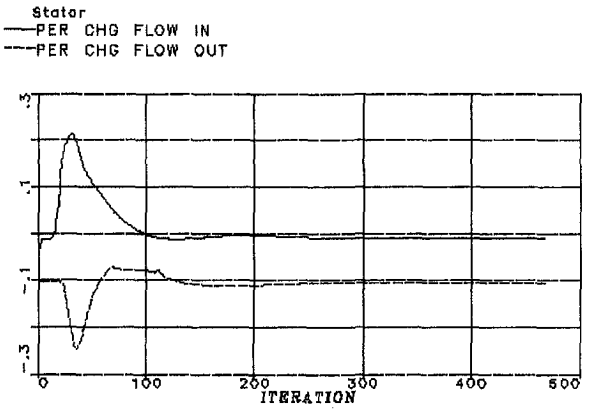

Fig. 19 Percentage change in mass flow versus iteration number at the inlet and exit planes of the 1st stator in the 1st stage of the turboprop

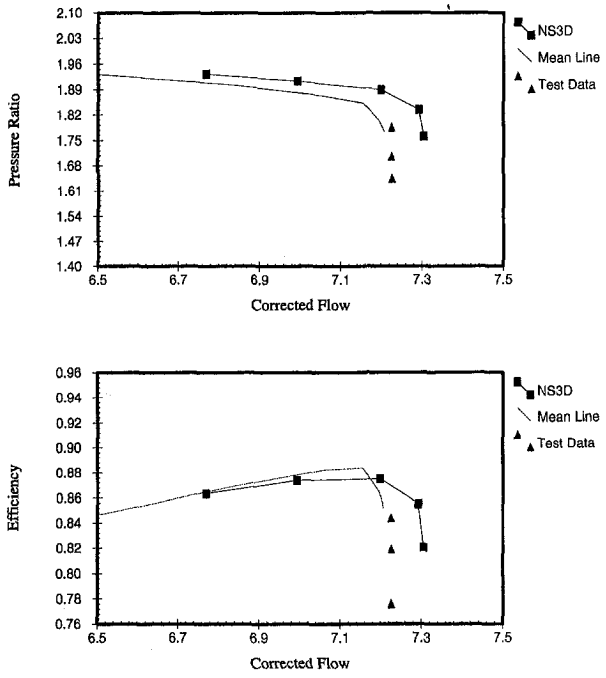

Fig. 20 Comparison of stage speed line prediction by NS3D, mean line model and test data; pressure ratio and efficiency versus corrected flow

stage without tip clearance is carried out. The rotor grid contains 43,750 nodes with 25 nodes in the spanwise direction, 25 nodes in the pitchwise direction, 21 nodes upstream, 41 nodes on the blade, and 10 nodes downstream. The stator grid contains 46,250 nodes

with 25 nodes in the spanwise direction, 25 nodes in the pitchwise direction, 10 nodes upstream, 41 nodes on the blade, and 25 nodes downstream.

A converged single-blade viscous solutions for the rotor and the stator are obtained before the interaction process between the rotor and the stator begins. It is observed that multistage calculations could not be started unless the percentage change in static pressure at the mixing plane, common to the rotor and the stator, is less than 20 percent.

The convergence history of the Navier-Stokes equations (N-S) for both rotor and stator (as a stage) is shown in Fig. 17. The L_2-residual for the rotor is two orders of magnitude greater than that of the stator. About 450 Newton iterations are sufficient to reduce the residuals of the governing equations by three orders of magnitude for both blade rows. Convergence of the stage calculation is not only based on residuals, but also on the change of physical quantities such as static pressure, total temperature, and mass flow across the mixing plane. Stage calculations are terminated when the change in mass flow, area-averaged static pressure, and mass-averaged total temperature at the mixing plane are less that 0.2, 0.5, and 0.1 percent, respectively. The percentage change in mass flow with iteration number, for each rotor and stator, is shown in Figs. 18 and 19.

NS3D over predicts choking flow by 1.03 percent, under predicts efficiency by 1.25 percent and over predicts pressure ratio by 2.4 percent.

Figure 20 shows the map predictions for the first compressor stage by NS3D, meanline model, and test data. In this figure, the predictions are compared with test data at the choking flow condition and to meanline model predictions at nonchoking conditions. The choking flow is over predicted by 1.03 percent with respect to the test data. The stage isentropic efficiency is under predicted by 0.97 percent and the pressure ratio is overpredicted by 1.98 percent with respect to the meanline model.

The potential reasons for the discrepancies observed in the predictions are due to two main causes:

1 The coarse mesh used,

2 Tip clearance is not modeled. This should reduce the predicted choking flow.

Acknowledgments

The authors would like to thank NSERC and FCAR for Operating, Strategic and Team grants under which the current work was performed.

References

Adamczyk, J. J., Celestina, M. L., Beach, T. A., and Barnett, M., 1990, "Simulation of Three-dimensional Viscous Flow Within a Multistage Turbomachine," ASME *Journal of Turbomachinery,* Vol. 112, No. 3, pp. 370–376.

Ait-Ali-Yahia, D., and Habashi, W. G., 1997, "A Finite Element Adaptive Method for Hypersonic Thermo-Chemical Non-equilibrium Flows," *AIAA Journal,* Vol. 35, No. 8, pp. 1294–1302.

Baruzzi, G. S., Habashi, W. G., Guèvremont, G., and Hafez, M. M., 1995, "A Second Order Finite Element Method for the Solution of the Transonic Euler and Navier-Stokes Equations," Special issue of the *International Journal for Numerical Methods in Fluids,* Vol. 20, pp. 671–693.

Dawes, W. N., 1992, "Toward Improved Throughflow Capability: The Use of Three-dimensional Viscous Flow Solvers in a Multistage Environment," ASME *Journal of Turbomachinery,* Vol. 114, pp. 8–17.

Dring, R. P., and Joslyn, H. D., 1986, "Through-Flow Analysis of a Multistage Compressor: Part I—Aerodynamic Input," ASME *Journal of Turbomachinery,* Vol. 68, pp. 17–23.

Dring, R. P., Van Seters, R. J., and Zacharias, R. M., 1993, "A 3D Navier-Stokes Calculation Applied to an Axial Compressor Rotor and Stator," ASME Paper 93-GT-113.

Giles, M. B., "Stator-Rotor Interaction in a Transonic Turbine," AIAA Paper 88-3093.

Rai, M. M., 1989, "Three-Dimensional Navier-Stokes Simulation of Turbine Rotor-stator Interaction, Parts I & II," *Journal of Propulsion and Power,* Vol. 5, No. 3, pp. 305–319.

Tam, A., 1998, "An Anisotropic Adaptive Method for the Solution of 3-D Inviscid and Viscous Compressible Flows," Ph.D. thesis, CFD Lab, Department of Mechanical Engineering, Concordia University, Montreal, Qc, Canada, May.

Numerical Study of Vortex Shedding From a Circular Cylinder in Linear Shear Flow

A. Mukhopadhyay

P. Venugopal

S. P. Vanka

Department of Mechanical and Industrial Engineering, University of Illinois at Urbana-Champaign, 1206 W Green Street, Urbana, IL
e-mail: s-vanka@uiuc.edu

A three-dimensional numerical simulation of linearly sheared flow past a circular cylinder has been performed for a shear parameter β of 0.02 and a mean Reynolds number of 131.5. A cylinder of 24 diameters span is considered. A second-order accurate finite volume scheme is used to integrate the unsteady Navier-Stokes equations. Present computations confirm both qualitatively and quantitatively, the aspects of cellular shedding as reported by several investigators through experimental studies. Up to five constant frequency cells of obliquely shedding vortices are observed. The nondimensional frequencies of these cells are observed to be lower than those given by parallel shedding correlations at the equivalent Reynolds numbers. It is also observed that the cell boundaries continuously move in time. Detailed distributions of vorticity and velocity components are presented to describe the flow. The influence of end-wall boundary conditions is studied by computing two cases, one with free-slip condition, and the other with no-slip condition on disks of radius of five cylinder diameters.

1 Introduction

Numerous studies of vortex shedding from bluff bodies placed in a uniform free stream have been reported (cf. Williamson, 1996) since the early work of Strouhal (1896). The general characteristics of flow over a bluff body of simple shape (circular and rectangular cylinders, flat plate, sphere) placed in a uniform stream are reasonably well understood. At low Reynolds numbers (until ~40), the flow has been observed to be steady. However, beyond a critical Reynolds number, unique to the given geometry, the flow is found to become unsteady, with periodic shedding of vortices from the top and bottom sides of the body. The flow field is two-dimensional (spanwise uniform, except at end regions) until a second critical Reynolds number, at which the spanwise uniform flow becomes three-dimensional. Regions of streamwise vorticity are observed to appear at spanwise intervals of 4 diameters (Mode A instability), and 1–1.5 diameters (Mode B instability) when the Reynolds number is progressively increased. Detailed reviews of previous studies on circular and rectangular cylinders in uniform flow are given by Berger and Wille (1972), Bearman (1984), and Williamson (1996).

In many practical situations, the inflow stream is not uniform, but has some form of shear imposed along the axis of the body. Such a situation is of relevance to the design of chimneys placed in the earth's boundary layer, marine risers, tethered buoys, and pillars of offshore platforms. In comparison to uniform flow, effects of shear on the vortex shedding mechanisms are relatively less understood. Only a few studies, primarily experimental, have been reported in which the shedding frequencies and drag forces have been measured. The most distinguishing feature observed for shear flow over a bluff body is the shedding of vortices in cells of constant frequency. Early experiments of Masch and Moore (1960) and Shaw and Starr (1972) measured the drag and Strouhal numbers for a circular cylinder in shear flow. Within the accuracy of the experiment, their study did not show any cellular shedding pattern. However, in several subsequent experimental studies (Maull and Young, 1973; Mair and Stansby, 1975; Peltzer, 1982) a distinct cellular pattern consisting of cells of constant frequency was noticed. Mair and Stansby (1975) conducted similar experiments on cylinders of various cross-sections and aspect ratios. They conjectured that there should be an upper limit to the spanwise size of the cells. The largest cell lengths observed have been usually in the range of $4D$ to $6D$. In their experiments, the base pressure coefficient based on local velocity was observed to be nearly constant along the span with variations only at the ends. For short cylinders, the end effects were more pronounced. It was also observed that the base pressure coefficient based on mean velocity varied linearly for most of the span and did not show any cellular pattern. This observation is inconsistent with that of Maull and Young (1973) who had earlier observed a definite variation of base pressure in the spanwise direction. The change in the slope of the base pressure curve was linked to the boundary of cells of constant frequency.

As a simplified analogue of shear flow over uniform cylinders, Gaster (1969, 1971) studied flow over slender cones and observed that there exists a spanwise coupling between regions of different characteristic frequency that introduces some amount of amplitude modulation to the shedding vortices. In a review paper, Griffin (1985) summarized the observations made by several investigators. It was shown that for various experimental conditions, cellular shedding pattern has been observed along with spanwise variation of base pressure. Noted among these are experiments by Woo et al. (1981), Peltzer (1982), and Peltzer and Rooney (1981). Peltzer (1982) also reported that the boundaries of the constant frequency cells, away from the ends show some temporal variation. However, the dynamics of the cell boundaries remain to be understood. Much of the theoretical work has been based on simple oscillator models, with modifications to include effects of three-dimensional geometry or upstream flow. Gaster (1971) proposed a simple model of three-dimensional vortex shedding using the Van der Pol equation with a chain of spanwise stiffness. Noack et al. (1991) presented similar phenomenological model for the spanwise cell formation in the near wake of the cylinder in nonuniform flow at low Re (0 ~ 160). However the accuracy of the model is limited by the appropriate selection of the coupling coefficients.

Balasubramanian and Skop (1996) have developed an elastically coupled Van der Pol oscillator model using a diffusive coupling in the spanwise direction. Their model could closely replicate the cellular nature of vortex shedding that has been observed in experiments. Anderson and Szewczyk (1996) investigated the con-

Contributed by the Fluids Engineering Division for publication in the JOURNAL OF FLUIDS ENGINEERING. Manuscript received by the Fluids Engineering Division April 20, 1998; revised manuscript received February 4, 1999. Associate Technical Editor: C. L. Merkle.

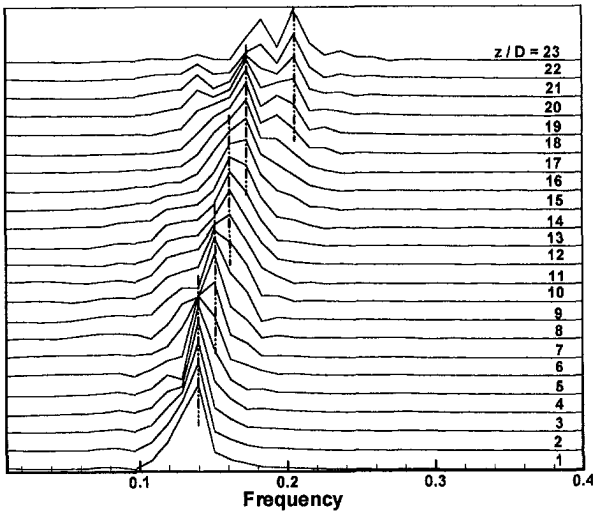

Fig. 1 Spanwise variation of frequency spectra of fluctuating v-velocity at $x = 1D$, $y = 0$ for the free slip condition at spanwise boundaries. The vertical axis is the power spectral density on an arbitrary scale. Curve for each spanwise location is plotted with a constant successive offset.

cept of universal Strouhal parameter that would remain invariant for a variety of bluff bodies and flow configurations, including shear in the upstream flow. Different dimensionless groupings of base pressure, wake width, and Strouhal number were investigated.

To our knowledge, there have been only a small number of computational studies of the three-dimensional vortex shedding phenomena arising out of either sheared upstream flow or body geometry. Jesperson and Levit (1991) conducted a three-dimensional computation of the flow over a tapered circular cylinder similar to the geometry considered by Piccirillo and Van Atta (1993). A time sequence of vortex formation and interactions was presented. Vortex dislocations were observed as seen in the experiments. Newman and Karniadakis (1997) recently presented results of a direct numerical simulation of flow past a freely vibrating cable at low Reynolds numbers (Re = 100 and 200). As a part of this study, a sinusoidally sheared upstream flow was considered. This direct simulation is probably the only numerical study that reports the vortex shedding process for nonuniform upstream flow. They showed that the effect of a shear in the approach flow is to produce a mix of both travelling and standing waves. While a sinusoidally sheared inflow condition is rather uncommon in practice, these computations show the impact of spanwise varying inflow on the vortex shedding process.

Despite the experimental and computational studies mentioned above, several issues relating to shear flow past bluff bodies are still not well understood. The issue of cellular vortex shedding itself is not conclusively resolved. It is not known precisely how many cells are normally formed, and how different flow parameters, such as the shear rate, Reynolds number, cylinder aspect ratio, and end conditions influence the cellular pattern. Also, not much is known of the dynamics of the downstream flow.

Table 1 Computed Strouhal numbers

Span of the cells	Strouhal number based on mean velocity	Strouhal number based on local velocity
$0D$–$7D$	0.1397	0.184–0.155
$8D$–$11D$	0.1513	0.166–0.153
$12D$–$15D$	0.1621	0.163–0.151
$16D$–$20D$	0.173	0.163–0.144
$21D$–$24D$	0.2048	0.176–0.165

In the present study, we have undertaken a three-dimensional numerical simulation of the flow over a circular cylinder with linear upstream shear. In order to minimize the complexities due to intrinsic three-dimensionalities that appear because of spanwise instabilities, we have kept the Reynolds number low. The minimum and maximum Reynolds numbers are 100 and 163, with a mean value of 131.5. At these Reynolds numbers, the Mode A and Mode B intrinsic three-dimensionalities are known not to appear (Henderson and Barkley, 1996). The spanwise domain is taken to be 24 cylinder diameters, giving a shear parameter $[\beta = (D/U_0)(\partial u/\partial z)]$ of 0.02. To minimize the effects of the end conditions, it would be necessary to consider a very long cylinder in the computations, or use a spanwise periodic boundary condition with a periodic upstream profile. For the linear shear case, this would imply using a saw-tooth profile. However, such a saw-tooth profile itself can become a source of vortex dislocations in the wake region. Therefore, effects of end conditions cannot be avoided, both in the numerical computations, as well as in the experiments.

Computations were performed with two different spanwise boundary conditions. The first simulation assumed free slip at the ends, while the second simulation imposed no-slip condition on disks of radius $5D$. Even though the no-slip boundary condition is more physically realistic over the free-slip case, the development of the boundary layers and consequent vorticity generation for the no-slip boundary case adds to the complexity of the wake flow. The free-slip condition, on the other hand, implies an abrupt change in the velocity gradient. Results from both the studies will be presented and a comparison of their effects on the frequency response and wake structure will be made.

Section 2 describes the solution procedure. Section 3 provides the computational details and Section 4 presents the results. Section 5 summarizes the observations.

2 Numerical Method

In the present study, the time-dependent three-dimensional continuity and momentum equations for an incompressible flow are solved on a general curvilinear grid. The solution variables in the momentum equations are selected to be the Cartesian velocity components. A collocated arrangement of pressures and velocity components at the centers of finite volumes is adopted. Spatial discretization uses second-order accurate central differencing. The pressure field is determined by the fractional step method. For time integration, a two-stage, second-order accurate Adams-Bashforth scheme is used. The first stage of the integration consists of solving

Nomenclature

D = cylinder diameter
f = frequency of oscillating velocity signals
p = pressure
Re = Reynolds number (UD/ν)
St = Strouhal number (fD/U)
t = time
U = mean free stream velocity
u, v, w = Cartesian velocity components
x, y, z = Cartesian coordinates, used for post processing of results

Greek Symbols

β = shear parameter $[(D/U)(\partial u/\partial z)]$
ξ, η = transformation coordinates
ν = fluid viscosity
ω = vorticity

Subscripts and Superscripts

local = spanwise local value
mean = spanwise mean value
x, y, z = cartesian components, used for post processing of results

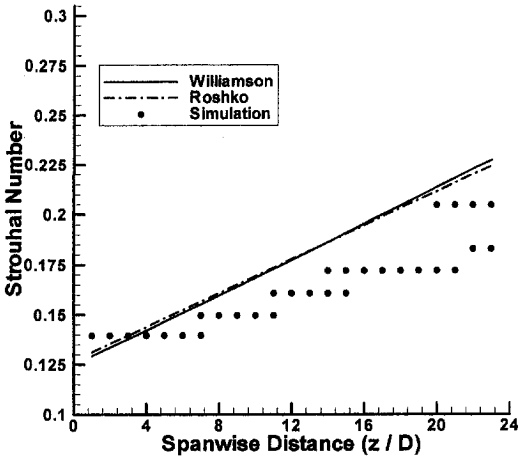

Fig. 2 Spanwise variation of Strouhal number for the free slip condition at spanwise boundaries

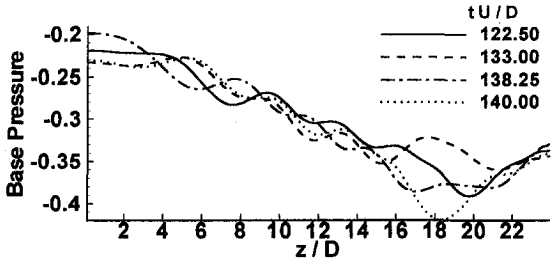

Fig. 4 Temporal variation of base pressure over the span of the cylinder at four different time instances

the momentum equations for an intermediate velocity field. This step is followed by the solution of a Poisson equation for pressure, p such that u_i^{n+1} satisfies the divergence-free condition imposed by the mass continuity equation. Discretization of pressure equation gives rise to a linear system of the form, $\mathbf{A} \cdot \mathbf{p} = \mathbf{b}$. In the present study, this linear system is solved iteratively using the conjugate gradient method. The pressure field is then used to update the volume fluxes and the Cartesian velocities.

As discussed earlier, we have considered both no-slip and free-slip boundary conditions in the spanwise direction. The no-slip conditions are imposed on disks of $5D$ radius. On the cylinder surface no-slip impervious boundary conditions are used along with zero normal pressure gradient. Away from the vicinity of the wake, the far stream boundary conditions are used. Within the wake region, the outflow boundary conditions are adopted from Oseen's solution. (Braza, Chassaing, and Ha Minh, 1986). Complete details of the numerical procedure are given in Wang (1996).

A code based on this algorithm has been implemented for parallel computing on distributed memory machines using the Message Passing Interface (MPI). The computer program has been initially validated for the cases of uniform flow, over circular and rectangular cylinders (Wang, 1996).

3 Computational Details

A curvilinear grid (ξ, η, z) has been considered around the circular cylinder. The domain extends in the η direction to 15 cylinder diameters. In the spanwise (z) direction a domain length of 24 cylinder diameters has been considered. The computational grid is generated in the cross-stream (ξ, η) plane and then stacked in the z-direction. Stretching functions in both radial (η) and azimuthal (ξ) directions are used for appropriate grid concentrations in the wake region and in the vicinity of the cylinder. The present computations are for a mesh size of $80 \times 80 \times 120$ cells in the ξ, η and z directions respectively. This results in a rather coarse grid spacing of $0.2D$ in the z direction. However, computations performed by Jesperson and Levit (1991) for uniform flow over a tapered cylinder suggest that a grid spacing of even $1D$ is sufficient to capture spanwise structures like vortex dislocations. This has been further confirmed by Zhang et al. (1995) who did $3D$ Direct Numerical Simulations of cylinder wake transition. According to them a Δz of 0.1–$0.2D$ is sufficient to resolve secondary spanwise structures with wavelengths around $1D$. Since most of the experimental studies on shear flow past circular cylinders have reported constant frequency cell sizes between $4D$ and $6D$, a grid spacing of $0.2D$ in the z-direction was considered adequate.

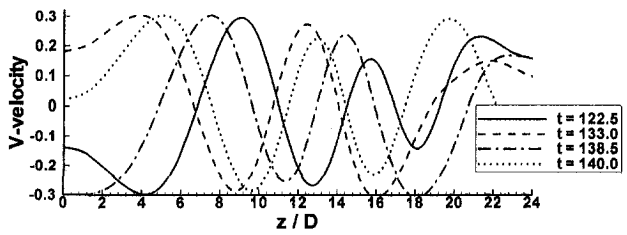

Fig. 3 Spanwise variation of crossflow velocity at a few time instances

The Reynolds number in the present computations varied from 100 to 163 from one end of the cylinder to the other for a shear parameter of 0.02. The nondimensional time step used was 2.5×10^{-3} so as to satisfy the CFL criterion. The computational domain has been split into a number of nonoverlapping subdomains and each domain was assigned to a separate processor. All computations have been performed on the IBM SP2 machines at the Maui High Performance Computing Center (MHPCC). Typical simulations were run on 8 processors and took about 24 hours of real time for 1400 time steps. The integration was started from a uniform sheared flow throughout the solution domain. After the initial transients have been convected out and a nearly stationary flow field has been set up, temporal data were collected for a total of 60,000 time steps, equivalent to 150 time units, and approximately 30 vortex-shedding cycles.

4 Results and Discussion

4.1 Frequency Response of Vortex Shedding. For the Reynolds-number range studied here, a nominally two-dimensional flow field is expected when the upstream flow is uniform along the span. However, with the presence of upstream shear, a complex three-dimensional flow field is generated even at very low Reynolds numbers. The frequency of vortex shedding, and the base pressure variation have been the primary quantities studied in previous experiments. In the present computations, the frequency of vortex shedding has been monitored by collecting the cross flow velocity signals at downstream locations of $x = 1D$, $y = 0$ along the span of the domain at intervals of one diameter. Figure 1 shows frequency spectra of these cross flow velocity signals. Barring the effects at the ends, the presence of five constant frequency cells is evident in this figure. Table 1 presents two sets of Strouhal numbers for different spanwise cells. Within each cell, the Strouhal number based on the mean velocity is constant, while the one based on the local velocity varies linearly, with sudden jumps across the cell boundaries.

The computed Strouhal numbers are somewhat lower than those experimentally measured by Maull and Young (1973). This may be due to the much higher Reynolds number in the experiments. However, our Strouhal numbers compare fairly well with measured values of Noack et al. (1991) for flow over a tapered cylinder. Although the equivalent shear parameter for their tapered geometry is lower than the value in our computation (0.01 *vs.* 0.02 in our study), the Reynolds number range is nearly the same. The lengths of the constant frequency cells in the present computation

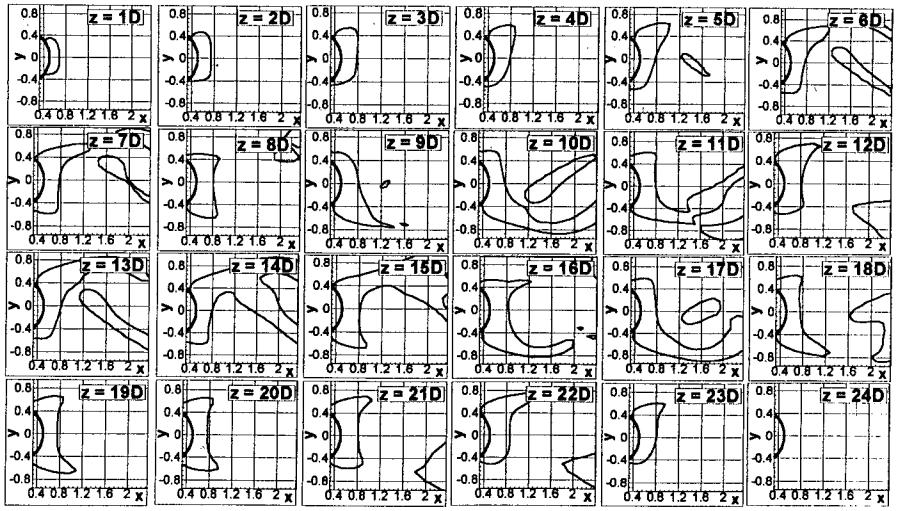

Fig. 5 Spanwise variation of crossstream vorticity at time, $t = 133$. Each frame shows the same contour ($\omega_y = 0.12$) on a (ξ, η) plane at the corresponding spanwise location from the low velocity (u) end

are observed to vary between $3D$ and $7D$. This observation is consistent with those of Maull and Young (1973), Woo et al. (1981), and Peltzer and Rooney (1981), despite the differences in the Reynolds numbers.

The observed frequencies for a sheared upstream flow may be also compared with the parallel shedding frequencies for a uniform flow at the corresponding local Reynolds number. We have hence modified the correlations presented by Roshko (1954) and Williamson (1989) to account for the varying local Reynolds number and the definition of the Strouhal number based on the centerline velocity. In Fig. 2, the computed Strouhal numbers are plotted against the modified correlations given by:

$$\mathrm{St}_W = -3.3265/\mathrm{Re}_{\mathrm{mean}} + 0.1816 \cdot \mathrm{Re}_{\mathrm{local}}/\mathrm{Re}_{\mathrm{mean}} + 1.6 \times 10^{-4} \cdot \mathrm{Re}^2_{\mathrm{local}}/\mathrm{Re}_{\mathrm{mean}} \quad (1)$$

$$\mathrm{St}_R = 0.212(\mathrm{Re}_{\mathrm{local}}/\mathrm{Re}_{\mathrm{mean}}) - 4.5/\mathrm{Re}_{\mathrm{mean}} \quad (2)$$

In the present case, the range of Reynolds numbers is 100 to 163 with a mean of 131.5. It can be seen that the computed Strouhal numbers are lower than those given by the correlations. Noack et al. (1991) made a similar observation in the case of a slender cone. They attributed this lowering of the frequency to the oblique nature of the shedding (resulting from the varying cylinder diameter), for which the frequency reduces as the cosine of the shedding angle (Williamson, 1988). Oblique shedding is also observed in the case of a sheared flow. However, a simple scaling of the frequency by the angle of shedding gives only a simple explanation. We observe that the lowering of the frequency is due to complex fluid dynamic interactions (described below) that are occurring in the near wake, as a result of continuous spanwise energy redistribution.

4.2 Instantaneous Flow Field. Ideally, one would expect that a continuous spanwise variation of the free stream velocity should result in a continuous variation in phase of the shed vortices. However, this is not the case. Because of the convective-diffusive coupling in the spanwise direction, the shed vortices maintain a certain degree of coherence. Thus vortices of finite lengths are shed alternately from the top and bottom sides of the cylinder. A cell may be identified by the span over which a top or a bottom shear layer is able to maintain coherence. Between two successive cells the crossflow (v) velocity will change its sign. Figure 3 shows the spanwise variation of the crossflow (v) velocity at a location of $x = 1D$, $y = 0$ at different time instants. It can be seen that there are five spanwise cells present at these times, with some effects due to the end conditions. Also, the cell boundaries move in time along the span and are not fixed. Such cellular behavior is also observed in the temporal variation of the base pressure along the span (Fig. 4). The details of the temporal behavior of the cellular shedding phenomenon will be discussed in Section 4.4. This has also been observed experimentally by Peltzer and Rooney (1981) and by Mair and Stansby (1975). Further, these instantaneous boundaries do not coincide with those shown in the frequency spectra (Fig. 1). The temporal dynamics are further discussed in a subsequent section of the paper.

We also see that near the cell boundaries there is a sudden change in the phase of the vortex shedding. This is exemplified by the distributions of cross-stream vorticity, shown in Fig. 5.

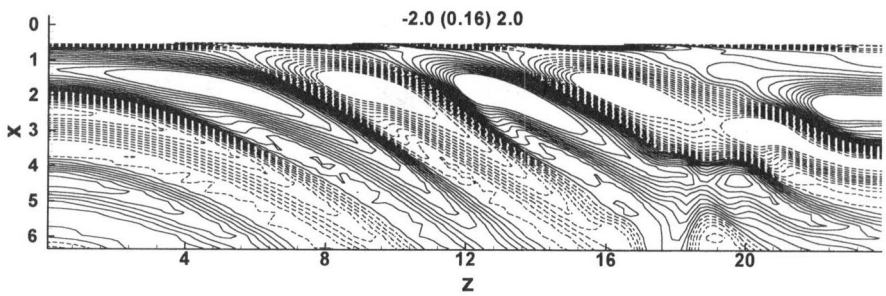

Fig. 6 Contours of spanwise vorticity on $y = 0$ plane at time, $t = 133$. Solid and dashed lines show positive and negative vorticities, respectively.

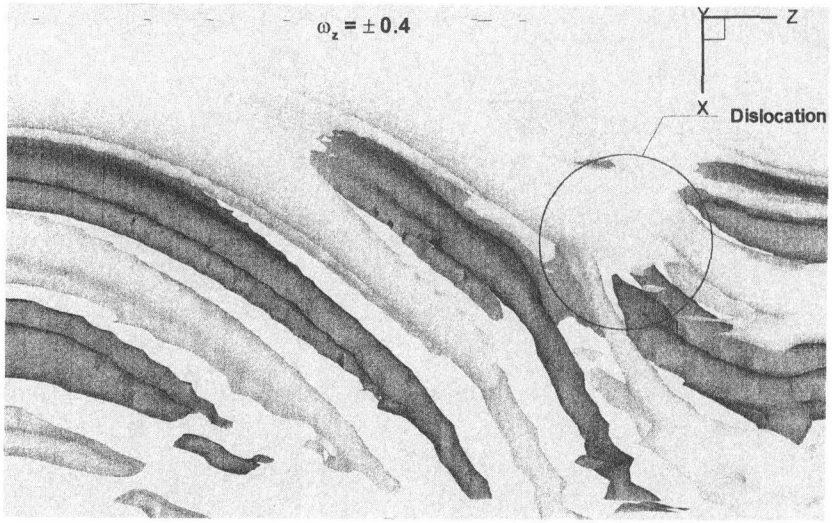

Fig. 7 Isosurfaces of spanwise vorticity ($\omega_z = \pm 0.4$) at time, $t = 133$

Figure 5 shows the distribution of (ω_y) at different spanwise locations at $tU/D = 133.0$. It can be seen that there is a monotonic pattern of ω_y between 0 and $7D$. This pattern suddenly changes between 7 and $8D$ when a new pattern of shedding from the bottom is initiated. There are again abrupt changes at $12D$, $16D$ and $20D$. These locations match fairly well with the zero-crossing locations of the v-velocity shown earlier in Fig. 3. The loss of coherence in the locally adjacent layers manifests in abrupt changes in ω_y. On either side of these changes, the shedding layers are aligned with each other. We therefore believe that the span of each shedding layer is determined by an extent of phase difference that can be supported by the coherence of the shedding vortices.

Within each cell, however, the axial velocity is not constant. As a result, the axis of the spanwise vorticity is slanted in the spanwise direction. This is evident in the contours of spanwise vorticity at $y = 0$, shown in Fig. 6. It is seen that these contours form closed loops, which progressively become more oblique with downstream distance. The cell boundaries are regions where the positive and negative vorticities meet. The characteristic alternate top-bottom shedding over finite distances with a phase difference along the span can be clearly observed in this figure. Very close to the cylinder ($x \approx 0.5D$), the positive and negative contours indicate that at this time instant, the bottom and top layers are alternately incident on the $y = 0$ plane. The spans of these positive and negative contours coincide well with the zero crossings of the v velocity, as well as with the shedding sequences of ω_y, thus confirming the cellular shedding pattern. As mentioned above, the obliqueness in the vorticity contours indicates a relative increase (across the span of a cell) of the convective velocity of these vortices. The obliqueness of the vorticity distribution can also be seen in Fig. 7, which shows isosurfaces of a particular value

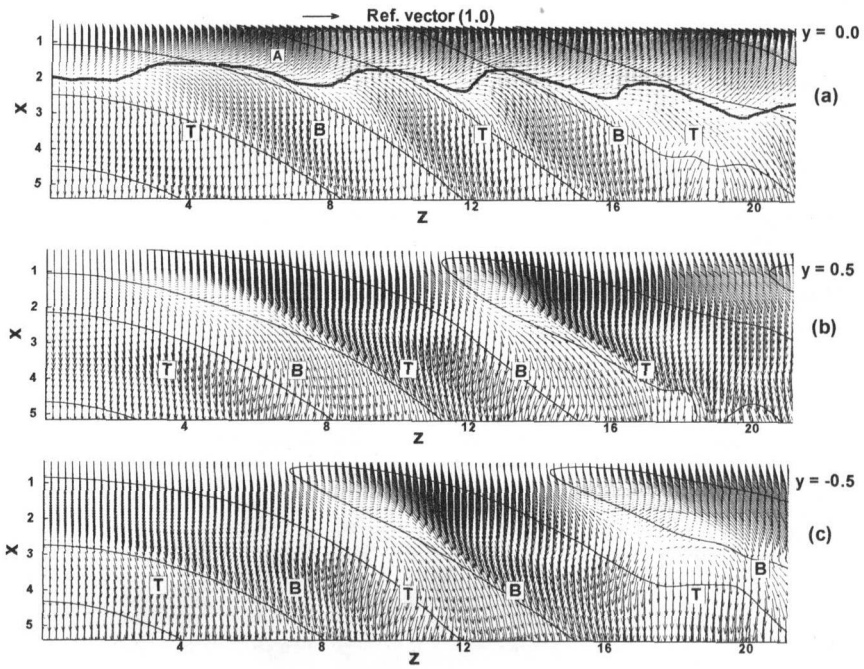

Fig. 8 In-plane velocity vectors (u, w) on various horizontal planes: (a) $y = 0.0$, (b) $y = 0.5$ and (c) $y = -0.5$. Solid lines show contours of $v = 0$. Thick wavy line in (a) represents $u = 0$ contour. T and B represent top and bottom shear layers.

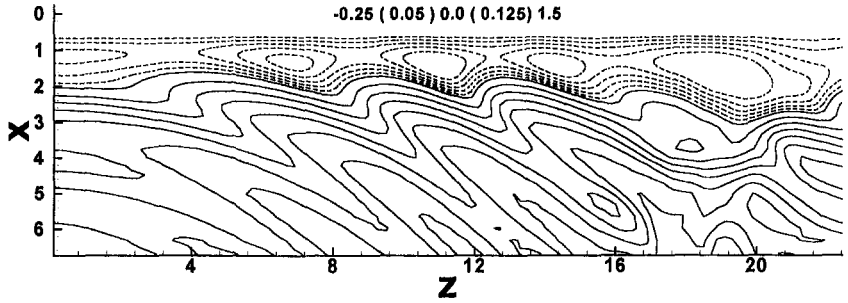

Fig. 9 Distribution of axial velocity (u) on the symmetry plane, $y = 0$ at time, $t = 133$

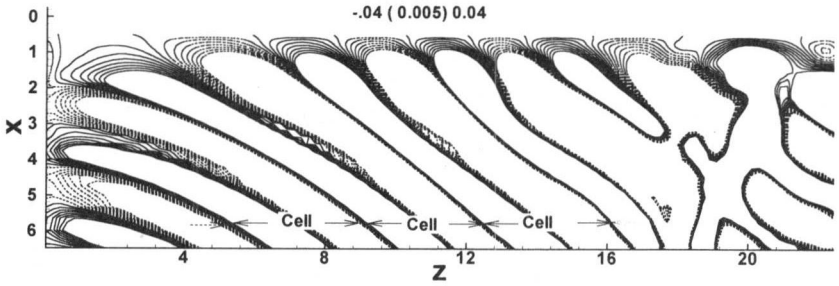

Fig. 10 Distribution of spanwise gradient of axial velocity ($\partial u/\partial z$) on the symmetry plane, $y = 0$, at time, $t = 133$

(magnitude) of ω_z. One can also observe the appearance of a dislocation at the high velocity end.

It may be further noticed from the spanwise vorticity distribution shown in Fig. 7, that the obliqueness of vorticity contours is not present in the immediate vicinity of the cylinder, where the axial velocity is negative. Thus, it appears that although the cellular pattern exists in this region as well, the nature of vorticity variation in this region is different from that outside. This is clear from Fig. 8 which shows the in-plane velocity vector (u, w) on three horizontal planes in the wake ($y = 0, \pm 0.5$). Also shown are contours of zero v-velocity locations, identifying the cells. Within each one of these cells, distinct flow patterns are seen inside the recirculation region and outside the recirculation region. Inside the recirculation region, the increasing strength of the base suction pressure gives rise to a spanwise velocity from the low velocity end to the high velocity end. Further, the axial and spanwise pressure gradients continually vary in time and in the span. Depending on the phase of vortex shedding, the pressure in the wake may be higher or lower than the corresponding base pressure. This gives rise to continuously varying u- and w-velocities within each cell. Consider cell A shown in Fig. 8(a). The line where u is zero is approximately sketched. Upstream of this line, the w velocity is always positive, and decreases toward the cell boundaries. Downstream of the zero u-velocity line, the u velocity is strong and positive. The w-velocity is very small. At locations where the shear layer reaches the $y = 0$ plane, the axial velocity is minimum and the in-plane velocity vectors are showing only spanwise velocities. The flow turns distinctly within a cell to develop the oblique shedding pattern whereas relatively farther downstream, the velocity vectors are getting realigned with the free-stream. Figures 8(b) and (c) show similar plots for $y = 0.5$ and $y = -0.5$. The imprints of the vortices shed from the top and bottom surfaces are marked (T) and (B) on these figures. Within each cell (say T), there is first a positive spanwise flow. When this

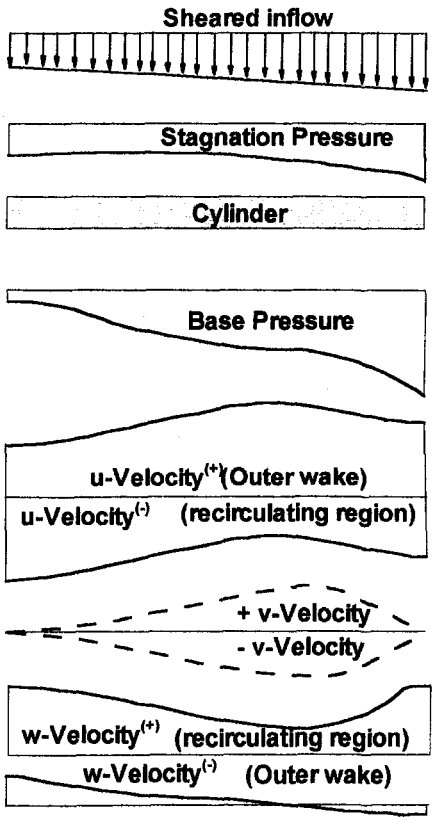

Fig. 11 Schematic representation of flow parameters within a constant frequency cell

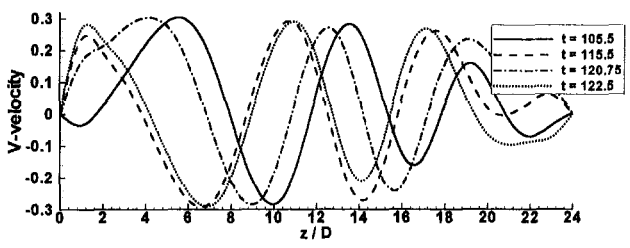

Fig. 12 Spanwise variation of crossflow velocity (with end plates) at four different time instances

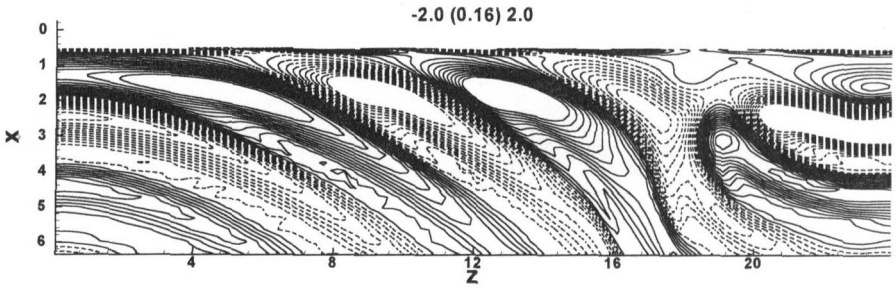

Fig. 13 Contours of spanwise vorticity on $y = 0$ plane (with end plates) at time, $t = 122.5$. Solid and dashed lines show positive and negative vorticities, respectively.

flow reaches the cell boundary, it turns with the adjacent cell (B), which convects it axially. Thus, there is a transfer of mass and momentum between adjacent cells. We believe that this transfer of mass to an adjacent cell gives rise to an increase in shedding frequency of its low velocity end, and a decrease in frequency for the high velocity end of the cell that transferred the mass.

Figure 9 shows instantaneous contours of u velocity at $y = 0$ plane. The regions of negative velocity, in the form of cells can be clearly seen. Figure 10 shows contours of spanwise derivative of axial velocity. The spanwise cell boundaries are locations of the minimum u velocity. Within each cell the spanwise gradient of u velocity has a pair of positive and negative regions. The locations where the gradient goes from negative to positive value correspond to cell boundaries. The maximum absolute velocity gradients are larger in magnitude than the imposed linear shear upstream. This also indicates that there is a significant redistribution of flow in the wake region.

Figure 11 shows hand sketches of the variations of the velocities and pressure within the span of an individual cell at $y = 0$. Upstream of the cylinder, there is the imposed shear, with a quadratically varying dynamic pressure distribution. However, even though there is a significant spanwise pressure gradient upstream of the cylinder, there is no significant spanwise velocity. Downstream of the cylinder (in the near wake), the pressure is negative throughout and has zero derivatives at the cell boundaries. The u-velocity shows zero derivatives and minimum magnitudes at the cell boundaries, while the v velocity is zero at the cell boundaries. On the centerline, the w velocity is positive throughout (i.e., flow is from the low velocity end to the high velocity end) in the near wake. Downstream however, it is positive for much of the span, and negative towards the high-velocity end. Eventually, the flow becomes mostly axial, with very small values of w velocity.

4.3 Results With End Plates. The results presented above correspond to a free slip boundary condition in the spanwise direction. We have also carried out a second simulation with no slip condition imposed over disks of radii of $5D$. Selected results from this simulation are presented below, and are compared with the results from the free-slip case.

Figure 12 presents the v velocity variation along the span at $y = 0$ and $x = 1D$ for four time instants. The zero crossings of the v velocity signals are indicative of the cellular shedding pattern. As in the case of the free-slip boundary condition, we see here also five cells. The range of v velocity fluctuation is also similar to that with free-slip condition. However, imposition of the no-slip condition produces some local effects at the ends. Figure 13 shows instantaneous contours of spanwise vorticity at $y = 0$. The alternate positive and negative vortices indicate shedding from top and bottom sides of the cylinder. From this plot, we can clearly observe that there are five cells. Near the high velocity end, we see some distortion of the vorticity contours. This is resulting from the formation of a dislocation in that region. The other two components of vorticity also indicate similar cell structure, and hence are not shown here. Figure 14 shows the iso-vorticity surfaces ($\omega_z = \pm 0.4$) at one instant in time. This figure should be compared with Figure 7 shown for the free-slip case. We see that these two figures are very similar, but for minor differences near the high velocity end. It appears that the imposition of the no-slip condition does not produce much distortion in the ω_z, as well as other vorticity distributions (not shown here).

Instantaneous base pressure plots, shown in Fig. 15 also support the existence of the cellular shedding pattern. The overall pressure distribution is again similar to the ones observed in the free-slip case, except for some differences at the high velocity end. Figure 16 shows the time average base pressure for the cases with and without the end plates. In both cases, the time-averaged base pressure plot, however, masks the cellular shedding pattern. Further, the overall range of variation of base pressure is smaller in the no-slip case than in the free-slip case. This decrease in the magnitude of base pressure is the result of the growth of the boundary layers on the end disks and also due to the flow diverting away from the end walls.

Figure 17 shows the frequency spectra of the v velocity at $x = 1D$, and $y = 0$, for spanwise locations separated by one cylinder diameter. From this figure, we see that there are only two (2) distinct frequencies of shedding in addition to one at the high

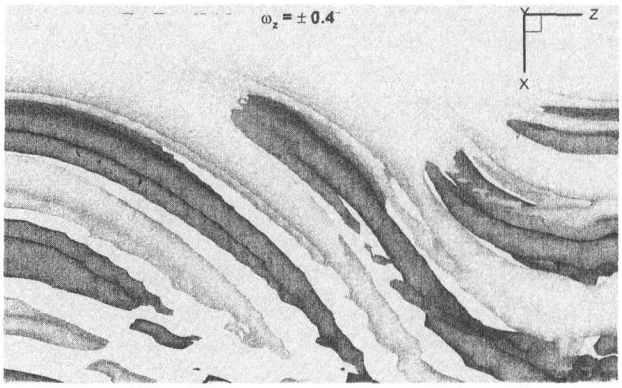

Fig. 14 Isosurfaces of spanwise vorticity ($\omega_z = \pm 0.4$) (with end plates) at time, $t = 122.5$: no significant difference with the free-slip case (Fig. 7)

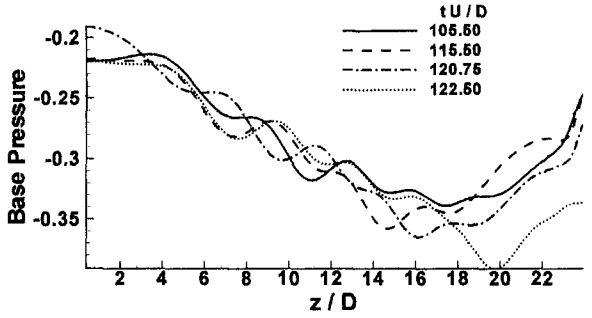

Fig. 15 Temporal variation of base pressure over the span of the cylinder (with end plates) for four different time instances

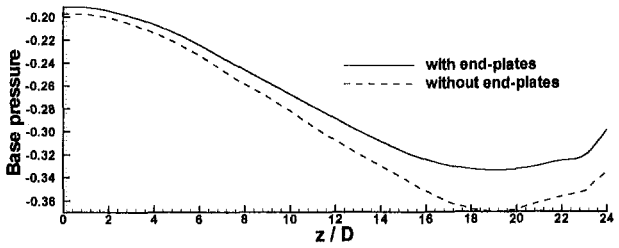

Fig. 16 Spanwise variation of time averaged base pressure for both cases—with and without endplates

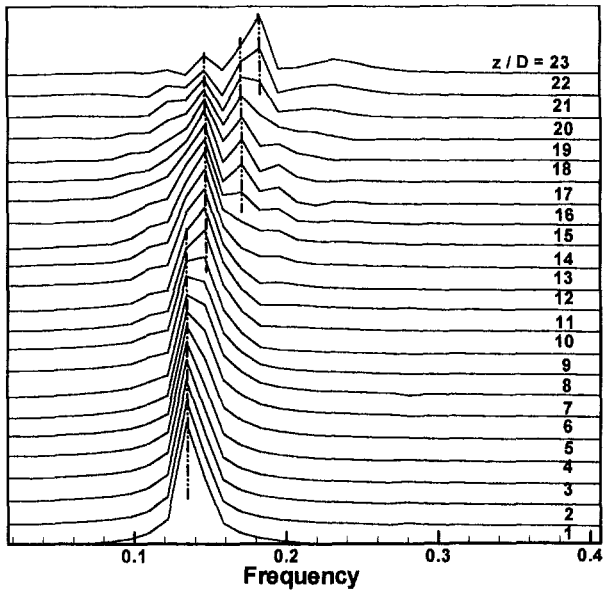

Fig. 17 Spanwise variation of frequency spectra of fluctuating v-velocity at $x = 1D$, $y = 0$ (with end plates). The vertical axis is the power spectral density on an arbitrary scale. Curve for each spanwise location is plotted with a constant successive offset.

velocity end. Although this may lead us into concluding that there are only two distinct cells of shedding, actually there are five cells, as seen in the distributions of the v-velocity, vorticity, and pressure. Thus, an incorrect conclusion can be reached by observing only the frequency spectra, and not the distributions of individual variables, such as the v-velocity. Further, the frequencies are relatively lower with the no-slip condition compared to the free-slip case. In the case of no-slip, the individual frequencies are 0.135 and 0.147 with another frequency of 0.183 at the high velocity end.

4.4 Temporal Dynamics. We observe that the cell boundaries are continuously moving along the span. This can be inferred from the temporal variation of base pressure over the span of the cylinder at four arbitrary time instants for both cases studied (Figs. 4 and 15). These variations are very similar to those reported by Maull and Young (1973). The cell boundaries are observed to coincide with valleys in the base pressure curve. These valleys can be seen to be at different spanwise locations at different instances. The pressure variations at the two ends are a consequence of the end conditions. However, for both cases studied, the time-averaged base pressure distributions are rather smooth curves along the span of the cylinder (Fig. 16). This may have lead previously (Peltzer and Rooney, 1981) to a conclusion that there is no discernible cellular shedding of the vortices.

Figure 18(a) shows the temporal variation of the cross flow velocity at $x = 1D$ and $y = 0$, in dimensionless time versus span coordinates for the spanwise free-slip case. From this plot, we see that after the initial transient evolution of the flow field, a travelling wave pattern is created. Dislocations are observed to occur at the high velocity end at time instants around 110, 129, and 147 and at different spanwise locations. As these dislocations are convected downstream, they are observed to grow in size. This can be also seen in earlier isovorticity plot (Fig. 7). The dislocation seen in Fig. 7 at a spanwise position of $18D$ corresponds to the one that appeared in Fig. 18(a) at time of 129 units.

The temporal variation of the v-velocity at $x = 1D$ and $y = 0$ for the end-plate case, is shown in Fig. 18(b). It shows a close resemblance with the corresponding figure for the free-slip case (Fig. 18(a)). There is an arbitrary time off set of 17 time units between the two cases (i.e., tU/D of 93 in the no-slip case corresponds with 110 of the free-slip case, and the plots should be

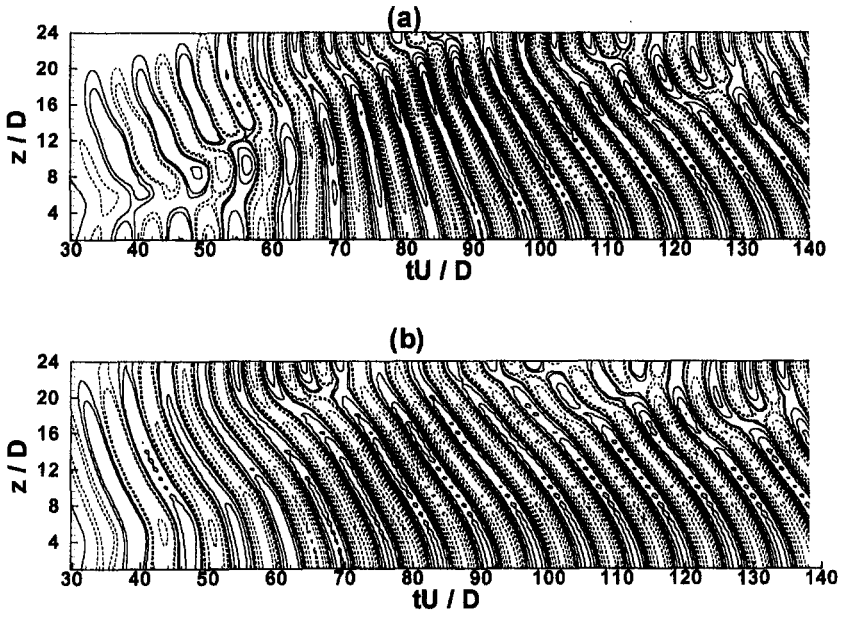

Fig. 18 Temporal variation of crossflow velocity at $x = 1D$, $y = 0$ for both cases—with and without endplates. The time signals at various spanwise locations are plotted on a dimensionless $z \sim t$ plane.

synchronized at these instants). The period between the occurrence of two consecutive dislocations is approximately 18 units in both the cases.

5 Summary

In the present study, two three-dimensional numerical simulations of a linearly sheared flow over a circular cylinder have been conducted. A fractional step method with central differencing of the spatial derivatives is used. The present computations confirm for the first time many of the features previously observed experimentally for shear flow over a circular cylinder. These computations reveal that the flow continually develops in time with the following features:

(*a*) A definite cellular pattern of vortex shedding along the span of the cylinder is observed. Up to five distinct cells for a cylinder of 24 diameters span have been observed. The lengths of the cells varied between 3 and 7 cylinder diameters.

(*b*) For the free-slip boundary condition, the Strouhal numbers based on centerline free stream velocity ranged between 0.14 and 0.205. With end plates at the spanwise boundaries, the corresponding limits were 0.135 and 0.183.

(*c*) Instantaneous base pressure plots show correspondence with cellwise shedding pattern, as reported by Maull and Young. However, the time averaged base pressure varies smoothly along the span (except for end effects) and masks the cellular pattern.

(*d*) Vortex dislocations are observed to form near the high velocity end, and to get convected to downstream.

(*e*) The results with end plates at the spanwise boundaries are very similar to those with free-slip condition, except for the end wall boundary layers and the corresponding vorticity that is generated. The cellular shedding is observed in both cases.

(*f*) The frequency spectra alone may not be the best indicator of the cellular shedding pattern. Detailed spanwise distributions of the velocity, vorticity and other quantities should be also studied along with the frequencies of vortex shedding.

In order to study the temporal dynamics in more detail, it is necessary to integrate the equations for much longer time. Also, in order to reduce the end effects, a much larger span should be considered. Such a simulation is currently in progress.

Acknowledgments

This work was supported by Office of Naval Research Grant N00014-96-1-0697. The computations were performed on the IBM SP2 cluster at the Maui High Performance Computing Center (MHPCC). The supports of these organizations and of the ONR technical monitor, Dr. Thomas Swean, are gratefully acknowledged.

References

Anderson, E. A., and Szewczyk, A. A., 1996, "A Look At A Universal Parameter For 2-D and 3-D Bluff Body Flows," *Journal of Fluids and Structures,* Vol. 10, pp. 543–553.

Balasubramanian, S., and Skop, R. A., 1996, "A Nonlinear Oscillator Model for Vortex Shedding from Cylinders and Cones in Uniform and Shear Flows," *Journal of Fluids and Structures,* Vol. 10, pp. 197–214.

Bearman, P. W., 1984, "Vortex Shedding from Oscillating Bluff Bodies," *Annual Review of Fluid Mechanics,* Vol. 14, pp. 195–222.

Berger, E., and Wille, R., 1972, "Periodic Flow Phenomena," *Annual Review of Fluid Mechanics,* Vol. 4, p. 313.

Braza, M., Chassaing, P., and Ha Minh, H., 1986, "Numerical Study and Analysis of the Pressure and Velocity Fields in the Near Wake of a Cylinder," *Journal of Fluid Mechanics,* Vol. 165, pp. 79–130.

Gaster, M., 1969, "Vortex Shedding from Slender Cones at Low Reynolds Numbers," *Journal of Fluid Mechanics,* Vol. 38, pp. 565–576.

Gaster, M., 1971, "Vortex Shedding from Circular Cylinders at Low Reynolds Numbers," *Journal of Fluid Mechanics,* Vol. 46, pp. 749–756.

Griffin, O. M., 1985, "Vortex Shedding from Bluff Bodies in Shear Flows: A Review," ASME JOURNAL OF FLUIDS ENGINEERING, Vol. 107, pp. 298–306.

Henderson, R. D., and Barkley, D., 1996, "Secondary Instability in the Wake of a Circular Cylinder," *Physics of Fluids,* Vol. 8, pp. 1683–1685.

Jesperson, D., and Levit, C., 1991, "Numerical Simulation of Flow Past Tapered Cylinder," AIAA, 91-0751, 29th Aerospace Sciences Meeting, Jan 7–10, 1991, Reno, NV.

Mair, M. A., and Stansby, P. K., 1975, "Vortex Wakes of Bluff Cylinders in Shear Flow," *SIAM Journal of Applied Mathematics,* Vol. 28, pp. 519–540.

Masch, F. D., and Moore, W. L., 1960, "Drag Forces in Velocity Gradient Flow," *ASCE Journal of Hydraulics Division,* Vol. 86, pp. 1–11.

Maull, D. J., and Young, R. A., 1973, "Vortex Shedding from Bluff Bodies in Shear Flow," *Journal of Fluid Mechanics,* Vol. 60, pp. 293–308.

Newman, D. J., and Karniadakis, G. E., 1997, "A Direct Numerical Simulation of Flow Past a Freely Vibrating Cable," *Journal of Fluid Mechanics,* Vol. 344, pp. 95–136.

Noack, B. R., Ohle, F., and Eckelmann, H., 1990, "On Cell Formation in Vortex Streets," *Journal of Fluid Mechanics,* Vol. 227, pp. 401–409.

Peltzer, R. D., 1982, "Vortex Shedding from a Vibrating Cable with Attached Spherical Bodies in a Linear Shear Flow," Naval Research Laboratory Memorandum Report 4940.

Peltzer, R. D., and Rooney, D. M., 1981, "Vortex Shedding, Base Pressure and Wake Measurements Behind High Aspect Ratio Cylinders in Subcritical Reynolds Number Shear Flow," ASME paper 81-WA/FE-10.

Piccirillo, P. S., and Van Atta, C. W., 1993, "Vortex Shedding Behind Linearly Tapered Cylinders," *Journal of Fluid Mechanics,* Vol. 246, pp. 163–195.

Roshko, A., 1954, "On the Drag and Shedding Frequency of Two Dimensional Bluff Bodies," NACA, Washington DC, Tech. Note 3169.

Shaw, T. L., and Starr, M. R., 1972, "Shear Flow Past a Circular Cylinder," ASCE *Journal of Hydraulics Division,* Vol. 98, pp. 461–473.

Wang, G., 1996, "Large Eddy Simulations of Bluff Body Wakes on Parallel Computers," Ph.D. thesis, University of Illinois at Urbana-Champaign.

Williamson, C. H. K., 1988, "Defining a Universal and Continuous Strouhal-Reynolds Number Relationship for the Laminar Vortex Shedding of a Circular Cylinder," *Physics of Fluids,* Vol. 31, pp. 2742–2744.

Williamson, C. H. K., 1989, "Oblique and Parallel Modes of Vortex Shedding in the Wake of a Circular Cylinder at Low Reynolds Numbers," *Journal of Fluid Mechanics,* Vol. 206, pp. 579–627.

Williamson, C. H. K., 1996, "Vortex Dynamics in the Cylinder Wake," *Annual Review of Fluid Mechanics,* Vol. 28, pp. 477–539.

Woo, H. G. C., Peterka, J. A., and Cermak, J. E., 1981, "Experiments on Vortex Shedding from Stationary and Oscillating Cables in a Linear Shear Flow," Fluid Mechanics and Wind Engineering Program, Colorado State University, Final Report on Contract N68305-78-C-005 for Naval Civil Engineering Laboratory.

Zhang, H., Fey, U., Noack, B. R., Konig, M., and Eckelmann, H., 1995, "On the Transition of the Cylinder Wake," *Physics of Fluids,* Vol. 7, pp. 779–794.

Biologically-Inspired Bodies Under Surface Waves—Part 1: Load Measurements

Promode R. Bandyopadhyay
Fellow ASME
e-mail: bandyopadhyay@c80.npt.nuwc.navy.mil

William H. Nedderman

James L. Dick

Naval Undersea Warfare Center,
Newport, RI 02841

Measurements have been carried out in a tow tank on cylindrical bodies submerged in proximity of traveling surface waves. Two bodies are considered: a reference plain cylinder and another cylinder containing a pair of wings (or hydrofoils) below the cylinder, not above. The latter body owes its origin to certain species of fish which has small wings for maneuverability. The wavelength of the surface waves (λ) is of the order of the cylinder length (L) or higher ($1 < \lambda/L < 10$). Temporal measurements of axial and vertical forces and pitching moments, phase matched to the surface elevation of traveling waves, have been carried out. The time periods of the waves and depth of water pertain to deep water and intermediate depth waves. The forces and moments exhibit characteristic phase relationship with water elevation. Towing affects only vertical forces in the speed range of 0 to 1 m/s. The effect of towing and surface waves on vertical forces is roughly additive. Within the low speed range of towing evaluated, the effects of surface waves dominate those of towing. The presence of the hydrofoil and intermediate depth waves bring in some additional effects which are not well understood. In intermediate depth waves, a small plain cylinder may encounter a resonance with traveling waves which can be averted by attaching a pair of small wings to dampen pitching moment and make it speed invariant, although at a cost of increased vertical forces.

1 Introduction

This work forms a part of the complicated hydrodynamics of small cylinders maneuvering in disturbed shallow waters. In such places, the wavelength of surface waves changes with the depth of water. The cylinder length (L) in the present work is roughly of the order of the wave length (λ) of the traveling waves or less ($1 < \lambda/L < 10$). Thus, a dynamic interaction can be expected—an expectation that has been met. Recent advances in understanding of forces and moments on submerged spheres can be found in Lee and Newman (1991), where (λ/D), D being the sphere diameter, was found to be the relevant variable. In the following, first, the bio-aquatic origin of the present work is traced. A biologically-inspired model is built and then dynamic measurements of phase-matched forces and moments are carried out.

At NUWC, the hydrodynamics and control theory of biologically-inspired control surfaces applied to small underwater bodies are being explored (in Part 2 of this paper, and Bandyopadhyay et al., 1997a; Singh and Bandyopadhyay, 1997). The following is a fundamental result from the control studies. Man made vehicles like aircraft have a moment based control, while biologically based maneuvering of engineering bodies is force based. One consequence perhaps of the latter is the faster underwater response allowing a greater agility. This opens the door to closed-loop control via dynamic control surfaces and subsequently a precision maneuvering. This part of the present paper provides a dynamic data base that has been used in Part 2 and by Singh and Bandyopadhyay (1997) to develop a feedback control theory for biologically-inspired maneuvering of a small body along a predetermined trajectory under traveling waves. This approach of biologically based engineering hydrodynamics has some potential in improving our ability to maneuver small underwater bodies.

The following aspects of the present work are also worth noting: the examination of the relevant biological concepts in the engineering context; the presentation of modern dynamic measurements of forces and moments that are phase matched to the wave elevation; measurements for winged bodies where the wings are underneath the cylinder; and measurements where the body is small, that is, its length is of the order of the wavelength of the traveling waves or smaller (not larger).

1.1 Role of Wings in Maneuvering.

Several species of fast yet agile fish (Fig. 1) have large pectoral fins. They do not have a gas bladder and retract these fins to control lift force. A modeling was carried out to determine the effectiveness of these pectoral fins in low speed maneuvering in an engineering context.

The computational modeling of cruise and turn was carried out on the cylinder shown in Fig. 2. Three simplified configurations are compared: a reference cylinder of diameter $D(=76$ mm) and two others where pairs of wings are attached that are $D \times D$ and $2D \times 2D$ in size. All three cylinders are provided with a pair of $D/3 \times D/2$ tail planes for stability. Note that, as in the fish in Fig. 1, the wings are of the order of the cylinder diameter. An in-house hydrodynamic model was used to compute the results shown in Figs. 3 to 6. The model is based on the law of motion where a large number of force and moment coefficients are included to account for the hydrodynamic effects. These coefficients are based on a large volume of experimental data and the limitation is that maneuvering performance is being computed based on steady state conditions. However, the breakdown of the coefficients is very detailed, and the following effects are accounted for: viscous and pressure drag on cylinders and wings, effects of induced drag, wing-cylinder juncture drag, effects of angles of attack and Reynolds number. The bodies are buoyant by +20%, +10%, 0%, −10% and −20% heavier than the displaced water, and the results for the +20% heavier case is shown here. The uncertainties are difficult to compute accurately, however, it is 10% or less of the differences observed in the three configurations. Put differently, because the uncertainty in the absolute values of the results computed is the same in the three configurations, the large differences between them can be attributed to the effects of the wings.

Contributed by the Fluids Engineering Division for publication in the JOURNAL OF FLUIDS ENGINEERING. Manuscript received by the Fluids Engineering Division December 20, 1997; revised manuscript received February 8, 1999. Associate Technical Editor: M. Triantafyllou.

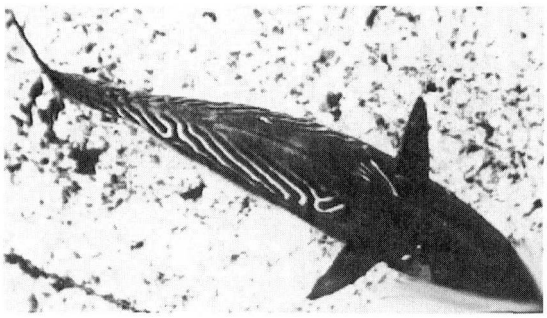

Fig. 1 Photograph of a euthynnid (Magnuson, 1978). The pectoral fins are swept back to change planform area and lift.

Figures 3 and 4 are for cruise condition and Figs. 5 and 6 are for turning. The angle of attack is the angle between the cylinder axis and the freestream direction in the vertical plane. A generic wing section with a section lift coefficient rate of 0.105 (C_l per degree) is used. The effect of wing aspect ratio is included. The body angle of attack is determined by balancing iteratively the vertical forces during cruise at each speed. In the turn rate calculations, the cruise results are used as the starting point. In Fig. 6, the turn radius for the $2D \times 2D$ case has first been assumed (a tight turn has been chosen from experience). In this first known turn case, in addition to the vertical force, a force balance in the horizontal plane, which is considered to be decoupled from the vertical plane, is carried out. The hydrodynamic forces are balanced against the force required to accelerate the vehicle toward the center of the turn. The turn radius for the remaining two cases is then computed. The wing contributes to the turn by means of a bank of the vehicle. A typical bank angle of 15 degree is used in the analysis.

Figure 3 shows that the winged cylinders require a lower angle of attack as to be expected. Figure 4 shows that the drag of the winged bodies is higher, but only slightly. Interestingly, at very low speeds, the winged bodies display a cross-over in their drag characteristic. Figure 5 shows the increase in the side force during turn. Clearly, the wings help produce a considerable amount of side force which assists turning. Finally, Fig. 6 shows the variation of r/L, which is a ratio of the turning radius to the vehicle length, in the three cases. Obviously, the winged bodies can make lower radii turns. These results give an indication that attaching a pair of wings that are of the order of the cylinder diameter, improves the low speed maneuverability. This result will now be used to build a model of an "agile cylinder."

1.2 Interaction of Traveling Waves and Submerged Cylinders. The present interest is in the dynamics of small cylinders approaching shallow waters from deep waters. The flow fields, in both cases of traveling sinusoidal surface waves on deep and finite waters, are given by classical linear theories (Lighthill, 1978, pp. 208–220 and Newman, 1978, p. 240). The present work is concerned with loads and moments on various bodies due to these flow fields. Attention will be paid here to when the water waves are not deep and the cylinder has attachments.

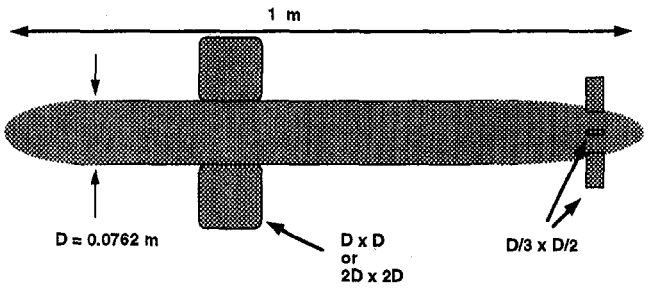

Fig. 2 Dimensions of a reference plain cylinder and two sets of wings used to model the maneuvering ability of winged bodies. The tail wings are always retained for stability. The dimensions are similar to the tow tank model described later.

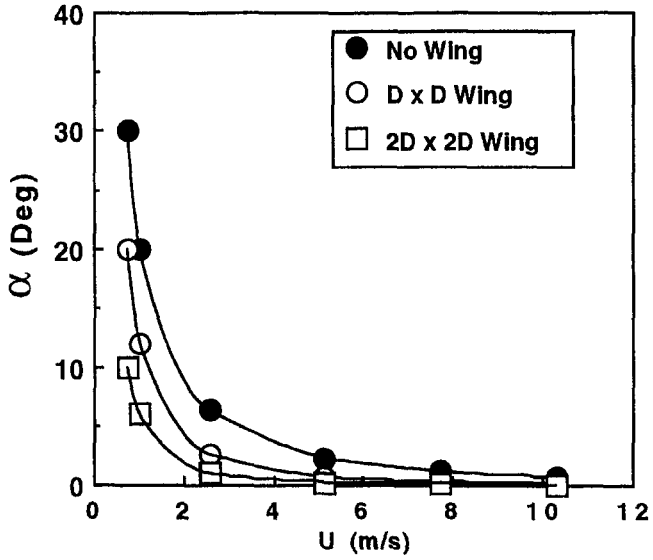

Fig. 3 Reduction of required angles of attack in winged bodies

The present flow problem is shown schematically in Fig. 7. From classical linear theory, it is known that the velocity vectors always oscillate in quadrature. The forces on a body due to these velocity components are shown schematically in Fig. 7. The finite depth of water distorts the velocity field compared to that due to deep water waves. In the experimental result presented below, the forces acting on submerged bodies due to surface water waves are presented in the framework of the classical linear theory. Also examined will be, how the amplitude and phase relationships may change in intermediate depth waves when additional lifting surfaces are present. There may also be differences in the wave interaction behavior of spheroids and cylindrical bodies.

It was shown earlier, that the attachment of a pair of small wings improves the low speed maneuvering capability: turn radius decreases, the vehicle can operate at lower speeds, time response to maneuvering commands improves, vehicle angle of attack drops and even drag could drop below certain speeds. Offsetting such a

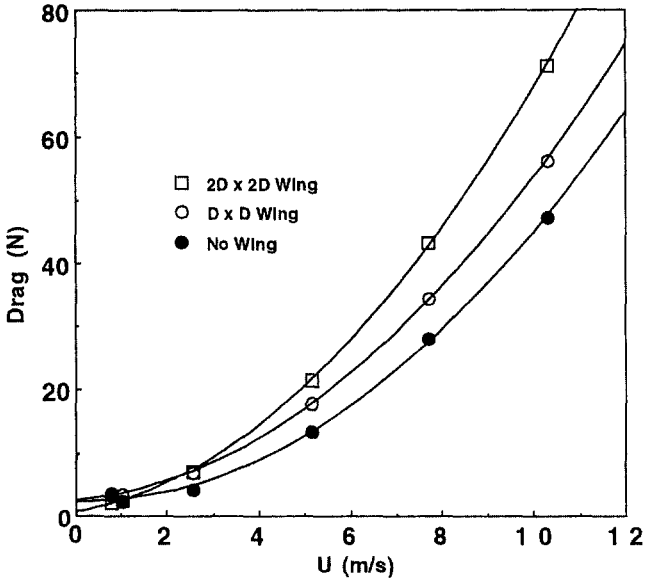

Fig. 4 Drag of winged bodies

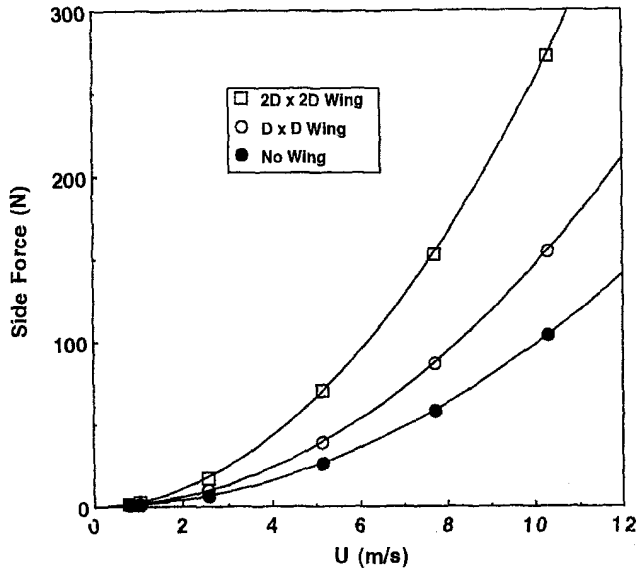

Fig. 5 Side force in winged bodies

wing could allow a very small vehicle to operate both underwater and on-surface (reduced wave drag). Such a model is shown in Fig. 8 (Bandyopadhyay, 1997). The present model is instrumented with a 6-component balance and wall-pressure taps. The forces and moments acting on this model submerged just under traveling (approximately) sinusoidal waves have been compared with those on a plain cylinder. The measurements are presented below.

2 Details of Model and Experiments

Figure 7 shows that the cylinder diameter D was taken as the scale of the vertical spacings in the present experiment. Two models were tested: a reference plain cylinder and another with an offset hydrofoil as depicted in Figs. 8 and 9. Figure 8 shows the complete model. The model also shows a dual flapping foil device at the tail cone. However, the results reported here are for the hydrofoil-cylinder assembly only that did not have the flapping foil device. Figure 9 shows a closeup of the offset hydrofoil-cylinder combination. The hydrofoil cross-section was a NACA0012 profile. The symmetric hydrofoil was mounted at an angle of +3 degrees to the cylinder. The cylinder-hydrofoil combination was made of resin and built as a single piece by a Stereo Lithography Apparatus. The hydrofoil and the cylinder contained surface pressure taps for measuring the distributions of pressure on the appendages. The cylinder diameter was 7.62 cm and consisted of an elliptic nose with an 8 cm long semi-axis, a constant diameter length of 65.3 cm and a conical tail of 15.7 cm length. The net model length was 89 cm. The half span of the hydrofoil was 11.43 cm and the chord varied from a maximum of 5 cm along the center line to a minimum of 1.1 cm at the tip. The hydrofoil was offset in the middle using a pylon of chord 5 cm. The leading edge of the pylon was located 34.2 cm from the nose. The pylon cross-section had a NACA0015 profile. A 2 mm long 1 mm deep rubber band was positioned at the junction of the elliptic nose and the cylinder to trip the boundary layer. The model is mostly hollow and is flooded with water. It is sting mounted from the carriage. The force balance, which is described below, is mounted at the strut location in the recess shown in Fig. 9. The forces are expressed in a Cartesian coordinate system (Fig. 7): F_x represents horizontal forces, F_z represents vertical forces and T_y represents pitching moment. The signs of the forces and moments can be clarified as follows: $-F_x$ indicates a backward movement of the model, $-F_z$ indicates a downward movement of the model and $-T_y$ indicates that the nose is experiencing a downward moment.

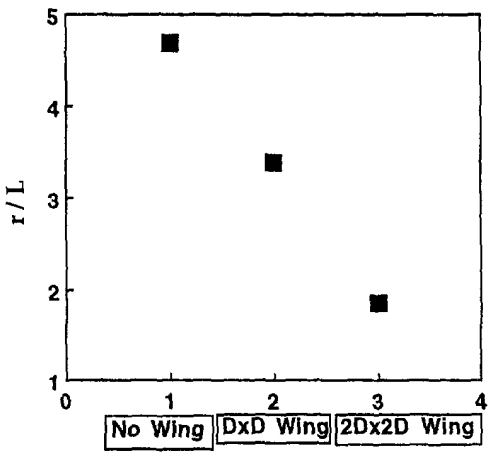

Fig. 6 Compared to their body lengths, winged cylinders make a shorter radii turn

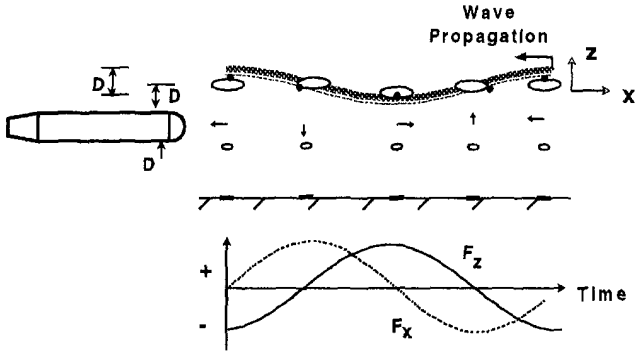

Fig. 7 Schematic of a surface wave propagating right to left over a submerged body. The velocity field and elliptic particle motion due to finite depth of water and the time signature of horizontal (F_x) and vertical (F_z) forces acting on the body are shown.

A six component force/torque sensor system (Model Mini FT3487, Assurance Technologies, Inc.) was used to measure the dynamic horizontal and vertical forces and pitching moments. The sensing range was ±80 N in the horizontal direction (F_x), ±240 N in the z-direction (F_z) and the torque T_y range was ±4 N-m. The resolution was 0.08 N in F_x, 0.24 N in F_z and 2.0 N-mm in T_y. The transducer is a monolithic structure which decreases hysteresis and increases strength and repeatability. A controller was used to convert the semiconductor strain gage data from the transducer to Cartesian force/torque components.

The measurements were carried out in the wave/towing tank at the Ocean Engineering Department of the University of Rhode Island at the Narragansett Bay Campus. The tank is equipped with a towing carriage and wave maker/wave absorber devices. A more detailed description of the wave quality and the wave absorption devices can be found in Mahoney (1996). The tank is 30 m long, 3.60 m wide and 1.80 m deep, with water depth upto about 1.5 m. Video photography of the model under traveling waves was carried out through a 2 m long and 1 m high side observation window located at the mid length of the tank. The maximum tow speed is 1.5 m/s. A hydraulically activated and computer controlled flap type hinged wavemaker paddle is located at one extremity of the tank. Regular waves with period $T = 0.5$ to 3 s and height $b = 0$ to 30 cm can be generated as well as irregular waves with random parameters within the same characteristics. A Macintosh II/Ci computer drives the wavemaker hydraulic piston. An arbitrary time series of piston strokes can be specified to produce required incident waves. The wave absorber, located at the tank extremity opposite to the wave maker, is made of three vertical plates with decreasing porosity whose spacing can be varied as a function of wave characteristics. The spacing was 64 cm between the first two

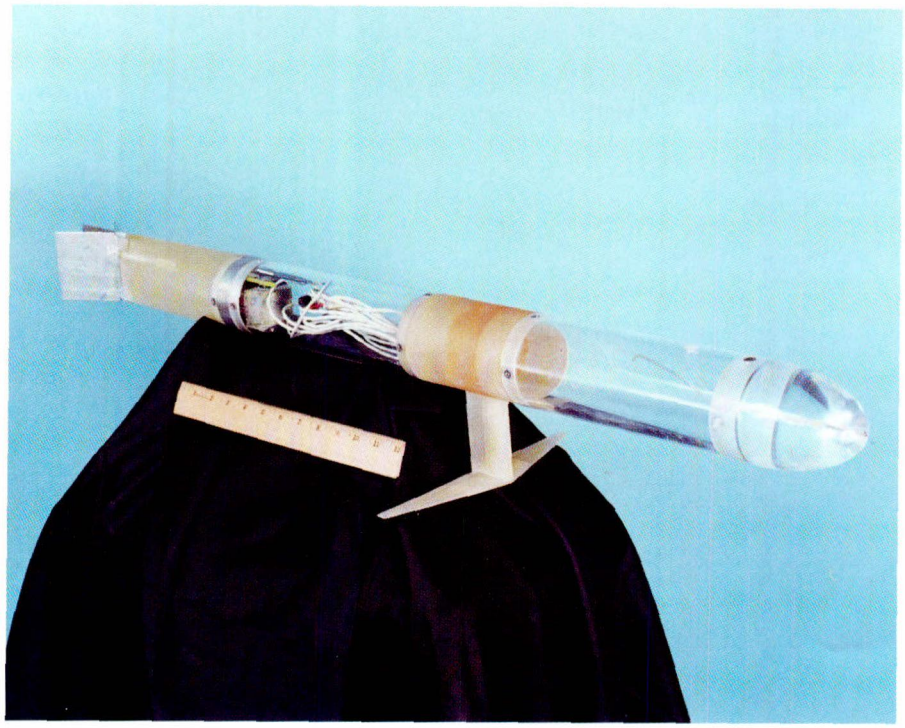

Fig. 8 Photograph of the cylinder-hydrofoil assembly

porous plates facing the waves, 80 cm between the next two plates and 80 cm between the third plate and back wall of the tank. The plate spacing were thus of the order of the length of the water waves. Absorption of wave energy of more than 95% can be achieved for $T = 0.5 - 2$ s, in optimal cases. The carriage can be rolled to any location and can be used for observation or for installing equipment above the water, and an overhead fixed bridge is located at mid length of the tank. Capacitance type wave gages are used for measurement of wave height with time. Determined visually, the results reported here pertain to non-breaking waves. Breaking of waves is a mechanism for dissipating some of the energy of wave resistance. We are thus operating in a flow regime where drag on the towed bodies is lower by a factor that is perhaps as large as three compared to that when waves are breaking due to towing (Duncan 1983). Furthermore, as we will see later, forces due to towing are less than those due to waves. The wave gage was positioned 1 m away from the force balance in the spanwise direction where the normal water elevation of the traveling waves did not appear to be disturbed by the presence of the models.

The water waves were two-dimensional and they traveled along the axis of the model (Fig. 7). The time period of waves T varied between 0.8–2.3 s (Fig. 10). The towing speed of the model varied between 0–1.23 m/s. The wave height was mostly ±4 cm, and in certain runs it was ±3 cm or ±5 cm (The results do not appear to strongly depend on wave height in this range probably because variation, if any, is within the uncertainty of wave heights). The top surface of the cylinder was 7.8 cm ($=D$) below the flat surface of the water and 1.155 m above the tank floor. It was observed that the model always remained under water in the present experiments. Analog signals representing water elevation, F_x, F_z and T_y were digitized at 100 Hz and stored for later analysis. The signals were low pass filtered at 20 Hz. Three coefficients are defined as follows:

$$C_{fx} = \frac{F_x}{\rho g b A_f} \tag{1}$$

$$C_{fz} = \frac{F_z}{\rho g b A_p} \tag{2}$$

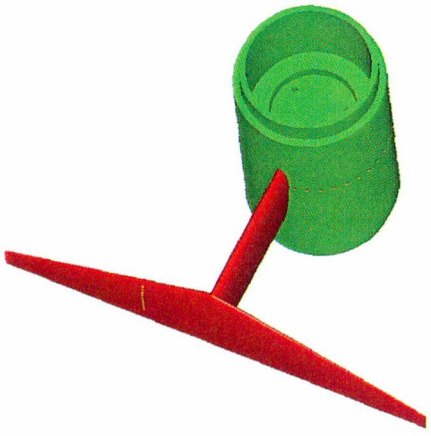

Fig. 9 Perspective view of the offset hydrofoil-cylinder part of the model shown in Fig. 8

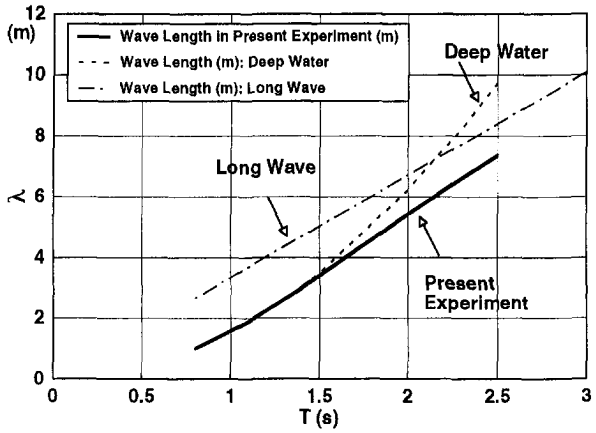

Fig. 10 Present experiment in the perspective of deep water and long waves. Depth of water = 1.155 m.

$$C_{Ty} = \frac{T_y}{\rho g b A_p \Delta} \tag{3}$$

where, C_{fx} is coefficient of horizontal force, C_{fz} is coefficient of vertical force, C_{Ty} is coefficient of pitching moment, ρ is fluid density, g is acceleration due to gravity, b is peak-to-trough wave height, A_p is planform area, A_f is frontal area and Δ is the offset of the hydrofoil leading edge from the model axis (=11.43 cm for the hydrofoil-cylinder model and $D/2$ for the plain cylinder). In case of the hydrofoil-cylinder model, it is unclear whether A_p should be calculated by treating the cylinder and the hydrofoil separately. Here A_p is taken equal to the net projected planform, that is, the overlapping area is not considered twice.

3 Results and Discussion

The flow regime of the present experiment can be set in the perspective of deep water (depth of water $h > \lambda$) and long waves (wavelength λ is a large multiple of depth h). For sinusoidal waves on water of uniform depth, the wave length is given by (Lighthill, 1978):

$$\lambda = \frac{gT^2}{2\pi} \tanh\left(\frac{2\pi h}{\lambda}\right) \tag{4}$$

For deep water, this reduces to:

$$\lambda = \frac{gT^2}{2\pi} \tag{5}$$

For long wave:

$$\lambda = T\sqrt{gh} \tag{6}$$

In the present experiment, h = 1.155 m. The variation of wave length of the water waves in the present experiment for constant h was calculated using Eqns. (4–6) and the results are shown in Fig. 10. The experiment covers a transitional range where departure from one of the limiting relationships (Eq. (5)) attributable to h can be studied. Note the departure of the deep water relation from the present experiment at $T \sim 1.5$ s. The results presented later are explained with reference to this time period.

The results of wave loading on the plain cylinder and the hydrofoil-cylinder models are presented separately for static and towed models. In the figures below, e is water elevation in the middle of the model where the load cell is located, with respect to a calm surface. Note that e is measured at a spanwise location off the model.

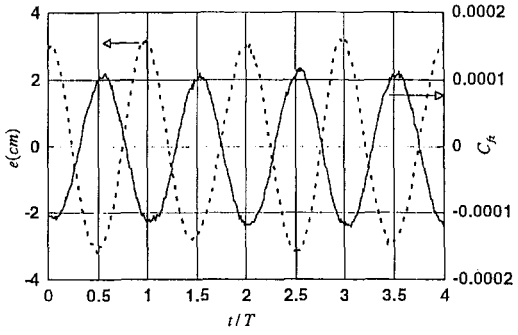

Fig. 11(*a*)

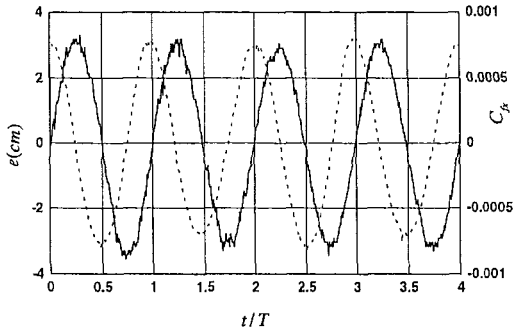

Fig. 11(*b*)

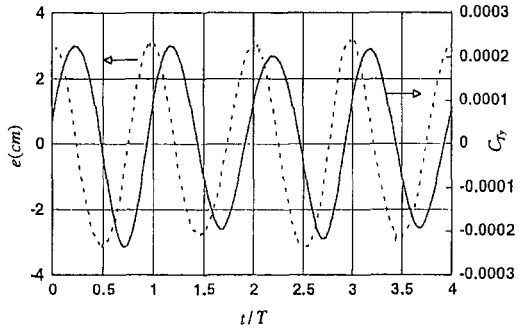

Fig. 11(*c*)

Fig. 11 Phase relationships with water elevation (broken line) of: (*a*) coefficient of vertical force, (*b*) coefficient of horizontal force, and (*c*) coefficient of pitching moment (solid lines). Static hydrofoil-cylinder model under deep water waves of period 1.08 s (λ/L = 2.1, λ/D = 25).

3.1 Static Hydrofoil-Cylinder Model. The periodic variation of the vertical and horizontal forces and pitching moment experienced by the hydrofoil-cylinder model is shown in Fig. 11. These results are for a time period of 1.08 s (λ/L = 2.1, λ/D = 25). With respect to water elevation, the vertical force lags by 180 degrees, the horizontal (axial) force lags by 90 degrees and pitching moment lags by 70–75 degrees. The horizontal and vertical forces are thus in quadrature as indeed the respective velocity components are as per classical linear theory of deep water waves. However, factoring in the areas A_f and A_p in Eqs. (1) and (2), the peak value of the vertical force produced by the hydrofoil-cylinder model turns out to be twice that of the horizontal forces. On the other hand, in the plain cylinder results presented below, the two peak amplitudes are equal as expected in the classical theory. An estimation suggests that the presence of an hydrofoil at an angle of attack has led to an increase in the positive and negative vertical forces in the hydrofoil-cylinder model.

3.2 Static Plain Cylinder Model. The periodic variation of the vertical and axial forces and pitching moment experienced by the plain cylinder model is shown in Fig. 12. These results are for a time period of 0.98 s (λ/L = 1.7, λ/D = 20), that is for deep water waves. With respect to the water elevation, the vertical force lags by 180 degrees and the horizontal force lags by about 90 deg. The forces are in quadrature. The pitching moment is not monochromatic, so a phase lag can not be determined. Factoring in the areas A_f and A_p in Eqs. (6) and (7), the peak amplitudes of the horizontal and vertical forces, however are equal as the respective velocity amplitudes are predicted to be in the classical linear theory of deep water waves. Unlike that in the hydrofoil-cylinder case, the pitching moment is not sinusoidal; it is asymmetric and reaches larger nose-down than nose-up values.

3.3 Effect of Towing on Hydrofoil-Cylinder Model. We now examine the combined effects of a moving body and traveling waves. The results for the hydrofoil-cylinder model are shown in Fig. 13. The recording covers segments of both towing and a static model. Towing increases the peak to trough levels of the vertical force by 20%, but it has little effect on the horizontal forces.

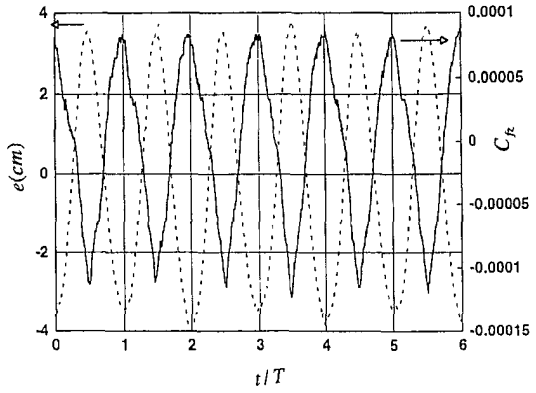

Fig. 12(*a*)

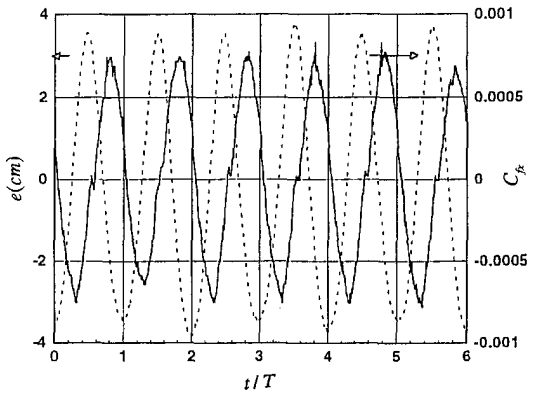

Fig. 12(*b*)

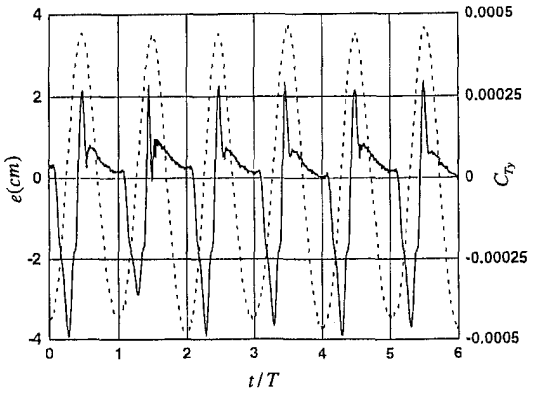

Fig. 12(*c*)

Fig. 12 Phase relationships with water elevation (broken line) of: (*a*) coefficient of vertical force, (*b*) coefficient of horizontal force, and (*c*) coefficient of pitching moment for a static cylinder (solid lines) under deep water waves of period 0.98 s (λ/L = 1.7, λ/D = 20).

Towing increases the peak to trough levels of pitching moment by only 5%. The effect of towing is therefore primarily on vertical forces.

3.4 Effect of Time Period of Waves on Hydrofoil-Cylinder. We now examine the effects of time period of waves. As shown in Fig. 10, this would allow us to understand the differences between the effects of deep water and intermediate depth waves. The two wave regimes in the hydrofoil-cylinder model case are compared in Figs. 11, 14, and 15. Increasing the time period from 1.08 to 1.4 s, or to 2.13 s (λ/L = 2.1 to 3.4 to 6.6; λ/D = 25 to 40 to 77), has no effect on the phase relationship with water waves of vertical and horizontal forces. When time period jumps from 1.4 s to 2.13 s (λ/L = 3.4 to 6.6; λ/D = 40 to 77), the phase lag of the pitching moment drops roughly to 50 degrees. This reduction in phase lag in pitching moment, apparently when time period 'jumps' roughly above 2 s (λ/L = 6.1, λ/D = 71), is observed in the plain cylinder case as well, but much more vividly (see Fig. 10 for the significance of T).

3.5 Effect of Time Period of Waves on the Static Plain Cylinder. The effects of time period of waves on the plain cylinder model are shown in Fig. 16. Only the effect on pitching moment is shown. When time period of waves jumps from 1.3 s

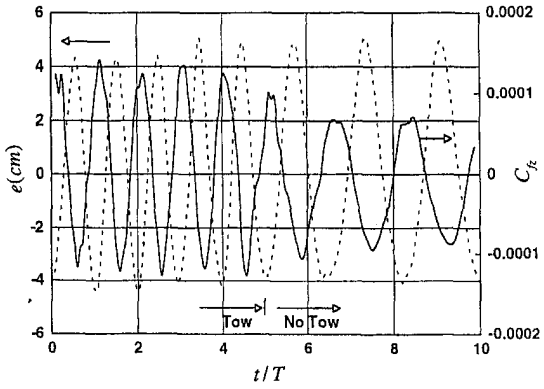

Fig. 13(*a*)

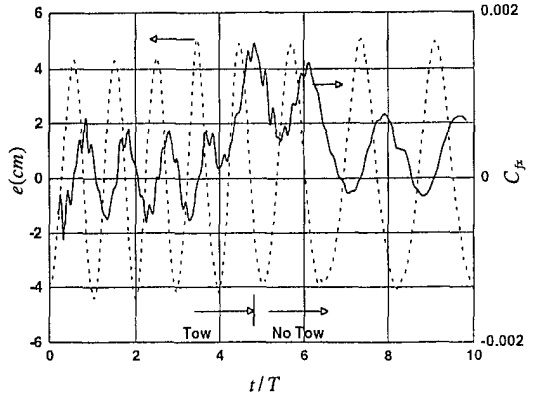

Fig. 13(*b*)

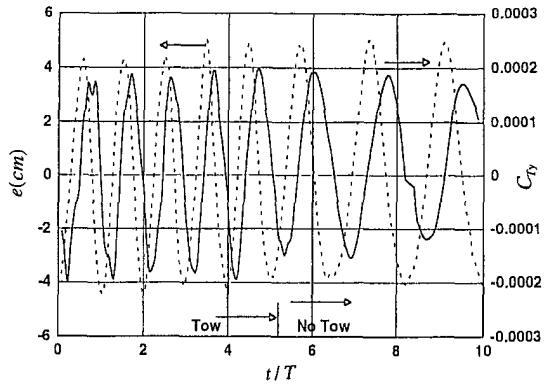

Fig. 13(*c*)

Fig. 13 Phase relationships with water elevation (broken line) of (*a*) coefficient of vertical force, (*b*) coefficient of horizontal force and, (*c*) coefficient of pitching moment for a hydrofoil-cylinder model (solid lines) towed at 1 m/s under deep water waves of period 1.08 s (λ/L = 2.1, λ/D = 25).

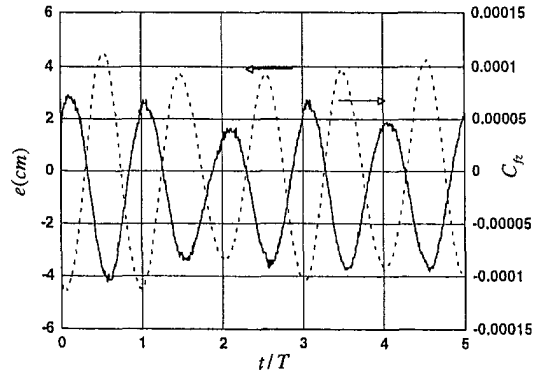

Fig. 14(*a*)

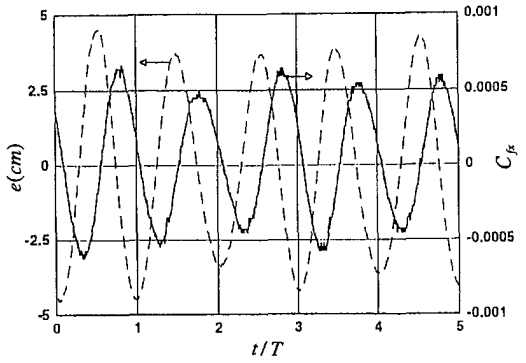

Fig. 14(*b*)

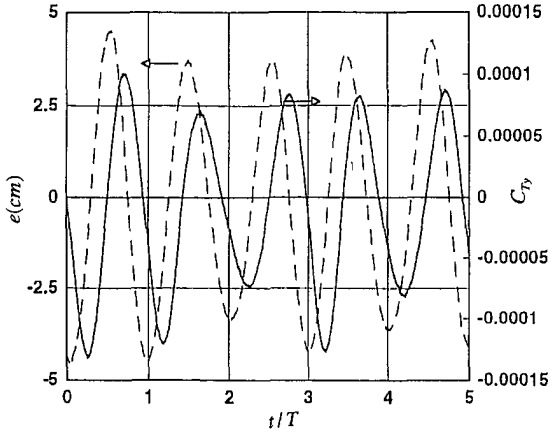

Fig. 14(*c*)

Fig. 14 Phase relationships with water elevation of (*a*) coefficient of vertical forces, (*b*) coefficient of horizontal forces, and (*c*) coefficient of pitching moment for a static hydrofoil-cylinder model under intermediate depth surface waves of period 1.4 s (λ/L = 3.4, λ/D = 40). Broken line: water elevation; solid line: forces (*a* and *b*) or moment (*c*).

to 1.7 s (λ/L = 2.9 to 5, λ/D = 34 to 58), pitching moment responds *in phase* with water elevation. Pitching moment then becomes sinusoidal. As time period increases from 1.7 s to 2.2 s (λ/L = 5 to 7, λ/D = 58 to 82), the peak to trough levels of pitching moment drops by half. Thus, in intermediate depth waves (Fig. 16(*d*) and (*e*)), in the plain cylinder case, we see a stronger effect on the behavior of pitching moment than that in the hydrofoil cylinder case (Fig. 15(*c*)). The phase match of pitching moment in intermediate depth waves opens the possibility for a resonance and instability of a small vehicle that is like a plain cylinder. Interestingly, the hydrofoil has a beneficial effect on motion because it prevents such a phase matching.

3.6 Resolved Effects of Waves and Towing. We now attempt to breakdown the effects of the traveling waves and towing the model. The dependence of the peak values of the forces and moments on tow speed is shown in Fig. 17 for the hydrofoil-cylinder model and in Fig. 18 for the plain cylinder model. Figure 17 shows that, in the hydrofoil-cylinder model, the pitching moment and horizontal forces are practically independent of speed in the range of the present experiments.

The dependence of the peak vertical force on speed is shown in Figs. 17(*b*) and 18, for the hydrofoil-cylinder and the plain cylinder, respectively. The uncertainty in the coefficient of vertical force is about ±0.00001. Three breakdowns are shown

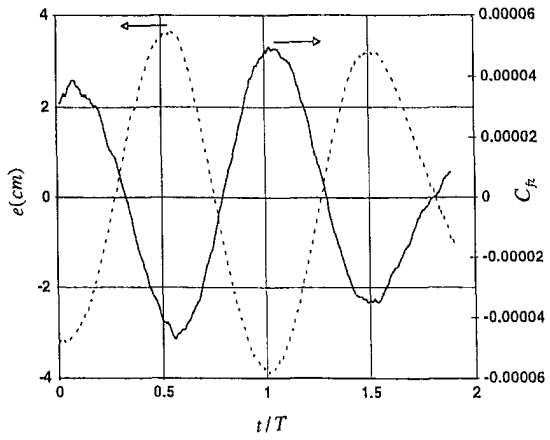

Fig. 15(*a*)

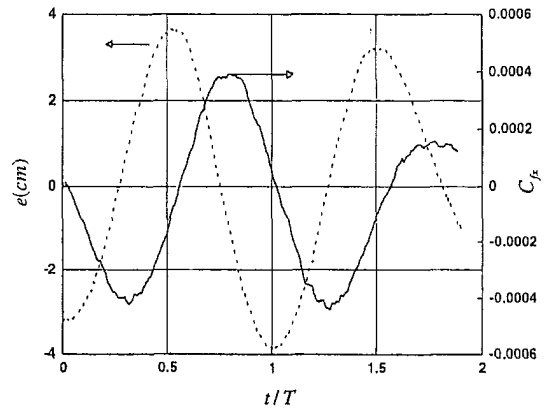

Fig. 15(*b*)

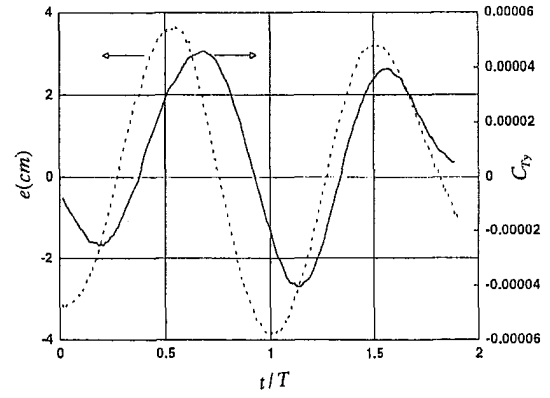

Fig. 15(*c*)

Fig. 15 Phase relationships with water elevation (broken line) of: (*a*) coefficient of lift, (*b*) coefficient of horizontal force, and (*c*) coefficient of pitching moment for a static hydrofoil model (solid line) under intermediate depth surface waves of period 2.13 s (λ/L = 6.6, λ/D = 77).

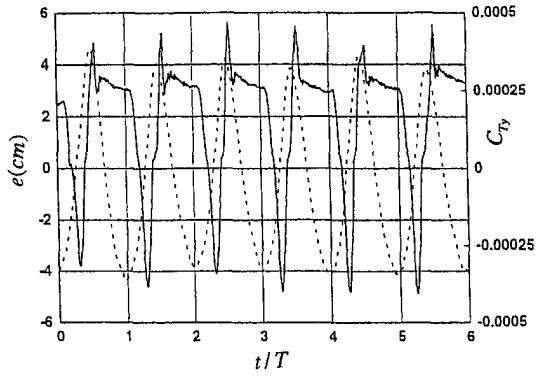

Fig. 16(*a*)

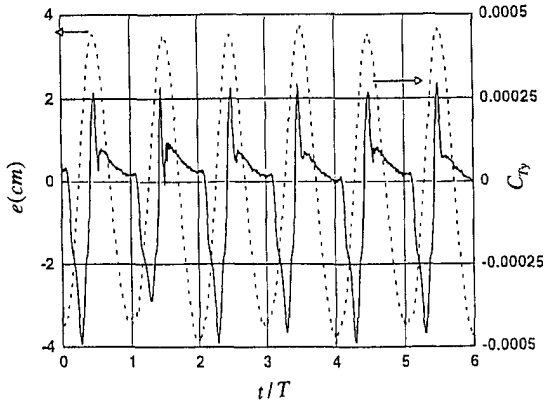

Fig. 16(*b*)

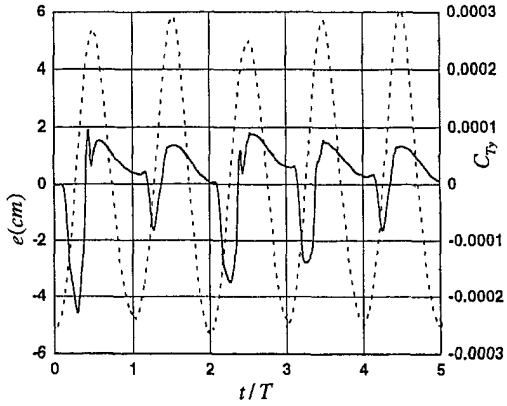

Fig. 16(*c*)

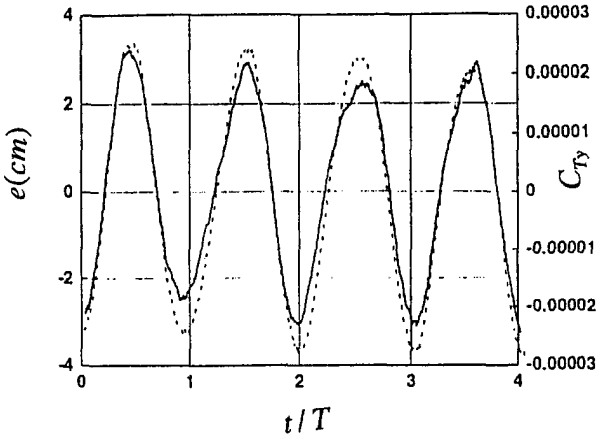

Fig. 16(*d*)

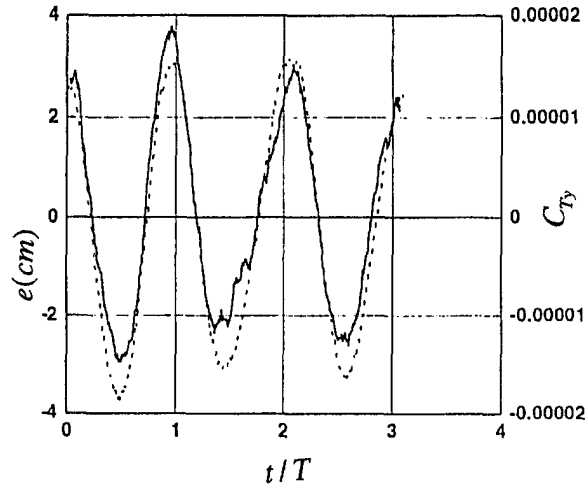

Fig. 16(*e*)

Fig. 16 Phase relationship between the coefficient of pitching moment (solid line) and water elevation (broken line) for a static plain cylinder. Time period of waves, λ/L and λ/D, respectively are: (*a*) 0.8 s, 1.1, 13; (*b*) 0.97 s, 1.7, 20; (*c*) 1.3 s, 2.9, 34; (*d*) 1.77 s, 5, 58; and (*e*) 2.2 s, 7, 82.

in the figures. The combined effects of towing and traveling waves vary in the same manner, namely roughly as $\propto\sqrt{U}$, in both models. The effect of waves on the static models is roughly of the same order in both models. (Note that, the value of A_p is lower in the plain cylinder case. Also note that the filled circle data are from runs after towing was stopped from speeds indicated.) The component of vertical force due to towing alone was obtained by differencing that due to towing under waves and the values for waves on the static models. It is interesting that lift forces due to wave actions alone (no towing) is nonzero, particularly in the plain cylinder case. The mechanism for producing lift forces both during towing alone or wave actions alone, is irrotational. At very low speeds, the lift forces due to towing alone are higher in the hydrofoil-cylinder case. The least square fit power law exponent varies between 1.68 and 2.67 in the hydrofoil-cylinder and the plain cylinder models, respectively. (The correlation of fit, which is the worst in the former, is 0.91.) These are roughly in the range of an exponent of 2.0 that follows from irrotational lifting line theory—via conformal transformation, or on dimensional ground (p. 443, Batchelor, 1967). In both the hydrofoil-cylinder and the plain cylinder models, because we are, more or less, recovering the exponent of 2.0, it can be concluded that vertical forces due to towing and waves are generally additive.

3.7 Discussion In a static cylinder, (Fig. 16), for $\lambda/L \approx 1$, C_{Ty} shows a positive spike—a nose-up pitching moment. Note that the wave elevation is being measured at the middle of the model where the load cell is located. The positive spike in moment occurs when the front half of the model is under a low elevation of water while the back half is below a higher elevation of water. The resulting distribution of F_z over the cylinder produces a torque. The moment is spikey during the negative excursion also, although not in a symmetric manner. The moment signature is asymmetric when the relationship $\lambda/L \gg 1$ is not followed. At high values of λ/L, the distribution of F_z follows the phase of e. Thus, in a static plain cylinder, the variation of C_{Ty} with T can be explained by whether $\lambda/L \approx 1$, or $\lambda/L \gg 1$. On the other hand, the hydrofoil adds to pitch and heave damping, whereby the spikes in moment are absent and the distribution is sinusoidal. This damping also explains why the maximum and minimum values of C_{Ty} are independent of

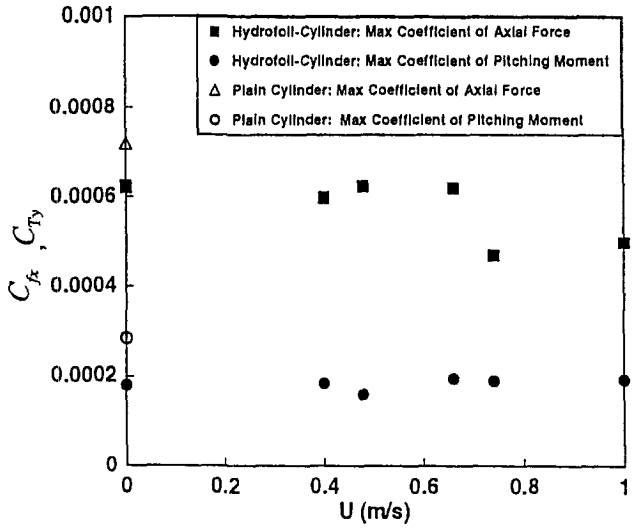

Fig. 17(*a*) Variation of the absolute values of the maximum or minimum values of the coefficients of axial forces and pitching moments with towing speed

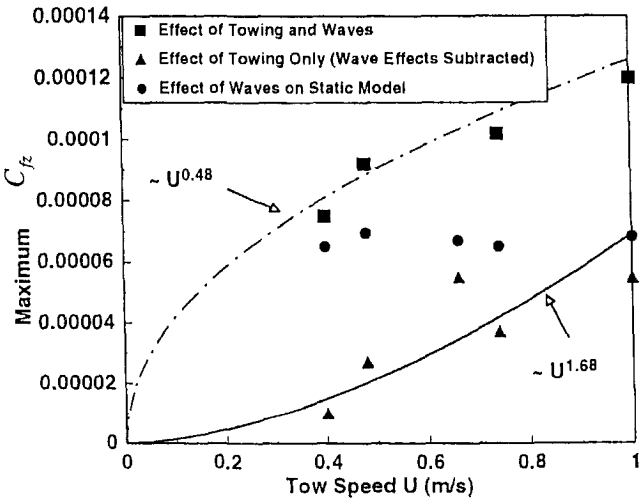

Fig. 17(*b*) Breakdown of vertical forces on the cylinder due to traveling waves and towing. Time period of waves: 1.08 s (λ/L = 2.1, λ/D = 25).

speed while F_z is not (Fig. 17(*a*) and (*b*)). Unlike that in a sphere, instead of λ/D, the relevant parameter in the present work is λ/L.

The vertical force is increased when the hydrofoil is attached. The effect of towing is also primarily on F_z. They are so because the hydrofoil is attached at an angle of attack of +3 deg.

4 Conclusions

Certain species of large fish are known to use their pectoral fins for lift control. Inspired by this, a coefficient based modeling has been carried out on small winged cylinders turning at low speeds. The wing dimensions are of the order of the cylinder diameter. It is demonstrated that winged cylinders can conduct a lower radius turn compared to a plain cylinder. This result is used to build a tow tank model of a winged cylinder and dynamic measurements have been conducted on it.

We have carried out measurements to determine the forces and moments imposed by traveling surface waves on submerged bodies in the range $1 < \lambda/L < 10$. The bodies considered are a hydrofoil-cylinder model and a plain cylinder. The effects of both deep water and intermediate depth waves are examined. The

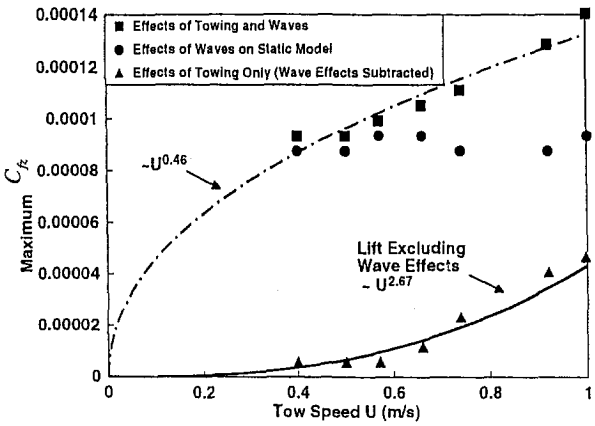

Fig. 18 Breakdown of vertical forces on the plain cylinder due to traveling waves and towing. Time period of waves: 1.08 s (λ/L = 2.1, λ/D = 25).

contributions due to waves and towing are compared. The results are presented in the framework of classical linear theory of deep water waves.

The quadrature phase relationship between vertical and horizontal forces, as the corresponding velocity components follow from the classical linear theory of deep water waves, is followed by both the plain cylinder and the hydrofoil-cylinder cases. In deep water waves, the amplitudes are equal in the plain cylinder case as predicted by the theory, but not in the hydrofoil case. In the latter, the vertical forces are about twice that of the horizontal forces.

The change from deep water to intermediate depth waves has no effect on the phase relationship of the components of forces in the hydrofoil-cylinder model. In the range $1 < \lambda/L < 10$, the difference in the pitching moment behaviors between hydrofoil and plain cylinders in deep and intermediate depth waves, has been documented. The possibility opens up that, as a plain-cylinder vehicle approaches the shore from the regions of deep water, the vehicle pitching could strike a resonance with the waves, which could then trigger undesirable instabilities. However, if the cylinder is fitted with a pair of wings (hydrofoils), this potential for resonance is averted.

When wave effects are excluded, towing produces lift forces on both the plain cylinder and the winged-cylinder. The effects of waves and towing on vertical forces are roughly additive in both the hydrofoil and plain cylinder cases indicating the presence of decoupled mechanisms. Within the tow speed range tested, 0–1 m/s, the peak vertical force due to towing alone varies as U^2 and that due to both towing and waves varies as $\sqrt{U}$.

Acknowledgments

This research was funded by the Office of Naval Research and NUWC Independent Research Program. Dr. T. McMullen and Mr. James Fein are thanked for encouragement.

References

Bandyopadhyay, P. R., 1997, Agile Water Vehicle, US Patent 5,673,645.

Bandyopadhyay, P. R., Castano, J. M., Rice, J. Q., Philips, R. B., Nedderman, W. H., and Macy, W. K., 1997a, "Low-Speed Maneuvering Hydrodynamics of Fish and Small Underwater Vehicles," ASME JOURNAL OF FLUIDS ENGINEERING, Vol. 119, No. 2, pp. 136–144.

Bandyopadhyay, P. R., and Donnelly, M. J., 1997b, "The Swimming Hydrodynamics of Pair of Flapping Foils Attached to a Rigid Body," *Proc. NATO AGARD Workshop on High Speed Body Motion in Water,* Kiev, Ukraine, Sept. 1–3, AGARD Report 827 (Feb. 1998) pp. 1.1–1.17.

Bandyopadhyay, P. R., Singh, S. N., and Chockalingam, F., 1998, "Biologically-Inspired Bodies Under Surface Waves. Part 2: Theoretical Control of Maneuvering," ASME JOURNAL OF FLUIDS ENGINEERING, Vol. 121, published in this issue pp. 479–487.

Batchelor, G. K., 1967, *An Introduction to Fluid Dynamics,* Cambridge Univ. Press, New York, NY.

Dean, R. G., and Dalrymple, R. A., 1984, "Water Wave Mechanics for Engineers and Scientists," *Advanced Series on Ocean Engineering,* Vol. 2, Prentice-Hall, Englewood Cliffs, NJ.

Duncan, J. H., 1983, "The Breaking and Non-Breaking Wave Resistance of a Two-Dimensional Hydrofoil," *Journal of Fluid Mechanics,* Vol. 126, pp. 507–520.

Lee, C. H., and Newman, J. N., 1991, "First- and Second Order Wave Effects on a Submerged Spheroid," *Journal of Ship Research,* Vol. 35, No. 3, pp. 183–190.

Lighthill, J., 1978, *Waves in Fluids,* Cambridge Univ. Press.

Mahoney, M., 1996, "Design of an Efficient Upright Porous Wave Absorber for a Large Scale Laboratory Wave Facility," M.S. thesis, Dept. of Ocean Engrg., URI.

Magnuson, J. J., 1978, *Fish Physiology,* Hoar, W. S., and Randall, D. J., eds., Academic Press, New York, p. 258.

Newman, J. N., 1978, *Marine Hydrodynamics,* MIT Press.

Singh, S. N., and Bandyopadhyay, P. R., 1997, "A Theoretical Control Study of the Biologically-Inspired Maneuvering of a Small Vehicle Under a Free Surface Wave," NUWC-NPT Tech. Rept. 10,816, Naval Undersea Warfare Center, Newport, RI.

Biologically-Inspired Bodies Under Surface Waves—Part 2: Theoretical Control of Maneuvering

Promode R. Bandyopadhyay
Naval Undersea Warfare Center,
Newport, RI 02841
Fellow ASME

Sahjendra N. Singh
Professor. ECE Department.

Francis Chockalingam
Graduate Student. ECE Department.

University of Nevada,
Las Vegas, NV

The theoretical control of low-speed maneuvering of small underwater vehicles in the dive plane using dorsal and caudal fin-based control surfaces is considered. The two dorsal fins are long and are actually mounted in the horizontal plane. The caudal fin is also horizontal and is akin to the fluke of a whale. Dorsal-like fins mounted on a flow aligned vehicle produce a normal force when they are cambered. Using such a device, depth control can be accomplished. A flapping foil device mounted at the end of the tailcone of the vehicle produces vehicle motion that is somewhat similar to the motion produced by the caudal fins of fish. The moment produced by the flapping foils is used here for pitch angle control. A continuous adaptive sliding mode control law is derived for depth control via the dorsal fins in the presence of surface waves. The flapping foils have periodic motion and they can produce only periodic forces. A discrete adaptive predictive control law is designed for varying the maximum tip excursion of the foils in each cycle for the pitch angle control and for the attenuation of disturbance caused by waves. Strouhal number of the foils is the key control variable. The derivation of control laws requires only imprecise knowledge of the hydrodynamic parameters and large uncertainty in system parameters is allowed. In the closed-loop system, depth trajectory tracking and pitch angle control are accomplished using caudal and dorsal fin-based control surfaces in the presence of system parameter uncertainty and surface waves. A control law for the trajectory control of depth and regulation of the pitch angle is also presented, which uses only the dorsal fins and simulation results are presented to show the controller performance.

Introduction

Biologically inspired maneuvering of man-made under water vehicles has the potential of being agile and quiet. The dorsal and caudal fins give a fish a remarkable ability for swift and complex maneuvers (Wu et al., 1975 and Azuma, 1992). Here, we examine their potential for maneuvering small agile vehicles at low speeds. Studies have been carried out on fish morphology, locomotion, and the application of biologically-inspired control surfaces to rigid cylindrical bodies (Bandyopadhyay, 1996; Bandyopadhyay and Donnelly, 1997; Bandyopadhyay et al., 1997 and Part 1 of this paper). Related research to produce propulsive and lifting forces using flapping foil devices has been conducted by several authors (Chopra, 1977; Bainbridge, 1963; Gopalkrishnan et al., 1994; Triantafyllou et al., 1993; Hall and Hall, 1996; Triantafyllou et al., 1991). However, as yet, control systems synthesis using caudal and dorsal fins has not been accomplished.

The contribution of the present research lies in the design of control systems for low-speed maneuvering of small undersea vehicles using dorsal- and caudal-like fins (Fig. 1). A hydrodynamic control scheme is developed so that the vehicle tracks a precise depth versus time trajectory. It is assumed that the hydrodynamic parameters of the vehicle are imprecisely known and surface wave-induced forces are constantly acting on the vehicle. Although the design approach can be extended to yaw control, in this study, only control in the dive plane is considered. Using the dorsal fin, a normal force is produced for depth control and flapping foils produce pitching moment for pitch angle regulation. For simplicity, it is assumed that the vehicle is equipped with a control mechanism that causes the vehicle to move forward with a uniform velocity. For the depth trajectory control, an adaptive sliding mode control law (Slotine and Li, 1991; Utkin, 1978; and Narendra and Annaswamy, 1989) is designed for the continuous cambering of the dorsal fins in the presence of seawaves. The sliding mode control law is nonlinear and discontinuous in the state space and has an excellent insensitivity property with respect to disturbances and parameter variations.

The hydrodynamics of flapping foils is rather complex. Although design based on the continuous control of the angular velocity of the caudal fins is more efficient, forces and moments produced by the caudal-like fins as functions of angular position and velocity are not well-understood. This study is limited to a periodic (sinusoidal) actuation of caudal fins. It is assumed that the foils have identical periods of oscillation that do not necessarily coincide with the period of the seawave. The amplitude and phase of force and moment acting on the vehicle caused by the disturbing wave are assumed to be unknown. Assuming that the vehicle pitch angle deviation is small, a linear discrete adaptive predictive control system (Goodwin and Sin 1984) is designed for the pitch angle control. The maximum travel of the tips of the foils is adjusted periodically at the completion of the cycle. Interestingly, for the design of the pitch controller, it is seen that Strouhal numbers, which characterize the moment produced by the foils (caudal fins), are key control variables. In the closed-loop system using the dorsal and caudal fin controllers, depth control and pitch angle regulation in the dive plane are accomplished. Furthermore, a control system is designed for the control of depth and regulation of pitch angle using only dorsal fins and simulation results are presented.

Contributed by the Fluids Engineering Division for publication in the JOURNAL OF FLUIDS ENGINEERING. Manuscript received by the Fluids Engineering Division November 3, 1997; revised manuscript received December 4, 1998. Associate Technical Editor: M. Triantafyllou.

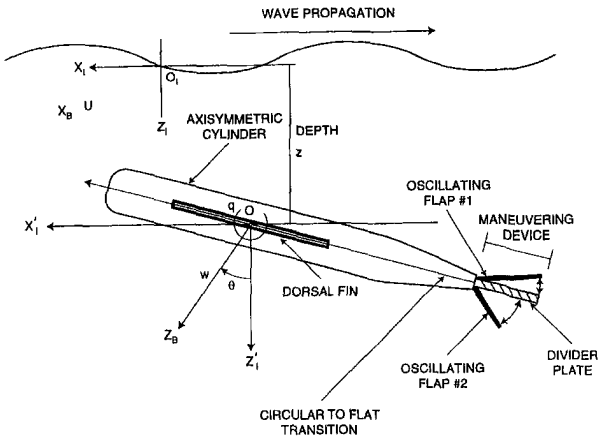

where:

$X_I - Z_I$ = Inertial Coordinate System (Origin at the Calm Surface).
$X_I' - Z_I'$ = Translation of Inertial Frame (Origin at Geometrical Center).
$X_B - Z_B$ = Body Fixed Coordinate System.

(Note that the long dorsal fins are actually mounted in the horizontal plane. The caudal fins are also mounted in the horizontal plane and are akin to flukes in whales.)

Fig. 1 Schematic of the maneuvering devices (Dorsal and Caudal Fins) and axisymmetric cylinder. Dorsal fin is shown uncambered.

Mathematical Model of Dive Plane Motion

Consider the vehicle motion in the dive (vertical) plane (Fig. 1). The heave and pitch equations of motion are described by coupled nonlinear differential equations. In a moving coordinate frame fixed at the vehicle's geometrical center, the dimensionless equations of motion for a neutrally buoyant vehicle are given by Papoulias and Papadimitriou (1995); Healy and Lienard (1993); and Smith et al. (1978)

$$m(\dot{w} - uq - z_G q^2 - x_G \dot{q}) = z_q \dot{q} + z_{\dot{w}} \dot{w} + z_q q + z_w w - C_D \int_{\text{tail}}^{\text{nose}} b(x)(w - xq)|w - xq|dx + z_\delta \delta + f_p + f_d,$$

$$I_y \dot{q} + m z_G (\dot{u} + wq) - m x_G (\dot{w} - uq) = M_{\dot{q}} \dot{q} + M_{\dot{w}} \dot{w} + M_q q + M_w w + C_D \int_{\text{tail}}^{\text{nose}} x b(x)(w - xq)|w - xq|dx - x_{GB} W \cos\theta - z_{GB} W \sin\theta + m_p + m_d, \quad (1)$$

where $\dot{\theta} = q$, $\dot{z} = -u \sin\theta + w \cos\theta + \dot{z}_f$, $x_{GB} = x_G - x_B$, $z_{GB} = z_G - z_B$, δ is the camber of the dorsal fins, $m_p = m_{p1} + m_{p2}$, m_{pi} is the moment produced by the ith foil, f_p is the net normal force produced by the flapping foils, $\dot{z}_f$ is the velocity of the fluid, and m_d and f_d are the force and moment acting on the vehicle caused by the surface wave. (Camber is the maximum cross-stream deflection of the dorsal fin). Here it is assumed that the forward speed is held steady ($u = U$) by a control mechanism. These nondimensionalized equations of motion (Eq. (1)) are obtained by dividing the original force and moment equations by $\frac{1}{2}\rho L^2 V^2$ and $\frac{1}{2}\rho L^3 V^2$ where L and $V = U$ are the reference values for length and velocity, and the time is scaled by (U/L). Thus z_δ, f_p, and m_p are the hydrodynamic coefficients of the vertical force and the pitching moment from the control fins.

In Part 1, Bandyopadhyay et al. (1998) have experimentally measured the forces and moments acting on winged bodies submerged in proximity of surface waves. The disturbance force and moment caused by surface waves are periodic, which can be

Nomenclature

A_i, A_2 = maximum cross-stream travel of a flap tip
A_p, b_1, A_c, B_c, D_c = system matrices
a_i, b_{ii} = system parameters
$u = U$, w = vehicle's forward and normal velocity
q = pitch rate
θ = pitch angle
z = depth
δ = camber
$Z_{\dot{q}}$, $Z_{\dot{w}}$, Z_q, Z_w, Z_δ = coefficients used in representing normal force
$M_{\dot{q}}$, $M_{\dot{w}}$, M_q, M_w = coefficients used in representing moment
x_B, z_B = coordinates of CB
x_g, z_g = coordinates of CG
C_d = coefficient used in crossflow integration
m, W = mass, weight of vehicle
m_{p1}, m_{p2}, m_p = moments produced by caudal fins
m_d, f_d = moment and force due to surface wave
I_y = moment of inertia
ω_f, ω_o = frequencies of oscillation of foils and of surface wave
α_1, α_2, α_o = phase angles
F_{io}, F_{ij}, M_{io}, M_{ij} = flapping foil force and moment terms
S_{t1}, S_{t2} = Strouhal numbers of foils
$U_c = (\delta, f_p, m_p)^T$ = control vector
$\xi = (z, w, q, \theta)^T$ = state vector
$y_o = z$ = output variable to be controlled
y_r = reference depth trajectory
ζ_r, ω_r = command generator parameters
z^* = target depth
S = switching surface
$e = (y_o - y_r)$ = depth tracking error
λ = switching surface parameter
α, $\Delta\alpha$ = known and uncertain functions
F_{d1}, F_{d2} = amplitudes of sinusoidal force components due to surface wave
$\hat{F}_{d1}$, $\hat{F}_{d2}$, $\hat{\eta}$ = estimates of parameters in control law
L_1, L_2, L_3 = weighting parameters in the Lyapunov function
V_o = Lyapunov function
K, μ = gain, feedback parameter used in sliding mode control law
$e = (z - y_o)$ = tracking error
θ^*, q^*, ω^* = equilibrium values
T_p = period
q_a = advance operator
a_{cij}, B_{cj}, a_{fi}, B_{fi} = elements used in discrete-time representation of dynamics
$\tilde{\theta}$ = pitch angle error
J = performance index
ν, β = polynomials used for predicting pitch angle
ν_l, β_i = coefficients of polynomials
$\hat{\nu}$, $\hat{\beta}$ = estimated polynomials
$\hat{\nu}_i$, $\hat{\beta}_i$ = estimates of ν_l, β_i
ψ, $\phi(k)$ = regressor vectors
p_o = parameter vector

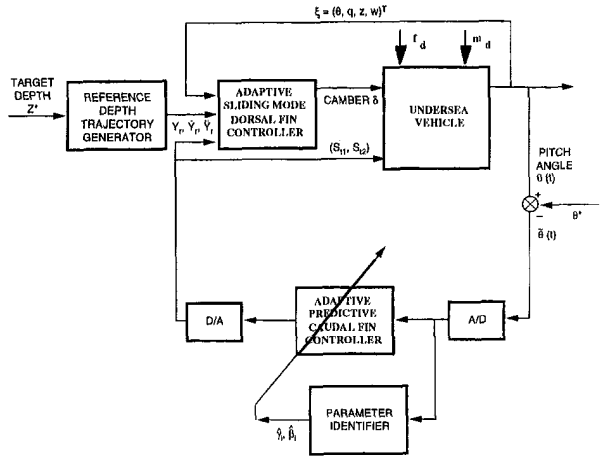

where

Z^* = Target Depth,
θ = Pitch Angle,
θ^* = Equilibrium Pitch Angle,
S_{t1}, S_{t2} = Strouhal Numbers of Foils,
A_1, A_2 = Maximum Travel of Foils,
δ = Camber of Dorsal Fins.

Fig. 2 Closed-loop system (including the Caudal and Dorsal Fin Controllers)

expressed by a Fourier series. For simplicity in presentation, consider that f_d and m_d are well approximated by their fundamental components and are given by

$$f_d = F_d \cos(\omega_o t + \alpha_o)$$
$$m_d = M_d \cos(\omega_o t + \hat{\alpha}_o), \tag{2}$$

where ω_o is the fundamental frequency of the surface wave, F_d and M_d are amplitudes, and α_o and $\hat{\alpha}_o$ are the phase angles.

The dorsal fin produces a normal force ($z_\delta \delta$) proportional to the camber δ of the fins and can be continuously varied for the purpose of control. The forces and moments produced by the flapping foils (caudal fins) are quite complex and depend on motion pattern (clapping and waving) as well as on the frequency of oscillation, maximum flapping angles, axis about which foils oscillate, and the speed U. The motions of the foil pair in the tail are called clapping and waving, because of the patterns they mimic; in the former, the flaps are out of phase while they are in phase in the latter. The choice of flapping parameters and the mode of oscillation can produce a variety of control forces and moments. Based on the experimental results and analysis, it had been shown by Bandyopadhyay and coworkers (Bandyopadhyay, 1996; Bandyopadhyay and Donnelly, 1997; and Bandyopadhyay et al., 1997) that flapping foils produce periodic forces whose period is equal to the period of flapping. Therefore, their periodic forces can be expressed by a Fourier series, but are dominated by their fundamental components. Although the approach of this study can be generalized, for simplicity, it is assumed that the flapping foils produce forces and moments of the form

$$f_p = F_{10}(S_{t1}, \omega_f) + F_{20}(S_{t2}, \omega_f) + F_{11}(S_{t1}, \omega_f)\cos(\omega_f t + \alpha_1) + F_{12}(S_{t2}, \omega_f)\cos(\omega_f t + \alpha_2)$$
$$m_p = M_{10}(S_{t1}, \omega_f) + M_{20}(S_{t2}, \omega_f) + M_{11}(S_{t1}, \omega_f)\cos(\omega_f t + \alpha_1) + M_{12}(t_{t2}, \omega_f)\cos(\omega_f t + \alpha_2), \tag{3}$$

where S_{ti} is the Strouhal number defined as

$$S_{ti} = \left(\frac{fA_i}{U}\right), \quad i = 1, 2 \tag{4}$$

and is a dimensionless angular frequency parameter, $\omega_f = 2\pi f$ is the frequency of oscillation (rad/s), and A_i is the maximum cross-stream travel of the flap tip. It is important to note that the Strouhal number of each foil is a key control variable that can be altered by the choice of frequency and the tip travel A_i independently, and, thus, one can control the contribution of each foil in force generation for the purpose of control.

For the purpose of control, it is assumed that the two foils are controlled independently and oscillate with the same frequency ω_f, but the maximum travel of each tip A_i is varied at the interval of T_p, the time period of oscillation of foils. A continuous change of A_1 and A_2 is not allowed here since the intention is to develop a periodic force by flapping, although such an imposed mode of oscillation does create a complex control design problem. Note that we are trying to imitate biolocomotion for slow speed maneuvers.

The problem of interest here is to design a control system for the independent control of depth (z) using dorsal fins and stabilize the pitch angle dynamics using flapping foils. This decomposition of the dive plane control problem simplifies the controller design. An adaptive sliding mode control system is designed for large magnitude depth (z), and a discrete adaptive predictive controller is designed for pitch angle regulation separately based on the decoupled rotational dynamics of the pitch angle of the vehicle. A judicious choice of controller design is essential since the dorsal fins are continuously cambered and the parameters of oscillations of the foils can be altered only at the completion of the cycle of flapping at discrete, but uniformly distributed, instants of time.

The system (Eq. (1)) can be written in a vector form as

$$\begin{pmatrix} \dot{z} \\ \dot{w} \\ \dot{q} \\ \dot{\theta} \end{pmatrix} = \begin{bmatrix} -U\sin\theta + w\cos\theta + \dot{z}_f \\ a_1 w + a_2 q + a_3(x_{GB}\cos\theta + z_{GB}\sin\theta) + a_4(w, q) + d_1 \\ a_5 w + a_6 q + a_7(x_{GB}\cos\theta + z_{GB}\sin\theta) + a_8(w, q) + d_2 \\ q \end{bmatrix} + \begin{bmatrix} 0 & 0 & 0 \\ B_{21} & B_{22} & B_{23} \\ B_{31} & B_{32} & B_{33} \\ 0 & 0 & 0 \end{bmatrix} \begin{bmatrix} \delta \\ f_p \\ m_p \end{bmatrix} \tag{5}$$

or

$$\dot{x} = Ax + g(x) + BU_c + Dd \tag{6}$$

where $x = (z, w, q, \theta)^T \in R^4$ is the state vector (T denotes transposition), $U_c = (\delta, f_p, m_p)^T$ is the control vector, $d = (\dot{z}_f, d_1, d_2)^T$, and D, a_i, A, B_{ij} and B are obtained by comparing (6), (7), and (8). The function $g(x)$ is the nonlinear function in (5), and A and D are constant matrices.

Dorsal Fin Control System

In this section, a dorsal fin control system is designed for depth control. Since depth (z) control is of interest, an output controlled variable

$$y_o = z \tag{7}$$

is associated with the system (Eq. (6)). Consider a reference trajectory, $y_r(t)$, generated by a second order command generator

$$\ddot{y}_r + 2\xi_r\omega_r\dot{y}_r + \omega_r^2 y_r = \omega_r^2 z^*, \tag{8}$$

where z^* is the target depth coordinate, $\xi_r > 0$, and $\omega_r > 0$. The parameters ξ_r and ω_r are properly chosen to obtain the desired command trajectories. The objective is to steer the vehicle using the dorsal fins so that $y_o = z(t)$ asymptomatically follows $y_r(t)$. As y_o tends to $y_r(t)$, the vehicle attains the desired depth since y_r converges to z^*.

For the derivation of a controller, an adaptive sliding mode control technique (Slotin and Li, 1991; Utkin, 1978; and Narendra and Annaswamy, 1989) is used and the sliding surface is defined as

$$S = \dot{e} + \lambda e, \tag{9}$$

where $\lambda > 0$ and $e = (y_o - y_r) = z - y_r$ is the tracking error.

Consider the motion during the sliding phase. During the period of sliding, one has $S(t) \equiv 0$, which implies from Eq. (9) that

$$\dot{e} + \lambda e = 0. \tag{10}$$

Thus, during the sliding phase, it follows that $e(t) \to 0$, that is, $z(t) \to z^*$ as $t \to \infty$ and the desired depth control is accomplished.

Now consider the design of a controller so that the trajectory beginning from any initial condition is attracted toward the switching surface. In obtaining a control law, differentiating $S(t)$ along the trajectory of the system (Eq. (6)), and substituting $\dot{\omega}$ from (5), gives

$$\dot{S} = \ddot{e} + \lambda \dot{e} \tag{11}$$

$$= \cos\theta B_{21}[\alpha(x, f_p, m_p, t) + \Delta\alpha(x, d, f_p, m_p, \ddot{z}_f, t) + \eta^T\psi(x) + F_{d1}\cos\omega_o t + F_{d2}\sin\omega_o t + \delta], \tag{12}$$

where $B_{21}^{-1}d_1 = F_{d1}\cos\omega_o t + F_{d2}\sin\omega_o t$. Here α and ψ are known functions, but $\Delta\alpha$, the parameter vector η, the amplitudes F_{d1} and F_{d2}, and B_{21} are unknown. It is assumed that the sign of B_{21} is known and $|\theta| \le \theta_m < \pi/2$. Without loss of generality, it is assumed that $B_{21} > 0$. The known functions α and ψ are computed using the nominal set of values of various parameters of the system.

The camber δ of the dorsal fin is continuously varied to steer any trajectory toward the switching surface. Assuming that the frequency ω_o of the surface wave is known, a control law is now chosen as

$$\delta = -\alpha(x, f_p, m_p, t) - \hat{\eta}^T\psi(x) - \hat{F}_{d1}\cos\omega_o t - \hat{F}_{d2}\sin\omega_o t - \mu S - K\,\mathrm{sgn}\,(S), \tag{13}$$

where $\mu > 0$, $\hat{\eta}$ and $\hat{F}_{di}$ are estimates of η and F_{di}, respectively, and K is a constant gain yet to be determined. Substituting control law Eq. (18) into Eq. (17), gives

$$\dot{S} = \cos\theta B_{21}[\Delta\alpha + \tilde{\eta}^T\psi(x) + \tilde{F}_{d1}\cos\omega_o t + \tilde{F}_{d2}\sin\omega_o t - K\,\mathrm{sgn}\,S - \mu S], \tag{14}$$

where $\tilde{\eta} = \eta - \hat{\eta}$, and $\tilde{F}_{di} = F_{di} - \hat{F}_{di}$.

Now, adaptation laws for $\hat{\eta}$, $\hat{F}_{di}$, and gain K must be chosen so that the surface S becomes attractive to any trajectory of the system. In deriving the adaptation law, consider a Lyapunov function,

$$V_o = ((B_{21}\cos\theta)^{-1}S^2 + \tilde{\eta}^T L_1\tilde{\eta} + \tilde{F}_{d1}^2 L_2 + \tilde{F}_{d2}^2 L_3)/2, \tag{15}$$

where $L_2 > 0$, $L_3 > 0$, and L_1 ($i = 1, 2, 3$) is any positive definitive symmetric matrix which are chosen to provide desirable response characteristics. The derivative of V_o is given by

$$\dot{V}_o = S(\Delta\alpha + \tilde{\eta}^T\psi + \tilde{F}_{d1}\cos\omega_o t + \tilde{F}_{d2}\sin\omega_o t - K\,\mathrm{sgn}\,S) - \mu S^2 + \tilde{\eta}^T L_1\dot{\tilde{\eta}} + L_2\tilde{F}_{d1}\dot{\tilde{F}}_{d1} + L_3\tilde{F}_{d2}\dot{\tilde{F}}_{d2}. \tag{16}$$

The function V_O is a positive definite function of S, $\tilde{\eta}$, $\tilde{F}_{d1}$, $\tilde{F}_{d2}$. In order to ensure that the surface $S = 0$ is attractive, adaptation laws and K are chosen so that $\dot{V}_o$ satisfies $\dot{V}_o \le 0$.

In view of Eq. (16), one chooses the adaptation laws of the form

$$\dot{\hat{\eta}} = -\dot{\tilde{\eta}} = L_1^{-1}\psi S,$$

$$\dot{\hat{F}}_{d1} = -\dot{\tilde{F}}_{d1} = L_2^{-1}S\cos\omega_o t,$$

$$\dot{\hat{F}}_{d2} = -\dot{\tilde{F}}_{d2} = L_3^{-1}S\sin\omega_o t \tag{17}$$

and the gain K is chosen to satisfy

$$K = k_1(\xi, d, f_p, m_p) + \epsilon, \tag{18}$$

where the function k_1 is a bound on the uncertain function satisfying

$$k_1 \ge |\Delta\alpha(x, d, f_p, m_p, \ddot{z}_f, t)|. \tag{19}$$

Substituting adaptation law (17) in Eq. (16) now yields

$$\dot{V}_o \le -\epsilon|S| - \mu S^2 \le 0. \tag{20}$$

Since $\dot{V}_o \le 0$, it follows that S, $\hat{\eta}$, and $\hat{F}_{di}$ are bounded. Furthermore, in view of Eq. (20), one concludes that $S(t) \to 0$, as $t \to \infty$, assuming that θ, q are bounded. This implies that the tracking error $(z - y_r) \to 0$ as $t \to \infty$. This completes the depth control system design.

Assuming that error $y_r(t) \to z^*$, and $\dot{y}_r \to 0$, the control law (Eq. (13)) asymptotically decouples (θ, q) dynamics from the remaining variables. Thus, the residual dynamics of the system essentially describe the rotational pitch motion. This residual dynamics, when the motion is constrained so that the error $y - y_r = 0$, is called the zero-error dynamics (Slotine and Li, 1991). For satisfactory performance in the closed-loop system, the state variables θ and q associated with zero-error dynamics must be bounded. In the next section, control of pitch angle using flapping foils is considered.

Flapping Foil Control of Pitch Dynamics

In this section, control of rotational pitch dynamics (zero error dynamics) is considered. First, a discrete-time linear model for pitch control is obtained.

Discrete-Time Pitch Dynamics. Since the sliding mode controller asymptotically controls z to z^*, the zero error dynamics is obtained from Eq. (1) by setting $\dot{e} = \dot{z} - \dot{y}_r = \dot{z} = 0$. Also, when $e(t) = 0$, $\dot{e}(t) = \dot{z} - \dot{y}_r = \dot{z} = 0$, one has for small θ

$$w = U\theta - \dot{z}_f \tag{21}$$

It is assumed that the two foils oscillate with identical frequency ω_f. The maximum travel A_i of each foil-tip is independently controlled periodically at the interval of T_p ($=2\pi/\omega_f$). This way the Strouhal numbers S_{t1} and S_{t2} of the two foils are independently controlled. The moments, $m_{pi}(S_{ti}, \omega_f)$, and forces, $f_{pi}(S_{ti}, \omega_f)$ ($i = 1, 2$), generated by the flapping foils are nonlinear functions of the Strouhal numbers. Since ω_f is a constant, expanding $f_{pi}(S_{ti})$ and $m_{pi}(S_{ti})$ in the Taylor series about $S_{t1} = S_{t2} = S_t^*$, a constant, and neglecting higher order terms gives

$$B_{33}m_{pi}(S_{ti}) + B_{32}f_{pi} \approx B_{33}\left[\frac{\partial M_{io}(S_t^*)}{\partial St_i} + \frac{\partial M_{1i}(S_t^*)}{\partial S_{ti}}\cos(\omega_f t + \alpha_i)\right]\tilde{S}_{ti} + B_{32}\left[\frac{\partial F_{io}(S_t^*)}{\partial S_{ti}} + \frac{\partial F_{1i}}{\partial S_{ti}}(S_{ti}^*)\cos(\omega_f t + \alpha_i)\right]\underline{\Delta}b_{ii}(t)\tilde{S}_{ti}, \quad i = 1, 2, \tag{22}$$

where $\tilde{S}_{ti} = S_{ti} - S_t^*$.

Next, pitch angle must be regulated to θ^*, a constant. Using Eqs. (16), (17), (20), and (21), the pitch dynamics about (θ^*, $q^* = 0$) obtained from (5) are given by

$$\dot{\tilde{x}} \underline{\Delta} A_p\tilde{x} + b_1[b_{11}\tilde{S}_{t1} + b_{22}\tilde{S}_{t2} + D_2(t)], \tag{23}$$

where $D_2 = d_2 + a_7 x_{GB}\cos\theta^* + a_8 + B_{31}\delta + a_5(U\theta^* - \dot{z}_f) + a_7 z_{GB}\sin\theta^*$, $b_1 = [1, 0]^T$,

$$\tilde{x} = (q, \tilde{\theta})^T, \ \tilde{\theta} = \theta - \theta^*,$$

and

$$A_p = \begin{bmatrix} a_6 & a_5 U + a_7(z_{GB}\cos\theta^* + x_{GB}\sin\theta^*) \\ 1 & 0 \end{bmatrix}$$

Since the control input $\tilde{S}_{ti}$ is to be implemented as a piecewise constant function changing at the interval T_p, a discrete-time model is obtained from Eq. (23) of the form

$$\tilde{x}(k+1) = A_c\tilde{x}(k) + B_c\tilde{S}_t(k) + D_c(k), \tag{24}$$

where $(k+1)$ denotes $(k+1)T_p$, $\tilde{S}_t(t) = \tilde{S}_t(k) = [\tilde{S}_{t1}(k), \tilde{S}_{t2}(k)]^T$ for $t\epsilon[kT_p, (k+1)T_p)$, and

$$A_c = e^{A_p T_p}$$

$$B_c = \int_{kT_p}^{(k+1)T_p} e^{A_p[(k+1)T_p-\tau)}b_1[b_{11}(\tau), b_{22}(\tau)]d\tau$$

$$D_c(k) = \int_{kT_p}^{(k+1)T_p} e^{A_p[(k+1)T_p-\tau]}b_1 D_2(\tau)d\tau. \tag{25}$$

Let $A_c = (a_{cij})$, $B_c = [B_{c1}^T, B_{c2}^T]^T = (b_{cij})$ for $i, j = 1, 2$, and $D_c(k) = (D_{c1}, D_{c2})^T$. Note that B_c is a 2×2 constant matrix since integration in Eq. (35) is performed over one period T_p and $\omega_f = 2\pi/T_p$, but $D_c(k)$ depends on kT_p due to the fact that $\omega_f \neq \omega_o$; that is, the flapping frequency differs from the frequency of the wave.

Autoregressive Moving Average Model. Next, a discrete adaptive predictive control technique is used for pitch control. For this, an expression for the predicted value of $\tilde{\theta}(k)$ is obtained and the advance operator q_a is introduced and defined as $q_a z_s(k) = z_s(k+1)$ for any discrete signal $z_s(k)$. Using Eq. (24) gives

$$q_a\tilde{q}(k) = a_{c11}\tilde{q}(k) + a_{c12}\tilde{\theta}(k) + B_{c1}\tilde{S}_t(k) + D_{c1}(k) \tag{26}$$

$$q_a\tilde{\theta}(k) = a_{c21}\tilde{q}(k) + a_{c22}\tilde{\theta}(k) + B_{c2}\tilde{S}_t(k) + D_{c2}(k). \tag{27}$$

Operating (26) and (27) by q_a^{-2} and q_a^{-1}, respectively, and manipulating the resulting equations, it can be shown that (for details, see Singh and Bandyopadhyay, 1997),

$$[1 + (-a_{c11} - a_{c22})q_a^{-1} + (a_{c11}a_{c22} - a_{c21}a_{c12})q_a^{-2}]\tilde{\theta}(k) = q_a^{-1}[B_{c2} + (a_{c21}B_{c1} - a_{c11}B_{c2})q_a^{-1}]\tilde{S}_t(k) + q_a^{-1}[D_{c2}(k) + a_{c21}q_a^{-1}D_{c1}(k) - a_{c11}q_a^{-1}D_{c2}(k)] \tag{28}$$

or

$$(1 + a_{f1}q_a^{-1} + a_{f2}q_a^{-2})\tilde{\theta}(k) = q_a^{-1}(B_{f1} + B_{f2}q_a^{-1})\tilde{S}_t(k) + q_a^{-1}a_{fd}(k), \tag{29}$$

where a_{fi}, B_{fi} and a_{fd} are obtained by comparing (28) and (29).

The discrete-time model of Eq. (29) is called an autoregressive moving average (ARMA) model. The ARMA model can be expressed in an alternative predictor form as

$$\tilde{\theta}(k+1) = (-a_{f1} - a_{f2}q_a^{-1})\tilde{\theta}(k) + (B_{f1} + B_{f2}q_a^{-1})\tilde{S}_t(k) + a_{fd}(k). \tag{30}$$

This is a useful representation of the pitch dynamics. It is assumed that the parameters a_{fi}, B_{fi}, and the signal $a_{fd}(k)$ are unknown. For the regulation of $\theta(k)$, one can design predictive control laws if the estimates of the unknown parameters and $a_{fd}(k)$ are known.

For the derivation of a control law, it is assumed that

$$a_{fd}(k+1) \approx a_{fd}(k). \tag{31}$$

Note that if the wave frequency ω_o is equal to the frequency of flapping and if either δ is small or $B_{31} \approx 0$, then $a_{fd}(k+1) = a_{fd}(k)$ for all k. In practice, it has been found that the predictive control technique works well even when parameters vary slowly and the condition of Eq. (31) is violated.

Under the assumption of Eq. (31), subtracting $q_a^{-1}\tilde{\theta}(k+1)$ from (30) gives

$$\tilde{\theta}(k+1) = [-a_{f1} + (a_{f1} - a_{f2})q_a^{-1} + a_{f2}q_a^{-2}]\tilde{\theta}(k) + [B_{f1} + (B_{f2} - B_{f1})q_a^{-1} - B_{f2}q_a^{-2}]\tilde{S}_t(k)\Delta\upsilon(q^{-1})\tilde{\theta}(k) + \beta(q^{-1})\tilde{S}_t(k), \tag{32}$$

where

$$\upsilon(q_a^{-1}) = \upsilon_0 + \upsilon_1 q_a^{-1} + \upsilon_2 q_a^{-2},$$
$$\beta(q_a^{-1}) = \beta_0 + q_a^{-1}\beta'(q_a^{-1}),$$
$$\beta'(q_a^{-1}) = \beta_1 + \beta_2 q_a^{-1}. \tag{33}$$

The coefficients β_i and υ_i are obtained from (32).

Adaptive Pitch Angle Control. Assuming that the parameters of Eq. (32) are known, now a weighted one-step ahead pitch control law is obtained. For this a suitable performance index of the form

$$J(k+1) = \tfrac{1}{2}[\tilde{\theta}(k+1) - \theta_r^*(k+1)]^2 + \tfrac{1}{2}\lambda_d\|S_t(k)\|^2 \tag{34}$$

is chosen, where $\lambda_d > 0$ and $\theta_r^*(k)$ is a suitable reference trajectory to be followed by $\tilde{\theta}(k)$. Note if $\theta_r^*(k) \to 0$, then $\theta(k) \to \theta^*$. By the choice of a suitable value of λ_d, a compromise between the rate of convergence $\tilde{\theta}(k+1)$ to $\theta^*(k+1)$ and the amount of control effort expended is achieved.

Substituting $\theta(k+1)$ from (32) in (34), for minimizing J differentiating with respect to $S_t(k)$, and solving gives

$$\tilde{S}_t(k) = (\lambda_d I + \beta_o^T\beta_o)^{-1}\beta_o^T[-\upsilon(q_a^{-1})\tilde{\theta}(k) - \beta'(q_a^{-1})\tilde{S}_t(k-1) + \theta_r^*(k+1)] \tag{35}$$

Notice that the Strouhal number at the instant kT_p depends on the present and past values of θ and the past values of input S_t, $\tilde{S}_t$.

Since $\tilde{S}_{ti}(k) \in [0, \tilde{S}_{tim}]$ where $\tilde{S}_{tim}$ is the same maximum allowed value of $\tilde{S}_{ti}$, control input $\tilde{S}_{ti}(k)$ given in (35) must be set to the lower or upper limits whenever the magnitude exceeds the prescribed limits.

Parameter Estimation. For synthesizing the control law, the parameters in Eq. (32) must be known. A practical solution to this problem is to obtain an estimate of these unknown parameters using an appropriate parameter identification technique. There are several kinds of algorithms based on the projection and the least square methods that can be used to obtain the estimates of these unknown parameters β_o, υ_i, and β_i in Eq. (32). Equation (32) can be written as

$$\tilde{\theta}(k+1) = \phi^T(k)\rho_o, \tag{36}$$

where

$$\phi^T(k) = [(1q_a^{-1}q_a^{-2})\tilde{\theta}(k), (1q_a^{-1}q_a^{-2})S_t^T(k)]$$
$$\rho_o^T = [(\upsilon_o, \upsilon_1, \upsilon_2), \beta_o, \beta_1, \beta_2]$$
$$(1, q_a^{-1}, q_a^{-2})S_t^T = (S_t^T, q_a^{-1}S_t^2, q_a^{-2}S_t^T)$$

Using a simple projection algorithm described in Goodwin and Sin (1984) for parameter estimation, the estimate $\hat{\rho}_o$ of ρ_o is obtained using an update law given by

$$\hat{\rho}_o(k) = \hat{\rho}_o(k-1) + \frac{a(k)\phi(k-1)}{c_1 + \phi^T(k-1)\phi(k-1)}[\tilde{\theta}(k) - \phi^T(k-1)\hat{\rho}_o(k-1)] \quad 0 < a(k) < 2,\ c_1 > 0 \tag{37}$$

These parameters are used in (35) for synthesis.

Now the adaptation law for adjusting the maximum travel of the tips of the two foils is easily computed using the definition of the Strouhal number and required adaptation scheme is given by

$$A_i(k+1) = \left[\frac{US_{ti}(k)}{(\omega_f/2\pi)} \right], \quad i = 1, 2, \tag{38}$$

where $S_{ti}(k) = \tilde{S}_{ti}(k) + S_t^*$.

The complete closed-loop system is shown in Fig. 2.

Dorsal Fin Control With Inactive Caudal Fins. In the previous sections, control systems using both the dorsal and caudal fins have been presented. A question of interest arises: Is it possible to maneuver the vehicle using only the dorsal fins? We examine this question in this section. It turns out that the vehicle model under consideration is non-minimum phase (i.e., the transfer function has unstable zero). As such, the sliding mode dorsal fin control law (Eq. (13)) derived in the previous section, cannot accomplish depth control with internal stability in the system and a new sliding mode dorsal fin control law must be derived.

When the caudal fins are inactive, $f_p = m_p = 0$, and (6) simplifies as

$$\dot{x} = Ax + g(x) + b\delta + Dd, \tag{39}$$

where b denotes the first column of B in (6). The system's transfer function with $g = 0$, $d = 0$, relating z and δ is

$$\bar{z}(s)/\bar{\delta}(s) = H(s) = C(sI - A)^{-1}b, \tag{40}$$

where $C = [1, 0, 0, 0]^T$, s is the Laplace variable, and $\bar{z}$, $\bar{\delta}$ denote the Laplace transforms. For the model (39), $H(s)$ is of the form

$$H(s) = k_p(s - \mu_1)(s + \mu_2)d_p^{-1}(s), \tag{41}$$

where $d_p(s) = s^4 + m_3s^3 + m_2s^2 + m_1s$, and $\mu_i > 0$. Thus, $s = \mu_1$ is an unstable zero and $H(s)$ is nonminimum phase.

For the derivation of a control system with internal stability, an approximate output variable z_a is derived such that

$$\begin{aligned} \bar{z}_a(s)/\bar{\delta}(s) = H_a(s) &= \tilde{C}(sI - A)^{-1}b \\ &= -\mu_1 k_p(s + \mu_2)d_p^{-1}(s). \end{aligned} \tag{42}$$

Following Chockalingam (1998), it can be shown that $\tilde{C}$ is given by

$$\begin{aligned} \tilde{C} = -\mu_1 k_p[0, 0, -1, -\mu_2] \\ \times [b, Ab, A^2b, m_3A^2b] + A^3b]^{-1}. \end{aligned} \tag{43}$$

Note that $H_a(s)$ does not have the unstable zero of $H(s)$.

Now a new controlled output variable can be defined as

$$z_a = \tilde{C}x \tag{44}$$

associated with the nonlinear system (39). For $d = 0$, $g(x) = 0$, in view of (40), (41), and (42), it follows that

$$\bar{z}(s) = -\frac{1}{\mu_1}(s - \mu_1) - \bar{z}_a(s), \tag{45}$$

which implies that

$$z(t) = z_a(t) - \frac{1}{\mu_1}\dot{z}_a(t) \tag{46}$$

From (46), it follows that if $z_a(t) \to z^*$, a desired depth, and $\dot{z}_a(t) \to 0$, then $z(t) \to z^*$, and the target depth is attained.

Now a control law is derived to control the new output variable z_a. The Lie derivatives of a function $a(x)$ with respect to the vector field $f(x) \triangleq Ax + g(x)$ are defined as

$$\begin{aligned} L_f(\alpha)(x) &= \frac{\partial \alpha}{\partial x} f(x) \\ L_f^j(\alpha)(x) &= L_f(L_f^{j-1}(\alpha))(x) \\ L_bL_f^k(\alpha)(x) &= \frac{\partial L_f^k(\alpha)}{\partial x} b. \end{aligned} \tag{47}$$

Define

$$L_DL_f^k(\alpha)(x) = \frac{\partial L_f^k(\alpha)}{\partial x} D. \tag{48}$$

Define

$$\begin{bmatrix} \xi_1 \\ \xi_2 \\ \xi_3 \end{bmatrix} = \begin{bmatrix} \tilde{C}x \\ L_f(\tilde{C}x)(x) \\ L_f^2(\tilde{C}x)(x) \end{bmatrix} \tag{49}$$

where $f(x) = Ax + g(x)$. Differentiating ξ_i along the solution of (39) gives

$$\begin{aligned} \frac{d}{dt}\begin{pmatrix} \xi_1 \\ \xi_2 \\ \xi_3 \end{pmatrix} = \begin{bmatrix} \xi_2 \\ \xi_3 \\ a^*(x) + b^*(x)\delta \end{bmatrix} + \begin{bmatrix} \psi_1 \\ \psi_2(x) \\ \psi_3(x) \end{bmatrix} d \\ + \begin{bmatrix} 0 \\ \psi_u(x) \\ 0 \end{bmatrix} d, \end{aligned} \tag{50}$$

where

$$\begin{aligned} \psi_1 = \tilde{C}D,\ \psi = [\psi_1, \psi_2, \psi_3]^T \\ a^* = L_f^3(\tilde{C}x)(x) \\ b^* = L_bL_f^2(\tilde{C}x)(x) \\ \psi_u = L_bL_f(\tilde{C}x)(x) \\ \psi = [\psi_1, L_DL_f(\phi_1)(x), L_DL_f^2(\phi_1)(x)]^T. \end{aligned}$$

For the derivation of control law, small values of ξ, η, δ, and d, functions ψd and $\psi_u\delta$ can be neglected to obtain an approximate representation of the nonlinear system as

$$\frac{d}{dt}\begin{bmatrix} \xi_1 \\ \xi_2 \\ \xi_3 \end{bmatrix} = \begin{bmatrix} \xi_2 \\ \xi_3 \\ a^*(x) + b^*(x)\delta \end{bmatrix} \tag{51}$$

Define $\tilde{\xi}_i = \xi_i - y_r^{(i-1)}$, $i = 1, 2, 3$, where $y_r^{(k)}$, is the kth derivative of the reference depth trajectory.

The sliding surface $S = 0$ is defined as

$$S = \tilde{\xi}_3 + \lambda_2\tilde{\xi}_2 + \lambda_1\tilde{\xi}_1 + \lambda_0\int_0^t \tilde{\xi}_1 dt, \tag{52}$$

which in view of (51) can be written as

$$S = \ddot{\tilde{\xi}}_1 + \lambda_2\dot{\tilde{\xi}}_1 + \lambda_1\tilde{\xi}_1 + \lambda_0\int_0^t \tilde{\xi}_1 dt. \tag{53}$$

The parameters λ_i are chosen such that the polynomial

$$\Pi(s) = s^3 + \lambda_2s^2 + \lambda_1s + \lambda_0 \tag{54}$$

is stable. Differentiating S and using (51) gives

$$\dot{S} = \lambda_2\ddot{\tilde{\xi}}_1 + \lambda_1\dot{\tilde{\xi}}_1 + \lambda_0\tilde{\xi}_1 + a^*(x) + b^*(x)\delta - y_r^{(3)}. \tag{55}$$

In view of (55) the sliding mode dorsal fin control law is given by

$$\delta = (b^*(x))^{-1}[-a^*(x) + y_r^{(3)} - \lambda_2(\xi_3 - \dot{y}_r) - \lambda_1(\xi_2 - \dot{y}_r) - \lambda_0(\xi_1 - y_r) - k_1 S - k_2 \text{ sgn } (S)]. \quad (56)$$

Substituting (56) in (55) gives

$$\dot{S} = -k_1 S - k_2 \text{ sgn } (S), \quad (57)$$

which implies that $S(t) \rightarrow 0$ and, therefore, according to (53), $\tilde{\xi}_1 \rightarrow 0$ as $t \rightarrow \infty$, since $\Pi(s)$ is Hurwitz. In the closed-loop systems (51) and (56), for $y_r = z^*$, a constant, $(z_a(t), \dot{z}_a(t)) \rightarrow (z^*, 0)$ as $t \rightarrow \infty$ and from (46) it follows that $z(t) \rightarrow z^*$. As $z(t) \rightarrow z^*$, the pitch angle also converges to zero since the transfer function H_a is minimum phase.

For the system (50), it can be proven that for small perturbations in x about the origin and small y_r and disturbance input d, with a proper choice of k_r, the trajectory error remains bounded (Chockalingam, 1998).

Simulation Results. In this section, results of digital simulation are presented. Although a combined dorsal and caudal fin control law has been derived, for simplicity in simulation, numerical results for the system (1) only with the dorsal fin control system (56) is presented and it is assumed that the caudal fins are inactive. The parameters used for simulation are given in the Appendix. For the nominal parameters, the transfer function has two zeros such that $\mu_1 = 4.5325$ and $\mu_2 = 11.3806$. Since the transfer function is nonminimum phase, the row vector $\tilde{C}$ is computed using (43) to yield

$$\tilde{C} = [-8.586e - 05, -0.0708, -0.8015, 1.009].$$

The reference trajectory is generated by the fourth-order system given by

$$(s + \lambda_c)^4 y_r - \lambda_c^4 z^* = 0,$$

where z^* is the target depth. The sliding mode parameters are $\lambda_2 = 17$, $\lambda_1 = 64$, $\lambda_0 = 20$. In order to avoid control chattering, sgn (S) was replaced by set (S/ϵ) with $\epsilon = 0.01$.

Define the tracking error for the depth variable $z_e = z - y_r$. Let z_{em}, $\tilde{\xi}_{1m}$, and δ_m be the maximum magnitudes of z_e, $\tilde{\xi}_1$, and camber δ, respectively. In the figures, $\tilde{\xi}_1 = z_a - y_r = \xi_i - y_r$ is denoted by e and u denotes δ.

A. Sliding Mode Dive Plane Control: Nominal System. The complete nominal closed-loop systems (1) and (56), with $f_p = m_p = d = 0$, were simulated. The λ_c of the command generator was chosen to be 0.45. The initial conditions were assumed to be $x(0) = 0$, $y_r^{(k)} = 0$, $k = 0, 1, 2, 3$. A command trajectory was generated for controlling the vehicle to a target depth $z^* = 1m$. The sliding mode gains $k_1 = 1$ and $k_2 = 0.0101$ are chosen. The responses are shown in Fig. 3. We observe smooth control of the vehicle in about 18 seconds. Interestingly, even though the modified output is used for controller design, the depth of the vehicle was controlled smoothly. Apparently, the neglected higher order term $(\psi_u \delta)$ in the design of the sliding mode controller has minor effect on the responses. The maximum depth error and the output errors are $z_{em} = 2.5$ cm and $\xi_{1m} = 2E - 6m$. In steady-state, the pitch angle settles to its equilibrium value zero and the vehicle attains the desired depth. The maximum pitch angle deviation was found to be 0.03°. The maximum camber is $\delta_m = 26.3$ mm. The steady-state values of the heave velocity and the pitch rate were also zero.

It is pointed out that the control magnitude can be reduced by choosing slower command trajectories y_r for the depth control. Simulation was done by setting $\lambda_c = 0.3$ in the command generator. In this case, the maximum control magnitude was reduce to 8 mm, and smooth control was accomplished, but the response time increased to the order of 30 s.

Figure 4 shows the response for a $4m$ ($z^* = 4$) command for a choice of $\lambda_c = 0.3$. This gave a response time of the order of 30 s. The maximum tracking errors are $z_{em} = 6$ cm and $\tilde{\xi}_{1m} = 4E - 5m$. In steady state, the pitch angle settles to its equilibrium value of zero and the tracking errors $\tilde{\xi}_1$ and z_e were found to be zero. The maximum pitch angle deviation was found to be 0.08°. The maximum camber was $\delta_m = 32.3$ mm.

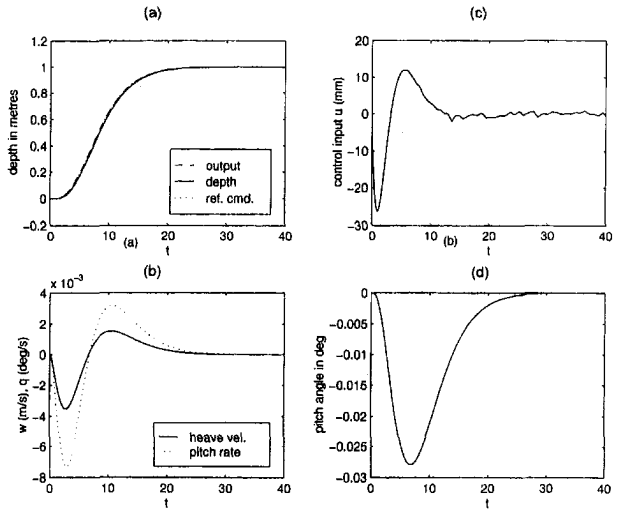

Fig. 3 Dorsal fin control: nominal parameters. (*a*) Output z_a, depth z, and reference command y_r; (*b*) heave velocity and pitch rate; (*c*) camber $\delta = u$; (*d*) pitch angle.

B. Sliding Mode Dive Plane Control: Off-Nominal Parameters. In order to examine robustness of control system, the closed-loop system was simulated with variation of ±25% in the hydrodynamic parameters. The remaining feedback parameters and initial conditions of Fig. 3 were retained. Selected response for +25% parameter perturbations is shown in Fig. 5. We observe smooth control of the vehicle. The steady-state error $\tilde{\xi}_1$ was zero. The pitch angle tends to 0° asympototically. The maximum values are $z_{em} = 2$ cm, $\tilde{\xi}_{1m} = 3E - 4m$, and $\delta_m = 16$ mm. Smaller control input is required in this case since control effectiveness matrix b has increased by an amount of 25%.

Simulation was also done with −25% parameter uncertainty. In this case also, smooth depth control was accomplished and the steady-state error $\tilde{\xi}_1$ was found to be zero. Unlike Fig. 5, larger

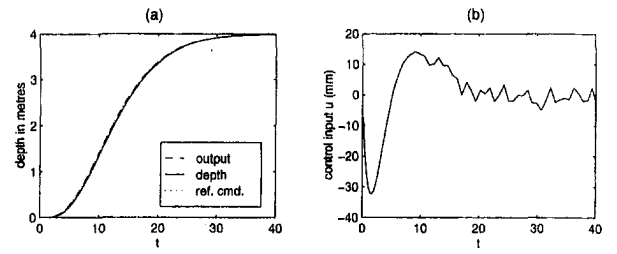

Fig. 4 Dorsal fin control: large command. (*a*) Output z_a, depth z, reference command; (*b*) camber $\delta = u$.

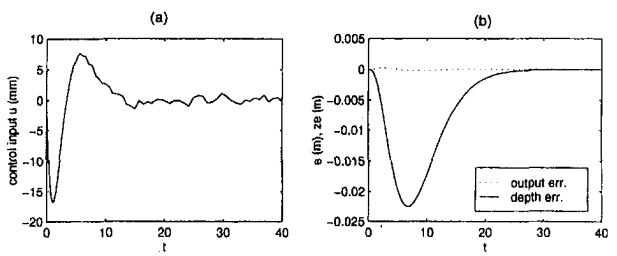

Fig. 5 Dorsal fin control: off-nominal parameters. (*a*) Camber $\delta = u$; (*b*) output error $e = z_a - y_r = \tilde{\xi}_1$ and depth error $z_e = z - y_r$.

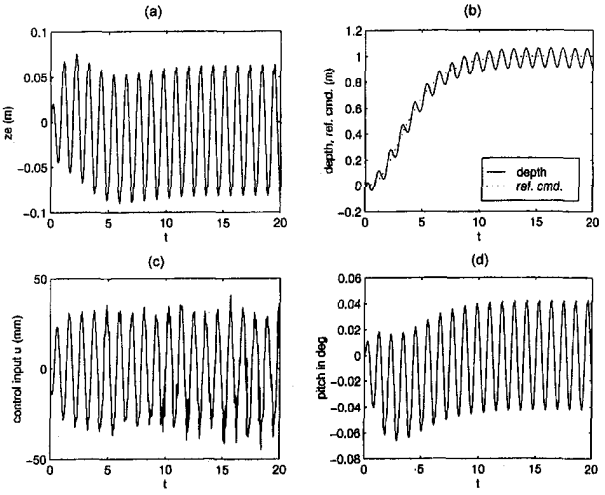

Fig. 6 Dorsal fin control: sinusoidal disturbance. (*a*) Depth error $z_e = z - y_r$; (*b*) depth z and reference command y_r; (*c*) camber $\delta = u$; (*d*) pitch angle.

control is needed for controlling depth since the value of b has decreased. The maximum values are $z_{em} = 5$ mm, $\xi_{1m} = 4$ mm, and $\delta_m = 35$ mm. Since the responses are somewhat similar to those given in Fig. 5 for positive parameter variation, these are not shown.

C. Sliding Mode Dive Plane Control: Sinusoidal Disturbance. Simulation was also done for the depth maneuvering in the presence of sinusoidal disturbance. It was assumed that $f_d = \exp(-0.1z)(0.3075)\ \sin\ (5.817t - \pi)$, $m_d = 0.3512\ \exp(-0.1z)\ \sin\ (5.817t + 70°)$ and $\dot{z}_f = 0.03\ \sin\ (5.817t)$. The frequency and phase angles of the disturbance are close to the values described in Bandyopadhyay et al. (1998). The feedback gains were set as $k_1 = 2$ and $k_2 = 0.01$. Responses for a target depth of $z^* = 1m$ are shown in Fig. 6. The maximum tracking errors were $\xi_{1m} = 7.6$ mm and $z_{em} = 23$ mm. The steady-state oscillation in the depth response is 8 mm. The steady-state oscillation in the pitch was almost negligible. The maximum deviation in the pitch was about 0.02°. The maximum value of the camber was $\delta_m = 31$ mm. It is pointed out that larger gains k_1 and k_2 can be used to attenuate the effect of disturbances of higher amplitudes. But this will require larger camber of the dorsal fins.

Conclusions

A theoretical study for the dive plane control system design for biologically inspired maneuvering of low speed, small undersea vehicles using dorsal and caudal fin-like control surfaces was considered. A hydrodynamic control scheme is developed so that the vehicle tracks a precise depth versus time trajectory. Normal force produced by the dorsal fin was used to control the depth of the vehicle and two flapping foils were used for the pitch angle control. An adaptive sliding mode control law was derived for the reference depth trajectory tracking. For the design of this control, a nonlinear vehicle model was considered for which the system parameters were assumed to be unknown, and it was assumed that sinusoidal disturbance force and moment are acting on the vehicle caused by surface waves. In the closed-loop system, including the sliding mode controller, depth control was accomplished and rotational pitch dynamics were asymptotically decoupled.

For the decoupled pitch dynamics, assuming that the pitch angle perturbations were small, a linear deterministic autoregressive model was derived. For the pitch angle control, the Strouhal numbers were chosen as key input variables. The Strouhal numbers of the two foils were periodically changed (at intervals of the time period of oscillations of the foils by altering the maximum tip travel). Both foils were oscillating at the same frequency. Using projection algorithms, the parameters of the pitch dynamics were identified. These estimated parameters were used to design an adaptive predictive control system for the regulation of the pitch angle. Thus, in the complete closed-loop system, including the adaptive sliding mode and adaptive predictive controllers, dive plane control of the underwater vehicle can be accomplished in the presence of large parameter uncertainty and sea surface waves. A dorsal fin control law was also designed for the control of the vehicle without utilizing caudal fins. Simulation results were presented which showed that depth control and pitch angle regulation can be accomplished by using only dorsal fins.

Acknowledgment

This work was sponsored by ONR (Dr. T. McMullen and Mr. James Fein) and NUWC IR (Dr. S. Dickinson). The support is gratefully acknowledged. This study was carried out while S. Singh served as an ONR Distinguished Faculty Fellow at NUWC Division Newport.

References

Azuma, A., 1992, *The Bio-Kinetics of Flying and Swimming,* Springer-Verlag, New York.

Bainbridge, R., 1963, "The Speed of Swimming of Fish as Related to Size and the Frequency and Amplitude of the Tail Beat," *Journal of Experimental Biology,* Vol. 35, pp. 109–133.

Bandyopadhyay, P. R., 1996, "A Simplified Momentum Model of a Maneuvering Device for Small Underwater Vehicles," NUWC-NPT Technical Report 10,552, Naval Undersea Warfare Center Division, Newport, RI.

Bandyopadhyay, P. R., Nedderman, W. H., Castano, J. M., and Donnelly, M., 1996, "A Small Maneuvering Device for Energetic Environment," NUWC-NPT Video, Naval Undersea Warfare Center Division, Newport, RI.

Bandyopadhyay, P. R., Castano, J. M., Rice, J. Q., Philips, R. B., Nedderman, W. H., and Macy, W. K., 1997, "Low-Speed Maneuvering Hydrodynamics of Fish and Small Underwater Vehicles," ASME JOURNAL OF FLUIDS ENGINEERING, Vol. 119, 1997, pp. 136–144.

Bandyopadhyay, P. R., and Donnelly, M. J., 1997, "The Swimming Hydrodynamics of a Pair of Flapping Foils Attached to a Rigid Body," *Proceedings of the AGARD Workshop on High Speed Body Motion in Water,* Kiev, Ukraine, Sept. 1–3, AGARD Report 827 (Feb., 1998) pp. 1.1–1.17.

Bandyopadhyay, P. R., Nedderman, W. H., and Dick, J., 1999, "Biologically-Inspired Bodies Under Surface Waves. Part 1: Load Measurements," ASME JOURNAL OF FLUIDS ENGINEERING, Vol. 121, published in this issue pp. 469–478.

Chockalingam, F., 1988, "Feedback Linearization of Nominimum Phase Systems and Control of Aeroelastic Systems and Undersea Vehicles," MS thesis, ECE Dept., Univ. Nevada, Las Vegas, April.

Chopra, M. G., 1977, "Hydromechanics of Lunate Tail Swimming Propulsion," *Journal of Fluid Mechanics,* Vol. 7, pp. 46–49.

Goodwin, G., and Sin, K. S., 1984, *Adaptive Filtering Prediction and Control,* Prentice-Hall, Englewood Cliffs, NJ.

Gopalkrishnan, R., Triantafyllou, M. S., Triantafyllou, G. S., and Barrett, D., 1994, "Active Vorticity Control in a Shear Flow Using a Flapping Foil," *Journal of Fluid Mechanics,* Vol. 274, pp. 1–21.

Hall, K. C., and Hall, S. R., 1996, "Minimum Induced Power Requirements for Flapping Flight," *Journal of Fluid Mechanics,* Vol. 323, pp. 285–315.

Healy, A. J., and Lienard, D., 1993, "Multivariable Sliding Mode Control for Autonomous Diving and Steering Unmanned Underwater Vehicle," *IEEE Journal of Oceanic Engineering,* Vol. 18, No. 3, pp. 327–338.

Kailath, T., 1980, *Linear Systems,* Prentice-Hall, Englewood Cliffs, NJ.

Narendra, K. S., and Annaswamy, A. M., 1989, *Stable Adaptive Systems,* Prentice-Hall, Englewood Cliffs, NJ.

Papoulias, F., and Papadimitriou, H., 1995, "Nonlinear Studies of Dynamic Stability of Submarines in Dive Plane," *Journal of Ship Research,* Vol. 39, No. 4, pp. 347–356.

Sastry, S., and Bodson, M., 1989, *Adaptive Control: Stability, Convergence, and Robustness,* Prentice-Hall, Englewood Cliffs, NJ.

Singh, S. N., and Bandyopadhyay, P. R., 1997, "A Theoretical Control Study of the Biologically-Inspired Maneuvering of a Small Vehicle Under a Free Surface Wave," NUWC-NPT Tech Rept. 10816, Aug.

Slotine, J. E., and Li, W., 1991, *Applied Nonlinear Control,* Prentice-Hall, Englewood Cliffs, NJ.

Smith, N. S., Crane, J. W., and Summery, D. C., 1978, "SDV Simulator Hydrodynamic Coefficients," NCSC Rep. TM-231-78, Naval Coastal Systems Center, Panama City, FL, June.

Triantafyllou, M. S., Triantafyllou, G. S., and Gopalakrishnan, R., 1991, "Wake Mechanics for Thrust Generation in Oscillating Foils," *Physics of Fluids,* Vol. 3, No. 12, pp. 2835–2837.

Triantafyllou, G. S., Triantafyllou, M. S., and Grosenbaugh, M. A., 1993, "Optimal Thrust Development in Oscillating Foils With Application to Fish Propulsion," *Journal of Fluids and Structures,* Vol. 7, pp. 205–224.

Utkin, V. I., 1978, *Sliding Modes and Their Application to Variable Structure Systems,* MIR Publication, Moscow.

Wu, T. Y. T., Brokaw, C. J., and Brennen, C., eds., 1975, *Swimming and Flying in Nature,* Vols. 1 and 2, Plenum Press, New York.

APPENDIX

Vehicle parameters:

$$x_{GB} = 0,$$

$$z_{GB} = 0.578802,$$

$$L = 1.282\text{m},$$

$$\rho = 1025.9\text{kgm}^{-3}.$$

Hydrodynamic parameters:

$$U = 3.6\text{m/s},$$

$$M_{\dot{q}} = 0.16E - 3,$$

$$M_{\dot{w}} = -0.825\text{E} - 3,$$

$$M_q = -0.117\text{E} - 2,$$

$$M_w = 0.314E - 2,$$

$$z_\delta = 0.3398,$$

$$z_w = -0.873\text{E} - 2,$$

$$z_{\dot{w}} = -0.569\text{E} - 2,$$

$$z_{\dot{q}} = -0.825\text{E} - 5,$$

$$z_q = -0.238\text{E} - 2..$$

Laminar Flow of a Nonlinear Viscoplastic Fluid Through an Axisymmetric Sudden Expansion

Khaled J. Hammad
Adjunct Faculty.

M. Volkan Ötügen
Associate Professor.

George C. Vradis
Associate Professor.

Mechanical, Aerospace and Manufacturing Engineering,
Polytechnic University,
Six Metrotech Center,
Brooklyn, NY 11201
e-mail: votugen@rama.poly.edu

Engin B. Arik
Vice President of Engineering,
Dantec Measurement Technology,
Mahwah, NJ

A combined experimental and computational study was carried out to investigate the laminar flow of a nonlinear viscoplastic fluid through an axisymmetric sudden expansion. The yield-stress, power-law index, and the consistency index of the yield shear-thinning test fluid were 0.733 Pa, 0.68, and 0.33 Pa · $s^{0.68}$, respectively, resulting in a Hedstrom number of 1.65. The Reynolds number ranged between 1.8 and 58.7. In addition, the flow of a Newtonian fluid through the same expansion was also studied to form a baseline for comparison. Velocity vectors were obtained on the vertical center plane using a digital particle image velocimeter (PIV). From these measurements, two-dimensional distributions of axial and radial velocity as well as the stream function were calculated covering the separated, reattached and redeveloping flow regions. These results were compared to finite difference numerical solutions of the governing continuity and fully-elliptic momentum equations. The calculations were found to be in good agreement with the experimental results. Both computational and experimental results indicate the existence of two distinct flow regimes. For low Reynolds numbers, a region of nonmoving fluid is observed immediately downstream of the step and no separated flow zone exists. For the higher Reynolds numbers, a recirculating flow zone forms downstream of the expansion step, which is followed by a zone of stagnant fluid adjacent to pipe wall characterizing reattachment.

Introduction

Viscoplastic fluids are commonly encountered in several industrial applications including those using rubber, plastic, paints, emulsions, and slurries. These fluids are characterized by the existence of a "yield stress," a critical shear stress value below which the fluid behaves like a solid. This critical stress value needs to be exceeded before the fluid can sustain a rate of deformation and thus flow. Once flow is established, if the stress-strain rate relationship is linear, the fluid is called a Bingham plastic. However, many fluids typically encountered in the industry are either shear-thickening or shear-thinning, which adds another layer of complexity in their analysis. These nonlinear viscoplastic fluids are also called Herschel-Bulkley fluids.

Despite their importance to many industries, the flows of Herschel-Bulkley fluids have so far received little attention from fluid mechanics researchers, perhaps partially due to the complexity involved in their analysis. In an earlier attempt, Chen et al. (1970) used an integral boundary layer method to calculate the laminar entrance flow of a linear viscoplastic fluid (Bingham plastic) in a circular pipe. This was followed by the study of Soto and Shah (1976) who obtained a numerical solution to the boundary layer equations for the same flow. The results of both studies indicated the strong influence of the yield number on flow development. The numerical analysis of Bingham plastic flows was extended to more complex geometries by Lipscomb and Denn (1984). They contended that once the fluid starts flowing, there must be complete yielding throughout the domain the fluid occupies with no regions of stagnant fluid. Vradis et al. (1993) used the fully elliptic governing equations to study the nonisothermal entrance flow into a pipe. The results showed that the influence of the yield stress is even stronger than had been found using the boundary layer equations. Although limited in scope, these computational studies of simple geometries clearly showed that the flow structure of viscoplastic fluids are quite distinct from those of Newtonian fluids and thus, results of Newtonian flows cannot be extrapolated to predict flows of viscoplastic fluids through complex geometries. This fact was further confirmed by the recent numerical study of the axisymmetric sudden expansion flow of Bingham plastics carried out by Vradis and Ötügen (1997).

The experimental studies of viscoplastic fluid flows reported in the literature are equally sparse. In an earlier attempt, Wilson and Thomas (1985) concentrated in the near-wall structure of the velocity field in a pipe flow of a Bingham plastic. The detailed experimental analysis of these fluids is particularly challenging owing to the limitation in the choice of measurement techniques that can be successfully employed. For this reason, a good number of experimental studies have been limited to global flow visualizations (see for example, Townsend and Walters, 1993; Abdul-Karem et al., 1993). To investigate spatially-resolved velocity, nonintrusive methods such as those based on lasers must be used. However, these optical techniques require that the fluid is optically transparent and the index of refraction is uniform, both of which are difficult to achieve. Park et al. (1989) and Wildman et al. (1992) used Herschel-Bulkley-type fluids with the proper optical characteristics to study the velocity field using laser Doppler velocimetry. Both studies concentrated in the turbulent flow through a circular, constant-cross section pipe. In the former study, additional measurements were made in the laminar and transitional regimes while, some results were obtained in an axisymmetric gradual contraction in the latter work. The bulk of the above experimental investigations was carried out in turbulent flows. Based on our knowledge, no systematic study of the laminar flows of nonlinear viscoplastic fluids has been reported in the literature covering a range of Reynolds numbers. Currently, the understand-

Contributed by the Fluids Engineering Division for publication in the JOURNAL OF FLUIDS ENGINEERING Manuscript received by the Fluids Engineering Division June 4, 1998; revised manuscript received March 15, 1999. Associate Technical Editor: M. N. Dhaubhadel.

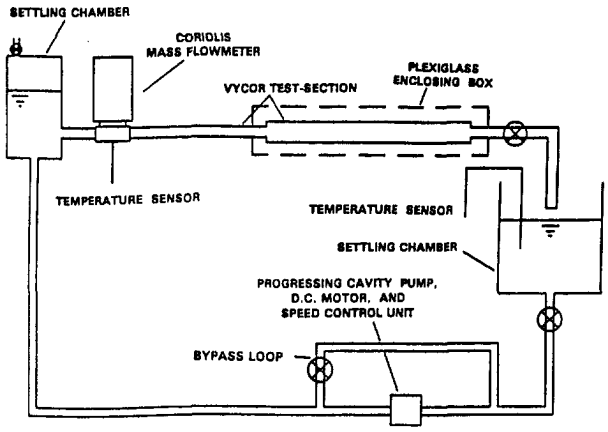

Fig. 1 Schematic of the closed-loop test facility

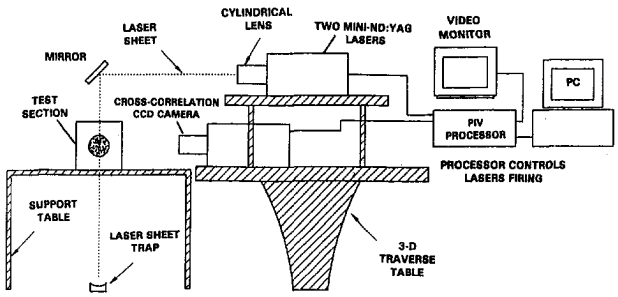

Fig. 2 Schematic of the PIV system

ing of the effect of these parameters on the flow structure is far from being complete.

In the present, the laminar flow of a Herschel-Bulkley fluid through an axisymmetric sudden expansion is studied. Flows through sudden expansions are frequently encountered in many industries, and therefore, are of strong interest from a practical point. In addition, although the flow is complex, typically exhibiting three distinct regions—separation, recirculation, and reattachment—the fact that the separation point is fixed at the edge of the sudden expansion (step) simplifies the analysis of the flow. Furthermore, the axisymmetric flow geometry affords a straightforward numerical implementation in cylindrical coordinates (Vradis and Ötügen, 1997). Measurements and computations were carried out for an axisymmetric 1:2 expansion (based on radii) with a yield-stress shear-thinning fluid. Some measurements were also made in a Newtonian fluid for comparison.

Experimental Details

Test Facility. A schematic of the closed-loop experimental system is shown in Fig. 1. The system is composed of a 12.7 mm diameter inlet pipe, a 25.4 mm diameter test section, a return loop, and a variable-speed dc motor-driven pump. There are also two settling chambers, one upstream of the inlet pipe and the other at the exit of the test section. The inlet pipe is 813 mm long which ensures a fully developed flow at the expansion step for all cases studied. The test section is 965 mm long which allows for the investigation of flow development downstream of reattachment. The material for the inlet pipe and the test section is Vycor, whose index of refraction matches that of the test fluids ($n_D = 1.46$). The test section is enclosed inside a 51 mm by 89 mm rectangular cross-section Plexiglas outer enclosure, which extends into the inlet pipe as shown in Fig. 1. During the experiments, the enclosure is filled with the working fluid in order to avoid the distortion of the PIV image by the curved surface of the test section. The steady flow rate through the system is monitored by a Coriolis mass flow meter throughout the experiments and different flow rates are obtained by changing the rpm of the pump motor. The liquid in the inlet settling tank is kept at a high level (300 mm) to prevent any significant static pressure variations in the test section.

PIV System. A digital PIV system is used for the planar simultaneous measurements of axial and radial velocities in the vertical plane passing through the test section centerline. The optical system is powered by two Nd:YAG lasers each with approximately 10 mJ of pulse energy and a duration of 8 ns. The firing of the lasers is externally controlled and the repetition rates and the cross-pulse delays are continuously adjustable. The laser outputs are frequency doubled to provide the 532 nm green line and the two beams are combined using a beam splitter in reverse. The combined beam is expanded into a sheet using a cylindrical lens. The 1 mm-thick laser sheet is directed through the test section via a mirror (Fig. 2). The sheet subsequently passes through a slot in the test section table and is terminated in a beam dump placed at the floor level. Silicon carbide particles are used as light scatterers with a nominal diameter of 18.2 μm. The image of the scattering particles in the measurement plane is collected at a right angle by a zoom lens and fed into a CCD camera. The 768 × 484 pixel image plane of the camera is divided into 32 × 32 pixel size sub-regions and the average particle displacement is calculated real-time for each of these sub-regions (interrogation areas) using a cross-correlation method. Therefore, each of these interrogation areas represents a single point in the flow field and the spatial resolution of the measurements is determined by the image size of the sub-regions and the thickness of the laser sheet. Based on these, the spatial resolution of the measured velocity is 0.36 mm and 0.45 mm in the radial and axial directions, respectively, and 1.0 mm along the third direction (depth). The data are stored on a personal computer for further analysis and graphing. The PIV system is placed on a three-dimensional traverse system so that different regions of the flow can be interrogated using the same alignment and optical settings. The positioning accuracy of the traverse system is determined to be 0.2 mm in the axial direction and 0.125 mm in the radial direction. Based on the predicted uncertainty in determining the particle displacement in each interrogation area and the accuracy in repositioning of the traverse system, the uncertainty in velocity is estimated to be better than 6

Nomenclature

d = diameter of upstream pipe
He = Hedstrom number, $\tau_y(\rho^n d^{2n}/K^2)^{1/2-n}$
K = consistency index
n = power-law index
n_D = index of refraction
P = pressure
p = nondimensional pressure, $P/\rho U_i^2$
R = radial coordinate
r = nondimensional radial coordinate, R/d
Re = Reynolds number, $\rho d U_i/K(U_i/d)^{n-1}$
U = streamwise velocity
U_i = inlet streamwise bulk velocity
u = normalized streamwise velocity, U/U_i
V = radial velocity
v = normalized radial velocity, V/U_i
X = streamwise coordinate from step
x = nondimensional streamwise coordinate, X/d
Δ_{ij} = rate of deformation tensor
$\dot{\gamma}$ = shear rate
μ = effective viscosity
μ_{eff} = nondimensional effective viscosity
ρ = density
τ_{ij} = stress tensor
τ_y = yield stress

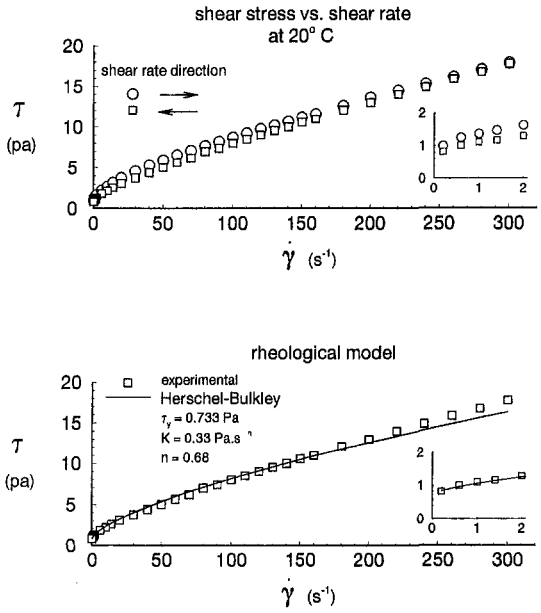

Fig. 3 Rheological characterization of the test fluid at 20°C

percent of the expected minimum velocity at each measurement plane.

Fluid Rheology. The main objective of the present effort is to characterize the laminar flow structure of a yield-stress shear-thinning non-Newtonian fluid through an axisymmetric sudden expansion. For comparison, measurements were also made with a Newtonian fluid in the same facility. The Newtonian fluid was diethylene glycol with an absolute viscosity of 0.038 Pa · s at 20°C. The base fluid for the non-Newtonian fluid was a mixture of 60 percent diethylene glycol, 20 percent benzyl alcohol and 20 percent water, all by weight. The yield stress was obtained by adding small amounts of silica particles to the base fluid. Increasing concentrations of the silica lead to increasing yield stress and consistency index values and decreasing power-law index (Hammad, 1997). Figure 3 shows the stress versus strain rate characteristics of the non-Newtonian fluid used in the present study. The concentration of the silica particles is 4.76 percent by weight. The rheological characteristics of the fluid were obtained using a cone-and-plate rheometer. However, additional measurements were made at low shear rates using a concentric cylinders rheometer in order to accurately determine the yield stress value. The figure indicates that there is no significant hysterisis in the stress strain-rate curve as it is approached from low and high ends of the shear rate. Most of the small hysterisis displayed in the flow curve can be attributed to the measurement uncertainty which was +/− 0.2 Pa in the present study. Additional tests established that the test fluid was insensitive to temperature variations (in the range of 20°C to 25°C). Further, the fluid exhibited good shear and storage stability characteristics. Based on the return curve from high-shear rates in Fig. 3 (with the solid line fit), the yield stress, power-law index and the consistency index are determined to be $\tau_y = 0.733$ Pa, $n = 0.68$ and $K = 0.33$ Pa · s$^{0.68}$, respectively. Therefore, the Hedstrom number based on the fluid properties and the upstream pipe diameter is He = 1.65.

Computational Method

The Governing Equations. The nondimensionalized governing elliptic equations for the steady, laminar, incompressible flow of a non-Newtonian fluid in cylindrical coordinates are

$$\frac{\partial u}{\partial x} + \frac{1}{r}\frac{\partial rv}{\partial r} = 0 \tag{1}$$

$$u\frac{\partial u}{\partial x} + v\frac{\partial u}{\partial r} = -\frac{\partial p}{\partial x} + \frac{1}{\mathrm{Re}}\left[\frac{\partial}{\partial x}\left[2\mu_{eff}\frac{\partial u}{\partial x}\right] + \frac{1}{r}\frac{\partial}{\partial r}\left[\mu_{eff} r\left[\frac{\partial u}{\partial r} + \frac{\partial v}{\partial x}\right]\right]\right] \tag{2}$$

$$u\frac{\partial v}{\partial x} + v\frac{\partial v}{\partial r} = -\frac{\partial p}{\partial r} + \frac{1}{\mathrm{Re}}\left[\frac{1}{r}\frac{\partial}{\partial r}\left[r2\mu_{eff}\frac{\partial v}{\partial r}\right] + \frac{\partial}{\partial x}\left[\mu_{eff}\left[\frac{\partial u}{\partial r} + \frac{\partial v}{\partial x}\right]\right] - 2\mu_{eff}\frac{v}{r^2}\right] \tag{3}$$

In the case of a yield-pseudoplastic fluid the relationship between the stress tensor τ_{ij} and the rate of deformation tensor Δ_{ij} is given by the following formula:

$$\tau_{ij} = \left[K\left(\frac{1}{2}\Delta_{ij}\Delta_{ij}\right)^{(n-1)/2} + \frac{\tau_y}{\left(\frac{1}{2}\Delta_{ij}\Delta_{ij}\right)^{1/2}}\right]\Delta_{ij} \quad \text{for} \quad \frac{1}{2}\tau_{ij}\tau_{ij} > \tau_y^2 \tag{4a}$$

$$\Delta_{ij} = 0 \quad \text{for} \quad \frac{1}{2}\tau_{ij}\tau_{ij} \le \tau_y^2 \tag{4b}$$

Here Δ_{ij} and $\Delta_{ij}\Delta_{ij}$ are the rate of deformation tensor and its second invariant, respectively. In cylindrical coordinates the function $\frac{1}{2}\Delta_{ij}\Delta_{ij}$ is given by:

$$\frac{1}{2}(\Delta_{ij}\Delta_{ij}) = 2\left[\left[\frac{\partial v}{\partial r}\right]^2 + \left[\frac{v}{r}\right]^2 + \left[\frac{\partial u}{\partial x}\right]^2\right] + \left[\frac{\partial v}{\partial x} + \frac{\partial u}{\partial r}\right]^2 \tag{4c}$$

As a result, the nondimensional effective viscosity is defined as:

$$\mu_{eff} = \left(\frac{1}{2}\Delta_{ij}\Delta_{ij}\right)^{(n-1)/2} + \frac{\mathrm{He}/\mathrm{Re}^{n/(2-n)}}{\sqrt{\frac{1}{2}\Delta_{ij}\Delta_{ij}}} \quad \text{for} \quad \frac{1}{2}\tau_{ij}\tau_{ij} > \tau_y^2 \tag{5a}$$

and

$$\mu_{eff} = \infty \quad \text{for} \quad \tfrac{1}{2}\tau_{ij}\tau_{ij} \le \tau_y^2 \tag{5b}$$

where, the Hedstrrom number, He, serves as a nondimensional yield stress.

Solution Technique. The numerical technique used in the present study is described in detail by Vradis and Hammad (1998). It is a second-order accurate, finite-difference approximations-based iterative technique in which the linearized equations are solved simultaneously along lines in the radial direction using an efficient block-tridiagonal matrix inversion technique. Only the convective terms are approximated with first-order differencing to warrant convergence. The linearization of the equations is accomplished by using the convective coefficients at the previous iteration level. In the core regions of the flow the effective viscosity, μ_{eff}, attains an infinite value since $\Delta_{ij} = 0$ in such regions. Large values of μ_{eff} create convergence problems since the coefficient matrix becomes very "stiff" due to large differences in the magnitude of its elements. In order to avoid such problems, μ_{eff} is "frozen" at a relatively high value of $\mu_{eff} = 1000$ when the value of $\sqrt{\frac{1}{2}\Delta_{ij}\Delta_{ij}}$ drops below a certain preset level thus, guaranteeing convergence. The same approach was adopted by other researchers in the past (O'Donovan and Tanner, 1984, and Lipscomb and Denn, 1984). The result of such an approximation is that the rheological behavior of the fluid is altered from that of an actual Herschel-Bulkley fluid to a bi-viscosity fluid. Through numerical experimentation, see Hammad and Vradis (1998), it was estab-

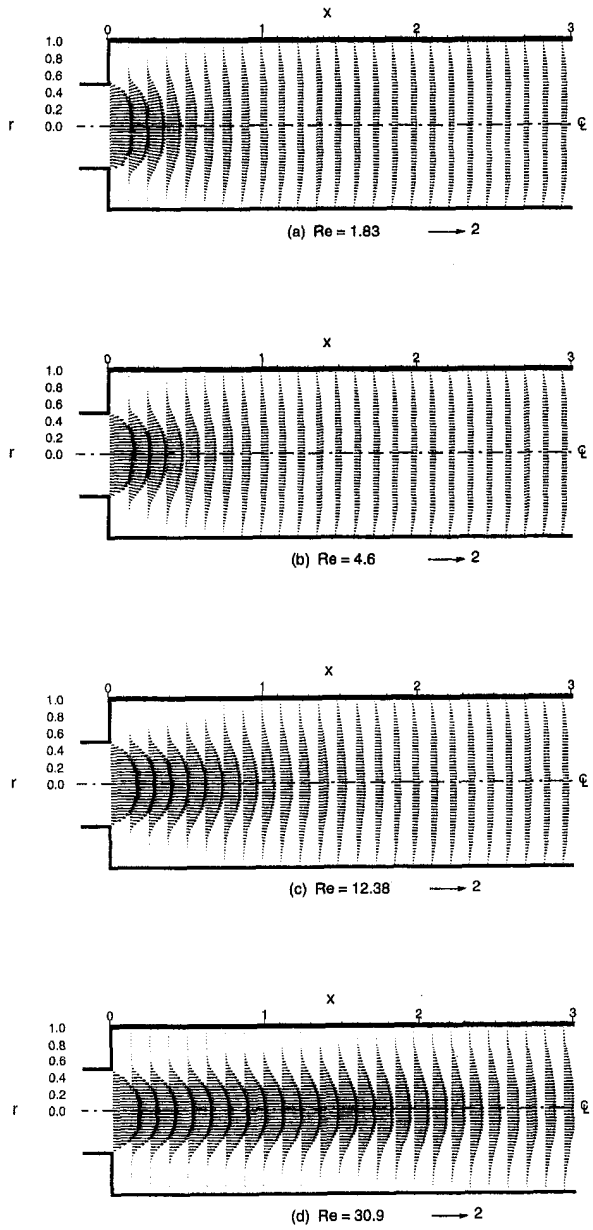

Fig. 4 Experimentally obtained velocity vectors for He = 1.65

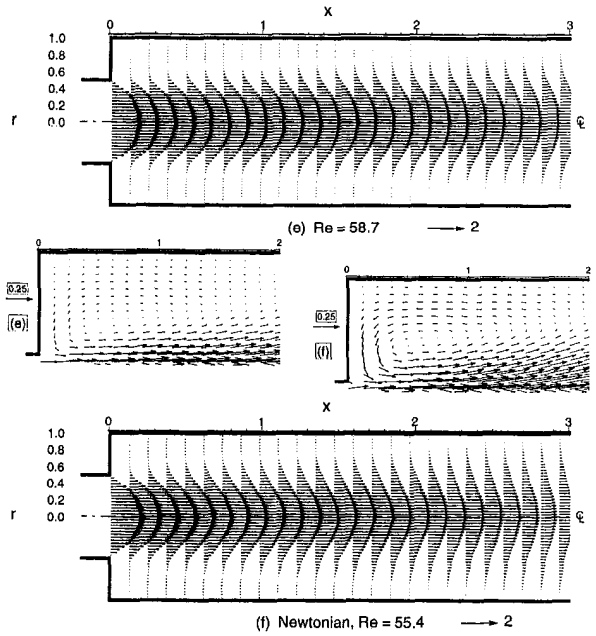

Fig. 4 (cont.)

lished that accurate results can be obtained based on a cut-off value of $\mu_{eff} = 1000$. Due to the sharp variations in the values of effective viscosity, in order to obtain convergence very strong under-relaxation of the effective viscosity is necessary from one iteration level to the next, especially in the earlier stages of the iterative procedure.

Discussion of Results

In the experiments, planar images of the flow field were obtained in small subregions of the domain of interest in order to achieve high spatial resolution and to capture the details of the complex flow structure. Each two-dimensional velocity image had a radial extent of approximately one step height and an axial extent of 1.6 step heights. Thus, four rows of images were obtained at each vertical level to cover the full radial extent of the flow. The number of images in each vertical strip varied from case to case in order to capture the development of the flow in the axial direction. In the end, the images were put together to form a composite picture of the complete flow field. The pulse time delay on the lasers was varied in different regions of the flow in order to optimize the particle displacement for highest measurement accuracy. For the calculations, the flow at the inlet ($x = 0$) is assumed to be fully developed with $u = u(r)$ and $v = 0$. The velocity profile at the inlet is obtained numerically by solving the problem of the fully developed flow of such a fluid in a straight pipe. At the exit plane of the computational domain, the flow is assumed fully developed. Thus, the streamwise derivatives of the velocity components are zero, while the pressure is uniform. The length of the computational domain depends on the Reynolds and yield numbers and is not known *a priori*. For each case, it has to be adjusted individually, sometimes through multiple trial runs. The 97 × 80 computational grid is variable in the streamwise (97) direction and uniform in the transverse (80) direction. It is finer close to the step and coarser toward the exit of the pipe. Extensive numerical experimentation using coarser and finer grids established that the present results are grid independent.

Figure 4 shows the experimentally obtained velocity vectors for the non-Newtonian fluid for a fixed Hedstrom number of 1.65 and at five Reynolds numbers. For comparison, the velocity field for the Newtonian fluid at Re = 55.4 is also presented. The fully developed velocity profiles at the expansion plane show plug zones around the centerline, where radial gradients of velocity are zero. The radial extent of the plug region becomes smaller as the Reynolds number increases. Downstream of the step, the initial plug zone is rapidly destroyed giving way to a velocity profile that shears throughout. Further downstream, when the flow reaches fully developed conditions again, a new central plug zone is formed. This downstream plug zone is observed in Figs. 4(*a*) through (*c*) where the flow becomes fully developed within the axial distance of $x = 3$. As the Reynolds number increases, the flow downstream of the step takes longer axial distances to reach a fully developed, self-similar state. For the non-Newtonian fluid flow up to Re = 30.9, there is no discernible recirculating flow near the step corner downstream of the expansion. For Re = 58.7, however, a weak reverse flow is observed. The insets in Figs. 4(*e*) and (*f*) compare the corner recirculation flow of the non-Newtonian fluid at Re = 58.7 with that of the Newtonian fluid at Re = 55.4. Clearly, the strength of the recirculating flow for the non-Newtonian fluid is weaker than that of the Newtonian fluid.

Profiles of the streamwise and the radial velocity are shown in Figs. 5 and 6 for He = 1.65 and for Reynolds numbers of 1.83 and 12.37, respectively. In each figure, the experimental (PIV) results

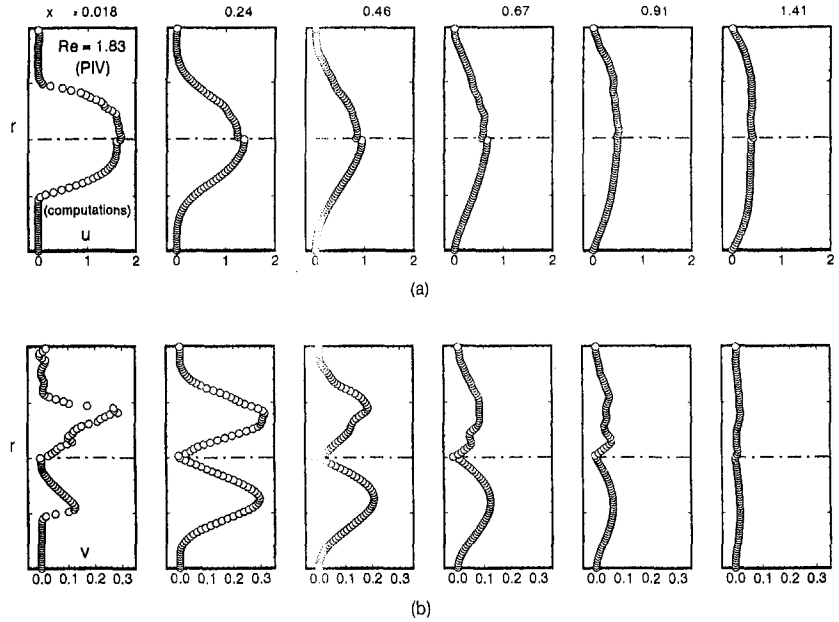

Fig. 5 Streamwise and radial velocity profiles for Re = 1.83; He = 1.65

are presented in the top half of the frames while the computational results are presented in the lower half. The experimental and computational results are in good agreement as each set of results display the same flow behavior. The presence of a plug zone at the expansion plane is again apparent from the streamwise velocity profiles. Further, the centerline value of the streamwise velocity at this location is smaller than 2. This is expected given that the fully-developed non-Newtonian fluid flows have fuller profiles than their Newtonian counterpart. The growth of the radial velocity is very rapid exhibiting a significant magnitude already at $x \approx 0.02$. For both Reynolds numbers, the radial velocity reaches its largest magnitude at $x \approx 0.25$. The radial velocity for the smaller Reynolds number of Re = 1.83 is consistently larger that for Re = 12.38 indicating a higher level of bulk transport in the radial direction for the smaller Reynolds number case. Indeed, the flow reaches a fully developed state within a streamwise distance of $x = 1.41$ for Re = 1.83 while for Re = 12.38, the fully developed conditions are not reached until about $x = 3.36$. Again, for both Reynolds numbers, there is no discernible flow near the step downstream of expansion. This finding is supported by laser sheet visualizations of the flow (Hammad, 1997). In these long duration visualizations no motion is detected in the region immediately downstream of the step. At larger Reynolds numbers (Re > 30.9), a recirculating corner flow is observed which becomes stronger with increasing Reynolds number. However, this recirculation flow is weaker than that for a Newtonian fluid at the same Reynolds number.

This is demonstrated in Fig. 7 which compares the streamwise velocity profiles of the non-Newtonian fluid at Re = 58.7 to the Newtonian fluid at Re = 55.4. Both sets of results shown in the

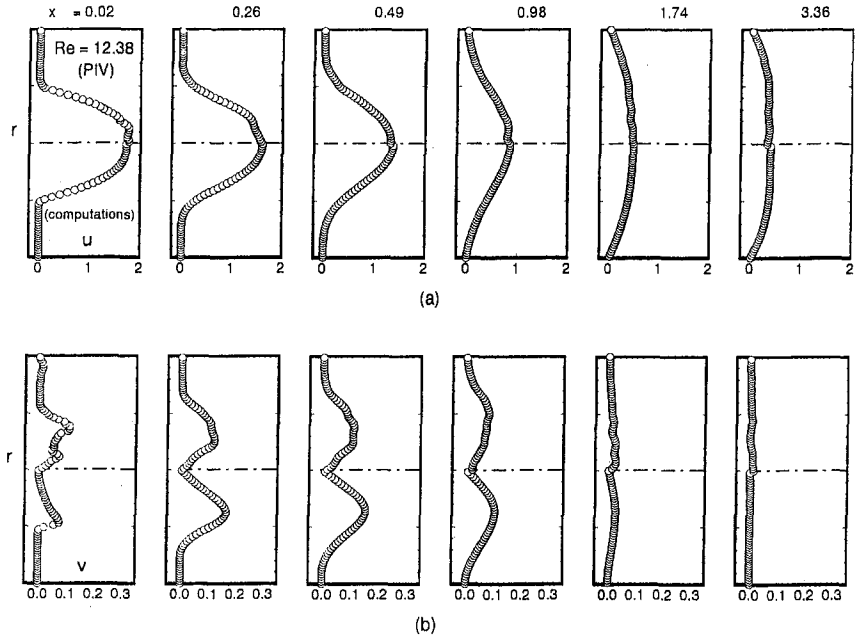

Fig. 6 Streamwise and radial velocity profiles for Re = 12.38; He = 1.65

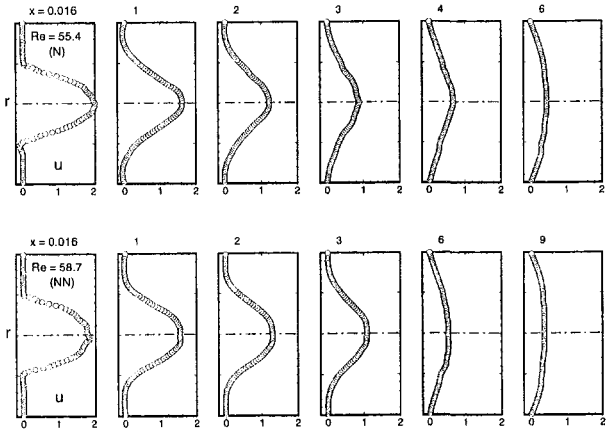

Fig. 7 Evolution of streamwise velocity for Newtonian and non-Newtonian fluids

figure are experimentally obtained. The upper half of the figure corresponds to the Newtonian flow (designated by *N*) while the lower half corresponds to the non-Newtonian fluid flow (designated by *NN*). In the Newtonian case, the normalized centerline velocity is 2 at the exit plane and 0.5 at $x = 6$ where the flow is again fully developed. These values correspond to the parabolic fully developed laminar pipe flow profile. In contrast, the inlet centerline velocity for the non-Newtonian case is slightly smaller than 2 indicating the existence of a plug flow zone. A plug zone is observed also at $x = 9$ where the flow is fully developed. The centerline value of the normalized streamwise velocity at this location is approximately 0.4. Comparing the velocity profiles at $x = 1$, it is observed that the magnitude of the near-wall reversed velocity is smaller for the non-Newtonian case. Further, the development of the non-Newtonian fluid flow is slower taking a significantly longer distance to attain a fully developed state.

The stream functions obtained from the experimental results are presented in Fig. 8 for a range of Reynolds numbers. For comparison, the Newtonian fluid flow results for Re = 55.4 are also presented. The stream function patterns are familiar for the Newtonian case showing a clear zone of recirculation. The stream functions for the non-Newtonian flows, on the other hand, show some distinct characteristics, especially in the region immediately downstream of the expansion step. It is evident that no flow recirculation exists for the three lowest Reynolds number non-Newtonian flow cases. For these cases, the fluid adjacent to the step seems to form a nonmoving block in the shape of a backward-facing ramp extending from the step over which the moving fluid gently expands as in a conical expansion. Such a flow scenario is possible considering the very low levels of stress encountered in this region which cannot overcome the yield stress value. However, for the case of Re = 30.8 and 58.7, the flow is sheared throughout and there is a detectable recirculation region. Figures 8(*e*) and 8(*f*) provide an interesting comparison. Although the Reynolds number of the Newtonian case is slightly smaller than that of the Non-Newtonian, the strength of recirculating flow is stronger for the Newtonian flow. On the other hand, it appears that the flow reattachment takes place at a longer axial distance from the step for the non-Newtonian case. Correspondingly, the approach of the flow toward a fully developed state is stretched out as well. In the case of the non-Newtonian fluid, two distinct rheological characteristics influence the behavior of the flow. At low shear rate regions such as the zone immediately downstream of the step, the yield stress controls characteristics of the flow by significantly retarding the fluid motion to the extent of completely stagnating it. Further downstream, where the shear rates are larger, the redevelopment of the flow is dominated not by the yield stress, but by the power-law index. In this region, the shear-thinning character of the fluid results in slower diffusion rates and hence

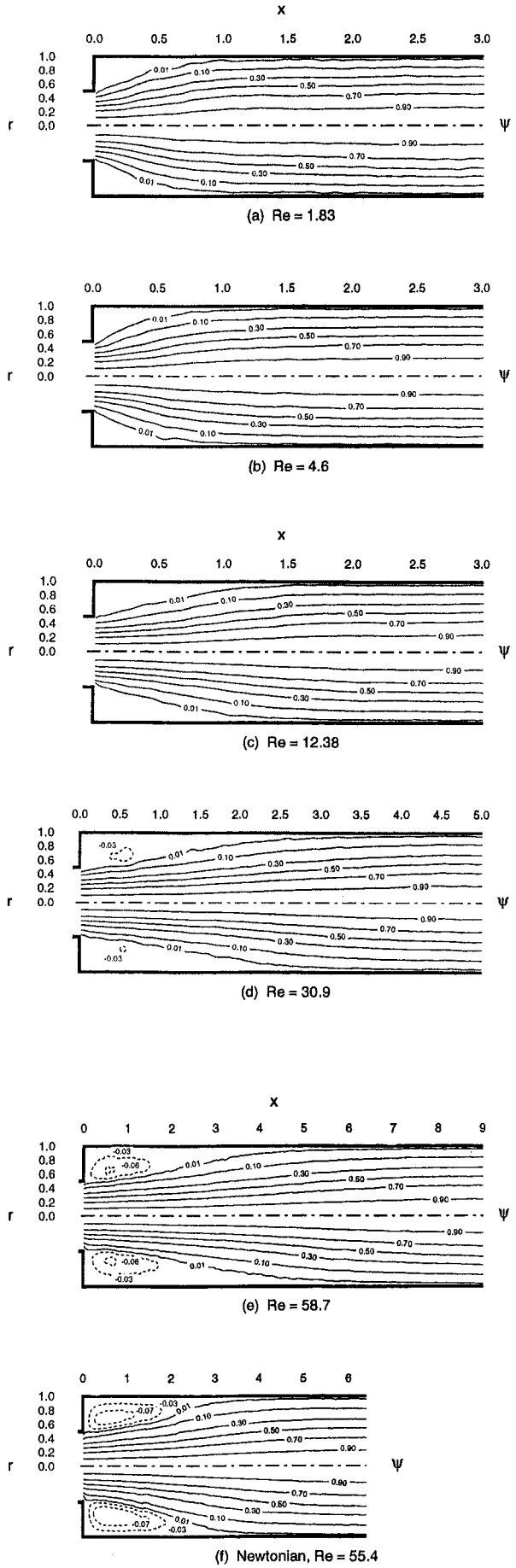

Fig. 8 Stream function distributions on the vertical plane

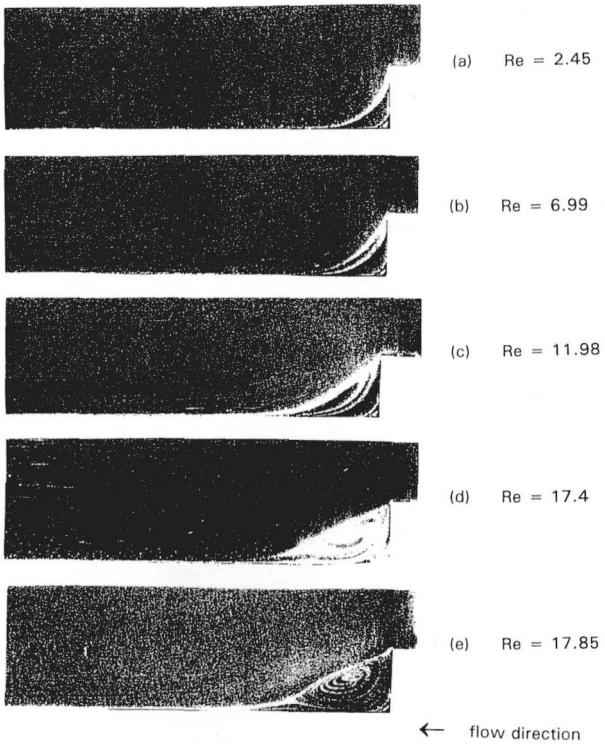

Fig. 9 Laser sheet visualization of the vertical half-plane of the non-Newtonian flow

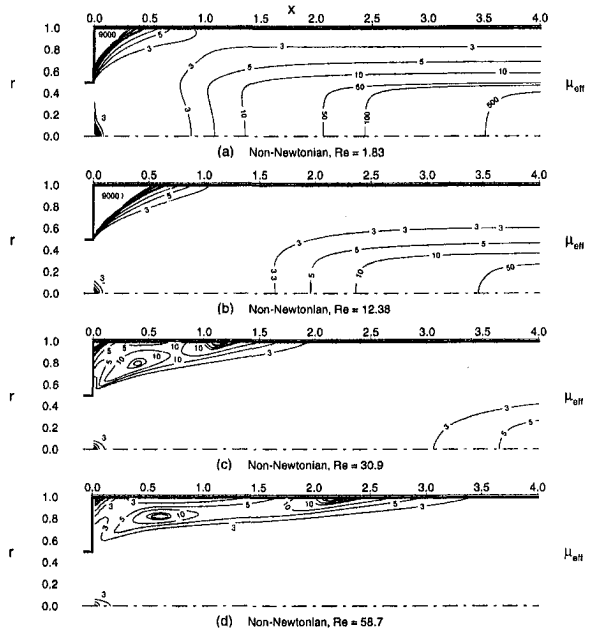

Fig. 10 Calculated effective viscosity contours

longer flow development distances compared to the Newtonian fluid.

In order to provide additional insight into the complex flow physics, planar laser sheet visualizations have also been performed for the non-Newtonian fluid flows. Figure 9 shows one such study where the flow is started from rest and the flow rate (hence, the Reynolds number) is increased gradually over a long period of time. A helium-neon laser illuminates the vertical centerplane of the test section and the fluid is seeded with the same silicon carbide particles used in the PIV measurements. In the photographs, the flow is from right to left. For flows with Re $<$ 17.4, it is clearly seen that there is no flow recirculation downstream of the step. Instead, the flow is at rest in this corner region. Immediately downstream of the step, the forward moving fluid gently expands over a slightly concave, what one might call a backward-facing ramp of stagnant fluid. This ramp zone is characterized by the concave streaks, which are regions of heavy concentration of seed particles. In each photograph, the outermost line represents the demarcation between the moving fluid and the non-moving fluid where large numbers of particles are deposited. Each of the additional streaks beneath this top layer represents the interface between the moving and nonmoving fluids for a previous (smaller) Reynolds number. The visualizations for a range of Reynolds numbers were carried out in a single experiment starting with the smallest Reynolds number and then gradually increasing this parameter. However, the steady state is established at each Reynolds number by running the system for several minutes, which, in turn, results in the formation of a new line of seed particles at the flow interface. As the Reynolds number increases, the size of the stagnant zone increases in the axial direction. When the Reynolds number reaches Re = 17.4, the fluid yields throughout the expansion step region and a recirculating flow is established at the corner (Figs. 9(*d*) and (*e*)). Figures 9(*d*) and 9(*e*) also show an interesting reattachment phenomenon. The reattachment of the flow is not defined by a single point but by a region of stagnant fluid, which protrudes a certain height into the flow from the wall. Within this three-dimensional zone of stagnant fluid, the overall stress distribution falls below a critical value and the flow does not sustain shearing. Lipscomb and Denn (1994) theorized that in complex flows of yield stress fluids no "stagnant zones" could exist. Obviously, the present experimental results contradict that claim and also validate the results of the present computational study that show the possibility of existence of such stagnant zones.

The plots of the computationally obtained effective viscosity are presented in Fig. 10. These computations accurately predict the different flow zones described above. For the two smallest Reynolds numbers of 1.83 and 12.38, the concave stagnant zone in the expansion corner is clearly evident. The outer edge of the ramp is outlined by the very large gradients of μ_{eff}. Inside this ramp, μ_{eff} assumes the maximum allowable (threshold) level indicating flow stagnation. For Re = 30.9 and 58.7, μ_{eff} is finite in this region. For these higher Reynolds numbers, the three-dimensional zone of stagnant fluid in the vicinity of flow reattachment is also evident in the plots of effective viscosity.

Conclusions

The laminar flow of a nonlinear viscoplastic fluid through an axisymmetric expansion was studied experimentally, using the PIV technique, and computationally, by solving the fully-elliptic governing equations. From the extensive velocity data gathered at a fixed Hedstrom number of 1.65 and various Reynolds numbers, several features of the non-Newtonian flow were observed. As expected, plug zones form in the fully developed flow regions, whose radial extent is a function of the Reynolds number. The approach of the flow toward a fully developed state is slower for larger Reynolds numbers.

For small Reynolds numbers of the non-Newtonian flow (approximately, Re $<$ 17), both the experiments (both PIV measurements and flow visualizations) and the computations show that there is no flow recirculation in the expansion corner. Here, the fluid is stagnant in a zone, which has the shape of an annular ramp. In effect, the moving fluid closer to the centerline gently expands over this ramp without any reversals. The surface of this ramp of nonmoving fluid is slightly concave. In contrast, for the non-Newtonian case of Re = 17.4 and higher, a recirculating flow region does exist. However, this recirculation is significantly weaker with smaller magnitudes of negative velocities than those for the corresponding Newtonian flow. Finally, at these larger Reynolds numbers where there is flow recirculation, the reattachment location is not characterized by a single point but by a

three-dimensional region of stagnant fluid protruding from the wall, again, caused by the small local strain rates which fall below the yield stress value of the fluid.

Acknowledgments

This project was partially funded by Exxon Education Foundation. The authors gratefully acknowledge this support.

References

Abdul-Karem, T., Binding, D.M., and Sindelar, M., 1993 "Contraction and Expansion Flows of Non-Newtonian Fluids," *Composites Manufacturing,* Vol. 2, pp. 109–116.

Chen, S.S., Fan, L.T., and Hwang, C.L., 1970, "Entrance Region of the Bingham Fluid in a Circular Pipe," *AIChE Journal,* Vol. 16, No. 2, pp. 293–299.

Hammad, K.J., 1997, "Experimental and Computational Study of Laminar Axisymmetric Recirculating Flows of Newtonian and Viscoplastic Non-Newtonian Fluids," Ph.D. dissertation, Polytechnic University, New York.

Lipscomb, G.G. and Denn, M.M., 1984, "Flow of a Bingham Fluid in Complex Geometries," *Journal of Non-Newtonian Fluid Mechanics,* Vol. 14, pp. 337–346.

O'Donovan, E.J. and Tanner, R.I., 1984, "Numerical Study of the Bingham Squeeze Film Problem," *Journal of Non-Newtonian Fluid Mechanics,* Vol. 15, pp. 75–83.

Park, J.T., Mannheimer, R.J., Grimley, T.A., and Morrow, T., 1989, "Pipe Flow Measurements of a Transparent Non-Newtonian Slurry," ASME JOURNAL OF FLUIDS ENGINEERING, Vol. 111, pp. 331–336.

Soto, R.J., and Shah, V.L., 1976, "Entrance Flow of a Yield-Power Law Fluid," *Applied Science Research,* Vol. 32, pp. 73–85.

Townsend, P., and Walters, K., 1993, "Expansion Flows of Non-Newtonian Liquids," *Chemical Engineering Science,* Vol. 49, pp. 749–763.

Vradis, G.C., and Ötügen, M.V., 1997, "The Axisymmetric Sudden Expansion Flow of a Non-Newtonian Viscoplastic Fluid", ASME JOURNAL OF FLUIDS ENGINEERING, Vol. 119, pp. 193–200.

Vradis, G.C., Dougher, J., and Kumar, S., 1993, "Entrance Pipe and Heat Transfer for a Bingham Plastic," *International Journal of Heat and Mass Transfer,* Vol. 36, pp. 543–552.

Vradis, G., and Hammad, K.J., 1998, "Strongly Coupled Block-Implicit Solution Technique for Non-Newtonian Convective Heat Transfer Problems," *Numerical Heat Transfer,* Part B, Vol. 33, pp.79–97.

Wildman, D.J., Ekmann, J.M., Kadambi, J.R., and Chen, R.C.,1992, "Study of Flow Properties of Slurries Using the Refractive Index Matching Technique and LDV," *Powder Technology,* Vol. 73, pp. 211–218.

Wilson, K.C., and Thomas, A.D., 1985, "A New Analysis of the Turbulent Flow of Non-Newtonian Fluids," *The Canadian Journal of Chemical Engineering,* Vol. 63, Aug. 1985.

Haim Kalman
Pearlstone Center for Aeronautical Engineering Studies,
Department of Mechanical Engineering,
Ben-Gurion University of the Negev,
P.O. Box 653,
Beer-Sheva, 84105, Israel

Amos Ullmann
Department of Fluid Mechanics and Heat Transfer,
The Faculty of Engineering,
Tel Aviv University,
Tel Aviv, 69978, Israel
e-mail: ullmann@eng.tau.ac.il

Experimental Analysis of Bubble Shapes During Condensation in Miscible and Immiscible Liquids

The initial volume of a condensing bubble released from an orifice and the shape oscillations of the bubble during the collapse process were studied. Results of a large number of original experiments of bubbles condensing in miscible and immiscible liquids were analyzed to evaluate the initial volume, the instantaneous shape, and the average aspect-ratio of the bubbles. The results were compared to common empirical correlations that were originally developed to evaluate these parameters for noncondensing bubbles. It is demonstrated that such correlations can satisfactorily predict the initial volume of condensing bubbles and their mean aspect ratio throughout the collapse process.

1 Introduction

In the present work two important parameters having a major effect on the rate of bubble condensation in direct contact heat exchangers were studied: the initial volume of the bubble following detachment and the instantaneous shape of the bubble during the collapse process. The focus in the present work is on the behavior of a solitary bubble of organic vapor released into a still media of sub-cooled liquid.

The volume of the bubble has a major effect on the bubble rising velocity and consequently on the shape of the bubble. The volume (and the interfacial area), the velocity, the shape and the shape oscillation of the rising bubble govern the interfacial heat and mass transfer rates which, in turn, determine the collapse rate of the bubble. Accurate prediction of the bubble collapsing rate is very important for designing direct-contact condensers. Such condensers are utilized, for example, for power production from low grade thermal energy sources (solar ponds, brines and geothermal sources etc.) (Kreith and Boehm, 1988) and for immersion cooling of electronic equipment (Kraus and Bar-Cohen, 1983; Letan, 1990).

The direct contact condensation and the collapse rates of a single bubble and bubble swarm were intensively studied theoretically and experimentally (Wittek and Chao, 1967; Isenberg and Sideman, 1970; Jacobs and Major, 1982; Kalman et al., 1986; Lerner et al., 1987; Kalman and Letan, 1987). These studies suggested various phenomenological models for the prediction of the instantaneous velocity and the collapse rate of condensing bubbles. However, in all of the aforementioned models the initial radiuses of the bubbles were arbitrarily chosen as a free parameter or were taken from experimental data. In addition, the bubbles were assumed to be spherical and the effects of the bubble shape oscillations were neglected. The ability to predict these parameters can considerably improve the performance of condensation rate models. Ullmann and Letan (1988 and 1989a), for example, demonstrated that taking into account the shape deformation of bubbles can improve the prediction of the instantaneous velocity of constant volume and evaporating bubbles.

An extensive literature survey revealed no previous studies which suggest any model or correlation for predicting either the initial volume of condensing bubbles or the instantaneous shape of the bubbles during the collapse process. In contrast, these subjects were extensively studied for the case of noncondensing bubbles. Comprehensive reviews of works in this area are given in Clift et al. (1978) and Cheremisinoff (1986). Despite their practical importance, the calculation of these values in advance remains essentially an unsolved problem and rigorous theoretical solutions are absent. Consequently, empirical or semi-empirical relationships are usually employed for the calculation of the bubble volume, shape and velocity. Some of these works will be discussed later.

In the present work, a large number of experiments of direct-contact condensation of a single bubble in both miscible and immiscible liquids are analyzed. The initial volume of the condensing bubbles and their instantaneous shape are studied, and the ability of standard correlations of non-condensing bubbles to predict these parameters is tested.

2 Description of the Experiments

Two cases of direct-contact condensation are described and discussed in the present study: the condensation of organic vapors in immiscible liquid (water) and the condensation of freon-113 in miscible liquid (freon-113). The freon-113, hexane and pentane (from "Aldrich") were "HPLC grade" and used without any further treatment. The water was double distilled.

The condensation experiments were conducted in a vertical square column, 10 × 10 cm in cross-section, and 60 cm high (Kalman et al., 1986). The walls of the column were made of glass plates. The column was filled with water or freon-113 and was open to the atmosphere. The temperature of the liquid in the column, T_∞, was maintained below the saturation temperature of the vapor, T_s, by a thermostatic controller. The temperature difference, $\Delta T = T_s - T_\infty$, provided the driving force for the condensation and collapse of the released bubble. At the present experiments, the temperature differences studied were in the range of 2.4 to 6.5°C. The temperatures were measured by iron-constantan thermocouples.

A vapor generator, made of a brass cylinder, was installed beneath the glass column. The generator was filled with water that was electrically heated, and thermostatically controlled. A copper tube passed through the vapor generator and was connected to a nozzle, 3 mm in diameter, which was placed at the center of the column floor. The flow rate of the evaporating liquid through the copper tube was regulated by a micrometric-valve that enabled the control of the bubble release frequency. The release frequency was kept low enough (1–6.5 bubbles per second) to minimize the

Contributed by the Fluids Engineering Division for publication in the JOURNAL OF FLUIDS ENGINEERING. Manuscript received by the Fluids Engineering Division October 24, 1997; revised manuscript received March 12, 1999. Associate Technical Editor: M. Sommerfeld.

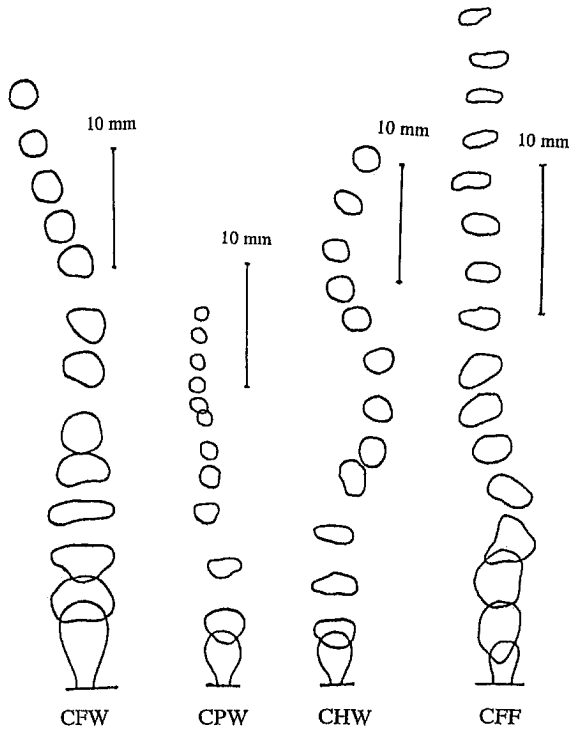

Fig. 1 Screen tracing of a video-taped collapse of bubbles of four systems: (*a*) freon-113/water; (*b*) pentane/water; (*c*) hexane/water; and (*d*) freon-113/freon-113

mutual effects of the bubbles, i.e., the effects of the leading bubble wake on the dynamics of the trailing bubble. According to Lerner and Leatn (1985), such effects start to be dominant only at higher release frequencies, i.e., $f > 8$, or even higher (Moalem et al., 1973).

The column was back-illuminated and the bubble collapse process was videotaped by using a Sony Rotary Shutter CCD, model RSC-1050. The pictures were recorded on a magnetic disk, and then projected on a monitor at the rate of 60 frames per second. The combination of the rotary shutter camera and the magnetic disk enabled us to halt a steady and clear picture of each frame on the screen and to make measurements of the bubble diameter, aspect-ratio and position. The time lapse between succeeding frames was measured by a video timer VTG-33 and was used to calculate the collapse rate and the bubble rising velocity.

2.1 Screen-Tracing. The videotaped collapse experiments were also screen-traced. The screen-tracings of a representative bubble of each of the following systems: freon-113/water, pentane/water, hexane/water and freon-113/freon-113 are shown in Fig. 1. The time lapse between two images is $\frac{1}{60}$ second.

The screen-tracing provides qualitative information on the behavior of the condensing bubble which includes the instantaneous size, the shape, and the vertical and horizontal location of the bubble. In addition, the instantaneous mean radius, aspect-ratio and height from the nozzle can be measured directly from the screen-tracing.

The instantaneous radius of each bubble was calculated using the measured horizontal and vertical diameters of the magnified bubble image on the screen-tracing. Assuming horizontal symmetry and ellipsoidal shape, the equivalent bubble radius was taken as

$$R = \frac{(D_H^2 D_V)^{1/3}}{2K_M} \tag{1}$$

where K_M is the magnification factor.

Figure 1 shows the behavior of the collapsing bubble from the moment it is detached from the orifice until termination of the

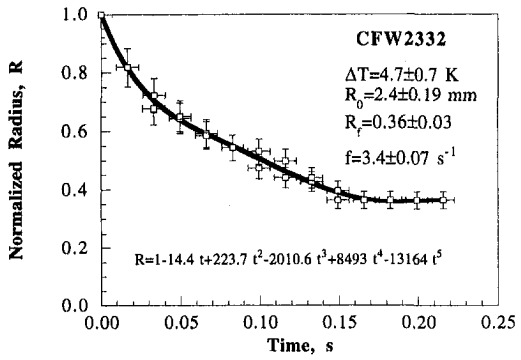

Fig. 2 Polynomial fit of the experimental instantaneous radius of a freon-113 bubble condensing in water

condensation process. Condensation is not completed at the end of the collapse process as a result of the presence of noncondensibles in the vapor. As discussed in previous works (Jacobs and Major, 1982; Ullmann and Letan, 1989b), the presence of noncondensibles reduces the apparent saturation temperature, and consequently, the temperature driving force for condensation. During the condensation process, the fraction of the noncondensibles increases and the collapse of the bubble is stopped when the apparent saturation temperature approaches the temperature of the surrounding liquid. This happens before the condensation process is completed. As shown in Fig. 1, the detachment of the bubble results in its strong deformation that is followed by a series of shape oscillations. The bubble oscillates between oblate and prolate shapes. As the collapse process in the water proceeds, the bubble gradually becomes spherical as a result of the decrease in its radius of curvature and the consequent increase of surface-tension forces (Figs. 1(*a, b,* and *c*)). For condensation in miscible liquids (Fig. 1(*d*)), the bubble remains oblate due to the low surface-tension of the organic liquid.

2.2 Condensation Rate and Velocity. Many experiments of bubbles condensing in miscible and immiscible liquids have been conducted and analyzed (Kalman et al., 1986; Lerner et al., 1987; Kalman and Letan, 1987). Although in these works a theoretical model was developed to predict the instantaneous bubble radius and velocity, a polynomial fit of the experimental results is used in the present paper. This method was chosen for simplicity, and in order to separate the present analysis of the bubble shape from any other effects which could have been imposed by the theoretical model. Thus, the experimental measurements are described by fifth and fourth order polynoms for the instantaneous radius and height, respectively. Such a polynomial fit for a representative experiment is shown in Figs. 2 and 3. The instantaneous velocity of the bubble is calculated by deriving the fourth order polynom.

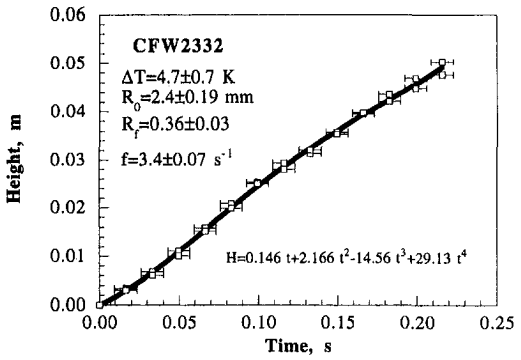

Fig. 3 Polynomial fit of the experimental instantaneous height of a freon-113 bubble condensing in water

2.3 Uncertainty Analysis. The uncertainty in measurements corresponds to timing, bubble size, and bubble position. The uncertainties of the non-dimensional groups, that will be presented later, correspond also to the properties of the vapors and liquids. For timing, the bubbles were videotaped at a frequency of 60 s^{-1}. The images projected on the screen were timed, and the time was digitally displayed with an accuracy of 0.01 s. The time lapse between two consecutive images corresponded to $\frac{1}{60} = 0.0167$ s. To overcome this difficulty, the evaluation of the time lapse was done by averaging the time lapses of at least ten images. This provides an accuracy of 0.001 s. However, since the time should be related to the moment of bubble detachment, which could occur between two following images, the time uncertainty is set to be $\Delta t = \pm 0.007$ s.

To determine the equivalent radius of the bubble, the horizontal and vertical diameters of the bubble were measured from the magnified bubble images projected on the screen (see Eq. (1)). The magnification factor was at least four. The error corresponded to the length measurements on the screen was about 0.5 mm, i.e., less than 0.12 mm of the actual diameter, or 0.06 mm of the actual radius. For a representative bubble with an initial radius of 2 mm, the uncertainty in a non-dimensional form is therefore ±3% at the beginning of the collapse. The uncertainty is increased to ±8% at the end of the collapse when the bubble attains its minimum size. Another uncertainty could be related to the difficulties in locating the bubble's interface (bubble's edge). In addition, an uncertainty should be considered to compensate for the assumption of ellipsoidal bubble shape in the calculation of the equivalent bubble radius (Eq. (1)). However, as can be seen in Fig. 1 and is further discussed below, the deviation from ellipsoidal shape is taking place mainly at the beginning of the collapse right after the detachment. Therefore, the total radius uncertainty is increased and taken as $\Delta R/R = \pm 8\%$ throughout the collapse.

For the position of the bubble, the height of the center-of-volume of any bubble along its path was measured from the center-of-volume of the initial bubble. The error in length measurements is again 0.5 mm on the enlarged scale, and 0.12 mm on the actual scale. Since it was difficult to locate the exact position of the initial bubble, the height uncertainty is extended and taken as $\Delta h = \pm 0.44$ mm.

The error bars of the time, non-dimensional radius and height are shown in Figs. 2 and 3. The bubble's instantaneous velocity is calculated by deriving the function obtained by a polynomial fit of the experimental bubble's height. The velocity uncertainty is accordingly calculated to be $\Delta u/u = \pm 5\%$.

3 Bubble Formation—The Volume of the Detached Bubble

Two stages of bubble formation on the orifice were observed (not shown in the screen tracing of Fig. 1). During the first stage, the bubble expands while its base remains attached to the orifice. During the second stage, a neck is created while the bubble begins to lift-off. Bubble necking is shown in Figs. 1(*a, b, c,* and *d*). The bubble detaches from the orifice as the buoyancy and inertia forces of the injected vapor overcome both the surface-tension at the necking and the drag forces acting on the lifting bubble. Similar stages of detachment for the formation of non-condensing bubbles have been observed and described by previous investigators. It is therefore reasonable to assume that, existing models originally developed for non-condensing bubbles can evaluate the volume of the detached condensing bubble too. This is particularly true for cases in which condensation during the bubble formation stage is negligible.

Previous experimental and theoretical works can be classified into three bubble formation conditions: constant-flow, constant-pressure, and an intermediate condition. In the present experiments, the hydrocarbon liquid was enforced to an evaporating chamber through a micrometric valve at a constant flow rate. The pressure of the vapor was increased due to evaporation, and the vapor was forced to exit the orifice as a sequence of bubbles. Since the liquid flow rate and the heat input to the evaporating chamber were kept constant, it is assumed that the bubble formation has a constant flow characteristics. In addition, the evaporating chamber and the orifice were connected with a relatively long capillary tube that caused a high pressure-drop restriction. Clift et al. (1978) have suggested that in such cases, the pressure fluctuations due to the formation of the bubbles are much smaller than the pressure drop in the capillary so the gas flow rate can be taken as constant.

Many of the mechanistic models proposed to describe bubble formation are based on a sequence of events suggested by photographic observation (Clift et al., 1978; Tsuge, 1986). These models apply a force balance for predicting one or more stages in bubble growth. For a constant vapor flow rate, the volume of the detached bubble, V, is dominated by the following variables: the vapor flow rate, Q, the surrounding liquid density, ρ, and viscosity, μ, the surface tension, σ, the internal diameter of the orifice, d_{or}, and the gravitational acceleration, g. For most practical purposes the bubble viscosity and density are much smaller than those of the surrounding liquid, $\mu_b \ll \mu$ and $\rho_b \ll \rho$, and therefore can be omitted.

For very low vapor flow-rates and low viscosity systems the volume of the detached bubble can be obtained by assuming that the bubble is spherical and performing a balance between the buoyancy and surface tension forces (Clift et al., 1978; Tsuge, 1986). Such a force balance yields

$$V' = V\frac{g\Delta\rho}{\sigma d_{or}} = \psi\pi \tag{2}$$

where V' is the dimensionless bubble volume and $\Delta\rho$ the density difference between the surrounding liquid and the bubble (for $\rho \gg \rho_b$, $\Delta\rho$ is taken as ρ). In Eq. (2) the mass balance is corrected by employing the Harkins-Brown correction factor, ψ (Clift et al., 1978). This correction factor accounts for the dispersed phase fluid retained at the orifice when detachment occurs, and is given below as:

$$\psi = \left[0.92878 + 0.87638\,\frac{d_{or}}{V^{1/3}} - 0.261\left(\frac{d_{or}}{V^{1/3}}\right)^2\right]^{-1} \qquad \left(0.6 < \frac{d_{or}}{V^{1/3}} < 2.4\right) \tag{3}$$

$$\psi = 1.0 - 0.66023\,\frac{d_{or}}{V^{1/3}} + 0.33936\left(\frac{d_{or}}{V^{1/3}}\right)^2 \qquad \left(0 \le \frac{d_{or}}{V^{1/3}} \le 0.6\right) \tag{4}$$

For higher flow rates or systems with a low surface tension, Davidson and Schuler (1960) have developed simple equations based on a one-stage model. The surface tension is neglected and for systems of low viscosity the bubble volume as a function of the flow rate, Q, is given as:

$$V = 1.378Q^{1.2}g^{-0.6} \tag{5}$$

or in a nondimensional form,

$$V' = 1.378(Q')^{1.2} \tag{6}$$

where

$$Q' = \left(\frac{\rho}{d_{or}\sigma}\right)^{5/6} g^{1/3}Q \tag{7}$$

For viscous liquids (high μ) and intermediate Q', Davidson and Schuler (1960) developed the following equation

$$V = 6.484\left(\frac{Q\mu}{\rho g}\right)^{0.75} \tag{8}$$

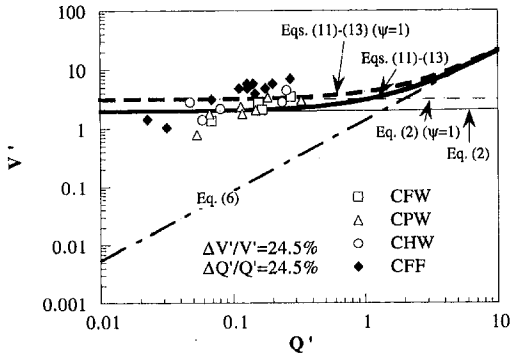

Fig. 4 Dimensionless initial volume of condensing bubbles as a function of dimensionless gas flow rate, a comparison of experimental results with correlations of non-condensing bubbles

or in nondimensional form,

$$V' = 6.484(Q'\mu')^{0.75} \tag{9}$$

where μ' is a dimensionless viscosity defined as:

$$\mu' = \frac{\mu}{\sqrt{\rho d_{or}\sigma}} \tag{10}$$

Ruff (1972) developed a semiempirical model which approaches Eqs. (2), (6), and (9) at the appropriate limits. Ruff's model belongs to the group of "two-stage models" in which the bubble formation is assumed to take place in two successive stages: the expansion stage and the detachment stage.

According to Ruff's model, the volume of the detached bubble is the sum of the volumes achieved in the two formation stages,

$$V' = V_1' + V_2' \tag{11}$$

The bubble volume obtained in the first stage is predicted from a force balance:

$$V_1' - 0.0578(V_1')^{-2/3}(Q')^2 - 2.417(V_1')^{-1/3}Q'\mu' - 0.204Q'\sqrt{\mu'Q'/V_1'} = \pi\psi \tag{12}$$

where the first term arises from buoyancy, the second from inertia and drag, the third and fourth from drag, and the term on the right-hand side from surface tension. The right-hand side is multiplied by the Harkins-Brown correction factor as an improvement of Ruff's original model as proposed by Garrett (1993). When the bubble volume exceeds V_1' the buoyancy force predominates and the bubble starts to move away from the orifice. During this stage, gas is supplied to the bubble through a neck and the bubble continues to grow for a finite period of time. The volume added in the second stage was correlated empirically by Ruff as

$$V_2' = (Q')^{1.2} + 4.0(Q'\mu')^{3/4} \tag{13}$$

Two similar stages of bubble formation were also observed in the present experiments of condensing bubbles. Therefore, a comparison between the experimental results and Ruff's model is in order. The experimental results, presented as the dimensionless bubble volume as a function of the dimensionless flow rate Q', are compared to Ruff's model, Eqs. (11)–(13), with and without the Harkins correction factor (Eqs. (3) or (4)) in Fig. 4. Also shown in Fig. 4 are lines corresponding to the single stage models, Eqs. (2) and (6). These simplified equations may be viewed as limiting cases for low and high vapor flow rates, respectively. Equation (9) is applicable only for high viscosity systems, $\mu' > 4$, (Clift et al., 1978) and therefore is not included in Fig. 4.

The experimental dimensionless bubble volume, V', was calculated by using Eq. (2) and the initial radius, Ro

$$V' = V\frac{g\Delta\rho}{\sigma d_{or}} = \frac{4}{3}\pi R_0^3\frac{g\Delta\rho}{\sigma d_{or}} \tag{14}$$

The uncertainty for the initial radius is 8% (see section 2.3), for the density ±1%, for the orifice diameter ±0.1% and for the surface tension ±5%. By an uncertainty calculation, the combined uncertainty of the dimensionless bubble volume was found to be $\Delta V'/V' = \pm 24.5\%$.

The experimental dimensionless flow rate, Q', was calculated by using Eq. (7), the initial radius and injection frequency, f

$$Q' = \left(\frac{\rho}{d_{or}\sigma}\right)^{5/6} g^{1/3}\frac{4}{3}\pi R_0^3 f \tag{15}$$

The uncertainty of the average injection frequency is assumed to be ±2% (the frequency was calculated by measuring the time interval for at least ten bubbles). This leads to an uncertainty of the dimensionless flow rate of $\Delta Q'/Q' = \pm 24.5\%$. The uncertainties of both the dimensionless bubble volume and flow rate are similar since they are mainly affected by the uncertainty of the initial radius that appears in the third power at their definitions.

Although, Ruff's equations agree (within ±15%) with most data appearing in the literature (Clift et al., 1978) it agrees less with the present experiments. Most of the present experimental bubble-volumes of the organic-liquids/water systems are located between the two lines of Ruff's model (with and without the correction factor). Some of the experimental points, particularly in the lower flow rate range, are below the values predicted by Ruff's model. This is probably due to the condensation of the vapor that takes place during the bubble formation stage in the present experiments, while Ruff's and other models were developed for bubble formation in isothermal systems. The effect of condensation on the volume of the released bubble is more pronounced in low vapor flow rates in which the bubble formation takes a longer time.

It should be pointed out, however, that some of the deviations from the predicted values are not real and could be attributed to the uncertainty in the determination of the initial bubble volume in the present experiments. The real initial bubble volume has to be measured exactly at the detachment. However, with the video system that recorded 60 frames per second it was very difficult to record the bubbles precisely at the moment of detachment. Most of the bubble images were either of bubbles that are still connected to the orifice or of bubbles that already detached. The initial bubble volumes reported here were measured from the first image recorded after the detachment. During the short time elapsed from the detachment (less than $\frac{1}{60}$ s) the bubbles were slightly condensed and therefore the reported values are smaller than the real ones. Indeed, the lowest bubble volumes shown in Fig. 4 are measured for the highest temperature differences. Obviously, the higher the temperature difference, the more noticeable is the condensation effect.

It can be therefore concluded that in the absence of any other validated theory, Eqs. (2) and (11)–(13) provide a reasonable prediction of the initial volumes of condensing bubbles. This in particular refers to the range of the present experimental conditions, i.e., vapor flow rates of: $0.07 < Q' < 0.3$ and temperature difference of: $\Delta T < 6.5$.

4 Bubble Shape During Condensation

Bubbles and drops tend to deform when subject to external fluid fields. Their shape is dictated by the balance between the interfacial tension and the viscous and inertia forces on the fluid-fluid interface. It is convenient to represent the shape of the bubbles and drops in terms of the aspect-ratio, E, which is defined as the ratio between the maximum vertical dimension and the maximum horizontal dimension. Small and medium bubbles and drops in free rise in infinite media under the influence of gravity generally have either spherical ($E \cong 1$) or ellipsoidal ($E < 1$) shapes. The spherical shape is typical of cases when the interfacial tension and/or viscous forces are dominant.

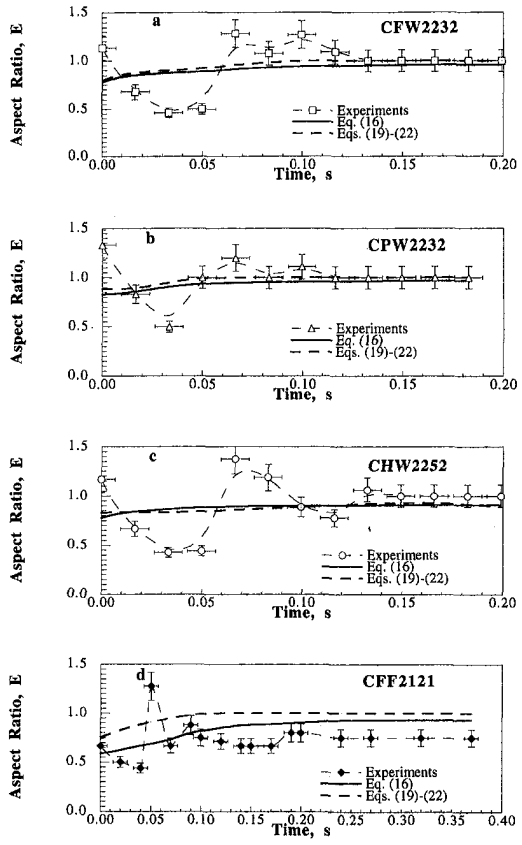

Fig. 5 Instantaneous aspect-ratio of condensing bubbles; a comparison of experimental results with correlations of noncondensing bubbles for four systems: (*a*) freon-113/water; (*b*) pentane/water; (*c*) hexane/water; and (*d*) freon-113/freon-113

Bubbles and drops may also undergo periodic shape oscillations during their rise. There are two main reasons for the onset of oscillations: the detachment of the bubble or drop from the orifice right after formation, and the vortex shedding during the late stages of rise. Most of the bubbles and drops are affected according to the first reason, while the second reason is common for ellipsoidal bubbles and drops with Reynolds numbers above 200.

The screen tracings of Fig. 1 show that the condensing bubbles also undergo an oscillatory shape deformation which starts right after detachment and continues during the collapse process. The bubble oscillates between an oblate shape (even disk shape in Fig. 1(*a*)) and a prolate shape. As the collapse process in the water proceeds the bubble gradually becomes spherical as a result of the decrease in its radius of curvature and the consequent increase of surface tension forces (Figs. 1(*a, b,* and *c*). During this stage, the shape oscillations cease and the wake shedding results only in a zig-zag or spiral trajectory of the rising bubble. For condensation in miscible liquids (Fig. 1(*d*)), due to the lower surface tension of the organic liquid, the final shape of the bubble is ellipsoidal with a low amplitude wobbling of the surface. The shape oscillations in terms of the aspect-ratio versus time for one representative experiment of each of the systems studied are shown in Figs. 5(*a–d*). The uncertainty of the aspect ratio was calculated to be $\Delta E/E = \pm 11.3\%$ and is shown by error bars in Fig. 5.

The major shape deformation of the bubbles occurs immediately after detachment. As we discussed above, the bubble is detached from the orifice as the buoyancy and inertia forces of the injected vapor overcome the surface-tension and drag forces. The detached bubble tends to undertake the least possible surface area. This results in a motion of the neck toward and sometimes even into the bubble (see Fig. 1(*a*)). Liquid from the surroundings is thereby entrained by the fast movement of the neck. It is well documented (Rabiger and Voelpohl, 1986) that for high gas flow-rates (above 70 l/h), the acceleration of this liquid is high enough to transport it beyond the upper contour of the bubble and to cause disintegration of the primary bubble. We did not observe such a phenomenon in our experiments since the vapor flow-rate was much lower (less than 2 l/h). However, the induced motion of the liquid was sufficient to cause a pronounced deformation of the detached bubble followed by a series of shape oscillations.

The initial large amplitude deformation of the condensing bubble decays after a few cycles (see Figs. 5(*a–d*)) as a result of the bridling effects of the surface-tension and the viscous forces. While the viscosity of the liquid remains constant during the collapse process, the effect of the surface-tension increases as the collapse process proceeds and the radius of the bubble decreases. As demonstrated in Figs. 5(*a–d*), the effect of the bridling forces is also manifested in the number of oscillation cycles until a steady shape is reached. The number of cycles varies for different systems. For example, the pentane/water system has the highest surface tension and viscosity among the organic-solvent/water systems. For this system, following the initial large decrease of the aspect-ratio of the collapsing bubble, the final spherical shape is obtained after a single low amplitude oscillating cycle (Fig. 5(*b*)). On the other hand, the hexane/water system has the lowest surface tension and viscosity (highest water temperature) and therefore an additional oscillation cycle takes place before the final shape is obtained (Fig. 5(*c*)). This effect is more pronounced in the case of the freon/freon system. This system has a similar viscosity but a much lower surface-tension and consequently the highest number of oscillations cycles (Fig. 5(*d*)). Further investigation and additional experiments are needed for characterizing the fluctuations and the effect of the surface tension.

While it is difficult to predict the instantaneous shape of rising bubbles, several attempts have been made to correlate the experimental data of the mean aspect-ratio, $\bar{E}$, of constant volume bubbles at their terminal velocities. For low Morton numbers, Wellek et al. (1966) provided a single equation for the mean aspect-ratio as a function of the Eotvos number:

$$\bar{E} = \frac{1}{1 + 0.163E_0} \quad (\mathrm{Eo} < 40,\ \mathrm{M} < 10^{-6}) \tag{16}$$

where the Morton number, M, is defined as:

$$\mathrm{M} = \frac{g\mu^4(\rho - \rho_b)}{\rho^2\sigma^3} \tag{17}$$

and the Eotvos number, Eo, as:

$$\mathrm{Eo} = \frac{g(\rho - \rho_b)(2R)^2}{\sigma} \tag{18}$$

An alternative correlation obtained by Tadaki and Maeda and extended by Vakhrushev and Efremov expresses the mean aspect-ratio of air bubbles as a function of the following dimensionless group (Clift et al., 1978):

$$\mathrm{Ta} = \mathrm{Re}\,\mathrm{M}^{0.23} \tag{19}$$

to give:

$$\bar{E} = 1 \quad (\mathrm{Ta} \le 1) \tag{20}$$

$$\bar{E} = [0.81 + 0.206 \tanh\{2(0.8 - \log_{10}\mathrm{Ta})\}]^3 \quad (1 \le \mathrm{Ta} \le 39.8) \tag{21}$$

$$\bar{E} = 0.24 \quad (\mathrm{Ta} \ge 39.8) \tag{22}$$

The above correlations are plotted in Figs. 5(*a–d*) together with the experimental instantaneous aspect-ratio of the condensing bubbles. In the above equations we used the instantaneous radius and velocity of the bubbles (see the discussion in Section 2.2). The average bubble density of the bubbles also varies during the

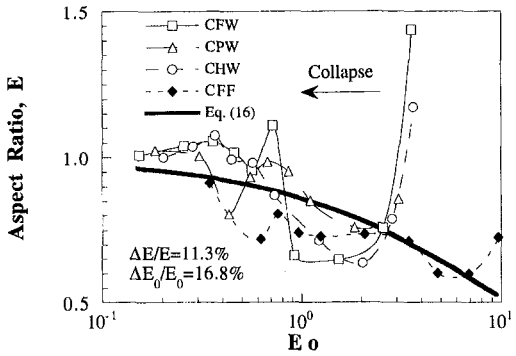

Fig. 6 Aspect-ratio as a function of Eo of a large number of experimental results; a comparison with the correlation of Wellek et al., Eq. (16)

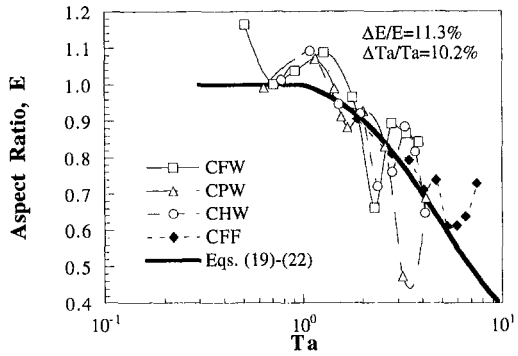

Fig. 7 Aspect-ratio as a function of Ta of a large number of experimental results; a comparison with the correlation of Vakhrushev and Efremove, Eqs. (19)–(22)

collapse process. As the condensation process proceeds the bubble contains increasing amounts of condensed liquid and decreasing amounts of vapor. Therefore, the average bubble density in Eqs. (17) and (18) is defined as:

$$\rho_b = \frac{\rho_v}{\bar{R}^3} \tag{23}$$

for condensation in immiscible liquids and $\rho_b = \rho_v$ for condensation in miscible liquids. $\bar{R}$ is the normalized radius, which is the ratio between the instantaneous radius, R, and the initial radius R_0.

Figures 5(a–d) show that for condensation of bubbles in immiscible liquids, Eqs. (16) and (21) give similar predictions of the mean aspect-ratio. Although these correlations were originally obtained from experiments for constant volume bubbles at their terminal velocities, they give a good prediction of the average aspect-ratio of the condensing bubbles. Furthermore, the mean aspect-ratio is well predicted by the correlations even during the initial stages when the detachment of the bubble from the orifice causes high amplitude oscillations of the bubble shape. Some discrepancies between Eqs. (16) and (21) appear in Fig. 5(d) for condensation of the freon-113 in its subcooled liquid. In this case, Eq. (16) provides a better prediction for the average aspect-ratio of the condensing bubbles but gives some higher aspect-ratios than the values obtained in the experiments. The discrepancy between the correlation and the experimental values may be attributed to an inaccuracy in the estimated surface-tension of the freon/freon system.

In Fig. 6, Eq. (16) is compared to a large number of experimental results. The experimental aspect-ratios in this figure are an average of 148 measurements for CFW, 191 for CPW, 190 for CHW and 424 for CFF. The wide spread is due to the oscillations. However, the oscillations approximate the values predicted by Eq. (16), particularly in the low Eo range. Condensation proceeds from large Eo numbers to the smaller ones. A similar comparison between experimental results and Eq. (21) is presented in Fig. 7. By an uncertainty analysis, the following uncertainties were calculated: Δ Eo/Eo = $\pm$16.8%, Δ Re/Re = $\pm$9.85, Δ M/M = $\pm$15.7% and Δ Ta/Ta = $\pm$10.2%.

5 Regime Diagram

Grace, Clift, and coworkers have developed a "regime diagram" to describe the behavior of bubbles and drops rising or falling freely in infinite media (Clift et al., 1978; Grace and Wairegi, 1986). In this diagram, the Reynolds number, Re, of the fluid particle is plotted against the particle Eotvos number. A family of lines, each characterized by a constant value of the fluid properties group, the Morton number (independent of the bubble size or velocity) is also plotted in the original diagram. Since Re is the only group that contains the terminal velocity, the regime diagram may be used to estimate the terminal velocity of the fluid particle. However, as stated by Grace and Wairegi (1986), more accurate methods have to be used to predict the velocity, and, therefore, the main use of the diagram is to predict the shape regime.

The experimental measurements of the condensing bubbles are plotted as Re against Eo in the classical regime diagram (Fig. 8). As can be seen, the regime diagram gives a good prediction of the bubble shape during the condensation process. The bubbles are at the wobbling ellipsoidal shape range at the initial stages of the condensation (large Re and Eo), even without considering the oscillation effect due to the detachment. At the final stages of condensation, the bubbles become spherical for condensation in immiscible liquids and remain ellipsoidal for most of the experiments when condensation takes place in a miscible liquid.

Since the original regime diagram has three parameters, Re, Eo, and M, while the experimental points are plotted using only Eo and Re, one can read the M number from Fig. 8. The logarithms of M, according to Fig. 8, are in the range of -10 to -12, where the highest M is of the freon/freon system (log M = -10) and the lowest is of the hexane/water system. The actual M numbers of the different systems are plotted in Fig. 9. The slight discrepancies between the actual M numbers and the values presented in Fig. 8 result in part from an inaccurate prediction of the terminal velocity as incorporated in the original regime diagram. In addition, the original regime diagram was obtained for constant volume fluid particles at their terminal velocities and the present experiments are for condensing bubbles at a time dependent motion.

It is also important to emphasize that for constant volume fluid particles, the M number is constant since it represents only the fluid properties. In contrast, for bubbles condensing in an immiscible liquid, M varies during condensation as a result of the change in the average density of the bubble (Eq. (23)). Variation in M

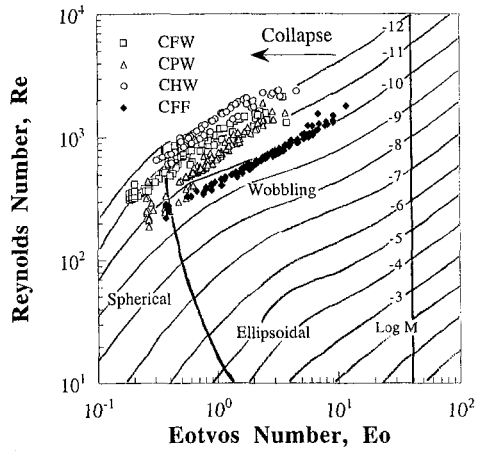

Fig. 8 Presentation of the experimental results of bubble collapse on the regime diagram of Grace et al. (1986)

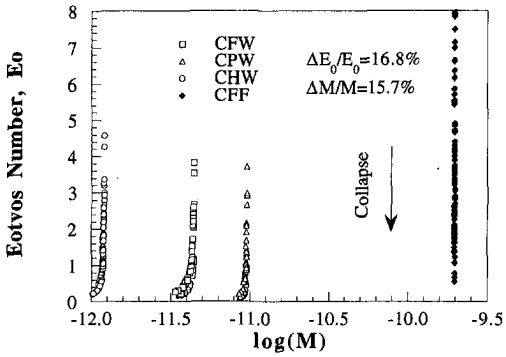

Fig. 9 Variation of the Morton number during the collapse process of bubbles condensing in miscible and immiscible liquids

during the collapse process is shown in Fig. 9 where the Eo number is plotted against the logarithm of M for the four systems. The freon/freon system is the only system to exhibit a constant M over the entire collapse process. Here the bubble is condensing in its sub-cooled liquid and the bubble density is constant.

6 Conclusions

A series of experiments of direct-contact condensation was analyzed in order to study the initial volume and the instantaneous shape of condensing bubbles. Two cases were considered: the condensation of organic vapors (freon-113, pentane and hexane) in immiscible liquid (water) and the condensation of freon-113 in miscible liquid (freon-113).

It was demonstrated that the initial volume of the condensing bubble can be reasonably predicted by employing Ruff's "two-stage model" that was originally developed for noncondensing bubbles. As can be expected, the best prediction of the model is for cases in which the condensation rate is slow relative to the rate of the bubble formation process. For high condensation rates the model is over-predicts the bubble volume.

The experiments show that the condensing bubbles undergo an oscillatory shape deformation during the collapse process. The major shape deformation occurs at the initial stages of the collapse and is a result of the bubble detachment from the orifice. The initial large amplitude oscillations decay after a few cycles as a result of the bridling effects of the viscous and the surface-tension forces. The latter increases with the decrease of the bubble radius as the collapse process proceeds. Thus, during the final collapse stages, only low amplitude oscillations can be observed, particularly for large bubbles or for low surface-tension miscible systems. However, these oscillations are a result of the wake shedding phenomenon.

While it is impossible to predict the precise shape of the condensing bubble, the present work shows that a qualitative prediction of the instantaneous bubble shape throughout the collapse process can be obtained by means of the classical "regime diagram." Furthermore, it is demonstrated that a quantitative evaluation of the instantaneous mean aspect-ratio of the bubbles can be achieved by correlations that were originally developed for constant volume bubbles at their terminal velocities.

It can be concluded that the present work provides, for the first time, tools to evaluate the initial volume and the shape of condensing bubbles. The ability to evaluate these parameters can help to improve models for predicting the condensation rate in order to appropriately design direct-contact condensers.

References

Cheremisinoff, N. P., ed., 1986, *Encyclopedia of Fluid Mechanics, Vol. 3 Gas-Liquid Flows,* Gulf Publish. Comp., Houston.

Clift, R., Grace, J. R., and Weber, M. E., 1978, *Bubbles, Drops and Particles,* Academic Press, New York.

Davidson, J. F., and Schuler, B. O. G., 1960, "Bubble Formation at an Orifice in an Inviscible Liquid," *Trans. Inst. Chem. Eng.,* Vol. 38, pp. 335–342.

Garrett, P. R., 1993, "Recent Developments in the Understanding of Foam Generation and Stability," *Chem. Eng. Science,* Vol. 48, pp. 367–392.

Grace, J. R., and Wairegi, T., 1986, "Properties and Characteristics of Drops and Bubbles," *Encyclopedia of Fluid Mechanics, Vol. 3 Gas-Liquid Flows,* N. P. Cheremisinoff, ed. Gulf Publish. Comp., Houston, pp. 44–57.

Isenberg, J., and Sideman, S., 1970, "Direct Contact Heat Transfer with Change of Phase: Bubble Condensation in Immiscible Liquids," *International Journal of Heat and Mass Transfer,* Vol. 13, pp. 997–1011.

Jacobs, H. R., and Major, B. H., 1982, "The Effect of Noncondensible Gases on Bubble Condensation in an Immiscible Liquid," ASME *Journal of Heat Transfer,* Vol. 140, pp. 487–492.

Kalman, H., Ullmann, A., and Letan, R., 1986, "Dynamics of a Condensing Bubble in Zones of Time-Dependent Velocity," *Proceedings, 8th International Heat Transfer Conference,* Vol. 4, pp. 1925–1930.

Kalman, H., and Letan, R., 1987, "Condensation of a Bubble in an Immiscible Liquid: Characteristic of the Thermal Resistance," *AIChE Symp. Series,* Vol. 83, No. 257, pp. 128–133.

Kraus, A. D., and Bar-Cohen, A., 1983, *Thermal Analysis and Control of Electronic Equipment,* Hemisphere, Washington.

Kreith, F., and Boehm, R. F., eds., 1988, *Direct-Contact Heat Transfer,* Hemisphere, Washington.

Lerner, Y., and Letan, R., 1985, "Dynamics of Condensing Bubbles: Effects of Injection Frequency," ASME paper No. 85-HT-47.

Lerner, Y., Kalman, H., and Letan, R., 1987, "Condensation of an Accelerating-Decelerating Bubble: Experimental and Phenomenological Analysts," ASME *Journal of Heat Transfer,* Vol. 109, pp. 509–517.

Letan, R., 1990, "An Immersion Cooling Unit: Condensation in a Remotely Subcooled Liquid," *Heat Transfer in Electronic and Microelectronic Equipment,* A. E. Bergles, ed., Hemisphere, Washington, pp. 521–536.

Moalem, D., Sideman, S., Orell, A., and Hetsroni, G., 1973, "Direct Contact Heat Transfer with Change of Phase: Condensation of a Bubble Train," *International Journal of Heat Mass Transfer,* Vol. 16, pp. 2305–2319.

Rabiger, N., and Vogelpohl, A., 1986, "Bubble Formation and its Movement in Newtonian and Non-Newtonian Liquids," *Encyclopedia of Fluid Mechanics, Vol. 3 Gas-Liquid Flows,* N. P. Cheremisinoff, ed., Gulf Publish. Comp., Houston, pp. 58–88.

Ruff, K., 1972, "Formation of Gas Bubbles at Nozzles with Constant Throughput," *Chem. Ing. Techn.,* Vol. 44, pp. 1360–1366.

Tsuge, H., 1986, "Hydrodynamics of Bubble Formation From Submerged Orifice," *Encyclopedia of Fluid Mechanics, Vol. 3 Gas-Liquid Flows,* N. P. Cheremisinoff, ed., Gulf Publish. Comp., Houston, pp. 191–232.

Ullmann, A., and Letan, R., 1988, "Motion of an Accelerating Droplet," ASME *Proceedings, 25th National Heat Transfer Conf.,* Vol. 2, pp. 455–460.

Ullmann, A., and Letan, R., 1989a, "Evaporation of Droplets Sprayed into an Immiscible Liquid," ASME 1989 National Heat Transfer Conf. HTD, Vol. 106, pp. 537–541.

Ullmann, A., and Letan, R., 1989b, "Effect of Noncondensibles on Condensation and Evaporation of Bubbles," ASME *Journal of Heat Transfer,* Vol. 111, pp. 1060–1067.

Wellek, R. M., Agrawal, A. K., and Skelland, A. H. P., 1966, "Shape of Liquid Drops Moving in Liquid Media," *AIChE Journal,* Vol. 12, pp. 854–862.

Wittke, D. D., and Chao, B. T., 1967, "Collapse of Vapor Bubbles With Translatory Motion," ASME *Journal of Heat Transfer,* Vol. 89, pp. 17–24.